RTO-MP-20
AC/323(HFM)TP/7

RTO-MP-20

NORTH ATLANTIC TREATY ORGANIZATION

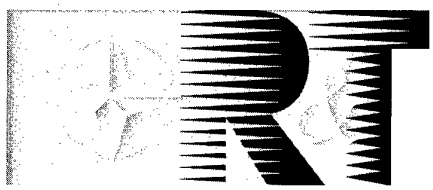

RESEARCH AND TECHNOLOGY ORGANIZATION

BP 25, 7 RUE ANCELLE, F-92201 NEUILLY-SUR-SEINE CEDEX, FRANCE

RTO MEETING PROCEEDINGS 20

Models for Aircrew Safety Assessment: Uses, Limitations and Requirements

(la Modélisation des conditions de sécurité des équipages : applications, limitations et cahiers des charges)

Papers presented at the Specialists' Meeting of the RTO Human Factors and Medicine Panel (HFM) held at Wright-Patterson Air Force Base, Ohio, USA, 26-28 October 1998.

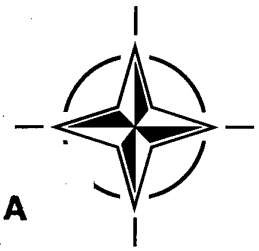

DISTRIBUTION STATEMENT A
Approved for Public Release
Distribution Unlimited

Published August 1999

Distribution and Availability on Back Cover

RTO-MP-20
AC/323(HFM)TP/7

NORTH ATLANTIC TREATY ORGANIZATION

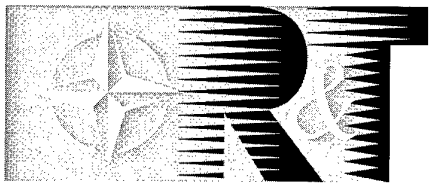

RESEARCH AND TECHNOLOGY ORGANIZATION

BP 25, 7 RUE ANCELLE, F-92201 NEUILLY-SUR-SEINE CEDEX, FRANCE

RTO MEETING PROCEEDINGS 20

Models for Aircrew Safety Assessment: Uses, Limitations and Requirements

(la Modélisation des conditions de sécurité des équipages : applications, limitations et cahiers des charges)

Papers presented at the Specialists' Meeting of the RTO Human Factors and Medicine Panel (HFM) held at Wright-Patterson Air Force Base, Ohio, USA, 26-28 October 1998.

20000110 125

The Research and Technology Organization (RTO) of NATO

RTO is the single focus in NATO for Defence Research and Technology activities. Its mission is to conduct and promote cooperative research and information exchange. The objective is to support the development and effective use of national defence research and technology and to meet the military needs of the Alliance, to maintain a technological lead, and to provide advice to NATO and national decision makers. The RTO performs its mission with the support of an extensive network of national experts. It also ensures effective coordination with other NATO bodies involved in R&T activities.

RTO reports both to the Military Committee of NATO and to the Conference of National Armament Directors. It comprises a Research and Technology Board (RTB) as the highest level of national representation and the Research and Technology Agency (RTA), a dedicated staff with its headquarters in Neuilly, near Paris, France. In order to facilitate contacts with the military users and other NATO activities, a small part of the RTA staff is located in NATO Headquarters in Brussels. The Brussels staff also coordinates RTO's cooperation with nations in Middle and Eastern Europe, to which RTO attaches particular importance especially as working together in the field of research is one of the more promising areas of initial cooperation.

The total spectrum of R&T activities is covered by 7 Panels, dealing with:

- SAS Studies, Analysis and Simulation
- SCI Systems Concepts and Integration
- SET Sensors and Electronics Technology
- IST Information Systems Technology
- AVT Applied Vehicle Technology
- HFM Human Factors and Medicine
- MSG Modelling and Simulation

These Panels are made up of national representatives as well as generally recognised 'world class' scientists. The Panels also provide a communication link to military users and other NATO bodies. RTO's scientific and technological work is carried out by Technical Teams, created for specific activities and with a specific duration. Such Technical Teams can organise workshops, symposia, field trials, lecture series and training courses. An important function of these Technical Teams is to ensure the continuity of the expert networks.

RTO builds upon earlier cooperation in defence research and technology as set-up under the Advisory Group for Aerospace Research and Development (AGARD) and the Defence Research Group (DRG). AGARD and the DRG share common roots in that they were both established at the initiative of Dr Theodore von Kármán, a leading aerospace scientist, who early on recognised the importance of scientific support for the Allied Armed Forces. RTO is capitalising on these common roots in order to provide the Alliance and the NATO nations with a strong scientific and technological basis that will guarantee a solid base for the future.

The content of this publication has been reproduced
directly from material supplied by RTO or the authors.

Printed on recycled paper

Published August 1999

Copyright © RTO/NATO 1999
All Rights Reserved

ISBN 92-837-1017-7

Printed by Canada Communication Group Inc.
(A St. Joseph Corporation Company)
45 Sacré-Cœur Blvd., Hull (Québec), Canada K1A 0S7

Models for Aircrew Safety Assessment: Uses, Limitations and Requirements

(RTO MP-20)

Executive Summary

The Human Factors and Medicine Panel (HFM) of the Research and Technology Organization (RTO) held a Specialists' Meeting on "Models for Aircrew Safety Assessment: Uses, Limitations and Requirements" at Wright-Patterson Air Force Base (WPAFB), Ohio, US, 26-28 October 1998. The Meeting was held to honour Dr Henning E. von Gierke, Director Emeritus, Human Effectiveness Directorate, Air Force Research Laboratory, WPAFB for his pioneering work in biodynamics and his extensive service to NATO/AGARD*.

Technological advances in computer speed and power have made modelling a feasible research and design tool. Computer simulations are being used extensively by safety experts to predict human physical and physiological responses, to reduce testing requirements, and to perform human safety-systems analyses. This Specialists' Meeting covered modelling of human body responses to environmental stressors, and the systems with which the body reacts for: impact, emergency escape, sustained acceleration, motion sickness, high altitude, mechanical shock, vibration, blast, extreme thermal conditions, directed energy and live fire. These studies impact on NATO aircrew safety issues in that they provide:

- new information on the extensive developments made in collecting biodynamic data for model development from animal and volunteer human testing for the past 30 years;
- further realization of the importance of good model and data-base validation and verification procedures, and the importance of standardization of recording systems and data bases to exchange data sources;
- confirmation of the significance of finite-element analysis, often when it is coupled with rigid-body modelling, for analyzing human-systems interaction during crash and other loading conditions;
- important new efforts in the human-systems integration of cardiovascular and cerebrovascular responses with the dynamics of anti-G protective hardware to sustained acceleration to address safety design issues; and
- new models and methods for describing or predicting:
  - mechanical shock that rely on biomechanical analysis rather than signal-processing techniques;
  - motion sickness that relate sensory information conflict between sensed and subjective (from past experiences) gravitational accelerations;
  - altitude decompression sickness that combine gas-bubble growth models with survival-analysis techniques;
  - impact of battlefield trauma on predicted task performance as exemplified by the Operational Requirement-based Casualty Assessment (ORCA) computer code for exposure to penetrations, blast, laser energy, and chemical, thermal and accelerative loading; and
  - body responses to vibration, radio frequency radiation, burns and blast overpressure.

With the increased emphasis on simulation and modelling in aircrew safety design, and the requirement for greater international collaboration, the recommendation is made that the RTO/HFM Panel assess the feasibility of establishing a series of biodynamics and trauma-injury data bases that would capture the relevant data available in the different aircrew environments. These data bases and any analogous pre-competitive modelling techniques, tools and ideas would conform to accepted procedures of standardization, validation and verification, and be available to all NATO nations conducting collaborative research and design.

* AGARD, the Advisory Group for Aerospace Research and Development, which merged with the NATO/DRG to form the RTO.

La modélisation des conditions de sécurité des équipages : applications, limitations et cahiers des charges

(RTO MP-20)

Synthèse

La commission des facteurs humains et médecine (HFM) de l'Organisation pour la recherche et la technologie de l'OTAN (RTO), a organisé une réunion de spécialistes sur « la modélisation des conditions de sécurité des équipages: applications, limitations et cahiers des charges » sur la base aérienne de Wright Patterson (Ohio USA), du 26 au 28 octobre 1998. Cette réunion a permis de rendre hommage au Docteur Henning E. von Gierke, Directeur émérite de la Direction des études sur l'efficacité humaine, au laboratoire de recherche de WPAFB, pour ses travaux novateurs dans le domaine de la biodynamique, et pour les nombreux services rendus à l'AGARD* dans le passé.

Les avancées technologiques en matière de vitesse et de puissance de calcul ont fait de la modélisation un outil pratique pour la recherche et la conception. Les simulations numériques sont largement utilisées par les spécialistes de la sécurité pour prévoir les réponses humaines, physiques et physiologiques, pour alléger les procédures d'essais et pour analyser des systèmes de protection individuelle.

Cette réunion de spécialistes a porté sur la modélisation des réponses du corps humain aux facteurs d'agression, ainsi que sur les systèmes avec lesquels le corps réagit en cas d'impacts, d'évacuation d'urgence, d'accélérations soutenues, de nausées liées aux mouvements, de vol à haute altitude, de chocs mécaniques, de vibrations, de souffle, de conditions thermiques extrêmes, et d'exposition à l'énergie dirigée et aux tirs réels. Ces études ont une incidence sur la sécurité des personnels militaires de l'OTAN dans la mesure où elles fournissent :

- de nouvelles informations sur les progrès considérables réalisés dans le domaine de la collecte des données biodynamiques pour le développement de modèles, basés sur les résultats d'essais effectués au cours des trente dernières années sur des animaux et des bénévoles humains;
- une nouvelle prise de conscience de l'importance des procédures de vérification et de validation pour les bases de données et les modèles, comme de la nécessité de disposer de bases de données et de systèmes d'enregistrement normalisés pour permettre un meilleur échange entre sources de données;
- la confirmation de l'intérêt de la méthode d'analyse des éléments finis, surtout lorsqu'elle est associée à la modélisation de corps rigides, pour l'analyse des interactions homme-système en cas d'écrasement ou de surcharge;
- d'importants efforts nouveaux visant l'intégration homme-système des réponses cardiovasculaires et cérébrovasculaires dans la dynamique des équipements de protection contre les forces d'accélération soutenues, afin de résoudre les problèmes de conception des équipements de protection individuelle et,
- de nouveaux modèles et de nouvelles méthodes pour la description et la prévision :
  - de chocs mécaniques; ces modèles et méthodes sont issus d'analyses biomécaniques plutôt que de techniques de traitement du signal;
  - de nausées liées aux mouvements, qui décrivent la perception d'informations sensorielles contradictoires relatives à des accélérations dues à la pesanteur, qu'elles soient senties ou subjectives (précédemment vécues)
  - du mal de décompression en altitude, qui associe des modèles d'accroissement des bulles de gaz aux techniques d'analyse de la survie;
  - des informations concernant l'impact des traumatismes subis sur le champ de bataille sur les prévisions en matière d'exécution des tâches, comme dans le cas du code de calcul de la méthode d'estimation du nombre des victimes par rapport aux besoins opérationnels (ORCA), relatif à l'exposition aux pénétrations, au souffle, à l'énergie laser, aux charges chimiques, thermiques et liées aux accélérations et les réponses du corps humain aux vibrations, aux rayonnements RF, aux brûlures et à la surpression due au souffle.

En raison de l'importance accrue accordée à la modélisation et à la simulation dans la conception liée à la sécurité des équipages, et étant donné que le besoin d'une plus grande collaboration internationale se fait sentir, il est recommandé à la commission RTO/HFM d'évaluer la réalisation d'une série de bases de données biodynamiques et de traumas/lésions, pour saisir les données pertinentes existantes dans les différents environnements opérationnels. Ces bases de données, ainsi que tout autre outil, technique ou concept concurrentiel analogue, se conformeraient aux procédures de vérification, validation et normalisation agréées, et seraient mises à la disposition de l'ensemble des pays membres de l'OTAN engagés dans la recherche et la conception collaboratives.

* NATO/AGARD, le Groupe consultatif pour la recherche et les réalisations aérospatiales, qui a fusionné avec le NATO/GRD, pour former la RTO.

Contents

	Page
Executive Summary	iii
Synthèse	iv
Preface	viii
Human Factors and Medicine Panel	ix
Acknowledgements	x

	Reference
Technical Evaluation Report by J.P. Landolt, I. Kaleps and L.A. Obergefell	T
Tribute to Dr. Henning E. von Gierke by J.W. Brinkley	TR
KEYNOTE ADDRESS 1	
Physical Models: The Good, the Bad, the Ugly by C.P. Hatsell	K1
SESSION I: MODELLING HUMAN RESPONSES TO IMPACT AND EJECTION ACCELERATION	
The AFRL Biodynamics Data Bank and Modeling Applications by J.R. Buhrman	1
Comparison of Vertebral Strength Properties of Anthropometrically Similar Male and Female using Quantitative Computed Tomography by M. DiCuccio, G. Paskoff, P. Whitley and M. Schweitzer	2
Modes of Human Head/Neck Response to Vertical Impact by M. Ziejewski, L. Obergefell, C. Perry and B. Anderson	3
A PC-Based Head-Spine Model by J.B. Bomar, Jr. and D.J. Pancratz	4
Neck Performance of Human Substitutes in Frontal Impact Direction by J.S.H.M. Wismans, A.J. van den Kroonenberg, M.L.C. Hoofman and M.J. van der Horst	5
Validation of the MADYMO Hybrid II and Hybrid III 50th-Percentile Models in Vertical Impacts by J.E. Manning and R. Happee	6
Strength of the Female Upper Extremity by J.A. Pellettiere, S.M. Duma, C.R. Bass and J.R. Crandall	7

SESSION II: MODELLING HUMAN-SYSTEMS INTERACTION DURING EJECTION AND IMPACT

Military Application of Biodynamics Models 8
by L. Obergefell, A. Rizer and D. Ma

Continued Development of an Integrated EASY5/ACESII-ATB Model for Ejection Seat Simulation 9
by D. Ma, L.A. Obergefell, L.C. Rogers and A.L. Rizer

Head Protection against Windblast for Crew Escape 10
by P.C. Chan, J.H-Y. Yu and J.H. Stuhmiller

The Use of Computer Finite Element Models of Humans and Crash Test Dummies for High Acceleration and Impact Biomechanics Studies 11
by K.H. Digges and P.G. Bedewi

Forces and Deformed Configurations of an Airbag during Inflation and Impact 12
by X.J.R. Avula, I. Kaleps and P. Mysore

MADYMO Validation of Side Facing Sofa Sled Tests 13
by A.M.G.L. Teulings, V. Gowdy, J.S.H.M. Wismans and B. Aljundi

KEYNOTE ADDRESS 2

Injury Measurements and Criteria K2
by K.H. Digges

SESSION III: SUSTAINED GZ ACCELERATION: CARDIOVASCULAR AND CEREBROVASCULAR RESPONSE MODELLING

A Model of Cardiovascular Performance during Sustained Acceleration 14
by C. Walsh, S. Cirovic and W.D. Fraser

Effect of High +Gz Accelerations on the Left Ventricle 15
by K. Behdinan, B. Tabarrok and W.D. Fraser

A Model of Cerebral Blood Flow during Sustained Acceleration 16
by S. Cirovic, C. Walsh and W.D. Fraser

Paper 17 withdrawn

Linear and Nonlinear Models of the Physiological Responses to Negative-to-Positive Gz Transitions 18
by A. Kapps and W.D. Fraser

SESSION IV: SUSTAINED GZ ACCELERATION: MODELLING HUMAN RESPONSES TO ANTI-GZ PROTECTION STRATEGIES

Hierarchical Modeling of the Baroreceptor Response to Gz Acceleration and Anti-Gz Protective Equipment 19
by W.D. Fraser

Modeling of the Physiological Responses to Non-linear G-suit and Positive Pressure Breathing Schedules 20
by W.D. Fraser, Z. Lu, V. Askari and A. Kapps

A Physiological Data Analysis Toolbox for the Analysis of Acceleration Data 21
by W.D. Fraser, V. Askari, Z. Lu and A. Kapps

Model Derived Timing Requirements for Gz Protection Methods 22
by D.B. Rogers

Mathematical Models for Predicting Human Tolerance to Sustained Acceleration 23
by R.R. Burton

KEYNOTE ADDRESS 3

Model Validation K3
by I. Kaleps

SESSION V: MODELLING HUMAN RESPONSES TO OTHER ADVERSE FLIGHT ENVIRONMENTS

A Biomechanical Approach to Evaluating the Health Effects of Repeated Mechanical Shocks 24
by J.B. Morrison, D.G. Robinson, J.J. Nicol, G. Roddan, S.H. Martin, M.J-N. Springer, B.J. Cameron and J.P. Albano

The Development of a Lumped-Parameter Model for Simulating the Vibration Response of the Human Body 25
by S.D. Smith

Modelling Motion Sickness 26
by J.E. Bos and W. Bles

Altitude Decompression Sickness (DCS) Risk Assessment Computer (ADRAC) 27
by L.J. Petropoulos, N. Kannan and A.A. Pilmanis

SESSION VI: MODELLING HUMAN RESPONSES TO HARSH CONDITIONS IN AIR ENVIRONMENTS

New Methodology for the Assessment of Battlefield Insults and Injuries on the Performance of Army, Navy, and Air Force Military Tasks 28
by D.N. Neades, J.T. Klopcic and E.G. Davis

Dosimetry Models used to Determine the Bioeffects of Directed Energy Exposure 29
by W.D. Hurt and P.A. Mason

A Submodel for Combat Casualty Assessment of Ocular Injury from Lasers 30
by R.E. Miller, II and B. Carver

Burn Prediction Using BURNSIM and Clothing Models 31
by F.S. Knox, D.B. Reynolds, A. Conklin and C.E. Perry

Thermal Output of Pyrotechnic Compositions and Evaluation of Skin Burns 32
by B. Lawton, R. Merrifield and R.K. Wharton

Biomechanical Modeling of Injury from Blast Overpressure 33
by J.H. Stuhmiller, P.J. Masiello, K.H. Ho, M.A. Mayorga, N. Lawless and G. Argyros

Preface

This Specialists' Meeting reviewed a variety of models applicable to the field of aerospace physiology and aircrew safety. These included lumped-parameter, rigid-body, finite-element, statistical, physiologic, and empirical models. These models described the human-body responses to environmental stressors, and the systems with which the body interacts. Also considered were the data bases and tolerance criteria used with these models. Special presentations focussed on the validations, limitations, and appropriate applications of different models.

The following topics were addressed:

- modelling human responses to impact and ejection accelerations:
  - biodynamic data-base development of material properties and mechanical characteristics of human tissue,
  - head/neck/spine responses and models,
  - finite-element model of upper extremity for assessing arm-airbag interaction, and
  - validation of the MADYMO mathematical-dummy model against Hybrid II and Hybrid III test dummies;
- modelling human-systems interaction during ejection and impact:
  - combining wind-tunnel data with the ATB occupant model to evaluate ejection-seat/crew-member interactions,
  - head protection against windblast, and
  - using airbags and optimal seating strategies to reduce injuries;
- modelling human-systems responses to sustained Gz acceleration for:
  - cardiovascular and cerebrovascular functions,
  - baroreceptor (pressure sense organ) function, and
  - anti-G protection strategies; and
- modelling human responses to harsh air environments in regard to:
  - mechanical shock based on human-response data,
  - whole-body vibration,
  - motion sickness as a conflict between subjective (from mental stores of past experiences) and sensed gravitational vectors,
  - altitude decompression sickness from gas-bubble and survival-analysis considerations, and
  - battlefield trauma (penetration, blast, laser, chemical, thermal and accelerative loading) by an Operational Requirements-based Casualty Assessment (ORCA) computer code in terms of predicted task performance.

Human Factors and Medicine Panel

Chairman:

Dr M.C. WALKER
Director, Centre for Human Sciences
F138 Building - Room 204
DERA
Farnborough, Hants GU14 6TD
United Kingdom

TECHNICAL PROGRAMME COMMITTEE
Chairmen

Dr I. KALEPS
AFRL/HESA
2800 Q Street, Bldg 824
Wright-Patterson AFB, OH 45433-7901
USA

Dr R.R. BURTON
AFRL/HEP
2509 Kennedy Circle
Brooks AFB, TX 78235-5118
USA

Members

Dr J.P. LANDOLT
Defence and Civil Institute of
Environmental Medicine
1133 Sheppard Avenue West
PO Box 2000
Toronto, ON M3M 3B9 CA

Dr J.S.H.M. WISMANS
TNO Road-Vehicles Research Institute
PO Box 6033
2600 JA Delft
The Netherlands

Mr W.D. FRASER
Defence and Civil Institute of
Environmental Medicine
1133 Sheppard Avenue West
PO Box 2000
Toronto, ON M3M 3B9 CA

Dr L.A. OBERGEFELL
AFRL/HESA
2800 Q Street, Bldg 824
Wright-Patterson AFB, OH 45433-7901
USA

HOST NATION COORDINATOR
Dr I. KALEPS

LOCAL COORDINATOR
Dr L.A. OBERGEFELL

PANEL EXECUTIVE

Mail from Europe and Canada

Dr C. WIENTJES
RTA/NATO
BP 25
7, rue Ancelle
92201 Neuilly sur Seine Cedex, France

Mail from USA

RTA/NATO/HFM
PSC 116
APO AE 09777

Tel. (33) 1 55 61 22 60/62 - Telex: 610176F
Telefax: (33) 1 55 61 22 99/98 - Email: wientjesc@rta.nato.int

Acknowledgements

The Technical Programme Committee conveys its appreciation to the following people and companies:

- For sponsoring social events:
  - Biodynamics Research Corporation, San Antonio, TX;
  - DynCorp, Dayton, OH;
  - First Technology Safety Systems, Plymouth, MI;
  - JAYCOR, San Diego, CA;
  - SEI-Ashville, Ashville, NC;
  - TNO-MADYMO North America, Northville, MI;
  - Veridian, San Antonio, TX.
- For other functions:
  - Ms Ellen Moore, Veridian, for meeting arrangements and registration;
  - Ms Jean Smart, AFRL/HEPA, for technical program coordination;
  - TSgt Shawn Brown, AFRL/HEPA, for audio-visual support;
  - Lt. Omar Viken, AFRL/HE, emcee for dinner reception;
  - Mrs Nancy Wisteard, DCIEM, for administrative support.

TECHNICAL EVALUATION REPORT

by

Jack P. Landolt, PhD
Defence and Civil Institute of Environmental Medicine
Toronto, Ontario, Canada M3M 3B9

and

Ints Kaleps, PhD
Louise A. Obergefell, PhD
Human Effectiveness Directorate
Air Force Research Laboratory
Wright-Patterson Air Force Base
Ohio 45433-7947, U.S.A.

1. INTRODUCTION

The Human Factors and Medicine (HFM) Panel of the NATO Research & Technology Organization (RTO) held a Specialists' Meeting on "Models for Aircrew Safety Assessment: Uses, Limitations and Requirements" at the Hope Hotel and Conference Center, Wright-Patterson Air Force Base (WPAFB) (near Dayton, Ohio), USA, 26 - 28 October 1998. The Meeting was held to address a topic of importance to the Panel, and to honour Dr Henning E. von Gierke, Director Emeritus, Human Effectiveness Directorate (HE), Air Force Research Laboratory (AFRL), WPAFB for his pioneering work in biodynamics and his extensive service to NATO/AGARD,* the antecedent organization to RTO addressing issues in aerospace research and development. Thirty-five papers, including three keynote addresses, were given from the NATO countries of Canada, The Netherlands, United Kingdom, and United States. These are included in this Meeting Proceedings, as is a paper by Mr James W. Brinkley, Director, AFRL/HE paying tribute to Dr von Gierke. There were 70 registrants for the Meeting including representatives from the NATO Partnership-for-Peace countries Lithuania and Poland, and Japan.

2. THEME

Significant advances have been made in modelling human physical and physiological responses to extreme environments. Additionally, technological advances in computer speed and power have made modelling a feasible research and design tool. The military and civilian aviation and land-vehicle communities are using computer simulations extensively to predict human physical and physiological responses, to reduce testing requirements, to rapidly design improved protective systems, and to perform human safety- systems analyses. These models are revolutionizing the way physiologists, mathematicians, and engineers assess aircrew safety. Furthermore, appropriately-validated models will render the collection of volunteer human and animal test data less and less necessary in the future.

3. PURPOSE AND SCOPE

The purpose of this Specialists' Meeting was to review a variety of models that will address current and future issues in aerospace physiology and aircrew safety.

The scope was broad covering the modelling of human responses to impact, emergency escape, sustained acceleration, mechanical shock, vibration, motion sickness, high altitude, blast, extreme thermal conditions, directed energy, live fire, and other hazardous conditions. A variety of models were considered, including lumped-parameter, rigid-body, finite-element, statistical, physiological, and empirical models. The models described the human body response to environmental stressors, and the systems with which the body interacts. Also considered were the databases and tolerance criteria used with these models. Special presentations - the keynote addresses - focussed on the validations, limitations, and appropriate applications of different models.

The participants included military and civilian experts in mathematical and computer modelling, biomechanics, biomedical and other engineering disciplines, radiology, physiology and other life sciences, physics, and human factors. Presentations were invited from industry, defence

* AGARD is the acronym for Advisory Group for Aerospace Research and Development

and other governmental research laboratories, universities, and health care centres.

4. SYMPOSIUM PROGRAM

Each day, the technical programme commenced with a keynote address that discussed in general terms different aspects of models, and criteria development and usage. These presentations were:

a. Keynote Address 1 - Physical Models: The Good, The Bad, The Ugly, by Dr Charles Hatsell, Biodynamic Research Corporation, San Antonio, TX, US;

b. Keynote Address 2 - Injury Measurements and Criteria, by Dr Kennerly H. Digges, National Crash Analysis Center, The George Washington University, Ashburn, VA, US; and

c. Keynote Address 3 - Model Validation, by Dr Ints Kaleps, AFRL/HE, OH, US.

The remaining papers were arranged in six Sessions as follows:

a. Session I - Modelling Human Responses to Impact and Ejection Accelerations
Chairmen: Dr J.S.H.M. Wismans, NE and Dr L.A. Obergefell, US

Seven papers described quantitative databases, and mathematical and physical models of human responses to impact and ejection.

b. Session II - Modelling Human-Systems Interaction during Ejection and Impact
Chairmen: Dr L.A. Obergefell, US and Dr J.S.H.M. Wismans, NE

Six papers addressed the issue of modelling human-systems interaction during escape and impact conditions.

c. Session III - Sustained Gz Acceleration: Cardiovascular and Cerebrovascular Response Modelling
Chairmen: Dr R.R. Burton, US and Mr W.D. Fraser, CA

Four papers discussed the subject of modelling systemic system responses to Gz.

d. Session IV - Sustained Gz Acceleration: Modelling Human Responses to Anti-Gz Protection Strategies
Chairmen: Mr W.D. Fraser, CA and Dr R.R. Burton, US

Five papers were given on modelling responses to anti-G suits, positive pressure breathing (PBG), and anti-G straining maneuvres.

e. Session V - Modelling Human Responses to Other Adverse Flight Environments
Chairmen: Dr J.P. Landolt, CA and Dr I. Kaleps, US
Papers on modelling responses to mechanical shock, vibration, motion sickness, and altitude decompression sickness (DCS) were given.

f. Session VI - Modelling Human Responses to Harsh Conditions in Air Environments
Chairmen: Dr I. Kaleps, US and Dr J.P. Landolt, CA

One paper described a new joint US Army, Navy, and Air Force model – Operational Requirement-based Casualty Assessment (ORCA) - that assesses the impact of trauma on performance; two others discussed sub-models for predicting injury that port into ORCA. The remaining three papers dealt with modelling the bioeffects of directed energy exposure, skin burns, and blast overpressure.

Additionally, there was a half-day technical tour of relevant biodynamic, bioacoustic and alternative-control-technology facilities at the AFRL/HE.

5. TECHNICAL EVALUATION

5.1 Keynote Addresses

Keynote Address 1 considered the different physical models in terms of their being good, bad or 'ugly'. Good models make predictions that are close to experimental measurements and provide important information regarding a process or system. Models are bad if they fail to account for all of the physical phenomena required to describe an outcome. So-called ugly models may not be technically incorrect, but they fail to provide any insight into a process or about a system.

In addition to their predictive and explanatory capabilities, good physical models also differ from bad models in that they are:

- simple in that they require the least number of equations, lines of software, or components necessary to provide a convincing answer,
- clear in that they can be understood and used by any knowlegeable person familiar with the problem,
- objective in that they are independent of human bias, and
- tractable in that the cost of carrying out the computation is affordable

(Casti, J.L. Would-be Worlds. New York: Wiley, 1997).

Keynote Address 2 discussed the types of injury measurements obtained from frontal- and side-impact dummies, and the associated injury criteria that have been specified by the US Department of Transportation in safety

standards from crash testing of motor vehicles incorporating these dummies. Injury criteria based on frontal-impact dummies concern measurements of head and chest accelerations, neck and lower legs forces and moments, chest deflections, and femur loads. Measurements for criteria from side-impact dummies are confined to accelerations of the ribs, spine, and pelvis. Criteria based on these measurements are set so that the risk of serious injury is no more than 30%. In general, injury criteria for frontal impacts are well established but still evolving; those of side impacts require considerable refinement and much more research.

Keynote Address 3 addressed the issue of validating predictive models, i.e., models that are based on fundamental mechanisms for which response properties can be measured. The level of validation considered is dependent on the ultimate application of the model. Applications may involve:

- better insight into physical phenomena,
- reconstruction of physical events,
- use as a design tool, and
- systems simulation.

Considerations in model design to facilitate model validation include:

- model complexity, e.g., degrees of freedom,
- completeness of representation,
- accuracy of observation of model variables, and
- range of validity.

Model credibility is dependent on two separate and distinct tests:

- verification process which establishes that a model (or simulation) accurately depicts what the designer intended and that the requirements are correctly implemented in software, and
- validation process which compares the degree to which a model (or simulation) represents the real world.

Full credibility is achieved only when both tests are taken into consideration.

In validating a model, the motto should be: keep it simple, but accurate. Only the relevant response characteristics should be considered. For example, only the essential degrees of freedom, variables that can be measured, and parameters that can be obtained from direct measurements should be used. Ambiguity and unnecessary complexity will do much to undermine model validity and acceptance.

5.2 Modelling Human Responses to Impact and Ejection Accelerations

Modelling and simulation are becoming increasingly important operations in the conception, design, research, development, test and evaluation of crashworthy seats, restraints, and escape systems. Critical to the success of these operations is the readily-available, massive amounts of biodynamic data that have been collected from volunteer human and animal testing for the past 30 years. These data have provided the design basis for anthropomorphic human analogues - computer models and mechanical dummies - that are used widely today for assessing body response and injury risk to mechanical forces.

Perhaps, it is fitting that this Specialists' Meeting should start off with a paper that discusses a topic that is central to Dr von Gierke's concerns (Buhrman (1)). It was at a symposium in 1977 that he proposed the notion of a national (US) biodynamics data bank (Aviat. Space Environ. Med. 49(1): 347, 1978). More specifically, Dr von Gierke stated that: *"... it appears essential that the material properties and mechanical characteristics fed into the mathematical models be based on all the relevant data available, and not on a few test results from an individual investigator. In view of the time, cost, and risk involved in obtaining this broad spectrum of experimental data, I think consideration should be given to the establishment of some kind of centralized data bank that would store: a) directly measured mechanical properties of human tissue, b) mechanical properties of tissues of animals most frequently used in biodynamic research, c) human injury/rupture information derived from accident analysis, d) human tissue/organ response characteristics derived from volunteer biodynamic tests, e) human body dynamic response data from volunteer tests, and f) animal body subcritical and critical response data. This data bank should be fed by all laboratories working in this field and its data should be generally available. In this way, model parameters and inputs could be compared to the best and, above all, to all types of response data available."*

Such a national biodynamics data bank never materialized. Buhrman's paper, however, provides an overview of the current status regarding the evolution and contents of the Biodynamics Data Bank (BDB) that was initiated in 1984 at WPAFB for the development and validation of impact simulation and injury models.

The BDB includes acceleration, force and motion data from a large number of tests conducted on man-rated facilities at WPAFB, including those from both horizontal and vertical motion devices. Such information as the time histories and peak biodynamic responses from impact tests, anthropometric measurements from test subjects, and bibliographic information from relevant references are included in the BDB. These data and pertinent summary information from past biodynamic test programs reside in the BDB through a Windows NT® server which will allow users elsewhere to seamlessly access information according to their own requirements. A test index enables the

accessing of all impact test parameters, including type of test facility, data acquisition system, seat fixture, restraint system, helmet, gender anthropometry, and input acceleration profile. Currently, the slow-motion videos, photographs and pertinent printed material from the impact tests are being digitized for future entry into the BDB.

Using quantitative computed tomography, Diccucio et al. (2) are collecting data from vertebral bones of anthropometrically-similar males and females. The vertebral geometry, bone density, end-plate cortical bone thickness, and trabecular bone architecture of a number of spinal vertebrae are being examined. Gender differences in these parameters may help explain differences in vertebral load bearing capacities. The authors intend to use the ensuing results in a multivariant regression equation that would predict vertebral injury risk during impact or ejection. Only preliminary results are given in their paper. Indications are that mean trabecular bone mineral densities in C2 and C5 vertebrae are significantly higher in females than in males. A gender comparison indicated that only the end-plate cross-sectional area in the L4 vertebrate was significantly higher in males; trabecular bone mineral density, area x bone mineral density, and predicted compressive strength were not statistically significantly different.

Neck loading from wearing helmet-mounted displays and night-vision goggles increases the chance of neck injury during ejection. To better understand the mechanisms involved and define the criteria for allowable helmet mass properties, Ziejewski and colleagues (3) studied the modes of head-neck response in females to vertical impacts. Acceleration levels (10 G peak) comparable to those experienced in the catapult phase of ACESII seat ejections were used. The helmet mass properties were varied to simulate those in current helmet-mounted systems. Five modes of head-neck response were identified: two representing forward neck and head rotation, two representing forward neck rotation and rearward head rotation, and one representing no significant neck or head rotation. Two experimental measurements, the initial linear (forward head) acceleration at the mouthpiece and the (head) pitch of the mouthpiece relative to a shoulder marker, uniquely defined the head-neck response. Other factors such as initial head-neck position, anthropometry, helmet type, its mass and centre of gravity, and acceleration level should also be investigated for their contributions in defining the modes of response.

Bomar and Pancratz (4) commenced their presentation with a historical overview of a head-spine model, developed by the USAF in the late 1970s, that found limited application because of the intractability of the code in which it was written. The US AFRL has had the model re-coded and improved for solution on a Personal Computer under a Windows® environment. The model is comprised of six types of elements as follows:

- rigid bodies representing the head, spine, pelvis, rib cage and viscera having mass properties and capable of six degrees of freedom in motion;
- springs to represent ligaments, vertebral articular facets and abdominal visceral elements, that produce a cubic force to strain and a damping force to rate of strain;
- cervical muscles that produce a force proportional to strain and the concentration of an 'activator molecule' governing muscle behaviour;
- hydrodynamic elements employing fluid-filled pentahedrons for modelling the articular facets;
- beams having two end-plates for modelling intervertebral discs attached to adjacent vertebrae or ribs; and
- environmental elements consisting of springs as restraints, elastic planes as contact surfaces, and motion constraints.

The authors described the numerical methods employed for solving the underlying equations of motion. They raised concerns regarding validation of all complex multi-body biomechanical models. One application of the model is for simulating spinal loads resulting from ejection-seat accelerations. To a question from the audience regarding choice of mathematical models, Bomar noted that their head-spine model estimates the internal forces and motions within the human at the anatomic level, whereas surrogates such as the MAthematical DYnamic MOdel (MADYMO) and Articulated Total Body (ATB) programs can simulate gross effects only.

(Details on the mathematical dummies MADYMO and ATB, and (see below) the mechanical dummies Hybrid II and Hybrid III, THOR (TAD-50M), and EUROSID-1 are given in AGARD-AR-330: Anthropomorphic Dummies for Crash and Escape System Testing.)

Meeting neck biofidelity performance requirements in current motor vehicle safety standards for frontal impacts is achieved by using the Hybrid III dummy in crash testing. The Hybrid III neck is used also in dummies for aerospace applications. Wismans et al. (5) reported on work conducted at TNO Road-Vehicles Research Institute, The Netherlands, that compared neck performance of the Hybrid III with that of the new frontal impact dummy, THOR, and a neck model developed for incorporation in MADYMO. The authors demonstrated that the neck of the new THOR dummy, which was developed by GESAC as an improved dummy for the US National Highway Traffic Safety Administration, was more biofidelic than the Hybrid III neck. Moreover, the mathematical neck model in

MADYMO, which incorporated cervical vertebrae, ligaments, and active neck musculature, was even more representative of human responses during frontal impacts than the mechanical neck models. Interestingly, the authors showed that acceleration-based responses from dummy sensors are poor discriminators of neck biofidelity.

In order to improve seats and other safety components, the military and the aviation industry require a better understanding of occupant reaction to vertical crash conditions. The Hybrid II and Hybrid III anthropomorphic test dummies have been designed and used extensively for analyzing motion kinematics and injury potential in frontal-impact automotive crashes. Manning and Happee (6) collected militarily-relevant, drop test data from 50th-percentile Hybrid II and Hybrid III male dummies secured by five-point harnesses to UH-60 (Black Hawk) helicopter crew seats. Results from the tests were incorporated into a MADYMO program that simulated the Hybrid dummies. Comparisons were made between the mechanical and mathematical dummies of acceleration data from the head, chest and pelvis; neck and lumbar loads and moments; and shoulder belt and lap belt loads. After accounting for any data acquisition errors that may have been introduced during the tests, the results showed a good correlation for acceleration and compressive loading. Some differences were noted for the lumbar shear force and bending moment, and the belt loads. The authors concluded that the MADYMO Hybrid model provided an effective tool for evaluating vertical crash conditions.

Pellettiere and colleagues (7) developed a finite-element model of the forearm of a 5th-percentile female for the purpose of assessing bone strength. The geometry of the model was based on computed tomographic scans of the radius and ulna bones. Subsequently, a transversely-isotropic material model, developed at the University of Virginia to provide the proper mechanical response of bone, was applied to the geometric model. This combination was then incorporated into an LS-DYNA3D, finite-element computer program. Simulations using the model for predicting bone behaviour during impact compared favourably to experimental test responses. This model should find application in a range of simulations including those for predicting injury in arm-airbag interactions. Additional drop-test results obtained from cadavers - 55-60 years of age - demonstrated dynamic bending strengths of 128 Nm for the humerus, and 58 Nm for the forearm of the 5th-percentile female. It was suggested by the authors that these results could be used as injury criteria in airbag studies.

5.3 Modelling Human-Systems Interaction during Ejection and Impact

Increasingly, multi-body and finite-element models are being used to represent human-systems interaction in crash and escape-system simulations. Multi-body (rigid bodies connected by joints) models are particularly useful for simulating the spatial dynamics and interactions of complex kinematical structures such as the human body with mechanical systems such as vehicle interiors or ejection seats. Finite-element models allow for the study of local stresses and strains during impact; however, in many instances, validated databases of structural and material properties of body components are not available yet. As these models improve, and databases are validated and standardized, simulations will become more realistic thereby reducing the need for human subject testing to assess aircrew safety to impact.

Obergefell and colleagues (8) described the use of biodynamic modelling in the AFRL for resolving different military equipment and personnel safety issues. In short, validated models are used to provide rapid evaluations when other test methods are too expensive or unfeasible. The ATB model, a multi-body occupant model, is used extensively to determine crew motion and contact with equipment and surfaces during systems design and test procedures. Here, modelling is used to evaluate human-systems interactions, to develop safe design criteria, and to predict crew response to test situations. Moreover, when unusual test results are given in employing new dummies, biodynamic modelling is applied to sort out discrepancies and to extend test measurement capabilities. Simulations of tests are also used to determine which equipment modifications will likely improve conditions or to narrow future test requirements. The ATB model is constantly updated from, and validated against, human and dummy impact-test results of realistic military applications.

Ma and colleagues (9) described recent model developments for assessing ejection-seat motion, occupant biodynamic response and seat-occupant separation. An ejection-seat model, EASY5/ACESII, was coupled with the ATB model, to simulate the dynamic interaction between the seat and human being during the early phases of the ejection process. The two models interacted synergistically. Wind tunnel data from the EASY5/ACESII model were used to provide the total aerodynamic forces on the occupant in the ejection seat. Then the ATB model calculated the component forces and torques on the individual segments of the seat occupant. When these components were subtracted from the total forces and torques, the force components acting directly on the seat were obtained. When an occupant-seat separation signal was generated in the EASY5/ACESII model to initiate restraint-harness release, it was immediately transferred to the ATB model, and the appropriate aerodynamic forces and torques were then applied only to the separated occupant. At the same time, the recovery parachute force from the EASY5/ACESII model was sent to the ATB

model, where the combined forces from gravity, recovery parachute, and aerodynamics separated the occupant from the ejection seat. Test validation studies demonstrated the utility of the model in successfully predicting the main features of ejection-seat motion and occupant dynamic response.

Ejection from the next generation of high-speed aircraft may significantly increase the risk of head/neck injury from windblast. Chan, Yu and Stuhmiller (10) provided details on the use of wind/water tunnel and sled test data, and biomechanical modelling for determining head protection against windblast in aircrew during seat ejections. Results indicated that the windblast load on the head interacts strongly with the inertial dynamics of an ejection-seat/test-dummy combination during aircrew escape. Inertially, yaw conditions, in addition to adding a significant load to the side of the head, continuously increased the lift forces on the head. Various protective 'wind flow stagnation' strategies were tested and modelled. Some subjected the head to unwanted oscillations; others significantly increased the head side forces. Test results and simulations employing computational fluid dynamics showed that a protective strategy using an 'open-brim' concept would reduce the lift forces and provide for smaller side-force increases. This paper clearly demonstrated the power of using combinations of tests, simulations and analyses for developing protective strategies in complex human-systems interactions.

High-power computer modelling employing finite-element analysis is being used extensively for evaluating and improving the protective environment in hazardous situations. Digges and Bedewi (11) have indicated that finite-element modelling is the most advanced tool for simulating an impact or high-acceleration event. Advantages of the finite-element method for simulating human-vehicle interaction in a crash environment over other methods include:

- having advanced algorithms of contact surfaces for determining structural deformations;
- having good material models, such as those for fabrics, elasto-plastics, etc., for simulating different structures and assessing crash dynamics;
- the ability to apply dissimilar material properties to different elements in the model;
- the ability to collect a large variety of data, including those of stress, strain, displacement, velocity, acceleration, energy, etc. anywhere in the model; and
- not being restricted to limitations imposed by other means for investigating protective environments; e.g., the lack of total biofidelity in many modern test dummies inhibits total analysis in many instances.

Digges and Bedewi described a finite-element model of a vehicle occupant that is based on a validated computer representation of a Hybrid III test dummy. Components of the human such as the arms, legs, head/neck, etc. can be continuously upgraded in a biofidelic sense, and the changes made may then be transitioned back into the full-body dummy model. This gives a Hybrid III computer model that becomes more human-like as improvements are made. The authors cited the example of the development of an improved lower-limb model embodying muscle activation which, when incorporated in the Hybrid III computer model, enabled previously-missing injury mechanisms to be discovered. Applications for this model would include:

- the design of protective gear for preventing trauma in athletes;
- improved automobile crashworthiness for the prevention of occupant injuries during impact;
- improved military aircraft crashworthiness for pilot protection during escape and impact; and
- improved civil aircraft crashworthiness for civilian occupant protection during non-catastrophic airline emergencies.

In situations where the occupant is seated in an out-of-position orientation in a vehicle, the pattern of the airbag unfolding during deployment could be a critical safety issue. Avula, Kaleps and Mysore (12) used the finite-element model, LS-DYNA3D, to investigate fabric density, bag elasticity, input gas temperature and extent of venting during the evolution of an unfolding airbag impacting with a solid sphere. The influence of these parameters on the contact during impact was significant. Lowering the material density resulted in a higher velocity of the unfolding airbag, which increased the sphere rebound velocity. Lowering the fabric elasticity resulted in an increased contact time and a higher sphere rebound velocity. At low input gas temperature, the airbag volume remained low, contact time with the sphere was long, and the sphere had a very low rebound velocity. The acceleration and rebound velocity of the sphere were the highest when there was no venting and the least for maximal vent area. These results have important implications for designing optimal occupant safety systems in survivable crashes of fixed- and rotary-wing aircrafts. (Research on incorporating airbags in aircraft is being studied seriously by the aerospace industry. The use of airbags and other inflated restraint systems for head injury protection in aircraft crashes was the subject of Papers #21 & #22 in AGARD-CP-597: Impact Head Injury: Responses, Mechanisms, Tolerance, Treatment and Countermeasures.)

Issues relating to the US Federal Aviation Administration (FAA) regulations for occupant protection in transport aircraft are being addressed by industry and

government agencies. In this regard, the FAA has conducted tests using the automotive side-impact dummy, EUROSID-1, for assessing the potential for injury of side-facing sofas in aircraft. Assessed were the effects of thorax impact on an interior rigid wall with and without padding, body-to-body contact, and upper-torso restraint loads. Teulings and colleagues (13) have developed and validated a MADYMO computer model that predicted the test results quite well. In particular, both the model and the tests demonstrated the benefit of wall padding in reducing injury. The MADYMO simulations should enable the assessment of additional factors, such as occupant-size effects and restraint-system geometry, more cost effectively than would be the case with test sleds.

5.4 Sustained Gz Acceleration: Cardiovascular and Cerebrovascular Response Modelling

The loss of aircrew and aircraft through G-induced loss of consciousness (G-LOC) continuous to be a serious problem for the NATO air forces. Further studies into the physiological effects of this phenomenon are required. In particular, good models need to be developed to better understand human tolerance to acceleration. For example, recent work involving negative-to-positive Gz transitions - the so-called push-pull maneuvre - during high-performance aircraft flights would indicate that, perhaps, human tolerance to acceleration may have been overestimated. This is supported by two recent papers which suggest that the push-pull effect represents a significant source of G-LOC risk for accidents in high performance aircraft in air combat training and during operational missions (Aviat. Space Environ. Med. 69(11): 1083 & 1104, 1998). Four papers described models for exploring the effect of sustained Gz acceleration, including the push-pull transition, on cardiovascular and cerebrovascular performance.

Walsh, Cirovic and Fraser (14) described a mathematical model of cardiovascular function to +Gz in which physiological reflexes were neglected. A closed-loop vascular network of uniform, flexible tube segments was used that incorporated lumped parameter models of the heart chambers. Valves were embedded in the segments representing veins, and in the entrance and exit chambers of the heart. The model had to incorporate at least one valve in the vena cava just below the heart; otherwise, the simulated blood would drain into the inferior systemic veins at physiologically-excessive speeds. Muscular contractions of the heart were simulated by a time-varying elastance model. Segmental blood flow was described in terms of blood wave propagation by a pair of first-order partial differential equations. The equations were solved numerically in a finite difference scheme. Results showed cardiac output decreasing and increasing, respectively, as Gz increased and decreased. Central arterial pressure, the factor that governs the generation of G-LOC, did not follow physiological principles, accompanying instead the rise and fall of the cardiac output. Cardiac output returned to normal during high Gz when the lower body and abdomen were both protected through G-suit inflation. Protection was significantly reduced by lower body coverage alone.

The effect of high acceleration on the left ventricle is most severe when it is directed along the body z-axis. During some flight maneuvres, aircrew are subjected to +Gz levels as high as 10 G. In a previous communication at a NATO symposium, Tabarrok and colleagues described a three-dimensional, finite-element model of the left ventricle that was reconstructed from medical images of the human heart to study stress-strain relationships to such high accelerations (see Paper #20 in AGARD-CP-516). In the current paper, Behdinan, Tabarrok, and Fraser (15) have developed a new model of the left ventricle that is comprised of 3300 finite elements. Although a recent NATO/AGARD Working Group established that no pathologic cardiac changes were evident from a retrospective echocardiographic study of pilots repeatedly exposed to high, sustained Gz acceleration (AGARD-AR-351), investigations with this model may further confirm these results. Alternatively, the model may give new insights into the types of conditions required for inducing deleterious stress-strain in, and gross distortion of, the left ventricle that could jeopardize subsequent normal heart function in pilots flying high performance aircraft. In that regard, preliminary results with the model showed that, under high accelerations, the heart elongates and greater stresses are obtained at the aortic end of the heart than at the apex of the left ventricle.

A good knowledge of cerebral blood flow helps to understand the mechanisms subserving impaired vision or G-LOC during excessive exposure to Gz. Cirovic, Walsh and Fraser (16) designed a model which demonstrated that a G-induced reduction of blood flow to the brain is primarily caused by venous collapse resulting from an increased vascular resistance in the extracranial veins. Accordingly, detailed jugular veins were incorporated in the model. Cerebrospinal fluid prevents the intracranial vessels from collapsing during Gz so blood flow is preserved therein. Therefore, this model included simplified intracranial vessels, which were represented by a vascular resistance that was independent of Gz. The extracranial arteries were accounted for by introducing a hydrostatic pressure drop from the heart to the head. Autoregulation of cerebral vascular resistance to changing cerebral perfusion pressures also was incorporated. The jugular veins were modelled using one-dimensional equations of fluid dynamics and a nonlinear relation between transmural pressure and local vessel cross-sectional area was introduced. Gz was varied from -5 to

+10 G which encompasses the high-G environment of current high performance aircraft. The model reproduced the cerebral blood flow drop with increasing +Gz, while autoregulation was ineffective at higher +Gz because of the dominance of the extracranial venous resistance. The model predicted an increase in cerebral blood flow for elevations of central venous and arterial blood pressures. This was attributed to the fact that an elevated central venous pressure maintained extracranial venous patency by preventing venous collapse.

Paper #17 was to have described a model of the physiological mechanisms subserving cerebral ischemia during increasing +Gz. However, this paper was not presented.

Kapps and Fraser (18) used a combination of linear and nonlinear models to describe experimental physiological responses (eye-level blood pressure vs. Gz) for the push-pull effect. In experimental data, a sub-group of subjects had physiological responses that were highly nonlinear. The remaining responses could be described by a low-order, linear transfer function to both push-pull and +Gz maneuvres. Interindividual variations were pronounced in subjects demonstrating nonlinear behaviour. Additional data will be collected to validate these results.

5.5 Sustained Gz Acceleration: Modelling Human Responses to Anti-Gz Protection Strategies

Extended coverage anti-G suits combined with positive pressure breathing (PBG) have significantly enhanced the protection of aircrew to high +Gz (and high altitude). Current life-support systems, however, do not adequately protect aircrew during complex push-pull maneuvres. Moreover, they fail to adapt to physiological changes in aircrew during a mission; in part, this is due to the inability of protective systems to adapt to the body's blood pressure regulating system, the aortic and carotic baroreceptors (body-pressure sense organs). Current mathematical models of baroreceptor function do not allow for representation of the extreme changes in blood pressure and blood distribution that follows the application of very high +Gz. Neither do they address the extreme pressure shifts generated by the anti-G life-support equipment. Using the Caltech software package GENESIS (GEneral NEural SImulation System), Fraser (19) is developing hierarchical models of baroreceptor function that will include neuronal interaction within the baroregulation centres of the brain, the transient dynamics of pressure-induced stretch in the baroreceptors, the effects of local pressure gradients within the baroreceptors, and the dynamic response to Gz of each of these subsystems. These are relevant factors that affect the body's response to Gz and the efficacy of life- support equipment in preventing G-LOC. In the presentation at this Specialists' Meeting, only preliminary work was demonstrated.

Current pressurization schedules produced by mechanical valves for anti-G protection appear as linear functions of the acceleration. These are not optimized for Gz protection because the physiological responses to acceleration and the true pressure schedules delivered are nonlinear due to time delays and the reflex actions of the cardiovascular system. Fraser and colleagues (20) have developed models describing physiological responses to nonlinear, G-suit pressure and PBG schedules which will be used as aids in the development of new Gz-protection strategies. Microprocessor-based G valves and regulators were used to generate nonlinear pressure schedules. The blood-pressure responses at heart level to three pressure categories were obtained for:

- G-suit pressure without PBG;
- G-suit and PBG pressures controlled by a single valve, with PBG proportional to G-suit pressure; and
- G-suit and PBG pressures controlled by separate valves.

In some instances different ratios of G-suit to PBG pressures were applied to determine the point at which blood-pressure gain was maximized. The responses to step, ramp, pulse, sinusoidal and random inputs were determined. Based on the analysis completed, it would appear that a single-zero, double-pole model adequately describes blood-pressure response to G-suit pressure with and without PBG at +1Gz and, possibly, at higher Gz levels. Intersubject variations in response to G-suit pressures were common and intrasubject response variations were noted at different times during an experiment. These findings might impede the development of subject-specific Gz-protection strategies.

Fraser and colleagues (21) also tried a nontraditional systems-identification approach to model the cardiovascular response to nonlinear, anti-G-suit and PBG pressure schedules for both +Gz and push-pull transitions. The goal was to develop an expert system - a Physiological Data Analysis Toolbox - that would enable those with little experience in analysis to work through a set of experiments. At another level, the purpose of the work was to provide a method of analysis for the development of customized pressure schedules for anti-G pilot protection, in general, and for push-pull countermeasures, in particular. Recorded parameters were chosen as the heart-level arterial blood pressure, the electrocardiogram (ECG), the respiratory rate, and the G-suit and PBG pressures. The Toolbox integrated the results for these measures through statistical, trend, higher-order spectrum, and fuzzy-logic analyses of the data. Using this Toolbox, the correlation and trend dependencies established between the highly nonlinear pressure schedules and the physiological responses provided important information for screening data and the choice of method of analysis for modelling

protective systems in the high-G environment.

Rogers (22) described a model that focused on the dynamic response of the cardiovascular system to Gz, including the effect from the push-pull maneuvre. This model employed a second-order transfer function to account for the blood-pressure response to changes in Gz and G transition rates. It provided a descriptive picture of how the heart responds to the G environment, which should give some insight into strategies for improving G-LOC protection. By way of example, this model suggested that the choice of acceptable centrifuge profiles has not been optimized to describe the cardiovascular system most effectively under G conditions.

Burton (23) had earlier published a mathematical model based on hydrostatic principles that accurately predicted G-level tolerance with and without the use of G-protection methods such as the anti-G suit, PBG, and the anti-G straining maneuvre (isometric muscle contraction) (Aviat. Space Environ. Med. 57(8): 733, 1986). This model was validated and found to be extremely practical; it has been used by engineers in cockpit design for predicting G-level tolerance to various personal protective measures, and by lecturers in teaching high-G physiology. With the availability of further physiological data, the model has now been refined to include the ability to assess tolerances to G-duration (to account for the additional contributions of anaerobic capacity, muscular strength, and muscle blood flow to the evolution of G-induced fatigue), and to improve G-level assessments (by including venous return for predicting both blackout and G-LOC conditions). With these modifications, the effectiveness of protective systems up to 12 G can be predicted accurately. In conducting high-G research and testing, one is always concerned with the risk to the safety of the subject. Accordingly, good practical, validated models such as this one proposed by Burton will increasingly reduce the need for human volunteer participation in future G studies, and insure their safety when testing is required.

5.6 Modelling Human Responses to Other Adverse Flight Environments

Papers on promising models in mechanical shock, vibration, motion sickness and altitude decompression sickness (DCS) were also invited to this Specialists' Meeting.

Repeated mechanical shocks long have been associated with low back pain and degenerative disorders of the spine. Methods of evaluating mechanical-shock exposure have relied on signal-processing techniques rather than on human-response data or biomechanical analyses. Morrison and colleagues (24) described a new method, called the Health Hazard Assessment (HHA), for evaluating the effects of repeated mechanical shocks on the health of vehicle operators. The HHA model formulates the risk of operator injury (output) in terms of vehicle-seat acceleration (input). There are four stages that are combined to produce the HHA model:

- Dynamic response models are used to predict the three-dimensional accelerations of the lumbar spine as measured at the occupant seat.
- Lumbar compressive forces at the L4/5 vertebral joint to shock inputs at the seat are estimated from peak lumbar accelerations derived from a biomechanical analysis.
- A dose model based on fatigue-failure tissue properties, and the compressive strength of the L4/5 vertebral joint calculate the effect of repeated compressive loading.
- Injury risk is then determined from the accumulated compressive dose, the tissue fatigue life, the variance from the vertebral-joint-strength data, and the cumulative probability of failure.

The HHA model predicts the risk of injury from a single exposure or from the cumulative shock effects of a lifetime of repeated mechanical shocks. This new model has shown promising results; however, it will require further rigorous testing before it is generally accepted by safety experts.

Vehicular whole-body vibration has long been associated with health problems, performance degradation, discomfort, and fatigue. Smith (25) conducted a series of tests, using small females and large males, to collect sensor (biodynamic) data of critical human body parts to vertical vibrations. Responses obtained from the data, using the driving-point impedance and transmissibility techniques both of which are characterized by input/output response ratios as functions of frequency, were subsequently compared with responses obtained from a five degree-of-freedom, lumped-parameter model. This model simulated the resonance behaviour of the human body when it was positioned in a rigid seat with and without the benefit of seat cushions. The model was quite effective in simulating many of the rigid-seat responses, particularly for the male. In evaluating aircraft seat cushions, the model showed the benefits of using such cushions, and some of the differences in vibration response between the male and female. The study also demonstrated the need for additional modifications to the model, e.g., improved leg representation, possible inclusion of other body parts, better coupling of parts, etc.

The quest for a sound model that will predict motion-sickness incidence satisfactorily has long been a goal of aerospace scientists. Bos and Bles (26) have developed a motion-sickness model wherein the organs of balance

(vestibular organs) together with control-systems concepts play an essential role. There are three important aspects to the model:

- From multisensory input information, the brain resolves a so-called sensed vertical vector representing the magnitude and direction of the sensed acceleration of gravity.
- At the same time, the brain uses an optimal-estimation strategy to create a subjective (anticipated) vertical that is based on past experiences.
- Motion sickness occurs when there is a conflict between sensed and subjective verticals.

The current paper described the model when it is restricted to resolving inputs solely from the vestibular system, i.e., otolithic (gravity and linear-acceleration sensing) and semicircular canal (angular-acceleration sensing) inputs. The true vertical is resolved by the brain through low-pass filtering of otolithic information, and rotation information is provided by the semicircular canals. The model predicts that the incidence of motion sickness for pure vertical transitions is greatest at a frequency of 0.16 Hz, a value observed experimentally. The model is expected to be responsive to other inputs, e.g., visual, proprioceptive, and even cognitive information, and anticipated to accurately predict the incidence of sea, air, simulator and other analogous sicknesses. A comment from the audience inferred that there was, in fact, visual perception involved during the vertical transitions in the example cited by the authors that was inadvertently omitted in the analysis.

Decompression sickness is thought to occur from the formation and growth of bubbles resulting from dissolved, tissue nitrogen gas coming out of solution with a large and rapid reduction in environmental pressure. Weakness, numbness, pain, paralysis, and even death can occur with DCS. Typically though, the incidence of altitude DCS is in the range of 25 - 30%; symptoms are usually mild, and mostly limited to joint pain which is cleared on return to ground level. The most significant variables that influence the occurrence of DCS risk include the pressure and exposure time at altitude, the preoxygenation time, and the level of exercise undertaken. Taking these factors into account, Petropoulos, Kannan, and Pilmanis (27) have developed an Altitude DCS Risk Assessment (ADRAC) computer that determines on-site estimates of the risk of DCS in real time for altitudes from 18,000 to 40,000 feet (5.5 to 12.2 km). The computational algorithm in ADRAC is based on a multi-component gas-bubble growth model and survival-analysis techniques for predicting DCS risk. Altitude-exposure profiles tested with ADRAC were within +/-5% error of observed values taken from an AFRL data bank of over 2000 altitude exposures.

5.7 Modelling Human Responses to Harsh Conditions in Air Environments

The final set of papers at this Specialists' Meeting addressed issues on modelling human responses to harsh conditions that would apply to all military services, not just those in the aviation environment.

Neades, Klopcic, and Davis (28) described a new methodology for assessing the impact of battlefield trauma on performance of military tasks. The methodology employs an Operational Requirement-based Casualty Assessment (ORCA) model that determines the anti-personnel effects associated with various weapon-induced threats. The ORCA computer code enables calculation of the anatomical damage resulting from exposure to kinetic energy (fragments), thermal, chemical, directed energy (lasers), blast, and accelerative loading threats. The effect of a computed injury is characterized by the predicted impairment of each of 24 human elemental capabilities (e.g., vision, cognition, and physical strength). ORCA then determines the effect of such damage on individual task performance. Thus, post-injury CAPABILITY IMPAIRMENT is compared to CAPABILITY REQUIREMENT associated with the individual's military job, task, or mission to determine if (s)he is an OPERATIONAL CASUALTY. Code outputs for discrete exposures (e.g., single fragment) include a physical damage summary, details of any deleterious processes (e.g., blood loss), and an indication of the remaining performance capability (incapacitation) as a function of time following trauma (immediate, 30 seconds, 5 minutes, 1 hour, 24 hours, and 3 days). ORCA can produce results to both single and multiple exposure conditions.

Hurt and Mason (29) described models for determining the energy absorbed by the human body when exposed to radio-frequency directed energy (dosimetry models). Of particular importance is the Specific Absorption Rate (SAR) which is manifested as heat energy during directed energy exposure. This can be measured using whole-body calorimetric or other thermometric methods. Accurate SAR values and distributions for the full-sized human analog are now possible using such pertinent biological data together with iterative numerical methods, such as the finite-difference time-domain method, that require powerful computer processing capabilities. The ultimate goal of this work should be the establishment or updating of radio-frequency safety standards using combinations of anatomical and mathematical models that are based on noninvasive measurements and do not involve human-subject exposure.

Miller and Carver (30) discussed a sub-model of ORCA designed to predict the probability of ocular injury from laser insults. Sub-model input parameters included:

- laser type, wavelength, energy density, and insult duration;
- ocular injury assessment in regard to corneal damage/photokeratitis, flashblindness, and retinal damage;
- relevant body components, i.e., right and left eyes and retinas; and
- elemental capability degradation in regard to visual acuity (including colour vision), night vision, field of view, and binocular vision (including ocular motility).

Examples were given illustrating the applicability of the sub-model when integrated into the ORCA code.

Burns resulting from fires or other thermal sources represent a significant threat to aircrew safety. Models that predict burns are important because there is an increasing reluctance to use animals to assess burn trauma in humans. Moreover, burn preventive techniques such as the use of protective clothing and improved vehicle design require good models to accurately predict and assess burn injury. Two papers discussed the issue at this Specialists' Meeting.

Knox and colleagues (31) developed BURNSIM, an interactive model employing a heat-conduction equation, for predicting burns, that is based on the work of several earlier investigators including that of Henriques (Arch. Path. 43(5): 489, 1947). They indicated that BURNSIM, which is being incorporated into ORCA, predicts with reasonable accuracy the heat transferred through clothing when the initial conditions and thermal conditions are adequately defined. The model also has found utility in assessing burn hazards from rocket exhaust during side-by-side ejections, aerothermal heating during pilot ejection at supersonic speeds, aircraft fires, and other thermal threats.

Lawton and colleagues (32) presented a method for accurately predicting first-, second-, and third-degree skin burns from conductive, convective, and high- and low-temperature radiation sources. Subject to certain allowances, Henriques' original theory was sufficient to describe all of these skin burns. The computer model used to determine burn damage was based on a one-dimensional, transient, heat-conduction equation. Thermal data collected from fireballs produced by ignition of pyrotechnic compositions were evaluated by this model. This burn damage function related heat input (skin temperature or heat dose), for different burn depths, to the time during and after exposure to a heat source. BURNSIM provided similar information.

Blast overpressure on the body caused by explosives or weapon impulse noise can rapidly collapse human air-bearing organs causing injuries ranging from isolated pathologies with no physiological effects to those having more critical consequences involving organ rupture and death. The US Army Medical Research and Materiel Command uses lethality and injury data from animals to correlate with the pressure-duration characteristics of free-field blasts. However, these correlations become meaningless in a reverberant environment such as that experienced when weapons are fired in an enclosure, or a portion of the blast energy is deflected back to the individual firing the weapon. Stuhmiller et al. (33) have developed a thoracic-injury, finite-element model that provides a realistic biomechanical basis for thorax motion under reverberant conditions. Moreover, by choosing tissue material properties judiciously, the model effectively correlates calculated internal stresses resulting from such blast loading with observed lung injury. This work is being considered as a new exposure standard for lung injury.

6. CONCLUSIONS AND RECOMMENDATIONS

This meeting dealt with the modelling of human responses and human-systems interactions to a variety of hazardous conditions in air environments.

There have been significant advances made in modelling human physical and physiological responses to deleterious aircrew stresses, and in modelling the interaction of aircrew with the mechanical systems upon which hazardous conditions are imposed. To a great extent these advances are due to the following:

- the large collection of animal and volunteer human test data taken over the past 30 years of subcritical material properties of relevant biological tissues, and biomechanical responses,
- the significant collection of injury tolerance data extracted from accident reconstruction and analysis, and controlled animal and/or cadaver tests over the past 30 years,
- the development of sophisticated biodynamic test facilities, many of them man-rated, for collecting biodynamic response data,
- the development of a wide variety of sensors having improved frequency responses, some of which are highly miniaturized, for rapid and unencumbered data collection,
- the inordinate cost reductions and advances in computer speed and power for data acquisition, data analysis and model development,
- the wide variety of models developed, particularly the progress made in finite-element analysis, for analyzing and modelling human responses, and

- the corresponding evolution in the understanding and modelling of the aerodynamic effects of normal and hazardous flight conditions affecting human-systems interactions.

Because of the extensive developments made in designing appropriate, validated, human biodynamic models, the requirement for the collection of animal and volunteer human test data will likely be reduced in the future.

Notwithstanding the important advances made in model development, many realistic representations of human physiology and cognition under different aviation stresses in simulated environments are still missing and will require more human and animal testing. Some examples may be cited in support of this position:

- Validated models of the non-linear dynamic stresses and strains of muscles, brain and other biological tissues during impact are missing. These could contribute substantially to the development of more reliable injury criteria, thereby enabling improved crashworthiness designs to be developed. Similarly, as demonstrated by Lawton, Knox, Hurt, Miller and their colleagues at this meeting (29 - 32), the highly nonlinear nature of extreme thermal conditions and directed energy make it difficult to develop predictive models of human-interaction phenomena.
- Although the behaviour of the cardiovascular and cerebrovascular systems, and the dynamics of anti-G protective hardware to sustained acceleration have been modelled quite effectively, as Fraser and his colleagues have demonstrated at this meeting (14 - 16), the integrative nature of these human-systems interactions is severely lacking though essential to adequately address design issues.

There is much hope that with increasing computer speed and power, finite-element analysis will progress significantly and become more prevalent in modelling human-systems interactions. Finite-element modelling has been used to model stresses and deformations in realistic ways; however, more exacting biomaterial properties must be obtained before this method can be fully exploited. The use of finite-element analysis, coupled with rigid-body modelling, has shown great promise in analyzing human dynamics under the loading conditions of crash and ejection accelerations. As exemplified during this meeting, the MADYMO computer program (6, 13), developed by TNO Road-Vehicles Research Institute in The Netherlands, effectively combines both finite-element and rigid-body (multi-body) structures to allow simultaneous simulation of gross body motion and deformation.

Computer models of the airframe, the cockpit including the ejection seat, and other critical aircraft subsystems are increasingly being used by decision-makers to reconcile design aims and to cut design costs in the procurement process. It is important that aircrew safety models be an integral part of this process. Moreover, such subsystem safety models employing validated biodynamic data bases will have to interoperate with these other aircraft subsystem models effectively if safe design conditions are to be optimized in a virtual prototype environment. The experiences of Ma and colleagues (9) in their presentation on evaluating ejection-seat/crew interaction are an example of such a simulation. Using the ATB model, developed by the AFRL/WPAFB, in combination with wind-tunnel test data, Ma and colleagues successfully demonstrated the key features of seat motion and crew-member responses during critical seat operation stages in ejection.

In the future, simulation within NATO defence organizations will combine models and analytical tools (i.e., constructive simulations) with pilot-in-the-loop synthetic environments (i.e., virtual simulations) that may or may not involve motion-based features. On the constructive side, scenario generators will provide the physical environment necessary to characterize aircraft flight maneuvres and threat conditions, and provide the conditions necessary for addressing and resolving critical human factors and human protection countermeasures. On the virtual side, by immersing the human in the synthetic environment, real safety systems and human performance may be assessed as to function, fit, capability, etc. Playing back and forth between constructive and virtual simulations should enable various options to be assessed and provide the performance tradeoffs required for improving safety system features, thereby reducing the need for subsequent live test requirements.

Inevitably, all NATO air forces will depend on constructive simulations for planning functions such as concept development, design, test and evaluation, and mission rehearsal. All of these functions impact on aircrew safety. However, current scenario generators representing automated personnel conducting operations in constructive simulations do not adequately depict human attributes and the human reactions in dealing with different combat stressors. Modelling the effects of fatigue, workload, combat injuries and other stressors on decision making in constructive simulations in a way that is usable by planners is a difficult though important challenge that should not go unheeded by model builders. Furthermore, such models should be time dependent in order that human performance deterioration with continuing stress is taken into account. Moreover, individual differences in the physiological and psychological composition of aircrew must also be a component of such models if aircrew safety is not to be compromised.

Because of the advancements made in digital technologies, simulation environments in the near future, employing either or both constructive and virtual simulations, will communicate over local- or wide-area networks. These systems will allow dissimilar models from NATO and other worldwide research and industrial locations to interact with each other on various data bases to form common simulations. This will facilitate the dispersion and use of aircrew safety models in design and test processes, but it will also require greater standardization of digital data recording systems and data bases to exchange data sources. Maintaining good model and data base validation and verification procedures will take on added importance.

Advances in simulation and distributed interactive networking provide opportunities for increased collaboration among NATO scientists and engineers working in widely different fields and locations to reach common goals in model and data base developments. Such databases and any analogous pre-competitive modelling techniques, tools and ideas developed should be generally available to all, and conform to accepted procedures of standardization, validation, and verification. An example of such a collaborative effort might include the setting up of data bases of trauma injuries and the development of combat-casualty submodels that port into models such as the ORCA software described at this meeting by Neades and colleagues (28).

As indicated earlier, Dr von Gierke, at a symposium in 1977, spoke to the need for a national biodynamics data bank that would store the essential material properties and mechanical characteristics for model development. This data bank would have been centralized, and fed into and shared by all laboratories working in the field. Perhaps, with the increased emphasis on simulation and modelling in the design process and the requirement for greater national and international collaboration, it is time to extend Dr von Gierke's proposal and strive for a series of international biodynamics and trauma-injury data bases within NATO defence research laboratories.

These data bases would capture the relevant data available in the different aircrew environments, e.g., data collected on impact/ejection/sustained accelerations, altitude, etc. in the different countries, and these would be readily available to all NATO nations conducting collaborative research and design. In particular, data from previous hazardous human experiments should be included in these data bases before these are lost, or rendered useless through aging recording media (film, paper, etc.) or because of incompatibilities between new versus old data transfer systems. It is unlikely that such data will ever be collected again because of the stringent (though necessary) institutional requirements now being mandated to protect human subjects during experimentation. Perhaps the HFM Panel of the NATO/RTO could take the lead in assessing the feasibility of establishing such a series of databases. Perhaps also, the HFM Panel could take the initiative in developing a strategy for a better sharing of pre-competitive modelling techniques, tools and ideas for aircrew safety.

7. ACKNOWLEDGEMENTS

We thank Mrs N. Wisteard for preparation of this manuscript and general administrative assistance.

DCIEM No. SL 1999-012

TRIBUTE TO DR. HENNING E. VON GIERKE

James W. Brinkley, SES
Director
Human Effectiveness Directorate
Air Force Research Laboratory
Wright-Patterson Air Force Base, Ohio, USA

It is my distinct honor to describe the distinguished career and highlight a few of the many outstanding scientific contributions of my good friend and mentor, Dr. Henning von Gierke. Although some of these accomplishments are well known to you, I will provide some additional insights and discuss his accomplishments from my personal perspective.

Dr. von Gierke's background and education are most interesting. Starting at the beginning, Henning was born in 1917 in Karlsruhe, Germany. His family, particularly his father, influenced him to become a scientist. His father was a well-known German pathologist who discovered a metabolic liver disorder, now called "von Gierke's disease." His father and his grandfather, who also was a well-known scientist, both taught at universities. So Henning was born into a "scientific family;" his interest in science and education were an integral part of his upbringing.

Henning earned his undergraduate degree in electrical engineering from the Technical University at Karlsruhe, Germany in 1943. After his graduation, he worked as a research assistant at the Institute for Theoretical Electrical Engineering and Communications Technique. He received his doctorate degree in Communications Engineering and Acoustics at the Technical University in 1944 and continued to work at the university as a scientist and academician until 1947.

Figure 1 – Dr. Hans Oestreicher, Dr. Henning von Gierke, Dr. Ernst Franke, and Dr. Wolf von Wittern

In 1947, Henning came to the United States as part of a program known as "Operation Paperclip." The program was designed to enhance American aviation science and technology research programs after World War II. Sixteen German scientists and technologists joined the Aeromedical Laboratory here at Wright-Patterson Air Force Base during this period.

Other scientists that came to the Aeromedical Laboratory with Henning included Drs. Hans Oestreicher, Ernst Franke, and Wolf von Wittern. Each of these four young scientists, shown in Figure 1, came to the Aeromedical Laboratory to pursue research in the area of bioacoustics.

These young men initially were housed in military barracks in an area that is now part of Wright State University. After a short time they moved into their first house. Their rather "modest" quarters are shown in Figure 2. They also shared the same means of transportation, also seen in the figure.

Henning's early work in the Aeromedical Laboratory focused on the effects of high-intensity sound on biological systems. With the advent of aircraft jet engines, the Air Force was concerned about the potentially harmful effects of sound and ultrasound on pilots and ground crews. In the course of this pioneering work, Henning developed an early conceptual model of all of the elements of the acoustic energy problem as well as their interactions. Since its publication, it has been used worldwide to understand how the mechanical energy of sound and ultrasound is transmitted through body tissue and how the

Figure 2 – Early home and automobile

Papers presented at the RTO HFM Specialists' Meeting on "Models for Aircrew Safety Assessment: Uses, Limitations and Requirements", held in Ohio, USA, 26-28 October 1998, and published in RTO MP-20.

energy affects various tissue and organs within the body. Henning's ability to understand and describe a theoretic basis for biodynamic interactions was, in my opinion, the foundation for his greatness in the fields of bioacoustics and biodynamics.

During this same period, the Air Force was exploring the feasibility of supersonic flight. Tests conducted with the X-1 and X-2 experimental supersonic aircraft demonstrated potentially hazardous noise and severe vibration problems that could both adversely affect aircraft crew as well as communities near Air Force bases and test ranges.

Most of you have seen popular movies that depicted some of the problems that were encountered during the early years of supersonic flight. Problems included severe aircraft buffeting, reversal of the effects of flight control surfaces, and unwanted flight control inputs from the pilot in reaction to the aircraft vibrations, which could lead to complete loss of flight control. The last problem was not well depicted in these movies. Unwanted flight control inputs have been referred to as a biomechanical feed through problem or as the problem of pilot-induced oscillations. It is a condition where the vibrations of the aircraft are transmitted through the body of the pilot into the aircraft controls. These motions then become unwanted control inputs that often act to exaggerate the motion of the aircraft.

The solution of these serious problems required a monumental effort on the part of aircraft designers and the scientists in the Aeromedical Laboratory. In many respects, the problem of defining the human capability to withstand and operate within these adverse flight environments became the key to permitting man to operate beyond the speed of sound. Most of the problems that were being encountered could not be completely eliminated. Aircraft designers were faced with cost and weight constraints. So, the problem became one of determining how much the pilot could withstand and still be an effective aircraft operator and decision-maker.

Henning became the leader of the scientific efforts within the Aeromedical Laboratory to define the human capabilities and limitations within hazardous noise and vibration environments. These efforts encompassed the study of the physical and physiological response to acoustical and vibration stresses.

In 1956, Henning's responsibilities expanded, and he became the director of the Biodynamics and Bionics Division of the Aeromedical Laboratory. In this capacity, his responsibilities in noise and vibration research expanded to include the effects of blast and transient acceleration as well.

As Henning progressed from a bench-level scientist to a director of a division, he greatly expanded his vision of the type of research that would be required to meet the Air Force's requirements. He developed a more global viewpoint and a sound theoretical foundation. Additionally, he defined the facilities and methods that would be required to provide answers to the questions that designers would face in developing advanced air and space systems. Much of the conceptual work that Henning accomplished for this purpose is reflected in his publications from about 1958 onward.

I first met Henning in about 1960, when he was preparing a lecture series that later became the foundation for his chapter on "The Effects of Shock and Vibration on Man" in the Shock and Vibration Handbook. I was working with Dr. Bob Headley to explore short-duration acceleration problems associated with emergency escape from high-speed aircraft and during space vehicle landing impact. We were assigned to a different division of the Aeromedical Laboratory that was investigating the feasibility of encapsulated emergency escape systems and very high-altitude bailout.

If you have read books such as Thomas Wolfe's *The Right Stuff*, or have seen the movie version, you know that the problems of supersonic flight frequently resulted in severe pilot injury during emergency escape or the loss of the pilot's life during a crash. At that time, it was commonly believed that the open ejection seat would not be able to provide safe escape during supersonic ejection. The first pilot to eject above Mach one and live, a test pilot by the name of George Smith, was so severely injured by the aerodynamic deceleration and windblast forces that his survival after ejection could only be called a miracle. Fortunately, he landed in water near a boat and was quickly rescued.

In view of this evidence, new supersonic aircraft that were being developed, such as the F-108 fighter, and the XB-70 and B-58 bombers, were to be equipped with ejection seats that encapsulated the pilot prior to ejection. More advanced supersonic systems, such as the F-111 fighter/bomber, used escape systems that would eject its crew encapsulated within the aircraft cockpit. The encapsulation concept provided outstanding windblast protection for the occupant at high airspeeds and dynamic pressures. However, these systems presented several, potentially serious hazards during their operation. The primary common hazard that we focused on was the landing phase. The impact accelerations could be very severe. The landing acceleration profiles were also quite varied in magnitude, duration, and rate of onset. The exact nature of the impact profiles depended upon the landing impact velocity, direction, and type of impact attenuator that was used.

During our experimentation, we discovered that the current acceleration limits published in the aircraft design handbooks were inadequate to handle the varied impact conditions and the relatively short-stroke impact attenuator designs that appeared feasible. These existing limits had been developed to control the design of ejection catapults and the aerodynamic deceleration of the ejection seats. The limits specified human tolerance to short-duration impact in terms of peak g and rate of onset. However our experiments with volunteers were demonstrating that the rate of onset limits were not the absolute limits implied by the published limits. We were routinely exceeding the limits by several factors. We were also demonstrating that for very short-duration impacts, velocity change was a more meaningful limit criterion.

Henning provided us with sound, physics-based insights and guided us to the work of others such as Sigfried Ruff, who had proposed a more theoretically based set of acceleration limit criteria for emergency escape systems.

Our work also had another aspect that paralleled the novel, *The Right Stuff*. We were, likewise, conducting research for NASA to define the design criteria for the emergency landing system for the Project Mercury capsule. As you may recall, the capsule was equipped with a small tower with rockets that would pull the capsule away from the main booster rocket in case of an emergency during liftoff. You probably also remember that the launch rocket, the ATLAS Missile, frequently exploded during liftoff. Therefore, it was critical that we define the accelerations that would be tolerable during emergency ejection and landing impact. The understanding we gained from Henning's physics-based insights allowed us to explore the Project Mercury landing impact conditions with more confidence. In these experiments we were able to demonstrate that very short-stroke impact attenuators constructed of 8-inch aluminum honeycomb columns could provide impact protection for subjects in a semi-supine couch at up to 30 feet per second impact velocities.

Soon after our experiments for NASA's Project Mercury were completed, NASA asked us to begin studies to define the landing impact criteria for a new vehicle, the command module for Project Apollo. Vice President Johnson had decided that he wanted the command module to land in west Texas rather than be recovered from the ocean like the Project Mercury capsule. Although this may seem to you to be a politically motivated venture, it also had a practical payoff. Launching a fleet to recover space vehicles is a very expensive operation. Recovering the module after a ground landing would be much less expensive.

To attack this problem, a small tiger team of individuals from different parts of the Aeromedical Laboratory was assembled. The commander of our Laboratory gave us the highest priority and we were able to begin experiments using a new impact facility within Henning's division. In a very short time we began to explore impact vector directions and rates of onset that had not been explored with volunteer subjects.

At this time, many of us within the Aeromedical Laboratory became excited about President Kennedy's call to place a man on the moon before the end of the decade. I was soon offered a position at NASA, at the new space center in Houston. However, I would end up turning this position down in order to have the opportunity to work for Henning.

I was scheduled to complete the arrangements for my transfer to NASA during a trip that our team was making to NASA to describe the progress of our experiments. During our meeting with the NASA project office, I heard Henning and another Aeromedical Laboratory scientist, Dr. Neville Clarke, speak. They clearly stood out as unparalleled leaders in the field of biodynamics. I decided then, that if I was to achieve my technical goals, I must work under their brilliant leadership and mentoring. I have never regretted my decision.

Within less than a year of that meeting, our laboratory was reorganized; Henning became responsible for all biodynamic research and applications. And, by the way, we were not able to prove that landing in west Texas was feasible within the command module design constraints. However, we did go on to demonstrate the safety of the Apollo module water-landing impact. We also demonstrated the safety of the retro-rocket landing of the lunar module.

I shall never forget the day Henning and I jointly signed the letter confirming to NASA that the command module landing system and the lunar landing system were safe for the mission to the moon.

Within the first year or so of working for Henning, I became very aware of his compelling vision for a biodynamics center of excellence. He periodically enlisted me in his efforts to describe the facilities required to comprehensively explore the human's response to mechanical forces. Each of the vibration and impact facilities was an essential part of his theoretically based vision of the work that was needed to meet the national needs.

I learned of the breadth of the biodynamics research being conducted within the division. In every case, the strong theoretical foundation that had been laid out by Henning and his colleagues formed the basis of all research projects.

I also recognized that there were strong forces at work to deter his plans for a center of excellence. Problems ranged from funding limitations to competing technical agendas and the ever-present accusations of duplication of efforts with our sister Services. Nevertheless, Henning was persistent, and usually patient, in his efforts to create his envisioned center of excellence. His accomplishments and contributions to the Air Force and to our nation stand as evidence of his success in achieving his very ambitious vision!

Henning's legacy includes the development of models and supporting data for noise exposure standards and noise protection that are used worldwide. With John Cole, he led the development of land-use planning models; these models still are in use today to plan our air bases and test ranges. Additionally, the work that he initiated to study speech and speech perception in noise environments continues to be pioneering.

As a consultant to the Environmental Protection Agency, Henning assisted in preparing the biomedical foundations for the Noise Control Act of 1972. He chaired the working group, which prepared the "Guidelines for the Preparation of Environmental Impact Statements with Respect to Noise," issued by the National Academy of Sciences in 1977.

Henning's leadership in the area of human vibration exposure and vibration protection also is most impressive; it has provided the basis for the majority of vibration standards in use today. One of Henning's key strategies for success in the field of biodynamics has been his recognition that publication of a technical report or journal article is an inadequate stopping point; one must "press on" to assure that the results are used, and used correctly! To turn his strategy into reality, Henning has served as a member and chairman in numerous standards organizations including the American National Standards Institute, the US Standards Committee on Bioacoustics, the Air Standardization Coordinating Committee, and NATO AGARD Committees on Biodynamics.

In the area of impact exposure and impact protection, Henning also has been a leader in standardization, in many of these same organizations. In these forums, Henning taught me that, if we were to successfully implement a standard, we had better be skilled statesmen and know how to build consensus! He also demonstrated the art of debating, as well as the use of wry wit to cajole adversaries into accepting a given viewpoint!

Henning's contributions to the NATO AGARD are numerous, as many of you know. He has participated for over 30 years in AGARD Aerospace Medical Panel (AMP) activities, symposia, specialist meetings, committees and working groups. He has published over a dozen papers in AGARD Conference Proceedings (CP) (e.g. No 44, 82, 145, 253, 443) on subjects such as vibration and impact stress, biodynamic models, combined physiological and psychological factors, noise exposure, and sonic boom effects. For AGARD Headquarters, Henning chaired a program committee for a broad interdisciplinary symposium "Principles and Practice of Bionics" (Brussels, 1968), also published as a book (AGARD CP No 44, 1970) edited by von Gierke, Kiedel and Oestreicher.

Dr. Henning E. von Geirke receives commemorative pen set from Mr. James Brinkley at RTO reception honoring him for his lifetime achievements and service to the AGARD Aerospace Medical Panel on 27 October 1998

He lectured on AGARD missions in Portugal, Germany, Belgium, and Norway and represented the AMP with invited papers at symposia of other Panels, such as Flight Mechanics, Structures and Materials, Flight Control, Fluid Dynamics, and Propulsion and Energetics Panels.

Henning acted as program chairman, technical evaluator and editor of the conferences on "Models and Analogues for the Evaluation of Human Biodynamic Response, Performance and Protection" (1978) and "Vibration and Combined Stress in Advanced Systems" (1974). He also served as deputy chairman on the AMP symposium on "Implications of Advanced Technologies for Air and Spacecraft Escape" (1989). In 1996, Henning presented a "Tribute to John Paul Stapp" at the AMP specialist meeting in 1996 on "Impact Head Injury".

While we all know Henning has authored or co-authored over 180 scientific and technical publications, I hope I have illuminated the "brilliance of the man behind the publications."

It truly has been my honor and my pleasure to recognize Dr. Henning E. von Gierke and his scientific accomplishments.

PHYSICAL MODELS: THE GOOD, THE BAD, THE UGLY

Charles P. Hatsell, PhD, MD
Biodynamic Research Corporation
9901 IH 10 West, Suite 1000
San Antonio, TX 78230, USA

Physical models span a spectrum from mathematical equations written on paper and solved in closed form, to a brassboard mock-up nearing what will be a prototype. Most scientists do physical or mathematical modeling nearly daily, usually to gain additional insight into some physical phenomenon. A complete project will usually include a series of increasingly complete and complex models which converge to a final design. For these reasons, a model may not be a good one. It may be bad. It may be ugly.

A Good Model:

On a positive note, let's start with a good model, the mass-spring-dashpot model shown in Figure 1. The mass M is assumed to be sliding on a frictionless surface, energy is stored and given up by a spring of constant K, and energy is dissipated by a viscoelastic dashpot with velocity constant C. The differential equation for this system is linear, second order, and given as Equation 1.

$$\ddot{X} + \frac{C}{m}\dot{X} + \frac{K}{m}X = 0 \qquad (1)$$

The solution to this model is well known and easy to come by; nevertheless, it reveals interesting things about masses springs and dashpots hooked together in this way. After having been given a shove, the mass may oscillate back and forth (under damped), just fail to have any oscillatory quality (critically damped), or return to its initial state in a uniform way (over damped). Of course, an experiment would reveal these things, but the model allows a precise statement about the relationships among M, K, and C which dictate these conditions. Experiments show that predictions made with the model will be close to measurements, the hallmark of a good model; however, precise measurement will show that the mass slows more quickly than predicted. More energy will have been dissipated at any given time than predicted by Equation 1. Friction causes the spring and dash pot to heat slightly, and the surface on which the mass slides in the laboratory is not frictionless (Figure 2). So the modeller accounts for friction force by adding a term to the model as shown in Equation 2. Now the differential equation is non-linear and cannot be solved in closed form.

$$\ddot{X} + \frac{C}{m}\dot{X} + \frac{K}{m}X + \mu\, g\, \mathrm{sgn}\,(\dot{X}) = 0 \qquad (2)$$

Due to the discontinuity in the sgn(.) function, writing a difference equation which may be used to solve Equation 2 on a computer must be done with great care in order that the model predictions will be useful. So, what may have seemed only a slightly more inclusive model is a very hard one to solve.

A Bad Model:

The best thing which may be said about producing a bad model is that it can be an important learning experience. As an example, consider an object falling onto the surface of a pond. It is desired to determine the deceleration of the object due to its interaction with the water. Figure 3 shows a falling cylinder, but it is always better to keep the model as general as practical. Since we are dealing with objects in motion which will encounter applied forces, an equation of great interest to us will be Newton's second law,

$$M\ddot{X} = F \qquad (3)$$

where M is the object's mass, F the force it encounters on impacting the pond's surface, and X the resulting acceleration. F is easily determined from Archimedes' principle which states that the force on the object is equal to the weight of the fluid displaced. If $\tau(x)$ is the volume displaced by the object when it has sunk a distance x in the water, then F is given by

$$F = g\, p\, \tau(X) \qquad (4)$$

and the equation of the resulting model is

$$M\ddot{X} = -\, g\, p\, \tau(X) + M g \qquad (5)$$

Calculation of the velocity versus time for a 1.5 foot diameter cylinder weighing 1000 pounds impacting the water at 14 feet-per-second produces the result shown in Figure 3. Clearly the accelerations are quite mild producing little initial acceleration. A reasonable conclusion from this calculation would be that such a water impact would be unlikely to damage the contents of such a cylinder if prudently packed. The conclusion is incorrect because the model is wildly wrong.

Papers presented at the RTO HFM Specialists' Meeting on "Models for Aircrew Safety Assessment: Uses, Limitations and Requirements", held in Ohio, USA, 26-28 October 1998, and published in RTO MP-20.

We have failed to account for the inertia presented by the water as the cylinder pushes it out of the way. One reason we may have done this is the way we stated Newton's second law. The law stated far more completely is:

$$\frac{d}{dt}(M\dot{X}) = F \qquad (6)$$

where a time changing mass is allowed. The equation governing the model now becomes

$$[M + p\tau(X)]\ddot{X} + p\dot{X}\dot{\tau} = Mg \qquad (7)$$

and the result of the same calculation with the cylinder is shown in Figure 4. Notice how much greater are the accelerations experienced by the cylinder (and its contents). Although this is a better model, due to the nonlinear behavior of a splash it probably overstates the accelerations; however, to have used the first model could have led to disaster.

An Ugly Model:

Ugly models are not necessarily technically incorrect; they may be valid representations of a process or system but provide absolutely no insight or extensibility. The following model was constructed over 20 years ago (Ref 1, Ref 2) and has stood the test of time well: it was ugly then and it is ugly now.

About 30 years ago McRuer and Jex (Ref 3) both individually and together developed a (not ugly, but very nice) model stated in classical control theory terms of the human performing a tracking task. This model was extensively verified and found a great deal of application in land and air vehicle design. Perhaps more importantly, the model yielded new and valuable insight into how humans do manual tracking and provided some very good estimates of certain descriptive parameters such as gain and lumped delay. As classical control theory gave way to so called modern control theory, a model based on state variables and Kalman filtering was put forth (Ref 4). While still a valid model which provided the feature of identification of parameters, it provided little, if any, insight beyond that given by the model of McRuer and Jex (at least in this author's opinion).

About 25 years ago, interest was growing about the application of information theory to modeling the human operator. Because information theory in the context of control systems handles non-linear as easily as linear systems and lumped parametric elements in the system are handled with equal facility, such a model construct has great appeal, at least superficially. Actually, the absence of these structural sensitivities guarantees that the model will probably fit the data quite well but will give minimal new insight.

Figure 4 shows the usual model of the human operator. X is the system driving event which usually is not directly observable. The human operator observes the error in control, E, and provides a control Y in an attempt to control the plant in such a manner that E is held to a minimum. A typical control task performed in the laboratory is to have the operator attempt to keep a spot on a screen centered by providing control inputs to a joystick. The dynamic characteristics of the plant and the bandwidth of X may be varied to control the difficulty of the task. Stressors may be included to add to the overall task difficulty. The most important element in the model is the summing node which is isolated and shown in Figure 5. Also shown in Figure 5 are some functions commonly used in information theory. Precise definitions of these quantities are beyond the scope of this presentation, but brief descriptions will probably be sufficient. H(A) is called the entropy of the process A: it a measure of the uncertainty of the value of A. I(A,B) is the amount of information which is common to A and B. The important relations among these quantities are shown in the equations in Figure 5. Obviously, good operator performance produces a great deal of information mutual to both X and Z (i.e., I(X:Z) tends to be large) while minimizing the information mutual to Z and the error E (i.e., I(E;Z) tends to be small). The basic model conjectures that the entire visual tracking ability of the operator is used up in performing the task. If this capacity is given by C, then the model is

$$I(X;Z) + I(E;Z) = C \qquad (8)$$

Data from heat stressed subjects (Ref 5) controlling two tasks were used to test the model. An estimate of channel capacity was determined from the data and the mutual information measures were calculated in a standard way. Figures 6 and 7 show the results of these calculations. There is apparently a very good fit by the model to the data; however, all we have is the relationship guaranteed by the summing node and the model. No additional insight has been gained.

Conclusion:

For physical models to be useful and extensible, they must be mathematically concise and heed carefully those physical laws which govern any underlying processes. Overly complex models frequently will be overparameterized leading to non-unique solutions. Yielding to temptations to depart from fundamentals in order to use techniques which are in vogue will frequently lead to difficulty.

Spring-Mass-Dashpot Model

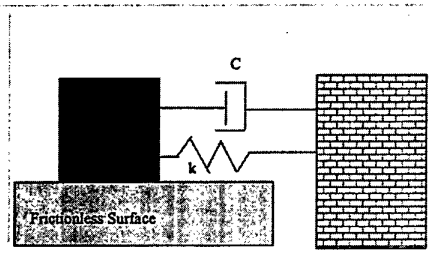

Figure 1

Spring-Mass-Dashpot Model

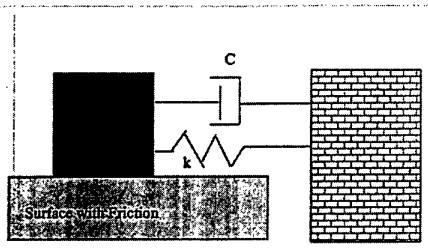

Figure 2

Cylinder Impacting Water

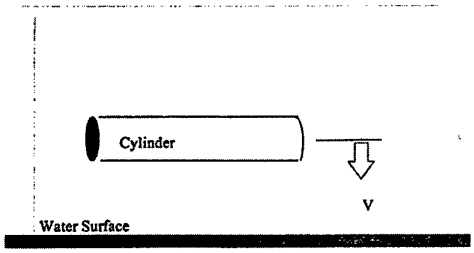

Figure 3

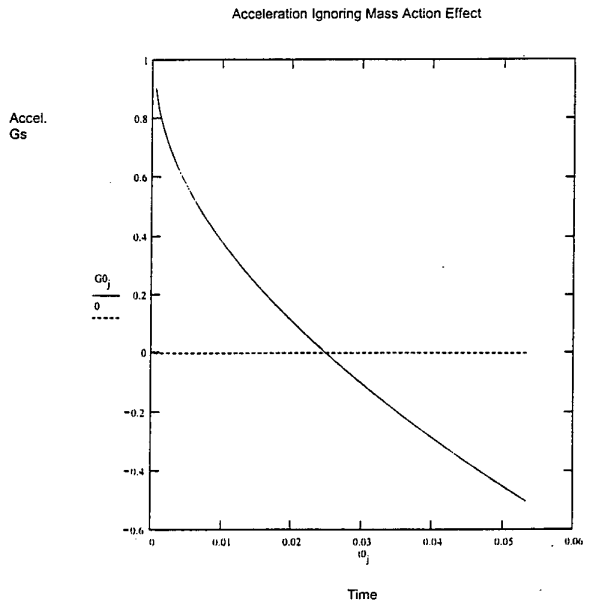

Figure 4

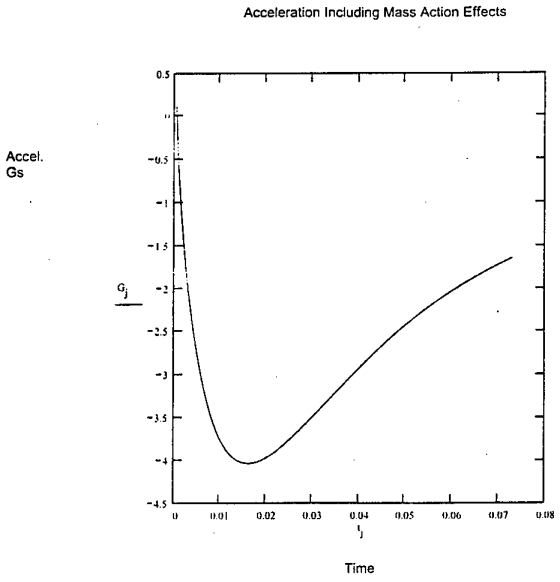

Figure 5

REFERENCES

1. Weidemann, H. L. Entropy analysis of feedback control systems. Advances in Control Systems, Vol. 7, Academic Press, Inc., pp. 225-255, 1969.

2. Hatsell, C. P. An information theoretic human operator model. Proceedings of The Tenth Annual Asilomar Conference on Circuits, Systems, and Computers, Pacific Grave, California, pp. 479-483, November 1976.

3. McRuer, D. T., and Jex, H. R. A review of quasi-linear pilot models. IEEE Trans., HFE-8, No. 3, pp. 231-249, September 1967.

4. Kleinman, D. L., Baron, S., and Levison, W. H. A control theoretic approach to manned-vehicle systems analysis. IEEE Trans. Auto Contr, Vol. AC-16, No. 6, pp. 824-832, December 1971.

The AFRL Biodynamics Data Bank and Modeling Applications

John R. Buhrman
Air Force Research Laboratory
Biodynamics and Acceleration Branch
AFRL/HEPA
2800 Q Street
Wright-Patterson AFB OH 45433
USA

1. SUMMARY

The Air Force Research Laboratory (AFRL) has studied the response of human volunteers and human surrogates to impact accelerations for over thirty years. The results of this research have been used to enhance the design of escape, crash protection, and life support systems, while providing invaluable biodynamic response data for the development and validation of impact simulation and injury models. The data that have been collected include accelerations, forces, and motions from in-house tests conducted on man-rated test facilities, including both a horizontal impulse accelerator and vertical deceleration tower. The test data and related summary information from these tests have been compiled and entered into a data bank residing on a server using MS Access, Excel, and Visual Basic software. The compilation of data and related software are referred to as the Biodynamics Data Bank (BDB). The contents of the BDB include general information describing the objective, test matrix, and results from seventy in-house test programs. Also included are the time history and peak biodynamic response data collected during these programs, encompassing approximately 5,000 impact tests. Anthropometry measurements from over 200 test subjects and bibliographic information from 10,000 related references are also included. Slow-motion videos of the tests are currently being digitized as AVI files for future entry into the BDB. Plans also include the scanning and subsequent entry of documentation photographs that will provide a visual image of each test set-up. To provide the user with more efficient access to the BDB, a test index has been developed which contains a complete list of all test parameters including the type of seat fixture, restraint system, and input acceleration profile. This index can be used to perform searches to create data sets of tests with specific parameters, thus enabling the researcher to address specific issues of interest. These features make the Biodynamics Data Bank an ideal source of test data for computer model development and validation.

2. INTRODUCTION

The AFRL has accumulated invaluable biodynamic response data through impact research experiments conducted over many years with both human and manikin test subjects. The data include accelerations, forces, and motions from approximately 5,000 in-house tests conducted on man-rated impact test facilities, including the AFRL Vertical Deceleration Tower (VDT) shown in Figure 1, the Horizontal Impulse Accelerator (HIA), Horizontal Decelerator (HD), Vertical Impact Device (VID), and Body Positioning and Retraction Device (BPRD). The experiments were conducted to answer specific questions regarding the safety of ejection seats and restraint devices, and to assess the potential for injury to human occupants during ejections under adverse conditions. The Biodynamics Data Bank (BDB) was established in order to provide the means for researchers to easily access and understand these data and their associated parameters. The data can then be used in conjunction with biodynamic computer models to perform analyses of dynamic state variables under impact conditions.

3. BACKGROUND

The BDB was established in 1984 by a team of researchers at the AFRL, then known as the Armstrong Aerospace Medical Research Laboratory (1). A computer data base management system called BASIS was used for the initial development of the BDB, which has since been changed to a standardized Windows based system. Although the AFRL maintains data from impact experiments conducted by Stapp and others as far back as the early 1950s, it was not until the 1970s that computer controlled data acquisition systems and storage methods became available for use by researchers at AFRL. This allowed for the relatively straight-forward transfer of data into the BDB from tests dating back to 1978 which were already in digital format and stored on magnetic tapes. However, data from tests during the period from 1972 to 1977 were stored in analog format and therefore required

Papers presented at the RTO HFM Specialists' Meeting on "Models for Aircrew Safety Assessment: Uses, Limitations and Requirements", held in Ohio, USA, 26-28 October 1998, and published in RTO MP-20.

digitization prior to entry into the data bank. This process is currently being implemented. Test programs conducted prior to 1972 have not yet been incorporated into the BDB since these data are stored on chart recordings and other media that can not be easily transferred into computer files. Future plans include incorporating these past test programs, as well as the entry of video and photographic test information from the more recent studies, and providing access to the data through the Internet.

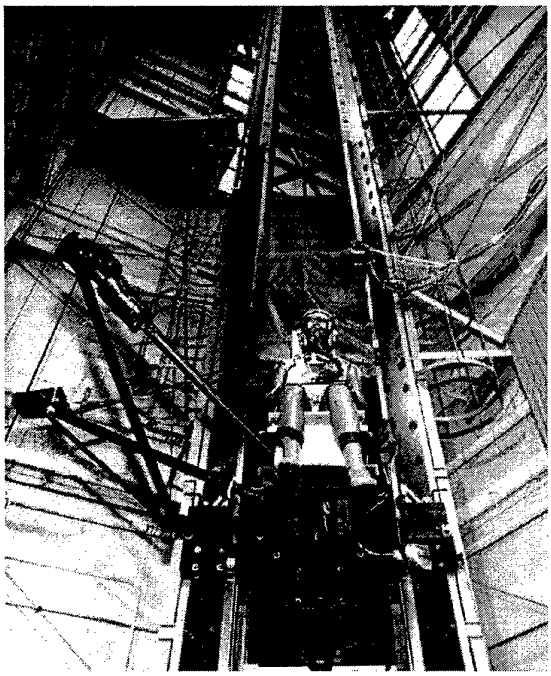

Figure 1. Manikin Test Subject on AFRL Vertical Deceleration Tower

4. METHODS

The current version of the data bank was developed using MS Access, MS Excel, and MS Visual Basic, and resides on a Windows NT server. Software is currently being developed in MS Visual Interdev that will allow users to log on via the Internet. The contents of the BDB include tables for General Study Information, Extrema Test Data, Bibliography Information, Anthropometry Data, and a Test Index. The time histories of the tests, including forces, accelerations, and displacements, have been formatted as MS Excel files and are linked to the Test Index by test number. Plot routines have been developed which can be incorporated into Excel and allow the user to plot any number of channels while viewing the data. The subsets of the data bank and their inter-relationships are shown in Figure 2. Information specified in the shaded boxes is generally available but has not yet been entered into the BDB.

The contents of the BDB subsets illustrated in Figure 2 are as follows:

Anthropometry: Sixty to eighty anthropometry measurements from each of approximately 200 human impact test subjects. These include both males and females from the AFRL Human Impact Test Panel.

Bibliography: Approximately 10,000 references on biodynamics and impact-related topics. References include title, author, abstract, citation, and reference location.

General Test Information: Summary information from seventy in-house test programs from 1974 to 1998, which were conducted to evaluate ejection seat designs, restraint systems, seat cushions, inertia reels, helmets/NVGs, and to establish neck and spinal injury criteria. Information is given on the program objectives, investigators, key words, test matrix, test equipment, instrumentation, and experimental results for each program.

Test Data: Sampled test data from approximately 5,000 in-house acceleration impact tests. Includes force and acceleration data collected with on-board data acquisition systems, and motion data from digitized 16mm films (1972-1990) and a SELSPOT infrared camera system (1990-present).

Test Extrema: Minimum and maximum data values with their corresponding time-to-peak values, and pre-impact harness tensions of all sampled test data.

Test Index: List of parameters for each impact test, including test facility, data acquisition system, acceleration axis, seat acceleration level, pulse duration, seat fixture, type of restraint, type of helmet, and subject weight, gender, and sitting height. The test index can be used to perform searches and create subsets of tests with similar characteristics.

Videos/Photographs/Reports: Slow-motion videos, technical reports, publications, and documentation photographs from the impact tests are currently being digitized for future entry into the data bank.

5. RESULTS

Conversion of the BDB to a standardized Windows format has allowed the seamless transfer of data from AFRL to biodynamic researchers at universities, government research institutes, and the automotive industry, as well as to laboratory in-house personnel. The data can be easily accessed by searching either by study or test using the appropriate index, and can then be transferred elsewhere for use in statistical analyses or modeling applications. The indexes can be used to perform searches to create data sets of tests with specific parameters, thus enabling the researcher to address specific issues of interest. By using the test index, the user can select tests with specific parameter values, such as a particular acceleration level or axis, restraint system, helmet type, etc. and generate subsets with only those tests which are of particular interest.

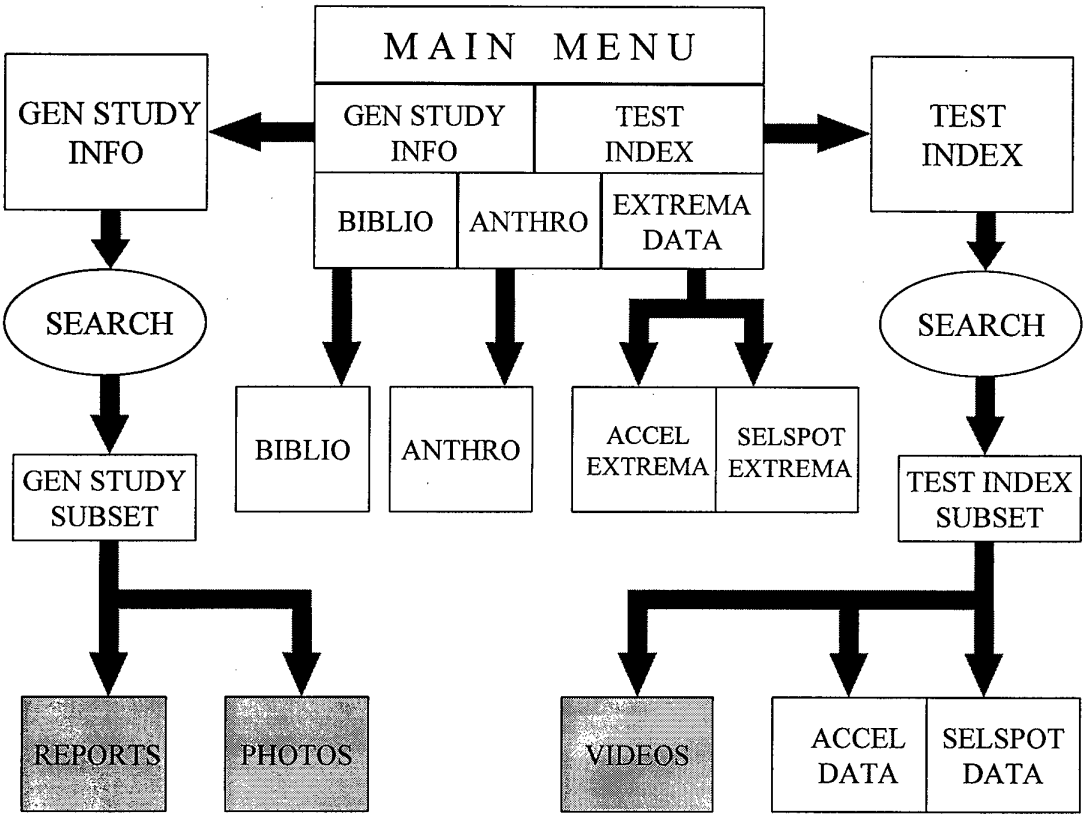

Figure 2. Subsets of the Biodynamics Data Bank and their Inter-Relationships

Data from the BDB have been used by researchers to establish spinal and neck injury criteria under various ejection conditions, and to verify the safety of ejection equipment designs and modifications. Acceleration, force, and motion data from head and neck responses of human and manikin subjects have been used extensively to predict dynamic cervical loads under conditions of varying helmet weights and high g-levels during simulated ejections. The BDB has also been an ideal source of test data for biodynamic model development and validation. Both computer models and lumped parameter injury prediction models have been used in conjunction with the BDB. In particular, it has been used extensively in the development and validation of the Articulated Total Body Model (ATB) (2,3). The ATB, developed by AFRL, is used to predict biodynamic responses of the crewmember and to evaluate injuries associated with diverse aircraft ejection events. The ATB Model can generate simulations of body motion in time history format using various dynamic state variables (Figure 3). The BDB has supplied ATB developers with

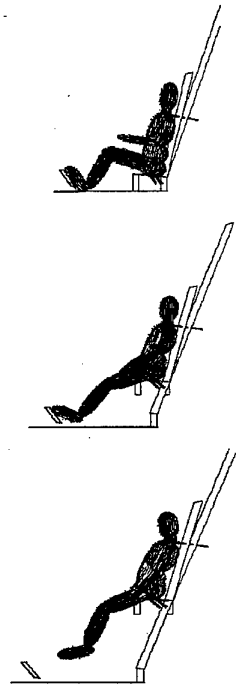

Figure 3. ATB Graphical Illustration of Three Stages of Manikin Inertial Response in Ejection Seat During Vertical Acceleration.

biodynamic response data in the x, y, and z axes for the purpose of validating the results of these simulations. Another biodynamic model often used in conjunction with the ATB is the Generator of Body Data (GEBOD) model, which is used to generate complete body data sets for biodynamic analyses (4). In a recent study at AFRL comparing male and female responses to impact, the BDB provided anthropometry data from male and female subjects tested under identical conditions. The data were then formatted and used as input sets to the GEBOD program. GEBOD then generated estimates of the masses of the subjects' upper body segments that were used in conjunction with upper torso accelerations, also taken from the data bank, to predict the forces present at the lumbar vertebrae of the test subjects. Biodynamic response data from the data bank have also been used to provide inputs to lumped parameter mass-spring-damper models which are used for ejection injury prediction. Two such models are the Dynamic Response Index and Multi-axis Dynamic Response Criteria. These models have utilized human response data from the BDB to compute and validate their equation coefficients which have included the natural frequency and damping ratios in the frequency and time domains (5). Data from the BDB have also been employed in the development and validation of a new Windows-based Head-Spine model (6). The BDB therefore continues to be an important contributor to the establishment of impact injury criteria and to modeling development and verification efforts at the AFRL and other biodynamic research institutes.

REFERENCES

1. Abrams T.S., Kaleps I., and Brinkley J.W. "The AAMRL Biodynamics Data Bank", Report No. AAMRL-TR-88-037, Air Force Research Laboratory, WPAFB, Ohio, 1988.

2. Fleck J.T., Butler F.E., and Deleys N.J. "Validation of the Crash Victim Simulator", Report No. DOT-HS-6-01300, 1982.

3. Obergefell L.A., Gardner T.R., Kaleps I., and Fleck J.T. "Articulated Total Body Model Enhancements, Vol II - User's Guide", Report No. AAMRL-TR-88-043, Air Force Research Laboratory, WPAFB, Ohio, 1988.

4. Cheng H., Obergefell L.A., and Rizer A.L. "Generator of Body Data (GEBOD) Manual", Report No. AL/CF-TR-1994-0051, Air Force Research Laboratory, WPAFB, Ohio, 1994.

5. Brinkley J.W. and Shaffer J.T. "Dynamic Simulation Techniques for the Design of Escape Systems: Current Applications and Future Air Force Requirements", Report No. AAMRL TR-71-29, Air Force Research Laboratory, WPAFB, Ohio, 1970.

6. Belytschko T. and Privitzer E. "Refinement and Validation of a Three-Dimensional Head-Spine Model", Report No. AMRL-TR-78-007, Air Force Research Laboratory, WPAFB, Ohio, 1978.

Comparison of Vertebral Strength Properties of Anthropometrically Similar Male and Female using Quantitative Computed Tomography.

Dr. M. DiCuccio[3], G. Paskoff[1], Dr. P. Whitley[2], and Dr. M. Schweitzer[3]

[1]Crew Systems Research and Engineering Department, Naval Air Warfare Center - Aircraft Division, Patuxent River, MD 20670-1906

[2]M Technologies, Inc., Huntingdon Valley, PA 19006

[3]Department of Radiology, Thomas Jefferson School of Medicine
111 11th Street
Suite 3390 - Gibbon Bldg
Philadelphia, PA 19107
USA

Summary

In determining the risk of injury in the military aviation environment, a male and female of the similar height and weight have been assumed to have the same risk of vertebral injury during an escape or crash scenario. A Quantitative Computed Tomography (QCT) study has been performed to analytically quantify the vertebral strength properties between men and women. The study's goals were to examine the vertebral geometry, bone density, end-plate cortical bone thickness, and trabecular bone architecture of the C2, C5, T12 and L4 vertebrae for a subject pool that consisted of 25 males and 25 females. Additionally, the development of a multivariant regression equation, which would predict the risk of vertebral injury for all individuals and would serve as a guide for designing escape and crash protection systems, was initiated. Preliminary analysis revealed that C2 and C5 trabecular bone mineral densities (BMD mg K_2HPO_4/cc) were significantly higher than those for T12 and L4. When separated by gender the same site relationship held. Female C2 and C5 trabecular bone mineral densities were significantly higher than those for males. Preliminary analysis of gender comparison of endplate cross-sectional area, area density (cross-sectional area x BMD) and predicted strength for the L4 vertebrae revealed that only endplate cross-sectional area was significantly different.

Introduction

In the analysis of injury risk to women and men in automotive crash, the scaling of biomechanical injury criteria has been based solely on general parameters such as height and weight. However, the shortcoming of this approach may be that these methods rely on the assumption of a proportional model. A gender correction does not factor into the scaling equations, and gender differences in anatomical, structural sub-systems are not considered. Using this approach, a man and a woman of the same size (height and weight) would be represented by the same manikin and also by the same injury assessment reference values (IARV). In the aviation ejection and crash environment, this fundamental assumption of the scaling process could prove to be invalid when evaluating injuries between gender. In a study of gender difference in lumbar vertebral size and bone density using quantitative computed tomography, there was found to be no difference in cortical or trabecular bone density between groups of male and female subjects. (Gilzantz et al, 1994) When a subset of this study group was matched for height, weight, bone density, vertebral body height, and age, a significant decrease in mid-plane cross-sectional area for the lumbar vertebrae studied existed for females in comparison to the matched males. The female lumbar vertebrae were 25% smaller in cross-sectional area. This smaller cross-sectional area also implied that the lumbar vertebrae in these female individuals experience 33% greater compressive stress than their male counter-parts under an equivalent load. When the authors considered the bending moment about the spinal motion segment, the female muscle force-coupled moment arm was shorter than that for males in the matched group which resulted in females experiencing a 9% increase in compressive stress. By their calculations, the increase in total compressive stress for axial compression plus bending would be 39%. This relationship implies that for some females, their vertebrae will fail at a lower acceleration level than an equivalent sized male due to a decreased load carrying capacity.

While this study's results are concerning, there are criticisms regarding their evaluations. (Genant et al, 1994) The creation of a sub-set of subjects might imply a hunt for an expected outcome rather than the test of a hypothesis. Additionally, using a more rigorous approach of multivariate correlation/regression to produce a predictive equation for lumbar vertebrae size based on anthropometry would be more useful. The production of such a prediction equation would come at the price of a great many subjects. It is not known whether this phenomenon exist for those who qualify for entry into military aviation. Several factors must be considered in the case of military ejection and crash injuries.

The Gilsanz studies were performed on general populations and, while the sizes were clearly in the area of interest, little is know about the activity level of these subjects.

Rather than being based solely on vertebral height, cross-sectional area and material properties, vertebral load bearing capacity could also be influenced by:

1. vertebral size (height and cross-sectional area)
2. bone density
3. endplate cortical bone thickness
4. trabecular bone architecture.

The correlation of true anthropometry/morphology, in addition to height and weight, may provide the needed factors to

Papers presented at the RTO HFM Specialists' Meeting on "Models for Aircrew Safety Assessment: Uses, Limitations and Requirements", held in Ohio, USA, 26-28 October 1998, and published in RTO MP-20.

describe the differences. Since male and female mass distribution is known to be different, differential loading of the vertebrae due to weight distribution may explain apparent differences in vertebral load bearing capacities.

This paper reports the preliminary results from a Quantitative Computed Tomography (QCT) study performed to analytically quantify the vertebral strength properties between men and women. The goals of the project were to examine the vertebral geometry, bone density, end-plate cortical bone thickness, and trabecular bone architecture of the C2, C5, T12 and L4 vertebrae for a subject pool that consisted of 25 males and 25 females. Additionally, the development of a multivariant regression equation, which would ultimately predict the risk of vertebral injury for all individuals and would serve as a guide for designing escape and crash protection systems, was initiated. For this paper, the results to be discussed will be the gender comparative subject pool anthropometry, the trabecular BMD and the predicted compressive strength.

Methods

Subject Pool

The subject pool consisted of 25 males and 25 females, between the ages of 18 to 40, between the weights of 120 to 150 lb. and with no limit on standing height. All subjects were required to be in good health. The subjects were recruited by announcement under a human use protocol approved by the Thomas Jefferson University Internal Review Board. The subjects were measured for anthropometry and were asked to complete a questionnaire about health, family and exercise history.

Anthropometry

An anthropometry kit from Seritex, Inc. (East Rutherford, NJ) was used to take the measurements. The list of anthropometry measures is given in the Table 3. The determination of the distribution of mass between and within genders was required to test the hypothesis that mass distribution was a predictor of vertebral characteristics due to the normal physiological loading during development. Toward this end, the following segment masses/volumes were determined (as shown in Table 1) for the vertebral levels examined within this study.

Table 1 Vertebral Supported Mass Calculations

Vertebra	Vertebral Supported Mass Calculations
C2	Head Volume
C5	Head Volume +Neck Volume
T12	Head Volume +Neck Volume + Thorax Volume
L4	Head Volume +Neck Volume + Thorax Volume + Right Upper Arm Volume + Left Upper Arm Volume + Abdominal Volume + ½ Pelvic Volume

The torso and total body volumes were also calculated for the purpose of comparison. For each segment volume a previously developed regression equation was used. The study of Young et al (1983) was used for female subjects and the study of McConville et al (1980) was used for male subjects.

Quantitative Computed Tomography and Image Analysis

Quantitative CT (QCT) was performed at the Thomas Jefferson Medical School (TJMS) using a GE High Speed Advantage scanner. Each patient underwent QCT scanning at the C2, C5, T12, and L4 levels (scan parameters: kV 80; mA 120; slice thickness, 10mm). Each QCT image included a density standard; the standard contained solutions of 0, 75, and 150 mg K_2HPO_4/cc. Image analysis was performed using vendor-supplied software and the commercially available package 3DVIEWNIX (Medical Image Processing Group, University of Pennsylvania, Philadelphia, PA). In brief, for BMD analysis, a linear relationship was determined from the density standard relating Hounsfield unit to concentration of K_2HPO_4. Elliptical regions of interest (ROIs) were defined in the midportion of the vertebral body, excluding obvious venous structures. The average Hounsfield unit in the ROI was then converted to milligrams of K_2HPO_4 using the linear relationship. The SCION Image software package was used to threshold the QCT images and then calculate the endplate cross-sectional areas.

Data Analysis

Data analysis was performed using Microsoft Excel and Number Cruncher Statistical System (NCSS). Data values were compared by gender factors using an Analysis of Variance (ANOVA) to test for statistically significant differences between factors. When an ANOVA was significant, a post-hoc Schieff's Multiple Comparison Test was performed to assess the relative differences within the levels of each factor. The level of significance for all tests was considered to be $p \leq 0.05$. Pearson's Product Moment correlation coefficient's were used to test for relationships between data values.

Prediction of L4 Compressive Strength

The compressive strength of the L4 vertebrae were predicted after the method described by Brinckmann et al (1989) using the following equations:

Males
Compressive Strength (kN) = 0.42 + 0.00314 x Trabecular BMD x Endplate Area

Females
Compressive Strength (kN) = 0.45 + 0.00315 x Trabecular BMD x Endplate Area

Trabecular BMD in mg/ml K_2HPO_4
Endplate Area in $(cm)^2$

Results

Subject Pool

The small weight range requirement created some problems in subject recruitment. While that range covered a large portion of the military female population (61.2% of distribution), that same range represented only 17.5% of the male military population. (Gordon et al, 1989) Particular difficulty was experienced in maintaining an ethnic diversity representative of a military population (Table 2). Since race does indeed play a role in BMD, attempting to balance race was deemed important. However, as can be seen in Table 2, in order to recruit smaller male subjects a disproportionately higher number of Asian subjects were used .

Table 2 Subject Pool Race Comparison

	Men			Women		
Race	**#**	**%**	**Army[1] %**	**#**	**%**	**Army[1] %**
White	16	73	64	20	80	46
Black	1	5	25	3	12	44
Hispanic	0	0	5.3	1	4	4.3
American Indian	0	0	-	1	4	-
Asian	5	22	2.2	0	0	2.6
	n=22*			n= 25		

* - three non-respondent males on race
1 - Gordon, 1996.

Anthropometry

The anthropometry results are shown in Table 3. The attempt was to recruit males and females that were the "same size" based on weight. As can be seen from Table 3, the differences between the two populations were statistically significant (shown in bold) by weight and several other measures.

Table 3 Anthropometry Means Comparison

	Men		Women		
	n=25		n=25		
Parameter	**Average**	**STDev**	**Average**	**STDev**	**p value**
Age	30.26	6.01	31.29	6.07	0.563
Thigh Circumference	51.34	4.44	55.76	5.14	**0.003**
Waist (omphalion) Circumference	81.75	5.47	75.60	5.53	**0.0004**
Waist (indentation)Circumference	79.32	5.73	72.18	4.51	**0.00002**
Chest Circumference	86.73	8.28	89.46	5.06	0.173
Neck Circumference	36.05	1.21	32.89	1.50	**0.00000**
Head Circumference	56.41	1.62	55.17	4.23	0.202
Chest Depth	21.65	1.64	23.53	1.87	**0.0007**
Bideltoid Breadth	45.69	2.12	42.24	3.05	**0.00006**
Forearm-Forearm Breadth	48.33	4.79	43.28	3.20	**0.00009**
Hip Breadth	36.91	2.32	38.34	2.35	**0.04**
Shoulder-Elbow Length	36.76	2.30	34.99	2.37	**0.01**
Forearm-Hand Length	46.70	2.11	44.59	3.01	**0.009**
Thumbtip Reach	77.33	5.70	75.78	5.74	0.364
Buttock-Knee Length	57.72	2.76	57.54	2.18	0.806
Popliteal Height	45.71	2.97	41.99	3.70	**0.0005**
Knee Height	55.77	3.20	54.18	4.04	0.144
Midshoulder Height	57.91	2.55	57.10	2.19	0.243
Eye Height	74.40	3.98	73.44	3.41	0.379
Buttock-Popliteal Length	45.65	2.94	46.18	2.29	0.494
Acromial Height	55.03	2.46	54.32	2.41	0.319

	Men		Women		
	n=25		n=25		
Parameter	**Average**	**STDev**	**Average**	**STDev**	**p value**
Sitting Height	87.18	9.78	83.33	3.49	**0.07**
Iliocristale Height	100.02	3.68	99.94	4.58	0.949
Tenth Rib Height	109.09	4.01	108.16	5.39	0.510
Height	172.16	5.59	165.08	6.81	**0.0004**
Weight	65.69	5.06	61.37	4.89	**0.005**
Head Volume (C2 Supported mass)	4132.03	238.62	3949.57	621.58	0.202
Neck Volume	851.19	61.49	768.80	70.19	**0.0001**
Thorax Volume	18610.45	1339.44	17465.24	1292.99	**0.005**
Abdominal Volume	1692.00	627.91	2184.52	828.92	**0.03**
Pelvic Volume	9492.37	1267.65	9050.15	1401.76	0.265
Right Upper Arm Volume	1625.11	137.51	1494.34	130.23	**0.0002**
Left Upper Arm Volume	1613.19	147.12	1482.37	140.97	**0.003**
Torso Volume	29781.83	2894.06	28695.13	3177.46	0.229
Total Body Volume	70428.16	5358.46	66091.69	5228.45	**0.007**
C5 Supported Mass	4983.2	268.5	4718.4	610.1	0.07
T12 Supported	23593.7	1148.8	22183.6	1549.8	**0.0025**
L4 Supported Mass	33270	2569.9	31869.9	2934.7	0.091

BOLD - $p<0.05$

For the comparison by gender of estimated vertebral supported masses only the T12 supported mass was statistically significant but the C5 and L4 were close to significance.

Trabecular Bone Mineral Density

The mean trabecular BMD are shown in Table 4. Of the vertebral levels tested, C5 was the only case where the differences between male and female trabecular BMD were statistically significant. The difference in C2 trabecular BMD, while slightly above $p = 0.05$, was determined to be different by the Schieff's Multiple Comparison Test.

Table 4 Trabecular Bone Mineral Density Means Comparison

	Men		Women		
	n=25		n= 25		
Parameter	**Average**	**STDev**	**Average**	**STDev**	**p values**
C2 BMD	269.60	45.96	297.19	57.44	**0.07***
C5 BMD	300.61	40.64	341.65	47.86	**0.003**
T12 BMD	184.91	35.64	193.05	23.58	0.345
L4 BMD	180.13	34.84	186.23	30.64	0.513

* - Schieff's Multiple Comparison Test

BOLD - $p<0.05$

Figure 1 shows the overall, male and female trabecular BMD graphically. The overall C2 trabecular BMD was significantly different from C5, T12 and L4. The overall C5 trabecular BMD was significantly different from C2, T12 and L4. The overall T12 and L4 trabecular BMDs were significantly different from C2 and C5. These differences held within gender for trabecular BMD comparisons by vertebral location. When trabecular BMD for males were compared to females the following statistically significant differences were found. The male C2 trabecular BMD was significantly different from female C2, C5, T12 and L4. The male C5 trabecular BMD was significantly different from female C5, T12 and L4. The male T12 trabecular BMD was significantly different from female C2 and C5. The male L4 trabecular BMD was significantly different from female C2 and C5. No statistically significant difference was found between male L4 or T12 trabecular BMD and the female L4 or T12 trabecular BMD.

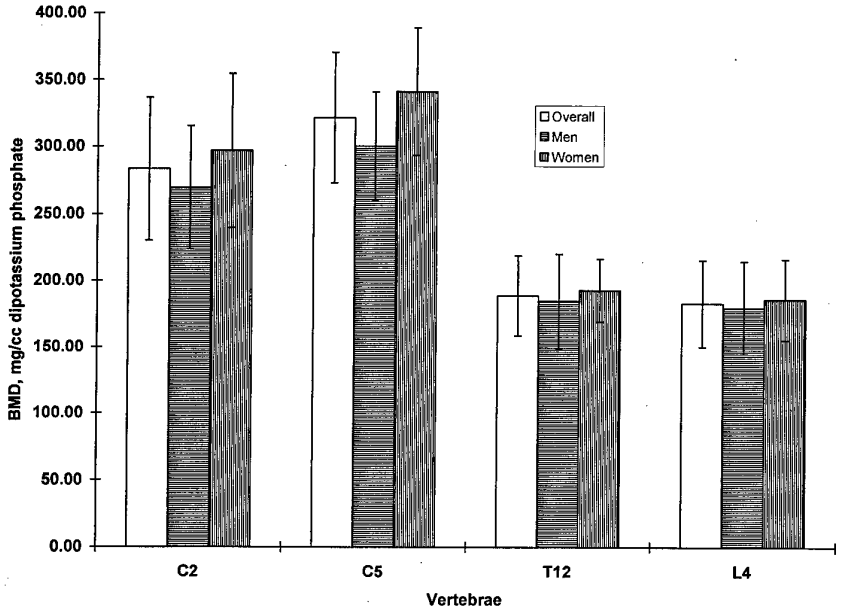

Figure 1 Overall, Male and Female Trabecular Bone Mineral Density by Vertebrae

Predictions of Compressive Strength

Only preliminary results for predictions of L4 compressive strength will be reported. Conclusions based upon the actual relationship must wait until further analysis. To date, 7 males and 12 females have been analyzed and the average data is shown in Table 5.

Table 5 Summary of L4 Compressive Strength Prediction

	Men		Women		
	n=7		n= 12		
Parameter	**Average**	**STDev**	**Average**	**STDev**	**p values**
Endplate Cross-sectional Area (cm^2)	14.6	2.11	12.5	1.66	**0.027**
Trabecular Bone Density (mg/cc K_2HPO_4)	172.2	38.6	200.1	33.4	0.115
Area x Density	2490	541	2496	508	0.979
Predicted Strength (kN)	8.23	1.7	8.31	1.6	0.923

BOLD - $p<0.05$

With the data set available at the time, the endplate cross-sectional area was seen to be significantly different across gender while the trabecular bone density. The area-density and the predicted L4 compressive strength were not statistically significantly different.

Discussion

Subject Pool

An attempt to control the subject pool mix by race to that equivalent to a military population was unsuccessful. Time constraints on the project rendered recruiting a subject pool that was representative of a military population in all aspects impractical. The fact that a large number of male (73%) and

female (80%) subjects were of one race may indicate that a separate analysis using the predominant race for both genders may be indicated to focus on the gender issue. Further data gathered in the other racial groups for comparison by gender may be necessary.

Anthropometry

Based on the contention of gathering a subject pool of the "same size" based on weight, one could conclude that since the gender weights are significantly different, the pools are not equivalent. However, the practical significance of a mean difference of 4.3 kg (9.5 lbs.) is unknown. None the less, of the anthropometry measures, 56% were significantly different by gender. While some anthropometry measures are expected to be significantly different based on gender, the fact that no hypothesis correlations were evident, points to further analysis using subject grouping based on several parameters to describe trabecular BMD relationships. Some of the measurement distributions were non-normal which could be traced to a race group. These outlier groups are further indication that some additional data reduction is required.

To fit within the required weight range, the males were typically thin with little difference in hip, waist and chest measurements. This body type is not surprising given the low percentile range of males with which this weight range corresponds. The females, since this weight range is more representative of the population, were typically more proportionate in hip, waist and chest measurements. Whatever the differences in apparent body type the various segment volumes calculated showed the male segment volumes were larger than the female volumes except for abdominal volume. This result is not surprising given the fact that the regression equations for segment volume that were used were based on height and weight. Given that the male study group was in the lower percentile range for males, using a regression equation that did not use segment specific parameters for calculation of segment volume may be erroneous. Equations that incorporate segment specific parameters may be more appropriate for the analysis.

Bone Mineral Density

This study is the only reported gender comparative QCT BMD studies of the C2 and C5 vertebrae. The result that the cervical BMD was higher than the thoracic and lumbar BMD can be possibly explained by the fact that while the thoracic and lumbar vertebrae experience higher loads they are larger in load bearing surface and so a lower BMD might be required. The result that the female cervical trabecular BMDs were higher than the male values was interesting and unexpected. Given no differences in actual loading, no difference would be expected between the populations by gender. Of the estimated vertebral supported masses, T12 was significantly different and C5 and L4 were close to the level of significance. No correlation was found between these vertebral supported masses and trabecular BMD. Further correlation will be conducted when the results of endplate cross-sectional area are available to factor in as an additional component of compressive strength with BMD.

Predictions of Compressive Strength

Since the results for L4 predicted strength were preliminary, only a limited discussion will be attempted. Endplate cross-sectional area was significantly different by gender and L4 trabecular BMD (just outside the level of significance) seemed to decrease with increasing endplate cross-sectional area in the random subset of subjects analyzed to date. One might extrapolate that a reciprocal relationship may exist between the cross-sectional area and trabecular BMD which would conserve predicted compressive strength. This relationship would be a convenient explanation of possible developmental, adaptive strength relationships and supported by traditional mechanics of materials concepts. However, the total subject pool response was such that no difference existed between trabecular BMD for L4 by gender. If the relationship for endplate cross-sectional area holds by gender however, the predicted L4 compressive strength would likely be less for female than for males.

References

Brinckmann, P, M Biggemann, D Hilweg. Prediction of the Compressive Strength of Human Lumbar Vertebrae. Clinical Biomechanics (Supplement), No.2, 1989, S1-S27.

Genant, HK, CC Gluer, JC Lotz. "Gender Differences in Bone Density, Skeletal Geometry, and Fracture Biomechanics." Radiology, 190:636-640, 1994.

Gilsanz, V., M.I. Boechat, R. Gilsanz, M.L. Loro, T.F. Roe, and W.G. Goodman. "Gender Difference in Vertebral Sizes in Adults: Biomechanical Implications." Radiology, 190:678-682, 1994.

Gordon, CC. U.S. Army Anthropometric Survey Database: Downsizing, Demographic Change, and Validity of the 1988 Data in 1996. NATICK/TR-97/003, October, 1996.(ADA 317 770)

Gordon, CC, T Churchill, CE Clauser, B Brandtmiller, JT McConville, I Tebbetts and RA Walker. 1988 Anthropometric Survey of U.S. Army Personnel: Methods and Summary Statistics. NATICK/TR-89/044, September, 1989. (ADA225094)

McConville, JT, TD Chruchill, I Kaleps, CE Clauser and J Cuzzi. Anthropometric Relationships of Body and Body Segment Moments of Inertia. AFAMRL-TR-80-119, December, 1980, (AD-A097 238)

Young, J, RF Chandler, CC Snow, KM Robinette, GF Zehner and MS Lofberg. Anthropometric and Mass Distribution Characteristics of the Adult Female. FAA-AM-83-16 (NTIS AD-A143 096) 1983.

MODES OF HUMAN HEAD/NECK RESPONSE TO VERTICAL IMPACT

Mariusz Ziejewski
Director of Impact Biomechanics Laboratory, College of Engineering
North Dakota State University
Dolve Hall 111
P O Box 5285
Fargo, North Dakota 58105-5285

Louise Obergefell
AFRL/HEPA
2610 7th Street
Wright-Patterson AFB, OH 45433-7901

Chris Perry
AFRL/HEPA
2800 Q Street, Bldg. 824
Wright-Patterson AFB, OH 45433

Beth Anderson
Veridian
5200 Springfield Pike, Suite 200
WP 441, Dayton, OH 45431
USA

SUMMARY

Helmet-mounted systems can change the helmet's mass inertial properties such as weight, moment of inertia, and center of gravity location, this change may alter the head/neck response and possibly change the pattern of neck loading during the catapult phase of ejection (i.e. vertical impact phase). To define the specifications or criteria for allowable head mounted mass and center of gravity location that is safe for the crew members, identification of the head/neck responses and the factors influencing those responses is necessary. The objectives of this study were to identify the modes of head/neck response to vertical impacts, to determine and assess the parameters influencing head/neck response, and to determine a method of predicting mode of head/neck response for a given subject under given conditions. The data used in this study came from five test cells of the Female Impact Program (FIP) study performed at the Air Force Research Laboratory (AFRL) on their Vertical Deceleration Tower (VDT) facility at Wright-Patterson Air Force Base, Dayton, Ohio. The subjects were exposed to acceleration levels comparable to those experienced in the catapult phase of ACES II ejections. The peak acceleration level for the tests used in this study was 10 G. Each of the subjects wore the same type of helmet. However, the inertial properties of the helmet were varied to simulate those of current helmet-mounted systems.

Five modes of head/neck response for vertical impact were identified and characterized. Modes A and B represent forward neck and head rotation. Modes C and D represent forward neck rotation and rearward head rotation. Mode E of head/neck response represent no significant neck or head rotation. Two experimental parameters, namely, linear x-acceleration of the head at the mouthpiece and head pitch as measured by the motion of the mouthpiece LED with respect to the shoulder LED, were found to be sufficient to uniquely define the mode of head/neck response. Three categories of parameters have been identified and suggested to be the determining factors in a given subject's mode of response for a given condition. The categories include initial position, anthropometry, and other factors such as helmet, weight, helmet center of gravity location and impact acceleration level.

INTRODUCTION

Helmet-mounted systems, such as night vision goggles and helmet-mounted displays, have come into increased demand in recent years. Though these devices enhance the pilot's performance, they may also increase the chance of neck injury during ejection.

There are two mechanisms of neck injury, direct impact to the neck and inertial loading of the head. During the ejection phase of escape, a direct impact to the pilot's neck is unlikely. However, the pilots are subjected to inertial loading of the head. During inertial loading of the head, forces are transmitted by the neck structure to the torso. The effect of the transmitted load on the pilot's neck depends on the magnitude and direction of the load and the direction of head motion since the neck appears to be at least three times stronger in resisting flexion than extension. [1]

Papers presented at the RTO HFM Specialists' Meeting on "Models for Aircrew Safety Assessment: Uses, Limitations and Requirements", held in Ohio, USA, 26-28 October 1998, and published in RTO MP-20.

The AFRL has carried out experimental evaluation of the effect of acceleration levels to human neck response during ejection. The main objective of their study was to define neck response during the catapult phase of ejection. High-speed film footage clearly showed that for identical test conditions, some subjects responded with neck flexion, while others responded with neck extension. To accomplish the ultimate objective of defining the specifications or criteria for allowable head mounted mass and center of gravity location that is safe for the crewmembers, identification of the head/neck responses and the factors influencing those responses is necessary.

OBJECTIVES

1. To identify the modes of head/neck response to vertical impacts.
2. To determine and assess the parameters influencing head/ neck response.
3. To determine a method of predicting mode of head/neck response for a given subject under given conditions.

EXPERIMENTAL DATA AND METHODOLOGY

The data used in this study came from experiments performed on the AFRL VDT facility. The VDT is composed of an impact carriage mounted on two vertical guide rails. [2] The test assembly, including a generic ejection seat, a restraint harness, and instrumentation, is mounted to the impact carriage. The carriage is then raised and allowed to free-fall along the vertical rails onto a water reservoir (hydraulic decelerator) at the base of the tower. A contoured piston mounted on the bottom of the carriage is guided into the reservoir where the displacement of water around the piston decelerates the carriage and produces an upward (+Gz) acceleration. The subjects are placed in the VDT seat in an upright position and restrained with a standard double shoulder strap-lap belt combination. Principal measured parameters include tri-axial linear accelerations at the head (mouthpiece or bitebar) and chest, angular accelerations about the lateral axis at the head and chest, seat and carriage vertical (z-axis) accelerations, and seat pan loads. Body displacements are measured by motion analysis using a SELSPOT infrared detection system.

The response mode study was based on five test cells of the FIP study. In the FIP study, 125 tests were performed using both male and female subjects of various anthropometric dimensions. The study used 12 female subjects with weight ranging from 45.00-65.25 kg and standing height ranging from 1.55-1.71 m. The study also used 15 male subjects with weight ranging from 60.75-102.60 kg and standing height ranging from 1.53-1.81 m. The subjects were exposed to acceleration levels comparable to those experienced in the catapult phase of ACES II ejections. The peak acceleration level for the tests used in this study was 10 G. Each of the subjects wore the same type of helmet. However, the weight and inertial properties were varied slightly to simulate those of current helmet-mounted systems.
The study of influential variables for head/neck response included the anthropometric parameters of the test subjects. The statistical analysis of the anthropometric parameters have been performed using over 600 tests from the FIP study and two additional AFRL vertical impact studies. This analysis was preceded by the analysis and selection of the most appropriate mathematical model representing the subject head response. It has been established that the most appropriate mathematical model for human response characterization is the non-linear extended rational function model of the form:

$$y = \frac{b0 + b1 * x + b2 * x^2}{1 + c1 * x + c2 * x^2}$$

MODES OF HEAD/NECK RESPONSE

A schematic diagram of the head/neck anatomical structure and a two-pivot linkage mechanism representation of the head and neck is given in Figure 1. The approximate locations of a reference coordinate system at the first thoracic vertebra (T1), the occipital condylar point and the approximate head center of gravity, is also identified in Figure 1.

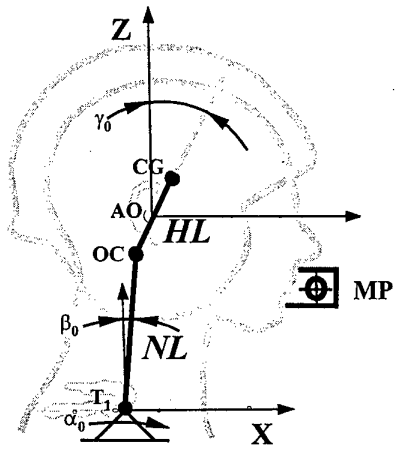

α_0 – Initial Torso Orientation
β_0 – Initial Neck Link Orientation
γ_0 – Initial Head Link Orientation
***NL* - Neck Link**
***HL* - Head Link**
T_1 - First Thoracic Vertebra
AO - Anatomical Origin
OC - Occipital Condylar Point
CG - Head Center of Gravity
MP - Mouth Piece

Figure 1. Schematic Diagram of head/neck structure.

For all tests considered in this study, the high speed film footage was viewed to observe the general trends of the subject's involuntary response. The available measured parameters were also considered. Based on the evaluation of the experimental parameters, it was determined that two parameters, namely, linear x-acceleration of the head at the

mouthpiece and head pitch as determined by the motion of the mouthpiece LED with respect to the shoulder LED, were sufficient to uniquely identify the head/neck mode of response. The positive x-acceleration designates forward acceleration and the positive head pitch designates a rearward head rotation.

Considering the physical constraints of the experimental setup, there are five possible modes of head/neck response as summarized in Table 1.

The first two modes, Modes A and B, represent forward neck and forward head rotation. Mode A differs from Mode B by the relative angular velocity of the neck in comparison to the head. Mode A has greater initial neck angular velocity than head angular velocity, while Mode B has greater initial head angular velocity than neck angular velocity. Schematic diagrams showing the kinematics for Modes A and B are given in Figures 2a and 3a, respectively. Figures 2b and 3b show example test data for initial linear x-acceleration of the head at the mouthpiece and head pitch as determined by the motion of the mouthpiece LED with respect to the shoulder LED for these modes. Actual high speed film footage is shown in Figures 2c and 3c.

The second two modes, Modes C and D, represent forward neck rotation and rearward head rotation. Mode C differs from Mode D by the relative angular velocity of the neck in comparison to the head. Mode C has greater initial neck angular velocity than head angular velocity. Mode D has a greater initial head angular velocity than neck angular velocity. Figures 4 and 5 demonstrate Modes C and D respectively.

Mode E of head/neck response has no significant head or neck rotation. Mode E is shown in Figure 6.

Theoretically, a subject can respond in any of the five modes of response. However, a combination of several parameters will determine the subject's mode of response for the given conditions. These parameters can be classified into three different categories and the role they play in the head/neck response can be determined with the help of statistical analysis. Category #1 is initial position, specifically initial head pitch and initial neck pitch. Category #2 is anthropometry. A preliminary statistical investigation of the influence of anthropometry was performed. It appears that four anthropometric variables such as sitting height, head length, chest circumference and weight are significant. These anthropometric variables were chosen as a preliminary set of variables to consider in defining the head/neck response modes as given in Table 1. Category #3 is labeled as others and includes helmet weight, helmet center of gravity location and impact acceleration level. The values for the parameters in these three categories are not yet available. A follow-up research project could determine those values that would complete Table 1, thus, providing a tool for predicting head/neck response for a given subject under given conditions. With this data, one can also classify the modes of response for the existing VDT test. This information can be used to study several different areas of interest such as gender differences and the effect of helmet configurations on head/neck response. It also can serve as a clustering method to reduce the variability of the test data included in the effort to develop the equation of head/neck response.

Using the described definition of head/neck response modes, the tests in the FIP study were classified in terms of mode of response. The frequency of each response mode for different test conditions is given in Table 2. In this research, five different test configurations were used. The baseline test included a standard helmet with no additional weight added. The second test configuration added 1.5 lbs weight and a center of gravity shift of 0.1 inches in the x direction. The third test configuration added 1.5 lbs weight and center of gravity shift of 1.59 inches in the x direction. The fourth test configuration added 4.5 lbs additional weight with a center of gravity shift 1.21 inches in the x direction. The last test configuration also added 1.5 lbs weight and a center of gravity shift of 0.1 inches in the x direction, as in the second test configuration, but the head rest was moved to one inch behind the seatback tangent line.

In the analysis of the data given in Table 2, the forward head rotation will represent the overall number of subjects responding according to Mode A or Mode B. The rearward head rotation will represent the overall number of subjects responding according to Mode C or Mode D. Based on the data in Table 2, it appears that for the baseline test (helmet with no additional weight), there was approximately an even split between the number of subjects responding with a forward head rotation (44.4%) and a rearward head rotation (48.1%). The second test configuration resulted in a similar ratio between forward head rotation (33.3%) and rearward head rotation (33.3%). Please note that for this scenario, the remaining 33.3% of the subjects did not reveal any significant forward or rearward head rotation. This number is four times greater than the number of subjects responding with no apparent forward or rearward head rotation in the baseline test. This observation might suggest that small adjustments in the center of gravity of the helmet may be used to reduce the extent of head rotation during ejection. The third test configuration resulted in the majority of subjects responding with a forward head rotation (66.7%) and 25.0% of subjects responding with a rearward head rotation. Similar results were obtained in the fourth test configuration with 64.0% of the subjects responding with a forward head rotation and 16.0% of the subjects responding with a rearward head rotation. The last test configuration resulted in only a small number of subjects responding with a forward head rotation (18.0%) and the majority of subjects responding with a rearward head rotation (72.6%). Based on the results of the last test configuration, it appears that the position of the head support is of significant importance and

possibly should be adjusted depending on the anthropometry of the subject and assumed bracing position of the subject.

SUMMARY AND CONCLUSIONS

1) Five modes of head/neck response for vertical impact were identified and characterized. The first two modes, Modes A and B, represent forward neck and forward head rotation. Mode A differs from Mode B by the relative angular velocity of the neck in comparison to the head. Mode A has greater initial neck angular velocity than head angular velocity, while Mode B has greater initial head angular velocity than neck angular velocity. The second two modes, Modes C and D, represent forward neck rotation and rearward head rotation. Mode C differs from Mode D by the relative angular velocity of the neck in comparison to the head. Mode C has greater initial neck angular velocity than head angular velocity. Mode D has greater initial head angular velocity than neck angular velocity. Mode E of head/neck response has no significant head or neck rotation.

2) Two experimental parameters, namely, initial x-acceleration of the head at the mouthpiece and head pitch as measured by the motion of the mouthpiece LED with respect to the shoulder LED, were found to be sufficient to uniquely define the mode of head/neck response.

3) Three categories of parameters have been identified and suggest to be the determining factors in a given subject's mode of response for a given condition. The categories include initial

Table 1. Modes of Head/Neck Response for Vertical Impact

		MODES				
		A	**B**	**C**	**D**	**E**
RESPONSE	Neck Rotation (β)	forward	forward	forward	forward	none
	Head Rotation (γ)	forward	forward	back	back	none
	Condition*	$\omega_\beta > \omega_\gamma$	$\omega_\beta < \omega_\gamma$	$\lvert\omega_\beta > \omega_\gamma\rvert$	$\lvert\omega_\beta < \omega_\gamma\rvert$	none
DIAGNOSTIC PARAMETERS	X - Acceleration *(Initial at mouthpiece)*	+	-	+	-	**0**
	Head Pitch *(Mouthpiece wrt shoulder)*	-	-	+	+	**0**
CATEGORY 1 *(Initial Position)*	Neck Pitch (deg)	**	**	**	**	**
	Head Pitch (deg)	**	**	**	**	**
CATEGORY 2 *(Anthropometry)*	Sitting Height (mm)	**	**	**	**	**
	Head Length (mm)	**	**	**	**	**
	Chest Circ. (mm)	**	**	**	**	**
	Weight (kg)	**	**	**	**	**
CATEGORY 3 *(Other Factors)*	Helmet Weight (kg)	**	**	**	**	**
	Helmet C. G.	**	**	**	**	**
	Acceleration Level (G)	**	**	**	**	**

*ω_β = angular velocity of the neck
ω_γ = angular velocity of the head

** Indicates the values not available at this time. Values to be determined in the follow up research.

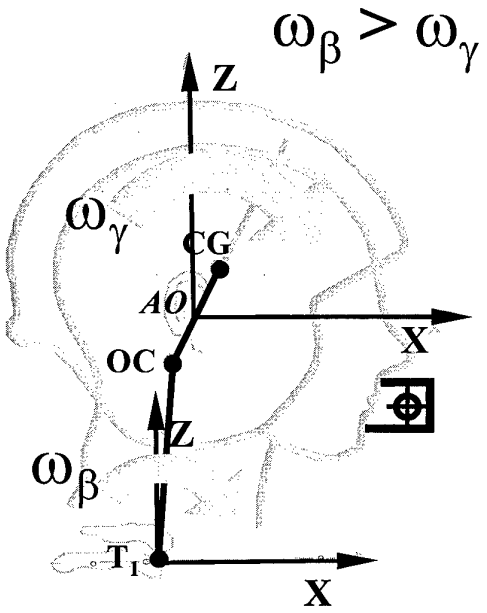

Figure 2a. Response Mode A - Diagram.

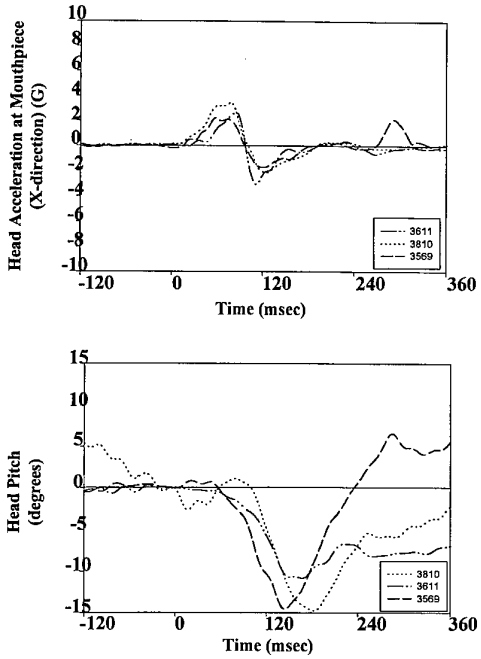

Figure 2b. Response Mode A - Data.

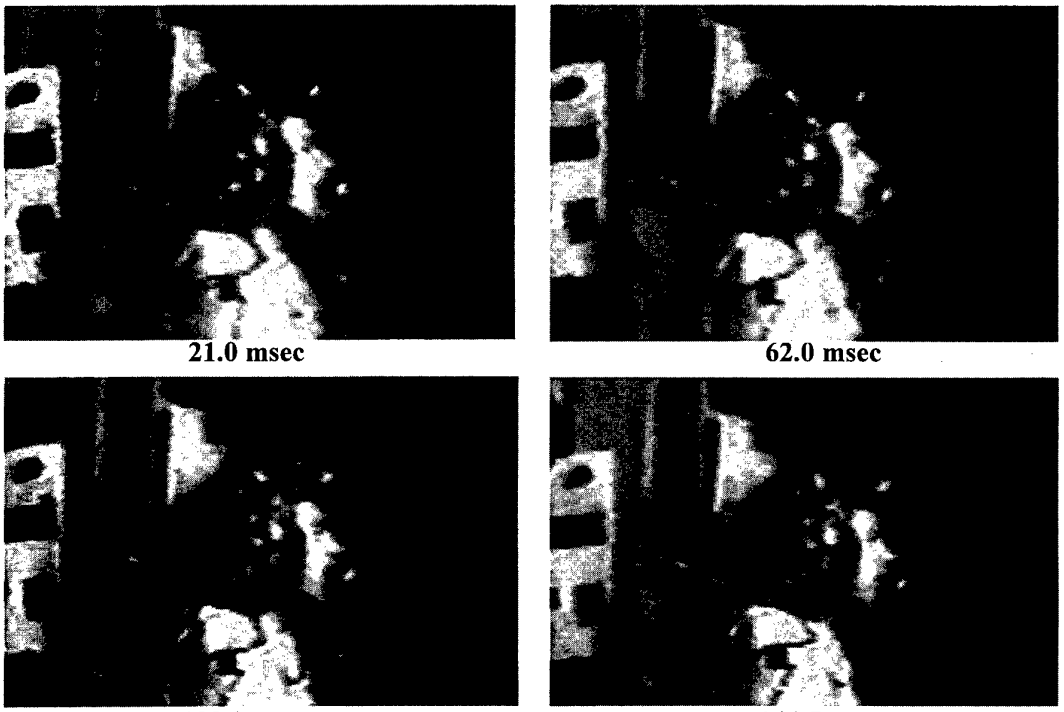

Figure 2c. Response Mode A - Selected frames from high speed film footage (Test 3569).

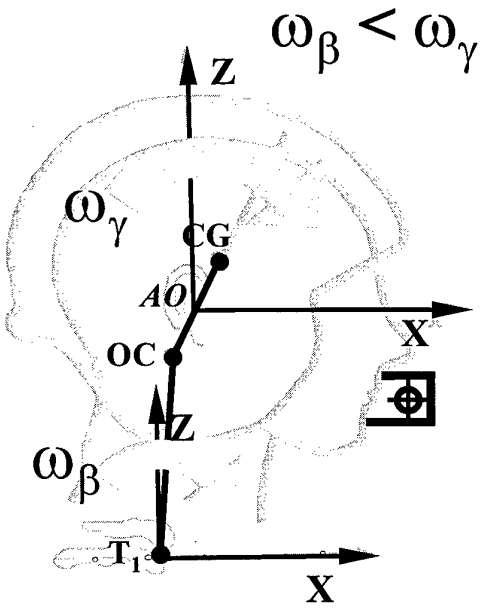

Figure 3a. Response Mode B - Diagram

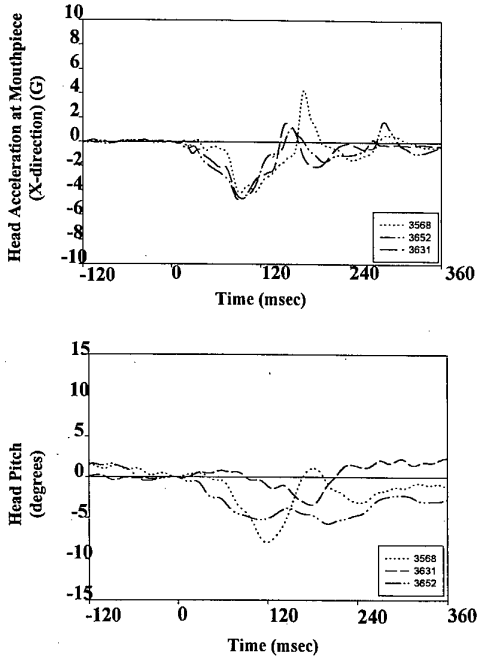

Figure 3b. Response Mode B - Data.

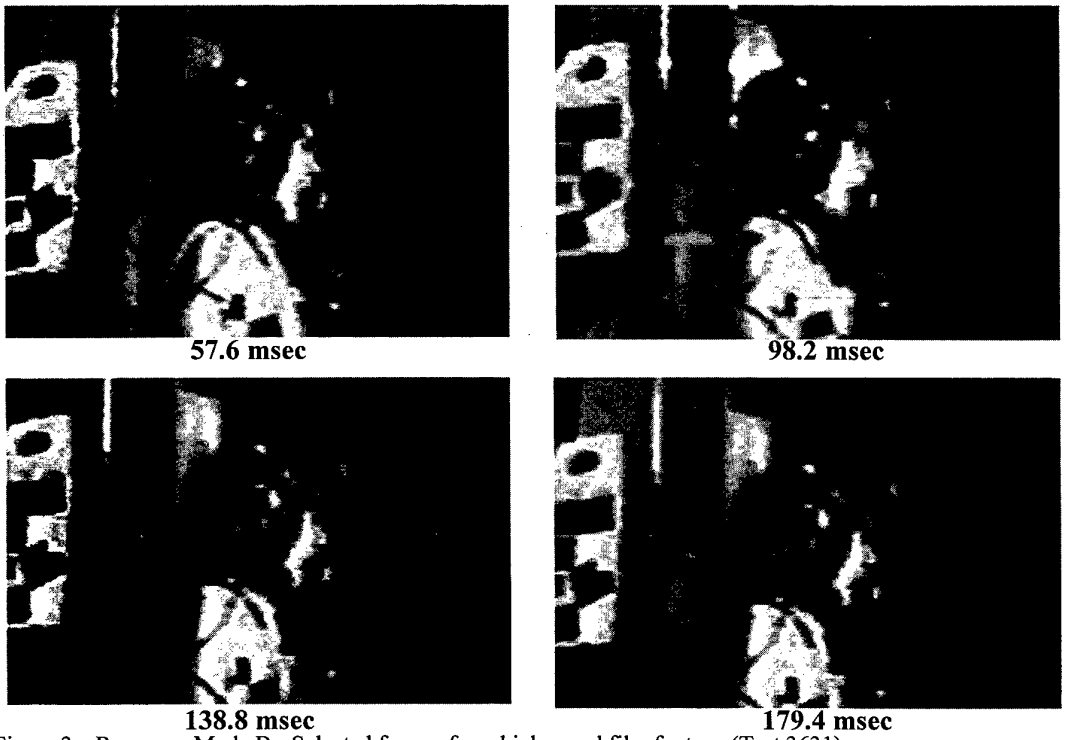

Figure 3c. Response Mode B - Selected frames from high speed film footage (Test 3631).

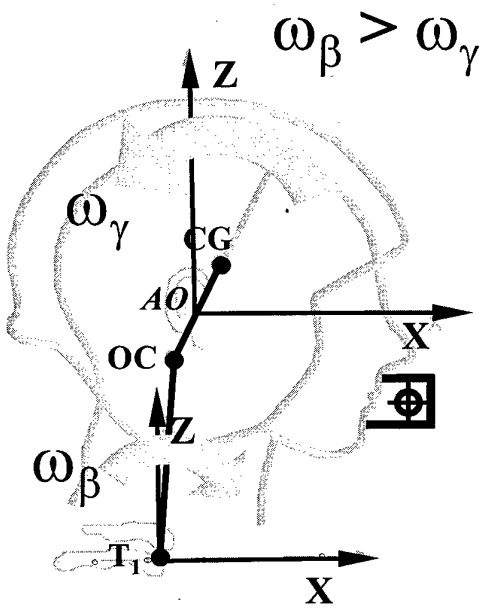

Figure 4a. Response Mode C - Diagram.

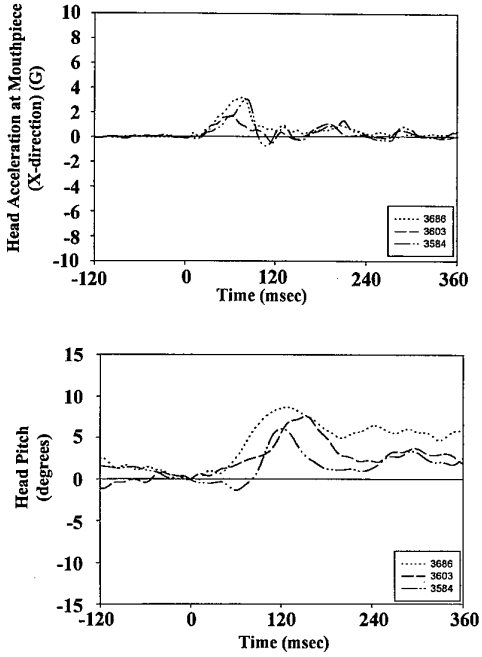

Figure 4b. Response Mode C - Data.

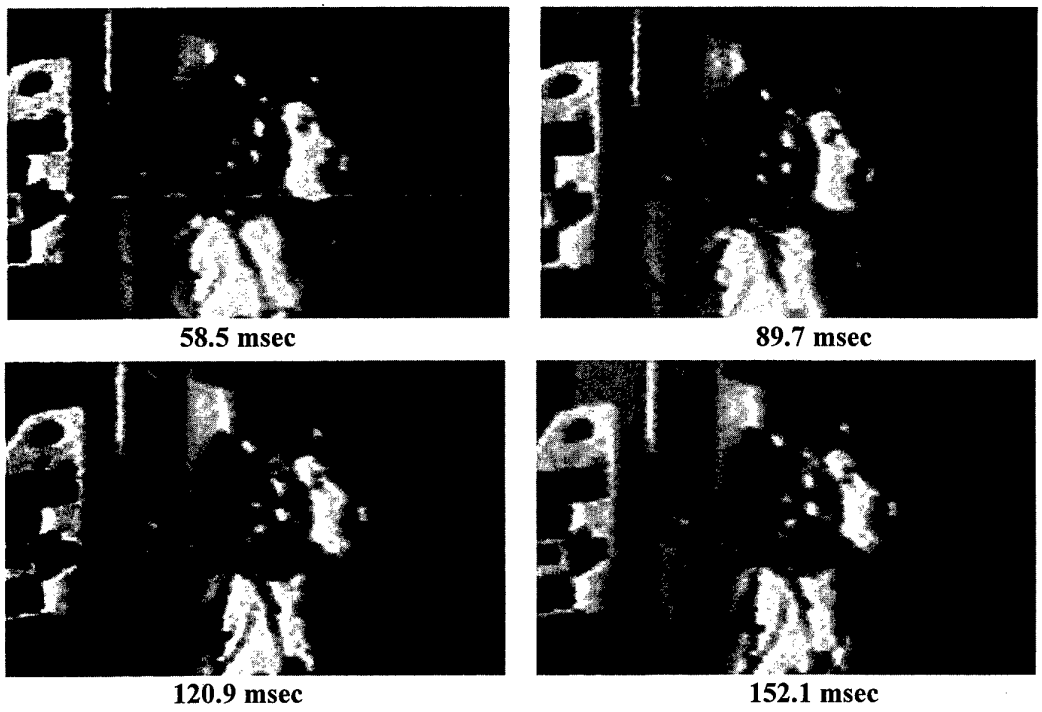

Figure 4c. Response Mode C - Selected frames from high speed film footage (Test 3584).

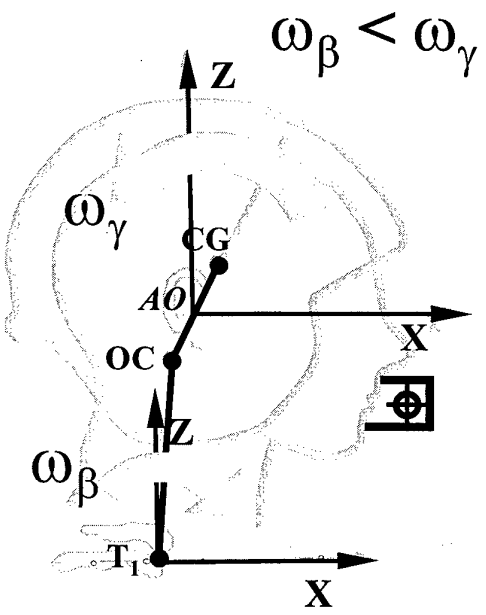

Figure 5a. Response Mode D - Diagram.

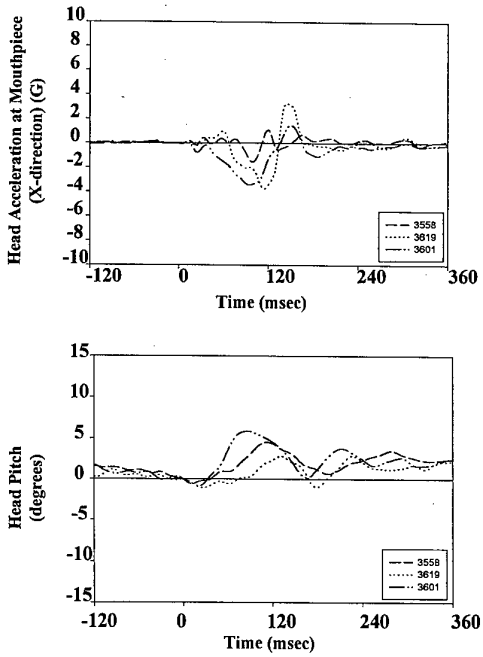

Figure 5b. Response Mode D - Data.

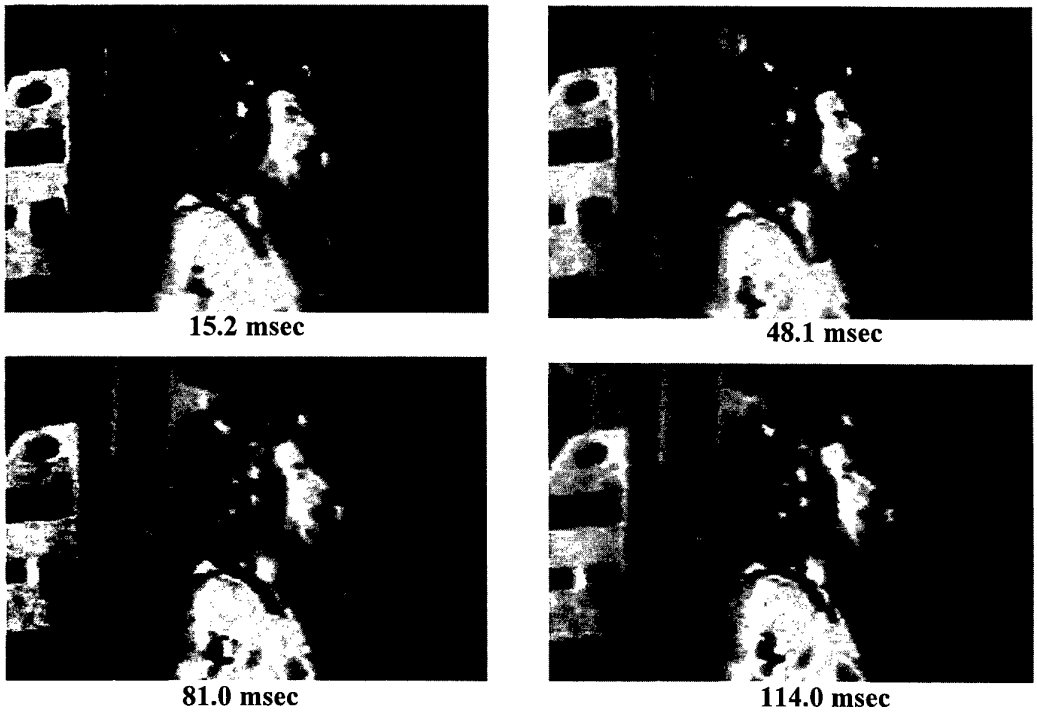

Figure 5c. Response Mode D - Selected frames from high speed film footage (Test 3558).

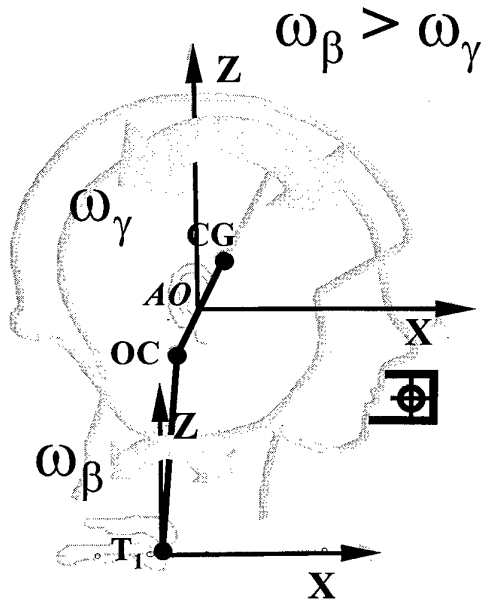

Figure 6a. Response Mode E - Diagram.

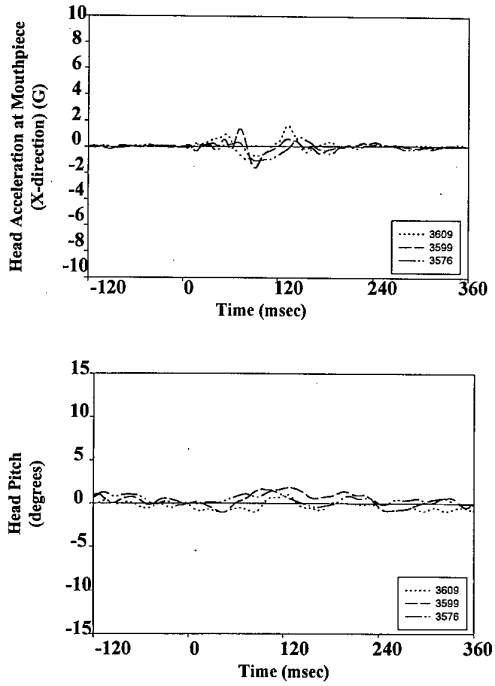

Figure 6b. Response Mode E - Data.

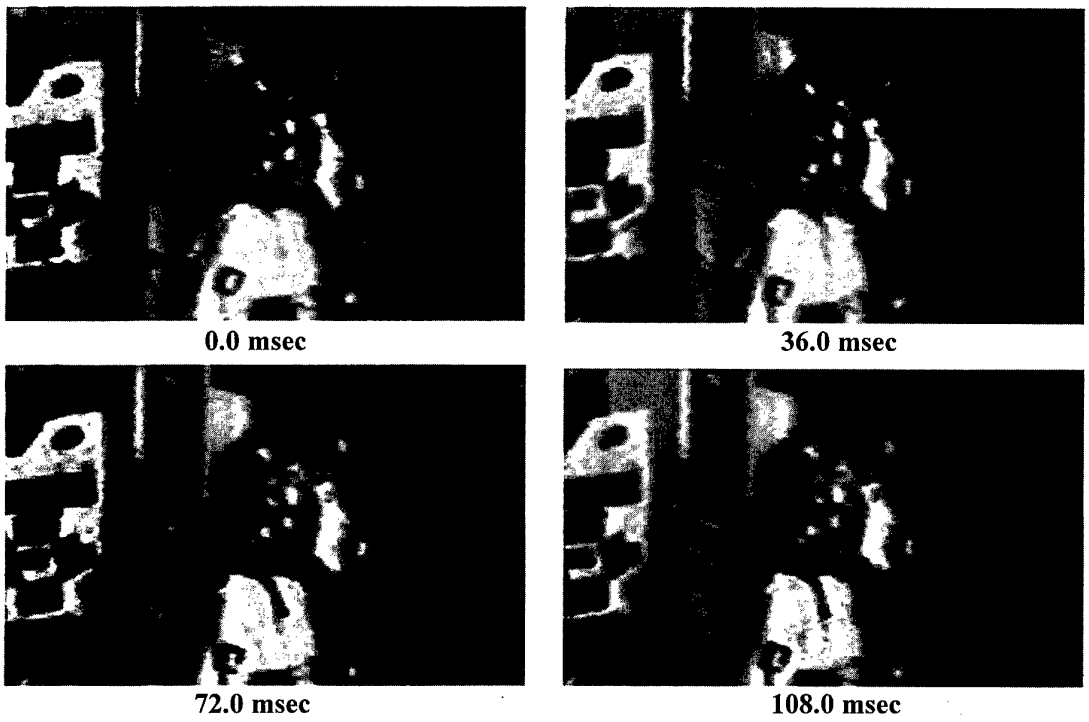

Figure 6c. Response Mode E - Selected frames from high speed film footage (Test 3576).

Table 2. Frequency of response mode for different test conditions.

ADDED HELMET WEIGHT (LB)	HELMET SYSTEM CG X.Y.Z. (IN)	MODES									
		A		B		C		D		E	
		Ratio	%	Ratio	%	Ratio	%	Ratio	%	Ratio	%
Helmet Only	-0.89, 0.01, 1.18	4/27	14.8	8/27	29.6	5/27	18.5	8/27	29.6	2/27	7.4
1.5	-0.79, 0.01, 0.73	3/27	11.1	6/27	22.2	4/27	14.8	5/27	18.5	9/27	33.3
1.5	0.70, 0.14, -0.10	7/24	29.2	9/24	37.5	2/24	8.3	4/24	16.7	2/24	8.3
4.5	0.32, 0.06, -0.14	6/25	24.0	10/25	40.0	2/25	8.0	2/25	8.0	5/25	20.0
1.5	-0.79, 0.01, 0.73	1/11	9.0	1/11	9.0	7/11	63.6	1/11	9.0	1/11	9.0

Note that for the last test condition, the headrest was moved to 1 inch behind the seatback tangent line.

position, anthropometry, and other factors such as helmet, weight, helmet center of gravity location and impact acceleration level.

4) When completed, the developed method will allow one to predict how a given subject will respond to a given vertical impact condition.

5) With the developed method, one can classify the modes of response for the existing VDT tests. This information can be used to study several different areas of interest such as frequency of response mode, gender differences, the effect of helmet configurations on head/neck response as well as to serve as a clustering method to reduce the variability of the test data included in the effort to develop the equation of head/neck response for modeling purposes.

REFERENCES

1. H. J. Mertz and L. M. Patrick, "Strength and Response of the Human Neck." SAE Paper No. 710855, Fifteenth Stapp Car Crash Conference, Nov. 17-19, 1971, Coronado, CA.
2. Perry, C.E., J.R. Buhrman, and F.S. Knox III, "The Effect of Head Mounted Mass on Males and Females Under +Gz Impact Acceleration," Aviation, Space, and Environmental Medicine (ASEMCG 68 {5}:216), Presentation at Annual ASMA Meeting, May 1997.

A PC-Based Head-Spine Model

John B. Bomar, Jr., Ph.D. and David J. Pancratz, M.S.
Biodynamic Research Corporation
9901 IH 10 West, Ste 1000
San Antonio, TX 78230, USA

Executive Summary:

Biodynamic Research Corporation (BRC) of San Antonio, TX, completed a government-sponsored project to port the Air Force's Head-Spine Model (HSM) to a personal computer environment, improve certain features of the software, and add a user-friendly interface. The impetus for this project was the desire to have a software tool capable of modeling the internal forces and motions of the human head and spine during impulsive acceleration events, such as aircraft ejections. The HSM was originally developed in the 1970's over a period of several years. BRC re-coded the model using modern programming techniques and renamed the software HSM-PC.

The HSM-PC is a collection of rigid inertial elements and mass-less deformable elements that represent the anatomy of the human spine. There are multiple versions of the model, with increasing levels of complexity. The HSM-PC simulation program consists of a graphical user interface, a computational module, and a database. The geometry and biomechanical data for the model are stored in Microsoft Access format, and can be viewed from the HSM-PC software or from Access directly. The user interface permits an operator to select different HSM models for a simulation; permits editing of the environment, or simulation parameters; and then allows the user to visually review the results of a simulation through an animation or graphs of desired data. The software stores element, environment, simulation, and other data in separate text files, so that additional simulations with a different environment, different forcing functions, or different body elements can be quickly accomplished. The software runs on Microsoft Windows 95, 98, or NT, and requires a Pentium CPU or equivalent for reasonable operation.

It is BRC's belief that there are still sections of the HSM-PC that must be improved to create a validated biomechanical tool with commercial potential. For example, old input files for the original HSM software were noted to have different element properties than published technical reports and journal articles. In many cases, the differences were several orders of magnitude. In addition, the original HSM software did not provide for a way to pre-load the elements of the model. BRC has introduced the concept of "settling" into the HSM-PC, so that the elements of the model have realistic forces and moments acting on them at the start of the simulation. Finally, the element models can be improved significantly. In particular, the muscle and intervertebral disc model can be improved to be more realistic.

Introduction and Literature Review:

The effort was conducted under Contract F41624-95-C-6010 through the Human Effectiveness Directorate of the US Air Force Research Laboratory. This effort emanated from the Air Force's desire to develop a mathematical tool which would estimate the internal forces and motions that occur within the human head-spine system during impulsive acceleration events and aircraft ejections in particular. Existing tools such as the Air Force Articulated Total Body (ATB) model, Dynaman, and MADYMO are able to simulate a human's gross motion to forces and accelerations, but are either unable or unvalidated for computing the internal forces and kinematics at an anatomic level. These internal forces and stresses can aid predictions of injury. The HSM-PC would be a useful tool for Air Force and commercial researchers and scientists in a variety of fields.

The Air Force Head-Spine Model (HSM) was initially developed for modeling pilot ejections from aircraft. In 1973-5, a three-dimensional model of the human spine and head was created at the University of Illinois, sponsored by the Air Force Aerospace Medical Research Laboratory.[1] The model consisted of rigid bodies, which represent skeletal segments, and deformable elements, which represent muscles, ligaments, cartilaginous joints, viscera, and connective tissues. The model can be separated into sub-models to study the response of different body segments to accelerations and loads. The original HSM was theoretically sufficiently general to be applicable to other acceleration environments. A technique for modeling other aspects of the environment, such as seat geometry and restraint harness, were also considered in the HSM. Output of the model included the forces and moments acting on the elements and the kinematics of the model elements.

The HSM was refined in 1976-7 during a second Air Force project.[2] During this project, four different versions of the model were created ranging from 32 to 252 degrees of freedom. The researchers also attempted to refine and validate the model using two methods -- by comparing the model's frequency response to the experimentally determined frequency response of humans to vertical acceleration, and by creating head-spine models for other primates and comparing the model output to experimental data. The work with the primate model also provided a methodology for scaling dynamic response and injury data between the primates and humans. Finally, spinal injury criteria were developed that use the computed stress in vertebral bodies to predict the likelihood of vertebral body failure

Papers presented at the RTO HFM Specialists' Meeting on "Models for Aircrew Safety Assessment: Uses, Limitations and Requirements", held in Ohio, USA, 26-28 October 1998, and published in RTO MP-20.

A database of head and cervical spine geometry and stiffness data was collected in a third project from 1978-80.[3] The geometry of the vertebrae and points of attachment of muscles, discs, and ligaments were obtained. Stiffness data were obtained or estimated from the literature. Inertia values were approximated from the geometry of the vertebrae and applying a uniform density. Simulations with the model were in relatively good agreement with experimental data for the first 150 milliseconds of response. After this time, the model output showed significant discrepancies that the authors attributed to poor modeling of the major muscles. Although this project focused on the head and cervical spine, it used portions of code from the entire HSM model. It is important to note that the simulations were initiated from an unstable configuration, with no forces or moments in the elements.

One final revision to the Head-Spine Model was an effort from 1980-4.[4] During this project, a model of the diaphragm was incorporated into the HSM that better represented the vertical load path through the viscera, abdomen, and rib-cage region. Additional work was done to create a proposed injury criterion for the cervical spine. Simulations with the head and cervical spine model in the fore-aft and side-to-side directions showed a good agreement to experimental data, which led the authors to believe the model was a viable tool for prediction of head-cervical spine kinematics in three dimensions.

A review of the literature reveals that only two other comprehensive biomechanical models of the spine, head and upper torso have been reported in the literature since the HSM was completed.[5,6] The first model, a Finite Element Model (FEM), did not include the head, however it did include descriptions of all the relevant tissues below the head. The paper reported static stress analysis of the model in the normal upright posture, however no dynamic analysis was mentioned or reported.[5] Generally speaking, FEM modeling capabilities are available only to specialists in structural analysis and not widely available to the entire biomechanics community. The second model[6] was a completely lumped model of the loading of the spine in the upright posture with the whole system modeled as a relatively simple mass-spring-damper system. Models with a high degree of lumping are useful for investigating a single posture, but are not flexible and are not capable of fully representing the effects of a dynamically changing posture.

There were several sub-segment models reported.[7,8,9, 10,11,12,13] These models fall into two categories: (1) models of the human head and cervical spine[7-9], and (2) models of sub-segments of the vertebral column[10-13].

The first head-cervical spine model described in 1978 by Huston, et al.[7] was a lumped parameter head-cervical spine model. That model included viscoelastic models for the soft tissues of the cervical spine (C-spine), while the head and bony structures of the C-spine and head are modeled as rigid bodies. There is no provision for active muscular reflex contraction in the model. Huston, et. al.[7] presented comparisons with that of a seated cadaver struck in the head by a mass suspended at the end of a pendulum. They concluded that the model's response compared favorably with that of the cadaver.[7] There was one independent evaluation of the Huston model.

In 1984, Merrill, et al.[8] described a three-dimensional model of the head and C-spine, which was an extension of a previously developed two-dimensional saggital plane model. Although the authors claimed that their model was "three-dimensional" only flexion-extension motion of the head and neck were modeled. No rotation was permitted at the intervertebral joints in the model. The viscoelastic properties of the intervertebral joints were modeled as lumped viscoelastic mechanical elements. Comparisons of the response of the model to impulsive acceleration with motions recorded in humans showed that the model's response did not agree well with the responses of human volunteers subjected to similar acceleration.[8]

The third C-spine model was described by de Jager, et. al.[9] in 1996. The de Jager model was built within the MADYMO[14] multi-body mechanical modeling environment. That model includes separate viscoelastic models for the soft tissues of the C-spine, as well as a contractile muscle model. The head and bony structures of the de Jager model are represented by rigid bodies. De Jager, et. al.[9] reported the model was too flexible when compared with "normal" human response to impulsive acceleration. However, they noted that when the soft tissue model parameters could be "scaled" to match the response of human volunteers, fairly good agreement was obtained between the model and the human subjects although no comparisons were presented.[9]

Two of the sub-segment models were more concerned with motion control in the spine than modeling the motion *per se*.[9,12] The others were FEM models of sub-segments in which detailed anatomical models of the vertebrae and intervertebral discs were modeled and subjected to a stress-strain analysis in FEM computer analyses.[10,11,13] None of these latter models offered information that was of use in the HSM-PC project.

Element Models:

The anatomic model of the HSM-PC consists of five types of elements.

Rigid Bodies: Rigid body elements model the vertebra, pelvis, ribs, and viscera of the HSM-PC. They are the only elements assigned mass properties and are capable of motion in six dimensions (translation and rotation). Rigid bodies have nodes that serve as attachment points for other elements. These elements are called "rigid bodies" because the nodes of a body cannot move relative to one another.

The dimensions of most these elements were obtained from the HSM software and are considered anatomically accurate. In the

case of the vertebra, however, the mass properties of the rigid body elements represents the properties of a horizontal slice of the body, rather than just the mass and inertia of the bone itself. The underlying assumption behind this approach is that horizontal slices of the body move together and can be associated with a corresponding vertebra. Rigid body elements are the only elements in the Head-Spine Model that have mass properties. Thus, to simulate the response of the HSM to a force or acceleration input requires Newton's Laws to be applied only to the rigid body elements. All other elements in the model produce forces and moments that act directly on a rigid body.

Each rigid body element has a primary node, representing the center of gravity for that body, and multiple secondary nodes. The rigid body elements also have multiple secondary nodes that represent attachment points for other elements. The secondary nodes can lie outside the physical representation of the body, since the vertebral bodies represent horizontal slices of the torso. The rigid body elements in the HSM-PC reflect the dimensions and mass properties from the original HSM database. A medical illustrator created anatomical representations of the vertebra and ribs for use in the graphical interface.

The equations of motion for a rigid body element are computed in a combination of body-fixed and global coordinates. Body coordinates are used to compute the acceleration and angular acceleration of each rigid body element due to forces from gravity and other elements. The position and angular orientation of the body is then integrated from velocities in global coordinates. Figure 1 describes the process for computing and integrating the equations of motion for each rigid body element.

BRC chose to use a set of four quaternion parameters to express the orientation of each rigid body internally. The quaternions are converted to conventional yaw-pitch-roll Euler angles for the HSM-PC output. The use of quaternions provides two benefits: there are no singularities in the expression of any orientation, and there is a redundant parameter that can be used as a Lagrange multiplier to speed the solution of the equations of motion.[15]

Figure 1 Solution for the Equations of Motion of Rigid Body Elements

$$(1)\ \sum F - ma - m\omega \times v = 0$$

The force vector equation permits the computation of acceleration in body coordinates, which can be integrated to obtain velocity in body coordinates. The total force on each body is calculated by computing the force in each element, rotating to the proper coordinate frame, and adding to the existing sum.

$$(2)\ \sum M - I\alpha - \omega \times I\omega = 0$$

The moment vector equation permits computation of angular acceleration in body coordinates, which can be integrated to obtain angular velocity in body coordinates. The total moment acting on each body is calculated by computing the forces and moments in each element that attaches to a body, rotating to the proper coordinate frame, and then summing.

$$(3)\ v_G = R_{BG}\, v_B$$

An algebraic expression permits the rotation of body velocity into global coordinates, which can then be integrated to obtain position in global coordinates.

$$(4)\ \omega_G = R_{BG}\omega_B$$

An algebraic expression permits the rotation of body angular velocity into global coordinates.

$$\begin{aligned}
\dot{e}_0 &= -0.5(e_1 p + e_2 q + e_3 r) \\
\dot{e}_1 &= +0.5(e_0 p + e_2 r - e_3 q) \\
(5)\ \dot{e}_2 &= +0.5(e_0 q + e_3 p - e_1 r) \\
\dot{e}_3 &= +0.5(e_0 r + e_1 q - e_2 p) \\
\lambda &= 1 - (e_0^2 + e_1^2 + e_2^2 + e_3^2)
\end{aligned}$$

Algebraic equations permit the computation of four quaternion parameter rates from the angular velocity in global coordinates, which can then be integrated to obtain quaternion parameters.

Springs: Spring elements are used to represent ligaments, some articular facets, and some abdominal viscera elements. They are one-dimensional elements that produce a cubic force from strain and a damping force from rate of strain. All of the ligaments are represented by tension-only springs. All of the abdominal viscera are represented by dual acting springs. It is possible to also add compression-only springs to the model. The force created by a spring is computed as follows:

$$\mathbf{F} = \mathbf{k1} \cdot \delta + \mathbf{k2} \cdot \delta^3 + 2 \cdot \omega \cdot \zeta \cdot \dot{\delta}$$

where, $\omega = \sqrt{k1 \cdot m}$

and where k1 is a proportional stiffness term, k2 is a cubic stiffness term, δ is the deflection from the unstretched state, is the $\dot{\delta}$ rate of deflection, ω is the natural frequency, and ζ is the damping ratio.

One of the major difficulties BRC had in implementing the spring element was the lack of unstretched spring element lengths – the biomechanical data from the original HSM software did not contain unstretched lengths for ligaments. Of course, in order to compute the tension in a ligament it is necessary to know its original length. Thus, in the HSM-PC, it was assumed that the initial endpoints of the ligament defined their unstretched length.

Muscles: Muscles are one-dimensional elements that produce a force proportional to strain and the concentration of an activator molecule that governs their behavior. The relatively simple model of the original HSM was employed[1], although more advanced models could be added in the future. Only the muscles in the cervical spine were modeled in the HSM-PC; there are no muscles from the thoracic or lumbar spine.

The muscle model, originally proposed by Apter and Graessley[16], appears to have the requisite characteristics without undue complexity. As illustrated in Figure 2, the model comprises a Maxwell element in parallel with a spring. All elements have variable parameters which depend on the concentration of an "activator molecule" released within the myofilaments in response to stretch or stimulation.

Figure 2 Muscle Model Schematic

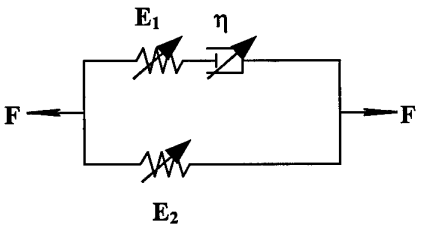

The muscle stress-strain relationships are described by two differential equations whose parameters are variables. The first equation describes the relationship between stress and strain and their rates of change:

$$\sigma + \frac{\eta}{E_2}\dot{\sigma} = E_1\varepsilon + \left(E_1 + E_2\right)\frac{\eta}{E_2}\dot{\varepsilon}$$

Where, $\sigma = \frac{\mathbf{F}}{\mathbf{A}}$, is stress with units of $F \cdot L^{-2}$, ε, is strain, which is unitless, and is defined by,

$$\varepsilon = \frac{\left(l - l_0\right)}{l_0},$$

Where, l_0, is the "no tension" length [L] of the muscle, E_1 and E_2 are elastic moduli [$F \cdot L^{-2}$], and η is viscosity [$F \cdot T \cdot L^{-4}$].

The second equation describes the relationships between the concentration of "activator molecule" [$M \cdot L^{-3}$], c, and its rate of change, the applied stimulus S(t) [$M \cdot L^{-3} \cdot T^{-1}$], and strain, ε.

$$\dot{c} = \mathbf{k}_2\varepsilon - \mathbf{k}_3 c + \mathbf{S(t)}$$

Where, $\mathbf{k}_3$ is a rate constant, and $\mathbf{k}_2$ relates the increase in strain to the rate of increase in activator molecule. The stress-strain model parameters vary as simple functions of the concentration of activator molecule. The relationships are:

$$l_0 = l_0^{\infty} + \frac{l_0^0 - l_0^{\infty}}{1 + \mathbf{k}_1 c}$$

$$\mathbf{E}_1 = \mathbf{E}_1^{\infty} - \frac{\mathbf{E}_1^{\infty} - \mathbf{E}_1^0}{1 + \mathbf{k}_4 c}$$

$$\mathbf{E}_2 = \mathbf{E}_2^{\infty} - \frac{\mathbf{E}_2^{\infty} - \mathbf{E}_2^0}{1 + \mathbf{k}_5 c}$$

$$\eta = \eta^{\infty} - \frac{\eta^{\infty} - \eta^0}{1 + \mathbf{k}_6 c}$$

Where, the superscripts " $^{\infty}$ " and " ^{0} " refer to the completely contracted ($c = \infty$) and completely relaxed ($c = 0$) states, respectively.

Many muscles in the spine actually follow curved paths across multiple vertebra and are attached at multiple locations along their length. The intermediary connections are called sliding nodes. The HSM-PC models sliding nodes by computing

separate lines of action for each segment of the muscle and applying a force to each vertebra that is contacted by a muscle segment.

Hydrodynamic Elements: A hydrodynamic element, employed to model articular facets, is a fluid-filled pentahedron element, with two triangular endplates that lie on adjacent vertebra. Three nodes, each as shown in Figure 3, define the triangular endplates. As the vertebra move relative to one another, the hydrodynamic element changes volume. By assigning a bulk modulus to the fluid in the element, the pressure within the hydrodynamic elements changes as the volume changes. A force proportional to the area of the triangular endplate is then produced on each of the adjacent vertebra. There is also a viscous damping term to reflect the highly damped nature of this interaction.

The pressure in the hydrodynamic element is a function of the volume and volume rate of change, according to the following relationship:

$$p = \mathbf{B}\Delta + \alpha \mathbf{B}\dot{\Delta} .$$

where, B is bulk modulus and Δ is defined by

$$\Delta = \frac{\mathbf{V} - \mathbf{V_0}}{\mathbf{V_0}}$$

and $\mathbf{V_0}$, is the original volume and **V** is the instantaneous volume.

The volume of the pentahedron is computed by separating it into four tetrahedrons and then computing the volume of each tetrahedron: $\mathbf{V} = \mathbf{V_{IJKL}} + \mathbf{V_{JLMN}} + \mathbf{V_{JKLN}}$, where $\mathbf{V_{pqrs}}$, is the volume of a tetrahedron defined by the global coordinates of its nodes. The force on each endplate is computed from the product of the internal element pressure and surface area of the endplate. The direction of this force is parallel to a line drawn from the centroid of the lower endplate to the centroid of the upper endplate. The force is then divided by three and applied evenly to the three nodes on each endplate.

Figure 3. Hydrodynamic Element

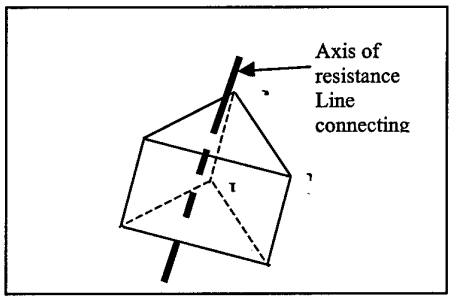

Beam Elements: Intervertebral discs and some of the connections of the rib cage in the Head-Spine Model are modeled with beam elements (also referred to as disc elements in many locations). There is one beam element between each set of adjacent vertebra, except at the level of the first and second cervical vertebra. Although there is not an intervertebral disc at this location, the original HSM software used a pair of matching hypothetical beam elements to model the interactions between these two vertebra. HSM-PC uses the same approach and includes this set of beam elements.

Beam elements are capable of providing axial and shear forces as well as bending and torsional moments when displaced from their original position, as shown in Figure 4.

Figure 4 Forces Produced by Beam Elements

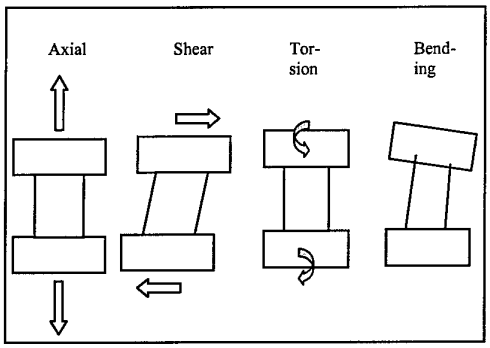

The beam elements in the rib cage do not have a shear force term. Each beam element has two endplates located on adjacent vertebra or ribs. The center of the endplate is attached to a secondary node of each vertebra or rib. The initial relative position and orientation between the two endplates is recorded before a simulation. Then, as the endplates move relative to one another during an HSM simulation, forces and moments are developed in the beam element that are transmitted to both endplates.

Environment Elements: The HSM-PC software relies on elements of the environment for all of the forcing function inputs to the model. There are three types of elements in the HSM environment: springs for modeling restraints, elastic planes for providing contact surfaces, and motion constraints.

The spring elements are identical to those in the HSM anatomy and can be used to model restraints. The springs can be tension-only (restraints), compression-only (cushions), or dual acting.

Planes represent the source for applying forces and accelerations to the HSM. Planes can be ascribed motion over time and produce a force proportional to deflection and rate of deflection when they interact with an element (secondary node) of the

HSM. The HSM-PC software permits planes to be assigned position, velocity, or acceleration time histories to force the HSM model. Springs in the environment can be attached on one end to a plane. This permits the representation of restraint systems, which connect to a force plane on one side and a rigid body node on the other.

Constraints, although not a physical element like springs and planes, can be used to affect the motion of the model. Any or all of the translational or rotational degrees of freedom of rigid body elements can be restricted with the use of constraint elements.

HSM-PC Software:

The HSM-PC consists of three modules: a user-friendly graphical user interface, a computational module, and a biomechanical database.

The graphical interface is a feature new to the HSM-PC. The original HSM software required users to make changes to simulations either by modifying code and re-compiling or by working directly in text files. Users of HSM-PC can perform all of the operations related to creating and running a simulation entirely from the user interface. For example, an operator can select and display a model for simulation, viewing it from any angle and selecting certain elements to be displayed or hidden. The environment for a simulation can be specified and viewed. Parameters related to a simulation such as duration and desired output variables can be specified. A simulation can be executed from within the interface, and then the results can be viewed through charts or an animation of motion. The interface also displays the messages generated during the solution of the model.

The HSM-PC computational module is an executable program written in Fortran 90 that acquires simulation data from the graphical interface, applies Newton's Laws to the model and integrates the resulting motion over time, and writes the specified output into a file for use by the graphical interface. Information from the user interface is communicated via a series of ASCII text files. Although these files are not optimal for conserving space, they allow an experienced user of the software to run simulations without the graphical interface. The program automatically adjusts the solution of the model to account for the number of elements -- re-compiling the HSM-PC is not necessary for different simulations. The computational module also performs some simplistic element checking before attempting to solve the model. For instance, the model will detect and report a ligament that is attached to a non-existent vertebra.

Finally, data for the HSM-PC is stored in the form of a Microsoft Access database. The database can be edited in a standalone fashion from the rest of the HSM-PC software. Although the graphical interface also allows parameters to be changed, those changes are temporary. Only changes to the database itself are permanent. The user can however save the changes in a separate file outside the database for future use. A separate interface was written to help users acquire data from the database. Figure 5 summarizes the functions of the three modules and their interactions with one another.

Figure 5 Schematic of the Operation of the HSM-PC Software

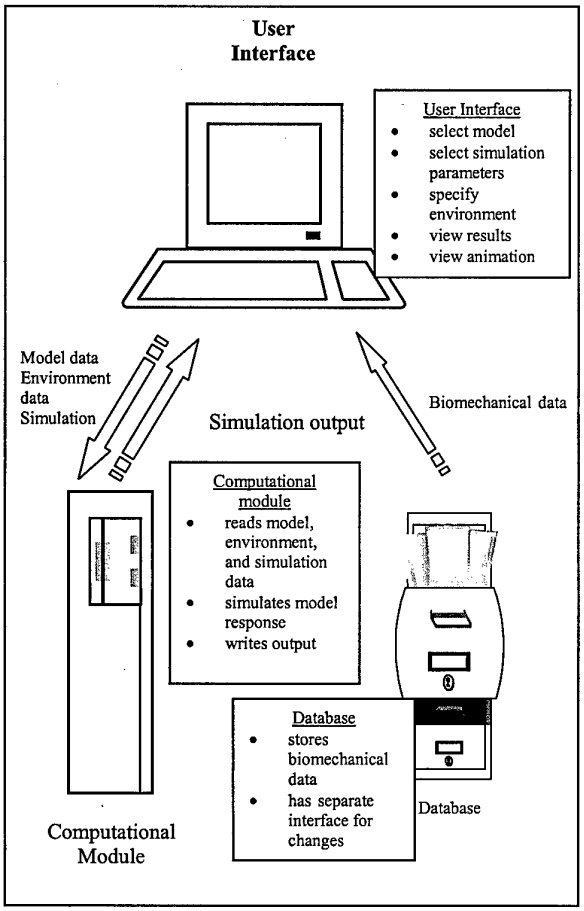

Simulations:

BRC conducted simulations with the several versions of the HSM model. The simplest version, the Head Cervical Spine Model (HCSM) was determined to be stable under gravity. Thus, BRC allowed this model to reach a "settled" position before loading the model.

Since the HCSM model was the most stable, BRC conducted a series of 3 simulations with the model forced at the thoracic first vertebra along the X (forward), Y (lateral), and Z (vertical) axes. The simulations were all started at the settled position described above. The response of the model to a 5.1 G vertical acceleration is shown in Figure 6. Figure 7 shows the response of the model to a 5.1 G forward acceleration. Finally, Figure 8 shows the response of the model to a 5.1 G lateral acceleration. Springs were used to attach the environment plane to T1 to avoid having the model loaded at multiple nodes by a plane. Note that the vertical and forward acceleration simulations result in sagittal plane motion of the head because the model is symmetric across the sagittal plane.

Figure 6 HCSM with 5.1 G Vertical Acceleration

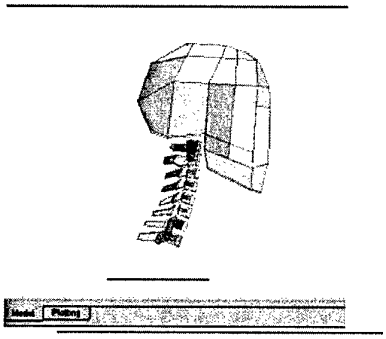

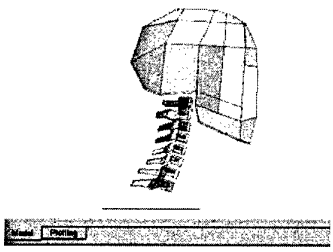

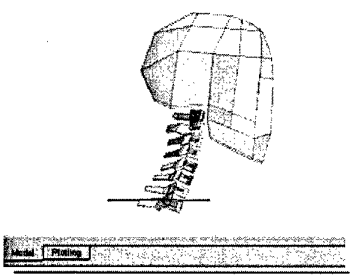

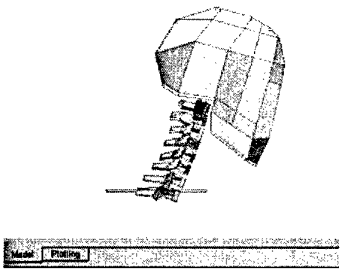

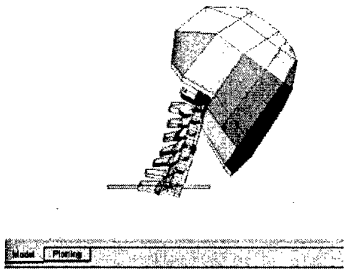

Figure 7 HCSM with Horizontal 5.1 G Acceleration

Figure 8 HCSM with Lateral 5.1 G Acceleration

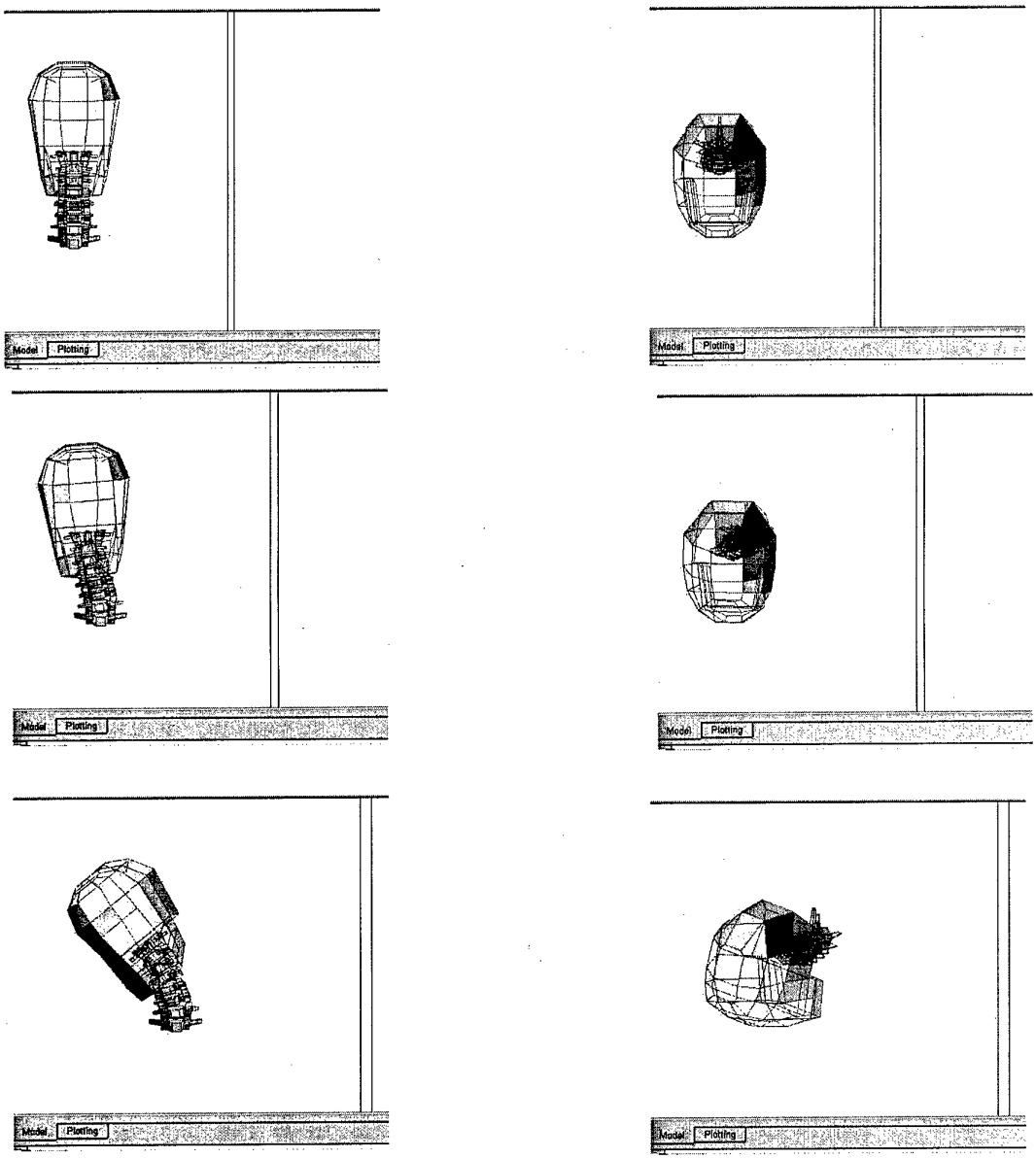

Conclusions:

BRC has created a development roadmap for the commercialization of HSM-PC, displayed in Figure 9. The plan calls for the HCSM to be improved and validated first, before proceeding to more complex models. The HCSM was the most stable of the models, probably because of the inclusion of neck muscles. It represents a good starting point for HSM-PC improvements. The first step will be to carefully audit the biomechanical and geometric data in the model. A muscle model with position feedback control would assist in positioning the model before simulations. Constraining the relative motion between vertebra and other elements would insure that motion was realistic.

With a validated HCSM, lumped lower spine bodies and elements will be added to obtain a simple complete model. The general response of this model will be validated before proceeding to the full HSM-PC.

Work on the full HSM-PC would include adding a full compliment of improved muscles to the spine below the Cervical Spine; standardization of element properties; addition of injury prediction models; improvements to disc models; and the addition of motion limits to all vertebrae. A hydrodynamic model for the viscera will also be added to provide a more realistic load path through the thorax and abdomen.

Improvements to the Environment Model are needed to develop an improved restraint model, allowing forces and moments to be employed as forcing functions in addition to the present kinematic forcing functions.

Graphic User Interface improvements will provide the ability to add or remove rigid bodies to create a new model by modifying an existing model. This would allow replacement of subsections of the spine with lumped models to reduce the total degrees of freedom in the model. Also, the GUI would include an injury estimation post-processor to aid analysis of force, moment, and motion results.

Figure 9. BRC Development Roadmap

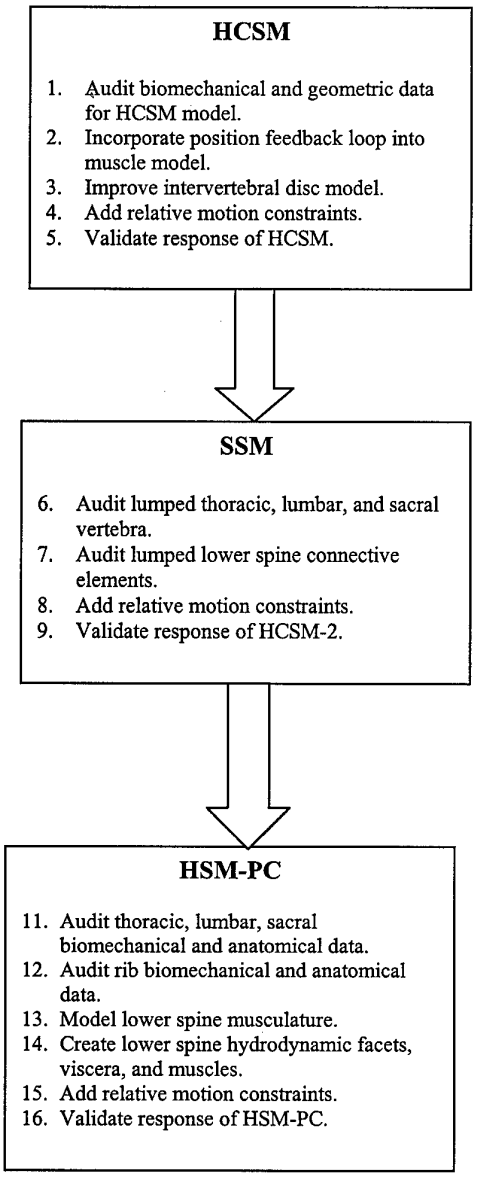

References

[1]Belytschko T., Schwer L., and Schultz A. A Model for Analytic Investigation of Three-Dimensional Head-Spine Dynamics. AMRL-TR-76-10; 1976.

[2]Belytschko T. and Privitzer E. Refinement and Validation of a Three-Dimensional Head-Spine Model. AMRL-TR-78-7; 1978.

[3]Williams T. and Belytschko T. A Dynamic Model of the Cervical Spine and Head. AFAMRL-TR-81-5; 1981.

[4]Belytschko T., Williams J., and Rencis M. Head-Spine Structure Modeling: Enhancements to Secondary Loading Path Model and Validation of Head-Cervical Spine Model. AAMRL-TR-85-019; 1985.

[5] Dietrich, M., and Kedzior, T. A Biomechanical Model of the Human Spinal System. Proc. Instn. Mech. Engrs. Vol 205, Part H:19-26, 1991.

[6] Soechting, J.F. and Paslay, P.R. A Model for the Human Spine During Impact Including Musclature Influence. J. Biomech. 6:195-203, 1973.

[7] Huston, R.L., Huston, J.C., and Harlow, M.W. Comprehensive, Three-Dimensional Head-Neck Model for Impact and High-Acceleration Studies. Aviat., Space, and Environ. Med. 49(1):205-210, 1978.

[8] Merrill, T., Goldsmith, W., and Deng, Y.C. Three-Dimensional Response of a Lumped Parameter Head-Neck Model Due to Impact and Impulsive Loading. J. Biomech. 17(2):81-95, 1984.

[9] Farfan, H., Gracovetsky, S., and Helleur. Cervical Spine Analysis for Ejection Injury Prediction. AFOSR-TR-33, Air Force Office of Scientific Research, Bolling AFB, D.C. Nov, 1982.

[10] De Jager, M., Sauren, A., Thunnissen, J., and Wismans, J. A Global and a Detailed Mathematical Model for Head-Neck Dynamics. SAE 962430. Society of Automotive Engineers, Warrington, PA, 1996.

[11] Yoganandan, N., Kumaresan, S., Voo, L., and Pintar, F.A. Jou. Biomech. Engr. 119(2):87-92, 1997.

[12] Gracovvetsky, S., Farfan, H.F., and Lamy, C. A Mathematical Model of the Lumbar Spine Using an Optimized System to Control Muscles and Ligaments. Symposium on the Lumbar Spine II, Othop. Clinics of N. America, 8(1):135-153, 1977.

[13] Lavaste, F., Skalli, W. Robin, S., Roy-Camille, R., and Mazel, C. Three-Dimensional Geometric Modelling of the Lumbar Spine. J. Biomech. 25(1):1153-1164, 1992.

[14] TNO Crash Safety Centre, Delft, The Netherlands. MADYMO User's Manual, Version 5.1, 1994.

[15] Rolfe, J.M. and Staples, K.J. Flight Simulation. Cambridge University Press. New York, NY. (1990)

[16] Apter, J. and Graessley, W. A Physical Model for Muscle Behavior. Biophysical Journal, (10):539-555.(1970).

NECK PERFORMANCE OF HUMAN SUBSTITUTES IN FRONTAL IMPACT DIRECTION

J.S.H.M. Wismans
A.J. van den Kroonenberg
M.L.C. Hoofman
M.J. van der Horst
TNO Crash-Safety Research Centre
P.O. Box 6033, 2600 JA Delft
The Netherlands

1. SUMMARY

In the past several laboratories have conducted human subject tests in order to derive biofidelity performance requirements for crash dummies and computer models. Both human volunteer and human cadaver tests have been conducted. Particularly noteworthy are the human volunteer tests conducted at the Naval Biodynamics Laboratory (NBDL) in New Orleans. In an extensive test program a large number of human subjects were exposed to impacts in frontal, lateral and oblique directions. Detailed analyses of these tests have been conducted and presented in various publications. Based on these results, a set of biofidelity performance requirements was developed. These requirements include trajectories and rotations of the head as well as acceleration requirements and data on the neck loads.

The objective of this paper is to compare the performance of various human neck models with the observed response in the volunteer tests. Concerning mechanical models, the neck of the Hybrid III dummy, which is the dummy currently specified in motor vehicle safety regulations, as well as the neck of the new THOR dummy will be evaluated. It will be shown that the neck of the THOR dummy offers more biofidelity than the Hybrid III dummy neck. Regarding mathematical neck models, a neck model developed in the MADYMO crash simulation program will be evaluated. It will be shown that the mathematical model which includes a representation of vertebrae, ligaments and active muscle response is able to reproduce the observed human subject response more accurately than the available mechanical models.

2. INTRODUCTION

Since 1967, human volunteers have been exposed to impact acceleration experiments in which the kinematic responses of the head-neck system have been measured. Most noteworthy are the experiments conducted at Wayne State University [1,2,3] and at the Naval Biodynamics Laboratory (NBDL) [4,5,6,7] in New Orleans. Fig. 1 illustrates the head-neck motions as they were observed in 15g frontal impact with human volunteers conducted at NBDL.

The results of this type of experiments have been analysed by a number of investigators and were used to define biofidelic performance requirements for crash dummy development. Well-known are the analyses of Mertz and Patrick [3] who defined neck performance requirements on the basis of the relationship between the moment of force about the occipital condyles due to the forces acting on the head and the angular position of the head relative to the torso. The mechanical neck of the Hybrid III dummy, which is the dummy specified in the current motor vehicle safety regulations, has been based on these requirements.

Fig.1 Human volunteer head-neck response in a 15.6 g frontal impact at NBDL

Papers presented at the RTO HFM Specialists' Meeting on "Models for Aircrew Safety Assessment: Uses, Limitations and Requirements", held in Ohio, USA, 26-28 October 1998, and published in RTO MP-20.

However, such a requirement is not a sufficient condition to ensure a humanlike response. In fact an infinitely stiff neck with a flexible joint at the top as a head-junction could theoretically fulfil the conditions defined by Mertz and Patrick. Both Mertz et al. [8] and Melvin et al.[9] discussed the need for additional displacement requirements, such as the trajectory of the head centre of gravity relative to the torso, but no such requirements were formulated by these investigators.

Wismans et al. [10] developed neck performance requirements in which the head trajectories were included. These requirements, which were formulated for frontal, lateral and oblique impacts, were based on the analysis of a large number of human volunteer experiments conducted between 1981 and 1985 at NBDL. In these analyses rotations of T1 were neglected. In 1987, the analyses of the frontal high severity experiments were extended with postmortem human subject (PMHS) experiments conducted at the University of Heidelberg [11]. The impact severity ranged from 15 - 23 g and the test set-up was identical to the set-up at NBDL. The head centre of gravity trajectories were of the same order of magnitude as in the volunteer tests but the head rotations were found to be larger in the PMHS experiments. The differences between the volunteers and PMHS response were largely attributed to the absence of muscle activity in the PMHS tests. In the PMHS tests T1 rotations of more than 20 degrees in frontal direction were observed. Comparison with the T1 measurements in the volunteer tests at NBDL revealed some inaccuracies in the measured volunteer T1 kinematic response, due to non-rigid mounting of the T1 instrumentation to the T1 vertebra.

More recently Thunnissen et. al. [12] performed a new analysis of frontal human head-neck volunteer tests. A correction method was developed to account for the observed errors in the human volunteer T1 response. As a result for frontal impacts a similar set of response data could be developed but now expressed relative to a rotating T1 co-ordinate system, thereby incorporating the rotations of T1. As a consequence the head excursion became smaller than in the earlier analyses.

The objective of this paper is to compare the performance of various human neck models with the observed response in the volunteer tests. Regarding mechanical models, the neck of the Hybrid III dummy, which is the dummy currently specified in motor vehicle safety regulations, as well as the neck of the new THOR dummy will be evaluated. Concerning mathematical neck models, a model with passive and active muscle response formulated in the MADYMO crash simulation program will be evaluated.

3 RESPONSE REQUIREMENTS

The set of biofidelity response requirements to be used here for assessment of the performance of mechanical and mathematical neck models is a subset of data presented in the analysis performed by Thunnissen et al. [12]. This subset consists of (see Fig. 2):

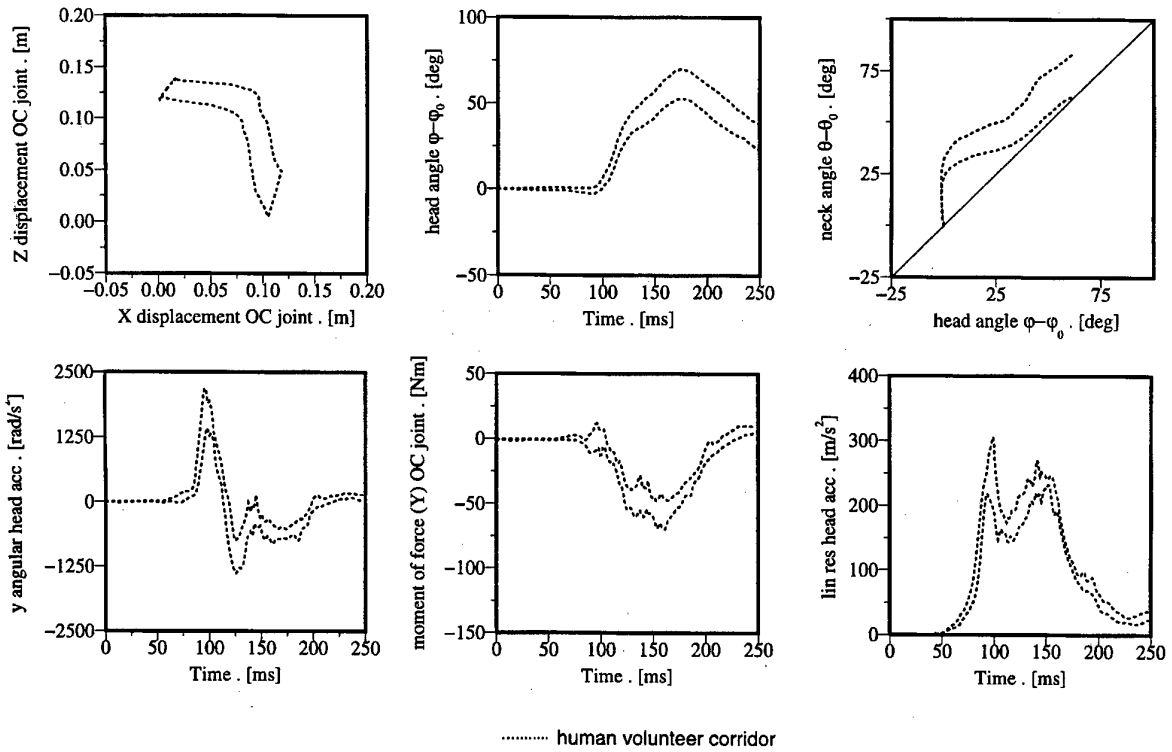

Fig. 2 Response corridors for frontal impacts based on Thunnissen et. al. [12]

1 the occipital condyle (OC) trajectory relative to T1
2 head rotation (flexion) as a function of time relative to T1
3 the neck angle as function of the head angle
4 the mid-sagittal head rotational acceleration as a function of time
5 the mid-sagittal moment of force with respect to the occipital condyles joint
6 the resultant head centre of gravity linear acceleration as a function of time

The neck angle is defined here as the angle between the T1 z-axes and a line connecting the origin of the T1 frame and the occipital condyles. From the neck angle vs. head angle relation, the so-called "head lag" can be observed during the initial part of the motion: the head translates and shows negligible rotation while the neck is already deforming.

The study of Thunnissen et al. [12] was based on 9 sled tests with 5 different subjects. The sled velocity change was 17 m/s and the peak sled acceleration approximately 15 g. The NBDL volunteers were strapped tightly into their seat, allowing just the head, neck and a small part of the upper thoracic spine to deform during the impact. The corridors shown in Fig. 2 represent the mean values minus and plus the standard deviation.

4 MECHANICAL DUMMY NECK PERFORMANCE

Two mechanical neck models were evaluated: the neck of the 50th percentile Hybrid III dummy and the neck of the THOR dummy (fig 3). The THOR dummy is a new frontal crash test dummy which has been developed in the US by GESAC under contract by NHTSA (US National Highway Traffic Safety Administration).

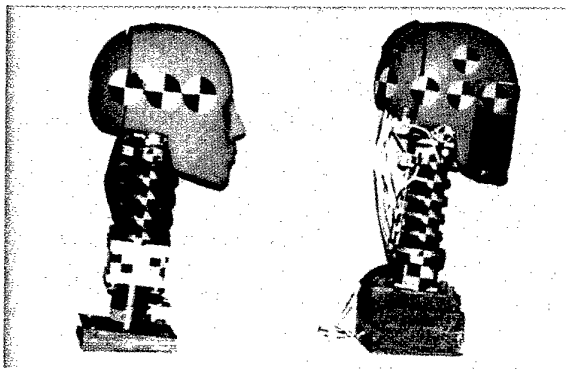

Fig. 3 Hybrid-III Head-Neck System (left) and THOR Head-Neck System (right)

Rather than testing the complete Hybrid III and THOR dummy, only the head-neck assemblies were evaluated . These are placed directly on a HyGe sled. Thunnissen et. al. [12] concluded that the linear T1 acceleration in X direction is the most relevant T1 motion parameter for the head-neck response during frontal impact at this high g level. Therefore, the two dummy head-neck systems are accelerated with a sled pulse equivalent to the average X-acceleration measured at the first thoracic vertebra of the NBDL volunteers (Fig. 4).

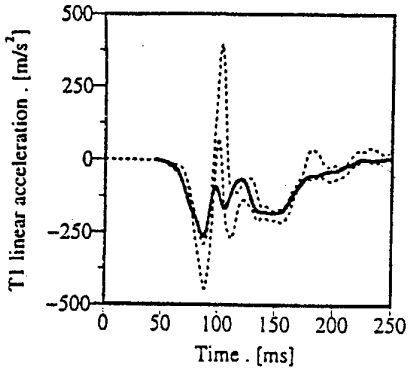

Fig. 4 Sled test acceleration in the dummy neck tests based on T1 accelerations in the NBDL volunteer tests

Figure 5 shows the results for both neck systems together with the frontal neck response corridors. More details of these tests are given by Hoofman et al. [13]. The most striking difference between the two dummy necks concern the occipital condyle trajectories: the trajectory of the THOR dummy approximates the response corridor quite well, only the forward displacement is somewhat too large. The excursion of the occipital condyles joint of the Hybrid-III neck is too small compared to the response corridors, particularly in Z-direction. The head rotation for the THOR dummy appears to be slightly too large. The shape of the head lag curve (neck angle as function of head angle) for the THOR neck is similar to the head lag performance requirement corridor, but still not within the corridor. The Hybrid-III head-neck system shows no head lag. The head angular acceleration of the THOR dummy appears to be quite realistic (the Hybrid-III head was not equipped with a nine accelerometer array). The torque at the occipital condyles joint of the Hybrid-III is too small compared to the requirement (no torque was available for the THOR occipital condyles). The resultant linear head centre of gravity accelerations of THOR and Hybrid-III are similar: both acceleration signals are close to the performance requirement corridor.

5 MATHEMATICAL NECK MODEL PERFORMANCE

De Jager [14] developed a detailed 3D mathematical model of the neck in the crash simulation program MADYMO. The model included the vertebrae as rigid bodies, the facet joints and ligaments. The most important muscles in the neck were represented by simple cord elements connecting the muscle attachment points. Active muscle behaviour was simulated. The model was compared with the frontal (and lateral) volunteer tests conducted at NBDL.

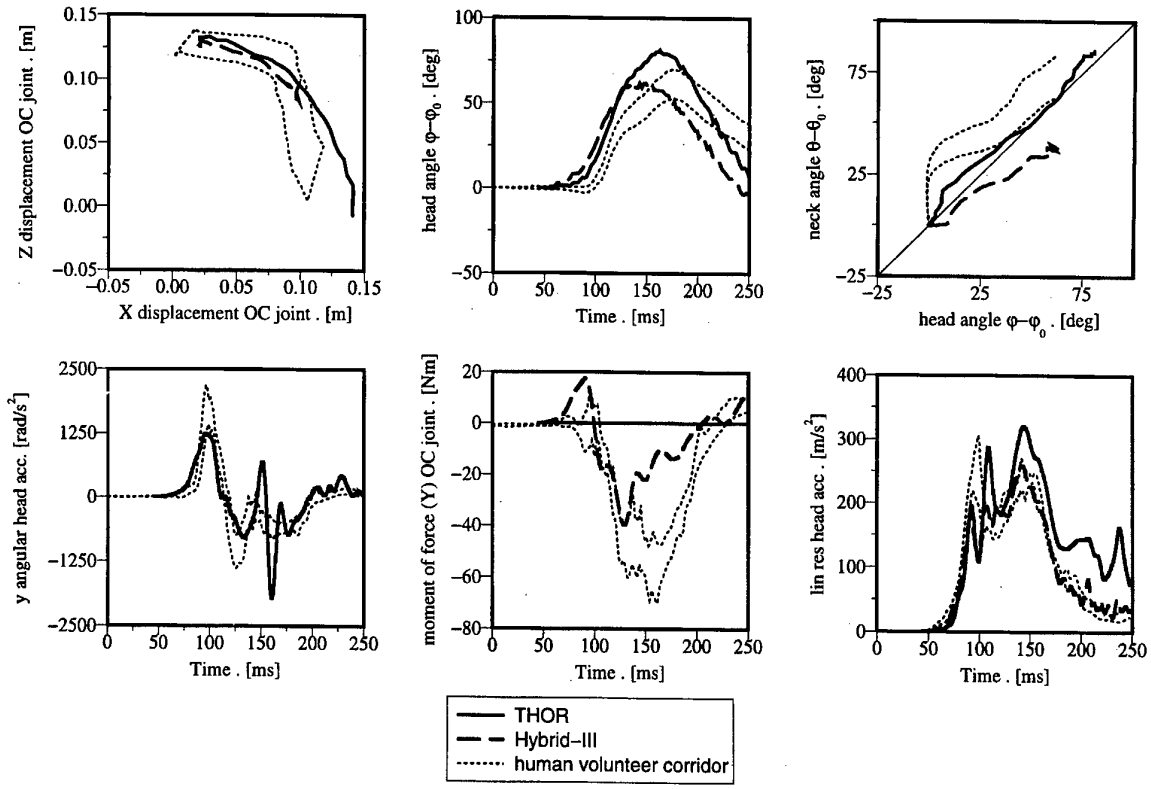

Fig. 5 Results for the Hybrid III and THOR neck in 15 g frontal tests together with a corridor derived from human volunteer tests

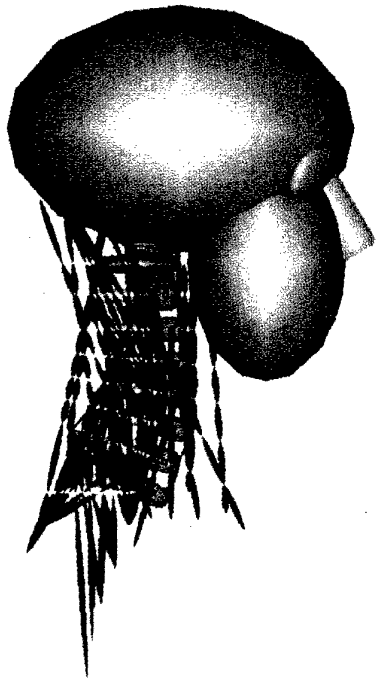

Fig. 6 3D neck model [15]

It was concluded that modelling the neck muscles as simple cords was not satisfactory. For this reason in a later study this neck model was enhanced by using a curved muscle model (fig. 6). Input for the model was the T1 acceleration measured in volunteer tests. Results were presented by van der Horst at the 1997 STAPP Conference [15]. The model was validated for frontal volunteer tests at different severity levels (3g, 6g, 8g, 10g, 12g and 15g). The study showed that muscle contraction has a large influence on the head-neck response.

Fig. 7 shows the model predictions together with the response corridors from the volunteer tests for the 15 g frontal pulse. Results for 2 different muscle activation levels are included, i.e. for passive muscle response (i.e. no muscle activation) and for 100% activated muscles. In case of passive muscle response the neck appears to be too flexible: trajectories and head rotations are much too large. In case of 100% activated muscles, the head-neck response appears to lie largely within the specified corridors for trajectories and head rotations. Also the head lag appears to be predicted accurately by the model with 100% activation level for the muscles. In case of passive muscle response the initial part of the head lag response in not affected. Furthermore it can be observed that the angular and resultant head accelerations are hardly affected by the muscle response. The torque-time histories show difference between the passive and active muscle response, and the active model is closer to the volunteer response.

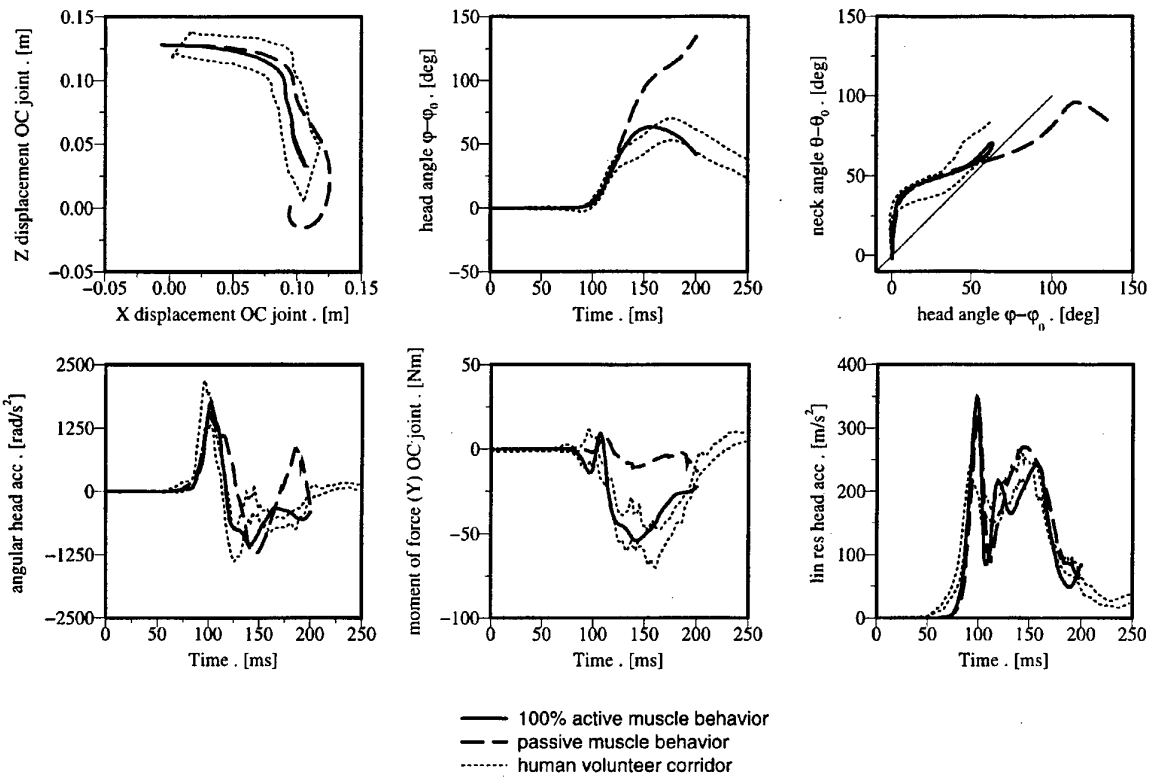

Fig. 7 Results from the 3D MADYMO neck model of van der Horst et al. [15] for passive and 100% active muscle behaviour in 15 g frontal tests together with a corridor derived from human volunteer tests

In the low severity simulations conducted by van der Horst et al. [15] it was observed that a lower activation level of the muscles and a larger reflex delay had to be introduced in the model in order to achieve realistic predictions for the neck response.

6 DISCUSSION AND CONCLUSIONS

A human-like mechanical or mathematical neck model must not only fulfil requirements on the external anthropometry and mass, but it should also describe the dynamic human head and neck response in a realistic way. In this study a set of response data is applied, based on analyses of human volunteer tests performed by Thunnissen et al. [12]. The set consists of occipital condyle trajectories relative to T1, head flexion time histories, the so-called "head-lag" which specifies the relation between the head and neck flexion, the occipital condyle torque time history and angular and resultant linear head acceleration time histories. These response data are more extended than the current Mertz response requirements for the Hybrid III, i.e. head rotation versus moment at the occipital condyles.

In interpreting these response data it should be realised that the tested subjects were young males, recruited from the U.S. navy population (active duty) and screened for good health, no history of cervical spine pain or injury and that they pre-tensed their muscles in order to reduce the effects of the impact. For a general population a less stiff response is expected. Other limitations to be considered include the effect of the volunteer head instrumentation mount, the effect of the initial head-neck position of the volunteers, and the limited impact severity in the volunteer tests compared to real-world crashes causing injuries. See for a discussion on these limitations Thunnissen et al. [12].

The behavior of the Hybrid III and THOR head-neck system has been compared to these response requirements. The comparison shows that the Hybrid III neck is too stiff to respond in a human-like manner during frontal impact. This seems to be a major limitation of the Hybrid III neck since in case of head impact the head might impact the vehicle structure in a different location than when a more biofidelic neck is used. The new THOR neck shows a more realistic response in particular for the head trajectories. But it should be noted that the design of the THOR neck is rather different compared to the Hybrid III neck. For example, the THOR neck is longer than the Hybrid III neck: the T1 location of the THOR neck is located about 65 mm above the neck base [13]. The effect of this is discussed in Ref. [13]. Due to this longer neck it can be questioned whether the selected test method where the measured T1 acceleration in the volunteer tests is applied to the neck base, is valid for the THOR neck. This should be further investigated.

The 3D computer neck model has been formulated in the MADYMO crash simulation program. This program combines both the multi-body and the finite element technique. For the presented model only multi-body techniques were employed. In order to achieve accurate model predictions simulation of active muscle response appeared to be of critical importance. A model with 100% activated muscles appeared to lie almost completely within the specified response corridors and as such appeared to be more humanlike than the THOR neck.

A final interesting observation is that the acceleration response corridors are closely approximated by all models including the models that show only limited biofidelity for the relative head trajectory. Therefore, acceleration based response requirements seem not to be a good discriminator for judging the biofidelity of neck motions.

7 REFERENCES

1 Patrick, L.M. and Chou, C.C. : "Response of the human neck in flexion, extension and lateral flexion." Report no. VRI-7.3, Wayne State University, Detroit, 1976.

2 Cheng, R., Mital, N.K., Levine, R.S. and King, A.I.: "Biodynamics of the living human spine during -Gx impact acceleration." In: Proceedings of the 23th Stapp Car Crash Conference, 1979. SAE paper 791027.

3 Mertz, H.J. and Patrick, L.M.: "Strength and response of the human neck." In: Proceedings of the 15th Stapp Car Crash Conference, 1971. SAE paper 710855.

4 Ewing, C.L. and Thomas, D.J.: "Torque versus angular displacement response of human head to -Gx impact acceleration." In: Proceedings of the 17th Stapp Car Crash Conference, 1973. SAE paper 730976.

5 Ewing, C.L., Thomas, D.J., Lustick, L., Becker, E., Willems, G., and Muzzy, W.H. III: "The effect of the initial position of the head and neck on the dynamics response of the human head and neck to -Gx impact acceleration." In: Proceedings of the 19th Stapp Car Crash Conference, 1975. SAE paper 751157.

6 Ewing, C.L., Thomas, D.J., Lustick, L., Muzzy, W.H., Willems, G. and Majewski, P.L.: "The effect of duration, rate of onset, and peak sled acceleration on the dynamic response of the human head and neck." In: Proceedings of the 20th Stapp Car Crash Conference, 1976. SAE paper 760800.

7 Ewing, C.L., Thomas, D.J. and Lustick, L.S.: "Multi-axis dynamic response of the human head and neck to impact acceleration." In: Proceedings Aerospace medical panel's specialist meeting. AGARD no. 153, 1978.

8 Mertz, H.J., Neathery, R.F. and Culver, C.C.: "Performance requirements and characteristics of mechanical necks". In: Human Impact Response, edited by King, W.F. and Mertz, Plenum Press, NY, 1973.

9 Melvin, J.W., McElhaney, J.H. and Roberts, V.L.: "Evaluation of dummy neck performance." In: Human impact response, edited by King, W.F. and Mertz, H.J., Plenum Press, NY, 1973.

10 Wismans, J.S.H.M., H. van Oorschot and H.J. Woltring: "Omni-Directional Human Head-Neck response". 30th Stapp Car Crash Conference, Proceedings P-189, p. 313-332, San Diego, October 1986. Society of Automotive Engineers Inc.

11 Wismans, J., Philippens, M., Oorschot, E., Kallieris, D. and Mattern, R. : "Comparison of human volunteer and cadaver head-neck response in frontal flexion". In: Proceedings of the 31th Stapp Car Crash Conference, 1987. SAE paper 872194

12 Thunnissen, J., Wismans, JS.H.M., Ewing, C.L. and Thomas, D.J.: "Human Volunteer Head-Neck Response in Frontal Flexion: A new analysis", 39th Stapp Car Crash Conference Proceedings, SAE paper 592721, 1995.

13 Hoofman, M, van Ratingen, M, and Wismans, J.S.H.M.: "Evaluation of the dynamic and kinematic performance of the THOR dummy : neck performance", in: 1998 International IRCOBI Conference on the Biomechanics of Impact, Göteborg, September 16-18, 1998

14 Jager, de M., Sauren, A., Thunnissen, J. and Wismans, J.S.H.M.: "A three-dimensional head-neck model: Validation for frontal and lateral impacts." In: Proceedings of the 38th Stapp Car Crash Conference, 1994. SAE paper 942211.

15 Horst, van der M.J., Thunnissen, J.G.M., Happee, R. Haaster, van R.M.H.P., Wismans, J.S.H.M.: " The influence of muscle activity on head-neck response during impact", 41th Stapp Car Crash Conference Proceedings, SAE paper 973346, 1997.

Validation of the MADYMO Hybrid II and Hybrid III 50th-Percentile Models in Vertical Impacts

J. E. Manning
Simula Technologies, Inc.
10016 South 51st Street
Phoenix, AZ 85044, USA

Dr. R. Happee
Schoemakerstraat 97
P.O. Box 6033
2600 Ja Delft
The Netherlands

1. SUMMARY

This paper describes the results of a project conducted by Simula Technologies, Inc., and TNO to validate TNO computer models of 50th-percentile Hybrid II and Hybrid III test dummies when used in a vertical crash condition. Drop tests were conducted at Simula utilizing military impact conditions for helicopter seat certification. After the tests were conducted, computer models of the simulation were made using the MADYMO 3D Crash Victim Simulation program and the test results were compared. The model showed good correlation to the tests in the parameters of interest.

2. INTRODUCTION

The MADYMO (MAthematical DYnamic MOdel) program is a computer analysis program used in the study of crash simulations and the forces and accelerations imparted to the occupants during these events. The MADYMO program was originally developed with automotive impacts in mind, but the input structure is flexible enough to allow for the evaluation of most kinds of impacts (1). The program provides output which can be used for the study and analysis of occupant reaction and injury parameters, as well as the dynamic and kinematic response of the surrounding environment.

A total of six tests were conducted: three using a 50th-percentile Hybrid II dummy, and three using a 50th-percentile Hybrid III dummy. Each dummy was subjected to the same test series. In one test, the seat and occupant were subjected to a pure vertical deceleration, and in the remaining two tests, the seat and occupant were pitched forward 30 degrees relative to the impact vector. The deceleration pulse utilized was based on information obtained from U.S. Military Specification MIL-S-58095 (Figure 1). The seat used in the drop testing was a crew seat from a UH-60 Black Hawk helicopter (Figure 2).

This paper discusses the correlation obtained between the drop tests and the corresponding computer models. The computer model of the Hybrid III dummy is Revision 5.5, an updated model which will be available as part of MADYMO v5.3.1. Extensive testing has been done on both the component and system level of the Hybrid III (2). The Hybrid II model is Revision 2.1, which will also be available with MADYMO v5.3.1. The current Hybrid II model has 13 bodies for the physical characteristics of the dummy and 13 ellipsoids representing the surface of the dummy, where the modified dummy has a setup similar to the Hybrid III with 32 bodies and 50 ellipsoids. Physical properties for the Hybrid II, such as joint stiffness and force deflection characteristics, were taken from the Hybrid III dummy.

Papers presented at the RTO HFM Specialists' Meeting on "Models for Aircrew Safety Assessment: Uses, Limitations and Requirements", held in Ohio, USA, 26-28 October 1998, and published in RTO MP-20.

3. DROP TESTS

Seat And Restraint

The UH-60 seat utilizes a five-point harness system in addition to an energy-absorbing (EA) mechanism which begins stroking at a pre-defined vertical axial load. The harness consists of two shoulder belts, two lap belts, and one anti-submarining belt. The shoulder belts tie together behind the neck, and the resulting single belt is attached to an inertia reel locking device which was manually locked prior to the testing. All of the belts are connected together by a padded buckle located in the abdominal region (Figure 2).

The downward motion of the stroking seat is guided by two tubes angled 4 deg from vertical, with a maximum possible stroking distance of 45.7 cm (18 in.). In allowing the seat to stroke, forces that normally would be imparted directly to the seated occupant are now limited by the EA to tolerable levels, thus reducing the possibility of severe spinal injury (3).

The seat bucket is made from Kevlar and is reinforced with steel plating placed below the bucket. The seat cushion in an operational UH-60 consists of three layers of foam designed to assist in the reduction of lumbar loads. This cushion was not used in the test, due to the potential difficulty of modeling the non-linear behavior of the multi-layered foam. A wood block, which was assumed to be incompressible, was attached to the seat in place of the cushion. The block was required to position the dummy at the proper height for correct routing of the harness around the lap and shoulders.

Dummies

The Hybrid II (Part 572, Subpart B), and the Hybrid III (Part 572,Subpart E) 50th-percentile dummies used in the tests were manufactured by the Applied Safety Technologies Corporation, formerly Vector Research, Inc., of Milan, Ohio. The Hybrid II was supplied with the straight lumbar spine, while the Hybrid III utilizes the curved lumbar spine.

Test Conditions

All of the dynamic testing was done on the 30-ft indoor drop tower at Simula Technologies, Inc., located in Phoenix, Arizona. The drop tower system is a solid steel cage in which the seat and dummy system are attached. The system is lifted by a winch to a specified height and then released. The cage drops vertically, and is guided by two vertical rails. Deceleration of the cage is provided by stacks of EA paper honeycomb placed below the cage (Figure 3). A program written by Simula is used to determine the drop height, size, and shape of the honeycomb stack required to achieve a specific initial velocity and deceleration pulse. A summary of the dynamic test conditions is shown in Table 1.

The dynamic testing was done according to requirements of MIL-S-58095. Each dummy was subjected to three tests. One test was done using a pure vertical position, Case 3 and 4 (Figure 1), and two tests were done using a modified version of Case 1. Two tests were done for the purpose of repeatability. For Case 1, only the 30-deg pitch was used for the seat; no roll was incorporated. The recorded cage accelerations for all tests were filtered at SAE Class 60 (Figure 4), and used as inputs in the corresponding MADYMO models.

Table 2 provides a complete listing of the data channels recorded for each test.

4. Computer Model

Seat

The seat geometry was converted from an Articulated Total Body (ATB) model, originally defined by Bark and Lou (4). The mass and mass moments of inertia were calculated based on a solid-geometry model of the seat bucket and frame. The EA device was modeled as two rigid segments connected by a translation joint. The load-versus-deflection characteristics of the translation joint were based on available data from the dynamic testing of the EA tubes. The EA data for a set of tubes was combined and applied to the translation joint as joint stiffness properties. For visualization, cylinders were attached to the two segments to represent the stroking EA tubes. A facet seat surface was generated and attached to the seat segment, although all contact interactions between the seat and the occupant were done using plane-ellipsoid contacts (Figure 5).

Review of the test films indicated that fore/aft flexing of the seat tubes was occurring near the floor attachment point. To account for this flex, the joint which connects the seat tubes to the floor was modeled as a revolute joint. Rotational stiffness of the joint was based on documentation from the program SOM-LA (5). Some torsional bending was noted in the test film, but no attempt was made to model this. Lateral flexion of the seat tubes was not noted in the film.

Harness

Both dummies were restrained using a combination of MADYMO conventional belts and finite element (FE) belts. The FE belts were positioned across the surface of the occupant and connected to the buckle and seat with the conventional belt segments. The anti-submarining belt between the seat and buckle was also a conventional belt segment.

The characteristics of the harness system were obtained from static testing done at Simula. For the anti-submarining belt and the lap belt, the pieces were installed in an Instron testing device and pulled at 1 in./min until failure occurred (Figure 6). The testing for the lap belt ended when the buckle of the lap belt snapped. In testing the upper harness, both the right and left sections were pulled at once. Testing for the upper harness was stopped when the belt began slipping in the tension adjuster, a mechanical device used by the pilots to adjust the fit of the belt.

The method for positioning the belts was the same as described in a MADYMO training course and further explained in the MADYMO User's Application manual (6). A model was set up with the FE belts in a flat plane positioned in front of the occupant. Rigid belts connected the FE belts to null systems and all joints of the dummy were locked. Motion was specified for the null systems, moving them to the seat anchor points. The force-strain curves for the rigid belts were defined much softer than the FE belts which allowed the rigid belts to stretch as needed. A long run time is used so that the harness system can move to the final anchor points and allow the FE belts to stabilize on the occupant. The FE nodal coordinate data was then copied to a second dataset for the final simulation.

For the final simulation, the dummy joints were unlocked, the rigid belts were modified to employ the correct force-strain data, and the rigid belt endpoints were attached to the seat instead of to null systems.

4. TEST AND MODELING RESULTS

Hybrid III

The following data acquisition errors were detected during the three tests with the Hybrid III dummy:

- The string potentiometer measuring seat stroke failed in all three tests
- The left shoulder belt load transducer in test 971094
- The neck shear force for all three tests.

The Hybrid III model used for the correlation study is an updated version available in the MADYMO v5.3.1 release. Enhancements made to the dummy model include:

- A new revolute-translation joint for the knees
- The foot and ankle, which are based on the FTSS 45-deg soft-stop ankle and foot
- Shoes implemented as separate bodies
- Additional ellipsoids defined for tibias
- Improved lumbar spine model
- Improved hip model based on the modified femurs available for the Hybrid III
- Improved mass redistribution around the lower lumbar and upper lumbar load cells.

Hybrid II

The following data acquisition errors were detected during the three tests with the Hybrid II dummy:

- The string potentiometer for Test 971089
- The neck of the Hybrid II broke during the latter portion of Test 971090.

The breaking of the neck occurred near the base of the neck after the seat fully stroked. Due to the

timing of the break, the failure is not apparent in the time duration used for the simulation. Depending upon the physical condition of the neck during this test and the previous test, some additional error could be present in the head accelerometer readings. The last test of the Hybrid II, Test 971092, was done utilizing a different dummy.

The Hybrid II computer model used for this study differs from the current production dummy in both shape and physical properties. The ellipsoid and joint properties have been copied and scaled from the v5.2 Hybrid III model. This enhanced dummy will also be available in MADYMO v5.3.1.

In addition to the enhancements made to both dummies, MADYMO v5.3 offers new features for the interactions between the ellipsoids and the nodes of a FE model. The new capability allows nodes to penetrate the surface of the ellipsoid, which can be used to represent compression of dummy skin.

The new contact feature was critical to this correlation study. The original correlation effort incorporated the inelastic ellipsoid-node algorithm which considers the ellipsoid as a rigid surface and the node as a point mass. When the position of a node is below the surface of an ellipsoid, it is placed back on the surface and contact forces are calculated. This contact force considers the relative velocity of the contact surface and the node in addition to the properties of the belt material (2).

Using the rigid surface contact method for the lap belt posed many difficulties. The placement of the belt is such that there is interaction with the ellipsoids for the hips and abdomen. During the stroking of the seat, the upper torso rotates forward. While this is occurring, the belt attempts to slip rearward on the hips but cannot, since contact with the abdomen requires the belt to stay at the surface of the abdominal ellipsoid. This action generated belt loads much higher than those recorded during the actual testing. The only alternatives that would lower the belt forces were either softening the belt properties or removing the contact with the abdominal ellipsoid and using an artificially high friction coefficient for the contact between the hips and belt. Both of these solutions were not deemed to be viable.

With the release of MADYMO v5.3, comes the capability to define an elastic ellipsoid-node contact. The compression characteristics of the dummy skin could then be used as part of the contact definition with the lap belt. This allowed the lap belt to slide back on the hips while at the same time partially penetrating the abdomen, simulating abdominal compression and thus reducing the lap belt loads in the simulation.

5. DISCUSSION

Head

The head accelerations recorded in the four 30-deg tests correlate reasonably well to the corresponding models in both the X (fore/aft) and Z (vertical) direction (Figures 7 and 8). During the first 60 msec of the tests, the dummy translates forward in the seat without noticeable upper body rotation. At about 60 msec, the forward motion of the dummy stops and the chest begins to compress due to belt loading. At this time, the head and neck begin to rotate. Some variance does occur during the 60-70 msec period. In the models, the dummy translates forward, but there is also some rotation of the upper body. Therefore, the rotation of the head and neck, relative to the upper torso, occurs later for the model than it does for the test. However, the primary peak, which occurs around 100 msec, matches well between the test and model.

For the vertical simulations, the head acceleration in the X direction has the trend of the test, but does not have the abrupt changes. A possible cause to this difference might be in the flex of the seat. In the film, it can be seen that as the seat flexes forward around 30 msec post-impact, the back of the dummy is pushed forward by the seat. In the model, interactions between the ellipsoids of the dummy's back and seat planes do not completely capture this reaction. For the Z component, the Hybrid II matches very well to the test, while the Hybrid III model has the correct shape, but occurs slightly sooner than the test.

Since the model does not account for torsional rotation of the seat, the Y component (lateral) of the accelerations were not considered in this report.

The X component of the chest acceleration for all 30-deg models is very similar to the test in both the peaks and overall shape of the curves (Figures 9 and 10). The Z component correlates well with a minor difference in the 40-60-msec region. The difference appears to be caused by the upper body rotation seen in the model and not in the test. When the upper torso region of the dummy begins to pitch forward, the Z component of the chest accelerometer reverses direction.

For the vertical simulation, the shape of the X component is representative of testing, while the peak values are slightly greater. Similarly, the Z component of the Hybrid II is a close match to the test, while the primary peak for the Hybrid III model is a little greater than seen in the test.

The accelerations for the pelvis generally correlate to the test for all three Hybrid III simulations (Figures 11 and 12). The X components were consistent in shape to the test, but tend to just miss the peaks. The Z component of the 30-deg cases matched the shape, timing, and peak values of the test, but failed to predict the second of three peaks which occurred in both tests. Due to the many interactions which occur with this body segment (belt interaction, buckle interaction, seat contact), minor differences are not unexpected.

The Hybrid II model under-predicted the pelvic acceleration of the test, and yet the shapes were very similar. Like the Hybrid III, the amount and complexity of the interactions involving the pelvic region can create these differences.

The lumbar forces and moments are shown in Figure 13 through15. The compressive forces on the lumbar correlate well to the test, while the shear force does in the beginning, but it is a little soft during the latter portion of the test. In the 30-deg tests, the shear force begins in the same fashion as the test, but as many different loads start acting on the occupant, the model under-predicts the test results. In the vertical tests, the shear force is more closely represented, due to the reduced amount of shear force acting on the lumbar.

The lumbar moment also displays some minor discrepancies when compared to tests. For the 30-deg model, the shape is consistent with test, but the magnitudes differ. Here, the values seen are greater than those recorded in the test. The combination of the model predicting greater bending moments and lower shear forces indicates that the lumbar in this particular Applied Safety Technology dummy is stiffer than the lumbar used in the building the MADYMO dummy.

Difficulty in predicting the lumbar shear force is likely due to the complexity of the interaction. Part of the load acting on the lumbar is passed through contacts with the pelvis or legs in addition to the abdomen and ribs. These are modeled separately in the dummy database, based on testing of a First Technology Safety Systems (FTSS) dummy. The correct representation of this is non-trivial, and some differences may exist between the FTSS dummy used to build the MADYMO dummy and the Applied Research dummy used in the test. Additionally, component testing at TNO has shown that there are differences in the stiffness between individual FTSS lumbar spines (7).

The dummy neck loads and moments are shown in Figures 16 and 17. Please note that the Hybrid II dummy does not have the ability to record neck loads or moments. Thus, the following discussion relates only to the Hybrid III dummy.

The fore/aft neck shear force differs significantly between the test and the computer model. Review of the film leads to the conclusion that the recorded shear values are incorrect, and that the actual values should have been higher. As a means to clarify this, several additional neck force plots were reviewed from tests involving either a nose-down or combined nose-down and yaw condition. The shear values recorded for those tests indicate a trend similar to that seen in the MADYMO model.

The neck moments for the model have a shape similar to that of the test, but are not as abrupt in occurrence as the test. For the nose-down tests, the cause would likely be the forward rotation of the upper torso seen in the model. Since the upper torso of the dummy rotates with respect to the lower torso, the bending moment between the neck and upper torso was reduced.

Comparison of the compressive loads for all three tests shows a very good correlation.

The belt loads are compared in Figures 18 through 21. In the 30-deg tests, the shoulder belt loads are high, but they have a similar shape. The lap belt loads reach the same peak, but do not unload like those of the test. The probable explanation for the difference could be that interference from the occupant during the test caused a mis-reading. The load transducer for the lap belts were placed on the upper leg, as close as possible to the free space between the dummy and the bucket. The shoulder belt transducers were placed on the upper portion of the chest, several centimeters below the clavicle. The ideal placement for the belt load transducer is off of the occupant on a piece of belt material that would not have any interaction with the dummy or seat. However, due to the tight confinement of the seat bucket, there was not enough space to accommodate this desired configuration.

Plots of the head motion are shown in Figures 22 and 23. The 30-deg cases for the Hybrid III show a good relationship between the testing and the model up until 60 msec. At this point, the curves begin to differ, due to the upper body rotation seen in the model, but not in the testing. The Hybrid II head motion matches well for Test 971092, but has some variance for the other two tests. Tests 971089 and 971090 were done using the neck which broke during Test 971092. Since the physical status of the neck is uncertain for these two tests, no conclusions about the head trajectories can be made.

Shoulder motion (Figures 24 and 25) correlates well between the model and the test for the Hybrid III in all three tests. For the Hybrid II, there is a timing discrepancy in the fore/aft direction for one 30-deg case (971090) and the vertical test (971089). The difference in the latter case is possibly due to the seat flex in the model not forcing the dummy forward as seen in the test.

6. CONCLUSION

A series of tests were done to validate the use of the 50th-percentile Hybrid II and Hybrid III MADYMO models in vertical applications utilizing military test conditions. The results of the comparisons indicate that the MADYMO models and new contact algorithms available in MADYMO v5.3 provide a good correlation, even when subjected to the extreme deceleration levels used in military helicopter test conditions.

7. REFERENCES

1. TNO, MADYMO v5.3 User's Manual 3-D, TNO Road-Vehicles Research Institute, 1997
2. TNO, MADYMO v5.3 Theory Manual, TNO Road-Vehicles Research Institute, 1997
3. Aircraft Crash Survival Design Guide, (Volumes I through IV), Simula Inc., Phoenix, Arizona
4. Bark, L. W., Lou, K., "Comparison of SOM-LA and ATB Programs for Prediction of Occupant Motions in Energy-Absorbing Seating Systems," American Helicopter Society Conference, 1991.
5. Laananen, D. H., Coltman, J. W., and Bolukbasi, A. D., "Computer Simulation of an Aircraft Seat and Occupant in a Crash Environment, Volume II - Program SOM-LA User Manual", DOT/FAA/CT-82/33-11-2, Federal Aviation Administration Technical Center, Department of Transportation, Atlantic City International Airport, New Jersey, 1983.
6. TNO, MADYMO v5.3 User's Application Manual, TNO Road-Vehicles Research Institute, 1997
7. Happee, R., Abramoski, E., Feustel, J., Kant, A. R., "The Load Path from Upper Legs to Chest in the Hybrid III Dummy; Experiments and Simulations", Enhanced Safety of Vehicles Conference, 1998.

Table 1. Dynamic test conditions				
Test Number	**Condition**	**Dummy**	**Initial Velocity (m/sec)**	**Peak G's**
971089	Vertical	Hybrid II - 50th	13.9	43.6
971090	30-deg - Pitch down	Hybrid II - 50th	15.7	46.4
971092	30-deg - Pitch down	Hybrid II - 50th	15.7	44.3
971093	30-deg - Pitch down	Hybrid III - 50th	16.1	44.6
971094	30-deg - Pitch down	Hybrid III - 50th	16.3	46.6
971095	Vertical	Hybrid III - 50th	14.1	46.1

Table 2. Data channels		
Data Acquisition	**Test Dummy**	
Channel	**Hybrid II**	**Hybrid III**
Cage Acc - North	x	x
Cage Acc - East	x	x
Head Acc - X	x	x
Head Acc - Y	x	x
Head Acc - Z	x	x
Chest Acc - X	x	x
Cheat Acc - Y	x	x
Chest Acc - Z	x	x
Pelvis Acc - X	x	x
Pelvis Acc - Y	x	x
Pelvis Acc - Z	x	x
Lumbar Force - X	x	x
Lumbar force - Z	x	x
Lumbar Moment - Y	x	x
Neck Force - X		x
Neck Force - Z		x
Neck Moment - Y		x
L Lab Belt Force	x	x
R Lap Belt Force	x	x
L Shldr Belt Force	x	x
R Shldr Belt Force	x	x
Seat Pan Acc - X	x	x
Seat Pan Acc - Y	x	x
Seat Pan Acc - Z	x	x
Seat Stroke	x	x

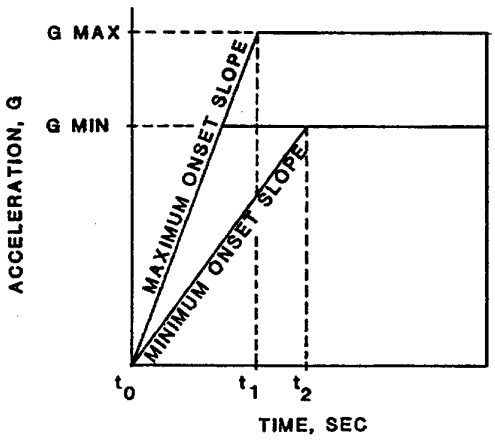

79 01001 294

TEST	CONFIGURATION	PARAMETER	COCKPIT SEATS LIMITS	CABIN SEATS LIMITS
1	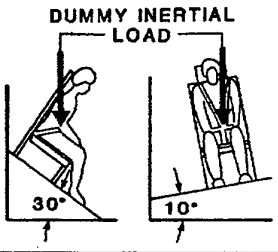	t_1 SEC	0.043	0.059
		t_2 SEC	0.061	0.087
		G MIN	46	32
		G MAX	51	37
		ΔV MIN, FT/SEC	50	50
2	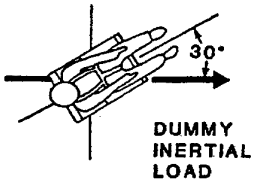	t_1 SEC	0.066	0.081
		t_2 SEC	0.100	0.127
		G MIN	28	22
		G MAX	33	27
		ΔV MIN, FT/SEC	50	50
3&4	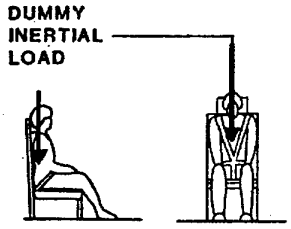	t_1 SEC	0.036	
		t_2 SEC	0.051	
		G MIN	46	
		G MAX	51	
		ΔV MIN, FT/SEC	42	

Figure 1.
Deceleration pulse from MIL-S-58095 used in drop testing.

Figure 2.
Crew seat from a UH-60 Black Hawk helicopter used for drop testing.

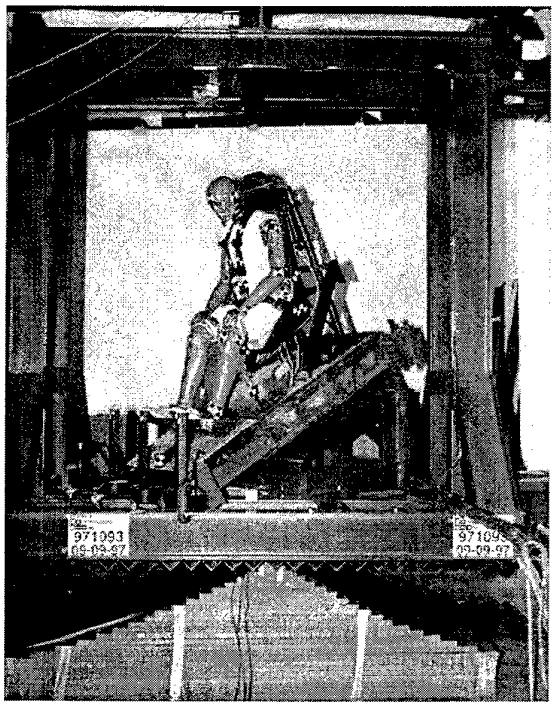

Figure 3.
Drop cage and energy-absorbing paper honeycomb.

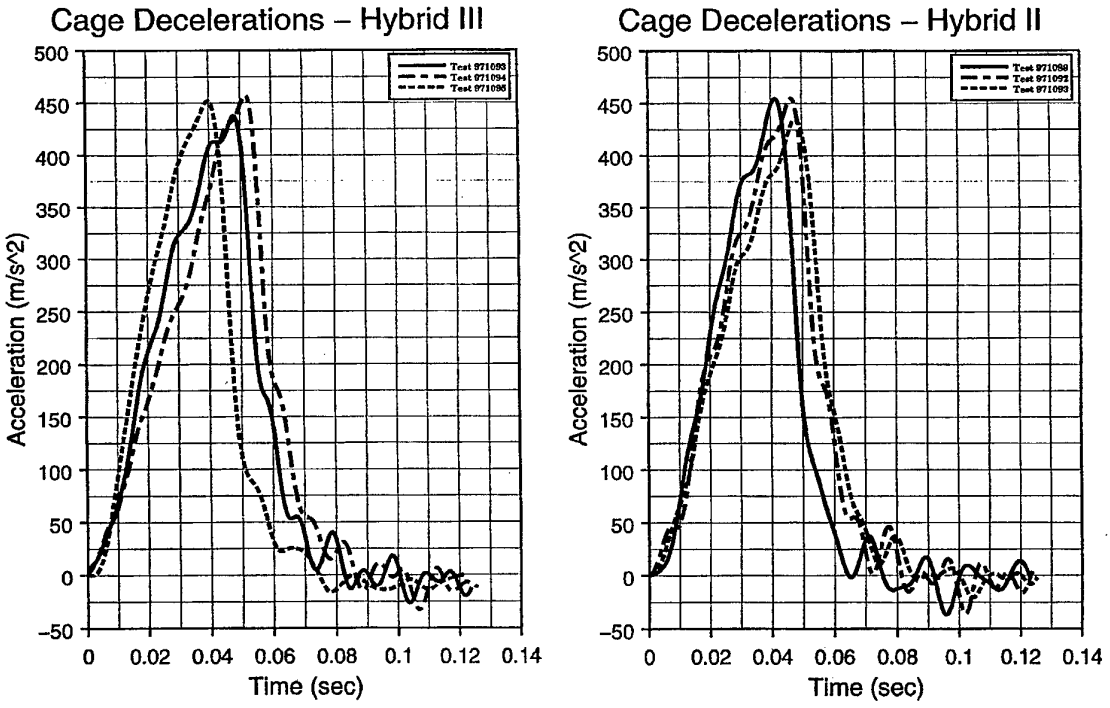

Figure 4.
Cage decelerations.

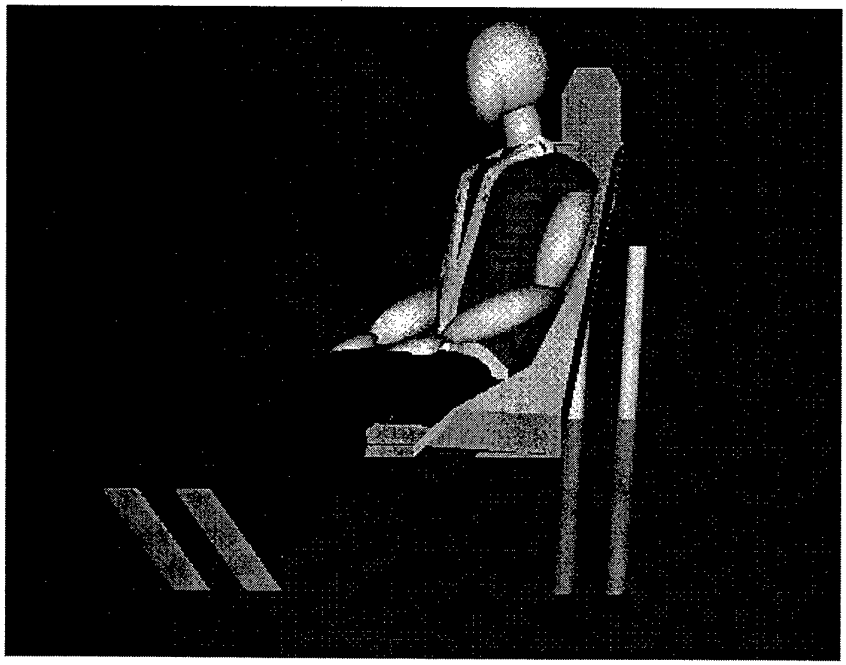

Figure 5.
UH-60 Black Hawk seat with MADYMO Hybrid III 50th-percentile dummy.

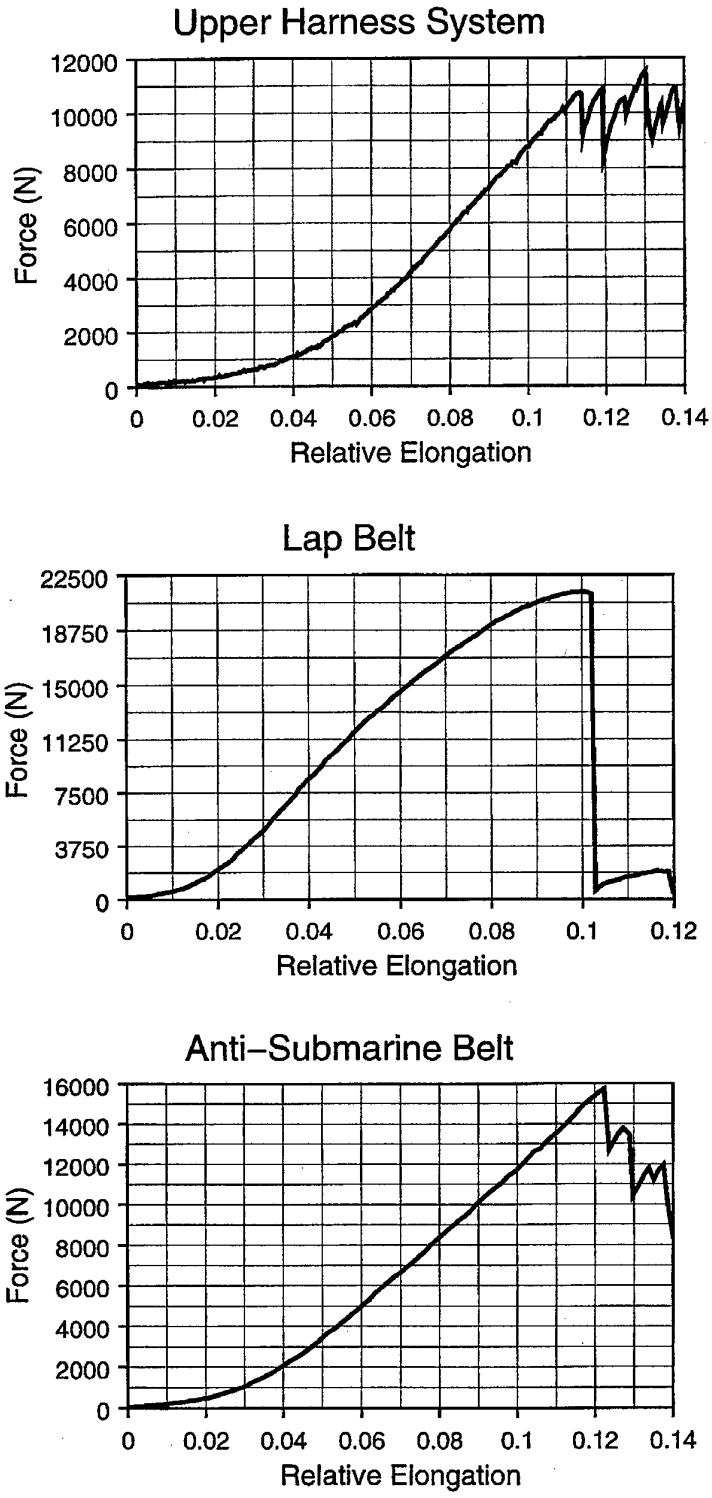

Figure 6.
Pull test of harness system.

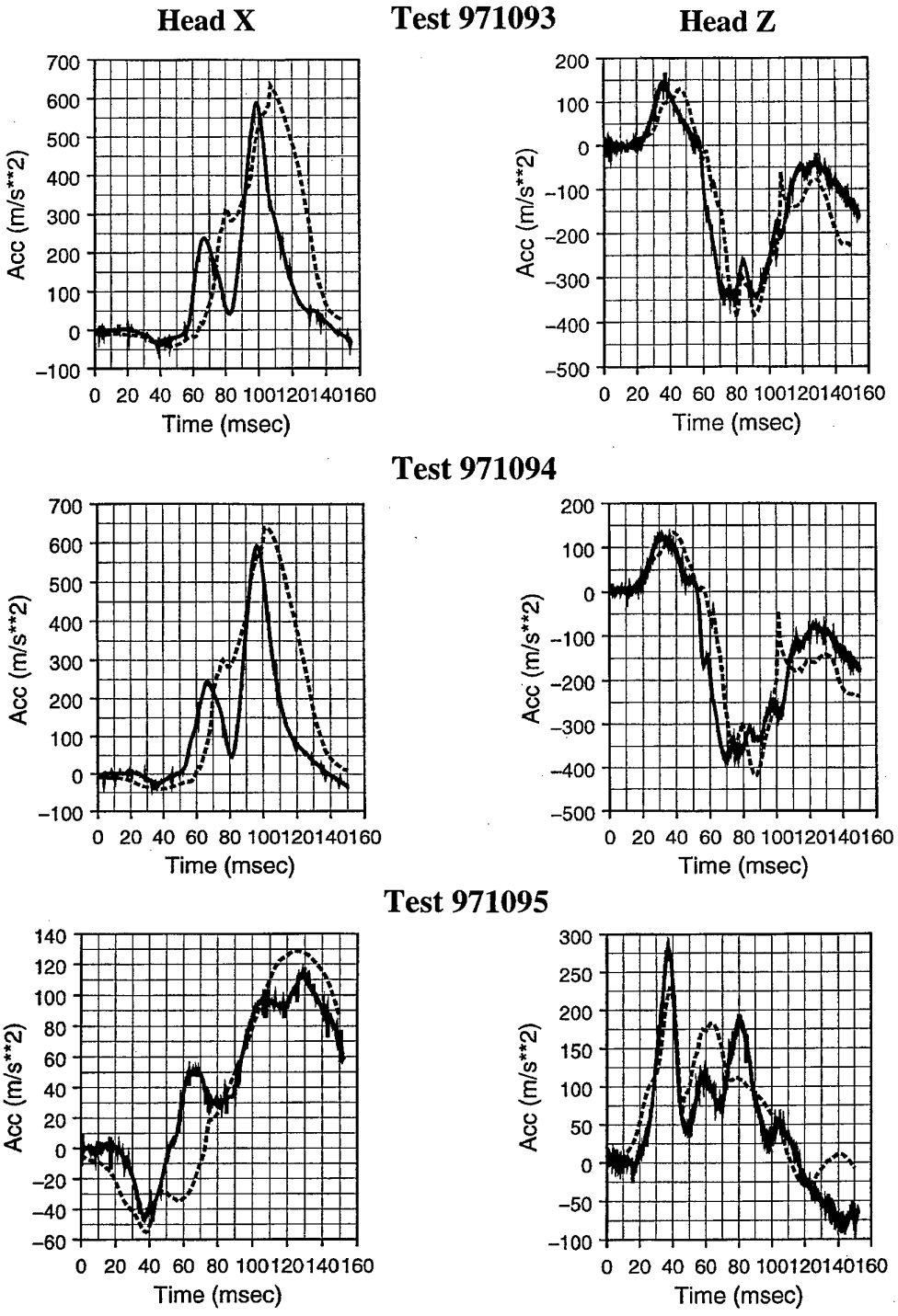

Figure 7.
Head accelerations for the Hybrid III.
(971093 and 971094 - Nose Down; 971095 - Vertical)
(Solid line - Test; Dashed line - Model)

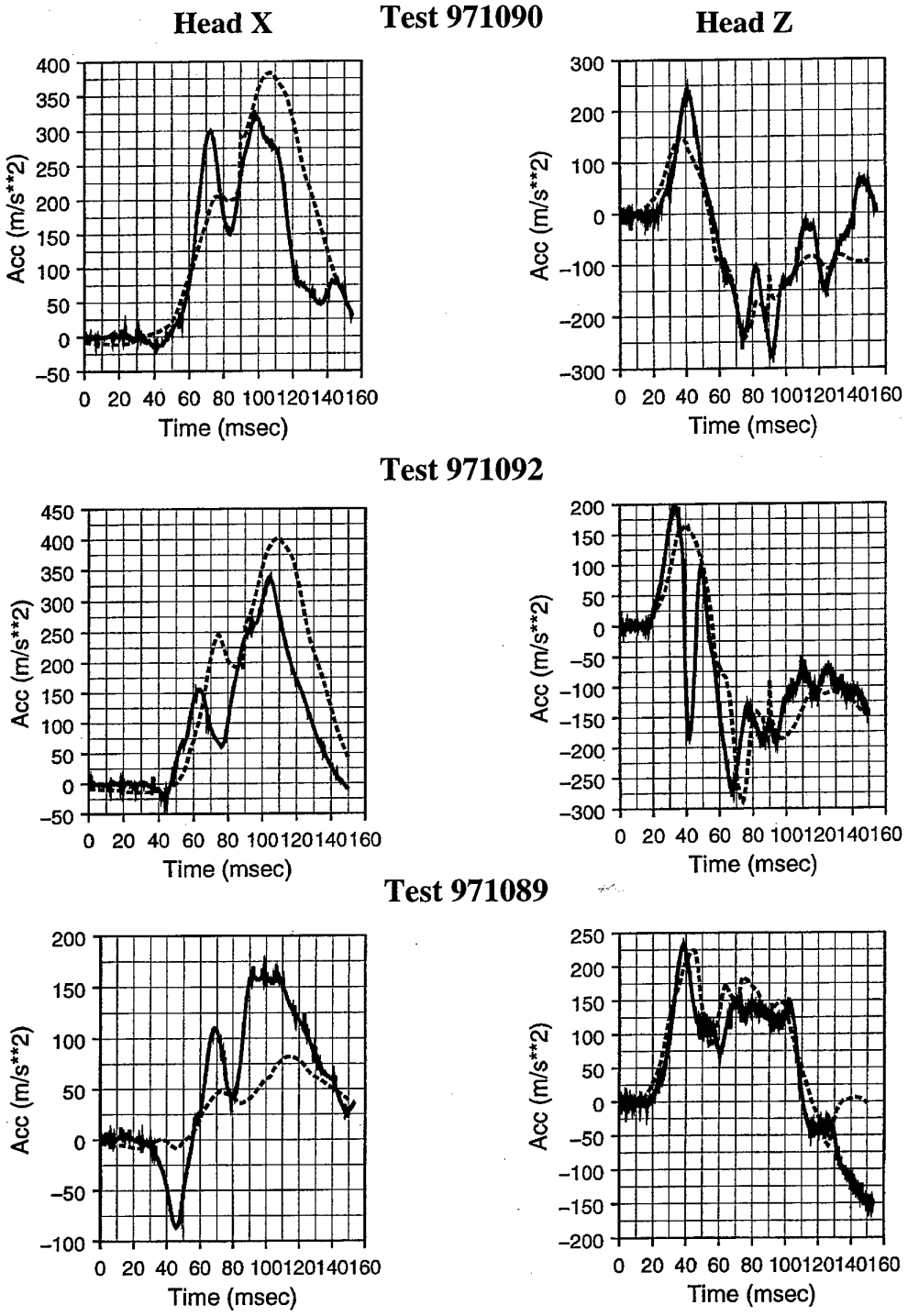

Figure 8.
Head accelerations for the Hybrid II.
(971090 and 971092 - Nose Down; 971089 - Vertical)
(Solid line - Test; Dashed line - Model)

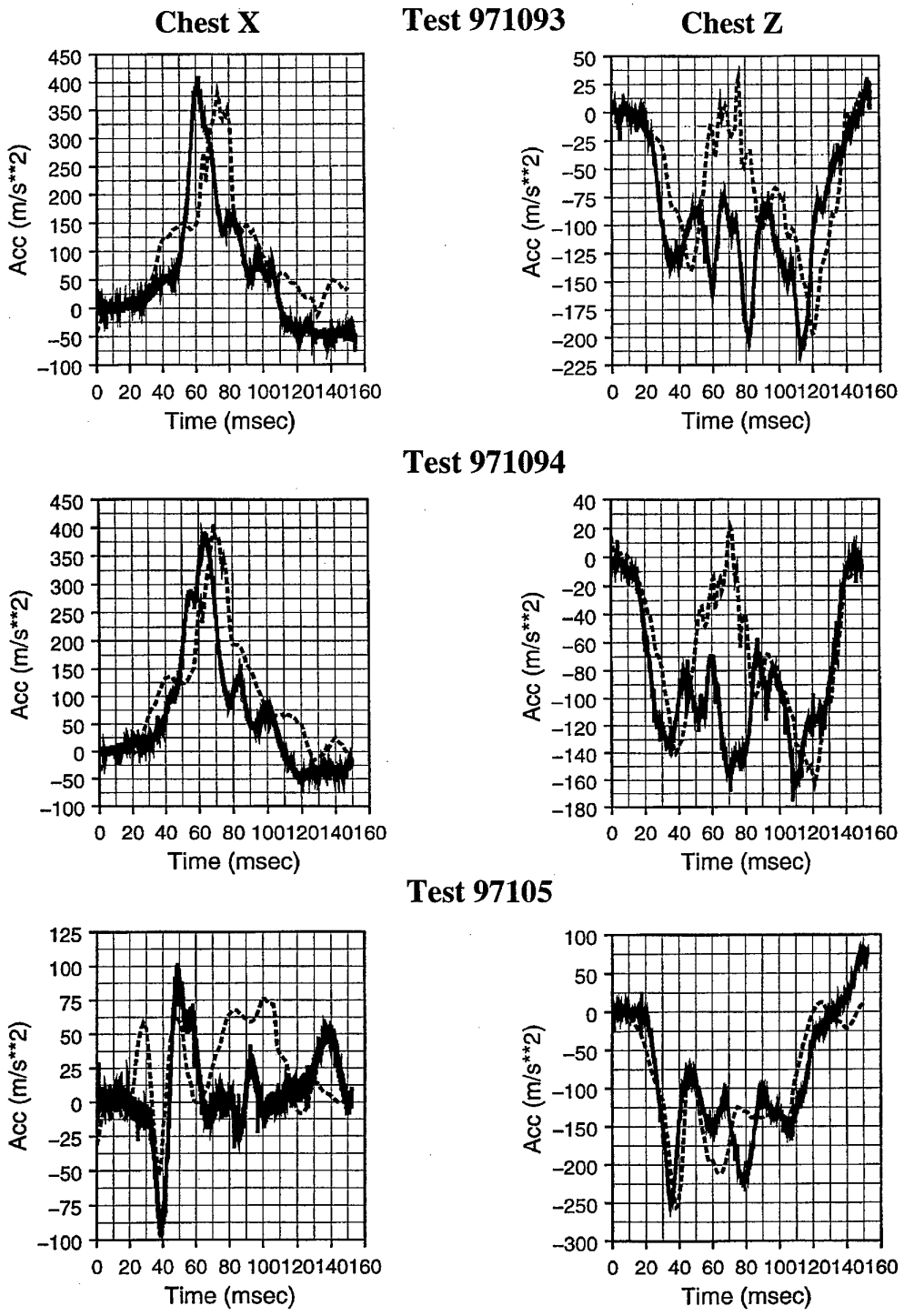

Figure 9.
Chest accelerations for the Hybrid III.
(971093 and 971094 - Nose Down; 971095 - Vertical)
(Solid line - Test; Dashed line - Model)

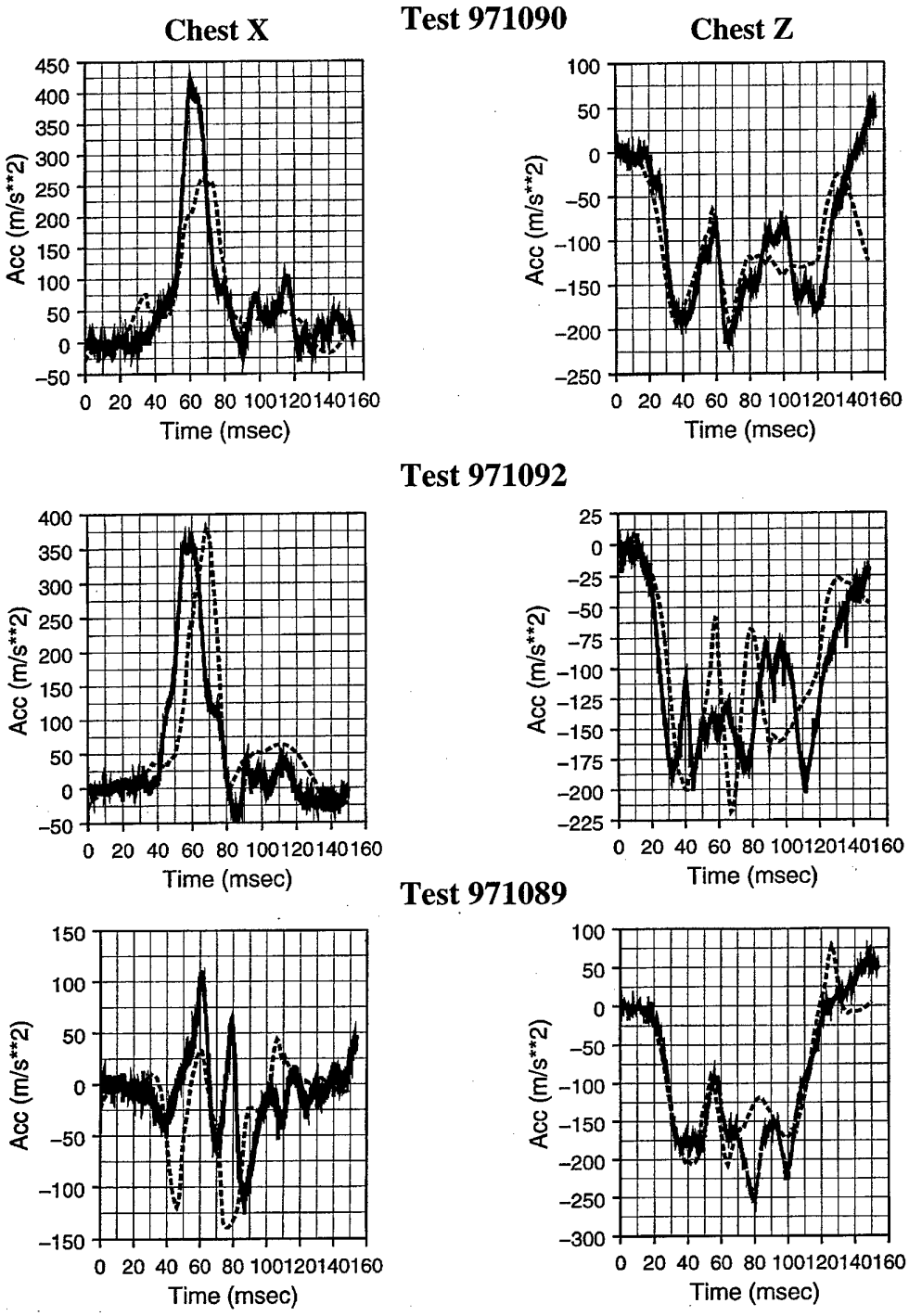

Figure 10.
Chest accelerations for the Hybrid II.
(971090 and 97192 - Nose Down; 97189 - Vertical)
(Solid line - Test; Dashed line - Model)

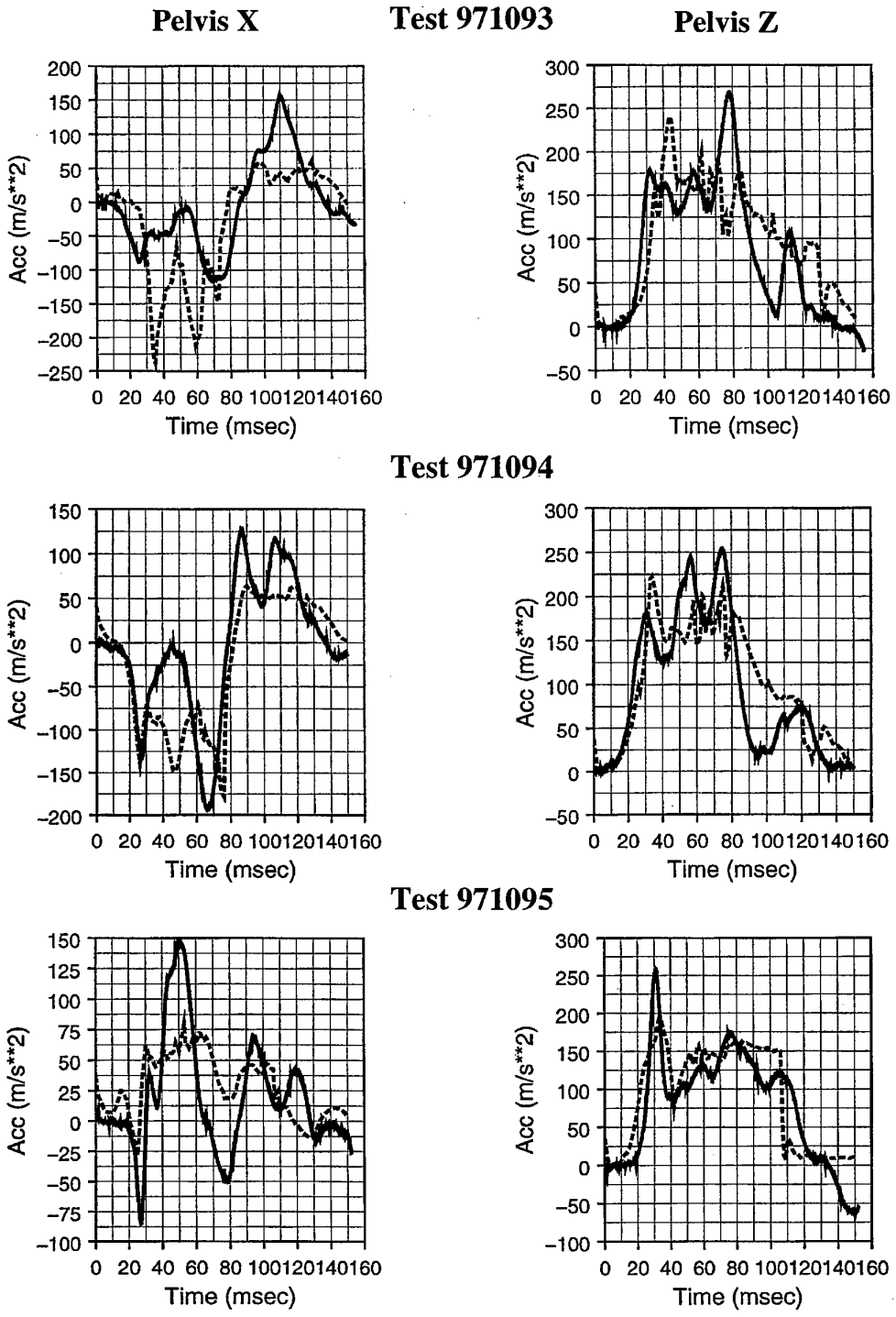

Figure 11.
Pelvic accelerations for the Hybrid III.
(971093 and 971094 - Nose Down; 971095 - Vertical)
(Solid line - Test; Dashed line - Model)

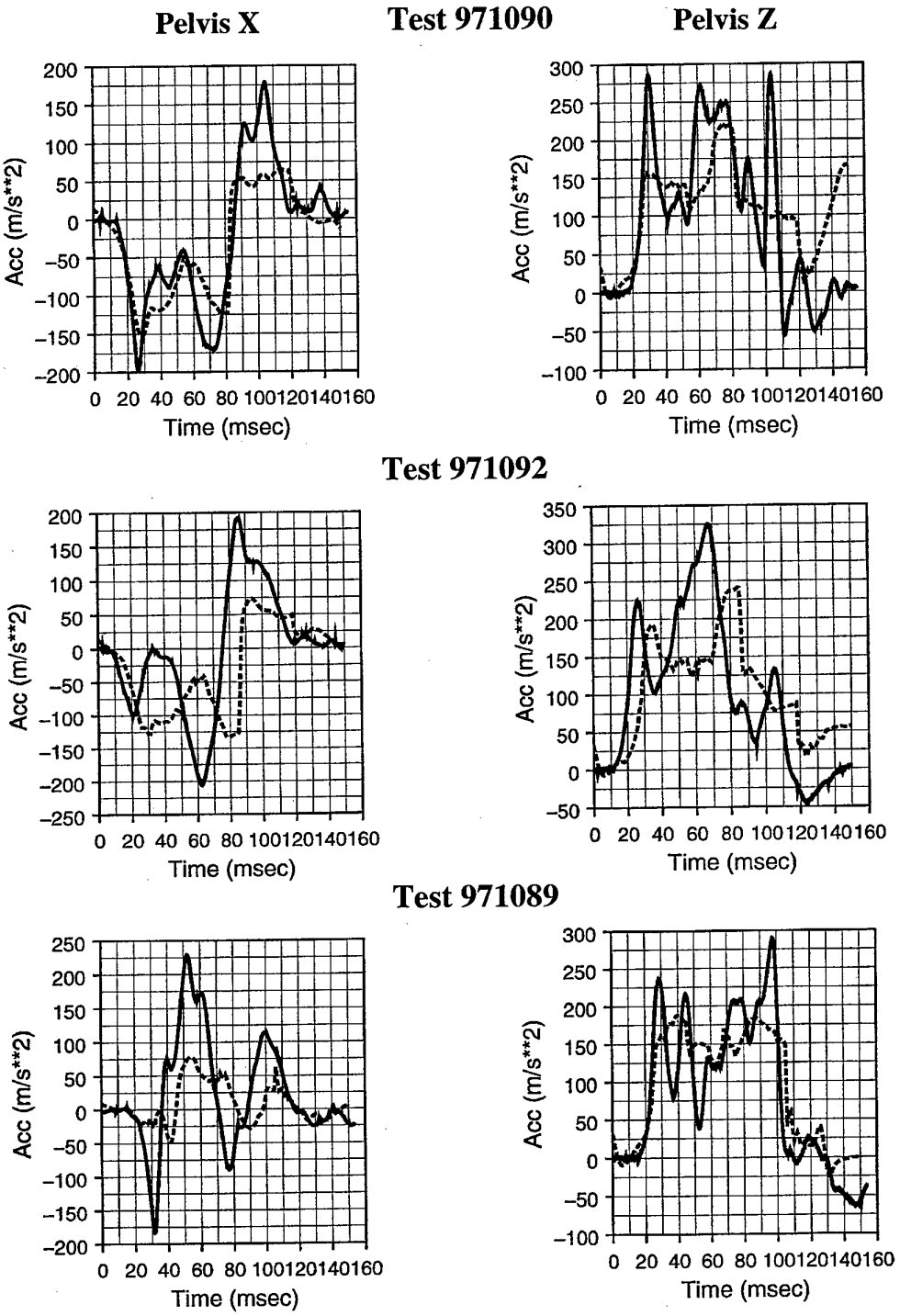

Figure 12.
Pelvic accelerations for the Hybrid II.
(971090 and 971092 - Nose Down; 971089 - Vertical)
(Solid line - Test; Dashed line - Model)

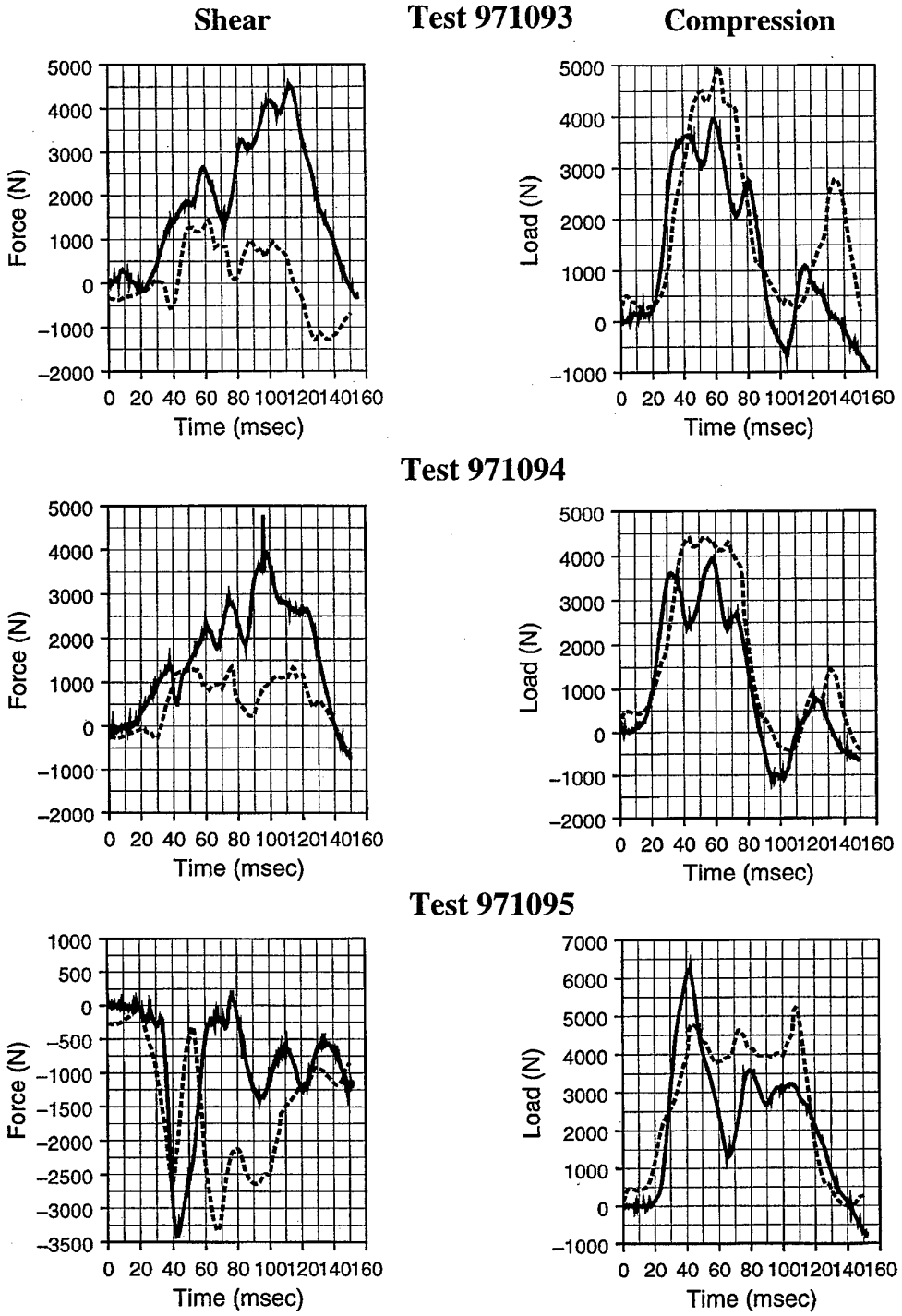

Figure 13.
Lumbar forces for the Hybrid III.
(971093 and 971094 - Nose Down; 971095 - Vertical)
(Solid line - Test; Dashed line - Model)

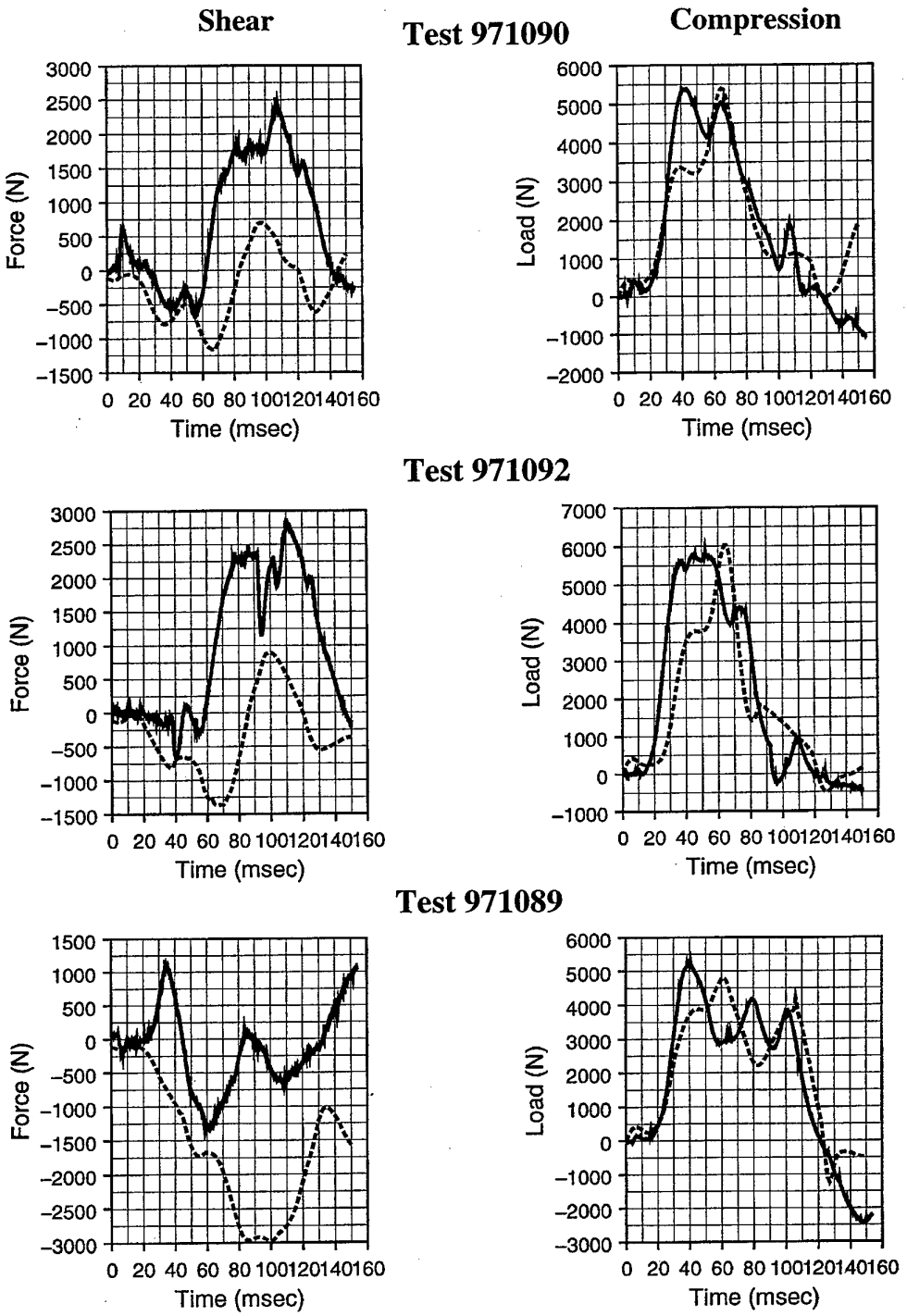

Figure 14.
Lumbar forces for the Hybrid II.
(971090 and 971092 - Nose Down; 971089 - Vertical)
(Solid line - Test; Dashed line - Model)

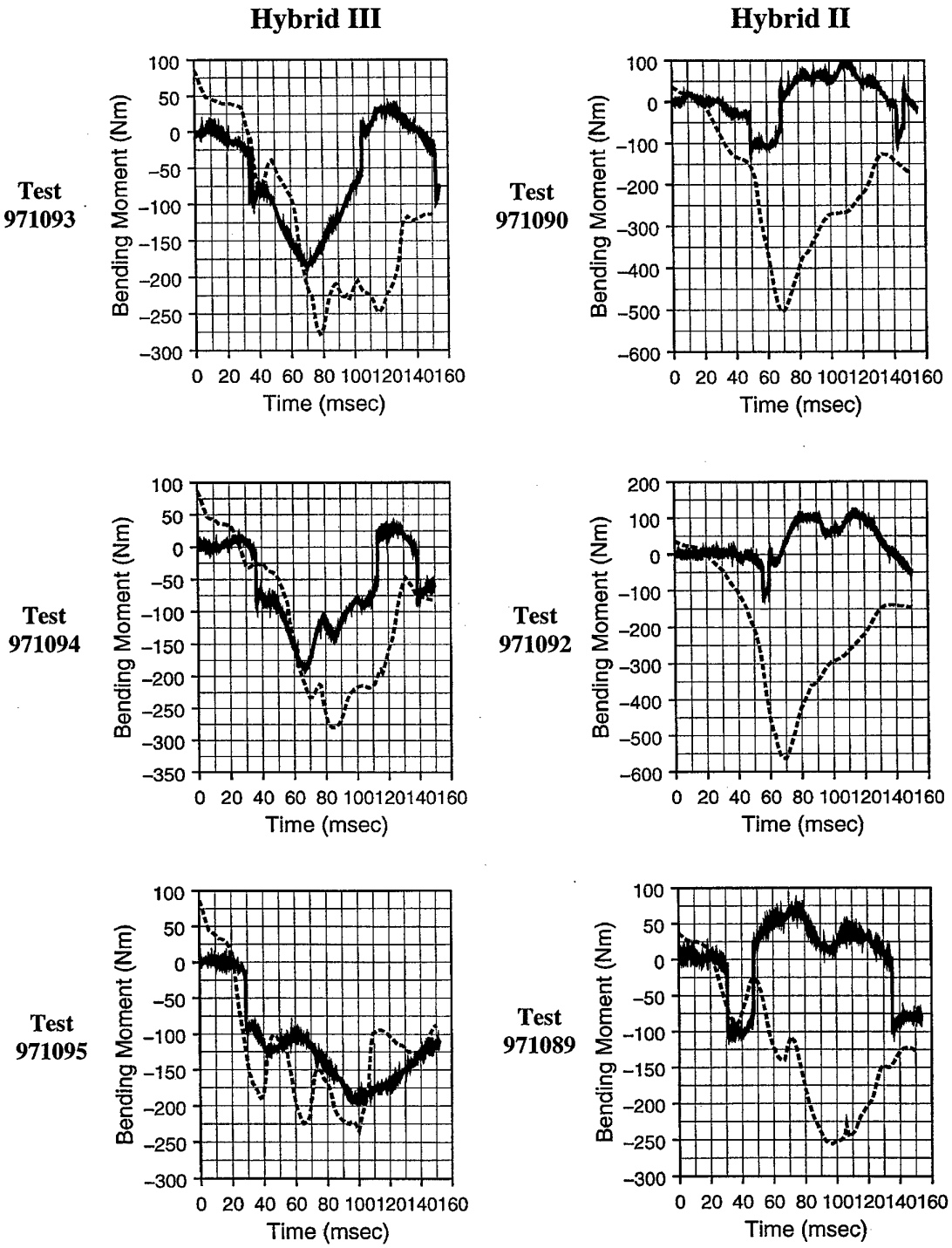

Figure 15.
Lumbar bending forces for the Hybrid III and Hybrid II.
(971093 and 91094 - Nose Down; 971095 - Vertical)
(Solid line - Test; Dashed line - Model)

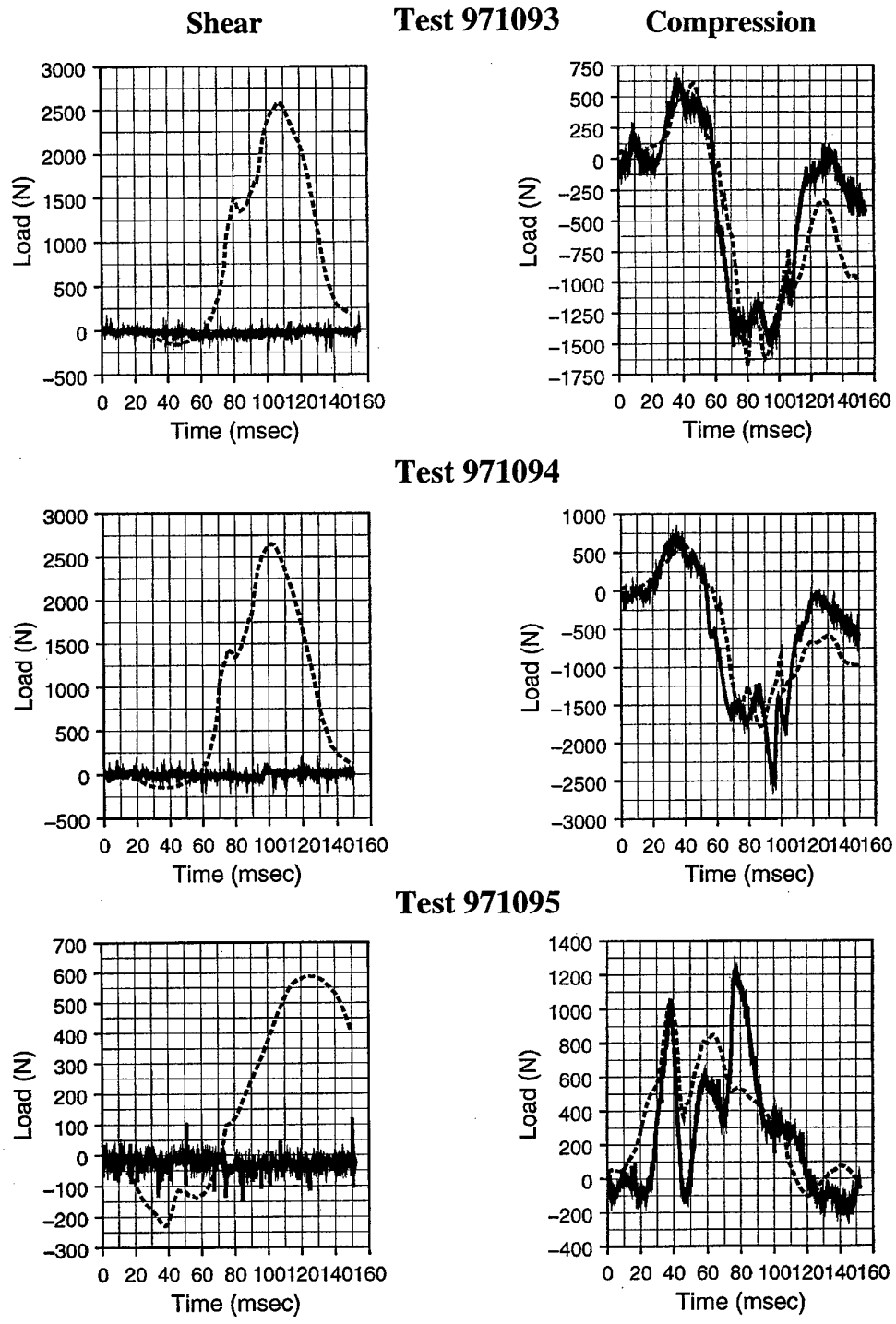

Figure 16.
Neck forces for the Hybrid III.
(971093 and 971094 - Nose Down; 971095 - Vertical)
(Solid line - Test; Dashed line - Model)

Hybrid III

Test 971093

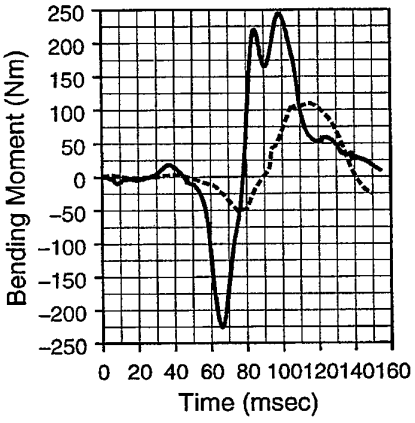

Test 971094

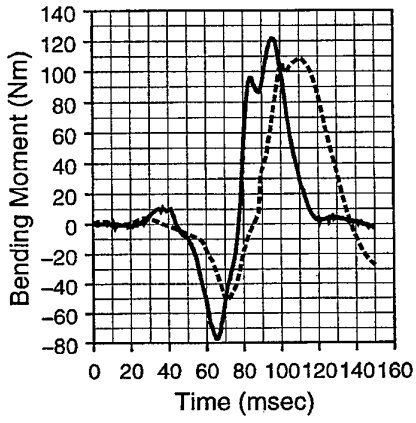

Test 971095

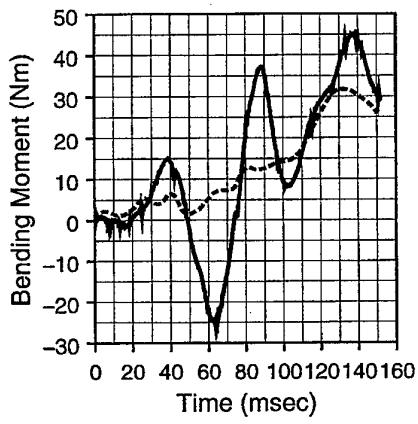

Figure 17.
Neck Bending Moments for the Hybrid III.
(971093 and 971094 - Nose Down; 97195 - Vertical)
(Solid line - Test; Dashed line - Model)

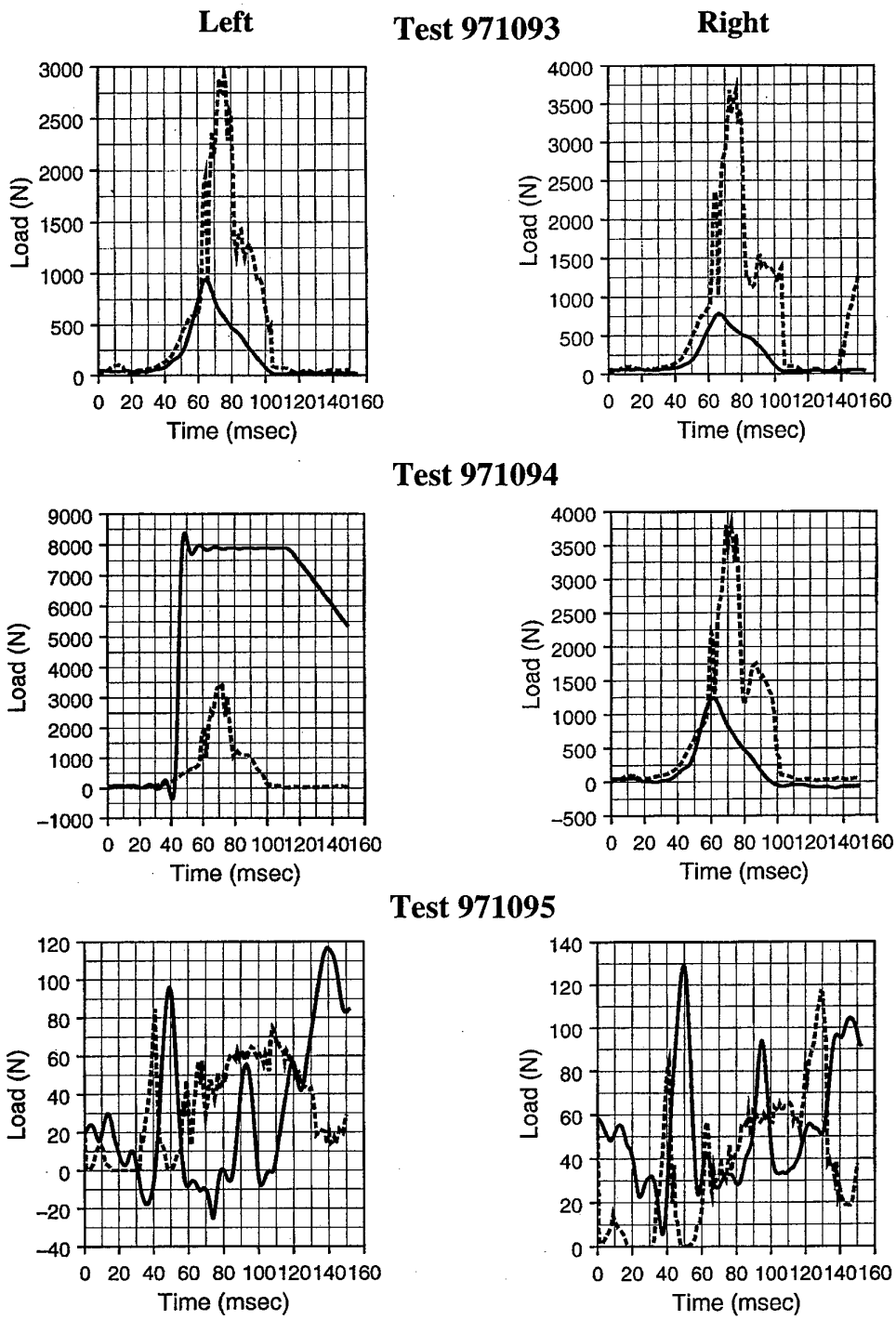

Figure 18.
Shoulder belt loads for the Hybrid III.
(971093 and 971094 - Nose Down; 971095 - Vertical)
(Solid line - Test; Dashed line - Model)

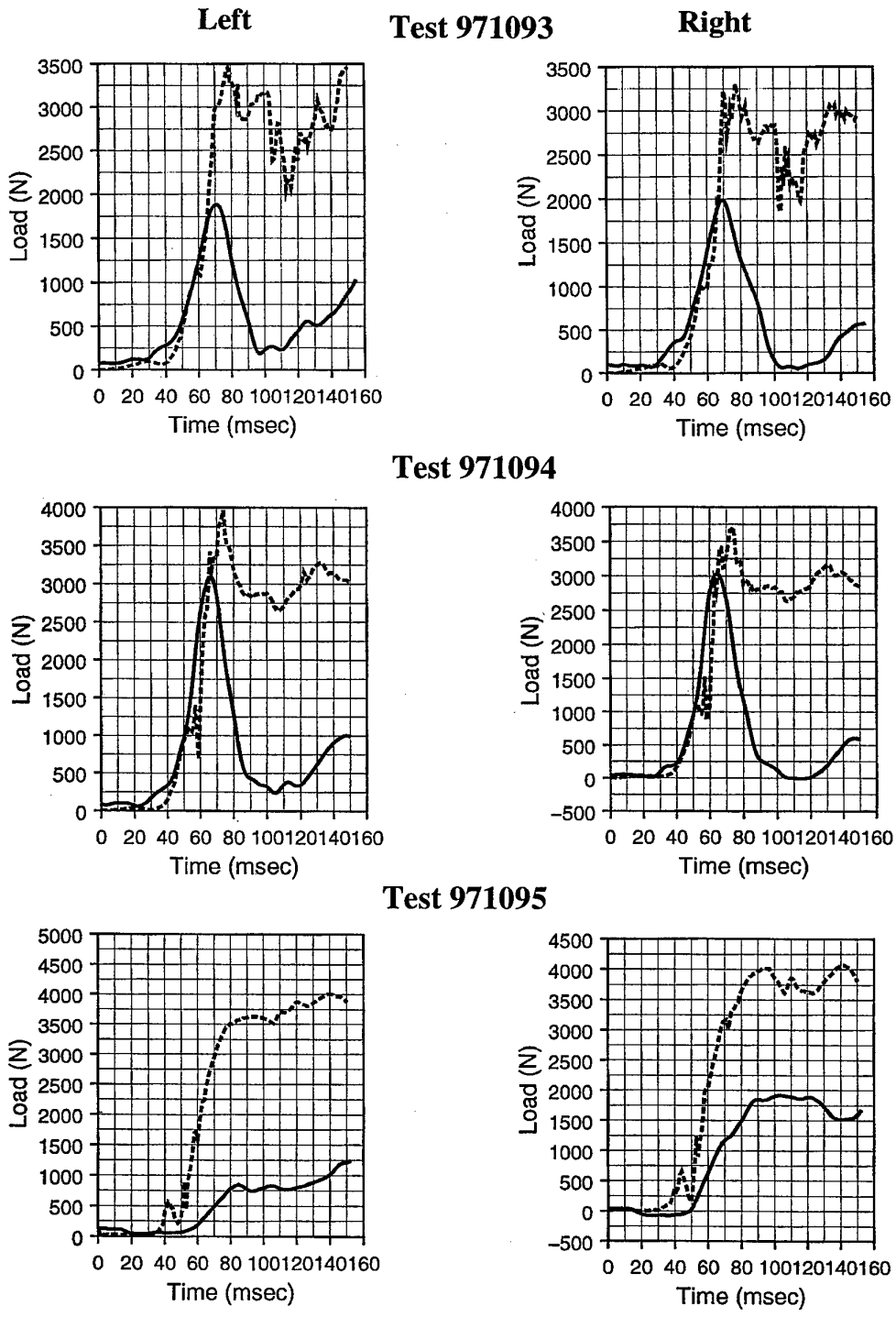

Figure 19.
Lap belt loads for the Hybrid III.
(971093 and 971094 - Nose Down; 971095 - Vertical)
(Solid line - Test; Dashed line - Model)

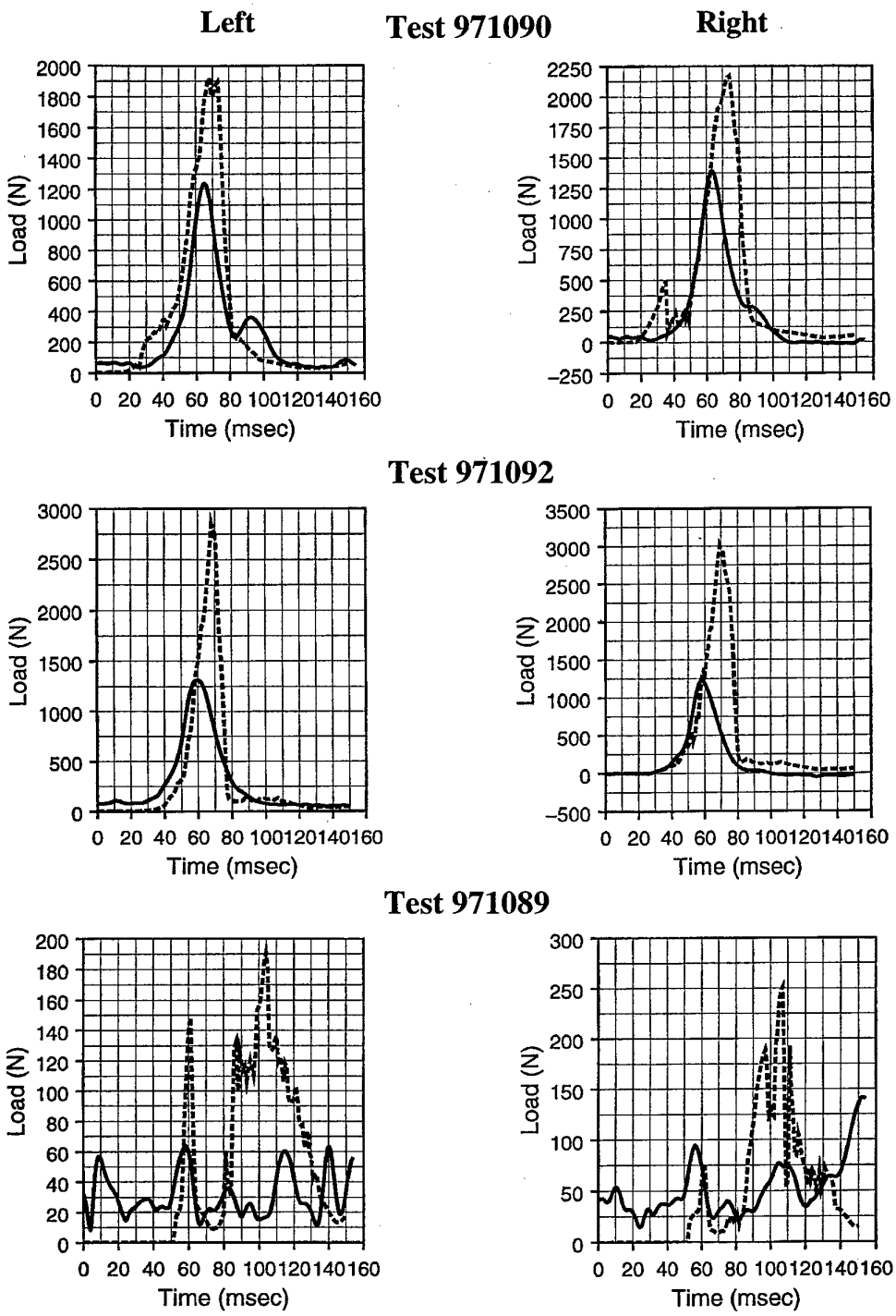

Figure 20.
Shoulder belt loads for the Hybrid II.
(971090 and 971092 - Nose Down; 971089 - Vertical)
(Solid line - Test; Dashed line - Model)

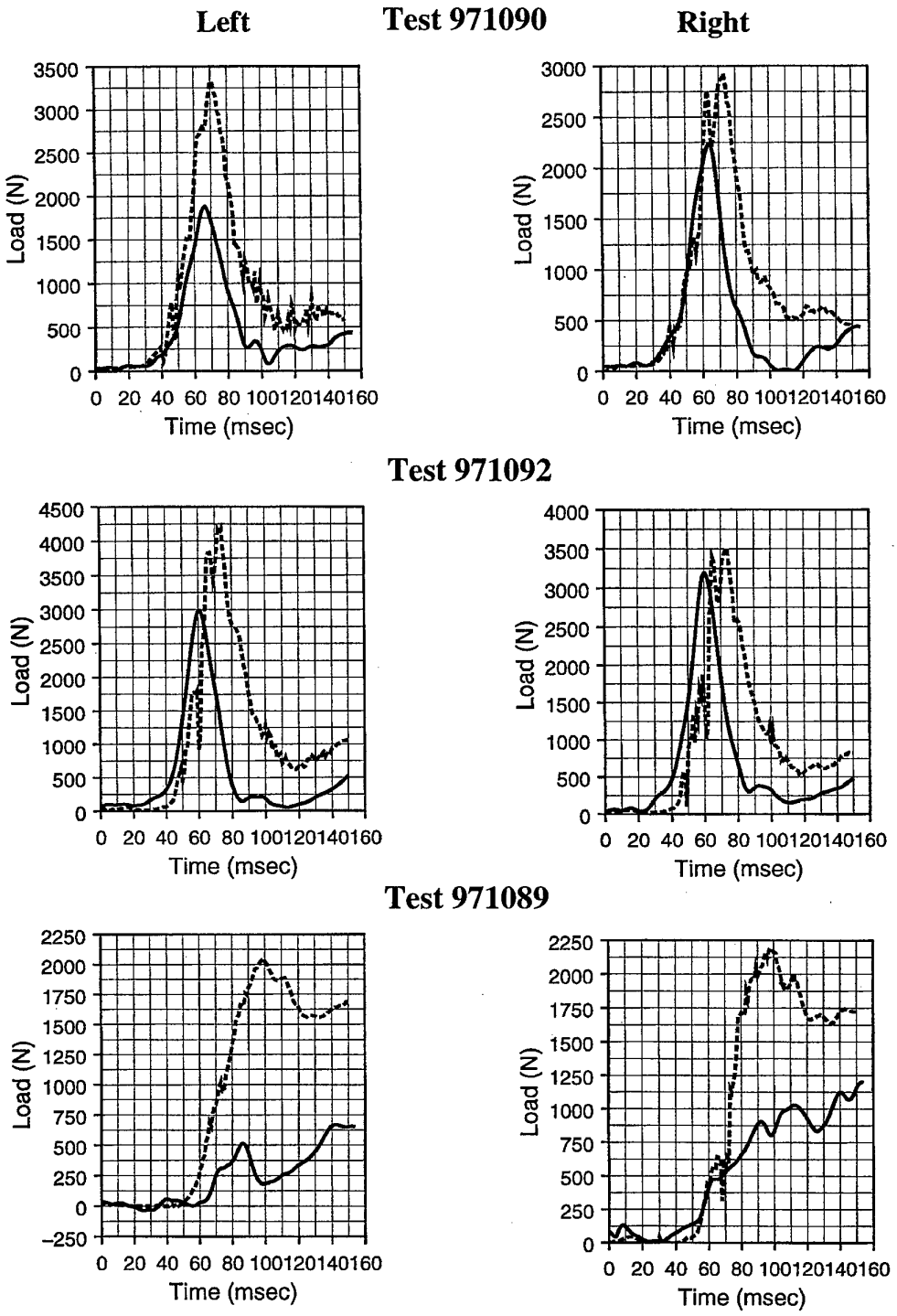

Figure 21.
Lap belt loads for the Hybrid II.
(971090 and 971092 - Nose Down; 971089 - Vertical)
(Solid line - Test; Dashed line - Model)

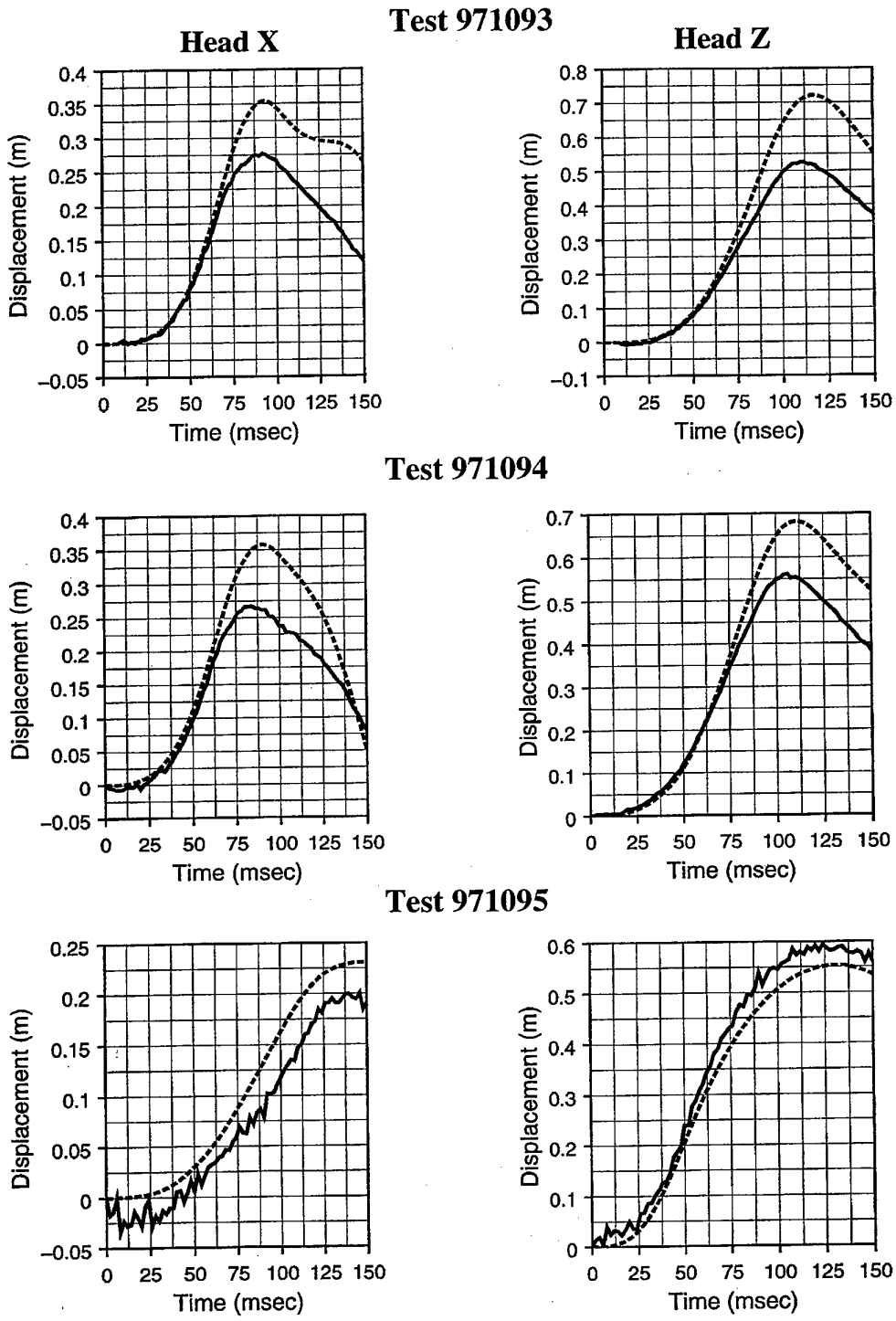

Figure 22.
Head trajectories for the Hybrid III.
(971093 and 971094 - Nose Down; 971085 - Vertical)
(Solid line - Test; Dashed line - Model)

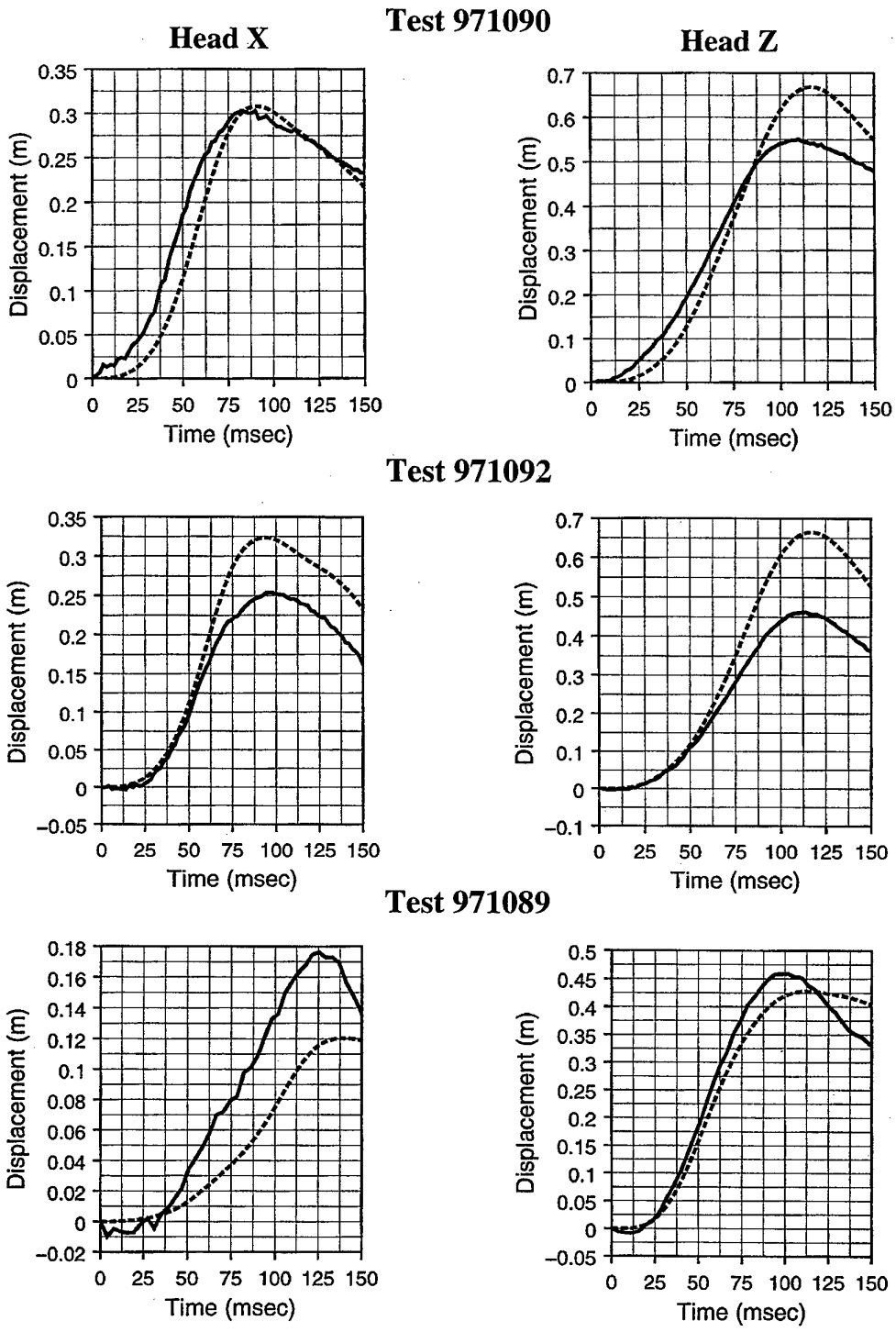

Figure 23.
Head trajectories for the Hybrid II.
(971090 and 971092 - Nose Down; 971089 - Vertical)
(Solid line - Test; Dashed line - Model)

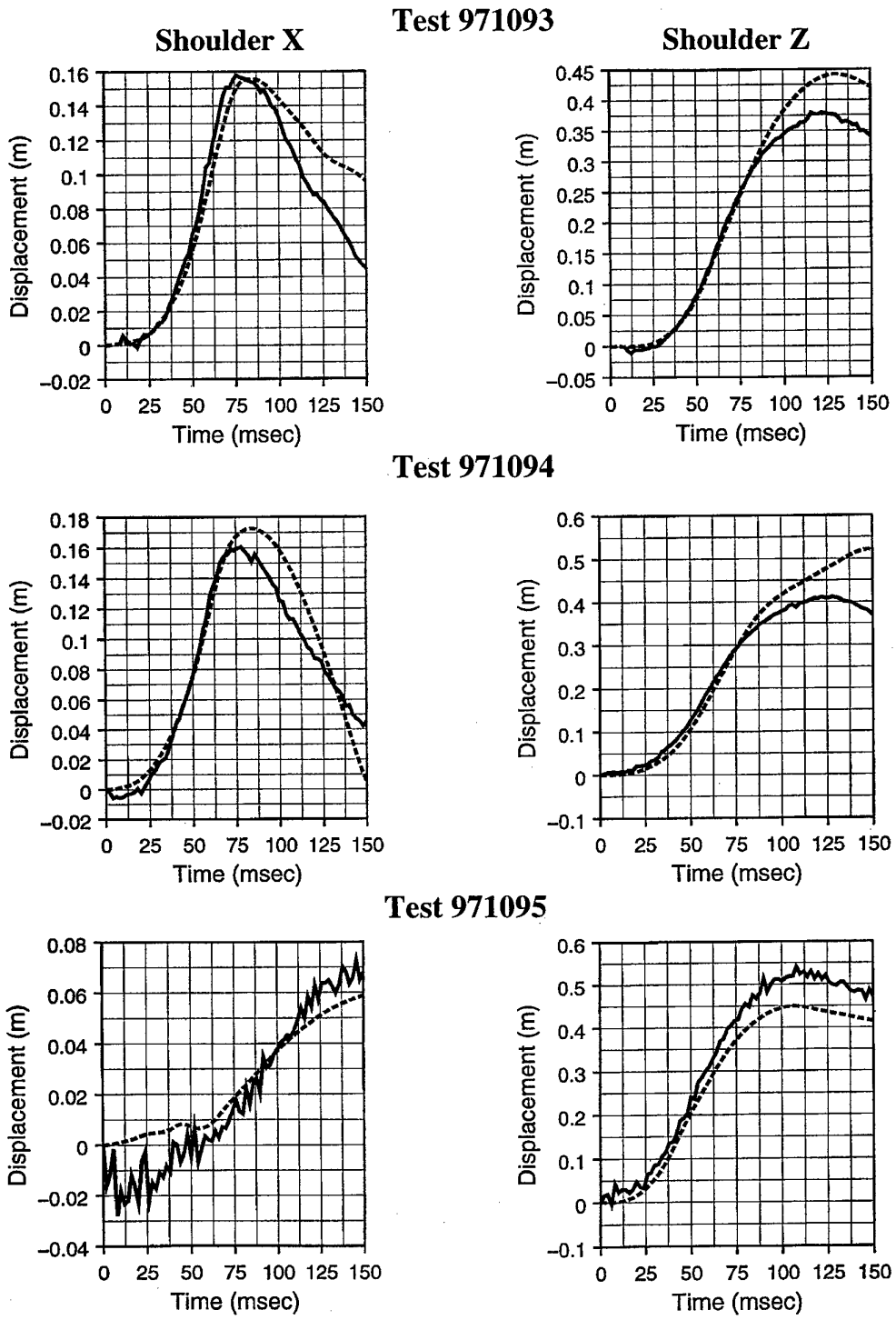

Figure 24.
Shoulder trajectories for the Hybrid III.
(971093 and 97194 - Nose Down; 971095 - Vertical)
(Solid line - Test; Dashed line - Model)

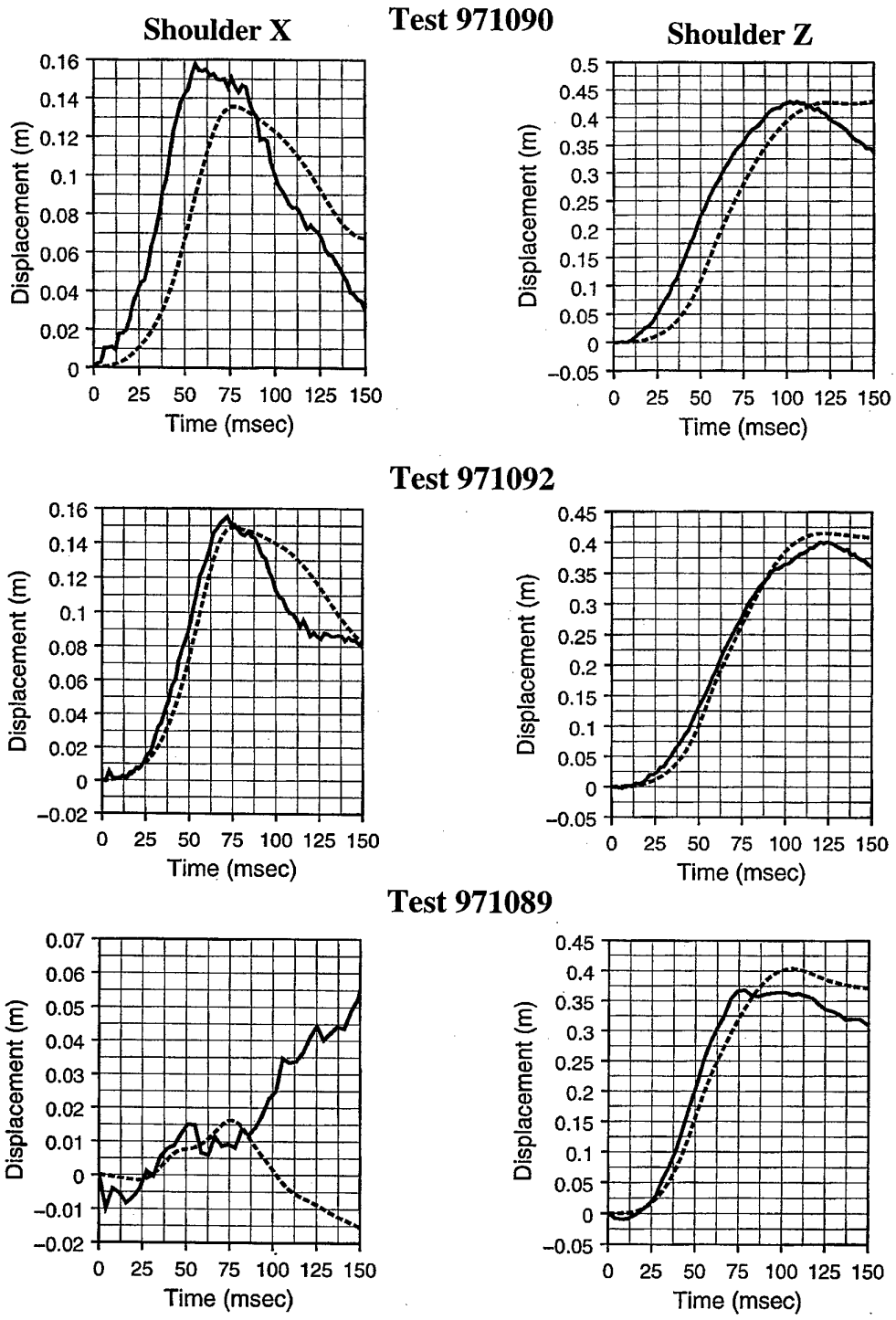

Figure 25.
Shoulder trajectories for the Hybrid II.
(971090 and 97192 - Nose Down; 971089 - Vertical)
(Solid line - Test; Dashed line - Model)

Strength of the Female Upper Extremity

J. A. Pellettiere[1], S. M. Duma[2], C. R. Bass[2], and J. R. Crandall[2]
1. Air Force Reseach Laboratory
AFRL/HEPA, 2800 Q Street
Wright-Patterson AFB 45433-7947

2. University of Virginia Automobile Safety Laboratory
1011 Linden Avenue
Charlottesville, VA 22902, USA

1 Abstract

A dynamic injury tolerance for the female upper extremity was derived from dynamic drop tests onto female cadaveric limbs. Twelve female humeri were tested at a strain rate of 3.7±1.3 strain/second. The ultimate failure moment (mass scaled to a 5% female) was measured to be 128±19 Nm. Ten female forearms were tested at a strain rate of 3.94±2.0 strain/second. The ultimate failure moment (mass scaled to a 5% female) was measured to be 58±12 Nm. A finite element model of the female forearm was constructed from computed tomography data. These data were the basis for the construction of the geometry of the female radius and ulna. A material model previously developed for modeling the mechanical behavior of bone under a variety of loading conditions was applied. Bending simulations of the radius and ulna, both quasi-static and dynamic, were computed, with the results comparing favorably with values available from the literature. Both the model and the testing show that the female foream is 21% stronger in a supinated (palm up) position than the pronated (palm down) position. The computer modeling demonstrates that with this material model, it is possible to create finite element models of human long bones for the purpose of using them in computational codes for predicting their strength.

2 Introduction

With the increased use of airbag protection systems there has been an increased emphasis on the study of extremity injuries in the automotive environment. These studies include the investigations of injuries to the upper extremities from deploying airbags [1, 2, 3, 4, 5, 6]. A recent National Highway Traffic Safety Administration (NHTSA) study of the National Automotive Sampling System (NASS) of cases involving airbags found an increased risk of upper extremity injury. When drivers were restrained only by a three-point belt, about 1% suffered upper extremity injuries. However, when the driver was restrained by a three-point belt and an airbag, the upper extremity injury rate increased to about 4% [1]. Case studies and NASS data have identified females to be at a higher risk of upper extremity injuries from deploying airbags. Factors contributing to this increased risk of injury include:

1. The seating position of women tends to be closer to the steering wheel, partially from the smaller stature, partially from driver behavior.

2. Women tend to have a lower bone strength due to lower bone mineral density, and smaller cross sectional areas, which correspond to smaller moments of inertia.

Concurrent with these modeling efforts, computed tomography (CT) data for analyzing the mechanical behavior and for creating finite element (FE) models of long bones have been used [7, 8, 9, 10]. These studies have included stress analysis of long bones under static loading conditions [7]. McBroom *et al.* [10] used CT data for predicting fracture in vertebral bodies. CT data have been used for determining the physical properties of the radius and ulna [9]. Keyak *et al.* [8] developed a process for automating the creation of FE models from CT data. While enough information was not provided to use these results directly, they demonstrate the current emphasis on using CT data to analyze human mechanical systems.

To address this situation, a methodology was created and tested to verify that CT can be used for creating FE models of long bones. These models achieve reliable results through the application of a material model that was developed for modeling the behavior of bone under a variety of load conditions. This material model was incorporated into a popular finite element package, LS-DYNA, and the use of this model is now available to the general population of researchers.

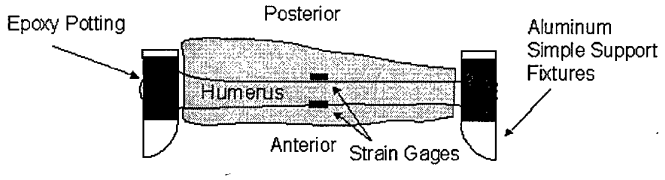

Figure 1: Humerus preparation and instrumentation

3 Experimental Testing

3.1 Humerus Tests

Twelve female humeri were prepared by disarticulating the upper extremity at the shoulder and elbow joints. The average age of these specimens was 57 ±11 years with an average body mass of 58.7 ±7.6 kg. Enough soft tissue was removed from each humerus to expose 50 mm of bone at the distal and proximal ends. The exposed ends were potted in PC-7 epoxy putty to a depth of 30 mm using removable molds. Simple support fixtures were attached to the hardened epoxy as shown in Figure 1. Strain gages (Micro Measurements, model CAE-13-125UN-350) were adhered mid-shaft on both the anterior and posterior sides of the humerus to provide maximum tensile and compressive strains. Pre-test CT scans of each humerus were taken (5 mm contiguous slices) to determine bone cross-sectional properties. Pre-test radiographs (frontal and sagittal views) were taken to identify any pre-existing skeletal conditions. If any abnormal bone pathology was noticed, the specimen was removed from the test population. Post-test radiographs (frontal and sagittal views) were taken and the humerus dissected to evaluate induced injury and classify fracture patterns.

Dynamic three-point bending tests were performed using a 9.48 kg impactor released from a drop height of 1.35 m. The impactor was guided by a vertical linear bearing track which resulted in a pre-impact velocity of 3.63 m/s. This velocity was chosen to match humerus strain rates as measured in cadaveric subjects under side airbag loading. The humerus was impacted mid-shaft in the posterior-anterior direction as shown in Figure 2. This direction was chosen to correspond with the direction of humerus loading that would be seen from a deploying seat-mounted side airbag. The impactor was brought to rest following fracture using a soft stop decelerator of crushable polystyrene. The proximal and distal simple supports each rested on greased plates. Each plate was supported by three quartz piezoelectric load sensors (PCB Piezotronics, model P212-B) aligned to measure force in the vertical direction. The impactor load was measured using three piezoelectric load sensors mounted in a similar fashion between the impactor blade and impactor mass. Accelerometers mounted to the impactor blade allowed for inertial compensation of the impact load. The initial contact between the impactor and the humerus was recorded by placing a conductive trigger switch on the humerus. Data were sampled at a rate of 20,000 Hz, and filtered at SAE class 1000. High speed video (Kodak, model 1000-E, 1000 fps) recorded impactor displacement during the event.

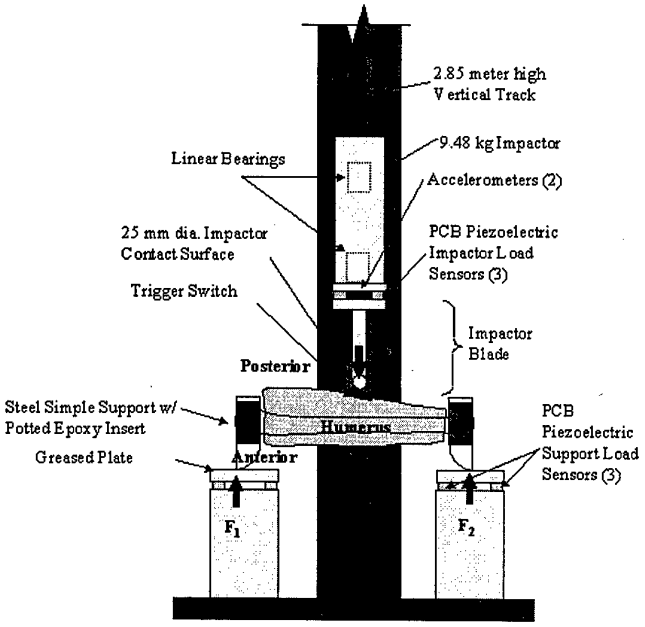

Figure 2: Drop test configuration for humerus tests

3.2 Forearm Tests

Ten female forearms were prepared by disarticulating the upper extremity at the shoulder and keeping the elbow joint intact. The average age of these specimens was 61 ±5 years with an average body mass of 59.1 ±11.6 kg (see Duma *et al.* [11] for subject anthropometry). Simple mounts were designed to attach to the posterior side of the forearm via two

tie wraps as shown in Figure 3. This mounting technique allowed for the forearm to be oriented in the supinated or pronated position prior to testing. The three-point drop test device used for the humerus tests was again employed with the drop height adjusted to 2.0 m, resulting in an impact velocity of 4.42 m/s. This velocity was chosen to match radius and ulna strain rates as measured in cadaveric tests with driver side airbags [12]. In both the pronated and supinated positions, the upper extremity was positioned such that the impactor struck the anterior surface of the forearm. The impact location was established as the distal third of the forearm, which was taken as two-thirds of the ulna length measured distally from the olecranon. This location was chosen due to the local minimum polar moment of inertia of both the ulna and radius at the distal third of the forearm [12]. Due to the lack of bone symmetry in the ulna and radius, strain gage rosettes (Micro Measurements, model CAE-06-062UR-350) where used so that the principal strains could be determined. One rosette was placed at the distal third mark on both the posterior radius and posterior ulna. The two-tailed Students t-test with alpha = .05 was used to compare the data averages.

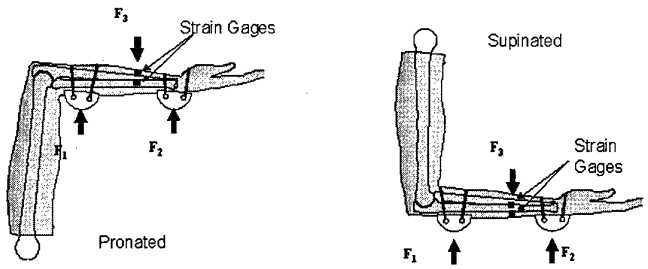

Figure 3: Specimen preparation for the supinated and pronated forearm tests

3.3 Experimental Humerus Results

The results from the humerus dynamic three-point drop tests are presented in Table 1. The average peak moment of 154 ±27 Nm can be mass scaled using the technique described by Eppinger *et al.*[13] to produce the injury tolerance for the 5th percentile small female humerus of 128 ±19 Nm. Although this value is very similar to the 134 Nm presented by Kirkish *et al.* [14], the similarity appears due to two opposing factors. The humeri in the study by Kirkish *et al.* were male and would tend to result in a higher value than female humeri; however, the tolerance was not scaled for dynamic testing: impact velocity of 0.22 m/s versus 3.6. m/s in the present study. Also, the relatively low standard deviation in the present study is a result of the close grouping of the small female sample population.

The average strain rates of 3.70 ±1.34 strain/second and -3.56 ±1.36 strain/second for the anterior and posterior gages, respectively, highlight the dynamic nature of the test and should be similar to humerus strain rates seen during side airbag loading. The strain gage wire was broken during the event in the two tests that is marked as "failed." Using simple beam theory and ignoring shear effects, the average dynamic elastic modulus was found to be 24.5 ±3.9 GPa. This was determined by plotting the stress, taken from the applied moment and cross-sectional bone properties, versus the strain directly measured from the in-situ strain gages. The slope of the linear region for each humerus was recorded and averaged. This dynamic elastic modulus should prove useful for finite element modeling of the humerus.

3.4 Experimental Forearm Results

Three matched pairs of forearms, tests 2.1 through 2.6, were tested with one forearm supinated and the other pronated to directly compare the differences. The results from all the forearm tests are presented in Tables 2 and 3 separated by test condition. The instance of peak strain is noted as "time" for all tests. The strain rates were calculated from the linear region before fracture from the strain time history plots. Within the three matched pair tests, the supinated position was significantly stronger (p = .02) than the pronated position, with a 21% higher average peak moment of 92 ±5 Nm versus 75 ±7 Nm respectively. Given this difference and the desire to produce a conservative injury tolerance, tests 2.7 through 2.10 were performed in the pronated position. Also, it is advantageous to choose this position given that typically the forearm is pronated while driving.

The average peak moment for the pronated forearms was 70 ±13 Nm, and when mass scaled for the 5th percentile female, the dynamic injury tolerance was determined to be 58 ±12 Nm. This value agrees reasonably well with the results presented by Bass *et al.* [12], who determined a forearm injury value of 67 ±13 Nm as the 50% risk of fracturing one bone in the forearm. This similarity suggests a preliminary validation of the biofidelity of the SAE instrumented upper extremity.

The average radius and ulna strain rates for the pronated tests were 3.64 ±1.12 and 2.70 ±1.32 strain/second, respectively. The relatively high standard deviation for strain rates

Table 1: Humerus dynamic three-point drop test results

Test	Subject	Ant. Strain (%)	Ant. Strain Rate (str/s)	Post. Strain (%)	Post. Strain Rate (str/s)	Peak Moment (Nm)	Elastic Modulus (GPa)
1.1	79 right	1.14	1.26	-1.09	-1.34	167	21.0
1.2	79 left	1.24	1.33	-1.49	-1.34	177	19.7
1.3	75 right	2.21	3.69	-1.22	-2.86	127	29.0
1.4	75 left	2.91	5.48	-1.75	-4.48	153	24.0
1.5	78 right	1.25	3.87	-1.09	-3.37	156	22.2
1.6	78 left	2.10	4.57	-1.72	-5.25	170	28.2
1.7	82 right	1.14	3.74	-1.20	-3.69	113	31.5
1.8	82 left	1.18	4.74	-1.06	-4.15	139	24.3
1.9	81 right	2.65	3.36	-1.17	-4.70	146	21.5
1.10	81 left	Failed	Failed	-1.18	-5.12	134	19.3
1.11	80 right	1.68	4.76	-1.13	-2.88	216	26.5
1.12	80 left	1.06	3.96	Failed	Failed	147	26.3
Average		**1.69**	**3.70**	**-1.28**	**-3.56**	**154**	**24.5**
Std. Dev.		**0.67**	**1.34**	**0.25**	**1.36**	**27**	**3.9**

Table 2: Supinated forearm dynamic three-point drop test results

		Radius			Ulna				
Test	Subject	Peak Strain (%)	Time (ms)	Strain Rate (str/s)	Peak Strain (%)	Time (ms)	Strain Rate (str/s)	Peak Moment (Nm)	Time (ms)
2.1	1013 left	1.180	4.7	6.78	.889	5.2	9.94	87	4.9
2.4	84 right	1.170	8.5	4.40	1.175	8.6	4.84	92	8.7
2.5	58 left	1.640	7.1	4.10	.757	7.8	4.30	96	7.5
Average		**1.330**	**6.8**	**5.10**	**.940**	**7.2**	**6.36**	**92**	**7.0**
Std. Dev.		**.270**	**1.9**	**1.50**	**.214**	**1.8**	**3.11**	**5**	**1.9**

may be due to variability in the initial positioning of the strain gages relative to the neutral axis, slight radius and ulna rotation during the impact, and the non-uniform geometry of the radius and ulna between specimens. There was no significant difference in radius and ulna strain rates between the two positions. The strain rates compare well to rates recorded for airbag loading, which ranged from 1.3 to 5.3 strain/second. The difference in loading between the pronated and supinated positions was investigated in more detail by examining the impact time histories as well as the forearm fracture patterns and locations.

3.4.1 Forearm Impact Time Histories

The in-situ strain gages were used to determine not only peak strain and strain rate, but also the fracture times of the radius and ulna. Since the trigger time depends on the amount of soft tissue and trigger strip placement for each test, the time history plots can be used only as a relative measure of fracture time within each test. In the supinated position the average difference in fracture time between the radius and ulna was a negligible 0.4 $\pm$0.3 ms. However, the pronated tests yielded an average difference in fracture time of 3.6 $\pm$1.2 ms, with the ulna breaking before the radius in every test. This difference is very significant ($p = .0001$) for comparing only the matched pairs, but is just significant ($p = .05$) for all tests. As illustrated in Figures 4 and 5, this trend implies that in the pronated position, the ulna and radius are loaded independently, while in the supinated position the ulna and radius are loaded together as a combined structure. These two figures also highlight the difference in peak strain values between the two positions. While the average radius peak strains for supinated and pronated tests were similar at 6.8 $\pm$1.9 % and 7.8 $\pm$2.2 % respectively, the average ulna peak strains were significantly different ($p = .03$) at 7.2 $\pm$1.8 % for the supinated tests and 4.3 $\pm$1.6 % for the pronated tests. Furthermore, in pronation the peak strain for the ulna was significantly less ($p = .0007$) than the

Table 3: Pronated forearm dynamic three-point drop test results

		Radius			Ulna				
Test	Subject	Peak Strain (%)	Time (ms)	Strain Rate (str/s)	Peak Strain (%)	Time (ms)	Strain Rate (str/s)	Peak Moment (Nm)	Time (ms)
2.2	1013 right	.775	4.8	4.50	.568	3.0	4.50	69	4.7
2.3	84 left	1.160	11.5	3.24	.525	7.9	1.85	82	11.4
2.6	58 right	1.830	9.2	2.05	.606	4.0	4.74	74	9.2
2.7	66 right	1.240	6.5	4.09	.241	3.7	1.24	48	6.5
2.8	72 right	1.880	8.9	2.54	.156	4.5	1.40	83	9.0
2.9	67 left	.961	5.3	5.62	.393	2.5	3.00	58	5.6
2.10	73 right	1.280	8.5	3.45	.286	4.2	2.17	73	8.6
Average		**1.300**	**7.8**	**3.64**	**.396**	**4.3**	**2.70**	**70**	**7.8**
Std. Dev.		**.380**	**2.2**	**1.12**	**.162**	**1.6**	**1.32**	**13**	**2.2**

peak strain in the radius.

4 Finite Element Upper Extremity Model

A cadaveric upper extremity that was approximately a 5th percentile female was selected. A computed tomography (CT) scan was acquired for this upper extremity. A scan was taken every 0.001 m for the length of the arm. The resulting information from the CT scans was in a digital format and was equivalent to a density plot of the cross section. The CT scans were converted to a 256 gray scale plot, Figure 4. The CT scans also provided information about the apparent bone density through regression equations. The density can be used to determine the local material properties.

The CT image was further processed using thresholding and edge detection algorithms, Figure 5. A threshold value of 128 was selected, as this gave the best boundaries for most of the bone sections. It was occasionally necessary to adjust this value up or down or to modify the image manually to provide an adequate boundary.

After the CT data were processed by detecting the edges, the output was converted to an input file that can be directly read into a computer-aided drafting (CAD)/pre-processing program, Figures 6 and 7. This conversion was accomplished using a program written to read in the data from the image processing software and add the necessary information for the CAD program. The conversion program smooths and refines the data to allow the creation of surfaces that are noise-free. After all the processing was completed, a solid mesh using eight-node brick elements was created from the CAD data, Figure 8. Two elements through the thickness were created with approximately 0.005 m edges.

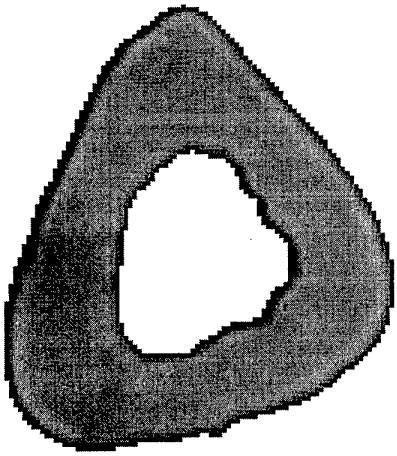

Figure 4: CT scan of bone slice

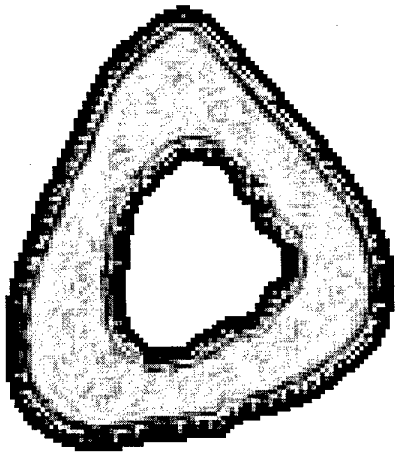

Figure 5: Processed image of CT scan of bone slice

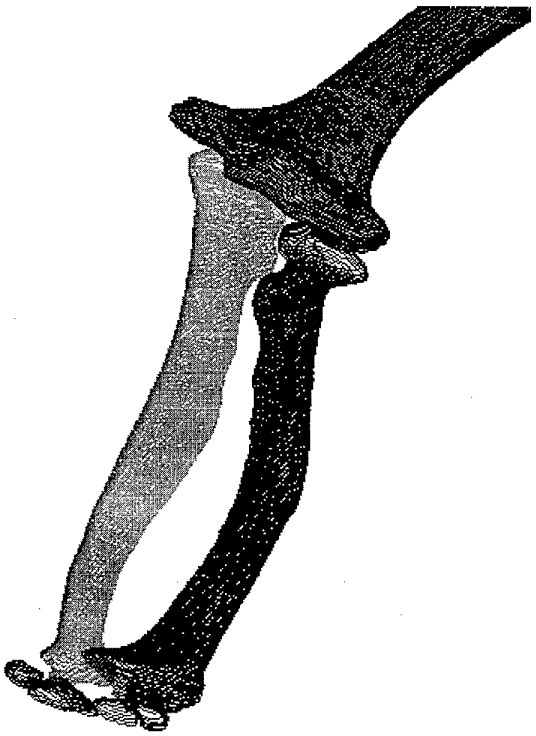

Figure 6: CAD geometry created from CT data

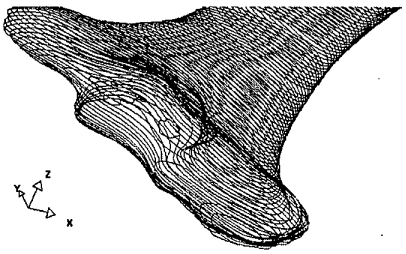

Figure 7: Closeup of CAD geometry

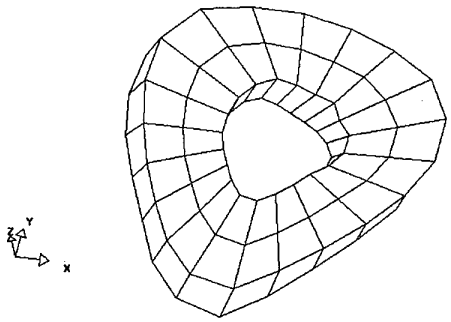

Figure 8: Meshed section of bone

5 Material Model

To achieve accurate, reliable results it was necessary to use a constitutive law that would incorporate the proper mechanical response of bone. While LS-DYNA contains a wealth of material models, a suitable one for modeling of bone was not included. This issue was solved by using a material model previously developed at the University of Virginia (UVA) [15]. This model treats bone as a linear transversely isotropic (TI) material for a fixed strain rate. Rate dependence is applied through a scaling of the longitudinal modulus determined from the relations derived by Carter and Hayes [16] as a function of the strain rate, $\dot{\varepsilon}$, and the density, ρ:

$$E_3 = 3790\dot{\varepsilon}^{0.06}\rho^3 \tag{1}$$

The transverse modulus was assumed equal to two-thirds of the longitudinal modulus. Carter and Hayes also developed a relationship for the ultimate stress for compressive loading

as:

$$\sigma_y = 68\dot{\varepsilon}^{0.06}\rho^2 \quad (2)$$

Perfect plasticity is assumed with a yield point that also scales with the strain rate, Figure 9. While only the results for a uniaxial compressive test are shown, this model has been validated for loading in any direction. The default properties presented in the derivation of the material model were used.

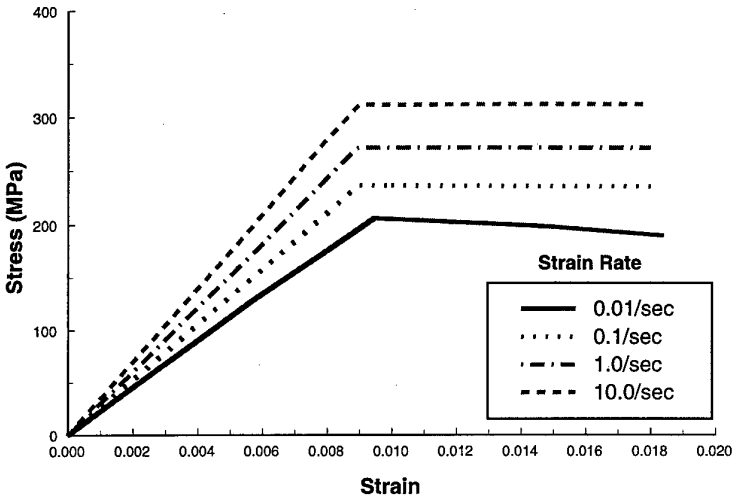

Figure 9: Stress - strain response for longitudinal compressive loading

6 Quasi-static Simulations

To verify the arm model and its material properties, simulations of quasi-static bending tests of the radius and ulna were conducted. These simulations provided confidence in the ability of the model to predict forces and moments from real-world tests. A density of $1.86*10^3$ kg/m^3 was selected, as this is approximately the cortical bone density of a healthy female [17]. The bones were supported on two rigid cylinders with a radius of 0.015 m and set 0.100 m apart. A massless rigid cylindrical impactor with a 0.015 m radius was applied on the anterior surface midway between the supports. The impactor was displaced with a rate of 0.050 m/s. While this loading rate is higher than typical rates for quasi-static testing, for computational purposes in LS-DYNA, it is actually quite slow. Several rates were tested and it was found that, with this loading rate, the inertial effects were negligible. The rigid impactor was used, as these simulations were to determine the breaking strength of a specific bone and did not include any soft tissue. The impactor was displaced until full failure through the bone was achieved.

Quasi-static simulations of the radius had a maximum measured force of 1240 N, which converts to a bending strength of 31.0 Nm, Figure 10. Quasi-static simulations of the ulna had a maximum measured force of 1234 N, which converts to a bending strength of 30.8 Nm, Figure 11.

In the literature testing shows an ultimate bending moment of the radius ranging from 23 Nm to 40 Nm and an ultimate bending moment of the ulna ranging from 28 Nm to 45 Nm [12, 18 - 21]. Part of this variability stems from incomplete subject data being available, i.e. age and gender. The studies of Messerer [18] show the bending strength of the female arm to be much lower than the bending strength of the male arm. Additionally, the studies by Motoshima [21] show a reduction in the bending strength as the age of the subject increases. For these reasons, it would be expected that the strength of the female radius would be toward the lower end of the values reported in the literature. Considering this, the FE model with the new TI material model compares quite well to testing previously conducted in the literature.

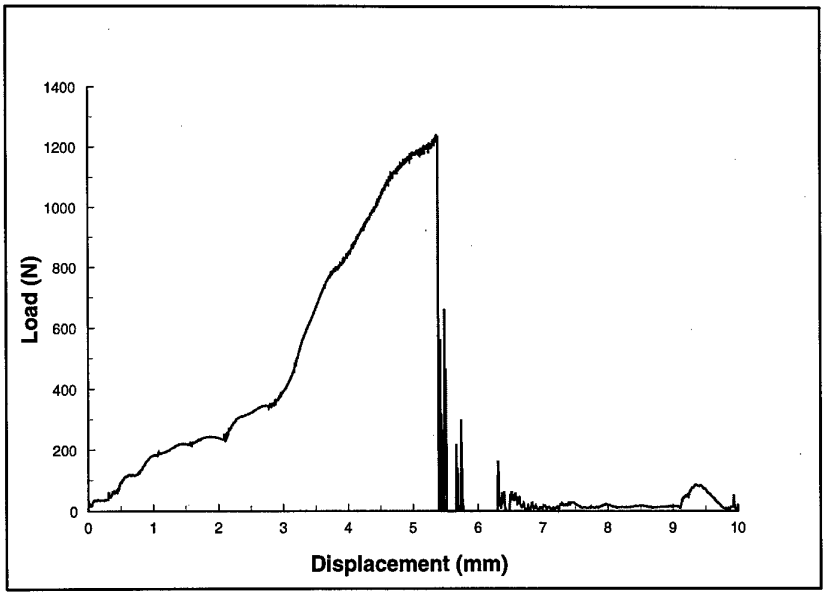

Figure 10: Quasi-static three-point bending of the radius using new TI material

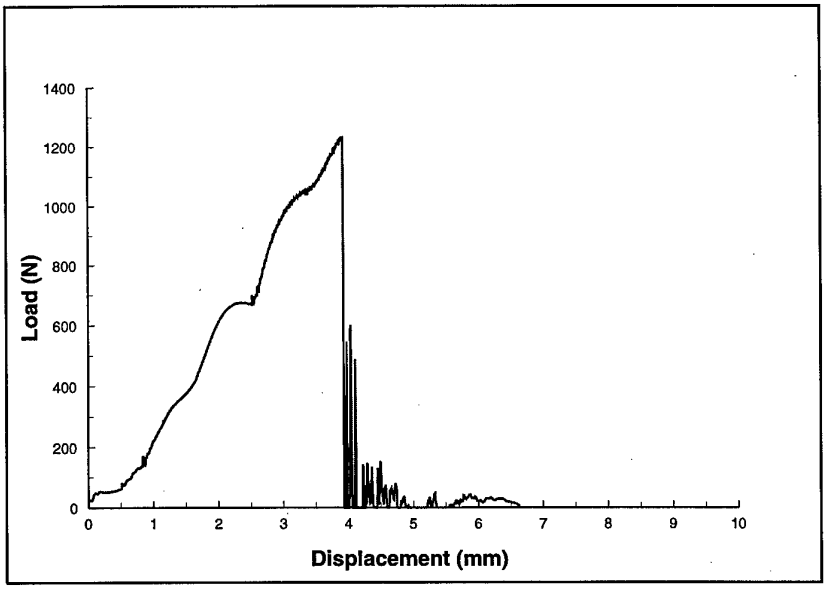

Figure 11: Quasi-static three-point bending of the ulna using new TI material

7 Dynamic Simulations

A simulation of a dynamic three-point bending test was created, Figures 12 and 13. The FE upper extremity was supported at the distal and proximal ends on two cylindrical supports and impacted with an elastic, cylindrical impactor. The supports were assigned a stiffness of 1000 MPa, and the impactor was given a stiffness of 100 MPa. A 9.0 kg impact mass with an initial velocity of 4.6 m/s was dropped mid-shaft on the anterior surface of the radius and ulna. The elasticity for the impactor and supports was incorporated to simulate the effects of the soft tissue on the impact. The arm

was placed in either a supinated position (palm up) or in a pronated position (palm down). Fracture of the model was defined as a complete failure of a line of elements through the entire model.

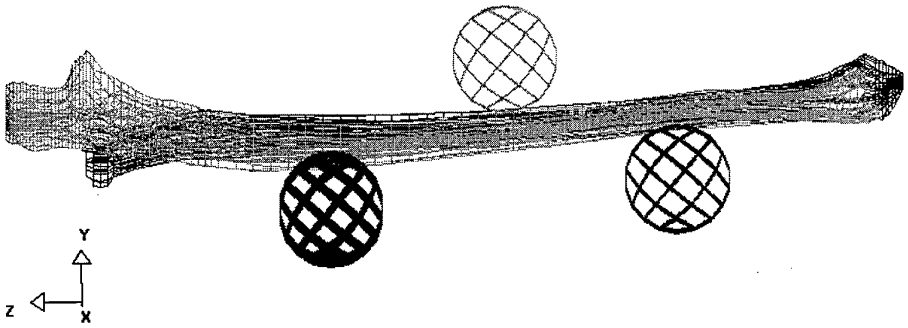

Figure 12: Setup for dynamic three-point bending test of upper extremity

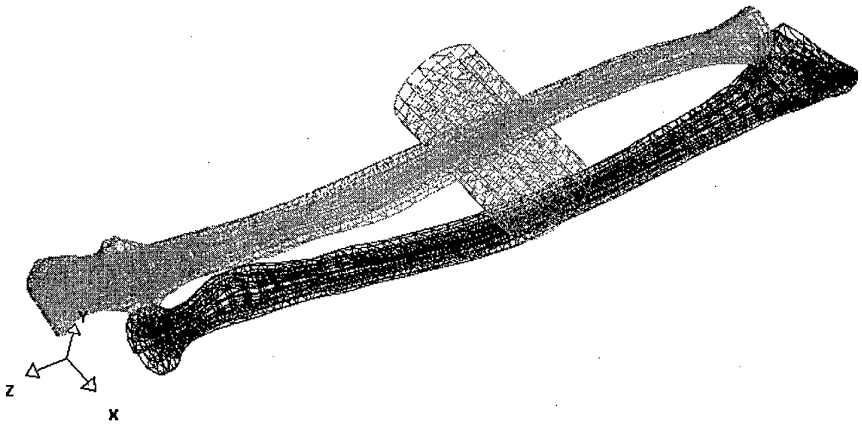

Figure 13: Setup of dynamic three-point bending test of upper extremity

When tested dynamically in the supinated position the maximum measured force to failure was 4000 N or 100 Nm, Figure 14. Failure of the radius occurred slightly before failure of the ulna. Changing the test condition to pronation reduced the maximum measured force to failure to 1860 N or 73 Nm, Figure 15. Now failure of the ulna occurred slightly before failure of the radius.

In the University of Virginia (UVA) testing of a female forearm [12], a failure moment of 115 Nm was measured for the supinated case and a failure moment of 80 Nm was measured for the pronated case. In the current set of tests, a failure moment of 92 $\pm$ 5 Nm was measured for the supinated case and a failure moment of 70 $\pm$ 13 Nm was measured for the pronated case. The value measured here in the simulation is quite close considering that this is actually the forearm from a different subject but from a similar group. Also, since there is no soft tissue included in this model, it would tend to be slightly on the conservative side. This is because the soft tissue spreads out the impact force and delays the contact with the bones. The elastic impactor also spreads out the contact force, but not to the same extent as the soft tissue. The elastic impactor did not delay the contact time.

7.0.2 Comparison of Supinated with Pronated

The maximum failure moment for the pronated case is lower than for the supinated case, as more load sharing exists for the supinated forearm. In the supinated case, both the radius and ulna are contacted simultaneously and loaded. Failure for both of these bones occurs concurrently, with one failing only at a slightly different time. For the pronated case, the ulna is the main load-carrying bone during the initial impact. As it is loaded and begins to fail, the radius begins to take up the load. This is easily noted from the large double peak, Figure 15, where once the ulna has failed and the load drops, it rises again to almost the same peak value until the radius fails. The findings here are that this model predicts the same trends in the failure patterns, as well as matching the peak moments quite well. The timing of the peaks is slightly different than what was measured in the tests, but this can be explained by the lack of soft tissue to delay the loading and energy transfer to the bones.

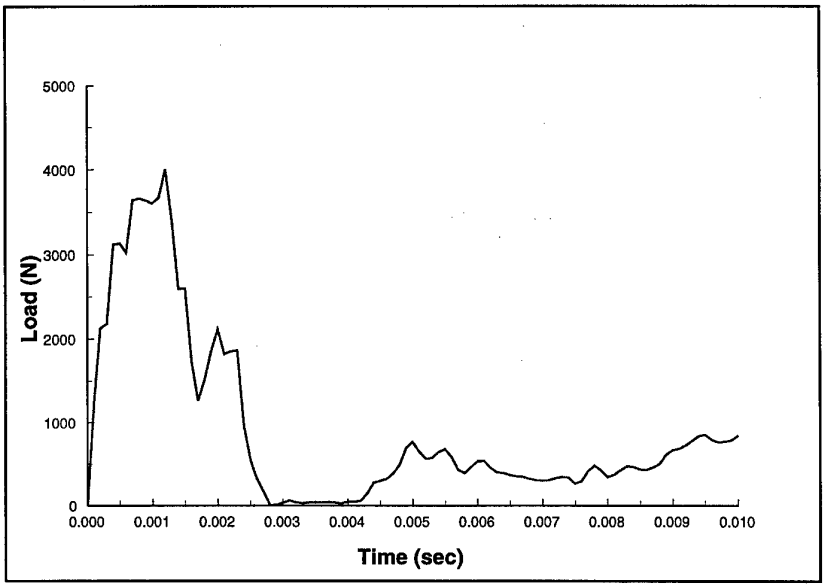

Figure 14: Force time history for a simulated drop test on a supinated forearm

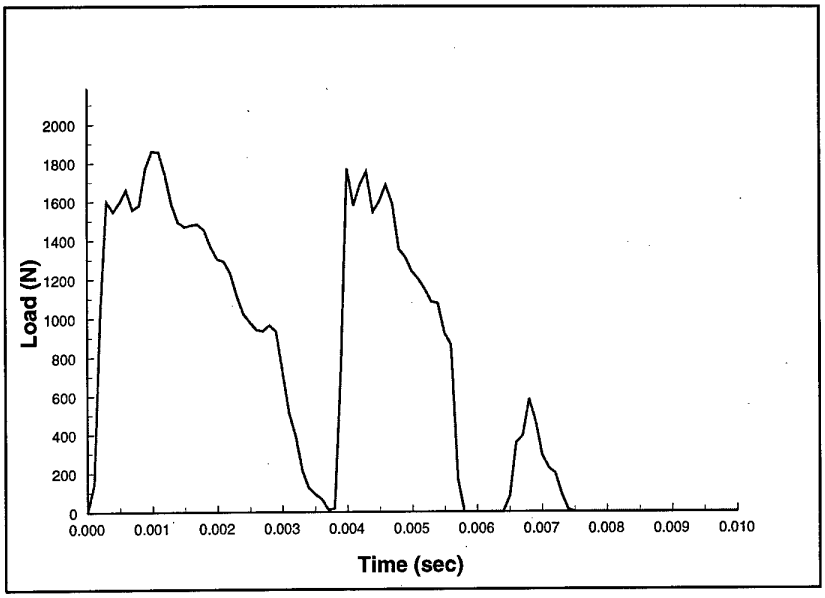

Figure 15: Force time history for a simulated drop test on a pronated forearm

8 Conclusion

A finite element model of a human upper extremity was created from computed tomography scan data. These data were the basis for the geometry, with the material properties determined from average values obtained from the literature. To this model, the newly developed TI material model was applied. Quasi-static bending simulations were conducted on the radius and ulna, and the results compared very well with information available in the literature. The radius and ulna were then simulated together in a dynamic three-point bending test, with elastic supports and an elastic impactor. These forearm bend simulations were conducted in both a supinated and a pronated position. The supinated position demonstrated a 20% increase in the bending strength, due mainly to the initial load sharing of the radius and ulna. This result is supported by the experimental tests where the forearm was shown to be 21% stronger in the supinated position for dynamic three-point bending tests. Because of these directional differences, an injury criterion should use the weaker position.

The dynamic bending strength of the 5th percentile female humerus was determined to be 128 Nm and the dynamic bending strength of the 5th percentile female forearm was determined to be 58 Nm. It is anticipated that these values could form the basis of an injury criterion that can be used in airbag investigations.

The new material model has been shown to be adequate for predicting injury. By using FE models created from CT data, several scenarios can be computed and the likelihood of injury predicted. Since the bone fracture is predicted directly from the material model, during the simulation, there is no need to compute the likelihood of injury from regression equations or post processing operations.

References

[1] S. Kuppa, C. Yeiser, M. Oslon, L. Taylor, R. Morgan, and R. Eppinger (1997) *SAE Paper No.* **970399**.

[2] R. A. Saul, S. H. Backaitis, M. S. Beebe, and L. S. Ore (1996), *Proceedings of the 40th Stapp Car Crash Conference, SAE Paper No.* **962417**.

[3] W. N. Hardy, L. W. Schneider, M. P. Reed, and L. L. Ricci (1997), *Proceedings of the 41st Stapp Car Crash Conference, SAE Paper No.* **973325**.

[4] P Palaniappan, P Wispauramonton, A. S. Tanavde, E. Lee, and P. Begeman (1998), *Proceedings of the 42nd Stapp Car Crash Conference, SAE Paper No.* **TBP**.

[5] P. Begeman, P Wispauramonton, A. S. Tanavde, and E. Lee (1998), *Proceedings of the 42nd Stapp Car Crash Conference, SAE Paper No.* **TBP**.

[6] C. R. Bass, S. Duma, J. R. Crandall, T Micek, E. M. Sieveka, M. Lange, N. Grillo, P. Martin, and W. D. Pilkey (1997), *24th International Workshop on Human Subjects for Biomechanical Research.*

[7] S. A. Marom and M. J. Linden (1990), *Journal of Biomechanics*, **23**, 399-404.

[8] J. H. Keyak, J. M. Meagher, H. B. Skinner, and C. D.

Mote (1990), *Journal of Biomedical Engineering*, **12**, 388-397.

[9] E. S. Hsu, A. G. Patwardhan, K. P. Meade, T. R. Light, and W. R. Martin (1993), *Journal of Biomechanics*, **26**, 1307-1318.

[10] R. J. McBroom, W. C. Hayes, W. T. Edwards, R. P. Goldberg, and A. A. White (1985), *The Journal of Bone and Joint Surgery*, **67A**, 1206-1213.

[11] S. M. Duma, P. Schreiber, J. McMaster, J. Crandall, C. Bass, and W. Pilkey (1998), *Proceedings of the 1998 IRCOBI Conference.*

[12] C. R. Bass, S. M. Duma, J. R. Crandall, R. Morris, P. Martin, W. D. Pilkey, S. Hurwitz, N. Khaewpong, R. Eppinger, and E. Sun (1997), The interaction of airbags with upper extremities, *Proceedings of the 41st Stapp Car Crash Conference, SAE Paper No.* **973324**.

[13] R. H. Eppinger, J. H. Marcus, and R. M. Morgan (1984), Development of dummy and injury index for NHTSA's thoracic side impact protection research program, *SAE Paper no.* **840885**.

[14] S.L. Kirkish, P. C. Begeman, and N. S. Paravasthu (1996), Proposed provisional reference values for the humerus for evaluation of injury potential, *SAE Paper no.* **962416**.

[15] J. A. Pellettiere (1998), *Proceedings of the 1998 NACOB Conference*, ASB.

[16] D. R. Carter and W. C. Hayes (1977), *Journal of Bone and Joint Surgery*, **59A**, 954-962.

[17] P. Ruegsegger, E. P. Durand, and M. A. Dambacher (1991), *Bone*, **12**, 99-105.

[18] O. Messerer, *Über Elastizität und Festigkeit der Menschlichen Knochen*, (Verlag der J. G. Cotta'schen Buchhandlung, Stuttgart, 1880).

[19] H. Yamada, *Strength of Biological Materials* (Williams and Wilkens, Baltimore, Maryland, 1973).

[20] J. M. Jurist and A. S. Foltz (1977), *Journal of Biomechanics*, **10**, 455-459.

[21] T. Motoshima (1960), *Journal of Kyoto Prefectural Medical University*, **68**.

Military Application of Biodynamics Models

Louise Obergefell, Ph.D.
Air Force Research Laboratory (AFRL/HESA)
2800 Q Street
Wright-Patterson Air Force Base OH 45433-7947
United States

Annette Rizer and Deren Ma, Ph.D.
Veridian
5200 Springfield Street, Suite 200
Dayton OH 45431
United States

1. SUMMARY

The Air Force Research Laboratory makes extensive use of biodynamics models to evaluate crew system designs and modifications, develop safe design criteria, and predict crewmember response. When special equipment is added to a cockpit for a test program, the Articulated Total Body (ATB) model is used to predict the crewmembers motion during an ejection. By simulating a large crewmember ejecting with his hands both on the firing control panel and on the side seat panel, the risk of significant arm contact is predicted. When the Army is concerned about detonating an item carried by a soldier during a fall from a truck or a parachute landing, the ATB model is used to predict the contact forces on the soldier if they land on a hard surface. When initial ejection seat tests with a new manikin have unusual results, biodynamics modeling is used to help sort out whether the response is due to the seat design or the manikin. Simulations of the tests with possible seat and manikin modifications are used to determine which modifications are most likely to improve results and to narrow future testing requirements. When ejection tests result in extreme manikin leg flail, ATB simulations are used to determine the loads in the hips, which are not measured by the manikin. The process used within AFRL to apply biodynamics modeling to these applications is described and the results presented.

2. INTRODUCTION

The Air Force Research Laboratory (AFRL) applies biodynamics modeling to many different military and civilian problems. Types of applications include evaluating crew system and personnel equipment designs modifications, supplementing test results, developing safe design criteria, and predicting crewmember response. The primary model used is the Articulated Total Body (ATB) model (Ref 1).

2.1 ATB Model

The ATB model is a three-dimensional coupled multibody dynamics program, which represents a crewmember's body as a linked set of segments (Figure 1). It has been primarily used to simulate human and manikin dynamics in aircraft crashes and ejection, automobile accidents, and other dynamic environments. It is distributed worldwide by AFRL and has capabilities to model most of the systems with which a crewmember or occupant are likely to interact. We have especially focused on developing simulation databases of human body properties.

The model has options for modeling joints, vehicle motion, environmental surfaces, belt and air bag restraints, and aerodynamic forces. The mass properties and surfaces are represented in the body segments. The joints have degrees of freedom, ranges of motion, and resistive torque properties. The GEBOD (Generator of Body Data) program has been developed to provide the required body properties for adult males and females, children and impact test manikins (Ref 2).

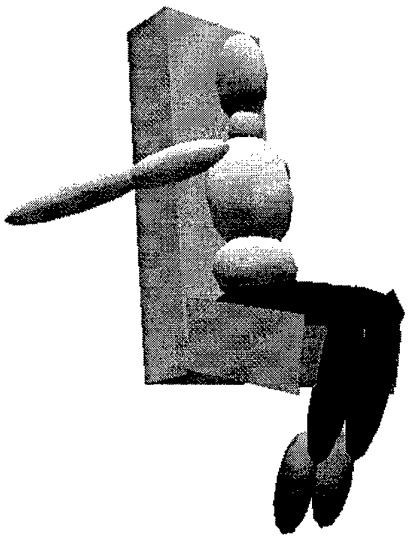

Figure 1 - Example ATB Model

Validation is the key to using a model such as the ATB and its body databases. We continually validate the ATB model against human volunteer and manikin tests. The human volunteer tests conducted in our laboratory are ideal tests for validation. Sim-ulations are set up using the test configuration with the proper body data set. Then simulation and test results are compared. These results include the overall body motion in films (Figure 2) and the available sensor data, such as accelerometers, load cells, and motion analysis.

A model's predictions are only as good as its validation. Predictive simulations are essentially interpolations and extrapolations of the validation simulations. Therefore, the validations need to be against tests that are comparable to the conditions of the planned applications.

2.2 General Process

Military applications for biodynamic modeling come to the AFRL from many sources. Typically, a program office calls with a safety concern and a need to know if their new system or proposed design is safe. Depending upon the stage of development, testing may or may not be practical. Either way,

Papers presented at the RTO HFM Specialists' Meeting on "Models for Aircrew Safety Assessment: Uses, Limitations and Requirements", held in Ohio, USA, 26-28 October 1998, and published in RTO MP-20.

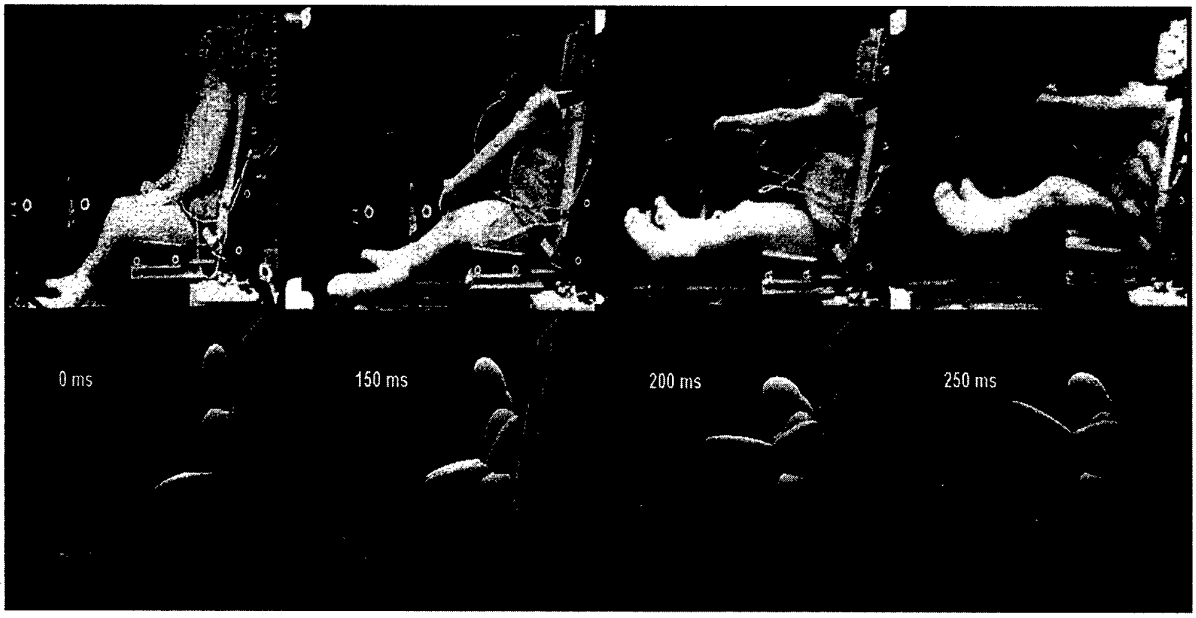

Figure 2 - 10G Frontal Impact Sled Test and ATB Simulation

simulations can often provide the answers or focus the testing. Each new problem usually requires a unique process to determine the simulations and/or experiments needed. But a general process covers the main steps in using biodynamics modeling. The steps are

- Analyze the problem
- Select a comparable simulation from available validation simulations
- Decide whether human or manikin properties are appropriate
- Modify the simulation data to represent the problem environment using available body and equipment properties
- Estimate unknown properties
- Run simulations with parameter variations on the estimated properties
- Analyze the results first for realism and then to draw conclusions regarding the problem

3. EXAMPLE APPLICATIONS

To demonstrate this process and the usefulness of biodynamics modeling, we present several example applications: special equipment clearance during ejection, detonation hazard during soldier fall, manikin performance evaluation, and supplementing test results.

3.1 Special Equipment Clearance During Ejection

VISTA (Variable Stability In-Flight Simulator Test Aircraft) is used as a test bed for many new aircraft systems. When a head tracking system was to be tested, the TMT (Tracker Magnetic Transmitter) needed to be mounted near the test pilots right shoulder. The risk of striking the TMT during ejection was unknown. We needed to know the injury risk to clear the head tracking system for flight testing. Therefore, an effort was made to determine whether a crewmember's arm would strike the TMT during ejection from the VISTA F-16 aircraft.

The approach was to conduct two ejection simulations with different arm positions. Case 1 was the normal situation with the pilot's hands on the ejection seat firing control handle. The second case was a worst case scenario with the pilot's hands on the seat side panels. This might be the case if the other crewmember pulled the ejection handle. Simulation conditions were set up to most closely represent an ejection during a VISTA test flight. An ACES II (Advanced Crew Escape System) F-16 ejection seat geometry with a 32° seat back angle was used with seat acceleration data from an ejection sled test. The TMT was positioned near the test pilot's shoulder based on the installation data. To consider a worst case scenario, a 95th percentile (based on height and weight) male was simulated.

The simulations showed that in the normal case, with the hands on the firing control handle, no contact with the TMT would occur. In Case 2 significant contact was predicted. The right lower arm contacted the TMT and seat side panel with forces as high as 5800 N (1300 lb) for 15 msec. This contact is large enough to possibly cause lower arm injury. This information allowed the test program to evaluate the added risk of flying with the TMT and the pilots to be briefed on positioning their hands during the unlikely event of an emergency ejection.

3.2 Detonation Hazard During Soldier Fall

Army soldiers carry a great deal of equipment, including detonators. Detonators triggered by impact pose a possible hazard if a soldier falls. To evaluate this risk, several simulations of various soldier falls were conducted, calculating the impact forces on the body. A large, fully loaded soldier was simulated tripping, falling out of a truck, and landing under a parachute. The predicted impact forces (Figure 3) are highly

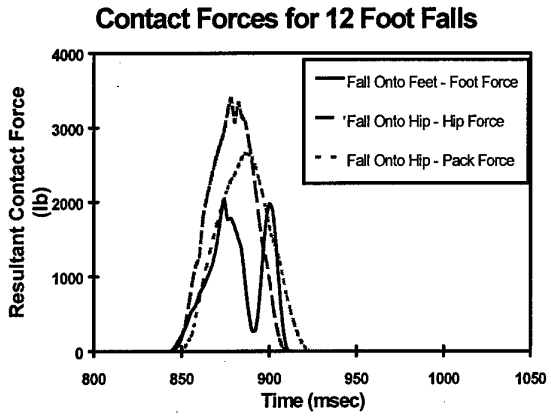

Figure 3 - Predicted Contact Forces During Soldier Falls

dependent on the contact properties of the body and the landing surface.

The worst case was found to be a 3.66 m (12 ft) parachute landing fall onto the hip (Figure 4). Therefore this case was further analyzed. The hip forces were analyzed based on the amount of body deformation caused by this contact. Since the deformation and force were greater than hipbone strength limits, the bone would fail in this scenario. The detonator initiation levels were then compared to the bone failure loads.

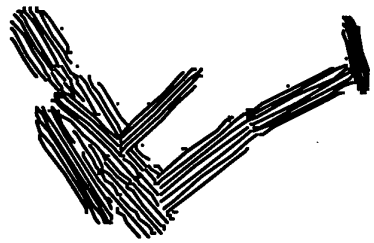

Figure 4 - Fully Loaded Soldier Falling on Hip

3.3 Manikin Performance Evaluation

When initial Joint Primary Aircraft Training System (JPATS) ejection tower tests had extreme manikin motion, computer simulations were used to help evaluate the results, determine feasibility of design options, and define future testing requirements. In the tower tests, the large JPATS manikin legs rotated forward pulling the hips extremely forward, as depicted in Figure 5. This caused the manikin to almost stand up in the seat. The resulting alignment of the spine could significantly increase a crewmember's injury likelihood. It was unclear whether this was due to the new manikin design or the ejection seat being evaluated. Several ATB simulations were conducted varying the manikin leg mass properties and the seat design. These simulations demonstrated that the manikin leg properties could affect the results and that the seat design had significant effect on the response. Using these results, a limited laboratory test program with a modified manikin was defined and conducted (Ref 3). These tests confirmed the simulation results. By conducting simulations and tests in conjunction, different concepts were easily evaluated, and the seat and manikin contributions to the motion were determined. This allowed the JPATS Program to go back to the ejection tower tests with a more biofidelic manikin and a modified seat and obtain successful results.

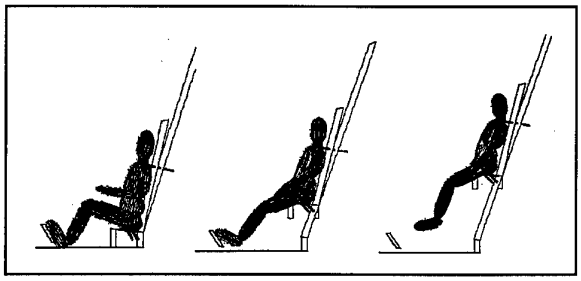

Figure 5 - ATB Simulation of Ejection Tower Test with Extreme Thigh Rotation

3.4 Supplementing Test Results

Another example of using biodynamic modeling to supplement test results occurred when extreme hip abduction (wishboning) was observed in an ejection sled test. Figure 6 shows the Advanced Dynamic Anthropometric Manikin (ADAM) during a 600 KEAS (knots equivalent airspeed) ejection test when this occurred. The ADAM manikin was designed to be highly biofidelic in its mass properties, joint degrees of freedom, and ranges of motion. However, its joint stops were designed for strength, not biofidelity. It is also a highly instrumented manikin, providing the hip rotations, but it does not measure the joint torques. Therefore the injury potential was unknown from the test data and simulations were used to determine what would happen to a human in this environment.

Figure 6 - Extreme Hip Abduction Observed in 600 KEAS Ejection Test with ADAM

The approach used was to calculate the upper leg angular velocity from the hip rotation test data. An ATB simulation of the ejection test was set up to start before the hips reached their stops. Because the interest was in the human injury potential, male human body data and hip joint properties were used. The GEBOD program was used to generate the human body data based on the ADAM dimensions. The hip joints were modeled as three degrees of freedom joints based on measured human voluntary range of motion and passive resistive torque data. The effects of active muscle response on the upper legs were not considered. To provide a controlled simulation, the lower torso was fixed to the seat. The thighs were given the orientation and initial angular velocity calculated from the test. The aerodynamic forces based on the seat velocity from the test were then applied.

The results of the simulation in Figure 7 clearly show that the hip rotation has passed the injury level. This is confirmed by the numerical data in Figure 8, where the hip joint exceeded 450 Nm (4,000 in-lb) in torque. This value is well beyond human tolerance levels. These results confirmed the conclusions made from the limited test data.

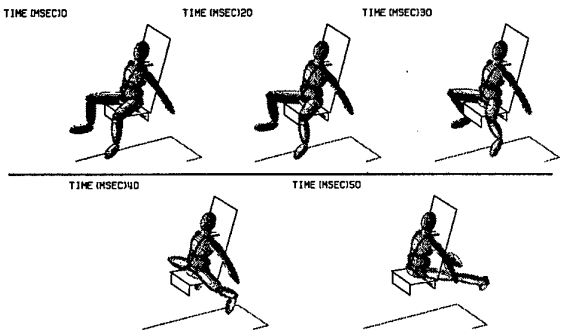

Figure 7 - Leg Flail Simulation

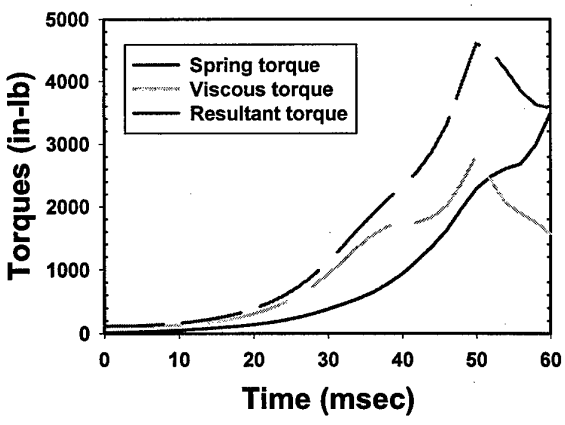

Figure 8 - Predicted Right Hip Joint Torques

4. SUMMARY

Biodynamics models such as the ATB model are applied to a variety of military environments. AFRL uses the model to provide evaluations in a short period of time, when testing is infeasible or too expensive. Simulations are even more valuable tools when used in conjunction with testing, defining test parameters and supplementing test results. It is important to recognize that the primary reason for the credibility of these examples' simulation results is the validation of the model. The ATB model is constantly being validated against human and manikin impact tests at AFRL. This continuous validation is required to have simulation data available when applications such as these arise.

5. REFERENCES

1. Cheng, H., Rizer, A.L., and Obergefell, L.A., "Articulated Total Body Model Version V, User's Manual," AFRL-HE-WP-TR-1998-0015, Wright-Patterson Air Force Base OH, February 1998.
2. Cheng, H., Obergefell, L.A., and Rizer, A.L., "Generator of Body Data (GEBOD) Manual," AL/CF-TR-1994-0051, Wright-Patterson Air Force Base OH, March 1994.
3. Buhrman, J.R., Andries, M.J., and Ma, D., "Risk Factors in Ejection Seat Design Associated with Upward Ejection for a Large Occupant," SAFE Symposium Proceedings, Phoenix AZ, September 1998, pp 361-370.

CONTINUED DEVELOPMENT OF AN INTEGRATED EASY5/ACESII-ATB MODEL FOR EJECTION SEAT SIMULATION

Deren Ma, Ph.D.
Systems Analysis & Research, Veridian
5200 Springfield Pike
Dayton, OH 45431

Louise A. Obergefell, Ph.D.
AFRL/HEPA
2800 Q Street
Wright-Patterson Air Force Base OH 45433-7901

Lawrence C. Rogers
ASC/ENFC
2530 Loop Road West
Wright-Patterson Air Force Base OH 45433-7101

Annette L. Rizer
Systems Analysis & Research, Veridian
5200 Springfield Pike
Dayton, OH 45431
USA

SUMMARY

This paper presents continued development and validation of an integrated ejection/crewmember model, specifically the modeling of aerodynamic effects and the crewmember/seat separation process. In a previous study, an ejection seat model, EASY5/ACESII (Engineering Analysis SYstem/Advanced Concept Ejection Seat), was coupled with a crewmember model, the ATB (Articulated Total Body) model. In this study, newly developed algorithms were incorporated into the integrated model to simulate the aerodynamics and seat/crewmember separation. Wind tunnel data from the ejection seat module are used to obtain total aerodynamic forces on the seat/crewmember combination. The crewmember module then uses an analytical method, based on air pressure and the exposed surface area, to calculate the aerodynamic forces and torques applied to the crewmember's individual body segments. These body forces and torques are then subtracted from the total forces and torques to obtain the force components applied directly to the seat in the ejection seat module. Once the man/seat separation signal is initiated, the aerodynamic forces and torques are applied only to the crewmember.

Dynamic interaction between the seat and crewmember during the very short period of their separation is complex and critically important. In this study, the harness release and crewmember/seat separation process algorithms were designed and implemented. When the release signal of the harness restraint is generated in the ejection seat module, it is transferred to the crewmember module. The harness belt in the crewmember module is then cut off. Meanwhile, the recovery parachute force from the ejection seat module is sent to the crewmember module. The combined forces due to gravity, recovery parachute, and aerodynamics separate the ejection seat and crewmember.

Simulations of F-16/ACESII sled tests were carried out to validate the newly developed features in the integrated model. Simulation results are reported and compared with results of ejection seat sled tests. The validation shows that the model successfully predicts the major features of the ejection seat motion and the crewmember biodynamic responses.

INTRODUCTION

Ejection seat dynamic characteristics and potential injury to its crewmember such as cockpit and aircraft clearance, and acceptable forces imposing on a crewmember during an ejection event are essential concerns for evaluating ejection seat performance. Because the crewmember's weight is on the same order of magnitude as the ejection seat weight, the crewmember's dynamic response during ejection has a direct impact on the ejection seat's stability and trajectory characteristics.

Ejection seat tests, including component level and full-scale tests, are the fundamental tools for the conceptual design and for the seat performance quantization. They are used to gather critical information and data of the ejection seat, such as the seat and crewmember's trajectories and the accelerations produced by the

Papers presented at the RTO HFM Specialists' Meeting on "Models for Aircrew Safety Assessment: Uses, Limitations and Requirements", held in Ohio, USA, 26-28 October 1998, and published in RTO MP-20.

seat on the pilot. However, due to the complexity of the ejection event scenarios and of the crewmember biodynamic, the limitation of the test equipment and data recording technology and high test costs restrict the types of ejections that the tests can simulate. Moreover, they are often not practical for certain studies such as the detailed evaluation of crewmember/seat interaction dynamics.

Computational modeling and simulation are commonly used in escape system development to predict performance and after testing to extrapolate performance for a wide variety of flight conditions. There are two types of computer models widely used in the escape system research community. The first type emphasizes modeling of the ejection seat and its components to predict the ejection trajectory and dynamic performance. The most popular models include the EASY5/ACESII model and ACCESS (Advanced Crew Capsule Escape System Simulation) model [1, 2, 3]. They are the multibody, six degrees-of-freedom programs designed for analyzing ejection seat stability and trajectory characteristics and for predicting the system performance throughout the escape envelope. Because the models treat the crewmember as a lumped point mass attached to the seat with springs and dampers, forces introduced to the seat from the crewmember and seat/crewmember interaction dynamics are largely overlooked. Therefore, it is not feasible to simulate the effects of CG (Center of Gravity) and MOI (Moment Of Inertia) changes during the ejection event. It is difficult to use this type of model for assessing the injury potential including those from inadequate limb restraint, poor body positioning and body segment collision with objects such as seat structure.

The second type concentrates on the modeling of crewmember and its surroundings to predict biodynamic responses of humans and manikins during aircraft ejection, aircraft crashes, automobile accidents and other hazardous events. The major three-dimensional codes in this category include the ATB model and its derivatives (CVS, CAL-3D, and DYNAMAN), MADYMO, and SOM-LA/TA[4,5]. However, these models require the input of the ejection seat motion data to predict the crewmember's biodynamic responses and to evaluate the potential for injuries. It is difficult to use models to simulate the operation process of the escape system, such as the event-time sequence control, rocket catapult firing, and parachute deployment. In addition, They only have limited or no aerodynamic capabilities to deal with the windblast effects.

To better assess the complete ejection seat/crewmember system, the EASY5/ACESII ejection seat model was integrated with the ATB crewmember model in a previous study [6]. The combined model emphasized not only the modeling of the ejection seat components, but also the detailed modeling of the crewmember and its surroundings. However, aerodynamics capabilities of both the ejection seat and crewmember models need to be integrated. Additionally, the seat/crewmember interaction and parachute modeling need to be further addressed. In this study the integrated ejection seat/crewmember model was reviewed. The existing aerodynamic models were integrated into the complete ejection seat/crewmember model. The seat/crewmember interaction and separation process algorithms were designed and implemented. Preliminary validation was performed against the 0-0 (zero airspeed - zero elevation) and 144 KEAS (Knot Equivalent Air Speed) ejection seat tests conducted on the High Speed Test Track at Holloman Air Force Base, New Mexico. Simulation graphics were reported and various simulation time histories were compared against those from the ejection seat tests.

EASY5/ACESII-ATB MODEL

The EASY5/ACESII ejection seat model and the ATB occupant model are the most prominent models widely used by the US Air Force and the escape system research community. The EASY5/ACESII ejection seat model's emphasis is on the modeling of ejection seat components, while the ATB model's is on the detailed modeling of the crewmember and their surroundings. To better make use of features and capabilities in both ejection seat and crewmember models and provide a powerful analytical tool for evaluating escape systems, the complete ejection seat/crewmember model is being developed by US AFRL (Air Force Research Laboratory).

The integrated model consists of four major modules: an ejection seat module, a crewmember module, an interface module, and an output module, as shown in Figure 1. The ejection seat module models the major seat components, including the firing control system, propulsion rockets, parachutes, and aerodynamic environment. It determines the seat motion based on the aircraft initial conditions, inertial properties of the seat, all forces and moments acting on the seat by rocket-catapult, STAPAC (STAble PACkge), the drogue and recovery parachute, windblast, the crewmember, and the restraint system, etc.

The crewmember module calculates the crewmember's biodynamic responses based on the ejection seat motion, body segment physical properties, seat interactions, windblast, and the belt restraint system. The module is based on three-dimensional coupled rigid body dynamics using Euler equations of motion with Lagrange-type constraints. A crewmember is described as a set of segments that are connected by kinematic joints. Outer surfaces of the segments are approximated by contact (hyper)ellipsoids that are used to determine the amount of contact, and application point for these forces. External forces are applied to the segments through interaction with other segments, planes, and harness restraint systems.

An interface module connects the ejection seat and the crewmember modules, and coordinates the numerical integration process. The ejection seat motion is transferred to the crewmember module and is used in calculating the crewmember's

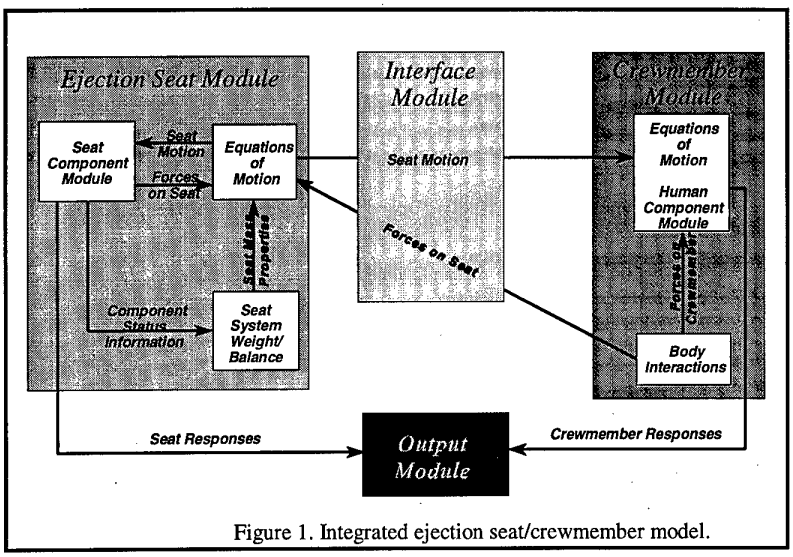

Figure 1. Integrated ejection seat/crewmember model.

biodynamic response. In the meantime, the forces and moments acting on the ejection seat by the crewmember and restraint system are sent to the ejection seat module to determine the motion of the ejection seat. An output module generates simulation results such as the ejection event-time sequence; any of the calculated dynamic state variables, and any forces and torques acting on the seat. With respect to the crewmember, the output includes the linear and angular positions, velocities, and accelerations of any body segment; the joint angles and torques; contact locations and forces, restraint belt forces, and aerodynamic forces acting on any body segment. These data are provided in time history format. Injury assessment information is also available, including the Dynamic Response Index (DRI), Multi-axial Dynamic Response Criteria (MDRC), lumbar and neck loads, seat/crewmember contact loads, and joint forces and torques.

NEW FEATURES

Aerodynamic Capabilities

Aerodynamic effects on ejection seat stability and potential injury to the crewmember are a major concern in design and evaluation of an ejection escape system. Classical methods used to model how aerodynamic forces and torques act on streamlined bodies are limited when applied to the blunt and jagged body shape of an ejection seat with a crewmember. Therefore, a combination of wind tunnel test data, CFD (Computational Fluid Dynamics) and multibody dynamics is used to study the aerodynamic performance of an ejection seat. There are two aerodynamic models in the combined ejection seat/crewmember model. One is from the ejection seat module, and another is from the ATB crewmember module.

In the ejection seat module, the aerodynamic characteristics for the ejection seat/crewmember combination are determined by accessing a large aerodynamic coefficient database that is primarily gathered on half scale models in AEDC's (Arnold Engineering Development Center) 16 foot transonic tunnel [7, 8]. Figure 2 shows the ACES II installation in AEDC wind tunnel. The coefficients vary with the Mach number, the seat orientation to the wind stream, and the crewmember size. Effects of propulsive rockets and aircraft proximity are also taken into account, as these will alter the pressure fields around the

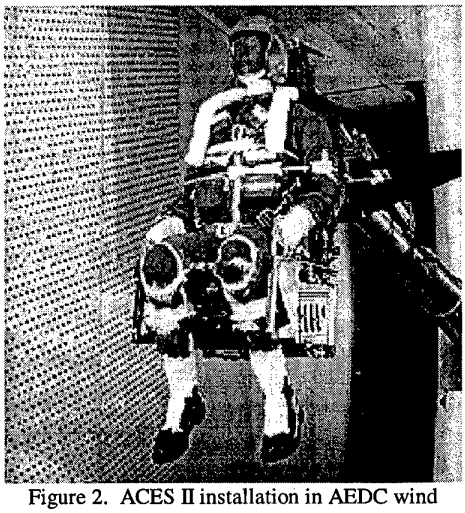

Figure 2. ACES II installation in AEDC wind tunnel.

seat/crewmember and change the aerodynamic coefficients. The ejection seat module uses the orientation, position and speed to find the force and torque coefficients in the wind tunnel-generated data matrix. The module starts to calculate aerodynamic forces and torques on the seat/crewmember combination as it passes through a wind stream plane fixed to the cockpit.

In the crewmember module, the aerodynamic forces are applied to any segments that penetrate a wind stream plane, as shown in Figure 3. Once a segment's ellipsoid penetrates the wind plane,

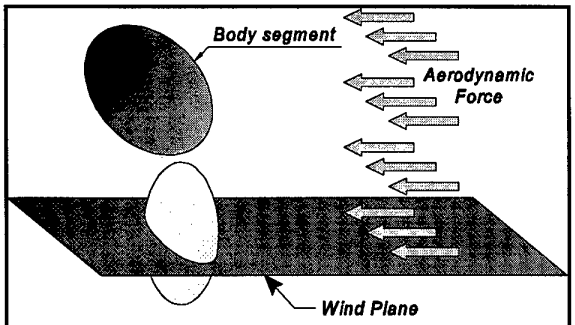

Figure 3. ATB aerodynamic model.

the projected area normal to the wind stream is calculated, and the forces are computed by multiplying the dynamic pressure by the wetted area and the drag coefficient. There are two types of wind pressure functions available in the crewmember module. The first is a time-dependent wind pressure function which gives three components of the wind pressure. The second type computes the wind pressure vector as a function of the relative velocity of a segment. Additionally, there is an option to account for the blocked wind where the body segments substantially overlap. Clearly, the windblast acts on the seat/crewmember combination in the ejection seat module, and applies repeatedly to the crewmember's body segments in the crewmember module. Therefore, the aerodynamic forces and torques acting on the crewmember are duplicated in the combined ejection seat/crewmember model. To integrate the aerodynamic capabilities of both models and to better use all the features available, the aerodynamic model in the ejection seat module is used to determine the aerodynamic effects on the seat. The aerodynamic model in the crewmember module, on the other hand, is employed to evaluate the aerodynamic forces and torques on the crewmember.

To this end, aerodynamic forces and torques on the seat are separated from those on the crewmember. Wind tunnel data from the ejection seat module are used to obtain the total aerodynamic force and torque on the seat/crewmember combination. The measured total aerodynamic force in the wind tunnel test $F_{seat/man}$ can be expressed as two components

$$F_{seat/man} = F_{seat} + F_{man} \tag{1}$$

where F_{seat} is the force component on the ejection seat, and F_{man} is the force component on the crewmember. At the same time, the aerodynamic force F_{man} on the crewmember is calculated using forces on each individual body segment from the crewmember module.

$$F_{man} = \sum_{i=1}^{n} F_{ith}^{seg} \tag{2}$$

where F_{ith}^{seg} is the aerodynamic force acting on the i^{th} body segment ($i = 1,n$). These forces and associated torques are applied to the body segments by the crewmember module. The crewmember aerodynamc force and torque are then transferred to the ejection seat module as shown in Figure 4, and subtracted from the total force and torque to obtain the components applied directly on the seat.

$$F_{seat} = F_{seat/man} - \sum_{i=1}^{n} F_{ith}^{seg} \tag{3}$$

This force and associated torque are applied to the seat by the ejection seat module. Once the seat and crewmember start to separate, the force and torque calculated from the crewmember module are applied only to the crewmember and no longer passed to the ejection seat. To implement these algorithms, the related codes were programmed and/or modified to facilitate the aerodynamic model integration.

Seat/Crewmember Separation Process

It is important to better understand the dynamic interaction between the seat and crewmember to fully evaluate the seat performance during the very short period of their separation. The crewmember/seat separation process starts when the harness release mechanism releases the crewmember from the seat, as the lap belt and inertial reel pins are withdrawn during the automatic recovery sequence. Release of the seat pan latch allows the seat lid to rotate and allows the survival kit to be withdrawn from the seat bucket. The recovery parachute then lifts the crewmember from the seat. This harness release and crewmember/seat separation process were investigated and the related algorithms were designed for the integrated ejection seat/crewmember model. When the release signal of the harness restraint was generated in the ejection seat module's control sequencer, it was sent to the crewmember module. The harness/belt in the

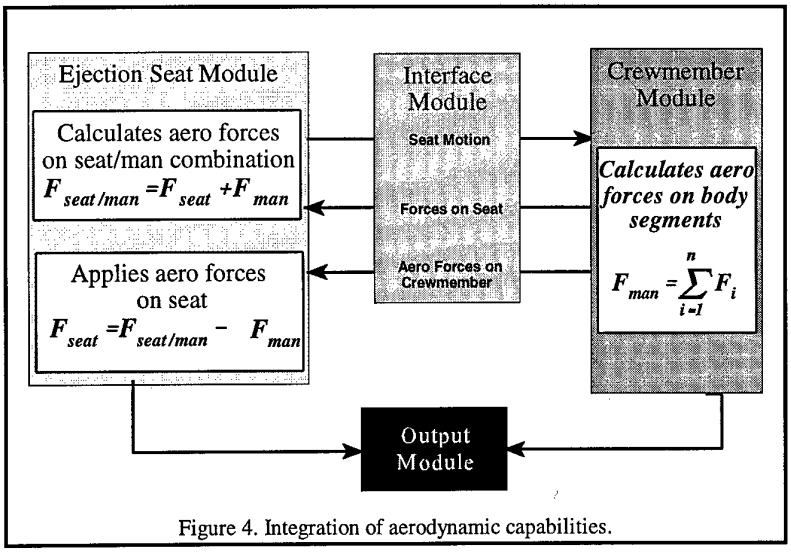

Figure 4. Integration of aerodynamic capabilities.

crewmember module was cut off and released the crewmember from the seat during the automatic recovery sequence. In the meantime, the recovery parachute force and torque from the ejection seat module was transferred to the crewmember module and applied to the crewmember's upper chest. The combined forces from gravity, recovery parachute, and aerodynamics separate the ejection seat and crewmember.

VALIDATION AND DISCUSSION

Ejection Seat Tests

Initial validation of the integrated model and newly developed features ensures that the simulation results have a satisfactory range of accuracy against ejection seat tests in predicting major features of both the ejection seat motion and of the crewmember biodynamic responses. Simulations of a wide variety of previously conducted ejection tests are planned. The first tests to be simulated are a zero airspeed-zero elevation and a 144 KEAS ejection seat tests [9, 10]. Both tests used a standard F-16 configuration seat with the ARS (Advanced Recovery Sequencer). The first test used a 95th percentile GARD (Grumman-Alderson Research Dummy) and the second one utilized a large ADAM (Advanced Dynamic Anthropomorphic Manikin). Both dressed in standard USAF personal flight equipment.

Simulation Input Description

In the simulation input files, fifteen body segments connected by fourteen kinematic joints were used to represent the dummy. Based on the mass and stature of the dummies, the inertial and geometric data for these body segments were generated using the GEBOD (GEnerator of BOdy Data) program. The cockpit layout, including the floor, seat, and rudder pedals, was based on the F-16 ACES II general configuration. The ejection seat back reclined 30° from vertical and the seat pan inclined 30° from horizontal as illustrated in Figure 5. The angle between the seat back and guide rails was 4.5°. In order to describe the compliance properties between the crewmember's segments and the seat panels, force-deflection characteristics were modeled and included in the simulation. A conventional double shoulder strap and a lap belt harness were used for restraining the crewmember. The contact force-deflection and belt stress-strain functions were taken from other validated occupant simulations.

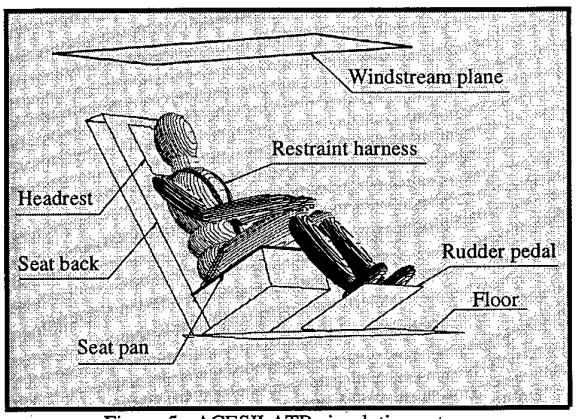

Figure 5. ACESII-ATB simulation setup.

0-0 Test Simulation Results

Figure 6 shows a graphic sequence portraying the crewmember and the ejection seat in the 0-0 ejection seat simulation. At time zero, the rocket-catapult fires and the seat starts to move up. As the seat approaches the top of the guide rails at about 180 ms, the STAPAC system ignites to provide a counter force to prevent extreme pitching. The recovery parachute mortar initiates at about 200 ms after rocket catapult ignition. The harness release thruster is actuated at about 450 ms, and the deploying parachute separates the crewmember from the seat. The parachute inflates to a reefed configuration until the reefing line cutters actuate to permit full inflation. Simulation view graphics present physically reasonable results.

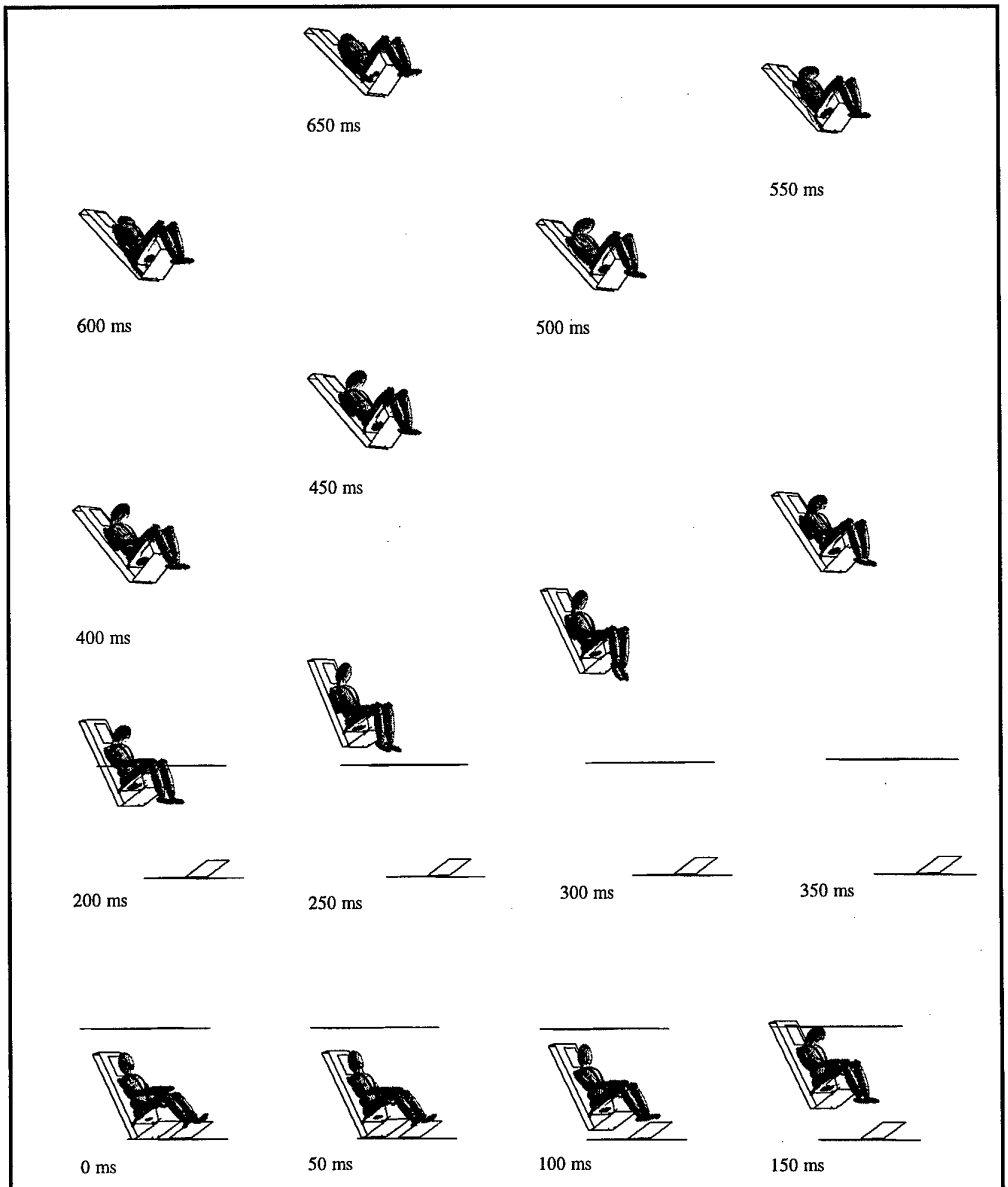

Figure 6. Graphic sequence of the 0-0 ejection seat/crewmember simulation.

The seat accelerations were measured using triaxial accelerometers installed in the seat pan. Figures 7 and 8 illustrate the comparison of the tested and simulated seat accelerations. The seat accelerations in the X and Z directions match very well with the test data up to STAPAC ignition and parachute deployment. However, there were some differences in the acceleration peak values after the parachute deployed. The simulated peak acceleration in the X direction was greater than that tested. On the other hand, the simulated peak acceleration in the Z direction was less than that tested. These differences were mostly due to the difficulty in accurately modeling the seat ballistic components and the unstable characteristics of the ejection seat system.

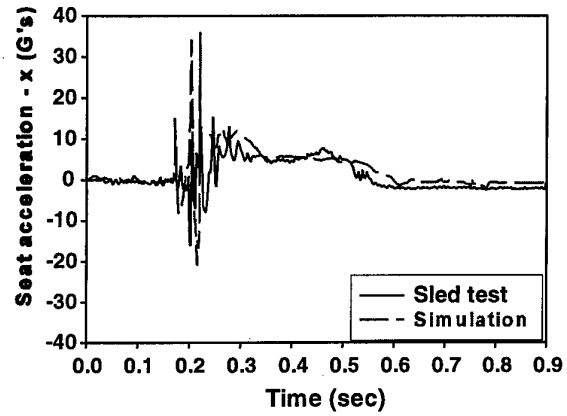

Figure 7. Comparison of seat accelerations - x (0-0 case).

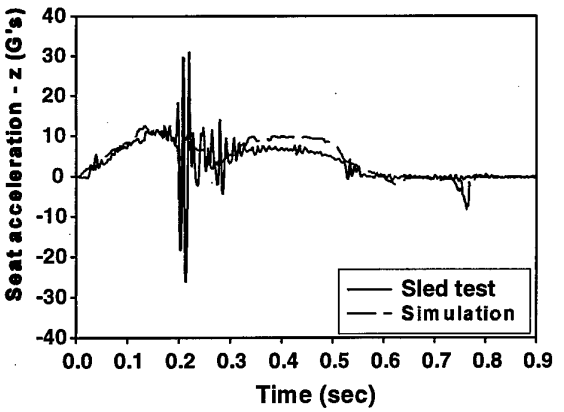

Figure 8. Comparison of seat accelerations - z (0-0 case).

144 KEAS Test Simulation Results

Figure 9 shows the graphic time sequence from the combined model simulating the 144 KEAS ejection seat test. The zero time frame shows the crewmember position just as the ejection is initiated. The graphic sequence portraying the crewmember and the ejection seat compares extremely well in dynamic response patterns with those of the film covering the test from seat initiation through the catapult and rocket phase, up until seat/crewmember separation. However, some differences have been observed. An approximately 100 ms time-shift between the test film and the simulation view graphics occurs after the seat/crewmember separation.

Transducer results were also used to validate the ACESII-ATB model. Figures 10 and 11 show comparisons of the tested and simulated seat accelerations. The accelerations in the X and Z directions match very well with those of the tested results. The predicted head accelerations in the Z acceleration as shown in Figure 12 also agree very well with that of the test in pattern and timing.

CONCLUSIONS

The complete EASY5/ACESII-ATB ejection seat/crewmember model was reviewed in this study. Aerodynamic capabilities were integrated into the combined model using features from both the ejection seat and crewmember modules. The aerodynamic forces and torques were described using wind tunnel test data combined with dynamic modeling techniques. Aerodynamic effects on the seat were calculated using the ejection seat module. Aerodynamic forces and torques on the crewmember's segments were modeled using the crewmember module. Because the ejection seat tests were not instrumented for aerodynamic force measurement, the validation was performed by correlating the overall dynamic responses in the simulations with those in the ejection sled tests. Additionally, the harness release and crewmember/seat separation process were investigated and the related algorithms were designed and implemented for the integrated ejection seat/crewmember model. Subsequent validation simulations including high speed ejection recovery modes are underway. Drogue and recovery parachute dynamics and modeling have also been closely analyzed for further implementation.

ACKNOWLEDGMENT

This work was supported by U. S. Air Force Research Laboratory, AFRL/HEPA and HSC/YA.

REFERENCES

1. Jines, L. A., "Computer Simulation of Ejection Seat Performance and Preliminary Correlation with Empirical Data," Technical Report AFFDL-TR-79-3150, Flight Dynamics Laboratory, WPAFB, Ohio, 1980.

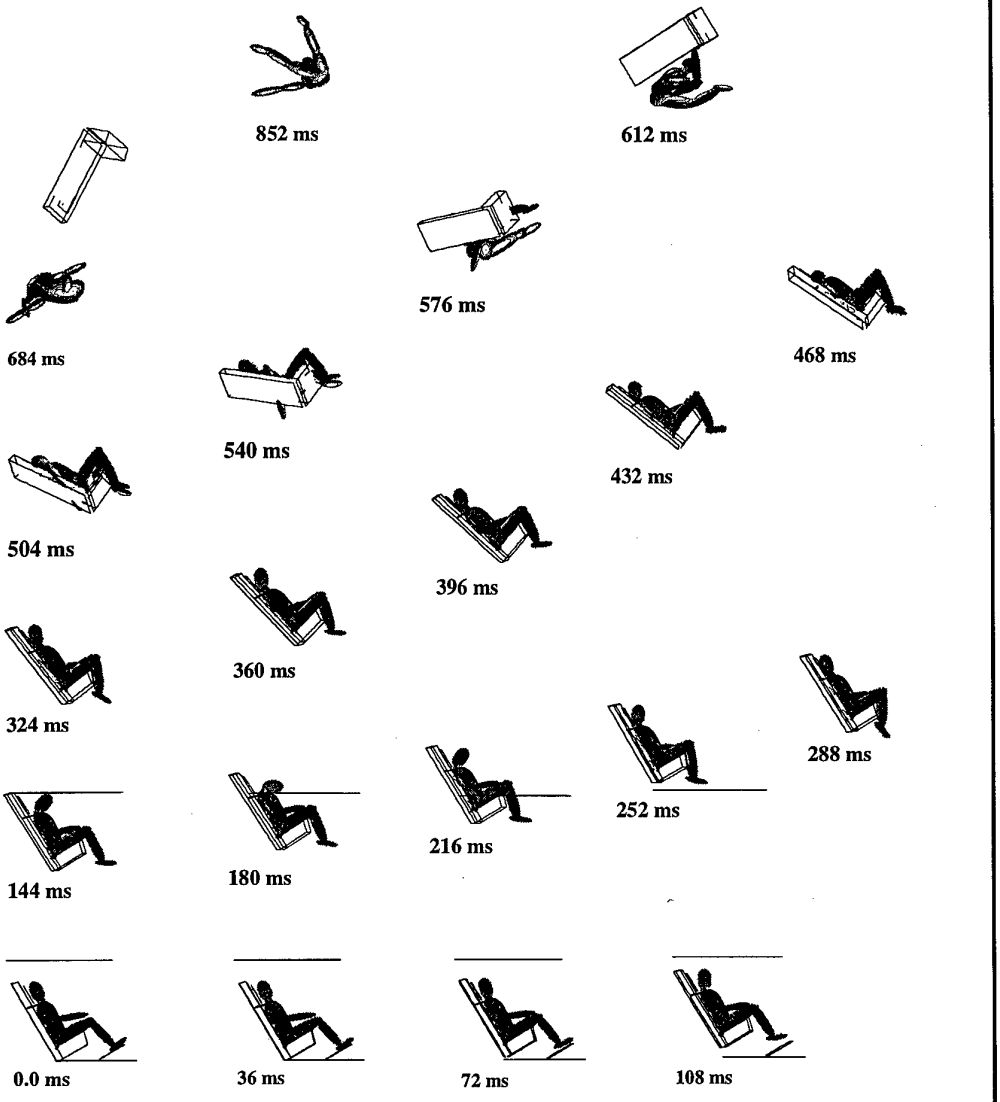

Figure 9. Graphic sequence of the 144 KEAS ejection seat/crewmember simulation.

2. Vian, J. L., "Ejection Seat Software Simulation Model Modification," Final Report CDRL B001, Boeing Defense & Space Group, Boeing Company, Seattle, WA, 1996.

3. Yeiser C. and Oslon, M., "Preliminary Report - Advanced Crew Capsule Escape System Simulation (ACCESS) Computer Program: ACCESS User's Manual Volume 2," Prepared for Naval Air Waterfare Center, Aircraft Division, Escape System Branch, Sept. 1992.

4. Obergefell, L. A., Gardner, T. R., Kaleps, I., and Fleck, J. T., "Articulated Total Body Model Enhancements,"

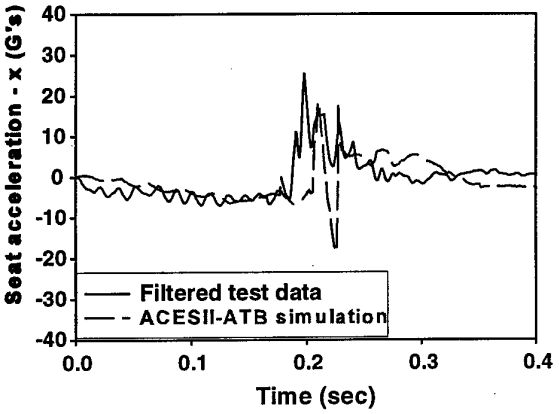

Figure 10. Comparison of ejection seat accelerations in x.

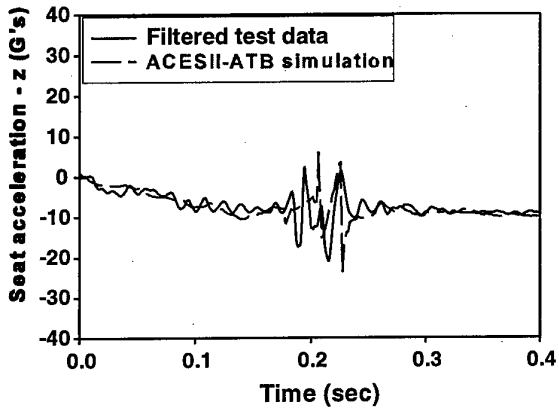

Figure 11. Comparison of ejection seat accelerations in z.

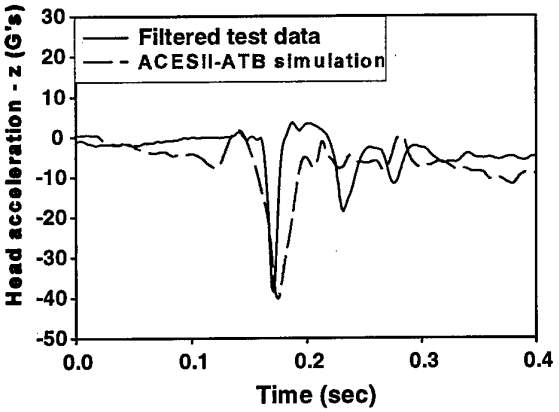

Figure 12. Comparison of the head accelerations in z.

Vol. II - User's Guide, Final Report No. AAMRL-TR-88-043, 1988.

5. Laananen, D.H., "Computer Simulation of an Aircraft Seat and Occupant(s) in a Crash Environment - Program SOM-LA/SOM-TA User Manual," DOT/FAA/CT-90/4, Federal Aviation Administration Technical Center, Atlantic City Airport, New Jersey, May 1991.
6. Ma, D., Obergefell, L. A., Rizer, A. L., and Rogers, L. C., "Development of an Integrated Ejection Seat/Crewmember Model," Proceedings of the 35th Annual Symposium, SAFE Association, pp317- 1997.
7. "Aerodynamic Characteristics of a Full Scale ACES-II Ejection Seat with a Small Female of Large Male Manikin at Mach Number from 0.2 to 1.4" AEDC-TR-87-16, Arnold Engineering Development Center, Arnold AFB, TN, 1987.
8. "Aerodynamic Characteristics of a Half Scale CREST Ejection Seat at Mach Number from 0.6 to 3.0," AEDC-TR-88-6, Arnold Engineering Development Center, Arnold AFB, TN, 1988.
9. Jackson, C. P., "ACES II Advanced Recovery Sequencer (ARS) System Qualification Test Program - Test 3," Technical Report MDC-K5261, Missile Systems Company, McDonnell Douglas Corporation, 1990.
10. Snyder, L., "CREST/AMIT Test Series - Tests 79E-A1 through 79E-L1 and Tests 70X-A1 through 70E-M1," Test Summary Report TSR-79E, Test Track Division, 46th Test Group, Holloman Air Force Base, NM, 1994.

HEAD PROTECTION AGAINST WINDBLAST FOR CREW ESCAPE

Philemon C. Chan
James H-Y. Yu
James H. Stuhmiller

Jaycor
9775 Towne Centre Drive, P. O. Box 85154
San Diego, California 92186-5154, USA
Tel: (619) 453-6580

SUMMARY

A pilot ejecting from an aircraft at high speed faces the possibility of windblast head/neck injury. To establish a phenomenological understanding of windblast protection for the head, three stagnation concepts, the unvented fence, the hood and the brim have been evaluated. As tested in the wind tunnel, the unvented fence and hood produce overstagnation which may subject the head to unwanted oscillations. The vented hood and the brim can reduce the normal head force without overstagnation, but with a significant increase of side head force. The side head force increase is caused by windward headrest flow stagnation, as confirmed by computational fluid dynamics simulations and subscale water tunnel model testing. Studies were performed to reduce the head rest flow stagnation using the open brim concept.

INTRODUCTION

A pilot ejecting from an aircraft at high speed faces the possibility of windblast head/neck injury. This threat can occur even for the future advanced seats while the pilot is still on-rail before the stabilization or active seat propulsion system is effective. The addition of stagnation devices around the head or the seat may be effective in mitigating the windblast threat.

The objective of this paper is to understand the phenomena controlling the windblast load to the head to guide the development of stagnation concepts by data analysis, subscale testing and computational fluid dynamics (CFD) studies. A large number of wind tunnel tests have been performed by the Air Force that can provide insight into the processes controlling windblast loading to the head. A variety of flow stagnation fences, with and without venting, have been tested [1, 2, 3]. The scope of the current effort was limited to a subset of the data we obtained related to three particular stagnation concepts: the unvented fence [4], the hood and the brim [5]. Subscale water tunnel tests and CFD simulations were used to understand the trends in the data to develop guidance for new concepts.

The derived phenomena understanding has benefited the development of the open cloth brim concept by the 4th Generation Escape Seat Demonstration Program of the Joint Air Force-Navy's CRew Escape Technology (CREST) Program [12]. The wind tunnel data for this open brim was also evaluated.

AIR FORCE WIND TUNNEL DATA ANALYSIS

Three stagnation concepts, the unvented fence, the hood and the brim, were evaluated based on the analysis of the Air Force wind tunnel data. Data analysis was performed using Jaycor's database software, SCATT, which can correlate test results across multiple test parameters, such as pitch, yaw and protection type. A basic seat means no protection is used.

The fence concept selected for the present study surrounds the whole seat with no venting, as shown in Figure 1a [4]. This fence was tested using a half scale seat-man model (tests Vought 637 and 644, and Calspan 08014). Four solid fences with increasing sizes were analyzed, together with one flex fence, which was the same size as the 2/3 solid fence. Mach number effects were tested for this half scale model.

The hood and the fence are attachments to the headrest (Fig. 1b-c). The hood is a headbox around the head, with controllable venting from the side and rear (Figure 1b) [5]. The brim is a hood without the sides, as shown schematically in Figure 1c. Both the hood and the brim were full scale tests using a 95th percentile manikin on an ACES II ejection seat (test Vought 756) [5]. Only low speed tests were performed for the full scale model.

Measured head/neck forces are compared to tolerances. According to the CREST criteria [6], the normal (lift) force should not exceed 300 lb. To prevent the head from flexing forward during ejection, the axial force should remain positive, which means that the wind load should always push the head to the headrest. As for the side force, a tolerance of 250 lb is selected based on a literature survey showing a range of thresholds from 154-418 lb. Consequently, based on the expected maximum

Papers presented at the RTO HFM Specialists' Meeting on "Models for Aircrew Safety Assessment: Uses, Limitations and Requirements", held in Ohio, USA, 26-28 October 1998, and published in RTO MP-20.

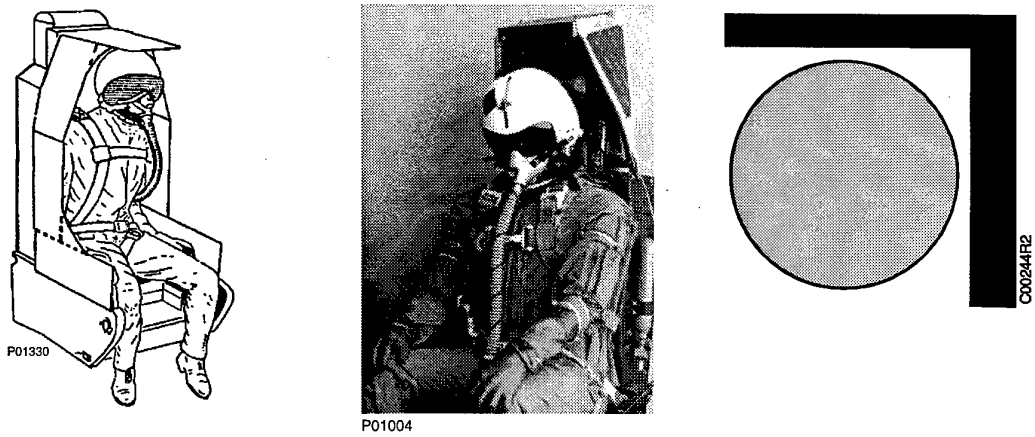

(a) Fence (unvented) (b) Hood (c) Brim

Figure 1. Air Force wind tunnel tests selected.

dynamic pressure of 2100 psf for advanced seats [7], the normal and side head force coefficients, CFHZN and CFHYN, should not exceed 0.323 and 0.269, respectively.

Without added protection, the basic seat data show that the normal head force coefficient exceeds the tolerance (CFHZN > 0.323) (Figure 2). The data confirms that head/neck protection is needed for future advanced aircraft.

As shown in Figure 2, the normal head force coefficient increases with the pitch angle α, with a recovery for α greater than 15°. This recovery is likely caused by knee shielding, which is expected to diminish with the yaw angle β, as shown by the full scale data in Figure 2. Knee shielding effect at high pitch angles can be observed by flow visualization studies in the wind tunnel and by streamline tracing using CFD results (Figure 3). The three-dimensional CFD simulation shown in Figure 3b was performed using Jaycor's Navier-Stokes code EITACC [8].

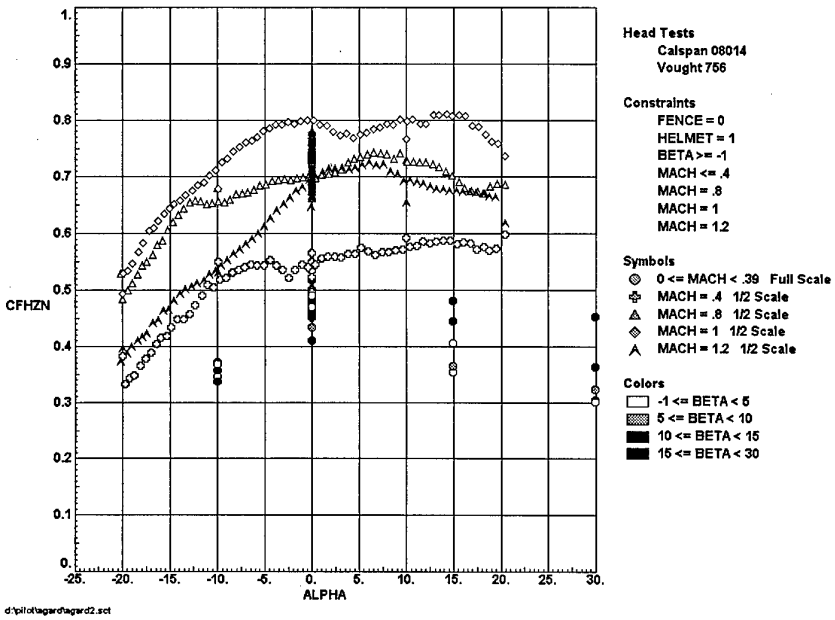

Figure 2. Basic model normal head force coefficient (Mach < 0.39 is full scale; Mach > 0.39 is half scale).

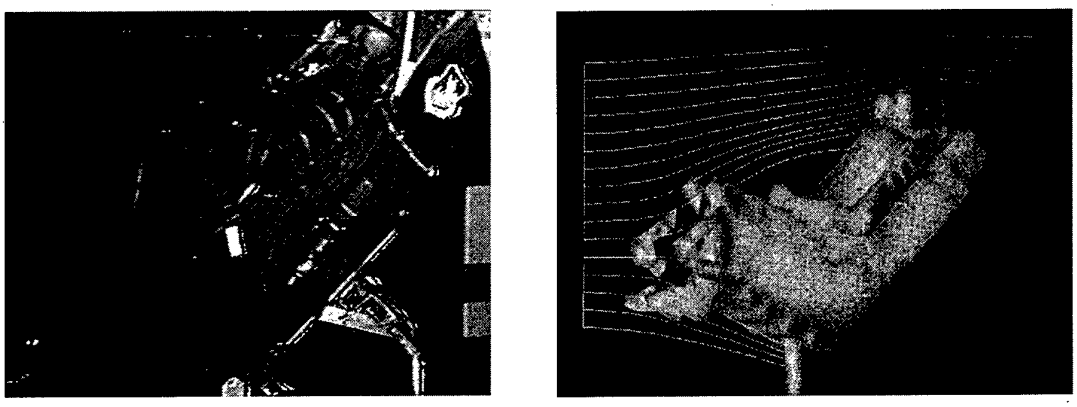

(a) Wind tunnel flow visualization (b) CFD simulation

Figure 3. Low speed flow over ejection seat at $\alpha = 30°$

The basic model normal head force coefficient also increases with Mach number, but with a supersonic recovery, as shown by the half scale data in Figure 2. Therefore, it is expected that the windblast threat to the head will increase with Mach number throughout the subsonic range.

The wind tunnel data indicate some data difference (at low speed) between the half and full scale tests that have not been resolved (Figure 2). This data difference could be due to the model difference between the half scale seat-man model and the full scale manikin-on-seat tests.

Figure 4 shows the effects of the unvented fence on the head force coefficients as scatter plots. The abscissa designates the fence size and type, as also indicated on the top of each plot. The basic model is always labeled as fence=0. To help bring out the β-effect as displayed by the symbols, the results for each fence size are spread out horizontally according to the yaw angle, β.

When unvented fences are added to the basic seat, both the normal and axial head force coefficients decrease with increasing fence size (Figure 4). (The flex fence is the same size as the 2/3 solid fence.) To obtain effective normal head force reduction (CFHZN < 0.323), the 2/3 and larger fences are required (Figure 4a). However, the axial head force is overstagnated when 1/2 and larger fences are added, as indicated by negative values of the axial head force coefficient CFHXN (Figure 4b). Due to the possibility of axial oscillation of the head, overstagnation is undesirable and should be prevented [9].

In contrast to the fence, the hood only surrounds the head and consists of a top brim with sides (Figure 1b). Three hood sizes, small, medium and large, were tested, including the effects of side and rear venting.

A large unvented hood is needed to reduce the normal head force coefficient below 0.323, (Figure 5a). With no venting, however, the medium and large hoods overstagnate the axial head force, as indicated by negative CFHXN (Figure 5b).

To reduce the normal head force effectively (CFHZN<0.323), a large vented hood is still required (Figure 6a). Venting for the hood does not affect the normal head force pattern significantly (Figures 6a and 5a). With side and rear venting, however, overstagnation of the axial head force is eliminated (CFHXN > 0) (Figure 6b).

The brim is the hood without sides (Figures 1b-c). Three brim sizes, small, medium and large, were tested. Figure 7 shows the effect of the brim on the normal and axial head force coefficients.

To reduce the normal head force adequately for all pitch, a large brim is required (Figure 7a). The small brim actually increases the normal head force coefficient at high α, suggesting a forward shift of the separation point on the helmet, resulting in loss of stagnation in the crown region to reduce lift (Figure 7a).

The brim does not produce axial overstagnation (Figure 7b). Furthermore, the brims eliminate the α-trend of the axial head force coefficient seen in the basic model (Figure 7b), indicating that flow stagnation can cause significant change of flow separation patterns [10].

Both the vented hood and the brim can reduce the normal head force without axial overstagnation (Figures 6-7), but the hood results in more unfavorable effects on the side head force (Figure 8). Figure 8 shows that adding the brim or the vented hood to the basic model increases the side head forces significantly. While the

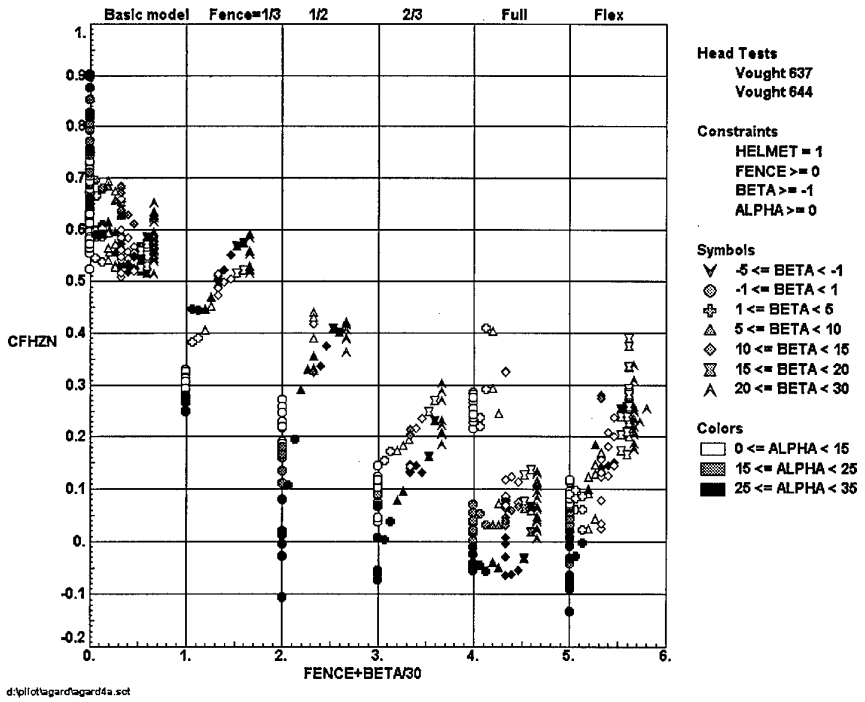

(a) Fence effect on normal head force coefficient

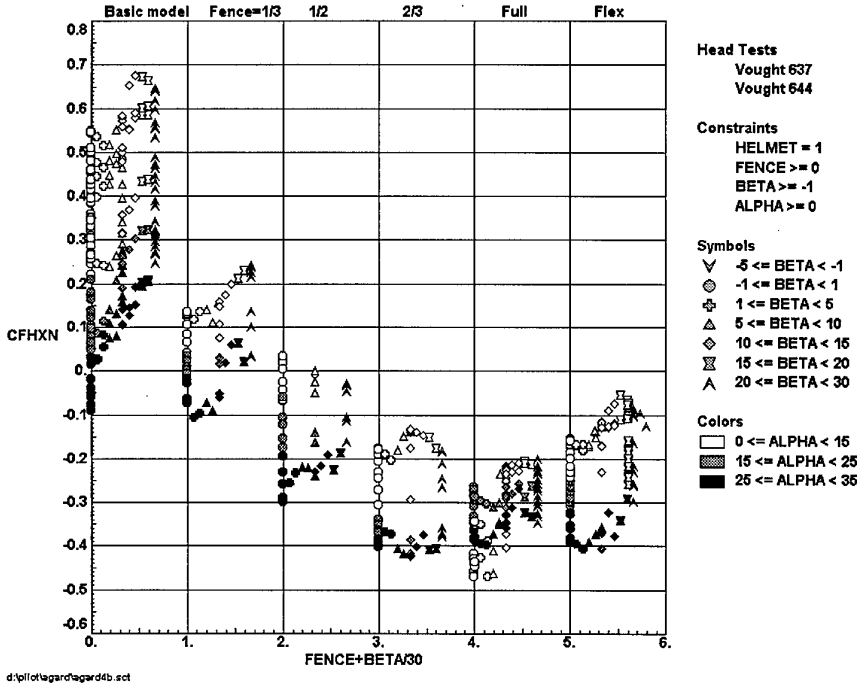

(b) Fence effect on axial head force coefficient

Figure 4. Unvented fence effect on head forces.

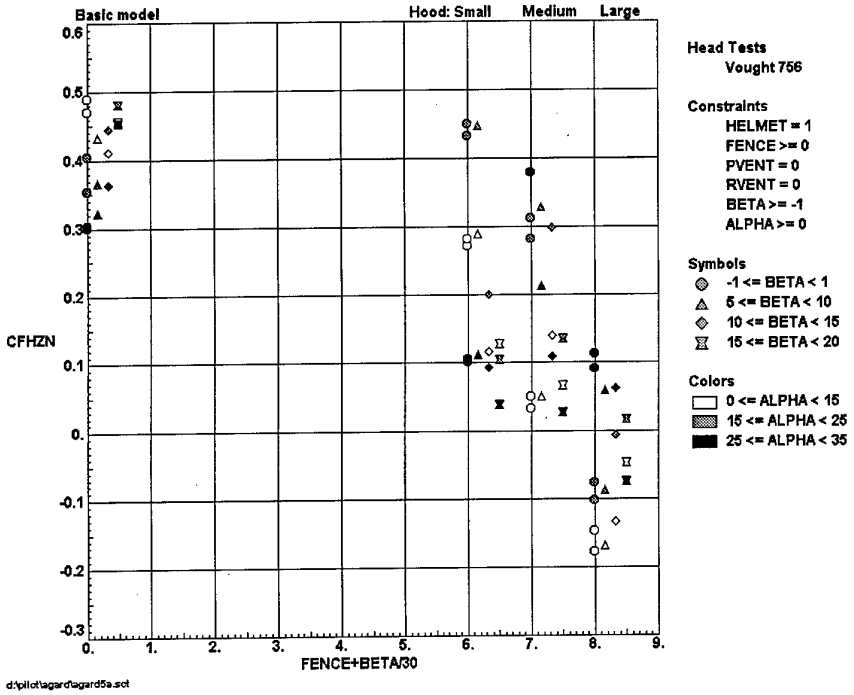

(a) Hood effect on normal head force coefficient with no venting

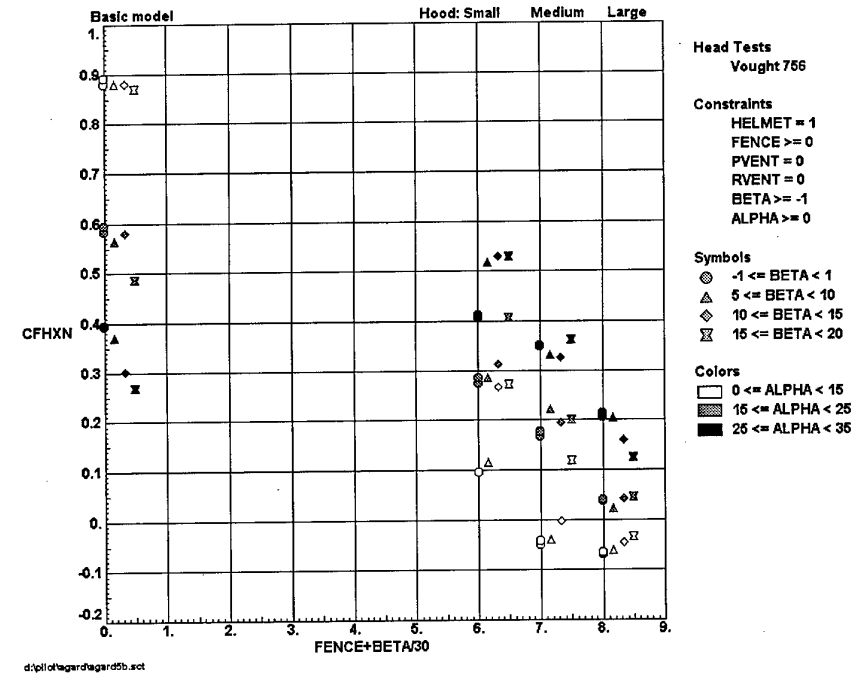

(b) Hood effect on axial head force coefficient with no venting

Figure 5. Unvented hood effect on head forces.

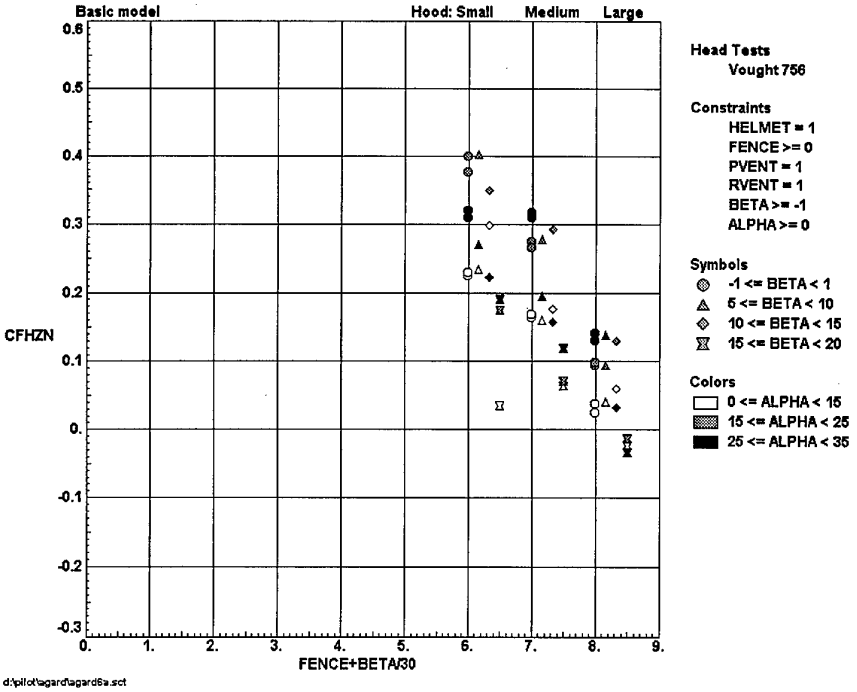

(a) Hood effect on normal head force coefficient with side and rear venting

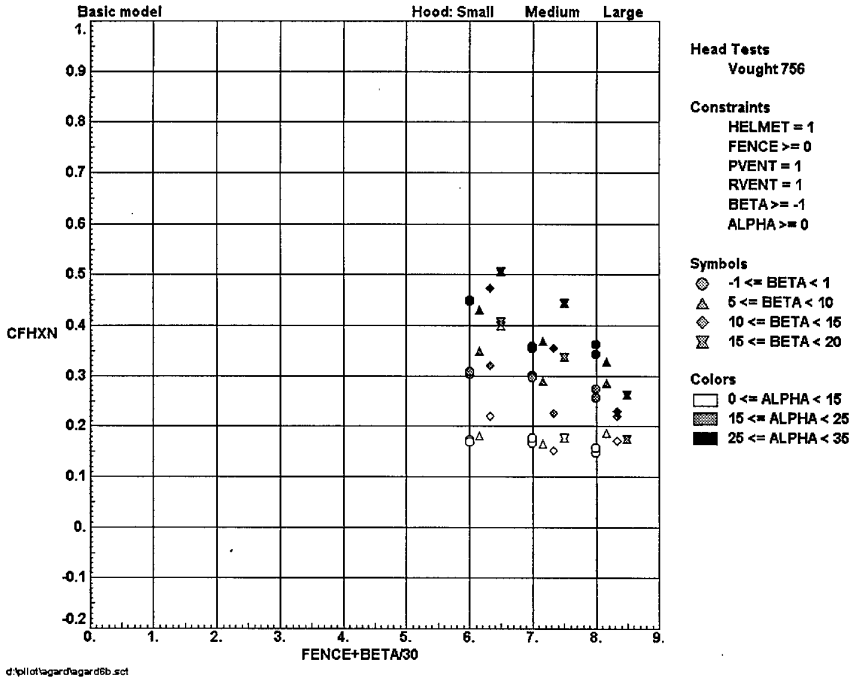

(b) Hood effect on axial head force coefficient with side and rear venting

Figure 6. Vented hood effect on head forces.

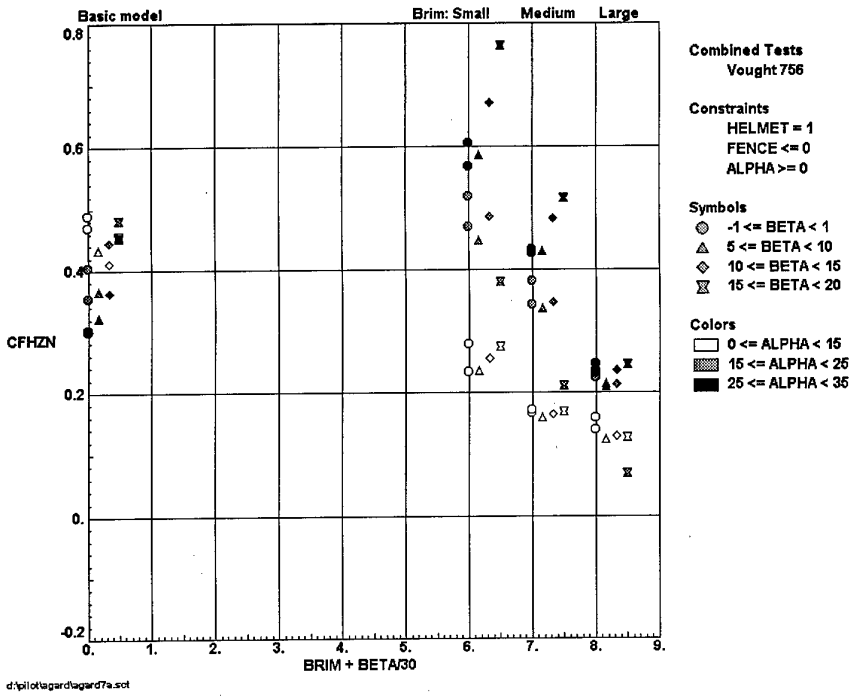

(a) Brim effect on normal head force coefficient

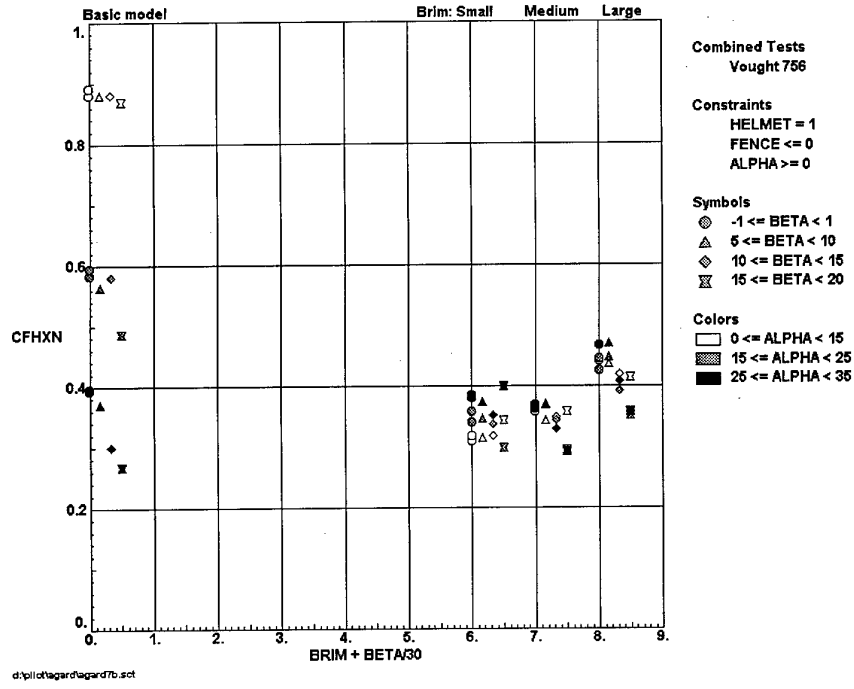

(b) Brim effect on axial head force coefficient

Figure 7. Brim effect on head forces.

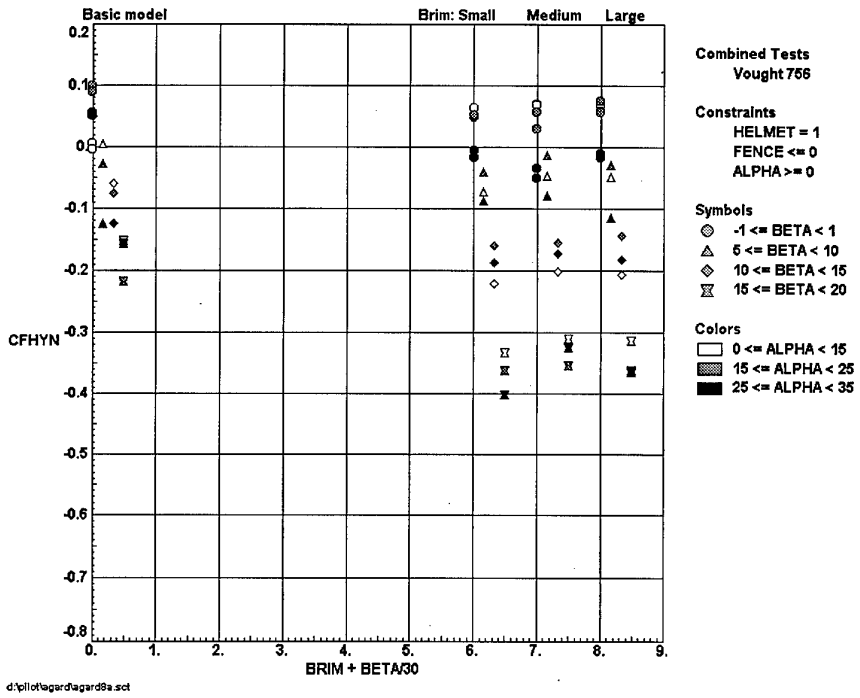

(a) Brim effect on side head force coefficient

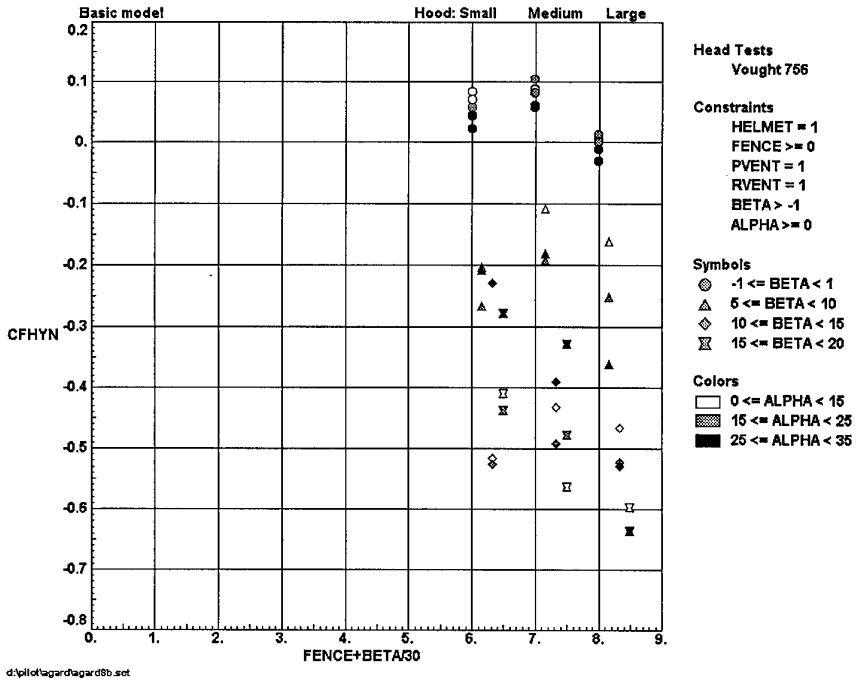

(b) Hood effect on side head force coefficient with side and rear venting

Figure 8. Brim and hood effects on side head force.

brims double the side head force coefficients (Figure 8a), the vented hoods increase the side head force coefficients by 3 to 4 times (Figure 8b). Side head forces and motions can result in serious neck injuries that should be prevented in these designs. Since both the hood and the brim increase the side forces, we need to understand the origin of this effect so the designs can be optimized.

CFD simulations indicate that windward headrest flow stagnation tends to increase the side head force. Using the EITACC code, the flow over an isolated cylinder at 20° yaw was calculated (Figure 9a), and the simulation was repeated by adding a headrest behind the cylinder (Figure 9b). The results show that just the addition of the head rest to the cylinder increases the side force coefficient by 4 times (Figure 9). In fact, the side head force coefficient of -0.2 observed for the full scale basic seat at 15° yaw (Figure 8a) is four times greater than the corresponding component of the drag on an isolated sphere (-0.05) [11]. This side head force increase over the geometric component is caused by windward flow stagnation on the headrest that can be further aggravated by additional stagnation devices (Figure 9b). Therefore, controlling side forces in a design is a matter of controlling the windward side flow stagnation.

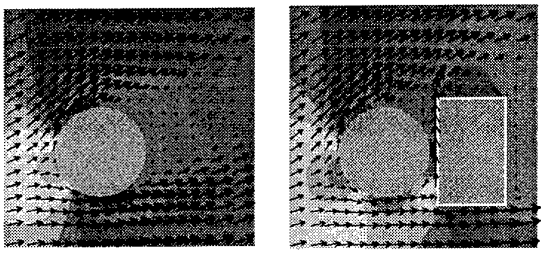

P01005

(a) Isolated cylinder, CFHYN = 0.14

(b) Cylinder with headrest, CFHYN = 0.55

Figure 9. CFD study of side head forces.

Three stagnation concepts, together with the basic model, have been analyzed. The basic model will exceed the CREST normal head force tolerance at a dynamic pressure of 2100 psf. The unvented fence and unvented hood overstagnate the axial head force. Both the large vented hood and large brim can reduce the normal head force without overstagnation, but with a significant side force penalty.

The reduction of the normal head force comes from flow stagnation above the head. The addition of sides tend to increase the side head force. An attractive design will produce high pressure above the head to reduce normal forces, while minimizing stagnation behind and on the windward side of the head.

WATER TUNNEL TESTS FOR OPEN BRIM

Subscale water tunnel tests were conducted to study the control of headrest flow stagnation for the brim concept. The Jaycor water tunnel is driven by gravity, with low turbulence level entering the test section. The test section used was 6×12 in. cross section, with a head Reynolds number of about 5×10^5 for a 2/9 scale model.

Three idealized head-torso models were tested (Figure 10). The basic model consists of a 2-in. sphere with an "upper torso" and a headrest (Figure 10a). To model a closed brim, a rectangular plate is added to the top above the head (Figure 10b).

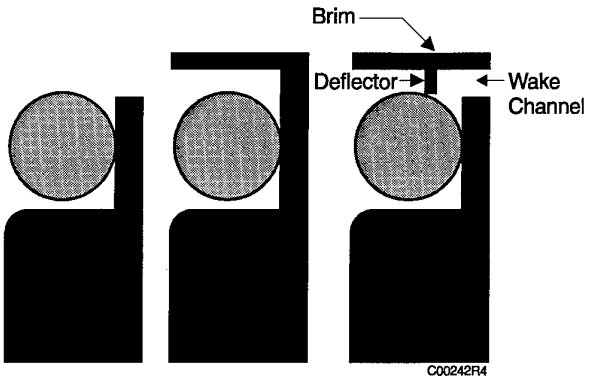

Figure 10. Idealized geometry considered.

The open brim concept consists of a brim with a crown deflector and a wake channel (Figure 10c). The crown deflector stagnates the flow above the head to reduce the normal force. The wake channel exposes the back of the head to the low wake pressure. Two brim sizes, medium and large, were tested for each brim geometry.

Since high pitch and yaw comprise the worst conditions, all tests were performed at α=30° and β=15°. Figure 11 shows the mounting of the open brim models in the water tunnel. Pressure and force data were taken. The test section dynamic pressure was about 2 psi. The run time for each test was about 30 sec.

Pressure data taken behind the head and on the windward side of the headrest confirm the reduction of windward stagnation effects by the open brim. Figure 12 shows that adding the medium or large closed brims to the basic model increases the pressure coefficients behind the head and on the windward side of the headrest significantly. When the open brim is used, however, both pressure

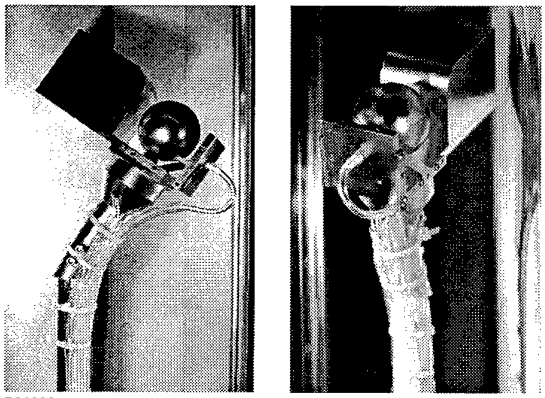

P01006

coefficients decrease by 25%, resulting in lower risk of overstagnation and reduced side head forces (Figure 12).

Three-dimensional CFD simulation results agree well with the observed data (Figure 13). The calculations show that the closed brim model results in the highest back plate pressure (Figure 13b). If the open brim is used, the back plate pressure is lowered but is still higher than the basic model, in agreement with data (Figures 12 and 13). The calculations confirm that the open brim crown deflector stagnates the flow above the head more effectively than the closed brim to reduce normal force (Figures 13b and c).

Figure 11. Water tunnel test fixtures.

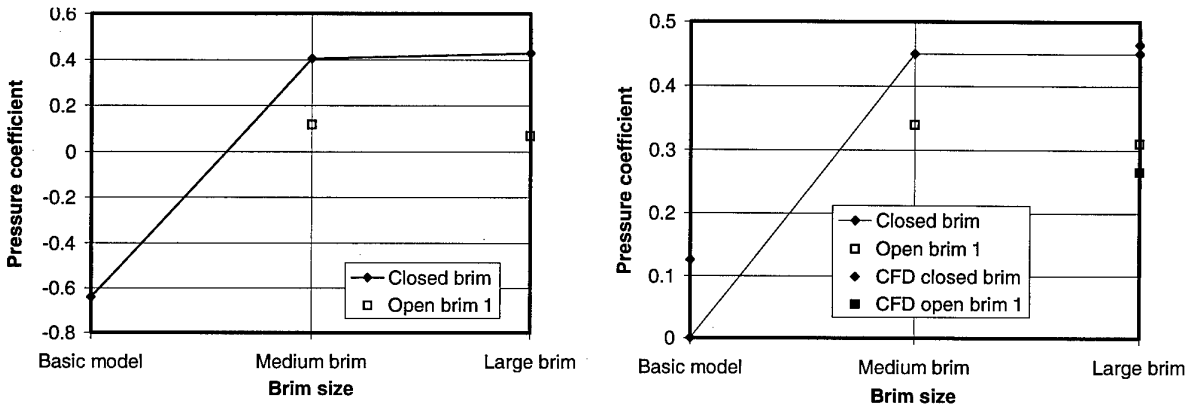

(a) Back pressure coefficient behind the head

(b) Windward head rest pressure coefficient

Figure 12. Water tunnel test results.

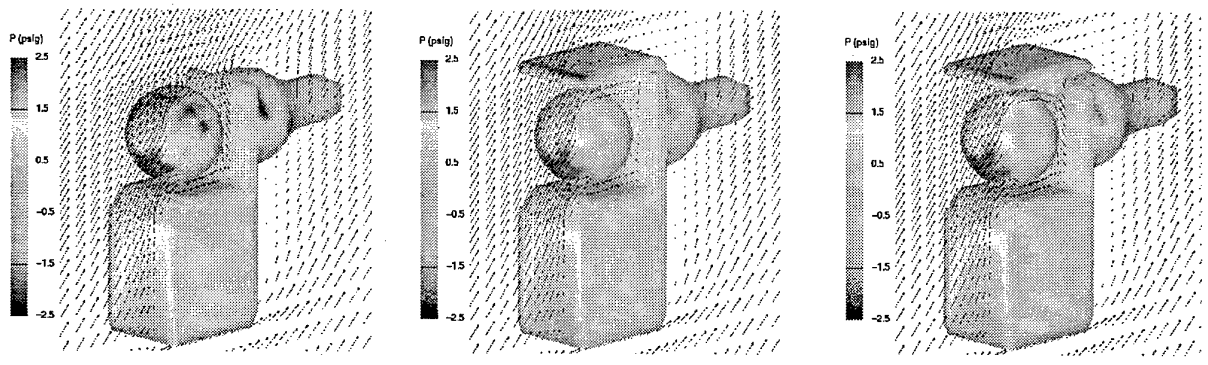

(a) Basic model

(b) Closed brim

(c) Open brim

Figure 13. CFD simulations of water tunnel tests, $\alpha = 30°$, $\beta = 15°$.

Both the water tunnel and CFD results indicate that if the brim is open, the headrest pressure can be lowered. The flow stagnation above the head can be achieved by using a crown deflector. These observable effects can be enhanced by optimizing the deflector size, brim shape and wake channel geometries.

EVALUATION OF 4TH GENERATION SEAT OPEN BRIM

The water tunnel results have benefited the development of the open brim used in the 4th Generation Escape System Demonstration Program sponsored by the CREST Program [12]. The open brim for the 4th Generation Escape System was developed subsequent to Jaycor's subscale water tunnel studies. Using the open brim concept, the 4th Generation brim is made of T-shaped fabric with a crown deflector above the head [13], as shown schematically in Figure 14. Compared to Jaycor's water tunnel model (Fig. 10c), the 4th Generation brim is more open on the sides (Fig. 14), with the intention to further relieve side force increase while achieving normal force reduction. The low speed wind tunnel data for the 4th Generation brim [13] is evaluated with comparison to the large closed brim tested by the Air Force. Besides using a 95th percentile male manikin, tests were also conducted for a tilted head and a 5th percentile female manikin to address accommodation issues.

Based on the wind tunnel data, the side force increase still limits the 4th Generation brim to provide head/neck protection for yaw less than 16° and pitch less than 40° (Fig. 15). Within this range of yaw and pitch, the 4th Generation brim keeps the side head force coefficient within tolerance, which is an improvement over the large closed brim (Fig. 15a). Both brims keep the normal head force coefficient within CREST limit (Fig. 15b).

When the head is tilted by 30°, the 4th Generation brim cannot keep the head/neck forces within tolerance for yaw greater than 14° (Fig. 16). (Data for $\beta<14°$ were insufficient.) Tilting the head also greatly increases the normal force to exceed tolerance (Fig. 16b), which indicates significant adverse effects when the head is out of position, making the crown deflector ineffective. It should be noted that side head motion or tilting at yaw is possible, especially when the side head force tends to increase with brim addition.

Head/neck force coefficients exceed the tolerances when a 5th percentile female manikin was tested (Fig. 17). A smaller manikin is farther below the brim and deflector. Compared to the large manikin, the side force coefficient increases significantly for the small manikin at yaw

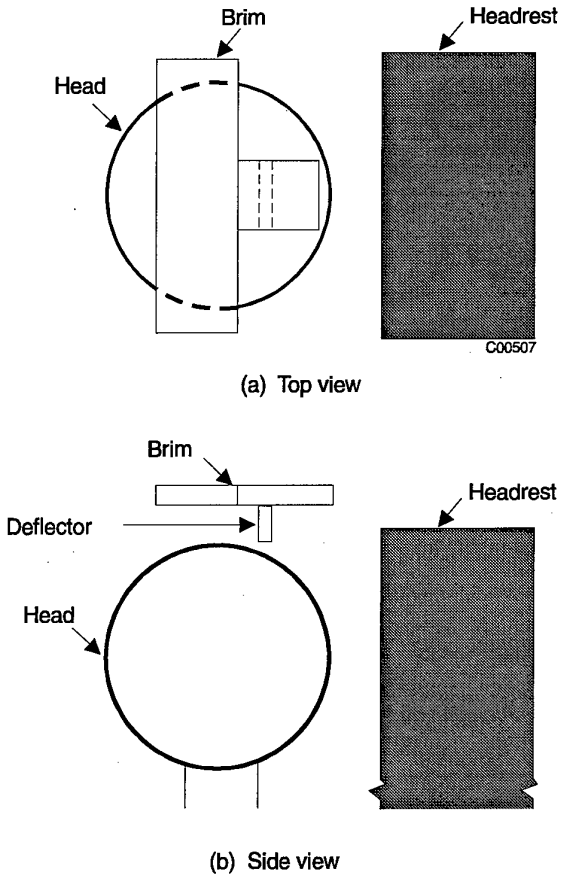

Figure 14. Open brim used in 4th Generation escape system.

greater than 14° (Fig. 17a). The normal force coefficients for the small manikin also exceed the tolerance (Fig. 17b). Lowering the brim by 1 in. does not show significant effect on head/neck forces (Fig. 17).

CONCLUSION

A phenomenological study of windblast protection by flow stagnation has been conducted by wind tunnel data analysis, fluid dynamics simulations and subscale testing. Wind tunnel data for the basic seat indicate that windblast protection of the head is required at high speed. CFD results confirm the observed knee shielding effect at high angles of attack. Knee shielding effect will diminish with yaw.

The vented hood and the brim can reduce the normal head force effectively with no axial overstagnation, but the side force is increased significantly. This side force increase is due to the windward headrest flow stagnation.

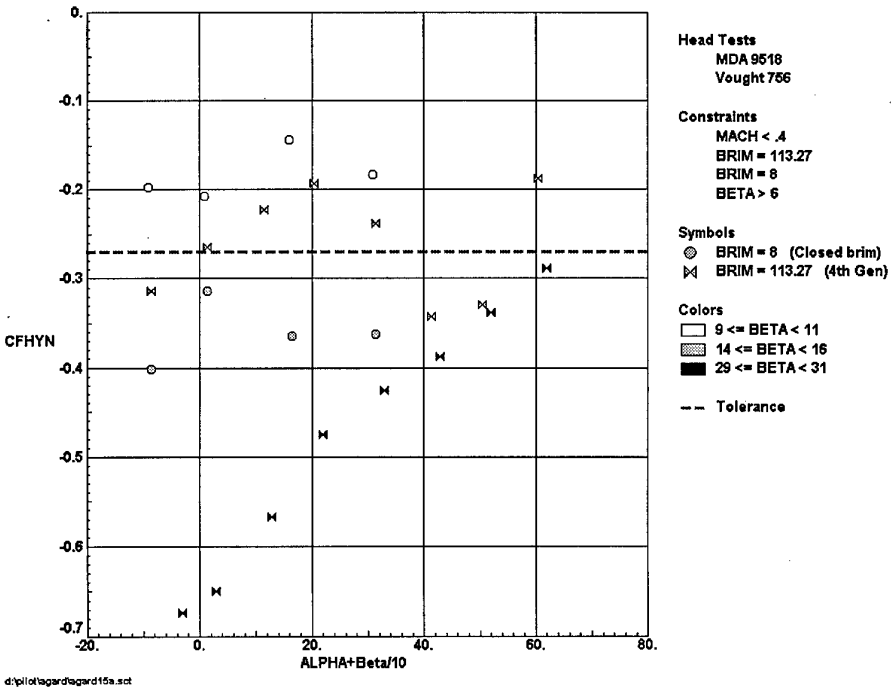

(a) Side head force coefficient

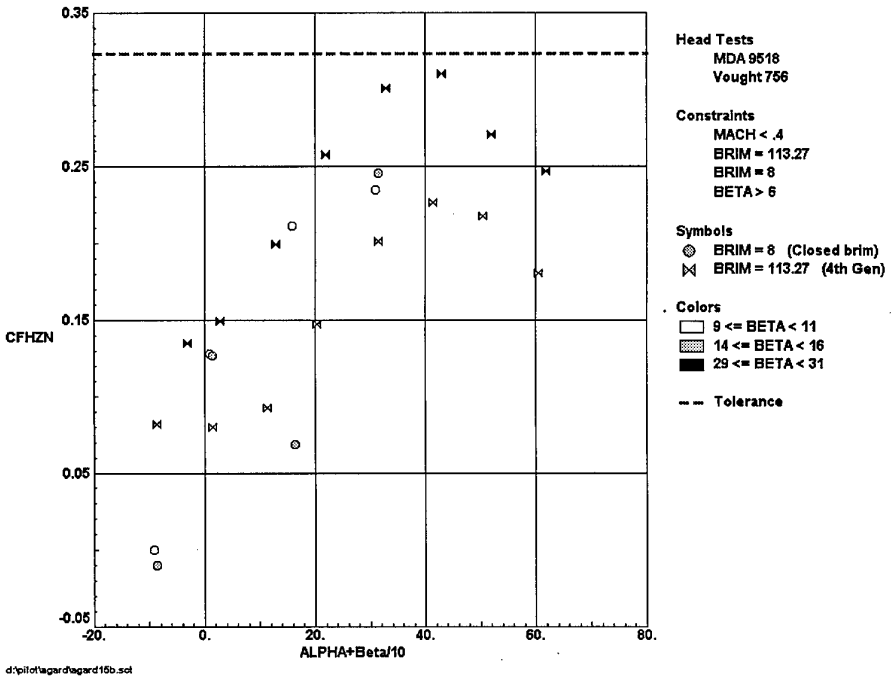

(b) Normal head force coefficient

Figure 15. Comparison of 4th generation brim with large closed brim.

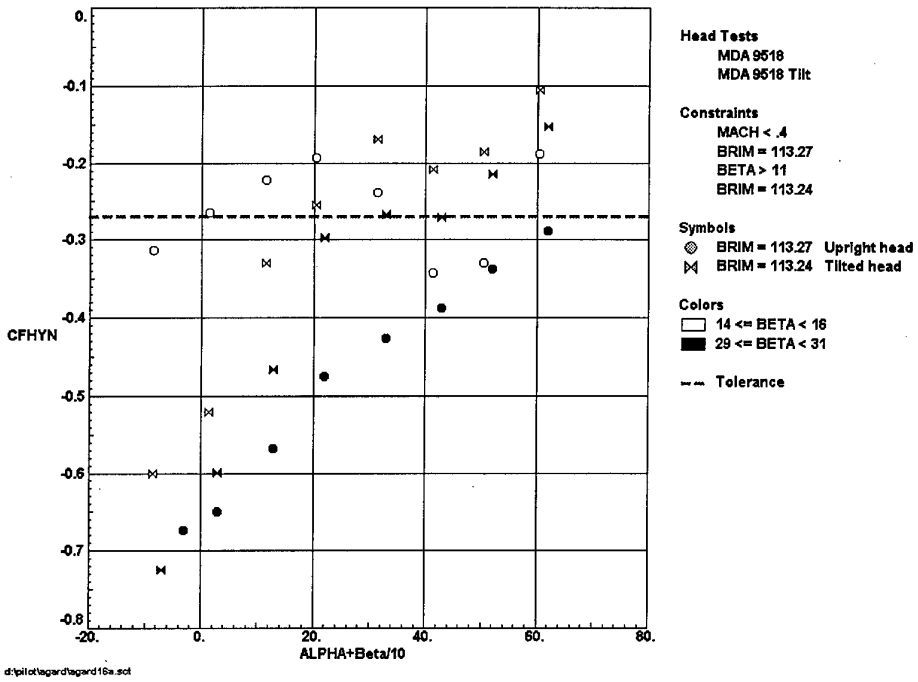

(a) Side head force coefficient

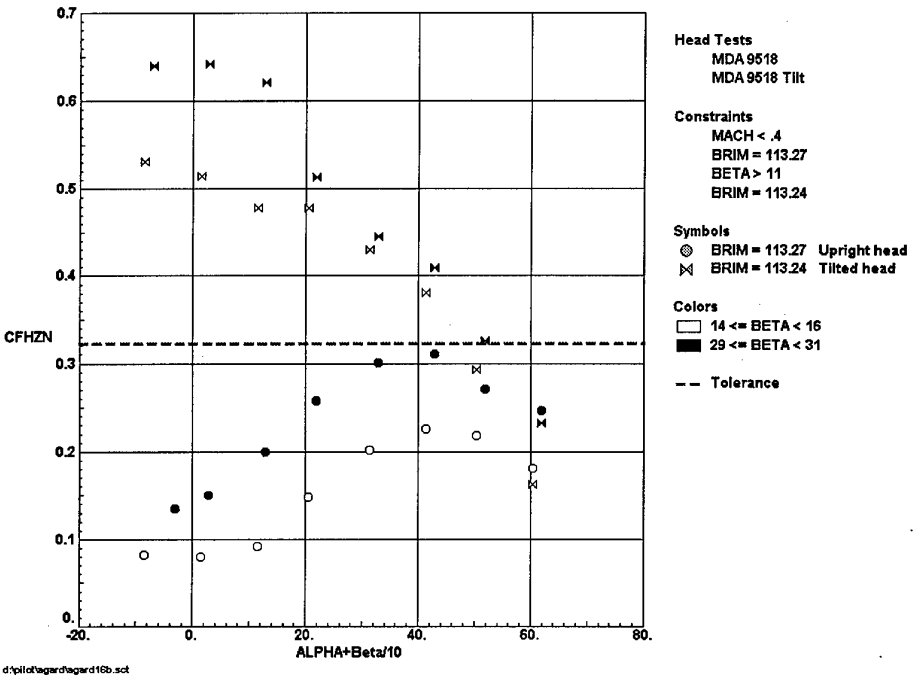

(b) Normal head force coefficient

Figure 16. Tilted head effects on 4th generation brim.

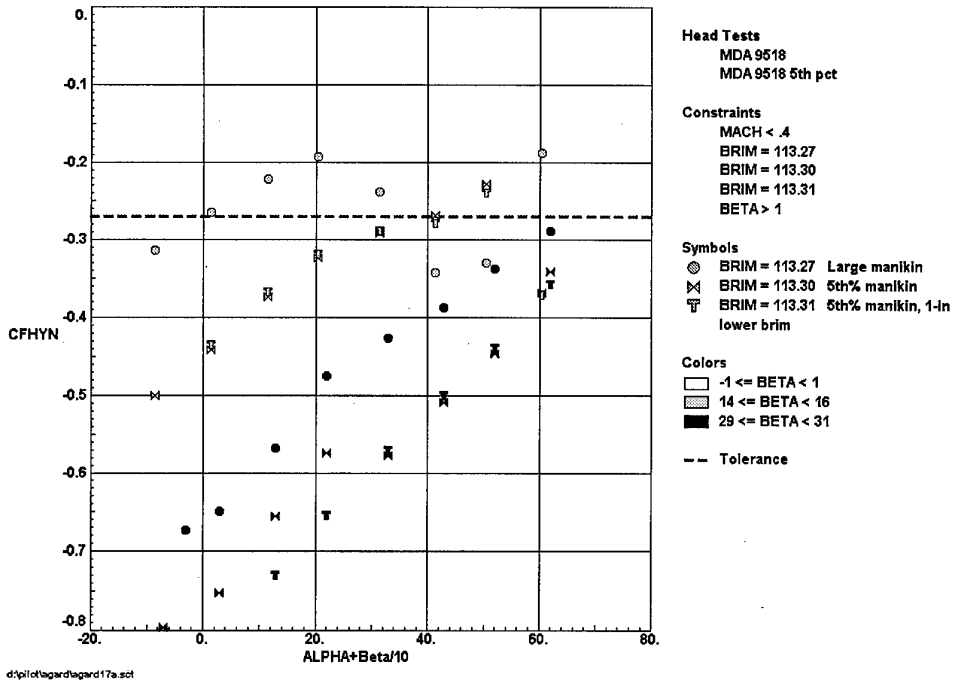

(a) Side head force coefficient

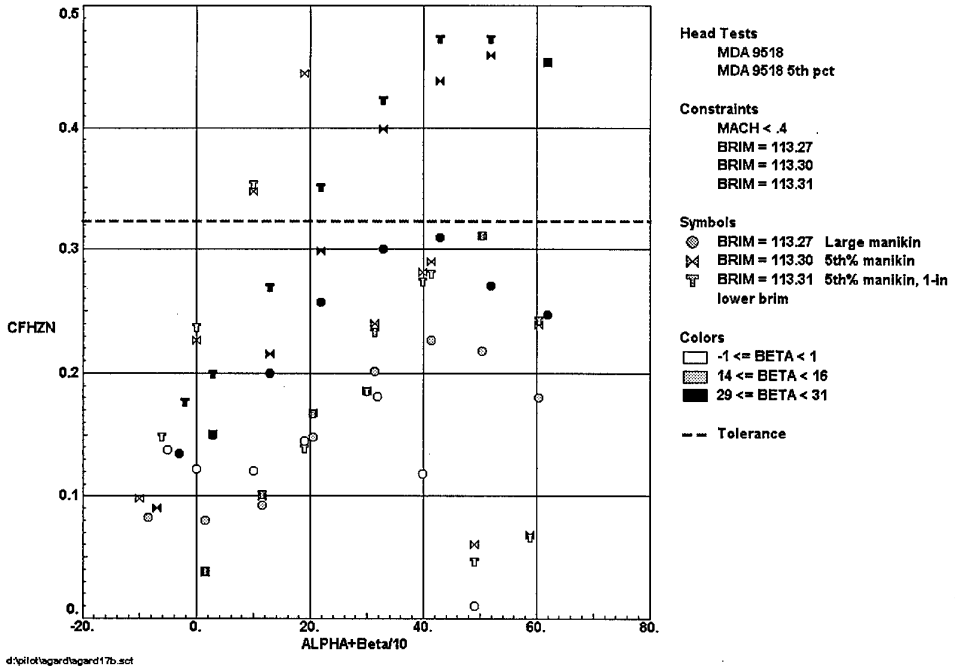

(b) Normal head force coefficient

Figure 17. Occupant size effects on 4th generation brim.

The open brim concept can reduce the side head force increase. Subscale water tunnel model tests and CFD results indicate that the open brim wake channel can mitigate the headrest flow stagnation, while the crown deflector can stagnate the flow above the head to reduce the normal force. Incorporation of these design principles has benefited the 4th Generation brim development and will help optimize the effectiveness of future windblast protection concepts.

Wind tunnel data show that the 4th Generation brim is an improvement over the large closed brim while concerns for accommodation issues of side head motion and small occupants still remain. The margin for side head force protection may still be inadequate, especially at higher yaw conditions. High yaw angles tend to lead to highly adverse conditions.

In addition to refining the parameters, other effects should be considered, including forebody interaction, dynamic loading and compressibility effects.

ACKNOWLEDGEMENT

This project was sponsored by the Human Systems Center (AFMC) under Contract No. F41624-95-C-6014. Mr. Lawrence Specker of the Air Force Armstrong Laboratory served as the project manager. The kind assistance of Mr. Lawrence Specker and Mr. John Plaga are appreciated. Part of the results were presented at SAFE Symposium 1995.

REFERENCES

1. "A Low Speed Wind Tunnel Test for the Air Force Aerospace Medical Research Laboratory to Obtain Buffet and Static Aerodynamic Data on a Man/Seat Combination Utilizing the Flow-Stagnation Protective Concept," LSWT 658, Vought Corporation, Dallas, TX., Aug., 1984.
2. "A Low Speed Wind Tunnel Test for the Air Force Aerospace Medical Research Laboratory to Obtain Buffet and Static Aerodynamic Data on a Man/Seat Combination Utilizing the Flow-Stagnation Protective Concept, Phase II," LSWT 666, Vought Corporation, Dallas, TX., Jan., 1985.
3. Reichenau, D. E. A., "Aerodynamic Characteristics of a Half-Scale CREST Ejection Seat at Mach Numbers from 0.6 to 3.0," AEDC-TR-88-6, Air Force Systems Command, July 1988.
4. Lundy, T. E. and Braddock, W. F., "Wind Tunnel Tests of the Flow Stagnation Protective Concept and Ejection Seat Stabilization Devices, Vol. I - Final Report," AAMRL-TR-85-053, Aerospace Medical Div. (AFSC), Wright-Patterson AFB, Ohio, Oct., 1983.
5. "An LTV Low Speed Wind Tunnel Test of a Vented Flow Stagnation Hood for Improved Wind Blast Protection," LSWT 756, LTV Missiles and Electronics Group, Dallas, TX, March 1992.
6. Fourth Generation Escape System Technologies Demonstration Statement of Work, Air Force CRew EScape Technology (CREST) Program, Aug., 1993.
7. Schoen, J. J., "Fourth Generation Escape System Technologies Demonstration Preliminary Design," *SAFE Journal*, Vol. 24, No. 3, Oct., 1994, pp. 46-56.
8. Chan, P. C. and Klein, H. H., "A Study of Blast Effects Inside an Enclosure," *ASME J. of Fluids Engr.*, Vol. 116, Sept., 1994.
9. Payne, P. R., "Notes on the Initiation of Limb Flailing," AMRL-TR-71-45, Aerospace Medical Research Laboratory, Aerospace Medical Div., Air Force Systems Command, Wright-Patterson Air Force Base, Aug., 1971.
10. Koenig, K. and Roshko, A., "An Experimental Study of Geometrical Effects on the Drag and Flow Field of Two Bluff Bodies Separated by a Gap," *J. Fluid Mech.*, Vol. 156, pp. 167-204, 1985.
11. White, F. M., Viscous Fluid Flow, McGraw-Hill, Inc., 1974.
12. Schoen, J. J. and McDonald, A. B., "Fourth Generation Escape System Technologies Demonstration Program Status," 34th SAFE Symposium, October 21-23, 1996, Reno, NV.
13. "Fourth Generation Escape System Technologies Demonstration, Low Speed Wind Tunnel Test Report," MDC 96K0201, McDonnell Douglas Aerospace, March 1996.

The Use of Computer Finite Element Models of Humans and Crash Test Dummies for High Acceleration and Impact Biomechanics Studies

Kennerly H. Digges
Paul G. Bedewi
The National Crash Analysis Center
The George Washington University
20101 Academic Way
Ashburn, VA 22011, USA

1. SUMMARY

The application of computer finite element models provides a valuable method for the study of human injury. The ability to model the complete human body is currently impractical. However, it is possible to model elements of the human body. These elements may be used independently, or in conjunction with models of crash dummies. In the latter case, specific crash dummy elements are replaced with human elements. The resulting model increases the accuracy of the model in predicting human response in high acceleration impacts.

The procedure for applying human elements to crash test dummy models is illustrated by substituting human lower limbs on a finite element model of the Hybrid III dummy. The model is validated by replicating tests of human cadaver lower limbs. The model is then applied to predict the effect of muscle activation.

2. INTRODUCTION

Injury is most commonly associated with some type of impact. The type of impact and forces involved will determine the level of stress on the body's structure.

In automotive crashes, the engineer must understand the biomechanics of impact and the events of the crash environment. To design for injury prevention, the causation must be known. Standard engineering practice would be to perform experimental tests to determine the loading mechanisms that cause failure in a structure. For the vehicle occupant, determining these characteristics directly, through some form of impact testing, using living human subjects, is neither reasonable nor ethical. This means it is necessary to develop some type of human surrogate. Because the human body is arguably one of the most complex structures in existence, it is in turn one of the most difficult to simulate. There are essentially five methods that have been used for human simulation in automobile accidents. These include the use of animals, cadavers, human volunteers, anthropomorphic test devices (ATD), and mathematical and computer models.

The use of animals, both living and post-mortem, is beneficial in that it provides a structure that often closely mimics the human body. Animals provide realistic patho-physiological response to impact injury. A closely estimated human response can be developed from the knowledge of how an animal responds in a similar situation. However, the use of animals has come under much scrutiny in the past several years. Although more cost effective, it has been deemed unethical and does not provide enough quality information to justify their use. In terms of a mechanical response and tolerance, animals are not the most desirable surrogate because of differences in anatomy and tolerance levels in comparison to the human.

For many applications, the human cadaver is a very good human surrogate for impact testing. They provide anatomical accuracy, proper weight distribution, and a response similar to that of a living human. A critical deficiency of cadavers is the lack of muscular tone, muscular response, and living tissue response. Muscular pretension prior to impact can have a significant effect on the kinematics of the human body. Other negative aspects include high cost because the subject is usually limited to one impact test, and the large variations in tolerance between each cadaver.

Human volunteer testing is not practical for

Papers presented at the RTO HFM Specialists' Meeting on "Models for Aircrew Safety Assessment: Uses, Limitations and Requirements", held in Ohio, USA, 26-28 October 1998, and published in RTO MP-20.

determining injury tolerance. It has provided valuable data on the static and dynamic response of human elements in sub-injury level environments.

Because of their many negative aspects, cadavers are not the ideal tool for assessment of injury tolerance. Differences in soft tissue response, lack of muscle tone, and a bias of available specimens toward the older population are among the many disadvantages. Large variability exists among specimens, requiring a large number of replicated tests to provide data with statistical significance. ATD's (commonly referred to as crash test dummies) have been developed to provide a human-like response and, more importantly, good repeatability in similar impact scenarios. Repeatability is necessary if the human surrogate is to be used for some type of regulatory test in which a standardized response is required. The most advanced ATD in common use is the Hybrid III developed by the General Motors Corporation in the 1970's [Foster, 1994 & Robbins, 1994]. In general, the Hybrid III shows good response to head and chest impact; however, it still lacks many realistic anatomical features and is not able to accurately represent the musculature associated with humans. It particularly lacks biofidelity in the lower limbs.

With the increasingly rapid development of higher powered computing techniques, computer modeling is becoming a more realistic and credible form to study the biomechanics of impact injury. The Finite Element Method (FEM) is currently the most advanced tool for simulating an impact event. It's advantages over other modeling techniques include advanced contact algorithms and material models for representation of the large deformations experienced in high speed impacts. Additionally, FEM allows for the collection of more data than any other type of modeling. This includes quantities such as stress, strain, displacement, velocity, acceleration, energy, etc. at virtually any location in the model. In the past, the FEM models were limited by the costs associated with computational power and time. Today the only issue is the user's ability to create a validated model for use in the simulations. Because physically testing humans is not possible and the three previously mentioned human surrogates have many limitations, the idea of creating a human model on the computer shows great potential.

For just over 30 years, computers have been used to mathematically model the dynamic response of a vehicle occupant involved in a collision event. Models developed range in complexity from simple one-dimensional mass-spring models to very detailed FEM models. FEM models have been limited in development for several reasons most of which concern the characterization of the biological properties needed to define a model. Other problems can be associated with the difficulty in understanding the complex FEM codes. Many biomechanics experts who thoroughly understand the complexities of the human body may be unfamiliar with the advanced FEM codes. Similarly, engineers experienced in FEM modeling do not have the necessary experience in biomechanics to create good models. This "generation gap" must therefore be linked in order to reach the full potential of this field.

3. THE FINITE ELEMENT METHOD

Virtually any phenomenon in nature can be described in terms of algebraic, differential, or integral equations with the aid of the laws of physics. Studying any physical phenomena requires the scientist to perform two steps: 1) mathematical formulation of the physical process, and 2) numerical analysis of the mathematical model. While in some instances it is possible to derive a mathematical formulation that accurately and completely describes the physical process, many times its behavior is too complex and thus impossible to describe in one operation. The solution to this problem is to divide the complex system into individual well defined components whose behavior is well understood; then, reassemble the system using the solutions found for the sub-components. When a system can be broken down into a finite number of sub-components or elements, it is termed discrete. This discretization of the continuum problem is the fundamental theory of the finite element method. Most commonly used in engineering solid mechanics, the finite element method has numerous applications from fluid dynamics to economics [Reddy, 1993, and Zienkiewicz,1989].

When a system's domain has been discretized, each sub-region is approximated with a simple function. In solid mechanics these sub-regions are most commonly simple geometric shapes that can be one-, two-, or three-dimensional in form. Any geometric shape can describe the system as long as there is an approximating function for this shape. The collection of the elements is known as the

mesh. The connecting points of the finite element mesh are the nodes. The approximating functions over the entire mesh form a system of equations which contains a set of undetermined coefficients. These undetermined coefficients are solved through the application of element boundary conditions and interpolating functions across the element. The degree of the interpolating functions depend on the number of nodes in an element and the order of the differential equation approximating the element.

Since approximating functions are being used to solve the problem, generally if the domain is more finely meshed (i.e. large number of smaller elements) it will return a more accurate solution. When the number of elements is continually increased, the solution will begin to move toward a certain value. This process is known as convergence. The accuracy of a mesh is the difference between the exact solution and the finite element solution returned. Accuracy can be improved in two ways: 1) increase the number of elements in the discretization, or 2) increase the order of the approximating functions over an element's interior. In both cases there is an increase in the computational costs needed to solve the problem. It is to the user's discretion to find a balance between the number of elements, order of the approximating functions, and accuracy of the solution.

A major advantage of the finite element method is that dissimilar material properties can be applied to different elements throughout the mesh. This makes it possible to formulate a solution for a problem involving very different components. Another feature, that results from having a large system of sub-components, is the ability to calculate certain quantities at specific points in the system. An example of this is finding the amount of deformation at a given point on an object involved in a collision event.

4. THE APPROACH TO FEM MODELING OF THE HUMAN LOWER LIMBS

The lack of biofidelity of dummies in assessing injury producing conditions in impact events may be circumvented by the use of FEM applied to dummies. The George Washington University has applied this approach to assess and overcome deficiencies in the Hybrid III dummy in measuring injury to the lower limbs. The approach has several elements as follows:

1. An FEM model of the human lower limbs has been developed. This model has the mass and geometric properties of a mid-size male – of similar size to the Hybrid III dummy. The model is validated by test data.
2. An FEM model of the Hybrid III dummy has been developed and validated. This model permits the assessment of the baseline performance of the Hybrid III dummy.
3. The model of the human legs are substituted for the dummy legs on the Hybrid III dummy model.
4. The response of the model with human legs is compared with the baseline Hybrid III model.

A model of the Hybrid III dummy has been developed and documented by staff of the National Crash Analysis Center, of The George Washington University [Noureddine, 1998]. Geometry for this model was created from the original blueprint specifications and CAD drawings of the Hybrid III. The model accounts for most of the materials present in the physical dummy. This includes all inner structures in detail, viscoelastic outer skin, rib dampers, as well as specified data measuring points similar to the actual dummy. The model totals approximately 18,000 elements. Validation for this model was performed using the standard calibration procedures for the Hybrid III. This includes a head drop test, neck pendulum test, and chest pendulum impact. Following the development of the Hybrid III dummy, there now exists a validated model of a human surrogate designed to represent the 50th percentile male. This model can then be used for any study of safety design via computer simulation rather than physical testing. Additionally, to obtain an even better representation of the human, more detailed human component models, such as the lower extremity model, can replace similar parts on the dummy.

5. DESCRIPTION OF LOWER LIMB MODEL

The FEM model created has accurate three dimensional geometry with much of the focus on biofidelic joint characteristics. The geometry for the finite element mesh consists of the pelvis, femur, patella, tibia, fibula, and the 26 bones of the foot. The digitized data for the geometry of a 50th percentile male was obtained from Viewpoint Datalabs [Viewpoint]. The geometric data is in Initial Graphics Exchange System (IGES) format

which can be imported into the finite element pre-processor for mesh generation and model development. The geometry may be scaled in the pre-processor for creation of the 5th percentile female model. The software package PATRAN/P7 is the pre-processor used to create the model.[134]

Once imported into PATRAN, the geometry was closely analyzed for accuracy and alignment. Most data sets created by Viewpoint are commonly used for animation purposes; therefore, they are constructed for aesthetics rather than the detailed accuracy needed for a finite element model. Some minor adjustments were needed because portions of the geometry were penetrating other adjacent segments. Alignment problems consisted of the femoral head penetrating the acetabulum of the pelvis, the femur and tibia were slightly overlapping at the knee, and the fibula was badly penetrating the tibia and the talus. Corrections were made to align the bones with two anatomy textbooks as references (Moore, 1992, and Marieb, 1992). The geometry is classified as medium resolution from Viewpoint, with the bones of the leg comprised of 5477 polygons. The units for the geometry in its original form was in inches. To maintain consistency and the ability to interact with other models used at the NCAC, the model was scaled to millimeters. The units of mass and time are metric tons (megagrams) and seconds, respectively.

A finite element mesh was applied to the bone segments and consisted of one element per polygon for a total of 5477 thin shell elements. The mesh was then divided into five groups: the pelvis (pelvic bone), thigh (femur), leg (patella, tibia, and fibula), talar region (talus), and the foot (calcaneus, cuboid, 3 cuneiforms, 5 metatarsals, navicular, and 14 phalanges). Because this is a level 2 model, each group was specified as a rigid material type or rigid body. This implies that all of the bones of a single group are not permitted to move with respect to each other; however, any given group may translate with respect to another group. For example, the tibia cannot move with respect to the fibula, but the thigh can move with respect to the pelvis. The individual segments are shown in Figure 5.1 (the talus has been included with the foot although they are separate entities.)

The thin shell elements were assigned a uniform unity thickness and the density of the elements were adjusted so that the mass of a segment would match that of the specified occupant. To do this, the surface area of the component is calculated in PATRAN and the densities are adjusted accordingly. The mass of a segment is adjusted so that it is representative of the entire segment rather than just the bones (i.e. the mass of the upper leg includes all masses of the skeletal and soft tissues, and not just the femur. LS-Dyna3D requires properties to be assigned for all materials, including rigid bodies. This is necessary for the purposes of calculating the time step and for contact interaction. For this, elastic properties of cortical bone were applied to all segments. A Young's modulus of 7300 N/mm^2 and a Poisson's ratio of 0.22 was used [Cowin, 1989].

The joints are defined using the joint definitions of LS-Dyna3D for a revolute (knee, ankle, and sub-talar) and a spherical (hip) joint. At each joint location, two identical joints are defined; the first carries the passive properties of the joint and the second carries the active properties. This feature has been added so that the active properties may be adjusted for a specific level of muscle tensing without disrupting the passive component of the joint. Essentially, the properties of each joint are represented by four torsional springs which carry the previously described properties for passive stiffness, active stiffness, passive damping, and active damping. Load curves for all joints in each degree of freedom are contained in the model. In addition, several different curves exist which represent various levels of muscle activation. For levels less than full activation, the values are simply scaled from the full muscle tensioning values. By simply changing the specified load curve assignment in the model, different scenarios of occupant bracing may be studied in a more efficient manner.

As previously mentioned, the center of rotation for a human joint may shift locations as the joint flexes or extends. Using the LS-Dyna3D joint definitions, the axis of rotation for each joint must remain fixed. This implies that the joint's center of rotation must be approximated. Based on various published studies including data found in the Clinical Measurements of Joint Motion, published by the American Academy of Orthopaedic Surgeons, these rotational axis' were defined [Nordin, 1989, and Green, 1994]. A singular point was specified for the hip which defined its center of rotation in all three degrees of freedom. The remaining joints of the knee, ankle, and sub-talar

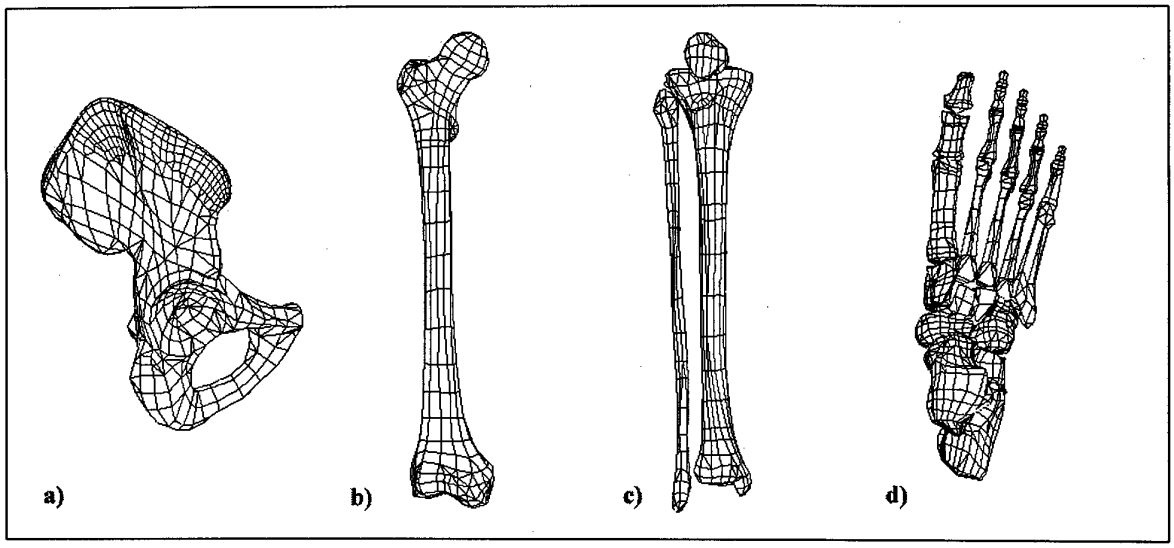

Figure 5.1: Finite element representation of the segments of the lower limb; a) pelvis, b) thigh, c) leg, and d) talar region and foot. (note: The segments are not displayed proportionally to each other.)

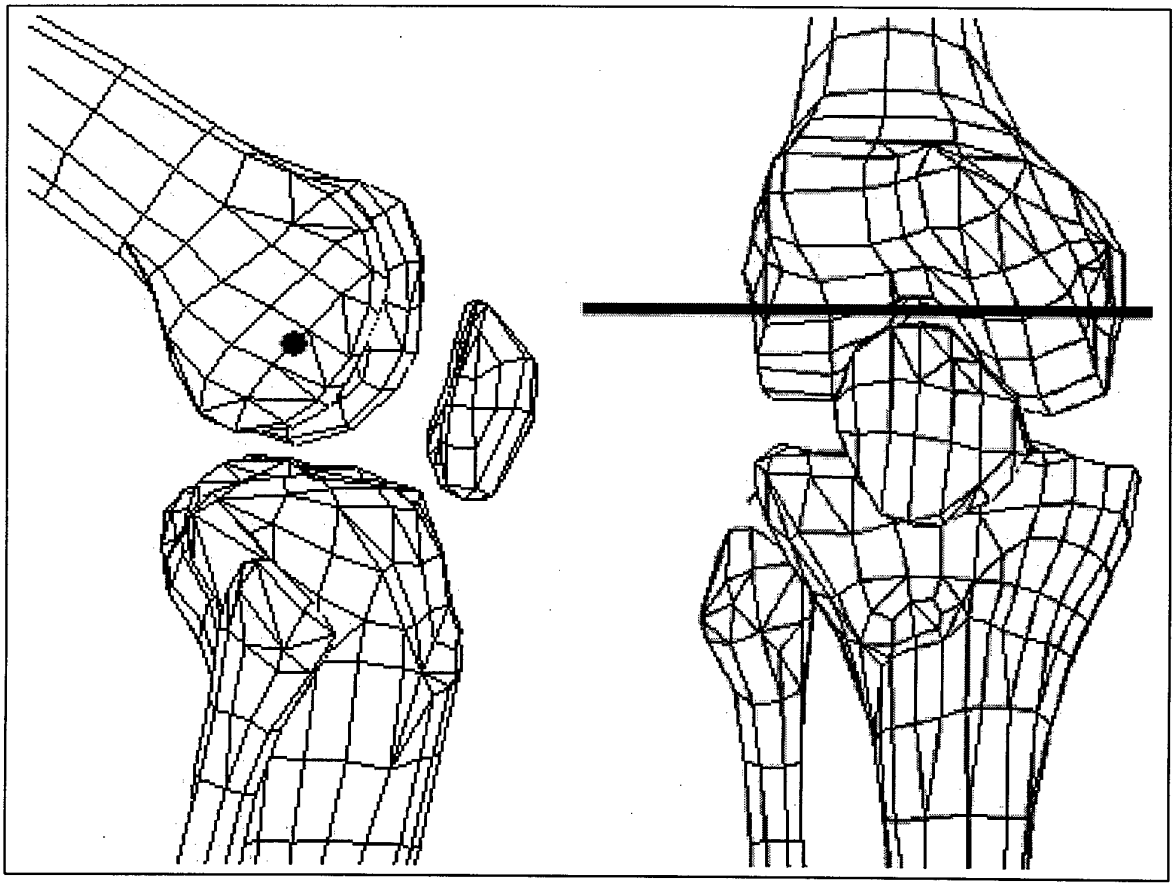

Figure 5.2: Axis of rotation for the knee joint providing for flexion and extension of the leg.

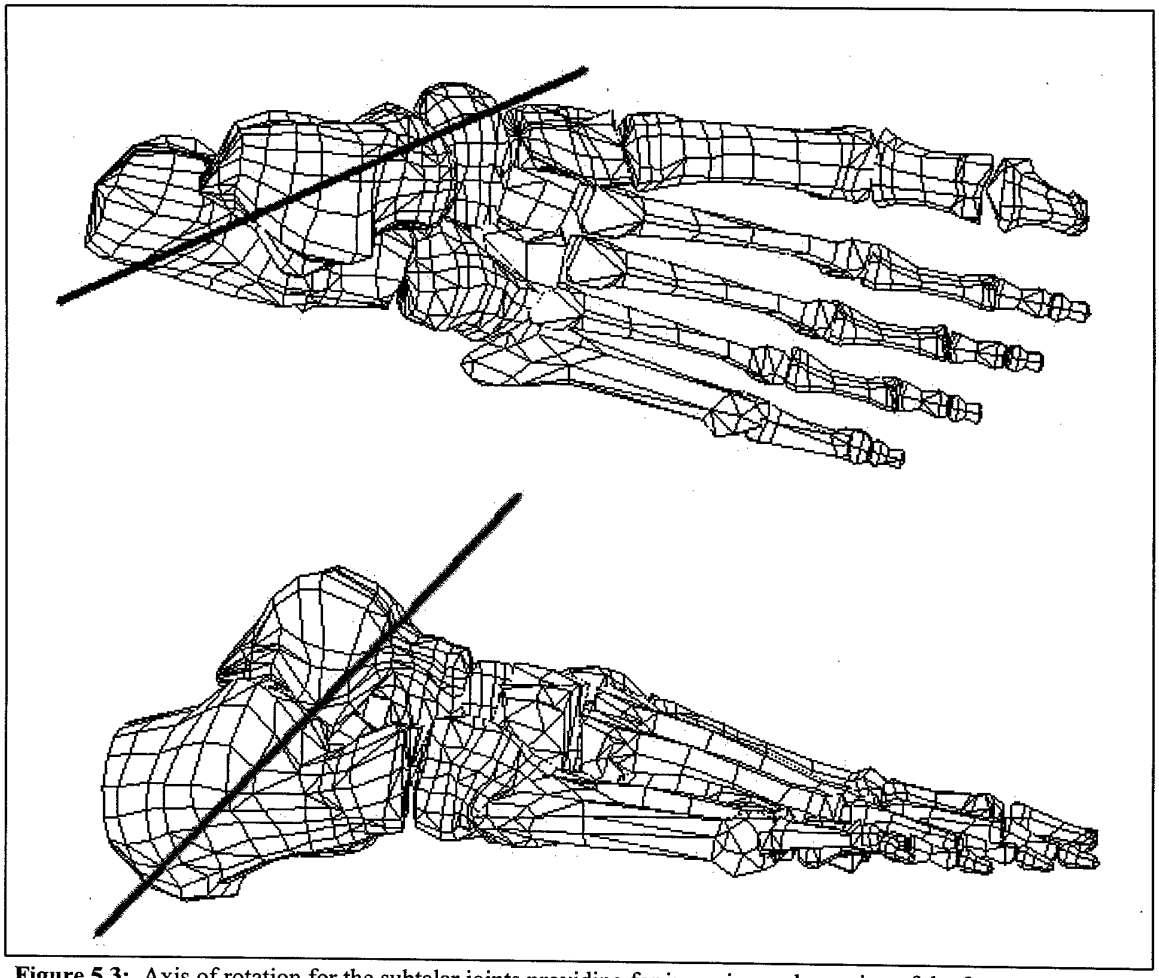

Figure 5.3: Axis of rotation for the subtalar joints providing for inversion and eversion of the foot.

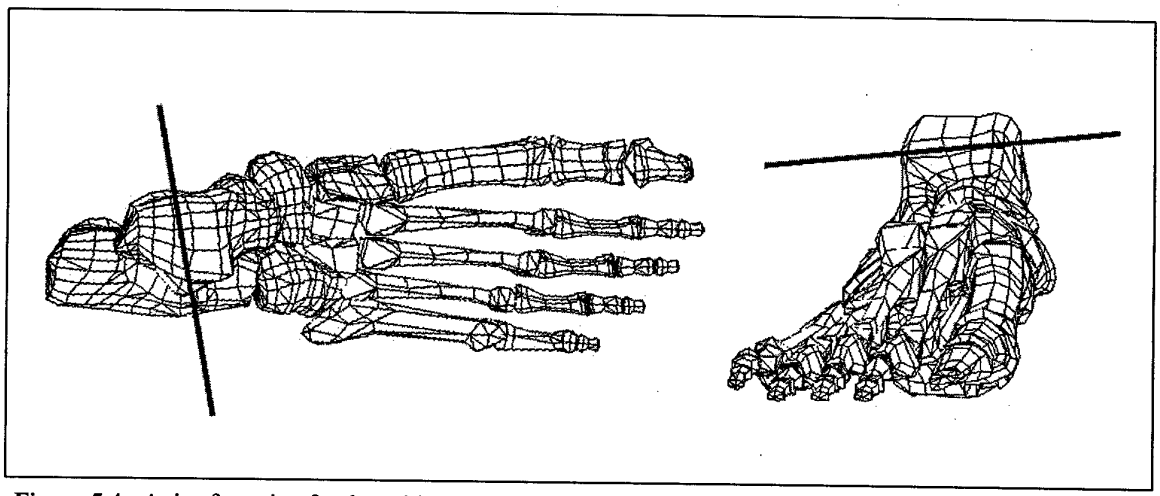

Figure 5.4: Axis of rotation for the ankle joint providing for plantarflexion and dorsiflexion of the foot.

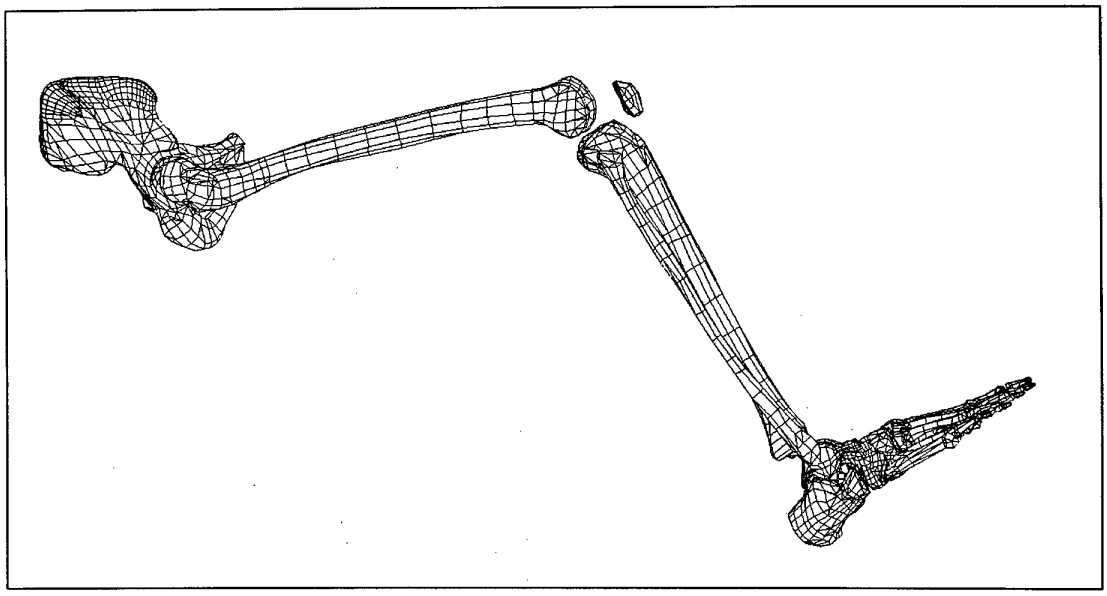

Figure 5.5: Lower extremity finite element model of the right limb in the seated occupant position.

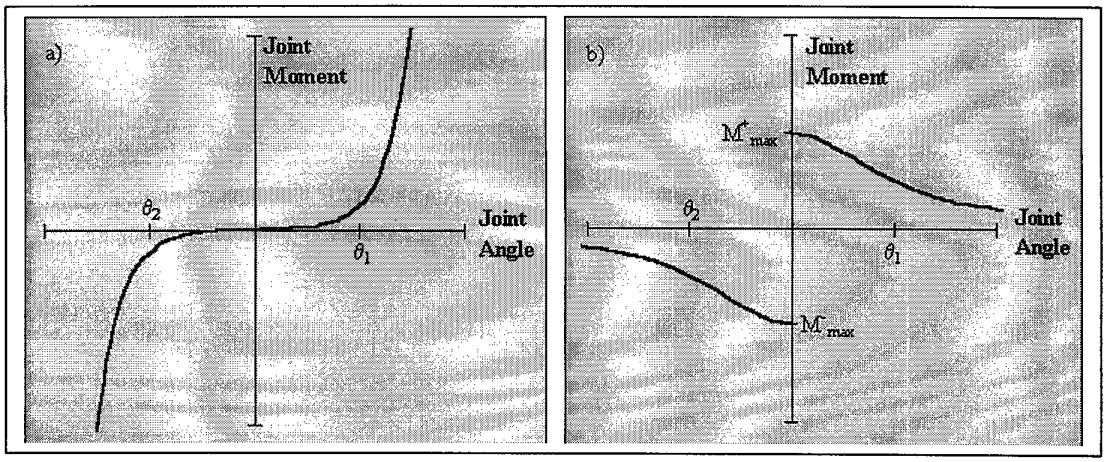

Figure 5.6: General form of the angle-torque curves for the human joints; a) the passive component, and b) the active component.

were constrained to one dimensional rotations via the revolute or hinge style joint. An axis defined by designated nodal points was determined for these rotations. This rotational axis is shown in Figures 5.2 to 5.4 for the respective joints. The assembled model is shown in Figure 5.5. The general form for the angle-torque curves for the human joints are shown in Figure 5.6.

Although the model can be used for numerous impact type problems, the primary use and intention for the development focuses on automotive safety. With the joints in place, the model can be articulated into the seated position of the vehicle occupant. Robbins reported the average seated position for a vehicle occupant [Robbins, 1983].

6. EXAMPLE OF MODEL VALIDATION

6.1 Basis for Validation

The validation of a model is equally as important as its creation. Although there are some acceptable standard methods for validating FEM models, human models do not fall into this category. Their validation is a constantly evolving process for a few reasons. Typical models can be compared to experimental tests. This is not possible for humans because these tests do not exist. Models must be compared to the best data available which is primarily through the use of cadavers and a minimal number of volunteer tests. This data will have inherent accuracy problems because the cadaver is simply not a living being with the same responses to impact. Therefore, when comparing the model to cadaver data, the engineer must be aware of what reactions will differ between the cadaver and a living system. For some components of the body, the response is not particularly different (bone fracture) but for others it is (internal organs).

The soft tissue structures which govern the response of the joints will have altered properties in under one hour post-mortem [King, 1993]. [As the deterioration of the muscles and tissues progresses, they tend to become more stiff losing much of the compliance of the tissues and flexibility in the joints. A certain level of passive damping will be maintained. With regards to the active component, there is for obvious reasons, no longer an active tension possible. In addition, the velocity dependence of the active damping component is eliminated. In a general sense, the total active component has been removed which reduces the total available moment or torque in a joint. At the same time, the passive component will have increased moments based on the hardening of the encompassing soft tissues. The total system response could be compared to a living human with some minimal level of muscle tension; however, most of the velocity dependence has been removed.

6.2 Response to Dynamic Dorsiflexion

The primary focus for validation of the model is on ankle joint behavior. The dynamic response of the ankle and subtalar joints has been characterized in a few studies, all of which have used cadavers as the test subject [Begeman, 1993, Begeman, 1994, Crandall, 1996, & Portier, 1997]. As previously mentioned the data published by Begeman and Prasad has been questioned based on the level at which the cadaver's limb was severed. The subsequent studies in the cooperative effort between Renault and the University of Virginia have attempted to address this issue in performing additional dorsiflexion tests.

For validation in dorsiflexion, two impact scenarios were set up; a pendulum impact using only the ankle joint, and a pedal acceleration using the entire lower extremity. The first was the pendulum impact test conducted experimentally by Begeman and Prasad (Figure 6.1). An impact load is applied to the foot via a 16.3 kg mass impacting at speeds ranging from 3.0 to 8.1 m/s. The impactor is a 25 mm diameter steel bar. The foot is initially positioned at 90° with respect to the leg. The foot is mounted to a 12 mm thick aluminum plate via two load cells at the heel and ball of the foot respectively. The centerline of the impactor is positioned 62.5 mm above the ankle joint. Four impacts were simulated for this test. These tests included:

1. 50^{th} percentile male with passive musculature
2. 50^{th} percentile male with 50% muscle activation

The impactor speed for each was 7.3 m/s. The test chosen to simulate was based on the cadaver used in the actual experiment. For this case, the cadaver best represented a 50^{th} percentile male, the cadaver was not injured from the impact, it was under 60 years of age, and did not suffer from a deterioration of muscle or bone tissue prior to expiration.

None of the cadavers were very representative of a

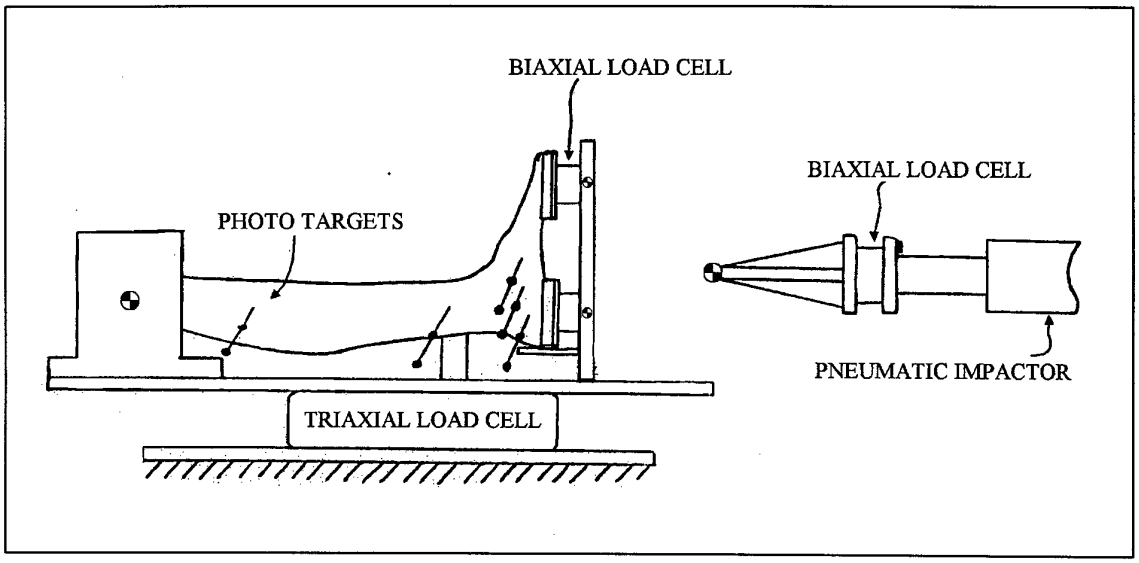

Figure 6.1: Experimental setup for Begeman and Prasad study.

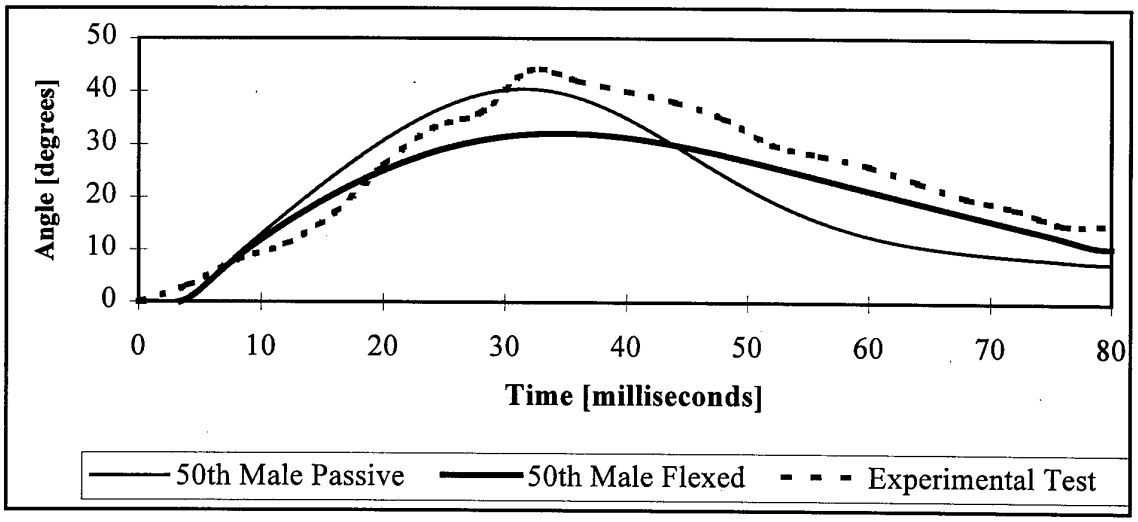

Figure 6.2: Dorsiflexion angle vs. time for Begeman and Prasad experiment and simulations.

5th percentile female or were too advanced in age with seemingly deteriorated tissues. Because of these circumstances, it was determined that it would be best to compare the 5th percentile model to the 50th percentile model under a similar impact scenario. While it is understood that the test subject is a cadaver which has been severed at the mid-shaft of the tibia, the experimental test is one resource available for validation of the model.
Results from the simulations indicate that the human ankle does not experience as much motion in dorsiflexion as the experimental tests would indicate. This was a foreseen result based on the type of specimen used in the test. The added musculature, which has been accounted for in the simulation, does limit the amount of dorsiflexion in the impact test. Table 6.1 summarizes the results and compares the simulations to the experimental test. Also as expected, the 5th percentile female experienced a higher degree of dorsiflexion than the male model. Figure 6.2 plots dorsiflexion angle with time for the four simulations and the experimental test.

Table 6.1: Results from simulations of Begeman and Prasad experiments.

Test Condition	Moment	Angle
Experiment	160 N·m	44°
50th - passive	110 N·m	40°
50th - flexed	106 N·m	32°

As with the experimental tests, the joint moments and forces did not correlate directly with joint angle. Generally, joint reaction forces were higher and moments lower for the simulations compared to the experiment. This is primarily due to the use of a rigid foot in the model. The human foot has a larger degree of compliance in the soft tissues at the impact point which will act to dissipate some of the contact force before it can be transferred to the joint. Likewise, the cadaver is more inclined to develop higher joint moments because it will reach its joint limits with less dissipation of energy from the musculature surrounding the joint. The model accounts for this musculature which has either been severed or lacks the active damping components in the cadaver. In this first validation effort, the model has shown to perform well.

6.3 Other Validation Tests

Additional validation for eversion and inversion, and for motion in the crash environment is reported in more detailed papers [Bedewi 1995, Bedewi, 1998]. These publications also document a human lower limb model of the 5th % female. The model has been applied to reconstruct the injury producing environment of an actual automobile crash. The 1998 publication quantifies the forces and motions which induced both dorsiflection and eversion induced ankle injuries.

7. COMPARISON AND CALIBRATION OF HYBRID III MODEL

The FEM model of the Hybrid III dummy has been validated by simulating the tests required for dummy calibration, and by simulating actual crash tests [Noureddine, 1998].

To compare the performance of the dummy lower leg with the human lower leg, the human lower legs were substituted on the FEM Hybrid III model. The response of the lower limbs in a representative car to car crash was examined. The car to car crash selected was similar to a series of research crash tests conducted by the Department of Transportation. In these tests, two cars, each traveling 35 mph are crashed together . The cars are offset so that their left front overlaps at the time of the crash. The overlap is 60% of the car width. The 50th % male Hybrid III driver dummy is restrained by a three point belt without an air bag. In this crash mode, the left limb is exposed to a more severe crash environment than the right limb.

Four different lower limb configurations are examined by the model. The results are depicted in Figures 7.1 and 7.2. Configuration A is the standard Hybrid III dummy lower limbs. Configuration B is the Hybrid III dummy lower limbs with a modified ankle to provide a soft stop. Configuration C is the 50th % male human leg without muscle tensing. Configuration D is the 50th % male leg with 50% muscle activation.

Figure 7.1 shows the dummy lower limb response shown at the beginning of the crash (1), and at three time increments during the crash (2 ,3 &4). An examination of the dummy lower leg response, shows that the left foot is displaced away from the floor. In contrast, the human foot has less displacement away from the floor. A second observation is that the improved dummy ankle undergoes large excursions in eversion and inversion. This response is further illustrated in Figure 7.2. The largest excursions of the left ankle

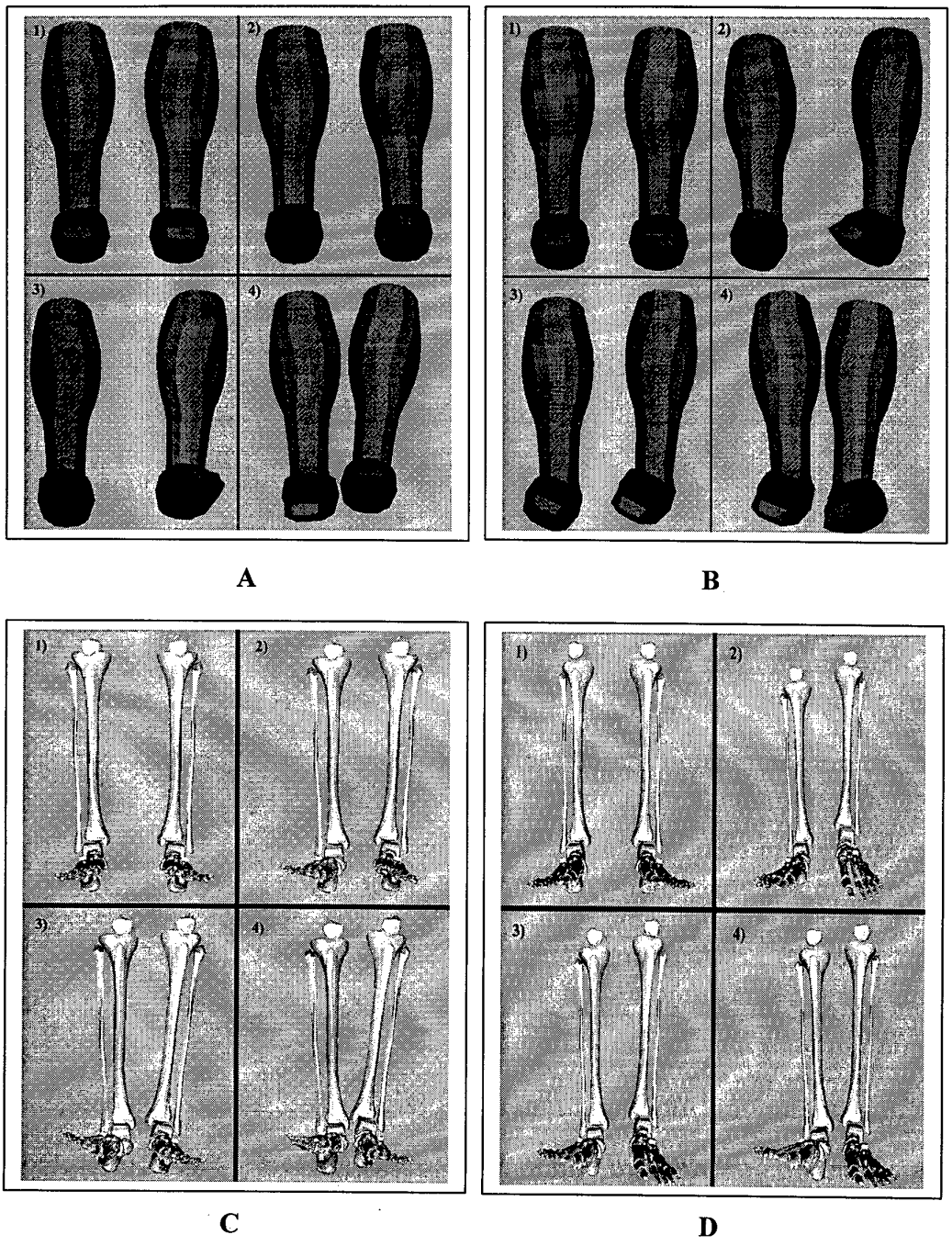

Figure 7.1 Lower limb response in car-to-car crash f or following models: (A) Hybrid III Dummy; (B) Hybrid III Dummy with improved ankles; (C) Human with passive muscles; (D) Human with 50% muscle activation

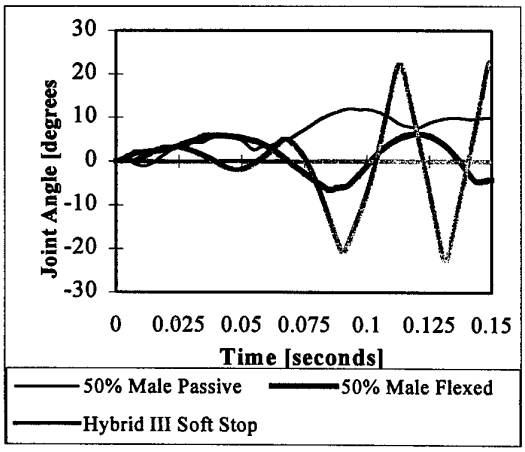

Left Leg Eversion/Inversion

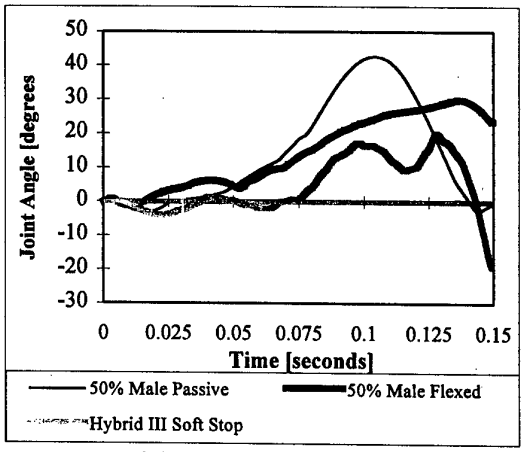

Right Leg Eversion/Inversion

Figure 7.2: Comparison of lateral sub-talar joint articulation for the soft stop dummy and two 50th percentile male human simulations. Positive values represent eversion while the negative are inversion. Left and right joint response shown.

are for the improved dummy ankle.

For the left foot, it is apparent that the improved ankle rattles from stop to stop in the lateral direction, under loading conditions representative of car to car crashes. The human response is much more benign. Muscle tensing tends to reduce the rotation of the foot.

8. APPLICATION OF FEM LOWER LIMB MODEL TO ASSESS THE EFFECT OF JOINT TENSING ON ANKLE LOADING

An inherent and beneficial quality of computer simulation modeling is the ability to make simple changes in a model and investigate a series of variables over a wide range of options. This can be done in a relatively short time frame. This ability to perform parametric studies quickly allows the engineer to optimize designs in a more efficient manner. This type of task was done using the lower limb model. The primary reason was to investigate the effects of muscle activation and bracing on lower limb response during an impact. Secondary to the actual study was demonstrating the ease and effectiveness of FEM modeling in performing such a task.

The setup was relatively simple. The boundary conditions of a typical car-to-car crash pulse were applied to the FEM model. Because the model has easily changed properties to represent different levels of muscle activation, these parameters were varied from 0% to 100% activation. This was done at the hip, knee, and ankle. A simulation matrix of 27 different runs were made. The hip, knee, or ankle could either be passive (0% activation), 50% activated, or 100% activated. Three joints with three different possible activation levels results in 27 test cases. From these simulations some trends were noticed. These include:

1. Increasing the activation level in the ankle decreased the maximum angle of dorsiflexion in the ankle.
2. Increasing the activation level in the hip increased the maximum angle of dorsiflexion in the ankle.
3. The effect of tensing the knee, while the ankle and hip remained constant, had no distinct pattern of results in ankle joint angle.
4. When the ankle was only passively activated, the peak dorsiflexion angle occurred early in the impact event, between 45 and 70 ms.
5. When the ankle was only passively activated, a second sharp increase in dorsiflexion was noted around 125 ms.
6. When the ankle was 50% or 100% activated, the peak dorsiflexion angle occurred later in the impact event, between 110 and 120 ms.

These trends indicate certain issues that are of interest to the automotive engineer who must protect against lower limb injuries. From a general human modeling point of view these results provide some insight into the necessary

techniques for representing the human. It was shown that the ankle had a high level of dependency on the musculature and activation at the hip joint. This indicates that someone focussing on ankle injury must not disregard the other joints of the body and their potential influence. The human body is a highly organized system and this must be taken into consideration when addressing human injury and response to loading.

9. Conclusions

A finite element model of the 50% male Hybrid III dummy has been developed and validated. A finite element model of the human lower limbs has been developed and validated. The two models have been combined to compare the performance of dummy vs. human limbs. The human lower limb model permits the simulation of both active and passive muscle action. The approach applied in this study is useful in assessing human response and injury mechanisms in high acceleration environments. The approach is applicable to other components of the human body in addition to lower limbs.

10. Acknowledgement

The authors express their appreciation to the Ford Motor Company, and The George Washington University for sponsoring the research reported in this paper.

11. References

Bedewi, Paul G., Human Finite Element Modeling with Applications for Vehicle Occupant Crashworthiness Simulations, (August 1995) Master's Thesis, The George Washington University, Washington, D.C.

Bedewi, P. G., The Biomechanics of Human Lower Extremity Injury in the Automotive Crash Environment, (May 1998) Doctoral Dissertation, The George Washington University, Washington, D.C.

Begeman, P. D., and Prasad, P., "Human Ankle Impact Response in Dorsiflexion," *Proceedings of the 34th Stapp Car Crash Conference*, (November 1990) SAE Technical Paper No. 902308. Reprinted in Hybrid III: The First Human-Like Crash Test Dummy, SAE PT-44, 1994.

Begeman, P., Balakrishnan, P., Levine, R., and King, A., "Dynamic Human Ankle Response to Inversion and Eversion," *Proceedings of the 37th Stapp Car Crash Conference*, (November 1993) SAE Technical Paper No. 933115.

Cowin, S. C., Bone Mechanics, (1989) ISBN No. 0-8493-4562-6, CRC Press, Boca Raton, Florida.

Crandall, J. R., Hall, G. W., Bass, C. R., Klopp, G. S., Pilkey, W. D., Hurwitz, S. R., Portier, L., Petit, P., Troseille, X., Eppinger, R. H., and Lassau, J. P., "Biomechanical Response and Physical Properties of the Leg, Foot, and Ankle," *Proceedings of the 40th Stapp Car Crash Conference*, (November 1996) SAE Technical Paper No. 962424.

Foster, J. K., Kortge, J. O., Wolanin, M. J., "Hybrid III - A Biomechanically Based Crash Test Dummy," *Proceedings of the 21st Stapp Car Crash Conference*, (1977) SAE Technical Paper No. 770938, pp. 973-1014. Reprinted in Hybrid III: The First Human-Like Crash Test Dummy, SAE PT-44, 1994.

Greene, W. B., and Heckman, J. D., The Clinical Measurement of Joint Motion, (1994) ISBN No. 0-89203-090-9, American Academy of Orthopaedic Surgeons, Rosemont, Illinois.

King, A. I., "Progress of Research on Impact Biomechanics", *Journal of Biomechanical Engineering*, (November 1993) Vol. 115, No. 4b, pp. 582-587.

Marieb, E. N., Human Anatomy and Physiology, (1992) ISBN No. 0-8053-4120-X, Benjamin/Cummings Publishing Company, Inc., Redwood City, California.

Moore, K. L. Clinically Oriented Anatomy, (1992) ISBN No. 0-683-06133-X, Williams & Wilkins, Baltimore, Maryland.

MSC/PATRAN, The MacNeal-Schwendler Corporation, 815 Colorado Blvd., Los Angeles, California 90041.

Nordin, M. and Frankel, V. H., Basic Biomechanics of the Musculoskeletal System, (1989) ISBN No. 0-8121-1227-X, Lea & Febiger, Philadelphia, Pennsylvania.

Noureddine, A., Development of a Finite Element Model and a Lumped Mass System to Address the Automotive Safety Issues Surrounding the Depowering of Airbags, (1998)

Doctoral Dissertation, The George Washington University, Washington, D.C.

Portier, L., Petit, P., Domont, A., Troseille, X., LeCoz, J. Y., Tarriere, C., and Lassau, J. P., "Dynamic Biomechanical Dorsiflexion Response and Tolerances of the Ankle Joint Complex," *Proceedings of the 41st Stapp Car Crash Conference*, (November 1997) SAE Technical Paper No. 973330.

Reddy, J. N., An Introduction to the Finite ElementMethod, (1993) ISBN No. 0-07-051355-4, McGraw-Hill, Inc., New York, New York.

Robbins, D. H., "Anthropomorphic Specifications for Mid-Sized Male Dummy," (December 1983), Transportation Research Institute Report No. UMTRI-83-53-2, United States Department of Transportation, National Highway Traffic Safety Administration Contract No. DTNH22-80-C-07502, Washington, D.C., 1994.

Viewpoint DataLabs - Database Catalog, Viewpoint DataLabs, 625 South State Street, Orem, Utah, 84058, Phone 801-229-3000, Fax 801-229-3300.

Zienkiewicz, O. C., and Taylor, R. L., The Finite Element Method, Volume 1: Basic Formulation and Linear Problems, (1989) ISBN No. 0-07-084174-8, McGraw-Hill, Inc., New York, New York.

FORCES AND DEFORMED CONFIGURATIONS OF AN AIRBAG DURING INFLATION AND IMPACT†

Xavier J. R. Avula*, Ints Kaleps, Prasad Mysore*◇**
*Department of Mechanical and Aerospace Engineering and Engineering Mechanics
University of Missouri-Rolla, Rolla, Missouri 65409-0050
**AFRL/HEPA, Wright-Patterson Air Force Base, Ohio 45433-7947, USA

SUMMARY
In this work, the evolution of forces and deformed configurations of an airbag during inflation and impact with a rigid sphere were investigated for various airbag parameters. The parameters considered were fabric density, bag elasticity, input gas temperature and vent size. The computations were performed using a non- linear finite element method coded in the LS-DYNA3D package. The influence of the above mentioned parameters on the contact during the impact was significant: lowering the fabric density resulted in higher bag velocity which in turn resulted in higher rebound velocity of an impacting sphere; fabrics of lower elasticity had shown increased contact time and higher rebound velocity; the lower the input gas temperature, the longer was the contact time and the lower the rebound velocity of the sphere. The acceleration and rebound velocity had an inverse relationship with vent area. These observations with additional studies could be used in the development of better occupant safety systems.

1. INTRODUCTION
In vehicle crashes, injuries can be drastically reduced by minimizing occupant movement and subsequent impact with the vehicle interior. Passive supplemental restraint systems, such as safety belts and airbags, are found to provide the best overall injury risk reduction. Viano [1] studied the fatality prevention effectiveness of airbags and concluded that they protected both belted and unbelted occupants. Digges [2] has examined the distribution of injuries to vehicle occupants and observed no patterns of serious injuries with the use of airbags.

The study of air bag occupant restraint systems includes the study of the airbag materials, sensors, inflators, airbag folding and deployment patterns, and finally the interaction of the airbag with an articulated occupant model. In recent years, the finite element technique has been used widely in the automotive industry for modeling and simulation of airbag inflation and its interaction with an occupant dummy. The finite element computations are most convenient for generation of bag inertia forces and direct incorporation of material properties. For accurate modeling of the airbag inflation, a gas inflation model based on the control volume concept is coupled with the airbag structure as documented by Wang and Nefske [3]. The model assumes that the gas is ideal, the specific heats are constant, no heat transfer, and uniform temperature and pressure within the airbag.

◇ Present address: EASI Engineering, 2025 Concept Drive, Warren, Michigan 48091

† Sponsored by Human Systems Center (AFMC), Brooks Air Force Base, Texas under the task "Modeling Airbag and Body Interactions" supported by the Engineering Services Contract No. F41624-95-C-6014 with Veridian, Inc. (formerly, Systems Research Laboratories), Dayton, Ohio.

Nieboer et al. [4] modeled inflated airbags with different kinds of boundary constraints associated with striking by impactors of different shapes and travelling at different velocities. These models are important to the simulation of airbag-occupant interactions when the occupants are of different sizes and shapes as in the case of females and children.

The most important aspect of airbag simulation is the prediction of occupant dynamics caused by the contact and interaction between an inflating airbag and the occupant. In the situation of an impact involving an occupant in the driver's seat, the pre-deployment folding pattern of the airbag is not critical because the duration of 30 to 40 milliseconds available for the airbag to assume full shape and volume provides adequate safety. In situations wherein the occupant is seated with his upper torso leaning on the steering hub or in another out-of-position orientation, the occupant could be in contact with the airbag during the early stages of deployment. In these situations, the pattern of the airbag unfolding could have a significant influence on occupant injury. Therefore, in simulations involving an out-of-position occupant, one should include the folding configuration of the airbag and investigate the effects of early interaction with the occupant due to the unfolding of the airbag. Lakshminarayan [5], Lasry [6] and Khalil et al. [7] have investigated the inflation of a folded airbags and resultant interactions with an occupant. Yang [8] has studied the forces between the occupant and airbag for two different folding configurations and two different airbag mounting angles.

Apart from the automotive industry, research on occupant simulation is being conducted in the aerospace industry to investigate the possibility of incorporating airbags in large aircraft and helicopters. The purpose is to provide maximum protection to the pilot and other crew members during survivable crashes. As in automobiles, deployment time for different folding configurations and various airbag parameters are of interest. The aim is to minimize the relative velocity of the body at the time of impact with internal vehicle components.

In this work, an attempt has been made to simulate the deployment of an initially folded airbag and predict the contact forces between a solid object that represents a particular part of the occupant's body and the airbag during the unfolding phase and after full inflation. A review of literature indicates that the influence of airbag parameters such as airbag fabric density, elasticity, input gas temperature, and extent of venting on contact force is worth investigating. In the present investigation, a parametric analysis was carried out to calculate the airbag response and resulting acceleration of a rigid sphere after impact with a deploying airbag.

2. AIRBAG INFLATION PROCESS
The supplemental inflatable restraint system module consists of an inflator, which produces a gaseous filling medium, and a

circular fabric bag housed in an appropriate location to encounter the impactor. The air bag material is woven nylon with self-venting pores or mechanical vents. The associated equipment includes a diagnostic system which serves three functions: it monitors the airbag system, acts as a backup against electrical power failure, and performs a readiness test at engine start-up.

The inflator produces nitrogen gas by igniting a material such as sodium azide (NaN_3). This material is mixed with certain proprietary oxidizers and binding agents so that the non-volatile byproducts form a slag which is removed by filtration. Ignition of the mixture is facilitated by use of a highly exothermic and easily ignitable substance such as boron potassium nitrate ($BKNO_3$). In order to achieve proper sequencing of combustion in the airbag inflation process, the two pyrotechnic materials are contained in separate chambers. Orifices at the exits of each of these chambers and a third chamber, which contains both a slag trap and a filter, control the gas flow rates. The filter in the third chamber consists of knitted and compacted wire mesh, screen or fibrous material. The function of this filter is to prevent droplets and condensed particulates from entering the gas stream that inflates the airbag. In the process, the gas stream loses a significant amount of heat.

The airbag inflation process is initiated by using a crash sensor located remotely from the passenger compartment. The sensor detects rapid deceleration, as in a collision, and sends an electric signal to trigger the inflator. In an automobile, the sensor is located such that a collision within a 60^0 arc in front of the vehicle triggers the inflator. After the sensor initiates inflation, the air bag is filled with gas to full inflation and then deflates as the gas escapes through vents. The deployment of the airbag usually occurs in 30 to 40 milliseconds.

3. AIRBAG MODEL FORMULATION

The airbag model formulation involves three aspects, namely:

1) Airbag fabric material characterization,
2) Modeling of the gas inside the airbag, and
3) Equation of state that describes the evolution of the gas pressure as a function of temperature and density.

The configuration of the fully inflated airbag is elliptic.

3.1 Fabric Model

The fabric material model used in the airbag analysis is described in the LS-DYNA3D theoretical manual [9]. The fabric exhibits a strong material nonlinearity and cannot sustain compressive and bending stresses. Further, only low levels of stresses are developed in the fibers until the material is stretched taut, which means there exists an initial slack. This behavior has been modeled by representing the modulus of the fiber as a function of fiber strain. The idealized model produces a zero modulus for compressive strains and piecewise linear modulus for tensile strains as described in [7]. This material model simulates the inability of the fibers to carry compressive stresses and allows initial fabric slack.

For the implementation of the material model, the Cauchy stress tensor σ_{ij} and the deformation tensor d_{ij} are transformed into the material coordinate system denoted by the subscript L. Then the stress state is incrementally updated in the material coordinates by;

$$\sigma_L^{n+1} = \sigma_L^n + \Delta\sigma_L^{n+\frac{1}{2}} \tag{1}$$

where,

$$\Delta\sigma_L^{n+\frac{1}{2}} = \begin{bmatrix}\Delta\sigma_{11}\\ \Delta\sigma_{22}\\ \Delta\sigma_{12}\\ \Delta\sigma_{23}\\ \Delta\sigma_{31}\end{bmatrix} = \begin{bmatrix} Q_{11} & Q_{12} & 0 & 0 & 0\\ Q_{12} & Q_{22} & 0 & 0 & 0\\ 0 & 0 & Q_{44} & 0 & 0\\ 0 & 0 & 0 & Q_{55} & 0\\ 0 & 0 & 0 & 0 & Q_{66}\end{bmatrix} \begin{bmatrix} d_{11}\\ d_{22}\\ d_{12}\\ d_{23}\\ d_{31}\end{bmatrix}_L \Delta t \,. \tag{2}$$

The terms Q_{ij} are defined as

$$Q_{11}=\frac{E_{11}}{1-\nu_{12}\nu_{21}},\ Q_{22}=\frac{E_{22}}{1-\nu_{12}\nu_{21}},$$
$$Q_{12}=\frac{\nu_{12}E_{11}}{1-\nu_{12}\nu_{21}},\ Q_{44}=G_{12},\ Q_{55}=G_{23},\ Q_{66}=G_{31} \tag{3}$$

Due to symmetry,

$$\nu_{21} = \nu_{12}\frac{E_{22}}{E_{11}} \tag{4}$$

where υ_{ij} is Poisson's ratio for the transverse strain in jth direction for the material undergoing stress in the ith-direction, E_{ij} are the Young's modulii in the ith direction, and G_{ij} are the shear modulii. After completion of the stress update, the stresses are transformed back into the local shell coordinate system.

Also, due to thermodynamic considerations, the following constraints are enforced at each time step:

$$|\nu_{12}| < \sqrt{\frac{E_2}{E_1}} \qquad |\nu_{21}| < \sqrt{\frac{E_1}{E_2}}\,. \tag{5}$$

3.2 Airbag Interior

The interior of the airbag could have been modeled by discretizing its domain using solid elements. The pressure-volume relation of the airbag would then be the sum of all elemental contributions. But this approach is numerically demanding and time consuming during the inflation phase of the airbag deployment and while the model is refined.

A less computationally demanding approach for modeling the contents of the airbag is the control volume approach. A control volume is defined as the volume enclosed by a surface called the control surface. In the present case, the control surface is the airbag fabric and the gaseous interior is the control volume. As the evolution of the control surface is known, i.e., the position, orientation and current surface area of the airbag elements, the control volume can be calculated by applying Green's theorem,

$$V = \oint \bar{x} \cdot \bar{n}\, d\Gamma = \sum_{i=1}^{N} x_i\, n_{ij}\, A_j \qquad (6)$$

where,

V = control volume,
N = number of elements,
$d\Gamma$ = elemental surface area enclosing the volume,
x_i = average distance for each element A_i,
n_{ij} = direction cosines of the unit normal of the jth element with respect to the coordinate axes
Aj = the surface area of the element j.

The above equation is integrated with respect to the direction of integration chosen to be parallel to the maximum principal moment of inertia of the surface.

3.3 Equation of State; Evolution of Gas Pressure

The pressure history in the airbag corresponding to the control volume is determined from an equation of state. The equation of state used for airbag simulation should relate the pressure to the gas density (mass per unit volume) and the specific internal energy of the gas.

The Gamma law equation of state as described in [7] is used to determine the pressure in the airbag:

$$P = (\gamma - 1)\rho e \qquad (7)$$

where P is the pressure, ρ is the density, e is the specific internal energy of the gas, and γ the ratio of the specific heats is

$$\gamma = \frac{C_p}{C_v} . \qquad (8)$$

The specific internal energy evolution equation corresponding to two states is given by

$$e_2 = e_1[v_2/v_1]^{(1-\gamma)} . \qquad (9)$$

in which v_1 and v_2 are the specific volumes at two different states.The time rate of change of mass flowing into the bag is given by the law of conservation of mass:

$$\frac{dM}{dt} = \frac{dM_i}{dt} - \frac{dM_o}{dt} \qquad (10)$$

where M_i is the mass flowing into the airbag and M_o is the mass flowing out of the airbag. This formulation is described in the LS-DYNA3D software [10] for modeling the airbag and its interior. Numerical results for the airbag model were calculated using the four-noded quadrilateral membrane shell element described in [10].

4. AIRBAG SIMULATION

The airbag simulation was carried out using the explicit nonlinear finite element program LS-DYNA3D. The dynamic nature of crashworthiness contact problems, such as airbag deployment combined with their complex geometry and highly nonlinear material behavior, makes them well suited for analysis using LS-DYNA3D. A typical driver side airbag of 720 mm diameter with 2 vent holes of 20 mm diameter was studied. The airbag was modeled using special fully integrated membrane elements in conjunction with the fabric material model. The fabric material model was chosen over the orthotropic material model as it was found to be less time-step sensitive compared to the other models presented in the menu of models in LS-DYNA3D [10]. The membrane element was found to be especially suitable for anisotropic fabric behavior and the wrinkling phenomenon. Though fabric material models are unable to support buckling due to compressive stress, the "no compressive stress" option was not used as wrinkling normally occurs in airbags. Damping was used in the fabric material model to reduce the excessive distortions caused by the large amounts of energy input to the bag. The numerical values used for the material and geo- metric parameters of the fabric material are given in Table I [10]. The computed mass of the airbag was 292 gm.

The airbag was folded using the folding option in the LS-INGRID mesh generator. The airbag was initially discretized as two separate layers using this mesh generator. The location of fold lines, direction of fold, folding radius and sequence of folds were specified in the input file. The nodal point locations were then checked to avoid element interpenetrations after folding. A series of thick folds were defined in the folding operation. The airbag model included 1496 quadrilateral membrane elements. The larger number of elements was needed in order to model the folded configuration. The orientation of the bottom fabric layer was at 0° and 90°. For the top layer it was -45° and 45°, as in an actual bag. A sequence of symmetric accordion folds

TABLE I: Material properties for the airbag fabric [12]

Parameter	Variable	Units	Value
Thickness	t	mm	0.35
Density	ρ_{fabric}	kg/m^3	1000
Young's Modulus	E	N/m^2	$1.0x10^{08}$
Poisson's Ratio	υ	-	0.4

perpendicular to the x-axis and a series of rolling and accordion folds about the y-axis were executed for the folds.

The Wang-Nefske equation of state, as given by Eq. (7) and the airbag model described in [3], based on the control volume approach, were used to model the thermodynamic behavior of the gas flow into the airbag. It was assumed that the gas behaved as an ideal gas, and that the process was adiabatic, and the pressure and temperature were distributed uniformly throughout the control volume. For a given inflator, the heat capacities at constant volume and pressure, temperature of the gas, ambient density and pressure, load curve for the mass flow rate and a mass-weighted damping factor were specified. The numerical values for the above are presented in Table II. The input gas temperature was considered to be constant with time. The outflow of the gas was defined by a coefficient of discharge and exit area. A mass flow rate curve was defined by averaging the mass flow rate data reported in [3]. The volume occupied by the gas was continuously monitored by calculating the volume of the finite element model of the airbag surface. Thus, knowing the volume occupied by the gas, the internal pressure was calculated from thermodynamic equations. This pressure was in turn applied to the finite element model to obtain the new bag shape and volume. This interchange between the gas model and finite element model provides the coupling between the two models.

As the airbag inflates, a considerable amount of energy is transferred to the surrounding air. This energy transfer decreases the kinetic energy of the bag as it inflates. In the control volume concept, this was simulated by using the mass-weighted option.

During the inflation stage of an airbag, surface folds come into contact with themselves while unfolding. To eliminate the interpenetration between the surface nodes during inflation, an airbag single surface slideline which was specially developed for airbags was used. A slideline is a contact algorithm to model the mechanical interaction between two bodies or two parts of the same body. The single surface slideline is based on a penalty formulation. For a single surface algorithm, a master surface need not be defined.

In this study the impact of an airbag with a rigid sphere was simulated. The evolution of volume and presssure of the airbag was studied for various parametric changes in fabric density, bag elasticity, input gas temperature, and vent size.

A sphere of 100 mm radius weighing 4.9 kgs initially at a center distance of 800 mm from the folded airbag was considered. In the computational scheme, a geometric contact entity approach was used to model the impacting sphere. The geometric contact entity was developed using a solid modeling approach described in [7, p. 264]. Using this approach for modeling the contact of curved rigid bodies impacting deformable surfaces requires much less storage and vastly reduced the computational time in comparison with the more general faceted contact which requires defining master and slave surfaces. For the contact phase, the nodes of the airbag were slaved to the impacting sphere. The simulation was carried out until 120 milliseconds elapsed and the results were post-processed.

5. RESULTS AND DISCUSSION

5.1. Verification of The Airbag Model

For the purpose of verification of the model, the case of pure inflation of the airbag was considered, and the results were compared with those obtained using the model of a generic driver side airbag from reference [11].

Figure 1 shows the configurations of the airbag at different stages of inflation. For the first 25 milliseconds, the airbag was in the unfolding process. After this, the bag started to undergo rapid deformation due to the high momentum. By 45 milliseconds, the bag had started to assume an ellipsoidal shape (Figure 1-d) and approached full inflation (Fig. 1-e). The wrinkling was caused by the expansion of the airbag in the z-direction. The wrinkling phenomenon in the present simulation was far less than that in a real airbag because of the smaller number of elements used to save computational time.

Figure 2 shows the input mass flow curve used in the simulation. The computed bag volume, bag pressure and gas temperature within the bag are compared with the similar data from reference [11] in Figures 3-5. The control mass flow rate curve being the one in Wang-Nefske model (see Ref. [3]), the two curves in these figures illustrate similar trends and reasonably close agreement.

The computed peak volume of 62.5 liters attained at 60 milliseconds in the present simulation (with the folding pattern shown in Figure 1- a) compared well with the volume measurements for an actual driver side airbag which varies from 62 to 68 liters. The high initial pressure was due to the

TABLE II : Thermodynamic properties of the gas and ambient air [12].

Material	Parameter	Variable	Units	Value
Nitrogen	Specific heat at Constant Volume	C_v	J/kg°K	741.0
	Specific heat at Constant Pressure	C_p	J/kg°K	1038.0
	Temperature	T	°K	700.0
Air	Density	ρ_{air}	kg/m^3	1.0
	Ambient Pressure	Pe	Pa	1.0E05

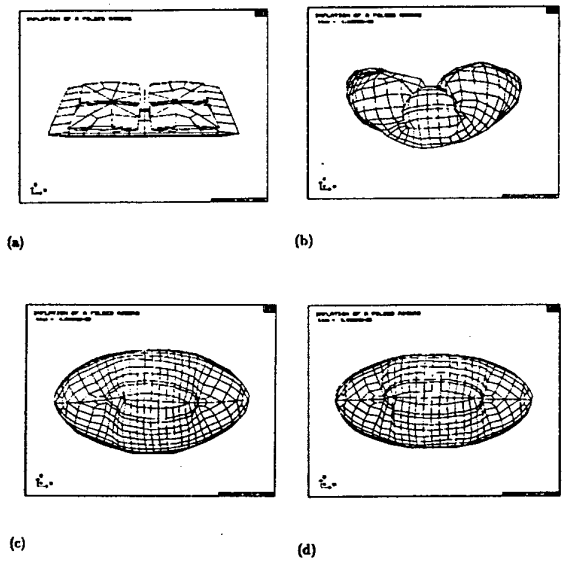

Figure 1. Inflation of a folded airbag in different stages: (a) oblique view before deployment, (b) side view at 15 msec, (c) at 28 msec, (d) at 45 msec, (e) at full inflation

gas flowing rapidly into the small volume of the folded airbag which resisted the expansion. Both the curves exhibited an initial peak at about 8-10 milliseconds. At the end of the simulation, both the curves had identical residual pressures. The temperature curves were in very good agreement throughout the simulation. It must be noted that while the input temperature was assumed constant with respect to time, the gas temperature in the expanding airbag will vary in accordance with the gas law.

5.2. Impact With a Sphere: A Parametric Study

After gaining confidence in the validity of the airbag model using LS-DYNA3D software, a parametric study was conducted to analyze the effects of airbag parameters such as fabric density, bag elasticity, input gas temperature, and vent size on the impact between a rigid sphere and a deploying airbag. The rigid sphere was initially at a distance of 800 mm from the base support and was travelling with a velocity of 10 m/s. As a measure of the effect, the acceleration of the rigid sphere as influenced by the airbag inflation phase was studied. The initial finite element setup of the airbag and the sphere is depicted in Figure 6. The material properties of the airbag were the same as presented earlier in Table I. The collision of the spherical entity with the inflating airbag is illustrated in Figures 7-9. Until 35 milliseconds, the airbag was inflated and the sphere travelled with a constant velocity without any contact between the two. Between 35 and 40 milliseconds the sphere came in contact with the airbag. By 80 milliseconds the sphere had penetrated the airbag reducing its volume. At the end of the simulation, which was 120 milliseconds, the

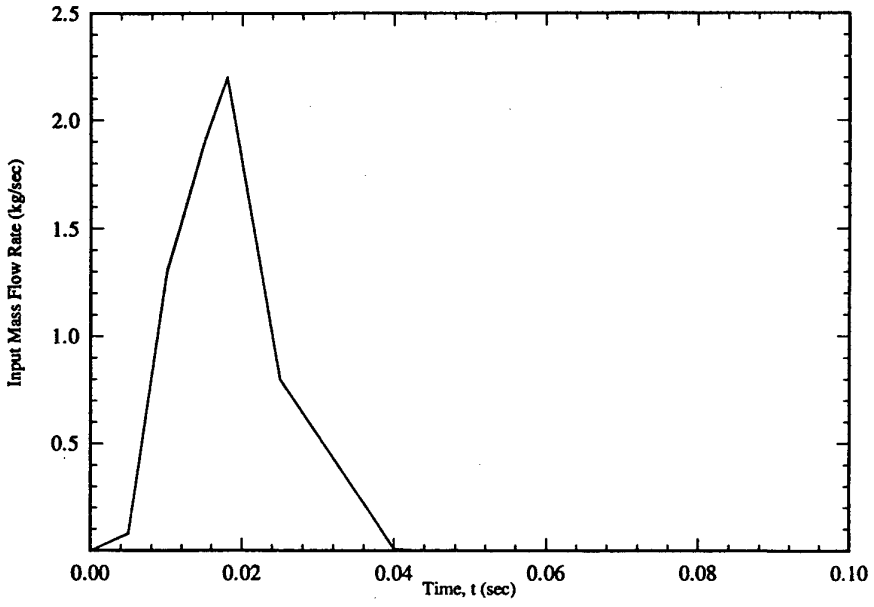

Figure 2. Input mass flow rate curve

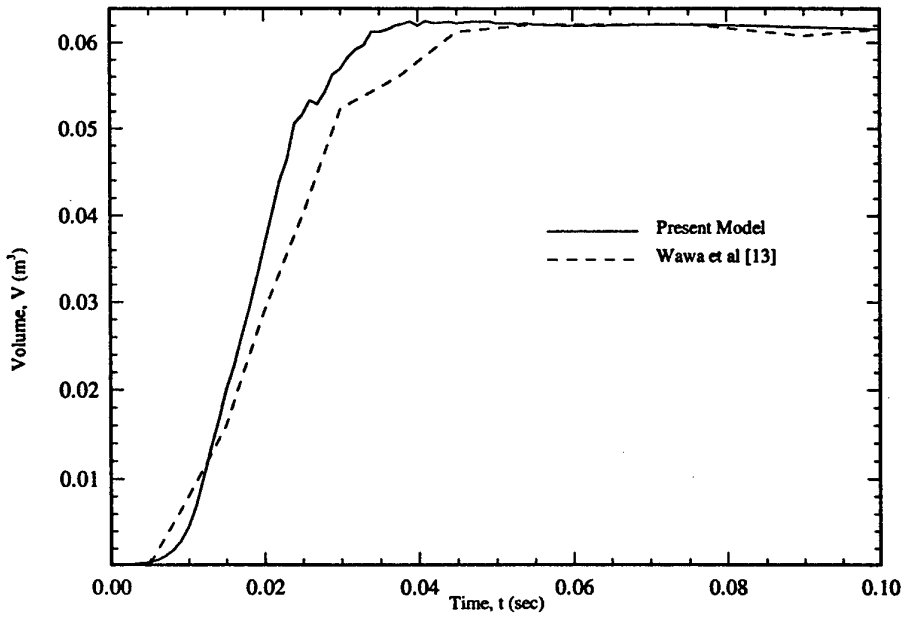

Figure 3. Time history comparison of the airbag volumes

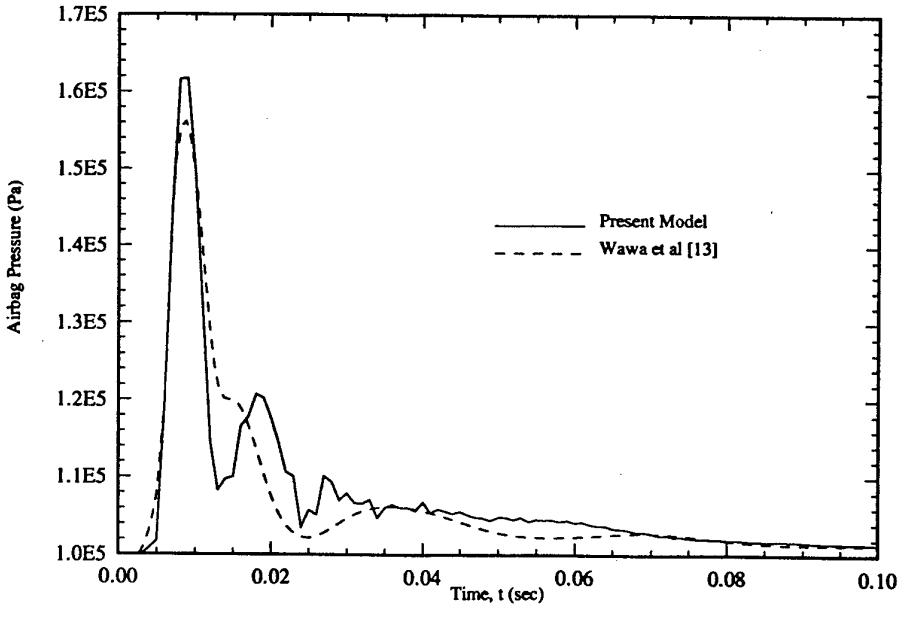

Figure 4. Time history comparison of the airbag pressures

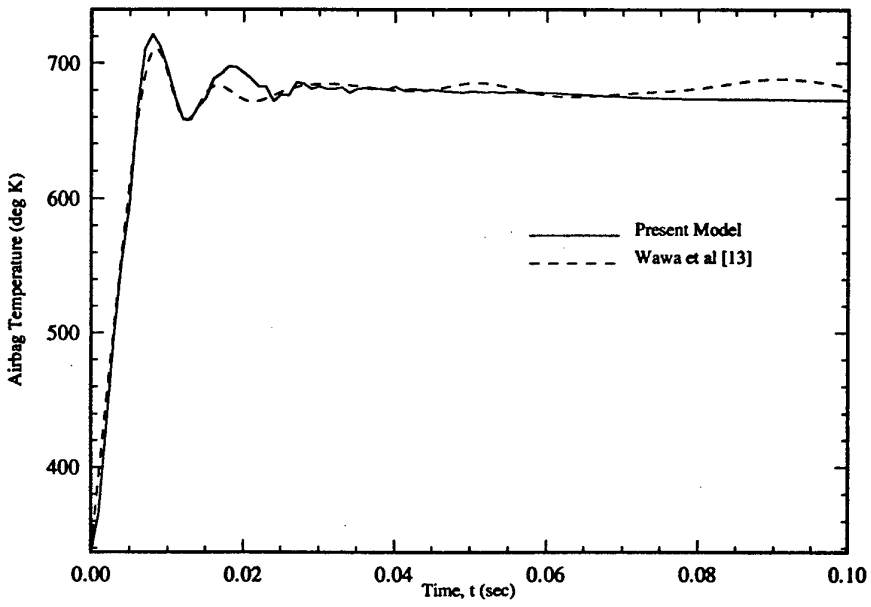

Figure 5. Time history comparison of the temperature within the airbag

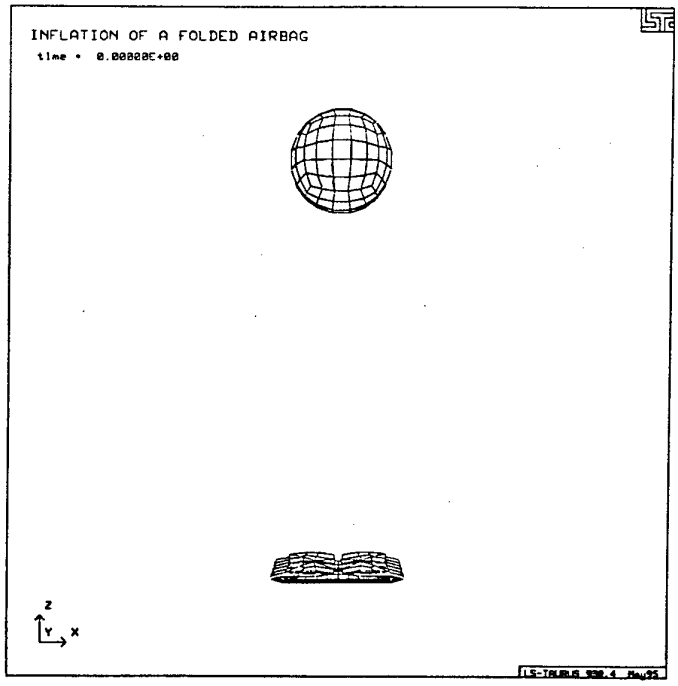

Figure 6. Initial configuration of the folded airbag and the rigid spherical entity

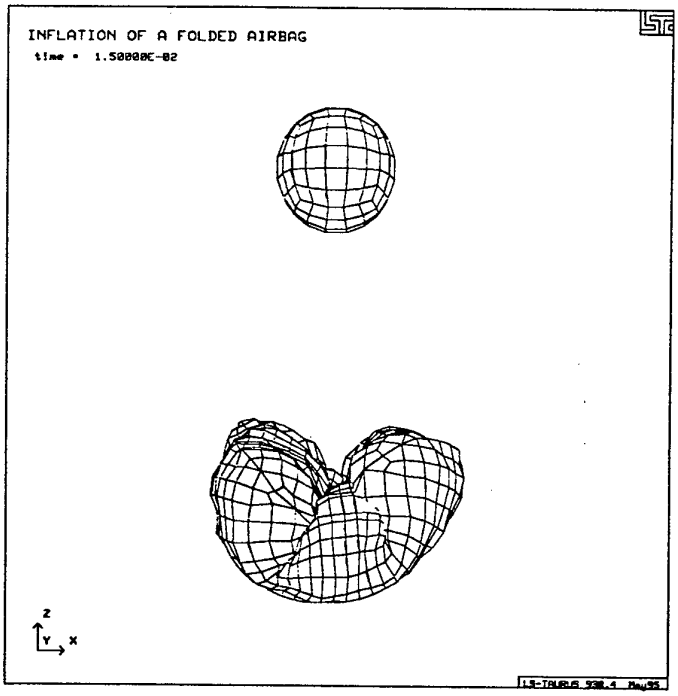

Figure 7. Side view of the unfolding airbag and the sphere at 15 msec

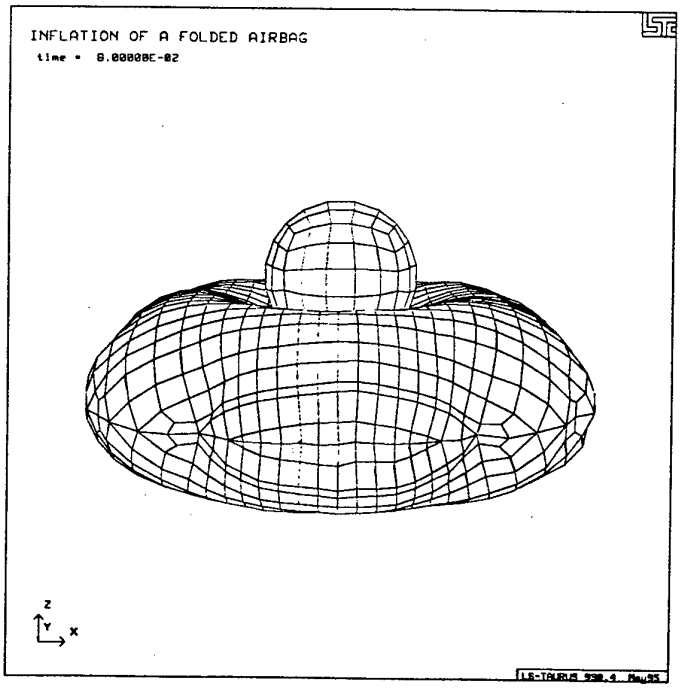

Figure 8. Side view of the rigid sphere penetrating the fully inflated airbag at 80 msec

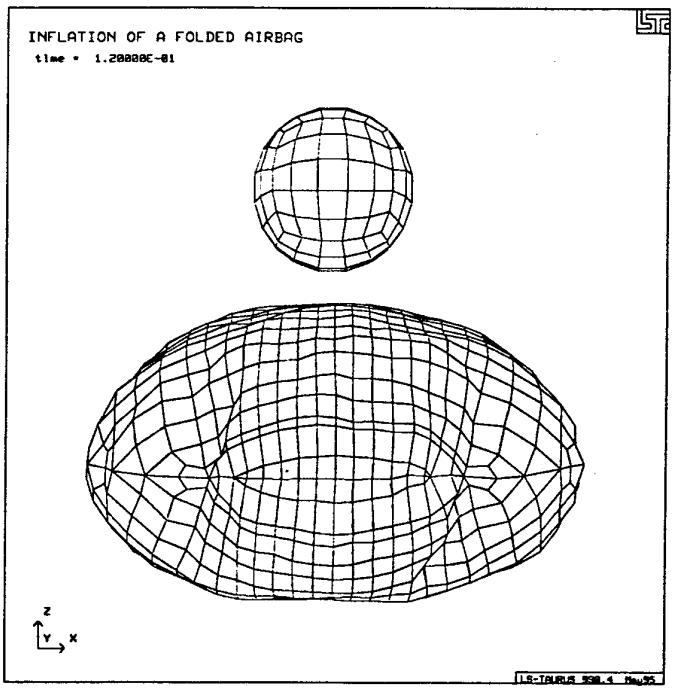

Figure 9. Side view of the rebounding sphere and that of the airbag regaining its shape at the end of the simulation

sphere had rebounded and was traveling away from the airbag. The accelerations of the sphere are in close agreement with the head accelerations from reference [12].

5.2.1. Effect of Fabric Density

To study the effect of fabric density on airbag deployment, a parametric study was carried out with airbags having fabric densities 500 kg/m^2, 1000 kg/m^2 and 1500 kg/m^2. Predictions of the resultant acceleration and z-velocity for the sphere are illustrated in Figure 10. The anticipated differences in times of initial contact by virtue of variations in material densities are indistinguishable in these figures for the three cases. However, the contact duration of 70 milliseconds remained the same for all the three cases. Peak accelerations ranging from 55 to 58 g's were observed for the sphere in all the simulations. The rebounding velocity of the sphere was highest for the fabric with lowest density which can be attributed to higher velocity of the airbag during unfolding and subsequent inflation as a consequence of low material density.

Figure 11 shows the volume and pressure histories. As expected, a higher bag volume and corresponding lower bag pressure were computed for the lowest bag density airbag model. The airbag volume was reduced during the contact phase, after which it began to regain its fully inflated shape. The pressure curves tended to converge once the gas generation stopped.

5.2.2. Effect of Bag Elasticity

Using the same material properties for the airbag but changing the bag elasticity, a parametric study was conducted to determine the dynamics of impact. Initial contact time was different for all the cases. For the fabric with 1.3x10^8 kg/m^2 elasticity, the acceleration was relatively higher compared to the other elasticity values used due to higher stiffness causing larger forces on the sphere. The larger contact time and higher rebound velocity of the sphere for 0.5x10^8 kg/m^2 elastic modulus value was attributed to greater bag stretch due to the lower elasticity. Rebound velocities computed were in the range of 7 to 8 m/sec in all cases as seen from Figure 12. The pressure curves in Figure 13 reveal marginally higher pressures for higher modulus of elasticity of the fabric. The softer (more compliant) material was found to cause larger bag volumes than a stiff material.

5.2.3. Effect of Input Gas Temperature

A parametric study was done on the effect of input gas temperature on the contact time and resulting acceleration of the rigid sphere. Figure 14 shows the accelerations and velocity time histories for input gas temperatures ranging from 600 to 800 deg K in steps of 100 deg K. For the 800 deg K case, the initial contact time was the earliest followed by simulations for 700 deg K and 600 deg K. The rebounding velocity for the case of 600 deg K input gas temperature was found to be significantly lower. At the end of the simulation, the sphere was still in contact with the airbag.

The evolution of volume and pressure in the airbag at different temperatures illustrated in Figure 15 show that the lowest value of input gas temperature results in low bag volume. All the pressure vs. time histories followed the same trend until contact after which they varied. This variation was attributed to gas escape through the vents in the airbag.

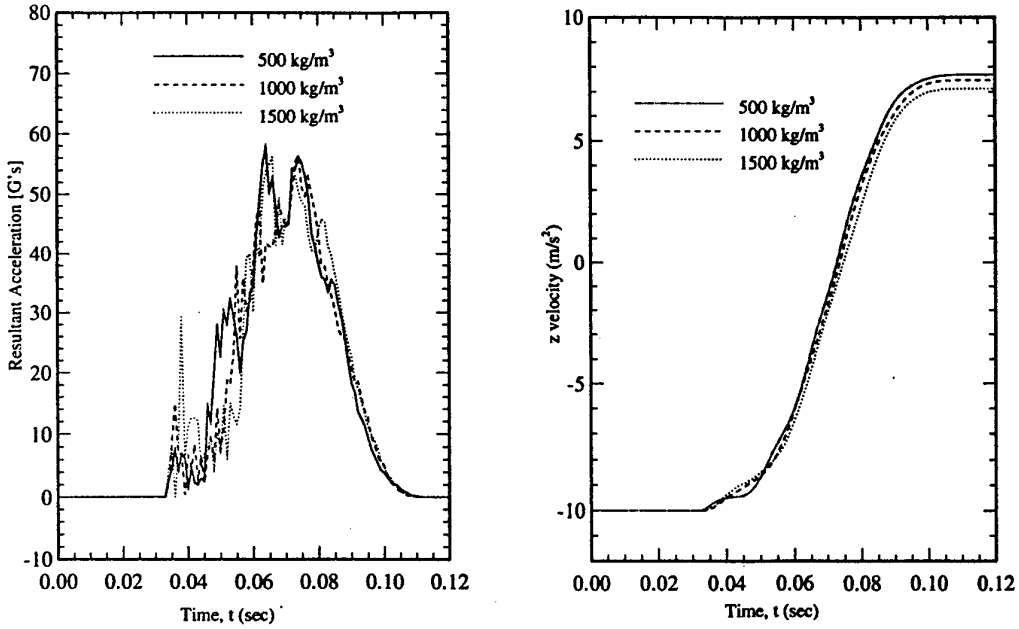

Figure 10. Resultant acceleration and velocity time histories of the rebounding sphere for various fabric densities

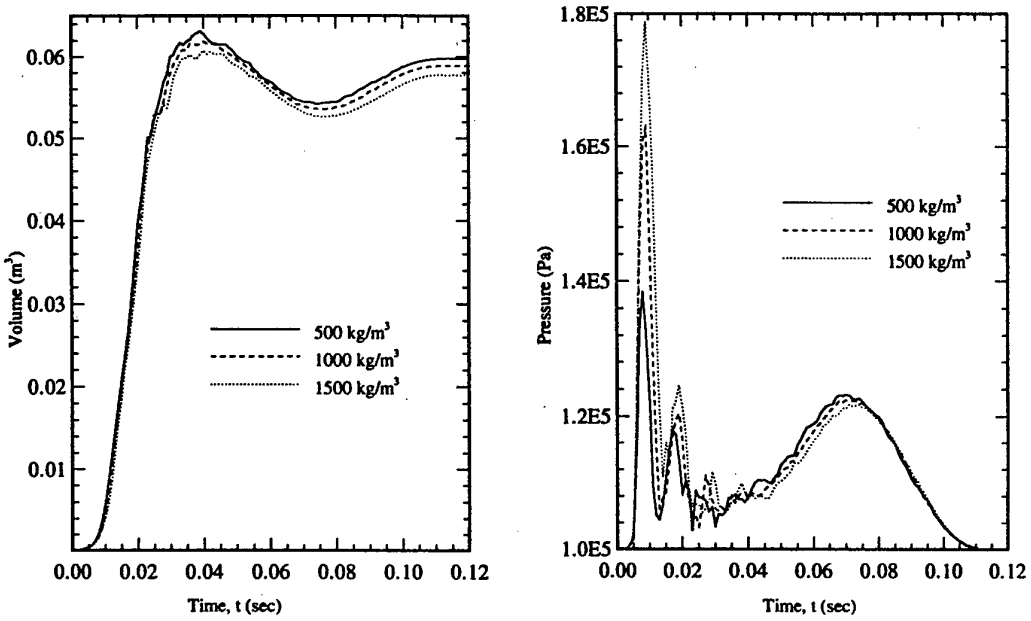

Figure 11. Time histories of volume and pressure in the airbag for various fabric densities

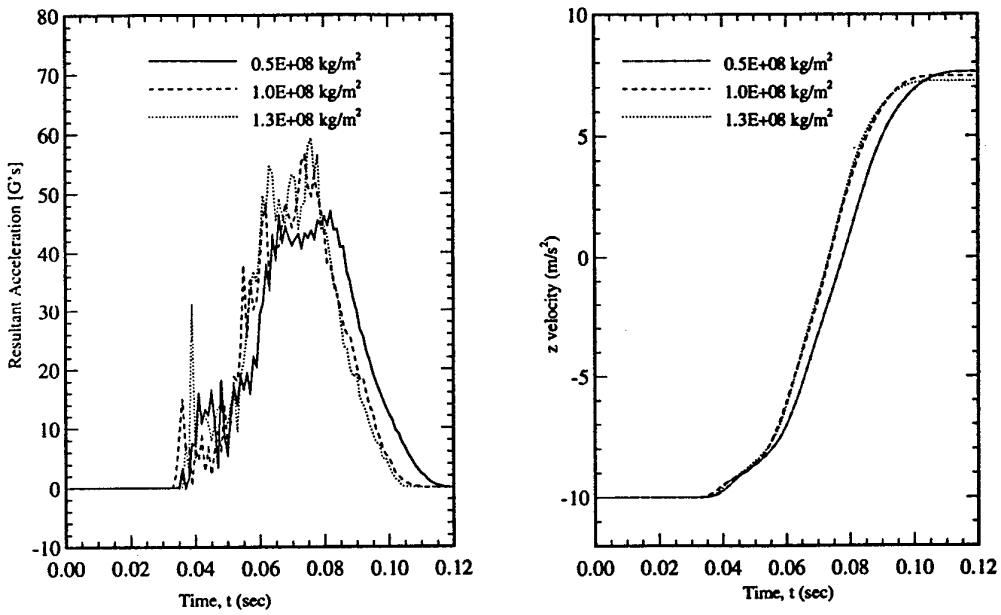

Figure 12. Resultant acceleration and velocity time histories of the rigid sphere for different values of bag elasticity

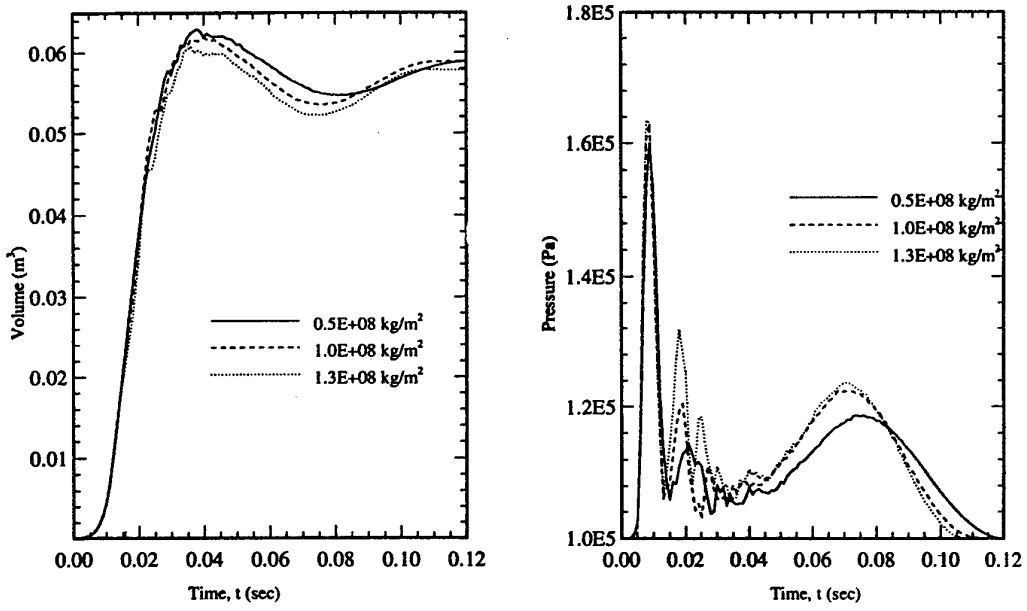

Figure 13. Volume and pressure time histories for the airbag for different values of bag elasticity

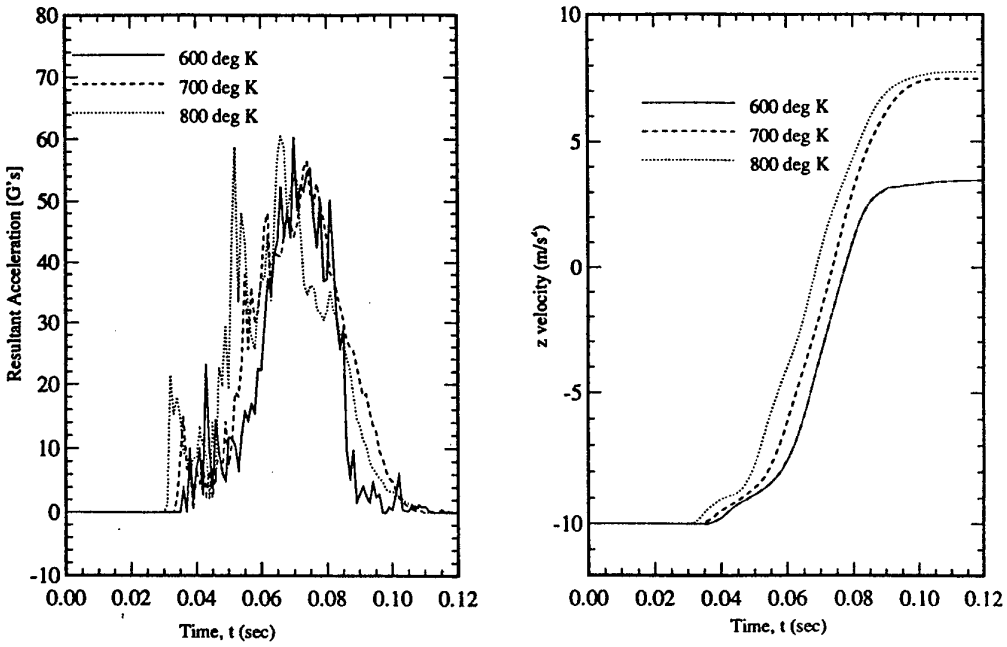

Figure 14. Time histories of the resultant acceleration and velocity of the rigid sphere for various input gas temperatures in the airbag

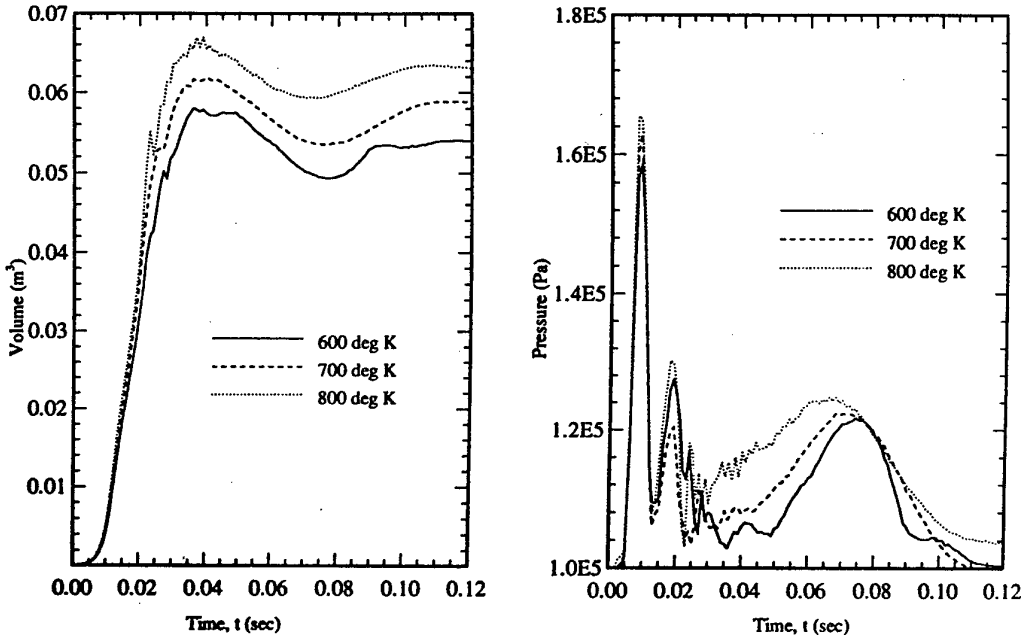

Figure 15. Time histories of the volume and pressure of the airbag at various input gas temperartures

5.2.4. Effect of Venting

Three cases were considered for studying the effect of venting on contact interaction. In the first case, no vent holes were defined and in the subsequent cases vent holes of areas 6.284 sq cm and 9.426 sq cm were considered. In all the simulations the coefficient of discharge of the venthole was assumed to be 0.7. The analysis of the velocity and accelerations from Figure 16 is instructive. The initial contact time which was at 35 milliseconds was found to be same for all the three cases as the mass of gas flowing out of the bag was negligible compared to the mass of the gas flowing into the bag until the input mass flow rate reached zero. After the gas generation stopped at around 40 milliseconds, the effect of venting could be seen. The resulting acceleration and z-velocity were the highest for the airbag model without venting and lowest for the model with the largest exit hole area.

The pressure and volume curves indicated in Figure 17 were identical until the flow of gas into the airbag stopped, after which they assumed different paths depending on the vent area.

6. CONCLUSIONS

A Finite Element simulation of the deployment of an initially folded airbag was carried out using the nonlinear three dimensional finite element program LS-DYNA3D.

The finite element airbag model implementation was verified by comparing the unfolding process and the evolution of pressure, volume, and gas temperature with previously reported simulation results. These results were in good agreement with the exception of some minute discrepancies which could be attributed to the difference in mass flow rate curves used for the two simulations.

A study was conducted to investigate the influence of the airbag parameters on contact during collision of the airbag with a rigid spherical object. The parameters considered were fabric density, bag elasticity, input gas temperature, and venting. It was inferred from the simulation that the fabric density did not have a significant effect on the resultant acceleration of the rebounding sphere while the bag elasticity had considerable effect on the acceleration as well as on the duration of contact. A low input gas temperature resulted in low bag volume and pressure. An increase in the vent area resulted in reduced acceleration for the impacting sphere. In an actual crash situation, the purpose of the airbag is to prevent injury and reduce the acceleration of the anatomical entity that may come in contact. The results in the present investigation fortify the idea of airbag deployment for occupant safety and call for additional studies for the development of robust occupant safety systems for aircraft.

REFERENCES

[1] Viano, C. David, " Effectiveness of Safety Belts and Airbags in Preventing Fatal Injury", SAE Paper No. 910901, 1991.

[2] Digges, H. K., Roberts, V., Morris, J. " Residual Injuries to Occupants Protected by Restraint Systems", SAE Paper No. 891974, 1989.

[3] Wang, J. T., Nefske, J. D., " A New CAL3D Airbag Inflation Model", SAE Paper No. 880654, 1988.

[4] Nieboer, J. J., Wismans, J., De Coo,P. J. A., "Airbag Modelling Techniques", SAE Paper No. 902322, 1990.

[5] Lakshminarayan, V.,Lasry D. , "Finite Element Simulation of Driver Folded Air Bag Deployment", SAE Paper No.912904, 1991.

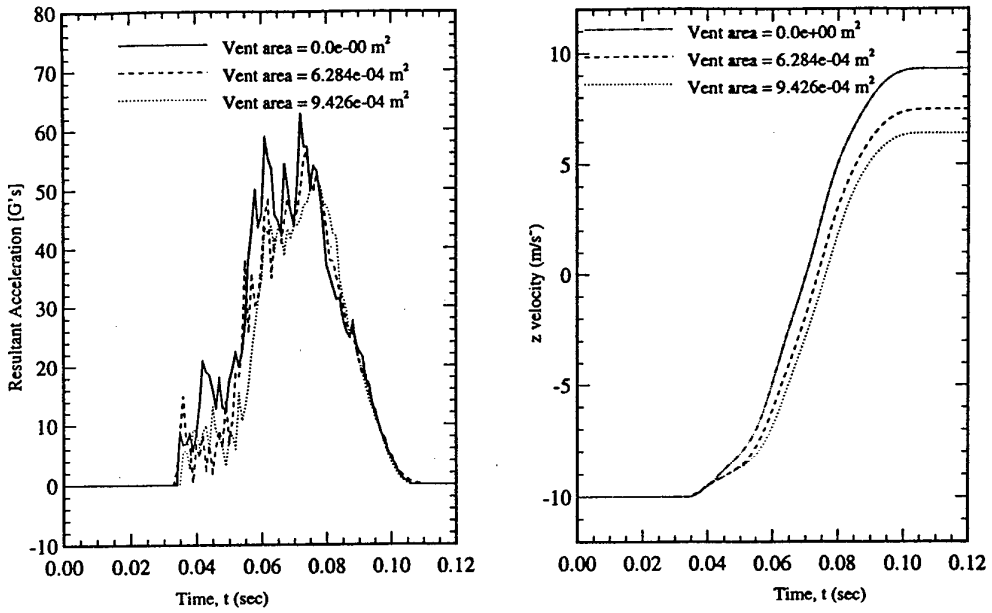

Figure 16. Time histories of resultant acceleration and velocity of the impacting sphere for different vent sizes of the airbag

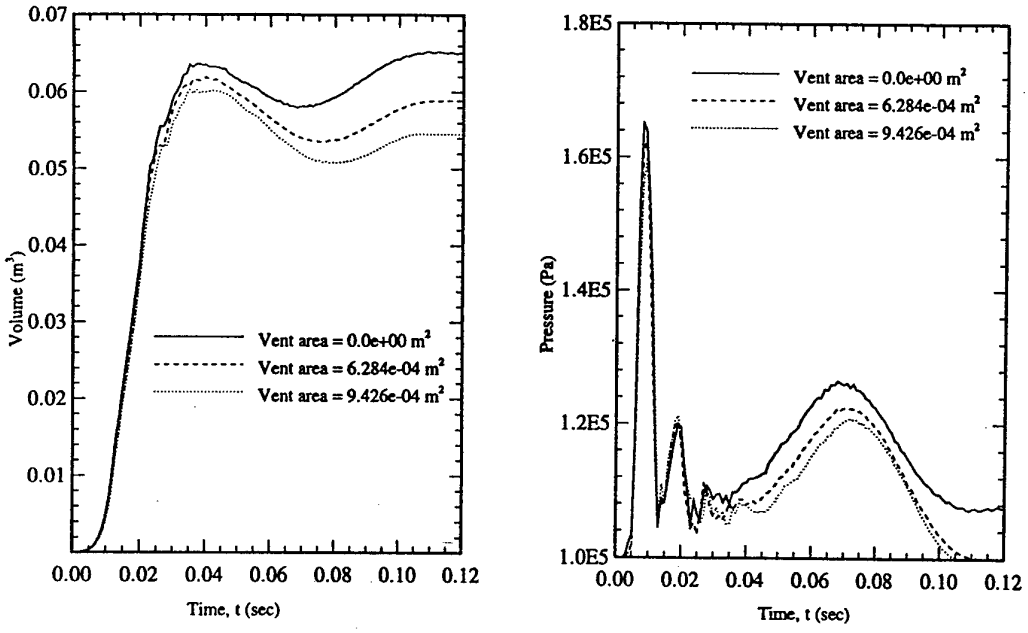

Figure 17. Time histories of the volume and pressure in the airbag at various vent sizes

[6] Lasry, D., Hoffmann, R., Protard, J.B. " Numerical Simulation of Fully Folded Airbags and Their Interaction with Occupants with PAM-SAFE", SAE Paper No. 910150, 1991.

[7] Khalil, T. B., Wasko, R. J., Hallquist, J. O., and Stillman, D. W., "Development of a 3-Dimensional Finite Element Model of Air Bag Deployment and Interactions with an Occupant Using DYNA3D, SAE Paper No. 912906, 1991.

[8] Yang, K. H., Li, Y. Q., " Effects of the Airbag Folding Pattern in Out-of-Position Frontal Impact With an Airbag", MD-Vol.169/BED-Vol. 25, Crashworthiness and Occupant Protection Systems, ASME 1993.

[9] LS-DYNA3D (Non-linear Dynamic Analysis of Structures in 3 Dimensions) Theoretical Manual, Livermore Software Technology Corporation, 1994.

[10] LS-DYNA3D (Non-linear Dynamic Analysis of Structures in 3 dimensions) User's Manual, Livermore Software Technology Corporation, 1995.

[11] Wawa, J. C., Chandra, S. J., Verma,, K. M., "Implementation and Validation of a Finite Element Approach to Simulate Occupant Crashes with Airbags: Part I - Airbag Model", AMD-Vol. 169/BED-Vol. 25, Crashworthiness and Occupant Protection Systems, ASME 1993.

[12] Wawa, J. C., Chandra, S. J., Verma, K. M., "Implementation and Validation of a Finite Element Approach to Simulate Occupant Crashes with Airbags: Part II-Airbag Coupling with Crash Victim", AMD-Vol. 169/BED-Vol. 25, Crashworthiness and Occupant Protection Systems, ASME 1993.

MADYMO VALIDATION OF SIDE FACING SOFA SLED TESTS

A.M.G.L. Teulings, TUE Eindhoven, Den Dolech 2, 5612 AZ Eindhoven, The Netherlands
V. Gowdy, CAMI Oklahoma 73125, USA
J.S.H.M. Wismans, TNO-wt, 2600 JA Delft, the Netherlands
B. Aljundi, TNO-MADYMO North America
Farmington Hills Corporate Centre, 21800 Haggerty Road, Suite 305, Northville, MI 48167, USA

1. SUMMARY

In order to investigate, and ultimately improve, the crash worthiness of side facing sofas a series of sled tests were performed. The EUROSID-1 dummy was used to measure various signals needed to assess injury potential. To facilitate a parametric study into injury potential related factors a MADYMO computer model of these tests was made and needed to be validated. The correlation between test and simulation signals warrents sufficient trust in the model for it to be used as a baseline model in a parametric study.

2. INTRODUCTION

Issues related to side facing seats and sofas for new aircraft that meet the objectives of the Federal Aviation Administration's (FAA) regulations for occupant protection are currently being addressed by various industry and government activities. A series of dynamic impact tests with a side facing sofa fixture were conducted at the FAA's Civil AeroMedical Institute (CAMI) using the EUROSID-1 and Hybrid-II dummy. In order to investigate the injury potential to the thorax, the test protocol included assessments of the effects of the thorax impacting on an interior rigid wall, body-to-body contact and loads induced by the upper torso restraint. The object of this study was to investigate parametric factors, such as the restraint system geometry, occupant size and their influence on injury potential. To this end computer simulations of these test conditions and configurations have been performed using the crash simulation software MADYMO to compare with the results acquired from the sled tests. These MADYMO simulations provided the means to assess the effect of parametric factors. Because injury potential was expressed in terms of injury criteria, emphasis will be placed on comparing these criteria from the test with the criteria deduced from the simulations.

3. TEST PROTOCOL, SETUP AND RESULTS

This section describes the protocol and setup for sled tests A98005, A98006 and A98008 conducted at CAMI in April 1998. The series of tests concerning the side facing rigid seat/wall fixture investigated the injury criteria as measured from a EUROSID-1 Articulated Test Dummy (ATD). The EUROSID-1 provided:

- Thoracic Trauma Index (TTI)
- Rib deflection data for each rib individually
- Pelvis-Y acceleration
- Pubic symphysis force
- Lateral abdominal force

The test setup represented a three place side facing sofa with a rigid wall at the forward end as shown in Fig. 1. The sofa had vinyl covered foam cushions and provisions for installing lap belts with a shoulder strap restraints at various anchor point locations.
For the tests presented in this report, the restraint anchor locations were considered typical of contemporary installations. The inertia reel was mounted on the top of the seat back near the left (or forward) shoulder of the ATD. The vertical wall at the end of the sofa is constructed with an approximately 13 mm thick aluminium plate supported by a steel triangular structure. Thus, the seat/wall representation can be considered completely rigid.

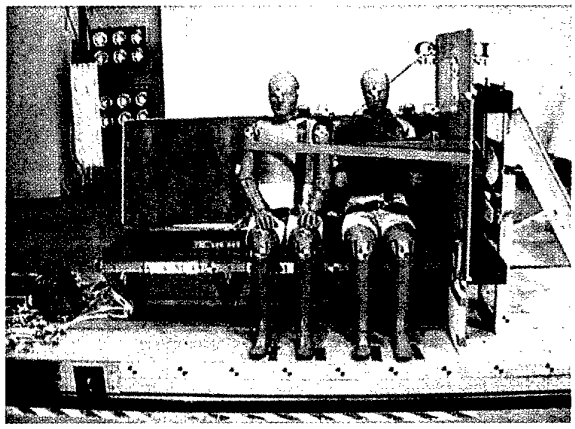

Fig 1: General test setup.

The orientation of the sofa was aligned with the sled, i.e., there will be no yaw component in the impact vector relative to the longitudinal axis of the sofa. The crash pulse, as prescribed by FAR, is defined by having an initial velocity of 13.4 m/s, with a triangular deceleration pulse of 16 g peak at 0.090 s.

All simulations were carried out up to 350 ms, which was beyond the influence of the crash pulse and was assumed to be long enough to contain the principal signals for the various dynamic variables.

Papers presented at the RTO HFM Specialists' Meeting on "Models for Aircrew Safety Assessment: Uses, Limitations and Requirements", held in Ohio, USA, 26-28 October 1998, and published in RTO MP-20.

3.1 Dummies

EUROSID-1. The European Side Impact Dummy (EUROSID-1) is specially designed for the evaluation of occupant safety in lateral impact and represents a 50th percentile adult male[1,2]. Sitting height of the dummy is 0.90 m and it's total body mass 72 Kg. The thorax consists of three separate, identical ribs. The following instrumentation is implemented in theEUROSID-1:

- *Head*
  A triaxial accelerometer
- *Chest*
  A displacement transducer on each rib
  A uniaxial accelerometer on each rib
  A triaxial accelerometer at the top and bottom of the thoracic spine
- *Abdomen*
  Three load transducers
- *Pelvis*
  A triaxial accelerometer in the sacrum block
  A load cell at the location of the pubic symphysis

Hybrid-II. One of the tests presented in this report, A98008, included a 50th percentile Hybrid-II ATD placed beside the EUROSID-1. This test condition was performed to investigate the effects of occupant-to-occupant contact. For the purpose of these tests the Hybrid-II was considered to account for its mass interaction with the EUROSID-1, and therefore it was not equipped with any instrumentation. The Hybrid-II had the same restraint provisions as the EUROSID-1.

3.2 Tests

Test A98005. The EUROSID-1 ATD was placed near a padded wall as shown in Fig. 2. The one inch thick padding was IV-3 foam, similar to Ensolite. The spacing from the ATD's arm to the wall was 15.2 cm. The ATD is supported during the pre-impact acceleration by means of the belt wrapping the upper torso and a break away cotton string supporting the ATD's head.

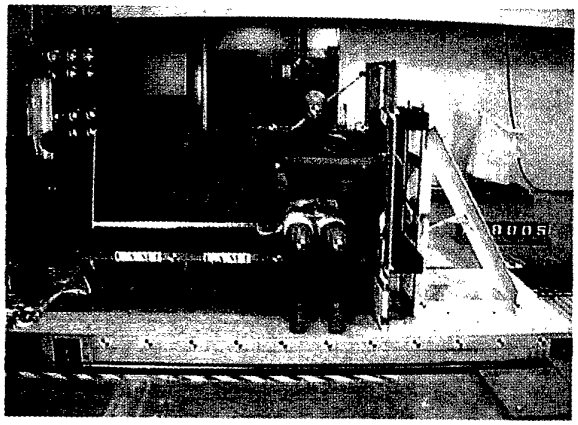

Fig 2: Test setup for test A98005

The measured impact test velocity was 13.6 m/s and the pulse maximum was16.36 g. In Table 1 the peak values of the various signals are listed.

Test 98006. The EUROSID-1 ATD was placed near a unpadded wall as shown in Fig. 3. The other parameters of the test setup are the same as in test A98005.

Test A98008. In this setup there are two dummies as shown in Fig. 4. The Hybrid-II is sitting in the middle seat and the EUROSID-1 in the forward seat. The wall is unpadded. The spacing from the EUROSID's arm to the wall is 5.7 cm. The ATD's were in shoulder to shoulder contact.

The impact velocity was 13.8 m/s and the pulse maximum was 15.95 g. In Table 3 the peak values are listed.

4. MODEL SETUP

The object of simulating these tests in MADYMO was to achieve a basemodel from where a parametric study can be conducted. The following section discusses the methods that where used to model the simulations[3,4].

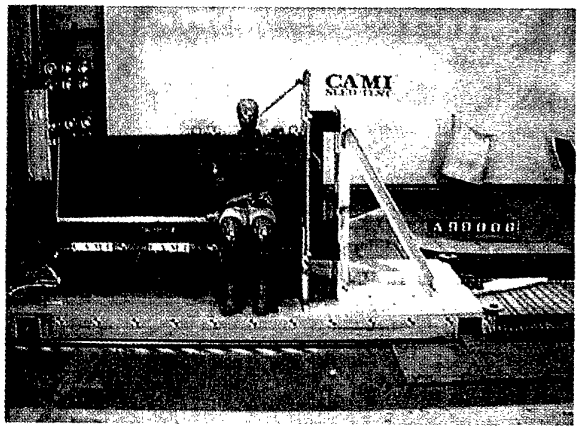

Fig 3: Test setup for test A98006

The impact velocity was 13.7 m/s and the pulse maximum was 16.64 g. In Table 2 the peak values are listed.

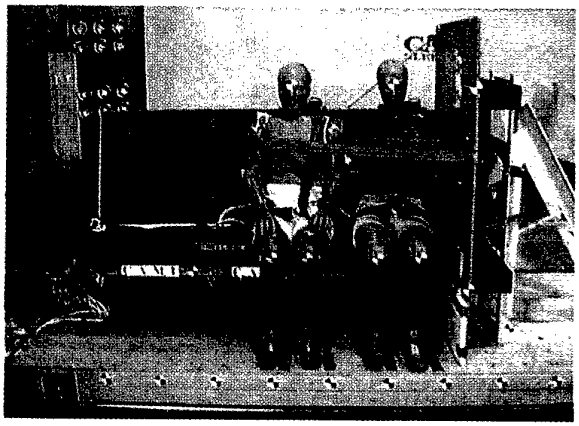

Fig 4: Test setup for test 98008

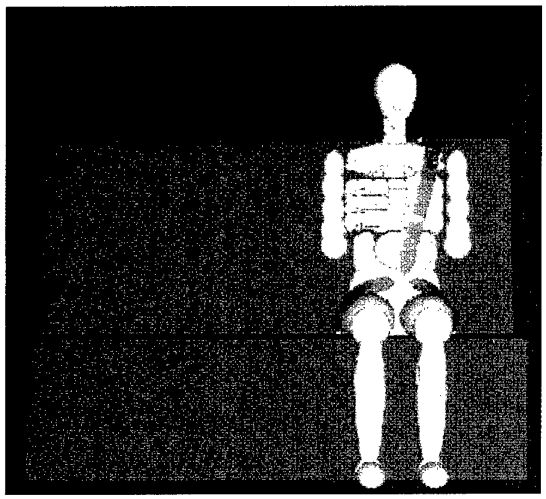

Fig 5: The MADYMO model

The bench seat and back were modelled as planes, see Fig. 5. The seat properties such as force deflection curve and static friction coefficient between seat and ATD were taken from experimental data supplied by CAMI. For the wall-dummy contact in simulation A98006 and A98008 only the contact characteristic of the dummy is regarded, thus assuming the wall completely rigid. The Hybrid-II dummy and the EUROSID-1 dummy were represented by the standard databases provided with MADYMO 5.3.

The belt and retractor properties were provided by the manufacturer: SHROTH Safety Product Gmbh. The belt was modelled as a combination of three conventional belt segments and three finite element belt segments. The finite element parts represent the shoulder belt and the lap belt on the left- and right hand side that are in contact with the dummy. Each of these parts are connected with a truss element support to the buckle. The three rigid body parts extend from the finite element belts and provide the coupling with the retractor and anchor points.

The simulation were carried out up to 250 ms. The actual pulse as recorded from each sled test individually was given as an input for the corresponding simulation.

4.1 Simulation A98005

This simulation describes the single EUROSID-1 with padded wall. The plots of these signals are included in the Annex. The computed peak values are listed in Table 1.

Table 1: Comparison test and simulation A98005

Injury parameter	Test	Simulation	Unit
Upper rib acc.	738	901	m/s^2
Lower rib acc.	706	989	m/s^2
Lower spine acc.	569	624	m/s^2
TTI	69	82	m/s^2
Pelvis-Y acc.	1030	983	m/s^2
Upper rib defl.	45.0	41	mm
Middle rib defl.	39.9	37	mm
Lower rib defl.	36.8	34	mm
Abdomen force	1361	1305	N
Pubic force	4780	4244	N

Note that because this EUROSID-1 database has no pubic load cell included*, the pubic force can not be directly assessed.
One can however approximate the pubic force by assuming that a linear relationship between the pelvis-Y acceleration and pubic force exists[1]. The accuracy of this approximation (and the constant, usually set on 4.5) can be determined by comparing the pubic force and pelvis-Y acceleration from the actual test. For this purpose each simulation has a plot subtitled *Pubic force Approximation* included in the Annex. A second plot compares the Pubic force with the Pelvis-Y acceleration from the simulation.

4.2 Simulation A98006

This simulation describes the single EUROSID-1 with unpadded wall. The results are listed in Table 2. The plots of these signals are include in the Annex.

Table 2: Comparison test and simulation A98006

Injury parameter	Test	Simulation	Unit
Upper rib acc.	1158	1232	m/s^2
Lower rib acc.	1040	1105	m/s^2
Lower spine acc.	608	642	m/s^2
TTI	90	99	m/s^2
Pelvis-Y acc.	1472	1400	m/s^2
Upper rib defl.	50.2	44	mm
Middle rib defl.	39.7	39	mm
Lower rib defl.	36.5	35	mm
Abdomen force	1580	1578	N
Pubic force	6726	6580	N

4.3 Simulation A98008

This simulation describes the EUROSID-1 and Hybrid-II with the unpadded wall moved closer to the ATD's. The results are listed in Table 3. The plots of these signals are include in the Annex.

* The next version of the EUROSID-1 database has a pubic load cell included. However this version was not yet available for these tests.

Table 3: Comparison test and simulation A98008

Injury parameter	Test	Simulation	Unit
Upper rib acc.	451	520	m/s^2
Lower rib acc.	461	531	m/s^2
Lower spine acc.	471	488	m/s^2
TTI	48	52	m/s^2
Pelvis-Y acc.	743	733	m/s^2
Upper rib defl.	59.0	46	mm
Middle rib defl.	46.2	43	mm
Lower rib defl.	40.9	41	mm
Abdomen force	1484	1454	N
Pubic force	3667	3657	N

5. DISCUSSION AND CONCLUSIONS

One of the primary objectives of this study was to establish a baseline mathematical model for design and optimization studies for improvement of side facing sofas in small business aircraft. For this purpose the EUROSID-1 dummy, which is developed for implementation in vehicle side impact crashes, has been tested in three different aircraft crash conditions. It appeared that this dummy quite well could be used for these conditions. Differences between the "vehicle crash condition" and the selected "aircraft crash" condition are in particular: the seating position (more straight-up in the aircraft condition), the pulse duration (almost twice as long in the aircraft condition) and the arm position (forward in the vehicle crash condition and along the thorax in the aircraft condition). In spite of these differences it appeared that the EUROSID-1 model, which mainly up to now has been validated in typical vehicle crash conditions, performed quite well in the selected aircraft crash conditions.

Most of the peak model results, but also the general shape of the time history, appear to be predicted quite realistically. The rib accelerations from the model all appear to be slightly overestimated. Further the unloading phase of the rib deflections shows large deviations in the single dummy tests. The thoracic deflection based injury criterion is solely based on the maximum deflection so it is not affected by the unloading phase[3].

Both the model and the test show the benefit of the introduction of padding: most of the injury parameters decrease after introduction of padding material (compare Table 1 with padding and Table 2 without padding).

The EUROSID-1 model used in this study (MADYMO version 5.3) is a so-called rigid-body database. More recently a more advanced database has been developed using partly flexible bodies. This database showed improved correlation in automotive applications. Also in the aircraft safety environment studied here a further improvement of the accuracy of the model predictions can be expected.

6. REFERENCES

[1] TNO Road-vehicles Institute, 'MADYMO database manual version 5.3', TNO 1997.

[2] TNO Road-vehicles Institute, 'EUROSID-1 users manual', TNO 1994.

[3] A.M.G.L. Teulings, V. Gowdy, B. Aljundi, J.S.H.M. Wismans, 'MADYMO validation of side facing sofa sled tests' (WFW 98.029), TUE 1998.

[4] T. Shams, Y.M. Zhao, N. Rangarajan, 'Safety of side facing seats in general aviation aircraft' (951164), SAE 1995.

[5] TNO Road-vehicles Institute, 'Dummy Newsletter No. 6', TNO May 1995.

A. ANNEX

Test simulation plots A98005.

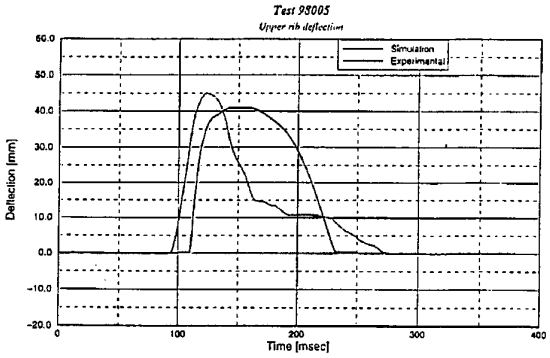

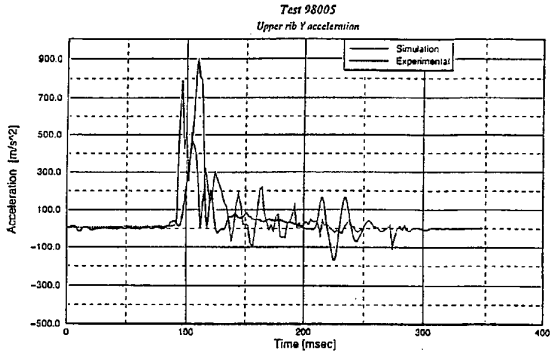

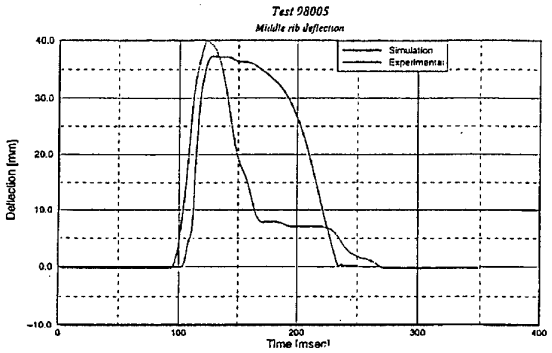

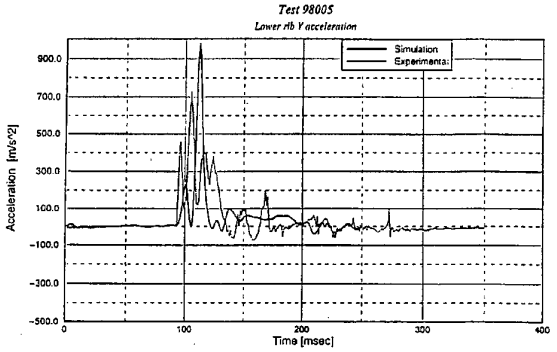

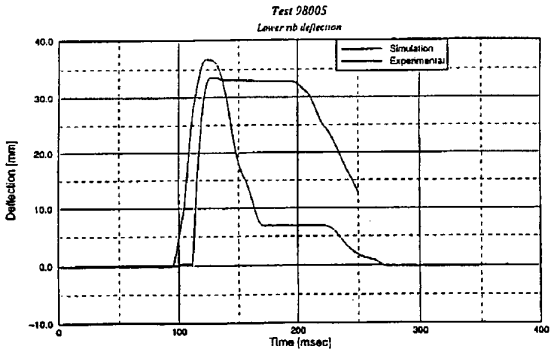

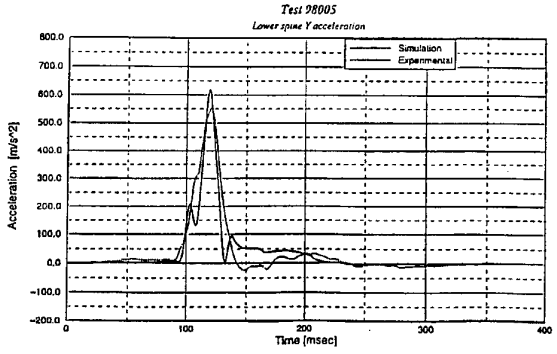

Test 98005

Pelvis-Y acceleration

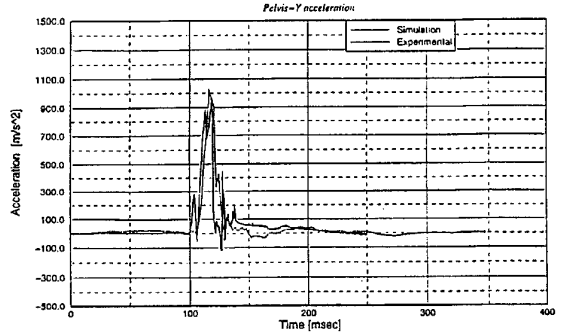

Test 98006

Upper rib deflection

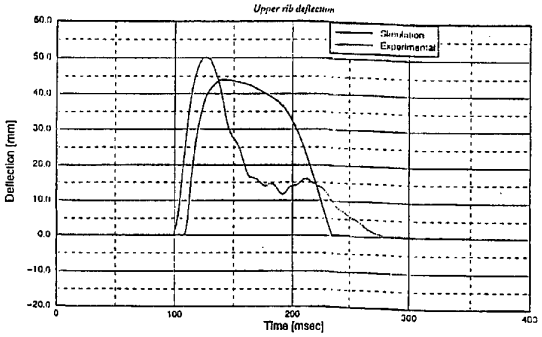

Test 98005

Pubic Force Approximation

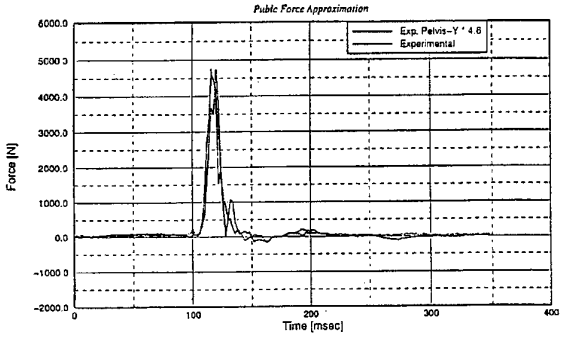

Test 98006

Middle rib deflection

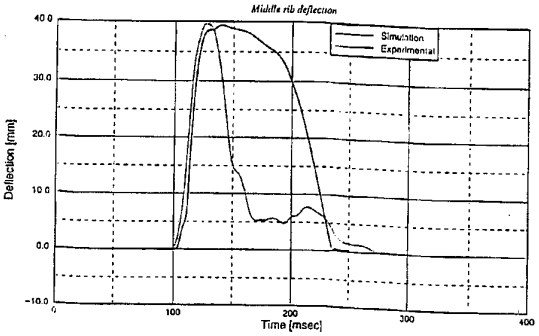

Test 98005

Pubic Force Approximation

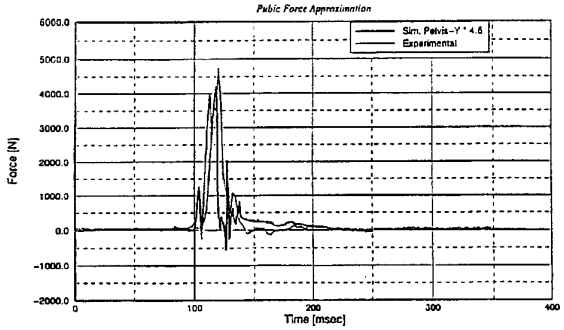

Test 98006

Lower rib deflection

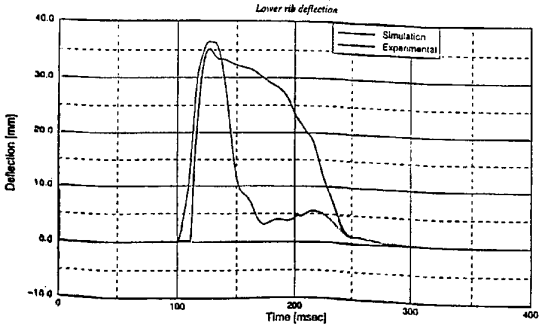

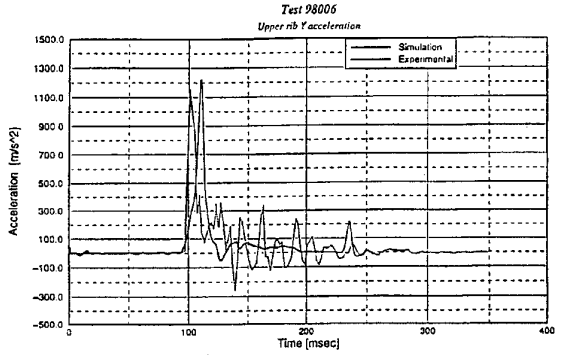
Test 98006
Upper rib Y acceleration
Simulation
Experimental
Acceleration [m/s^2]
Time [msec]

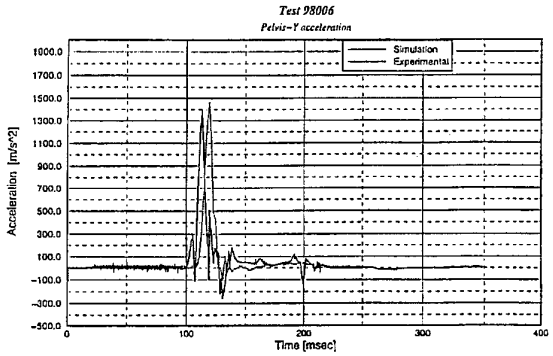
Test 98006
Pelvis-Y acceleration
Simulation
Experimental
Acceleration [m/s^2]
Time [msec]

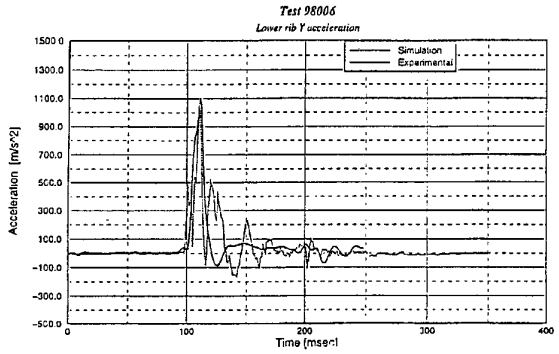
Test 98006
Lower rib Y acceleration
Simulation
Experimental
Acceleration [m/s^2]
Time [msec]

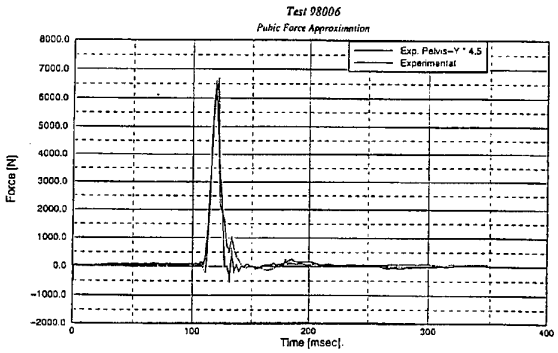
Test 98006
Pubic Force Approximation
Exp. Pelvis-Y * 4.5
Experimental
Force [N]
Time [msec]

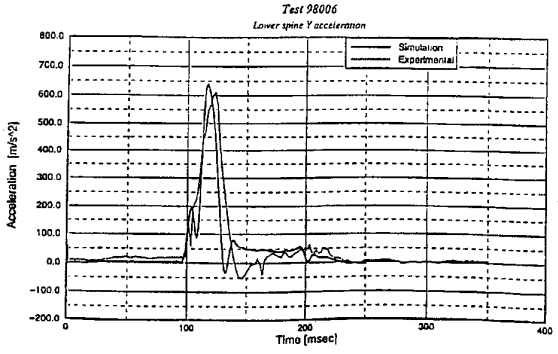
Test 98006
Lower spine Y acceleration
Simulation
Experimental
Acceleration [m/s^2]
Time [msec]

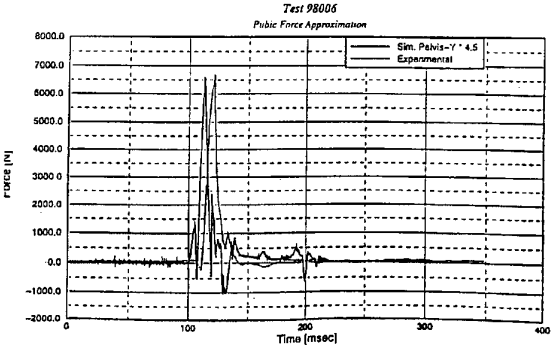
Test 98006
Pubic Force Approximation
Sim. Pelvis-Y * 4.5
Experimental
Force [N]
Time [msec]

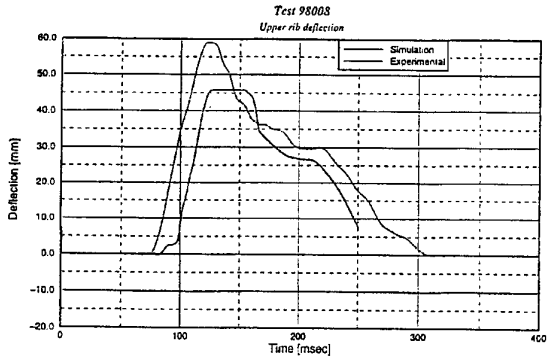
Test 98008
Upper rib deflection
Simulation
Experimental
Deflection [mm]
Time [msec]

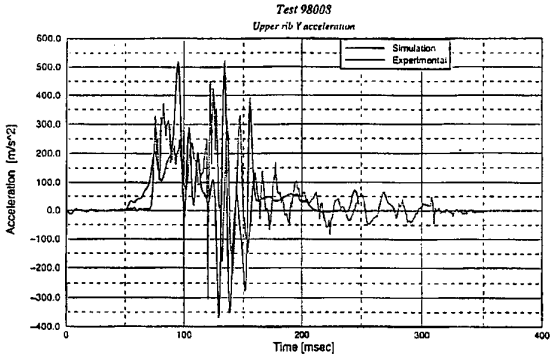
Test 98008
Upper rib Y acceleration
Simulation
Experimental
Acceleration [m/s^2]
Time [msec]

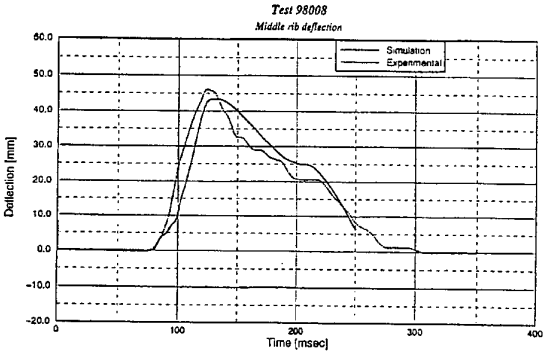
Test 98008
Middle rib deflection
Simulation
Experimental
Deflection [mm]
Time [msec]

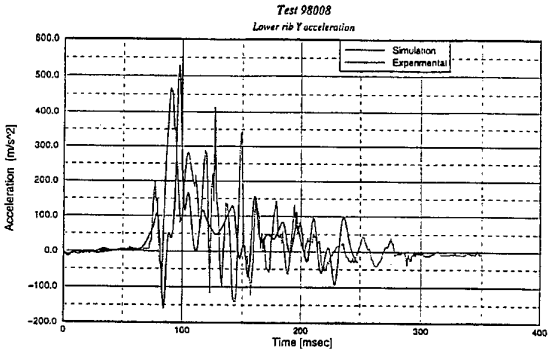
Test 98008
Lower rib Y acceleration
Simulation
Experimental
Acceleration [m/s^2]
Time [msec]

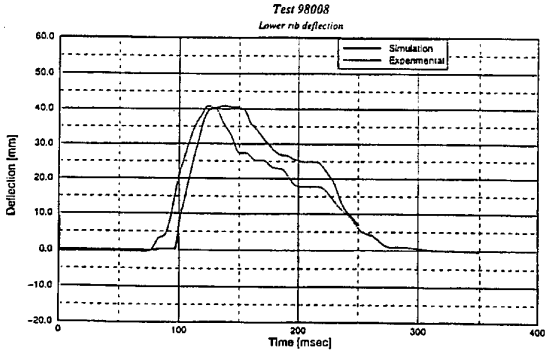
Test 98008
Lower rib deflection
Simulation
Experimental
Deflection [mm]
Time [msec]

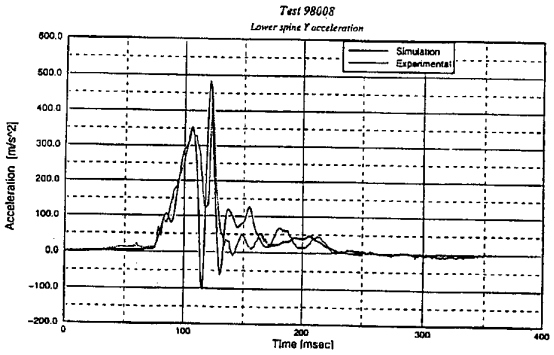
Test 98008
Lower spine Y acceleration
Simulation
Experimental
Acceleration [m/s^2]
Time [msec]

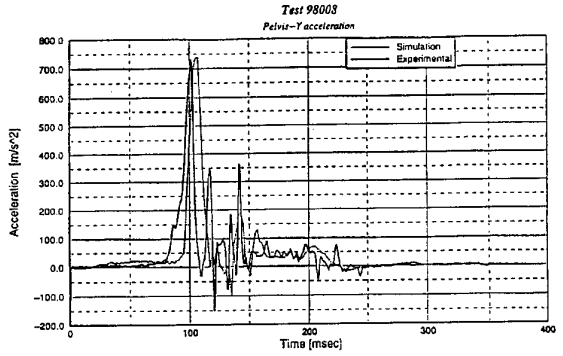
Test 98003
Pelvis-Y acceleration
Simulation
Experimental
Acceleration [m/s^2]
Time [msec]

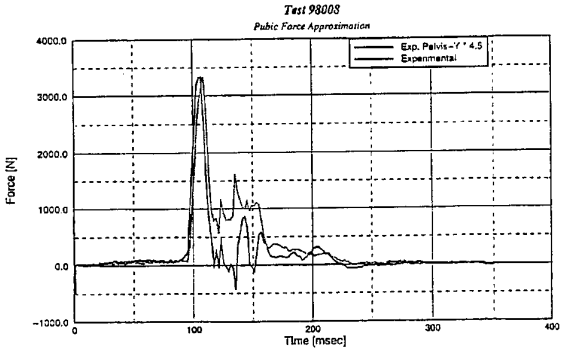
Test 98003
Pubic Force Approximation
Exp. Pelvis-Y * 4.5
Experimental
Force [N]
Time [msec]

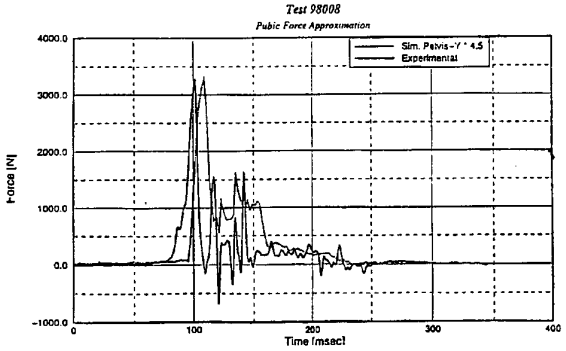
Test 98008
Pubic Force Approximation
Sim. Pelvis-Y * 4.5
Experimental
Force [N]
Time [msec]

Injury Measurements and Criteria

Kennerly H. Digges
The National Crash Analysis Center
The George Washington University
20101 Academic Way
Ashburn, VA 22011, USA

1. SUMMARY

The US Federal Motor Vehicle Safety Standards have established injury measurements intended to insure minimum safety levels in severe crashes. These tests require crash test dummies and associated injury criteria. In the paper, the injury criteria specified in the US Department of Transportation are summarized and the research to support the criteria is cited.

For complete-vehicles tested in frontal crashes, the crash test dummy measures head and thorax acceleration, thorax deflection, and femur loads. The allowable injury measures are: Head Injury Criterion (HIC) of 1000; 60G's of acceleration and 76 millimeters of chest deflection; and 10,000 Newtons of force on the femurs.

A recent addition to the frontal standard has been an instrumented neck and associated injury criteria. The neck injury criteria are: Compression – 4000 N; Tension – 3300 N; Shear – 3100 N; Flexion – 410 Nm; Extension – 125 Nm.

For full-vehicle side-impact tests, the thorax criterion (TTI) is based on rib and spinal acceleration. The allowable values are 85 to 90 G's. The allowable pelvic criterion is 130 G's of acceleration.

2. INTRODUCTION

Automotive safety standards developed by the US Department of Transportation require crash testing of motor vehicles. An essential basis for passing the test is the injury measurements recorded by the crash test dummies.

Safety regulations proposed in the early 1970's required a frontal crash into a rigid barrier at 56 km/hr. The Hybrid II dummy used in the tests was instrumented for measurements at three body regions – head acceleration, chest acceleration and femur load.

In the late 1980's, the Hybrid III dummy was phased into the frontal crash safety standards. This dummy provided additional measurements of chest deflection, forces and moments on the neck, and forces and moments on the lower legs.

Also, in the 1980's, the Side Impact Dummy (SID) became available and was phased into the side impact standard. The SID measured accelerations, of the ribs, spine, and pelvis.

The injury measurements allowed in the standards for these dummies are the most widely accepted injury criteria in the United States. The injury levels set by these tolerances do not guarantee that no injury will occur. Rather, the tolerance is set so that there may be a small injury risk of a serious injury - possibly as high as 30%.

Research in biomechanics is continuing to refine human injury criteria. In this paper, the criteria used in the Federal Motor Vehicle Safety Standards are summarized, along with the emerging criteria proposed for future standards.

3. HEAD INJURY

The basis for head injury tolerance is the Wayne State Tolerance Curve, shown in Figure 3.1. The relationship was based on military data published earlier (Eiband, 1959), and on tests of cadaver heads. In the cadaver tests, the foreheads were impacted against rigid and padded surfaces. The linear acceleration of the head was related to whether or not the impact produced fracture of the frontal bone.

The initial head injury criterion published in US standards was applied to a head form used to test vehicle interior surfaces. The criterion was a maximum of 80 G's for not more than 3 milliseconds. The Wayne State Injury Tolerance Curve becomes asymptotic to the pulse duration

Papers presented at the RTO HFM Specialists' Meeting on "Models for Aircrew Safety Assessment: Uses, Limitations and Requirements", held in Ohio, USA, 26-28 October 1998, and published in RTO MP-20.

axis at about 80 G's.

The Gadd Severity Index was a more refined head injury criteria (Gadd, 1966). This index was based on the product of the resultant head acceleration raised to the 2.5 power and the pulse duration. The index was limited to an acceleration pulse similar to that used in the cadaver tests.

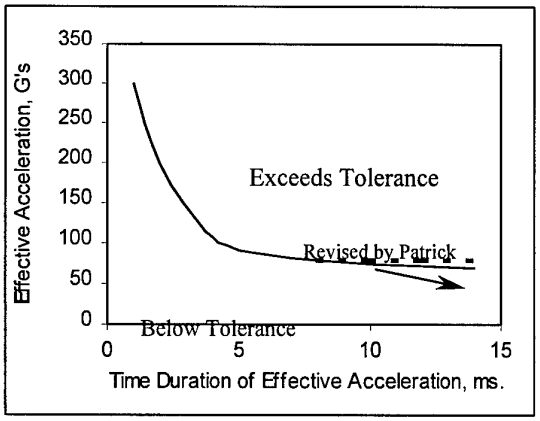

Figure 2.1: The Wayne State Head Injury Tolerance Curve (Initial 15 milliseconds)

The present Head Injury Criterion (HIC) is based on the Gadd Severity Index, modified to accommodate more complex acceleration pulses (Versace, 1971). The HIC is defined, based on the instantaneous head acceleration (A_R) as follows:

$$\mathbf{HIC} = \mathbf{Max}\ t_2,t_1\ [(t_2-t_1)\ [1/(t_2-t_1)\ \int_{t1}^{t2} A_R(t)\ dt]^{2.5}]$$

It should be noted that HIC varies depending on the selection of the time increment over which the integration is performed. Initially, the Federal Motor Vehicle Safety standards required the HIC to be less than 1000 for all magnitudes and locations of time increments. The most recent standards have limited the time increment over which HIC can be calculated to 35 milliseconds.

Mertz reanalyzed the available cadaver test data and concluded that for a HIC value of 1000, the risk of serious injury is less than 20% (Mertz, 1996).

Several limitations of the HIC have been of concern to biomechanics researchers. One concern is that HIC is based on skull fracture, not brain injury. In on-the-road collisions, brain injury may occur without skull fracture. Further, HIC does not include the detrimental effects of rotational acceleration, which has been shown to induce certain types of brain injury. Numerous other head injury criteria have been proposed, but none has been accepted in US safety standards.

4. CHEST INJURY

The chest injury criteria for frontal impacts was initially based on the resultant chest acceleration measured on the Hybrid II dummy. This early dummy did not have the capability of measuring chest deflection. Consequently, acceleration was the preferred tolerance measurement.

In the crash tests, the dummy needed to distinguish the presence of air bags in the vehicle. In cars of the early 1970's, the air bags reduced the chest acceleration substantially, compared with the test condition in which the dummy impacted the steering system and dashboard without safety belts or air bags. Therefore, high precision in the injury criteria was not mandatory for regulatory purposes. The magnitude of chest acceleration allowable for the air bag was based primarily on human volunteer tests. Military tests with harness type belt systems demonstrated that humans could withstand 45 G's for short duration pulses (44 milliseconds) without injury. A human impact with distributed chest loading produced 49 G's without injury (Mertz 1971). The injury tolerance for the air bag standard was set at 60 G's. This was in recognition that the distributed loading of the air bag was more benign than the loading in the human volunteer testing. The standard permitted the chest G's to rise above 60 G's for a period not more than 3 milliseconds.

The 60-G chest acceleration criterion developed for air bags is not conservative for the automotive belt systems of the 1990's. The Hybrid III dummy permits a chest deflection measurement that is intended to more accurately predict injury from a variety of restraint systems.

Initially, the proposed allowable chest deflection for the Hybrid III dummy was 51 millimeters for shoulder belt loading, and 76 millimeters for air bag loading. A regulation effective in the early 1990's required air bags and safety belts for the driver and front outboard passenger of all passenger vehicles. The chest deflection of 76

millimeters is allowed for the air bag only and for the air bag plus safety belts.

A regulatory proposal in 1999 uses a "Combined Thorax Index" (CTI) which includes both chest acceleration and chest deflection. The allowed value of CTI is 1.0. CTI is defined as follows:

$$\mathbf{CTI = (Amax/Aint) + (Dmax/Dint)}$$

Where:
Aint = 85 G's
Dint = 102 mm.
Amax = Maximum measured chest G's
Dmax = Maximum measured chest deflection, mm.

With regard to the US side impact safety standard, the chest injury is based on the combined rib and spinal accelerations, measured on the Side Impact Dummy (SID). The injury tolerance is called Thoracic Trauma Index (TTI). The formula is as follows:

$$\mathbf{TTI(d) = \tfrac{1}{2}\,[G_R + G_{LS}]}$$

Where:
G_R = greater of the peak accelerations of either the upper or lower ribs, expressed in G's.
G_{LS} = the peak lower spinal acceleration in G's.

TTI was based on whole cadaver tests. In the tests, the instrumented cadavers were impacted at various speeds against rigid and padded walls and vehicle interiors. Acceleration measurements of the ribs, thoracic spine, and pelvis were made. The TTI was found to be the best function to separate injuries by severity (Morgan 1986). The standard requires a TTI of 85 to 90. The higher number is the allowable for 2 door cars.

Compression tests of the human chest show a velocity dependent response. Biomechanics researchers have proposed that both compression and rate of compression should be considered in the chest injury criteria. Lau proposed a "Viscous Criterion" based on his analysis of cadaver and animal tests (Lau, 1986). The Viscous Response (V*C) is the product of instantaneous rate of chest deformation (V) and the instantaneous chest compression (C). The chest compression is defined as ratio of the instantaneous chest deflection to the initial chest thickness. The Viscous Response was found to be applicable to chest impacts in the velocity range of 2 to 20 m/s. The proposed Viscous Criterion was: [V*C]max = 1.0 m/s.

A difficulty in using V*C Criterion is the limitation of crash dummies used in existing standards. The SID dummy is can not measure V*C due to limitations in instrumentation and biofidelity. The Hybrid III can measure chest compression and velocity at a central point on the sternum. The biofidelity of the Hybrid III has not been certified for the chest velocity measurement. The V*C Response is frequently computed for research purposes. However, V*C has not been required by US standards.

5. FEMUR INJURY

The Hybrid II and Hybrid III dummies both have load cells in the femur to measure the axial load. The allowable femur load for frontal crashes is based on cadaver tests (Patrick, 1966, and Melvin, 1969, 1975). In most of the tests, a padded or rigid striker impacted the knee, loading the femur axially through the patella and femoral condyles. Based on the cadaver testing, the allowable femur load was specified at 10,000 Newtons.

The femur injury criterion is the only lower limb measure that is used in US motor vehicle safety standards. A principal concern is that it does not adequately address injuries below the knee. These injuries are frequent, costly, and disabling. A number of improvements to the Hybrid III dummy's lower limbs are now available, and associated injury criteria have been proposed for measuring knee, tibia, and ankle injuries.

6. PELVIC INJURY

A pelvic injury criterion is specified in the US side impact standard. The pelvic injury criteria is based on an analysis by Haffner of lateral cadaver tests (Haffner, 1885). The allowable maximum lateral pelvic acceleration is 130 G's.

7. NECK INJURY

The Hybrid III dummy permits a six-axis load cell between bottom of the skull and the top of the neck. The federal standard for frontal air bags (FMVSS 208) specifies criteria for three forces and the fore and aft moments about the neck. The allowable values for axial compression, tension, shear, and bending moments are shown in Table 7.1.

Table 7.1: Allowable Neck Loading in Federal Standard 208

Loading	Allowable
Axial Compression	4000 N
Axial Tension	3300 N
Fore & Aft Shear	3100 N
Flexion Bending Moment	190 Nm
Extension Bending Moment	57 Nm

The basis for the axial compression allowable was the reconstruction of football injuries by Mertz (Mertz, 1978). The allowable tension and shear loads were based on reconstruction of real world collisions by Nyquest (Nyquest, 1980). Tolerance levels for fore and aft bending moments were based on human volunteer and cadaver sled tests reported by Mertz (Mertz 1971).

A proposed revision to FMVSS 208 provides an optional neck injury criteria, Nij. The Nij criteria is defined by the following equation:

$$Nij = (Fz/ Fzc) + (My/ Myc)$$

The values measured on the dummy are Fz, the maximum axial force, and Mz, the maximum flexion/extension moment. The reference values are shown in Table 7.2.

Table 7.2: Reference Values for Calculation Nij

Symbol	Loading	Value
Fzc	Compression	3600 N
Fzc	Tension	3600 N
Myc	Flexion	410 Nm
Myc	Extension	125 Nm

Two allowable values of Nij have been proposed – 1.0 and 1.4 (DOT 1998). In the event the Nij criteria is adopted, the allowable value will be published in the final rule, expected during 1999.

8. CONCLUSIONS

Injury criteria for the head, chest and femur in frontal crashes have been in use for more than 25 years. Improvements and refinements in these criteria are continuing to evolve.

For the side impact, the injury criteria are less mature. The principal US criterion for chest injury uses rib and spinal accelerations. More recent criteria suggest the use of thorax deflection and velocity. The SID dummy is limited to measuring accelerations. A dummy with biofidelity in chest deflection and deflection rate, and with associated measurement capability will be needed to use this criteria.

The discussions in this paper are limited to the injury criteria for a mid-size male. Additional criteria are being proposed for small female and child dummies. In addition, criteria and measurement capabilities for the arms and lower limbs are the subjects of sponsored research by the US Department of Transportation.

9. BIBLIOGRAPHY

Department of Transportation (1998), "Occupant Crash Protection; Proposed Rule", Federal Register, Vol. 63, No. 18, pp. 49978, 1998.

Eiband, A.M., (1959), "Human Tolerance to Rapidly applied Acceleration: a Summary of the Literature", Memorandum 5-19-59E, NASA Lewis Research Center, Cleveland.

Gadd, P.,(1966), "Use of Weighted Injury Criterion for Estimating Injury Hazard", SAE 660793.

Haffner, J. H., Marcus, J. H., and Eppinger, R. H., (1985), "Synthesis of Pelvic Fracture Criteria for Lateral Impact Loading", 10th ESV Conference,.

Lau, I. V., and Viano, D.C., (1986),"The Viscous Criterion – Bases and applications of an Injury severity Index for Soft Tissues", SAE 861882

Melvin, J.W., et.al., (1975), "Impact Response and Tolerance of the Lower Extremities", 19th Stapp Car Crash Conference.

Melvin, J.W., et.al., (1969), Human Head and Knee Tolerance to Localized Impacts", SAE 690477.

Mertz, H. J., (1978), "An Assessment of Compressive Neck Loads Under Injury Producing Conditions", Physicians and Sports Medicine, Vol. 6, No. 11, pp. 95-106.

Mertz, H. J., and Patrick, l. M., (1971), Strength and Response of the Human Neck, SAE 710855.

Mertz, J. H., Prasad, P., and Nusholtz, G., (1996), "Head Injury Risks Assessment for Forehead Impacts", SAE 960099.

Morgan, R. M., Marcus, J. H., and Eppinger, R. H.,

(1986), "Side Impact: The Biofidelity of NHTSA's Proposed ATD and Efficacy of TTI", SAE 861887.

Nyquest, G., et. al., (1980), "Correlation of Field Injuries and GM Hybrid III Dummy Responses for Lap-Shoulder Belt Restraint", Journal of Biomechanical Engineering, Vol. 102, pp. 487-493.

Patrick, L. M., Mertz, H.J., and Kroell, C. K., (1967) , "Cadaver Knee, Cheat, and Head Impact Loads", 11th Stapp Car Crash Conference.

Versace, J., (1971), "A Review of the Severity Index", SAE 710881.

A MODEL OF CARDIOVASCULAR PERFORMANCE DURING SUSTAINED ACCELERATION

C. Walsh[1]
S. Cirovic[2]
W. D. Fraser[3]

1. Department of Mechanical Engineering, Ryerson Polytechnic University, Toronto, Ontario, Canada
2. Institute for Aerospace Studies, University of Toronto, Toronto, Ontario, Canada
3. Defence and Civil Institute of Environmental Medicine, Toronto, Ontario, Canada

DCIEM, Building 54, ALSS
PO Box 2000
1133 Sheppard Avenue West
Toronto, Ontario, Canada
M3M 3B9

ABSTRACT

During aerial combat maneuvers, G_z can cause visual impairment or loss of consciousness (G-LOC). Anti-G suits, positive pressure breathing, and anti-G straining maneuvers reduce the risk of G-LOC. However, complex G-profiles are problematic. To assist in designing G-protective measures for such profiles, we are developing a model of human cardiovascular performance. We present preliminary results from a model that deals with the mechanical aspects of cardiovascular response to G_z. Physiological reflexes are neglected.

We consider a closed loop vascular network with a time varying elastance heart model. Blood flow is modeled by a one-dimensional (1-D) approximation: a pair of first order partial differential equations govern continuity and momentum. The blood pressure is determined by the external pressure and a tube law. The dominant physical phenomenon is wave propagation. The vasculature is modeled as a network of uniform flexible tubes. Valves are placed at the entrances and exits to the ventricles, and in the veins. The equations are solved numerically using a split coefficient matrix method. The algorithm is first order, and it is suited to wave propagation. The boundary conditions are implemented using the method of characteristics.

The results show cardiac output falling as G_z increases and rising again when G_z is reduced. Because there are no physiological reflexes, the central arterial pressure rises and falls with cardiac output, rather than being regulated to its physiological value. G-suit inflation, during periods of high G_z, returns the cardiac output to resting values when both the lower body and abdomen are covered. Protection is significantly reduced if only the lower body is covered. Simulations, in which G_z increases from 1 G to 4 G, are only plausible when there is at least one valve in the inferior vena cava.

1 INTRODUCTION

Rationale

The G_z values generated in aerial combat maneuvers are large enough to modify the blood circulation of the air crew. There is an increase in the hydrostatic pressure difference between the heart and each of the organs, and blood pools in the lower extremities, reducing venous return and cardiac output. Therefore, organs above the heart, particularly the eyes and brain, tend to experience lower blood pressure and lower perfusion. In unprotected individuals G-induced loss of consciousness, G-LOC, results at approximately 4.5 G. Although G-LOC is reversible, and causes no permanent damage in centrifuge experiments [4], when it occurs during combat maneuvers it poses grave risks to the air crew and aircraft [2].

The goal of the current project is to develop a numerical simulation of cardiovascular performance and cerebral perfusion. This simulation will give insights into the mechanisms of G-LOC during complex G-histories, and be of help in the design of advanced air crew life support systems.

Physiological background

For relaxed upright posture, during gradual onset rates of acceleration (GOR) cardiovascular reflexes, which are fully mobilised after approximately 20s [23], provide some protection. Typically, the carotid sinus reflex leads to peripheral vaso-constriction, increased heart rate and increased blood pressure [10], while the venous capacitance is reduced to maintain venous return [18]. As the body's regulatory mechanisms are overwhelmed, visual impairment occurs first [3]. This is because the high intra-ocular pressure makes the eyes more susceptible than the brain to low blood pressure. Thus, the normal sequence of events is peripheral vision loss (gray out) followed by total vision loss (blackout) and finally G-LOC. However, G-LOC can occur without preliminary visual impairment [25]. For GOR, the G-values at which these

Papers presented at the RTO HFM Specialists' Meeting on "Models for Aircrew Safety Assessment: Uses, Limitations and Requirements", held in Ohio, USA, 26-28 October 1998, and published in RTO MP-20.

phenomena occur become independent of time provided the cardiovascular reflexes are established. In contrast, for rapid onset rates (ROR), G-LOC occurs after an interval of approximately 4.2s that is independent of the G-rate or magnitude: cerebral blood flow ceases and the neurological cells must rely on their stored energy reserves.

Vascular networks

We are interested in closed loop vascular networks that incorporate a model of the heart [13, 14, 15, 17, 19, 22, 24]. The essential goal is to simulate cardiovascular performance with a set of material properties and governing equations. These are hyperbolic: the physics of the cardiovascular system is dominated by wave propagation.

The simulations with the greatest physiological detail are generally lumped parameter approximations. However, the lumping process typically leads to a spatial discretisation that is badly suited to wave propagation, and has poor stability characteristics for the parameter values of interest. One-dimensional (1-D) continuum models, in which the network element is a tube, permit difference schemes that can be tailored to the governing equations and boundary conditions [6, 7, 9, 17, 21]. The huge number of vessels present in the microcirculation cannot be modeled in detail. Instead, groups of small vessels in parallel are combined into equivalent tubes.

Approximate governing equations

1-D flow models focus on the bulk transport of blood mass and momentum through the vascular system. The governing equations, which can be derived from integral expressions of mass and momentum conservation, take the form

$$\frac{\partial V}{\partial t} = -\frac{\partial F}{\partial x} + S \tag{1}$$

where

$$V = \begin{pmatrix} A \\ U \end{pmatrix} \tag{2}$$

$$F = \begin{pmatrix} AU \\ U^2/2 + P_t/\rho \end{pmatrix} \tag{3}$$

$$S = \begin{pmatrix} \Psi \\ -\dfrac{8\pi\mu U n_v}{\rho A} - \dfrac{1}{\rho}\dfrac{dP_e}{dx} + g\cos\theta \end{pmatrix} \tag{4}$$

The first component of the vector equation (1) is the continuity equation, the second component is the momentum equation. Here t is time, x axial distance along the tube, A the tube cross-sectional area, U the mean flow speed, $P_t = P - P_e$ the transmural pressure, P the blood pressure, P_e the external pressure on a tube, and ρ the blood density. The source term S comprises: in the continuity equation, a leakage function Ψ; and, in the momentum equation, viscous dissipation, the gradient of external pressure, and the acceleration body force. The blood is assumed to be Newtonian

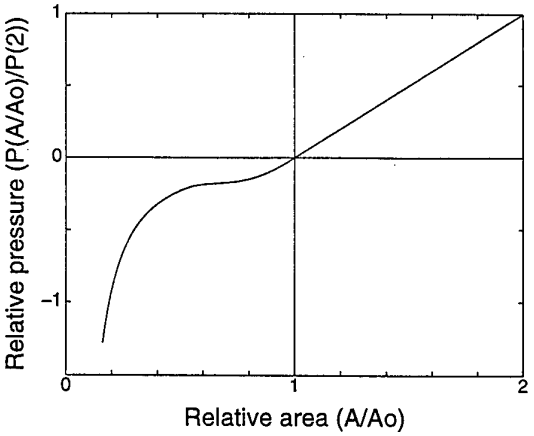

Figure 1: The tube law used by Sheng *et al.* [21].

with viscosity μ, and n_v parallel vessels are combined into one equivalent tube. θ is the angle between the tube axis and the body force.

Equation (1) comprises two equations in the three unknowns A, U, and P_t. A further approximation, called a tube law, expresses P_t as a function of the relative area A/A_0,

$$P_t = \mathcal{P}(A/A_0) \tag{5}$$

Here A_0 is the area of the vessel when P_t is zero. Corresponding expressions give the pressure as a function of volume for the heart chambers. Mathematically, the tube law closes the system of equation. Physically, it defines a long wave speed c as

$$c^2 = \frac{A}{\rho}\frac{\partial \mathcal{P}}{\partial A} \tag{6}$$

Common forms of $\mathcal{P}$ are either purely linear, or a combination of the similarity solution of Flaherty *et al.* [8], for $\mathcal{P} < 0$, with the linear law for $\mathcal{P} > 0$. Numerical algorithms generally demand some degree of differentiability, therefore a number of authors have smoothed the patch area as indicated in Figure 1 [5, 21].

There is a strong analogy with the equations of compressible gas and open channel flows [20], and a number of effective stable algorithms can be found in computational fluid dynamics publications [1, 11, 12]: the method of characteristics [6, 7], flux splitting [9], split coefficient matrix methods [1, section 6-4], and the MacCormack method [17, 21]. Although equation (1) is compact, the vascular geometry is complex and there are many internal boundaries. However, the method of characteristics provides a powerful tool for handling the boundary conditions.

Discussion

In general, there appears to be a strong consensus, amongst both the continuum and the lumped parameter closed loop

studies, regarding cardiac and arterial models. These incorporate a distributed arterial network with sound treatments of the arterial and cardiac mechanics, and of the baroreceptor reflexes [14, 15, 17, 19, 22, 24]. However, there is no such consensus regarding the model of the venous mechanics. The systemic veins may be lumped into a single element [14, 17, 22] or represented as a distributed network [15, 19, 24]. However, if autoregulation is modeled, control of venous compliance is also included [14, 17, 15]. Finally, none of the models cited in this paper includes lower body venous valves.

Objectives

The scope of the current study is limited to treating the mechanical and numerical issues that arise in a cardiovascular simulation. The model will be closed loop with a distributed venous and arterial network, and the simulation will allow G-histories, G-suit inflation, and positive pressure breathing. Given the preliminary nature of the work, no attempt will be made to produce a detailed cardiovascular model. However, the inclusion of anti-G protective measures demands that at least the cerebral, abdominal, and lower body capillary beds be differentiated. The new features introduced in this study are the use of a split coefficient matrix method, and inclusion of lower body vein valves.

2 METHODS

Program overview

The algorithm involves a large number of scalar function calls within nested loops. Problems of this type are most efficiently handled using compiled code. Our simulation is implemented in C. The hierarchy of structures used in the code is illustrated in Figure 2. At the top level is the flight environment, the principal members of which are an air crew list and a list of flight environment variables. Results are presented below for a single air crew member with the G-vector as the only flight environment variable. We propose

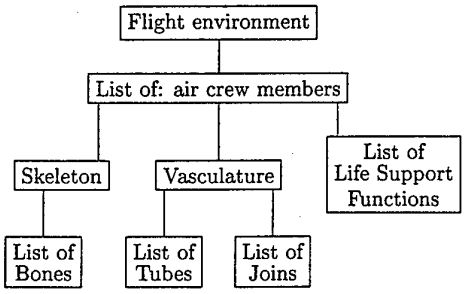

Figure 2: The higher level C structures used in the cardiovascular simulation.

to include cabin pressure as a flight environment variable in a later phase of the study that will deal with a lung model.

Each crew member comprises a vasculature, a skeleton, and a list of life support functions. We can currently simulate G-suit inflation, and the effects of positive pressure breathing on the systemic blood dynamics. Results are presented only for G-suit inflation. The skeleton comprises a list of 'bones': foot, calf, thigh, spine, neck, upper arm, and lower arm. For each of these we specify the rotation from the perpendicular to the floor of the environment, and thus the posture (sitting, standing, lying, etc.) of the crew member. The limbs are symmetrically placed, and results are presented below for the case of standing.

The vasculature is defined by first projecting all blood vessels onto a coronal plane, associating each blood vessel with a bone in the skeleton, and defining the angle between the bone and the vessel in the plane. With this information we calculate the orientation of each vessel in the flight environment, and the component of the G-vector acting along the axis of each vessel. Currently we assume that the G-vectors always lie in the sagittal plane of the crew member, and in the current study all bones are aligned with each other and the G-vector. The mechanical properties of the tubes are stored in the list of tubes, while the list of joins records whether inter-tube junctions have valves or resistances. In addition the tubes are oriented so that they have a beginning and an end, and both lists cross-reference each other: each tube has pointers to the join at its beginning and end; and each join has pointers to all of the tubes attached to it and flags to indicate whether it is the beginning or the end of the tube that is attached.

Physiological approximation

The vascular networks used in this paper are shown in Figure 3, where the circle denotes the left heart, the symbols > denote valves, and the arrows indicate the positive flow direction for each vessel. The line elements are blood vessels connecting the heart to three capillary beds represented in the diagram by the horizontal rectangles and in the model by pure resistances. The right heart and pulmonary circulation have been neglected, and the left heart simplified to a single chamber. These restrictions will be removed once the physiological reflexes are modeled. However, including the pulmonary circulation and all of the heart chambers will introduce no new mechanical problems, while substantially increasing the number of parameters that we need to estimate for the model. Furthermore, cardiac filling is largely passive, so that a plausible simulation can be obtained with no atria, and the principal mechanical determinants of venous return are associated with the systemic veins, which are modeled.

The vertical rectangles to either side of the network indicate two levels of G-suit coverage. The smaller one on the left covers only the lower body, while the larger one covers the lower body and abdomen. Each of the four horizontal

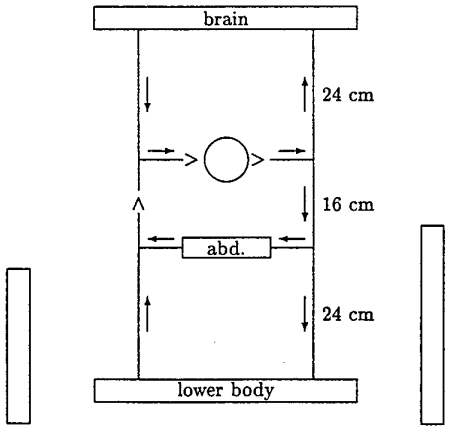

Figure 3: Vascular network

vessels is 8 cm in length. Some results will also be shown for a simpler network with no venous valve and one lower body capillary bed connected to the heart by an aorta and an inferior vena cava, each of length 40 cm. The vessel properties are the adapted from Sheng *et al.* [21].

G-suit

The G-suit model is based on the original Franks Flying Suit [16]: a water-filled garment covering the lower body and abdomen. We assume that, in the area of coverage, the G-suit exerts an external pressure equal to the hydrostatic pressure relative to the heart.

Valve model

All valves are passive. They open instantaneously under a forward pressure gradient, and are closed instantaneously, regardless of the pressure gradient, by back flow. When closed, valves do not leak. The valves have no equations of motion, but enter the governing equations through the tube boundary conditions. When a valve is open it has no effect. When it is closed it isolates the otherwise connected tubes and imposes a zero flow condition at the respective tube ends.

Heart model

The ventricular pressure P_v is defined as:

$$P_v = P_e + E_v(t)(\frac{V_v}{V_0} - 1) \quad (7)$$

$$E_v(t) = E_m + E_a \max(0, \sin(2\pi t/T)) \quad (8)$$

$E_v(t)$ is a variable elastance with period T, V_v is the ventricular volume, and V_0 is the ventricular volume at which $P_v - P_e = 0$.

When the central venous pressure (CVP) is greater than P_v, *i.e.*, during diastole, the mitral valve opens and the ventricle fills passively through a mitral resistor. When P_v is greater than the central arterial pressure (CAP), *i.e.*, during systole, the aortic valve opens and the heart empties actively, with the ejection flow speed determined by a momentum equation. The rate of filling or ejection in turn determines the rate of change of V_v. The heart properties are adapted from Ozawa [17].

Split coefficient matrix method

In the split coefficient matrix (SCM) method we rewrite equation (1) in terms of the Jacobian, A, of the flux vector and $\partial V/\partial x$.

$$\frac{\partial V}{\partial t} = -A\frac{\partial V}{\partial x} + S \quad (9)$$

where

$$A = \frac{\partial F}{\partial V} = \begin{bmatrix} U & A \\ c^2/A & U \end{bmatrix} \quad (10)$$

We can now diagonalise A using its eigenvalues $U \pm c$ and the array L of left eigenvectors, and split A into additive components $A_\pm$ that are associated with signals propagating in the positive and negative directions along the tube axis, [1, section 6-4].

$$L = \begin{bmatrix} c/A & 1 \\ -c/A & 1 \end{bmatrix} \quad (11)$$

$$A = L^{-1}\begin{bmatrix} U+c & 0 \\ 0 & U-c \end{bmatrix} L \quad (12)$$

and

$$A = A_+ + A_- \quad (13)$$

For supercritical flow, *i.e.*, $|U| > c$, one of the arrays $A_\pm$ will be zero the other will be equal to A. For subcritical flow, *i.e.*, $|U| < c$,

$$A_\pm = \frac{1}{2}(U \pm c)\begin{bmatrix} 1 & \pm A/c \\ \pm c/A & 1 \end{bmatrix} \quad (14)$$

For the discrete problem we use the notation V_i^n, where the superscript indicates the time level and the subscript the node number. $t^{n+1} = t^n + \Delta t$, where the time step Δt is the same for all tubes. On any tube the nodes are numbered sequentially with $x_{i+1} = x_i + \Delta x$, where the the space step Δx is constant on any tube, but can vary from tube to tube. We use a forward time difference, a backward spatial difference for the A_+ term, and a forward spatial difference for the A_- term. The difference equation is then

$$\frac{V_i^{n+1} - V_i^n}{\Delta t} = \begin{array}{l} -A_+\left(\frac{V_i^n - V_{i-1}^n}{\Delta x}\right) \\ -A_-\left(\frac{V_{i+1}^n - V_i^n}{\Delta x}\right) \\ +S_i^n \end{array} \quad (15)$$

Consistency, stability and convergence

The consistency of the discrete equation (15) with equation (1) is apparent from the very simple form of the difference expressions. On proving consistency by using Taylor series expansions of the differences, the truncation error is seen to be first order. A von Neuman stability analysis [11, Chapter 8] shows that the linearised form of equation (15) is stable provided the Courant-Friedrich-Lewy (CFL) condition is satisfied:

$$\frac{|c \pm U|\Delta t}{\Delta x} <= 1 \qquad (16)$$

Thus, we expect that the nonlinear equation (15) will be stable if the boundary conditions are treated correctly.

Initial conditions

The initial state for each simulation is $U_i^0 = 0$ everywhere with A_i^0 determined as follows: at arterial and venous roots, let the blood pressure be the anticipated mean blood pressure for that location; establish separate hydrostatic equilibria for the veins and arteries branching from their respective roots; use the tube laws to calculate the corresponding A_i^0; and assign volumes to each of the heart chambers. This leads to a pressure discontinuity at the capillary bed. This is desirable since the capillary flow begins immediately, reducing venous return artifacts during the first beat of the simulation.

Boundary conditions

The boundary conditions are applied using the method of characteristics following Hirsch [12, Chapter 19]. The principal boundary types are two-tube and multi-tube boundaries. All two-tube boundaries allow discontinuity of material and flow properties at the boundary and may include a boundary resistor and a valve. Two tube boundaries occur: at the heart; at the boundaries between tubes used to represent a larger vessel with varying properties; at the location of venous valves; and at the capillary bed in coarse vascular networks where we do not wish to treat the details of the vessels supplying the micro-circulation. Neither valves nor resistors can occur at multi-tube boundaries which represent arterial branching or venous convergence. Currently, we do not incorporate separation losses at any of the boundaries. Such losses can be modeled following Cancelli and Pedley [5] at sudden expansions, and Wolf [26] at branches.

Only the venous valve boundary is described for the case of subcritical flow. This case is illustrated in Figure 4. We assume that two tubes join at a valve with the positive direction for each tube going from left to right. The subscript $_l$ denotes valve boundary quantities from the left tube, and subscript $_r$ quantities from the right tube. Following Hirsch [12, section 16-4], we can define characteristic variables $w_\pm$ that are governed by first order ordinary differential equations (ODE) on characteristic paths $C_\pm$ as:

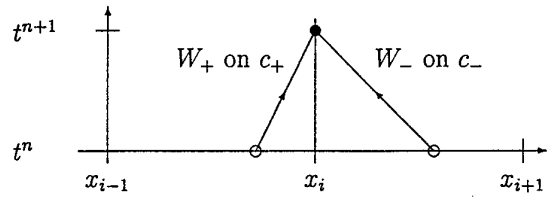

Figure 4: The method of characteristics applied at a subcritical boundary at $x = x_i$.

$$w_\pm = U \pm \int \frac{c}{A} dA = U \pm \mathcal{U}(A) \qquad (17)$$

with $C_\pm$ defined by

$$\frac{dx}{dt} = U \pm c \qquad (18)$$

Thus, a pair of characteristic paths meet at the valve at time t^{n+1}, with w_+ propagating from the left tube along C_+, and w_- propagating from the right tube along C_-. To first order the paths are straight lines, and we can use linear interpolation to determine the $w_\pm$ at time t^n, and then solve the governing ODE's to obtain estimates of the $w_\pm$ at time t^{n+1}. Now, using the two estimates for $w_\pm$, flow continuity and a momentum equation, we can solve for the values of A_l, U_l, A_r, and U_r. When the valve is open we have

$$\begin{aligned} U_l + \mathcal{U}(A_l) - w_+ &= 0 \\ U_r - \mathcal{U}(A_r) - w_- &= 0 \\ A_l U_l - A_r U_r &= 0 \\ P_l + \rho\frac{U_l^2}{2} - P_r - \rho\frac{U_r^2}{2} - U_l A_l R &= 0 \end{aligned} \qquad (19)$$

where R is a resistance to flow at the tube boundary. When the valve is closed we have

$$\begin{aligned} U_l &= 0 \\ \mathcal{U}(A_l) - w_+ &= 0 \\ U_r &= 0 \\ \mathcal{U}(A_r) + w_- &= 0 \end{aligned} \qquad (20)$$

In general these equations are nonlinear and cannot be solved analytically. Fortunately, the values of the unknowns at time t^n provide an excellent approximation to the values sought at t^{n+1}, and Newton's method converges very quickly.

Mass conservation

The SCM method does not enforce exact mass conservation, and numerical errors change the total blood volume. In this closed loop simulation, such errors lead to spurious changes in the blood pressure. Therefore, at each time step, when V_i^n and V_i^{n+1} are both still available, we adjust the volume

of each tube by estimating the error in the continuity equation using centred time and space differences. With this procedure the total blood volume varies by less than 0.005% during 16 cardiac cycles.

Model restrictions

Two simplifications have been made to reduce the computational costs associated with applying the method of characteristics at the boundaries: the vessel tube laws are assumed to be linear, corresponding to distended vessels, and the case of supercritical flow, *i.e.*, blood flow speed greater than the wave speed is not handled. The principal consequence of these restrictions is that the description of flow in the highly collapsed veins above the heart will be poor. Consequently, the mechanism for the action of positive pressure breathing cannot be effectively examined in the current study.

3 RESULTS

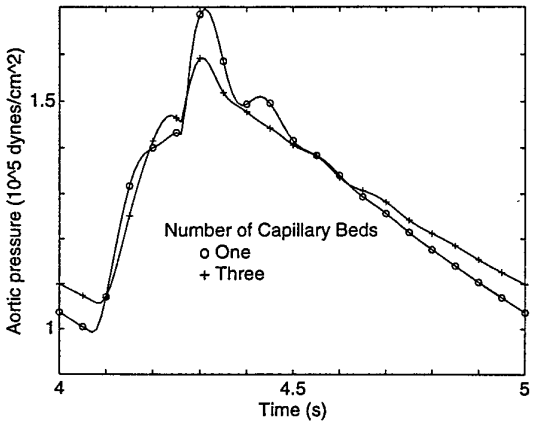

Figure 5: The effect of network complexity.

The aortic pressure is shown in Figure 5 during the fifth beat for the networks with one and three capillary beds. The principal difference between these results is the presence of large reflected waves in the one bed case. These are due to poor termination of the aorta, and are substantially reduced in the three bed case.

The G-history illustrated in Figure 6, where G_z=1.3 G for $5.5 \leq t \leq 11$, was applied to the one bed network, and the resulting ventricular volume history is shown in Figure 7. As expected, we see a drop in cardiac output during the period of elevated G_z. However, the magnitude of the drop is unreasonably large for such a small increase in G_z. It appears that the lower body veins defined by Sheng *et al.* [21] may be too compliant. Numerical experiments suggest that the vein stiffness in the lower body should be comparable with the arterial stiffness in order that the cardiac response

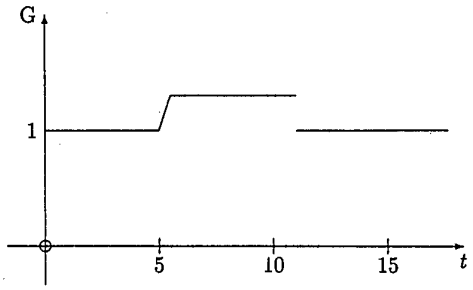

Figure 6: G-history, no G-suit inflation.

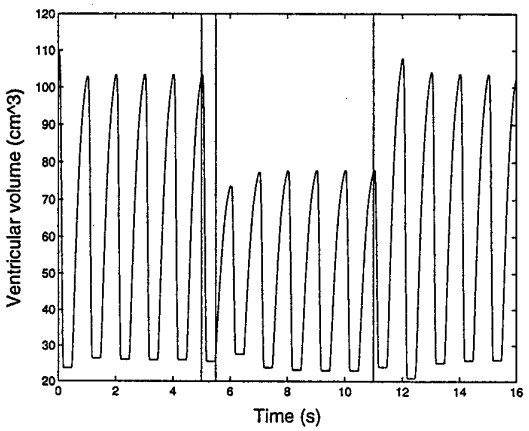

Figure 7: Ventricular volume for the one bed network subjected to the G-history in Figure 6.

to G be reasonable. The G-profiles in Figures 6 and 8 both involve discontinuities, and in neither case was there any numerical difficulty, suggesting that the algorithm is robust.

The G-history illustrated in Figure 8, where $G_z = 4\,\mathrm{G}$ for $5.5 \leq t$, and the G-suit is inflated at $t = 11$, was applied to the three bed network with the lower body vein stiffnesses raised to arterial levels. The resulting CAP and CVP are shown in Figure 9. In performing the simulation it was apparent that a valve was needed in the inferior vena cava to prevent high speed back flow in that vessel. With the valve present a reasonable simulation was obtained with a large drop in CAP and also cardiac output. Note that in a real cardiovascular system the baroreceptor reflexes would quickly act to return CAP to the normal range. Here we see that inflating the G-suit raises the CAP, and that the suit covering the lower body and abdomen is markedly superior to the one that covers only the lower body.

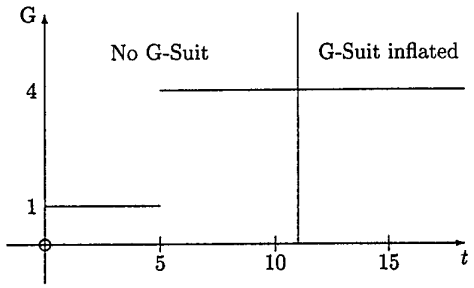

Figure 8: G-history, with G-Suit inflation.

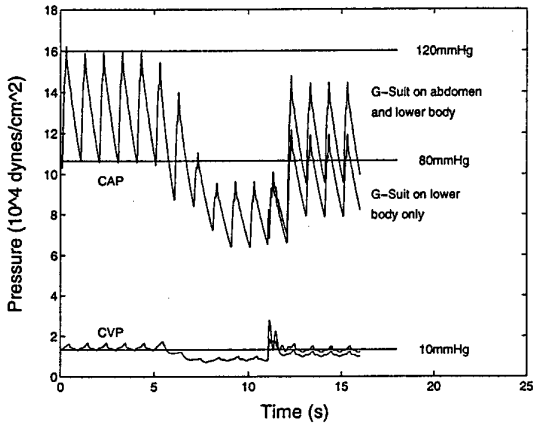

Figure 9: CAP and CVP for the three bed network subjected to the G-history of Figure 8.

4 CONCLUSIONS

The SCM method with a method of characteristics boundary treatment provides a robust and effective algorithm for cardiovascular simulations. At higher values of $G_z$it appears that at least one valve is needed in the inferior vena cava to maintain physiologically reasonable behaviour, and that the commonly used vessel material models are too compliant for the lower body veins. It is possible that the distended vessels have moved to a much stiffer operating point on the nonlinear vein response, or that the stiffness of the lower body vessels is dominated by the surrounding muscles and not their own properties. Both of these possibilities suggest that direct determination of *in vivo* vein tube laws should be made over the physiological range of transmural pressures.

When a G-suit is inflated during high $G_z$it markedly improves cardiovascular performance, and coverage of both the abdomen and lower body produces much better results than coverage of only the lower body.

5 ACKNOWLEDGEMENTS

This work has been generously supported by the Canadian Department of National Defence. DCIEM Research Paper No. 98-P-XX

6 REFERENCES

[1] Anderson, D. A., J. C. Tannehill, and R. H. Pletcher (1984). *Computational Fluid Mechanics and Heat Transfer.* Hemisphere.

[2] Banks, R. D., M. L. Brush, and H. L. Wright (1997). Operational implications of push-pull effect. In *The Aerospace Medical Association, 68th. Annual Scientific Meeting, Chicago Illinois.*

[3] Burton, R. R., S. D. Leverett, and E. D. Michaelson (1974). Man at high sustained +Gz acceleration: A review. *Aerospace Medicine 45*(10), 1115–1136.

[4] Cammarota, Jr., J. P. (1994). *A Dynamic Percolation Model of the Central Nervous System Under Acceleration (+Gz) Induced Ischemic/Hypoxic Insult.* Ph. D. thesis, Drexel University.

[5] Cancelli, C. and T. J. Pedley (1985). A separated-flow model for collapsible tube oscillations. *Journal of Fluid Mech. 157*, 375 – 404.

[6] Collins, R. and J. Maccario (1979). Blood flow in the lung. *Journal of Biomechanics 12*, 373–395.

[7] Collins, R. and E. Mateeva (1991). Assessment of physiological requirements for protection of the human cardiovascular system against high sustained gravitational stresses. In *High Altitude and High Acceleration Protection for Military Aircrew*, AGARD Conference Proceedings, 516, pp. 18–1 – 18–12.

[8] Flaherty, J. E., J. B. Keller, and S. I. Rubinow (1972). Post-buckling behaviour of elastic tubes and rings with opposite sides in contact. *SIAM Journal of Applied Mathematics 23*, 446–455.

[9] Gaffie, D., P. Quandieu, P. Liebart, D. Cohen-Zardy, T. Daumas, and A. Guillaume (1991). Circulatory biomechanics effects of accelerations. In *High Altitude and High Acceleration Protection for Military Aircrew*, AGARD Conference Proceedings, 516, pp. 19E–1 – 19E–15.

[10] Gauer, O. H. and G. D. Zuidema (1961). *Gravitational Stress in Aerospace Medicine.* Little, Brown & Co.

[11] Hirsch, C. (1990a). *Numerical Computation of Internal and External Flows*, Volume 1. John Wiley & Sons.

[12] Hirsch, C. (1990b). *Numerical Computation of Internal and External Flows*, Volume 2. John Wiley & Sons.

[13] Hyndman, B. W. (1973). An example of digital computer simulation: Investigation of the human cardiovascular system. In E. Haga, R. D. Brennan, M. Ariet, and J. G. Llaurado (Eds.), *Computer Techniques in Biomedicine and Medicine. Simulation and Modeling, Health Care, and Image Processing*, Chapter 5, pp. 98–120. Philadelphia.: Auerbach.

[14] Jaron, D., T. W. Moore, and C.-L. Chu (1984). A cardiovascular model for studying impairment of cerebral function during +Gz stress. *Aviation, Space, and Environmental Medicine 55*, 24–31.

[15] Moore, T. W., D. Jaron, and P. Vieyres (1992). Mathematical modeling of the cardiovascular system to study acceleration stress. *The Physiologist 35*(1), S180–S181.

[16] Nader, R. (1992). *Canada Firsts*. Toronto: McClelland & Stewart.

[17] Ozawa, E. T. (1996). *A Numerical Model of the Cardiovascular System for Clinical Assessment of the Hemodynamic State*. Ph. D. thesis, Massachusetts Institute of Technology.

[18] Rothe, C. F. (1983). Reflex control of veins and vascular capacitance. *Physiological Reviews 63*(4), 1281–1342.

[19] Samn, S. (1993). A multi-branched model of the cardiovascular system: Application to G-research. Technical Report AL/AO-PC-1993-0034, Armstrong Laboratory (AFMC), Aerospace Medicine Directorate, Clinical Sciences Division, Brooks AFB TX 78235-5117.

[20] Shapiro, A. H. (1977). Steady flow in collapsible tubes. *Journal of Biomechanical Engineering 99*, 126–147.

[21] Sheng, C., S. N. Sarwal, K. C. Watts, and A. E. Marble (1995). Computational simulation of blood flow in human systemic circulation incorperating an external force field. *Med. & Bol. eng. & Comput. 33*, 8–17.

[22] Snyder, M. F., V. C. Rideout, and R. J. Hillestad (1968). Computer modeling of the human systemic arterial tree. *J. Biomech. 1*, 341–353.

[23] Stoll, A. M. (1956). Human tolerance to positive g as determined by the physiological end points. *Aviat. Space Environ. Med. 27*, 356–367.

[24] Sud, V. K., R. S. Srinivasan, J. B. Charles, , and M. W. Bungo (1992). Mathematical modelling of flow distribution in the human cardiovascular system. *Med. Biol. Eng. Comput. 30*, 311–316.

[25] Whinnery, J. E. and R. M. Shaffstall (1979). Incapacitation time for G-induced loss of consciousness. *Aviat. Space Environ. Med. 50*, 83–85.

[26] Wolf, T. (1990). *An Experimental/Theoretical Investigation of Parallel Inhomogeneities in Respiratory Flows*. Ph. D. thesis, Dept. of Mechanical Engineering, Massachusetts Institute of Technology.

APPENDIX 1 VASCULAR DATA

The joins and tube tubes are numbered to identify them, and the positive direction of flow is defined for each tube. Thus, at a join, the the positive direction for each attached tube is either inflow or outflow. At joins involving only two tubes there can be valves or resistors. The resistance values are given in Tables 4 and 5.

Join	Inflow tubes	Outflow tubes	Valve
1	1	2	Yes
2	2	3, 9	No
3	3	4, 7	No
4	4	5	No
5	5, 8	6	No
6	12, 13	11	No
7	7	8	No
8	9	10	No
9	10	12	No
10	6	13	Yes
11	11	1	Yes

Table 1: Join data for the vascular network.

The data for the tubes in Table 2 is adapted from Sheng *et al.* [21]. A_0 is the tube area at zero transmural pressure, and θ is the angle between each tube axis and the G-vector. $E_l = Eh/(2R_0)$ is the elastance, where E is the Young modulus, h is the vessel wall thickness, and $A_0 = \pi R_0^2$. The elastance values for the lower body veins were increased by a factor of 10 from those given by Sheng *et al.* [21] in order to reduce the lower body compliance to maintain some venous return under G. The resistances used in the current model were chosen to establish flow rates in the physiological range.

The G-suit covers the entire lower body upto a designated level below the heart. The two cases considered are given in Table 3.

Tube	Length cm	A_0 cm^2	E_l Pa	θ deg
1	See heart data			
2	8	6.697	0.2219×10^5	90
3	16	3.597	0.2373×10^5	0
4	24	0.999	0.2873×10^5	0
5	24	7.260	0.1436×10^5	180
6	16	7.548	0.1008×10^5	180
7	8	1.498	0.3393×10^5	90
8	8	2.945	0.1077×10^5	90
9	24	2.224	0.2978×10^5	180
10	8	5.100	0.8000×10^5	0
11	8	12.078	0.0200×10^5	90
12	16	5.100	0.0800×10^5	0
13	8	7.548	0.1436×10^5	180

Table 2: Tube data for the network.

Height below heart of G-suit upper edge (cm).
12, covers lower body and abdomen
20, covers lower body only

Table 3: G-suit coverage.

Left Ventricle	
E_{max}	1.89×10^4 Pa
E_{min}	1.20×10^3 Pa
T	1.0 s
V_{lv0}	15 cm^3
$V_{lv}(0)$	110 cm^3

Table 4: Data for the left ventricle.

Blood		
ρ	1.00 gm cm^{-3}	
μ	0.004kg m^{-1} s^{-1}	
Resistances (Pa m^{-3})		
4	5.00×10^8	Lower body resistance
7	6.27×10^8	Abdominal resistance
8	1.28×10^9	Cranial resistance
11	4.00×10^6	Cardiac filling resistance
Miscellaneous		
g	9.8m s^{-2}	
Δt	5×10^{-3} s	
Δx	8 cm	
P_{aI}	80 mm Hg	
P_{vI}	10 mm Hg	

Table 5: Miscellaneous data

KEYWORDS

CARDIOVASCULAR
SIMULATION
ONE-DIMENSIONAL
G-LOC
SPLIT COEFFICIENT MATRIX

DCIEM 98-P-91.

EFFECT OF HIGH +Gz ACCELERATIONS ON THE LEFT VENTRICLE

K. Behdinan,
Department of Mechanical Engineering, Ryerson Polytechnic University
350 Victoria St.
Toronto, Ontario M5B 2K3

B. Tabarrok,
Department of Mechanical Engineering, University of Victoria
Victoria, BC

W. D. Fraser
DCIEM, Toronto, ON, Canada

1 SUMMARY

During certain manoeuvers, fighter pilots are subjected to high accelerations reaching 10g levels. The effect of this acceleration on the left ventricle is most severe when it is directed along the body z axis. Under such accelerations it is difficult for the heart to function and supply the body with blood and further more there is concern that the heart may suffer tissue tear as a result of high stresses on the heart tissue.

In this study a detailed finite element analysis is carried out to determine the stress state of the left ventricle under high Gz loading. To develop the FE model, surface geometry data was acquired from view Point Data Lab in Utah. The surface data for the interior and the exterior of the left ventricle was then used with a software from XYZ Scientific Application Inc. of Livermore to develop a 3D FE model. The model is made up of 3830 solid elements with three layers between the inner and the outer surfaces. Finite element results for deflections, strains and stresses are obtained for a number of acceleration levels. The analysis accounts for geometric nonlinearities and uses the updated Lagrangian method in the MARC finite element program.

2 INTRODUCTION

The ongoing development of high performance aircraft, capable of providing positive accelerations under certain maneuvers, has created substantial research work dealing with physiological reactions affecting a pilot's judgement.

The inertia force acting along the vertical axis of an upright body is denoted as +Gz. Under high +Gz loading conditions, the heart and other organs are displaced downwards and depending upon the level of elevated stresses, can be severely damaged.

Physiological responses to the +Gz acceleration range from less severe temporary loss of peripheral vision to unconsciousness and, in the ultimate case, damage to heart tissue. For safety reasons, there is a need to investigate the effects of +Gz inertia forces on the cardiovascular system (see [1,2,3]).

From experiments conducted in a safe environment using a centrifuge, the average blackout level observed for an unprotected individual is between +3.5 to +4.0 Gz. However, when fitted with an anti-G suit and using straining maneuvers (muscle testing with controlled breathing) a pilot can be exposed to accelerations up to +10Gz for short periods of time [4,5,6]. Over longer periods such high loadings may bring about abnormalities in the electrocardiogram in men [7] as well as sub-endocardial hemorrhaging and pathological changes of the myocardial tissue in animals [8].

Reports of endocardial hemorrhaging and myo-fibrillar degradation in tests with swine (see [8,9]), undergoing sustained +Gz accelerations, raise questions regarding the possibility of cardiac tissue damage in humans subjected to high +Gz loading.

In general, the distribution of stress in the ventricles of the heart depend upon
1)the three dimensional geometry and fibrous architecture of ventricular walls.
2)the boundary conditions imposed by the ventricular cavity and pericardial pressures and structures like the fibrous valve ring skeleton at the base of the ventricles.

Papers presented at the RTO HFM Specialists' Meeting on "Models for Aircrew Safety Assessment: Uses, Limitations and Requirements", held in Ohio, USA, 26-28 October 1998, and published in RTO MP-20.

3)the three dimensional mechanical properties of the myofibrils and the collagen interactions in the relaxed and actively contracting states. Many of these determining factors have been quantified in experimental studies [10,11,12,13,14].

Difficulties in cardiological techniques used during experiments on the human heart provide insufficient data to determine the presence of any localized cardiac damage. Accordingly, the use of computational schemes becomes necessary to obtain estimates of stress levels in the human heart under high +Gz loading conditions.

The simplest models used by some researchers [15,16,17], are made up of regular geometrical shapes such as spheres, ellipsoids, cones or a combination of such geometries (see also [18]). These models do not describe the geometry of the heart adequately. Further, they are almost always used for small deformations.

For the present research, where deformations are expected to be large, it is essential to adopt a more realistic geometric model. The flexibility and power of the finite element method (FEM) to deal with complicated shapes and take account of the effects of material and geometrical nonlinearities makes it an ideal tool for analyzing the stress-strain behavior of the human heart under +Gz acceleration.

3 FINITE ELEMENT MODEL DEVELOPMENT

A model of 60000 points was bought from View Point Data Lab, Utah (see also [28]). This model describes the interior and exterior surfaces of a life size heart of a male.

The data on the coordinates of a large number of points on the exterior and interior surfaces of the heart had to be very extensively processed before a finite element model could be developed. First the proximity of the coordinate points had to be specified. This information was provided through the connectivity of the coordinate points. Thus the coordinates and their connectivity produced polygons on the surface geometries of the heart. To describe the surface geometry semi analytically, for purposes of finite element development, it was necessary to fit specific curves to the coordinate points. This is essentially a Computer Aided Design process. To this end the CAD program TRUE GRID was used for creating multi block stretched FE meshes. The essential idea is to project a block of finite elements in a regular mesh, onto a curved surface.

Making a mesh with TRUE GRID is analogous to sculpting. Pieces of the block mesh are removed so that its topology matches that of the object to be meshed. Portions of the mesh are moved, positioned along curves, projected to surfaces, etc. Interpolation, smoothing, and zoning requirements are used to fine-tune the mesh. Parts created separately are "glued" (merged) together automatically by specifying a tolerance.

Following the above procedure two models of the left ventricle were developed. The first model is comprised of 3300 solid elements (8 nodes) whereas the second model, being far more refined, is made up of 88000 elements. Both models have used three layers of elements through the thickness. The coarser model is small enough to allow computations on a workstation. It was planned to gain experience on the analysis of the coarser model and using this experience to analyse the finer model on a super computer. Typical difficulties encountered include: unacceptable element shapes, errors in node numbering, improper connection of parts etc. much of these errors had to be found and corrected through numerous check runs.
Finite Element Software

3.1 Importing the FEM Model into MARC

Having completed the data processing within the TRUEGRID program [28] it was necessary to import the developed model, with its data files, into the MARC finite element program. Next the objective was to examine the model, from different perspectives, in the MARC program. Figure 1 shows a view of the smaller model.

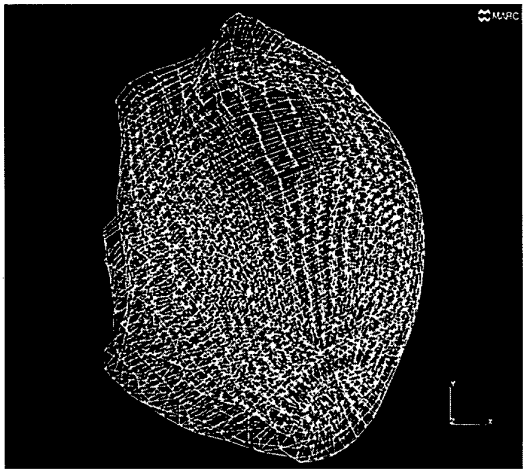

Figure 1: 3300 brick element model viewed in the MARC program.

3.2 Testing the Model within the Frame Work of MARC

Once the model geometry had been verified through a number of check runs in the MARC environment [28], it was necessary to ensure that the material data and boundary conditions were properly registered in MARC. To this end a trial run was carried out under +5Gz acceleration. In this run a linear analysis was carried out where the material density was taken as 9.15×10^{-5} slug/in^{3}and for elastic properties, Hooke's laws were used with $E = 142.8$ psi and $\nu = 0.45$, i.e. a soft nearly incompressible material.

The results obtained are shown in Figures 2 and 3. It is emphasized that this analysis was undertaken merely to ensure that the solution process can be carried out on the 3300 element model.

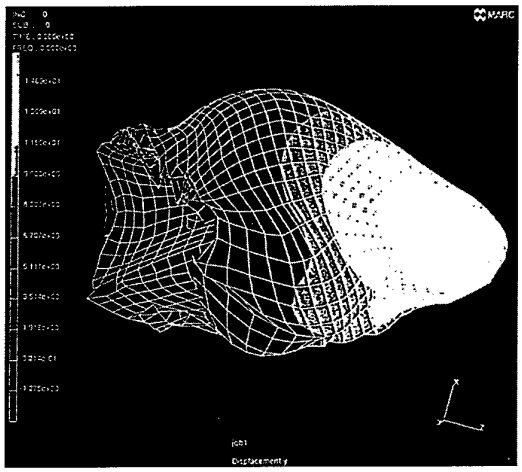

Figure 2: Displacement distribution in the left ventricle, linear check run.

3.3 Biomechanics of The Heart Muscle

The heart consists of two pumps, the right and the left ventricles, connected in series and anatomically intimately linked together into one organ. The right heart maintains blood flow in the systemic circulation. The left heart is by far the stronger of the two heart pumps. It develops a pressure of about 16 kPa which is four to five times the pressure developed by the right heart. Consequently more musculature is developed in the left than the right ventricular myocardium. The initial stages of cardiac disfunction are generally found in the left ventricle.

This study is mainly related to the left ventricular modelling. The mechanical performance of the left ventricle is the result of cooperative contractile action of the muscle cells in the left ventricular wall. Therefore, insight into the mechanics of the left ventricle, at the level of muscle cells, is important for understanding the pumping action of the heart. For that reason, quantifications of local ventricular wall mechanics have been stimulated against the following information:

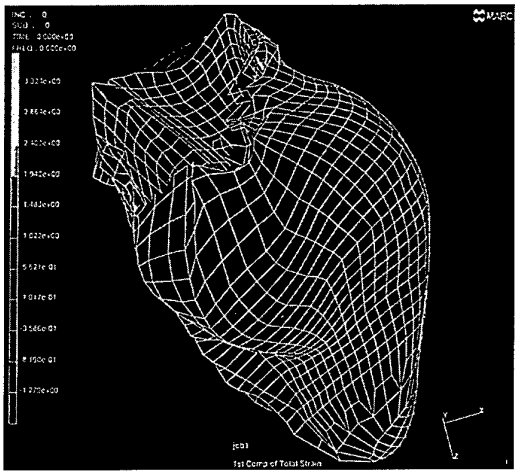

Figure 3: Strain distribution in the left ventricle, linear check run.

1- Myocardial wall stress and deformation are some of the primary determinants of myocardial oxygen consumption.
2- Myocardial oxygen supply is dependent upon coronary blood perfusion, which has a direct dependence upon the mechanical state of the myocardial tissue.
3- Wall deformation is believed to be the feedback signal that governs myocardial growth. For example, ventricular hypertrophy is the result of excessive loading of the heart.
4- Diagnosis of the heart is usually done on the basis of global data of cardiac function. Interpretation of these data in terms of local myocardial disfunction requires a thorough insight into the fundamental mechanisms underlying the ventricular action.

Important quantities for the description of the mechanical state of the left ventricle are the local deformations and stresses. At present, local deformations can be measured accurately only at a limited number of sites in the left ventricular wall. Reliable measurement of left ventricular wall stress is difficult, because insertion of a force transducer damages the tissue.

Here we will present a possible material model for consideration

in the heart muscle biomechanics. First, the main features are sketched for a continuum theory for blood perfused porous medium, largely deformable soft tissue. Next the constitutive law for the myocardial tissue, describing the dependency of stress on tissue deformation, will be addressed.

3.3.1 Continuum Mechanics theory of The Heart Muscle

Heart muscle is a mixture of many different components: muscle fibers, collagen fibers, coronary vessels, coronary blood and interstitial fluid. A rigorous integrated porous medium continuum theory of myocardial deformation and intramyocardial coronary flow has been developed by Huyghe [19]. In this finite deformation mixture theory the differential equations describing the state of the myocardium are derived by means of a formal averaging procedure. The tissue is composed of a solid phase and a spectrum of fluid phases representing the different coronary microcirculatory components.

In this section the major features of the above-mentioned theory will be specified for the simplified situation where the spectrum of fluid phases is condensed into one liquid component, and the transmural pressure differences across blood vessel walls are neglected. This simplification yields considerable computational advantages but retains the salient mechanical aspects of the heart tissue in the resulting so-called deformation model.

3.3.1.1 Equilibrium Equations

The state of stress in the liquid component of the biphasic mixture is described by an intramyocardial pressure p. The stress in the solid is a full 3D stress tensor. The stress in the deformed mixture is best understood as follows. Say the solid phase is subjected to a deformation in the absence of the fluid phase. The stress σ_{ij}^{eff} in the solid induced by this deformation and measured per unit bulk surface area is called the effective stress. The word effective indicates that this part of the stress is the only part depending directly on the deformation. Now we inject a fluid at a pressure p into the deformed solid matrix. The pressure p will effect both the fluid and the solid. So, the total Cauchy stress in the mixture may be written as:

$$\sigma_{ij}^{tot} = \sigma_{ij}^{eff} - p\ \delta_{ij} \qquad i,j = 1,2,3 \tag{1}$$

In the absence of inertia forces, the equilibrium equation of the deformed myocardium may be written as:

$$\sigma_{ij,\ j}^{eff} - p_{,i} = 0 \tag{2}$$

In the above equations we have used the conventional notations in continuum theories.

3.3.1.2 Blood Flow through Porous Myocardium

To simulate the redistribution of coronary blood in the ventricular wall during deformation, the liquid phase is allowed to flow relative to the solid. To generalize the relationship to the porous myocardium, where the pore length is a variable, we use Darcy's law, i.e., the fluid flow is proportional to the local intramyocardial pressure gradient.

Neglecting transmural pressure differences across blood vessel walls, Darcy's law yields the following equation in the Eulerian form:

$$Q_j = -\ K_{ij}\ p_{,i} \tag{3}$$

where Q_j is the Eulerian spatial fluid flow vector and K_{ij} is the permeability tensor with respect to the current configuration. Neglecting the stretching of blood vessels and assuming the ratio of the current and the initial blood volume fractions to be independent of the vessel diameter, the following expression holds for K_{ij}, [20],:

$$K_{ij} = \left(\frac{J-1}{R_{av}} + 1\right)^2 K_{ij}^{o} \tag{4}$$

where K_{ij}^{o} and R_{av} are the permeability and the averaged porosity of the undeformed tissue, respectively, while J is the jacobian of the deformation gradient tensor.

3.3.1.3 Continuity Equation

The cardiac tissue is considered as a mixture of an intrinsically incompressible solid and an incompressible fluid. Consequently any change in the volume of this solid-fluid mixture is equal to the amount of fluid being squeezed out or sucked in. Then, conservation of mass requires:

$$\dot{U}_{i,i} + Q_{i,i} = 0 \tag{5}$$

in which $\dot{U}$ is the material time derivative of the displacement of the solid.

3.3.2 Constitutive Behavior of Myocardial Tissue

The constitutive law for the myocardial tissue is expressed as a relationship between the effective second Piola-Kirchhoff stress tensor S_{IJ}^{eff}, the Green-Lagrange strain tensor E_{IJ} and time t, where:

$$S_{IJ}^{eff} = J\ F_{mI}^{-1}\ \sigma_{ij}^{eff}\ F_{mI} \tag{6}$$

and

$$E_{IJ} = \frac{1}{2}\left(F_{mI}\ F_{mJ} - \delta_{IJ}\right) \tag{7}$$

Here F_{mI} is the deformation gradient tensor.

The effective stress S_{IJ}^{eff} may be written as the sum of a passive stress S_{IJ}^{p} and an active stress S_{IJ}^{a}:

$$S_{IJ}^{eff} = S_{IJ}^{p} + S_{IJ}^{a} \tag{8}$$

3.3.2.1 Passive Constitutive Behavior

The stress tensor S_{IJ}^{p} is split into two components, one resulting from elastic volume change of the myocardial tissue S_{IJ}^{v}, the other from viscoelastic behavior of the myocardial tissue S_{IJ}^{ve}, i.e.:

$$S_{IJ}^{p} = S_{IJ}^{v}\left(E_{IJ}\right) + S_{IJ}^{ve}\left(E_{IJ}, t\right) \tag{9}$$

The elastic stress S_{IJ}^{v}, due to volume change, may be derived from the isotropic strain energy function $\mathcal{W}$ as:

$$S_{IJ}^{v}\left(E_{IJ}\right) = \frac{\partial \mathcal{W}}{\partial E_{IJ}} \quad ; \quad \mathcal{W} = \frac{c_v}{2}\ (J-1)^2 \tag{10}$$

where c_v is the volumetric modulus of the empty solid matrix.

The viscoelastic component S_{IJ}^{ve} is described in a spectral form of quasi-linear viscoelasticity as proposed by Fung, 1993, i.e.:

$$S_{IJ}^{ve}\left(E_{IJ}, t\right) = \int_{-\infty}^{t} H(t-\tau)\frac{d}{d\tau}S_{IJ}^{e}\left(E_{IJ}(\tau)\right)\, d\tau \tag{11}$$

where S_{IJ}^{e} is the anisotropic elastic response of the material. The reduced relaxation function $H(t)$ is a scalar function derived from a continuous relaxation spectrum.

The elastic response S_{IJ}^{e} is generally taken to be orthotropic. The three axes of orthotropy are specified in Figure 4 by the three orthonormal vectors e_1, e_2 and e_3. The vector e_3 is parallel to the initial local fibre direction.

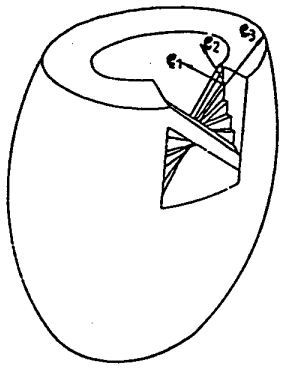

Figure 4: Orthonormal vectors e_1, e_2 and e_3 specifying axes of orthotropy. e_3 is parallel to the initial local fibre orientation. e_1 is perpendicular to the wall.

In this local coordinate system the components of the stress S^e and the Green-Lagrange strain E are written as:

$$S_{IJ}^{e} = e_I \cdot \left(S^e\ e_J\right) \quad ; \quad E_{IJ} = e_I \cdot \left(E\ e_J\right) \tag{12}$$

The passive constitutive behavior is described by a strain energy function $W\left(E_{IJ}\right)$ that relates S_{IJ}^{e} to E_{IJ}:

$$S_{IJ}^{e} = \frac{\partial W}{\partial E_{IJ}} \tag{13}$$

The functional forms of the strain energy function $\mathcal{W}$ (describing volumetric changes) and W are chosen so that:
$\mathcal{W}$ and W are zero in the unstrained state and positive elsewhere.

S_{IJ}^{v} and S_{IJ}^{e} are zero in the undeformed state.

The expression (10) for $\mathcal{W}$ satisfies these conditions.

The most comprehensive expression for $W\left(E_{IJ}\right)$, satisfying the above conditions, has been proposed by Huyghe [21], and is considered as a full orthotropic description of the tissue behavior.

3.3.2.2 Active (Contractile) Constitutive Behavior

Cardiac muscle is striated across the fibre direction. The sarcomere length is the distance between the striations, and may be used as an objective measure of muscle fibre length. In experiments it has been found that active stress, generated by cardiac muscle cells, depends on time, sarcomere length and the velocity of shortening of the sarcomeres (Fung [22]).

The active stress generated by the sarcomeres is directed parallel to the fibre orientation. Consequently the active stress tensor S^a_{IJ} can be written as:

$$S^a = e_3 \cdot \left(S^a\ e_3\right) \tag{14}$$

Since the first Piola-Kirchhoff stress tensor P^a_{IJ} is easily obtainable in experiments, we may use this stress measure instead of the second Piola-Kirchhoff stress S^a_{IJ} and therefore we have:

$$\begin{aligned} P^a &= \left\|F \cdot e_3\right\| S^a \\ &= \frac{l_s}{L_s} S^a \end{aligned} \tag{15}$$

where l_s and L_s are the current and the initial local sarcomere lengths, respectively.

We may write the first Piola-Kirchhoff stress P^a as (see Huyghe [23]):

$$P^a = P^a_o\ A_t\left(t_s\right)\ A_l\left(l_s\right)\ A_v\left(v_s\right) \tag{16}$$

where the constant P^a_o is associated with the load of maximum isometric stress. The factors $A_t\left(t_s\right)$, $A_l\left(l_s\right)$ and $A_v\left(v_s\right)$ represent the time dependency and the length dependency and the velocity dependency, respectively, of the active stress development ($v_s = dl_s/dt$). Figure 5 shows the above relationship. More detail on these coefficients can be found in Huyghe [23].

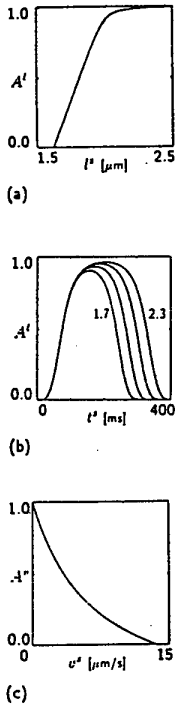

Figure 5: Active material behavior: (a) length dependence of active stress, (b) time dependence of active stress for sarcomere length of 1.7, 1.9, 2.1, and 2.3 μm , (c) stress-velocity relation.

3.4 Sources of Nonlinearities in Finite Element Analysis

Nonlinearities in finite element analysis arise due to
1- significant changes in geometry,
2- nonlinear constitutive relations,
3- contact problems.

For the present project, all three sources of nonlinearity are present. Certainly the geometry of the heart changes significantly under high +Gz loading. The tissue constitutive relations, found experimentally, are nonlinear and under large deformations the heart will contact other parts in the body. However for this study, nonlinear boundary conditions, due to contacts, will be neglected. This is in part due to the fact that the information on the geometry of other parts, in the vicinity of the heart, is not available.

By neglecting the nonlinear boundary conditions the computed results will be on the conservative side, i.e. the deformations will be larger than those resulting when the heart contacts other

parts.

3.5 Finite Element Results of Deformation and Stresses in the Human Heart under High +Gz Acceleration

In this study, a quasi-static analysis is performed for the diastolic phase of the left ventricle under +Gz loading conditions (see also [28]). After checking the 3300 elements model of the left ventricle, a geometric nonlinear analysis was carried out for different levels of acceleration. A full nonlinear formulation, including nonlinearities in the material of the human heart, has been outlined in the previous sections. Due to complication of the model, the initial analysis was carried out for geometrical nonlinearities alone. Here several test runs were made under different loading conditions. For this analysis, the myocardium is modelled as an isotropic soft elastic material with a Young modulus of 14.28 psi and Poisson's ratio 0.3.

Results obtained for the +5G loading are shown in Figures 6, 7, and 8. In Figure 6 one can see that displacements increase cumulatively as one proceeds from the constrained nodes, at the top to the bottom nodes. In Figure 7 the Von Mises stresses are shown across a vertical cut through the left ventricle wall. The highest stresses arise in the vicinity of the constrained nodes, at the top of the model. Figure 8 depicts the distribution for the first component of stress, σ_{xx}, in the global coordinate system (X).

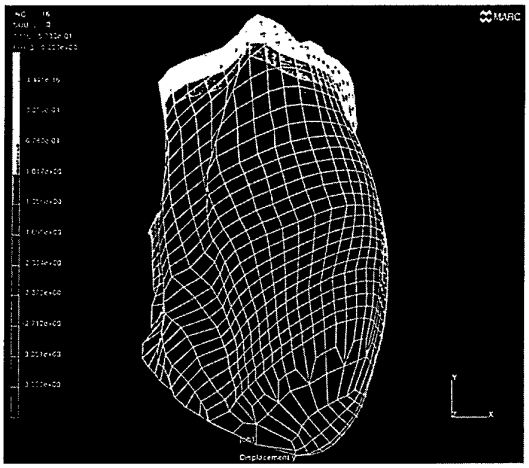

Figure 6: Displacement distribution, geometrically nonlinear analysis.

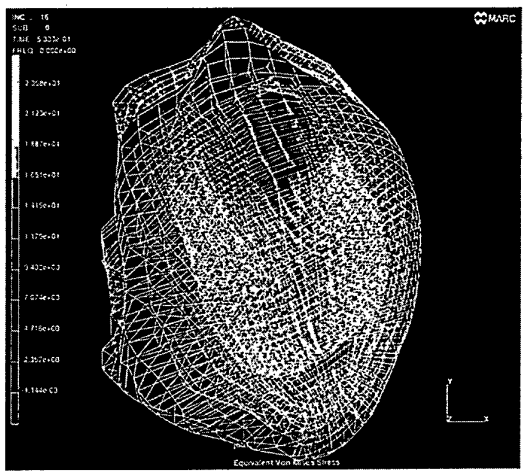

Figure 7: Von Mises stresses, distribution, geometrically nonlinear analysis.

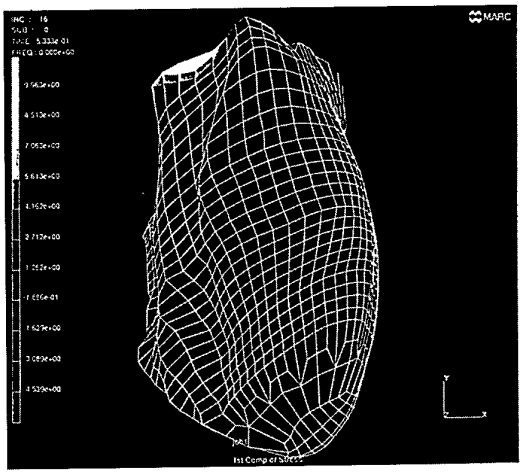

Figure 8: First component of stress, geometrically nonlinear model.

4 CONCLUSIONS AND FUTURE WORKS

The key objective in this study has been the investigation of the +Gz loading on the human heart. To this end it was necessary to generate an accurate geometrical model of the left ventricle. This data was processed by an advanced CAD tool named TRUEGRID. Next the model was discretized via the projection technique introduced in the TRUEGRID software. Two finite element models were developed, one with approximately 88000 eight-node brick elements and the other with 3300 eight-node brick elements.

For numerical processing it was decided to use the MARC finite element program. To run the model on the MARC program it was essential to find and correct poorly shaped elements. Such elements can give rise to ill conditioning during the solution process.

Once the model was suitably improved for element connectivity and the poor shaped elements were eliminated, a linear run was carried out. This run took about 10 minutes on a Sun Ultra work station. The results obtained were consistent with anticipated deformations in the model. Next a series of cases were run for different levels of accelerations. In these runs geometric nonlinearities were taken into account. From the results obtained one can see that under high acceleration the left ventricle becomes longer while its "diameter" diminishes. This is in agreement with one's expectations on physical grounds. The resulting stresses show high values at the constrained end and relatively low values at the apex of the left ventricle. There is a nonuniform stress distribution on the surface of the left ventricle as well as across the wall of the left ventricle.

Due to its high flexibility the heart elongates and changes its shape significantly, under high accelerations. If the distortions are not excessive; that is the case for relatively low acceleration levels, the elements almost retain their initial shapes. However, at high accelerations the element shapes become highly distorted leading to numerical problems. To overcome this difficulty it is essential to remesh the heart model when the distortions become excessive. This requires the transfer of information, such as nodal displacements and stresses from the initial mesh to the updated mesh. This is done by interpolation of the information to be transferred. This task remains to be undertaken in the next phase of this project.

To incorporate the material nonlinearities a detailed literature search was carried out. At this stage it appears that the Ogden model [24] is the most suitable for describing the nonlinear elastic behavior of the heart tissue. This model includes several parameters which must be determined by the "best fit" method to the experimental data presented in the literature [25,26,27]. This task and further refinements to the model will form the main focus of the future studies. Subsequent to that the porous media (section 3.3.2) will be used in the modeling.

5 ACKNOWLEDGEMENT

The funding for this research provided by Defence and Civil Institute for Environmental Medicine of Canada is greatly acknowledged.

6 REFERENCES

[1] Burton, R.R., and Whinnery, J.E., 1985, "Operational G-induced loss of consciousness: Something old; Something new", *Aviation, Space and Environmental Med.*, **8**, 812-817.

[2] Erickson, H.H., Sandler, H., and Stone, H.L., 1976, "Cardiovascular function during sustained +Gz stress", *Aviation, Space and Environmental Med.*, **7**, 750-756.

[3] O'Bryon, J.F., "Unlocking G-LOC", Sept. issue, *AIAA*, 60-63.

[4] Burton, R.R., Meeker, L.J., and Raddin, J.H., 1991, "Centrifuges for studying the effects of sustained acceleration on human physiology", *IEEE, Engrg. Med. and Biol.*, March, 56-65.

[5] Clarck, C., "Acceleration and body distorsion", *Human Factors in Atylical Environment, Ch. 4,* 65-85.

[6] Danaher, C., "Air force evaluates acceleration effects on cardiac function with HP ultrasound imaging system", 10-12.

[7] Leverett, S.D., Jr., Burton, R.R., Crossley, R.J., Michaelson, E.D., and Shubrouks, S.J., Human Physiologic Response, 1973, "Human Physiologic Responses to High, Sustained +Gz Acceleration", *USAFSAM TR,* 73-21.

[8] Mackenzie, W.F. and Burton, R.R., 1976, "Ventricular pathology in swine at high sustained +Gz", *AGARD Conf. Proc.*, **189**, The Pathophysiology of High +Gz Acceleration.

[9] Stone, H.L., Sordahl, L.A., Dowell, R.T., Lindsey, J.W., and Erickson, M.M., 1976, "Coronary Flow and Myocardial Biomechanical Responses to High Sustained +Gz Acceleration", *AGARD Conf. Proc.*, **189**, The Pathophysiology of High +Gz Acceleration.

[10] Nielsen, P.M.F., LeGrice, I.J., Smaill, B.H., and Hunter, P.J., 1991, "A mathematical model of the geometry and fibrous structure of heart", *Am. J. Physiol.*.

[11] Ter Keurs, H.E.D.J., Rijnsburger, W.H., Van Heuningen, R., and Nagelsmit, M.J., 1980, "tension development and sarcomere length in rat cardiac trabeculae: Evidence of length-dependent activation", *Circ. Res.*, **46**, 701-771.

[12] Yin, F.C.P., 1981, "Ventricular wall stress", *Circ. Res.*, **49**, 829-842.

[13] Humphery, J.D., and Yin, F.C.P., 1988, "Biaxial mechanical behaviour of excised epicardium", *ASME J. Biomech. Engrg*, **110**, 349-351.

[14] Lee, M.C., Fung, Y.C., Shabetai, R. and LeWinter, M.M., 1987, "Biaxial mechanical properties of human pericardium and canine comparisons", *Am J. Physiol.*, **253**, 75-82.

[15] Van den Bos, G.C., Elzinga, G., Westerhof, N., and Nobel, M.I.M., 1973, "Problems in the use of indices of myocardial contractility", *Cardiovasc. Res.*, **7**, 834-848.

[16] Woods, R.H., 1892, "A few applications of a physical theorem to membranes in the human body in a state of tension", *J. Anat. Physiol.*, **26**, 362-370.

[17] Sandler, H., and Dodge, H.T., 1963, "Letf ventricular tension and stress in man", *Circ. Res.*, **13**, 91-104.

[18] Moore, J.E., 1994, "Analysis of +Gz Acceleration Induced Stresses in the Human Ventricle Myocardium", Ph.D. Thesis, Mechanical Engineering Department, University of Victoria.

[19] Huyghe J.M., 1986, "Nonlinear Finite Element Models of The Beating Left Ventricle and The Intramyocardial Coronary Circulation", Ph.D. thesis, Eindhoven University of Technology, The Netherlands.

[20] Huyghe J.M., Oomens C.W., Van Campen D.H., Heethaar R.M., 1989, "Low Reynolds Number Steady State Flow Through a Branching Network of Rigid Vessels, I: A Mixture Theory", *Biorheology*, **26**, 55-71.

[21] Huyghe J.M., Van Campen D.H., Arts T., Heethaar R.M., 1991, "The Constitutive Behaviour of Passive Heart Muscle Tissue: A Quasi-Linear Viscoelastic Formulation", *J. Biomech.*, **24**, 9, 841-849.

[22] Fung Y.C., 1993, "Biomechanics: Mechanical Properties of Living Tissues", Springer-Verlag, New York.

[23] Huyghe J.M., Arts T., Van Campen D.H., Reneman R.S., 1992, "Porous Medium Finite Element Model of The Beating Left Ventricle", *Am. J. Physiol.*, **262**, H1256-H1267.

[24] Ogden, R.W., 1972, "Large deformation isotropic elasticity: on the correlation of theory and experiment for compressible rubberlike solids", *Proc. Roy Soc. London Ser.*, **A 328**, 367-583.

[25] Demiray, H., and Vito, R.P., 1976, "Large Deformation Analysis of Soft Biomaterials", *Int. J. Engrg. Sci.*, **14**, 789-793.

[26] Fung, Y.C., 1973, "Biorheology of soft tissue", *Biorheology*, **10**, 139-155.

[27] Yin, F.C.P., Strumpf, R.K., Chew, P.H., and Zeger, S.L., 1987, "Quantification of the mechanical properties of noncontracting canine myocardium under simulataneous biaxial loading", *J. Biomechanics*, **20**, 577-589.

[28] Behdinan, K., Tabarrok, B., and Fraser, W. D., 1998, "The Effects of +Gz Accelerations on Human Heart (Left Ventricle) Myocardium", *Technical Report,* Mechanical Engineering Department, University of Victoria, 1-100.

A MODEL OF CEREBRAL BLOOD FLOW DURING SUSTAINED ACCELERATION

S. Cirovic[1]
C. Walsh[2]
W. D. Fraser[3]

1. Institute for Aerospace Studies, University of Toronto, Ontario, Canada
2. Department of Mechanical Engineering, Ryerson Polytechnic University, Toronto, Ontario, Canada
3. Defence and Civil Institute of Environmental Medicine, Toronto, Ontario, Canada

DCIEM, Building 54, ALSS
PO Box 2000
1133 Sheppard Avenue West
Toronto, Ontario, Canada
M3M 3B9

ABSTRACT

Rationale: Radial accelerations generated in modern combat aircraft maneuvers (Gz) may result in impaired vision or loss of consciousness (G-LOC). We are interested in developing mathematical models of cerebral blood flow during exposure to Gz. Our previous model [1] showed that intracranial vascular resistance does not change with Gz since the vessels are protected from collapse by the cerebrospinal fluid and that reduction of the blood flow to the brain is mainly due to the increased vascular resistance of the large extracranial veins.
Methods: Based on the previous results, we propose a model with simplified presentation of the arteries and intracranial vessels and a more detailed description of the jugular veins. The extracranial arteries are accounted for by the hydrostatic pressure drop from the heart to the head level. The intracranial vessels are represented by a resistance independent of the mechanical effects of Gz. However, a model of cerebral autoregulation is incorporated, which involves active change in the cranial vascular resistance in reaction to the change in blood pressure at the head level. The jugular veins are modeled using one dimensional equations of fluid dynamics and a non-linear relation between the transmural (blood minus external) pressure and the local vessel cross-sectional area. The central arterial and venous pressures are taken to be 105 $mmHg$ and 5 $mmHg$ respectively and Gz was varied from -5 to +10. To simulate the effects of positive pressure breathing, blood pressures at the arterial and venous ends of the model were elevated by the same amount, so that the perfusion pressure was always maintained at 100 $mmHg$.
Results and conclusions: The model is successful in reproducing the drop in cerebral blood flow with +Gz. This reinforces our belief that the elevated venous resistance plays a significant role in G-LOC. The autoregulation has a positive impact at moderate +Gz but is ineffective at higher +Gz. This is mainly due to the fact that the venous resistance becomes absolutely dominant at high +Gz and a further decrease in the cranial vascular resistance makes little difference. The model predicts an increase in the blood flow in the case when the central venous and arterial pressures are elevated. We attribute this to the fact that an elevated central venous pressure prevents the venous collapse and maintains the extracranial veins patent.

1 INTRODUCTION

It is known that exposure to $+Gz$ acceleration can cause inadequate perfusion of the retina and brain leading to loss of vision and/or loss of consciousness [2]. When Gz is greater than the normal gravitational acceleration of the earth (+1 Gz), the weight of the blood is increased, and at approximately +5 Gz blood pressure at the level of the head can be expected to be zero. However, in a closed system with no net change in potential energy, such as the circulatory system, an increased hydrostatic gradient is not sufficient to explain the decrease in cerebral blood flow. If the blood vessels were rigid the cerebral perfusion would not be affected by Gz force, since the hydrostatic gradients on the arterial and venous side are equal and of the opposite sign, and the vascular resistance is independent of Gz stress. Blood vessels, however, have elastic walls and their cross-sectional area is a function of the transmural (internal minus external) pressure. In particular, thin-walled compliant vessels, such as veins, have tendency to collapse when subjected to negative transmural pressure. Therefore, in the case when vessels are compliant the vascular resistance is affected by the hydrostatic gradient, central arterial and venous pressures, and the external pressure acting on the vessels.

We have used opened loop mathematical models of the cerebral vascular system to model cerebral perfusion under Gz stress. Figure 1 shows a resistive network of compliant vessels representing the cerebral vascular tree. The extracranial portion of the network is represented by carotid and vertebral arteries and by jugular veins, which extend vertically, from the heart level to the cranium. The intracranial vessels are enclosed in a rigid container representing skull and surrounded by the cerebrospinal fluid (CSF). The results from the network suggest that the drop in cerebral blood flow dur-

Papers presented at the RTO HFM Specialists' Meeting on "Models for Aircrew Safety Assessment: Uses, Limitations and Requirements", held in Ohio, USA, 26-28 October 1998, and published in RTO MP-20.

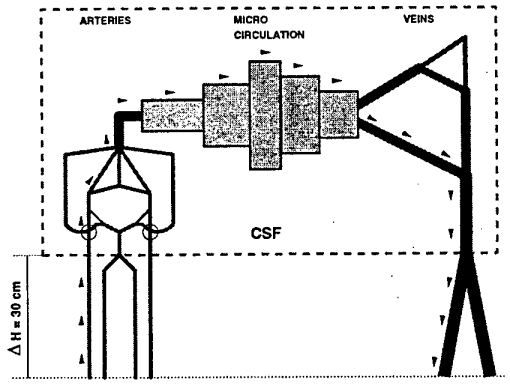

Figure 1: This anatomically complex resistive network was used in an earlier study to represent the cerebral circulation. The vessels surrounded by the broken line are cranial vessels subjected to the cerebrospinal fluid pressure (P_{CSF}).

ing high $+Gz$ is mainly due to an increased resistance of the collapsed extracranial veins. On the other hand, the vessels inside of the cranium are protected from collapse, since the CSF pressure (P_{CSF}) is always close to the venous pressure.

Based on the above results we propose a much simpler model geometry (Figure 2) which, however, gives a more accurate mathematical description of the flow in the extracranial veins, and incorporates a simple model of the cranial autoregulation. Also, we examine the effect of positive pressure breathing during $+Gz$ by elevating central arterial and venous pressures.

2 METHODS

Model

In the model geometry shown in figure 2, the network begins and ends at the heart level. Extracranial arteries are represented by a hydrostatic drop in pressure, from the heart to the head level. The intracranial vessels are assumed to be at the elevation of 30 cm above the heart. The external pressure acting on the blood vessels inside of the cranium is that of the CSF. Cranial arteries and veins are represented by their respective capacitances, whereas the cranial vascular resistance is lumped at the level of micro circulation. The extracranial veins are represented by a single distributed elastic vessel. The parameters used in the model are given in table 1.

Mathematical formulation

The model assumes that the viscous resistance in the extracranial arteries is insignificant. Therefore, the pressure drop from the heart to the head level is due to gravitational effects only. The intracranial arterial pressure (P_{AC}) is then

Central arterial pressure: P_{AHn}	105 $mmHg$
Central venous pressure: P_{AHn}	5 $mmHg$
Elevation: ΔH	30 cm
Cranial resistance: Rc_n	0.1333 $mm\ Hg\ min\ cm^{-3}$
Cranial arterial volume: V_{ACn}	15 cm^3
Cranial venous volume: V_{VCn}	60 cm^3
Stiffness constant: $Kp_{(AC)}$ (cranial arteries)	22.5 $mmHg$
Stiffness constant: $Kp_{(VC)}$ (cranial veins)	3.75 $mmHg$
Stiffness constant: $Kp_{(JV)}$ (jugular veins)	2.0 $mmHg$
Cross-sectional area A_0 (jugular veins)	0.43 cm^2
Density of blood: ρ	1000 kg/m^3
Viscosity of blood: μ	0.004 $kg/m\ s$

Table 1: Parameter values used in the model. Subscript n indicates normal values ($Gz = 1$).

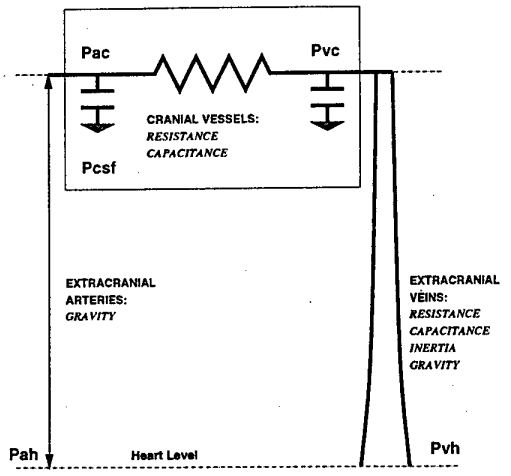

Figure 2: The simplified model of the cerebral circulation focuses on the mechanical properties of the jugular veins. The model begins at the root of common carotid and vertebral arteries, and ends with the internal jugular veins. The vessels surrounded by the box are cranial vessels subjected to P_{CSF}.

given by

$$P_{AC} = P_{AH} - \rho G z \Delta H \tag{1}$$

where P_{AH} is the arterial pressure at the heart level, ΔH is elevation of the cranial vessels, and ρ is blood density. In the cranium, it is assumed that the viscous pressure drop occurs only at the level of the micro circulation. The cranial resistance is independent of Gz, but a model of cerebral autoregulation can be incorporated. Therefore the intracranial venous pressure (P_{VC}) is given by

$$P_{VC} = P_{AC} - R_c Q \tag{2}$$

Where Rc and Q are cranial vascular resistance and blood flow rate, respectively. Rc is taken to be constant when autoregulation is not included, otherwise it is determined from

$$\frac{1}{Rc} = \frac{1}{Rc_n}\{1 - \frac{1}{\pi} tan^{-1}[(\frac{QRc}{(P_{AC} - P_{VC})_n} - 1)\pi]\} \tag{3}$$

[9]. The subscript n denotes normal values ($Gz = 1$). The intracranial arteries and veins are modeled as lumped capacitances without resistance. The intracranial arterial and venous volumes are functions of the transmural pressure.

$$\begin{aligned} P_{AC} - P_{CSF} &= K_p \left[\left(\frac{V_{AC}}{V_{ACn}}\right)^{20} - \left(\frac{V_{AC}}{V_{ACn}}\right)^{-1.5} \right] \\ P_{VC} - P_{CSF} &= K_p \left[\left(\frac{V_{VC}}{V_{VCn}}\right)^{20} - \left(\frac{V_{VC}}{V_{VCn}}\right)^{-1.5} \right] \end{aligned} \tag{4}$$

Where V_{AC} and V_{VC} are the arterial and the venous intracranial volume, respectively, and K_p is a vascular wall stiffness constant. The jugular veins are modeled following Shapiro's solution for a steady flow in a collapsible tube [7]. This is a one-dimensional distributed model including viscous resistance, gravitational effects and fluid inertia. The local cross-sectional area of the jugular vein is obtained from the following differential equation.

$$\frac{1}{A}\frac{dA}{dx} = \frac{1}{\rho}\frac{\rho G_z - \mathcal{R}(A)Q}{c^2 - U^2} \tag{5}$$

where x is the spatial coordinate and c is the local wave speed. $\mathcal{R}(A)$ is the viscous resistance term which is defined in the Appendix. For more details on the mathematical formulation the reader should refer to the Appendix.

Solution procedure

The equation 5 can be solved numerically, using a standard method for ordinary differential equations such as Runge-Kutta method [5]. However the flow rate Q is also unknown and therefore a "shooting" method has to be applied. The solution procedure is as follows:

- The flow rate Q is guessed.
- P_{VC} is determined from equation 2. If the cerebral autoregulation is incorporated, Rc has to be determined from equation 3.
- The solution is obtained for equation 5 for the guessed value of Q and P_{VC} as the boundary condition. P_{VH} obtained by solving equation 5 is compared with the assigned value of P_{VH} and a new value of Q is guessed.
- The procedure is repeated until the value of P_{VH} obtained from equation 5 and the assigned value of P_{VH} are close enough.
- P_{CSF} is determined from equation 4.

3 RESULTS

Blood and CSF pressure

Figure 3 shows blood pressures at the head level as a function of Gz. Arterial pressure is a linear function of Gz, as formulated in equation 1. The venous pressure curve is linear only in the region where the veins are distended. As soon as the venous pressure is negative, the curve becomes non-linear, with the gradient much smaller than that of the arterial pressure. Consequently, at high $+Gz$ the pressure difference driving the blood flow at the head level (cerebral perfusion pressure) is significantly diminished.

The relation between the Gz force and P_{CSF} is displayed by the line with solid squares in figure 4. The line with hollow squares shows venous pressure at the head level. For zero Gz the model predicts a P_{CSF} of 9 $mmHg$ which is well within the physiological range [8]. Venous and the CSF pressures stay closely together for the whole

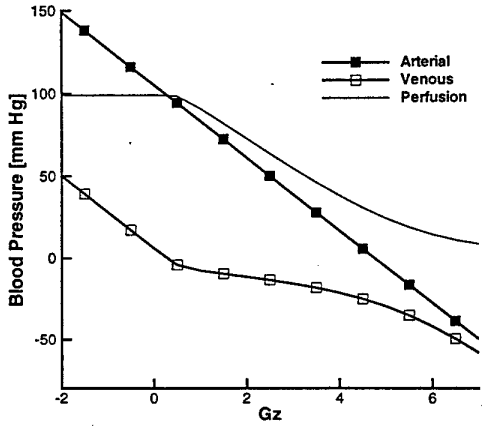

Figure 3: Blood pressure at the level of the head as a function of Gz. Solid squares: Arterial pressure. Hollow squares: Venous pressure. Faint line without symbols: Difference (cerebral perfusion pressure).

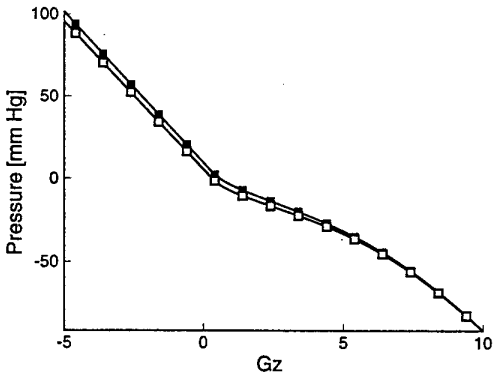

Figure 4: CSF and the venous blood pressure for Gz ranging from -5 to $+10$. Solid squares: P_{CSF}. Hollow squares: Venous pressure at the head level.

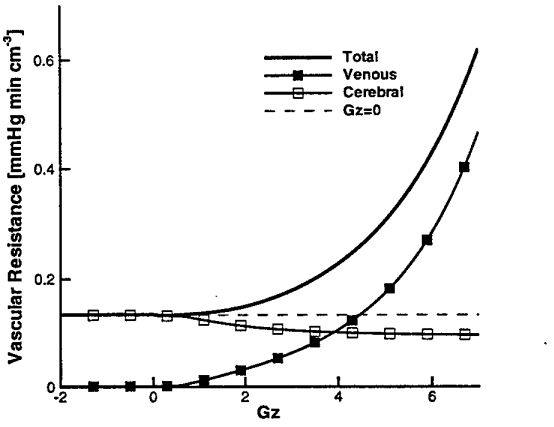

Figure 5: Vascular resistance as a function of Gz. Thick line without symbols: Total cerebral resistance. Solid squares: Venous resistance. Hollow squares: Cranial vascular resistance. Broken line shows the normal value of cerebral resistance.

range of Gz examined. Since the venous pressure at the head level is the lowest pressure in the system, the cranial vessels should never be collapsed.

Vascular resistance and blood flow

Figure 5 shows vascular resistance as a function of Gz. The total cerebral vascular resistance rises exponentially with $+Gz$. At approximately $+4.5$ Gz the resistance is doubled. In this model, the increase of the vascular resistance is exclusively due to an increase of venous resistance outside of the cranium. The cranial vascular resistance drops for moderate $+Gz$ but it levels at higher $+Gz$.

Due to increased vascular resistance, cerebral blood flow is diminished for $+Gz$, but it does not cease even when the arterial pressure becomes negative. At approximately $+5$ Gz, blood flow is below the minimum required for maintaining normal brain perfusion [3] . Autoregulation helps maintain normal perfusion only at moderate $+Gz$.

The effect of elevated central arterial and venous pressures

In order to simulate the effect of positive pressure breathing, arterial and venous pressures at the heart level were elevated from their normal values. The pressures were increased by the same amount, so that the difference was always maintained constant. Gz was kept constant at $+5$. Figure 7 shows vascular resistance in terms of the pressure increase.

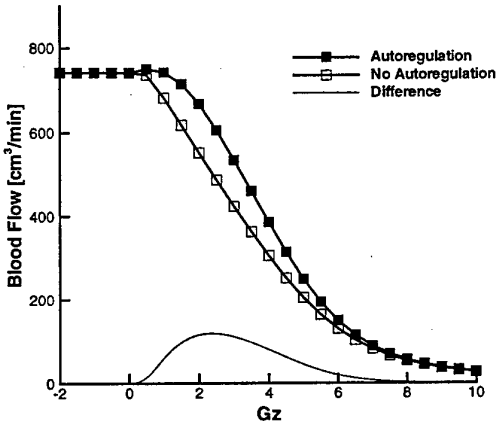

Figure 6: Cerebral Blood flow predicted by the model for Gz ranging from -2 to 10. Solid squares: Model with autoregulation. Hollow squares: Model without autoregulation. Faint line without symbols: Difference.

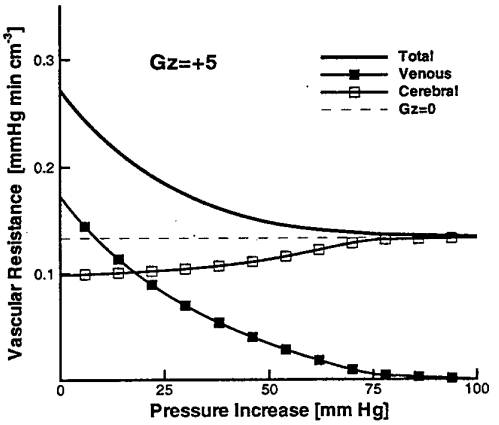

Figure 7: Vascular resistance at $+5$ Gz as a function of blood pressure increase. Thick line without symbols: Total cerebral resistance. Solid squares: Venous resistance. Hollow squares: Cranial vascular resistance. Broken line shows the normal value of cerebral resistance.

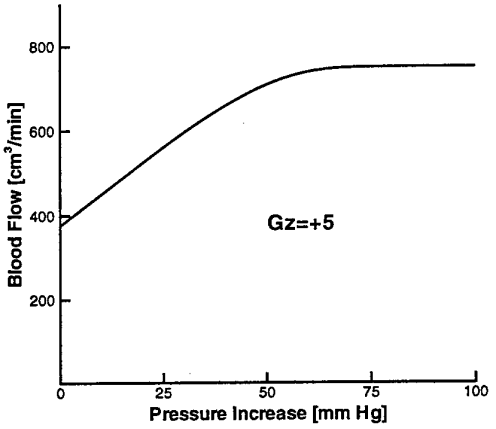

Figure 8: Cerebral blood flow at $+5$ Gz as a function of blood pressure increase.

The effect of the elevated blood pressure is to return vascular resistance to its normal value. Once the normal resistance is restored, further pressure increase has no effect. This is also reflected in the flow curve. Blood flow initialy increases with elevated blood pressure and then it levels at the normal value.

4 DISCUSSION

Vascular resistance and blood flow

This study indicates that even if the normal perfusion pressure is maintained, the increase in venous resistance caused by gravitational stress may lead to inadequate cerebral perfusion. The effect of the Gz-dependent jugular resistance can be discussed in terms of the extent to which pressure recovers as the blood descends towards the heart. If the veins were rigid (siphon), R_V would have been constant and negligible and the blood flow would be

$$Q_{MAX} = \frac{P_{AH} - P_{VH}}{R_C} \tag{6}$$

The other extreme case is the one in which viscous losses in jugular veins exactly equal the hydrostatic pressure component (waterfall). In this case blood pressure is P_{VH} everywhere in jugular veins, and blood flow is given by

$$Q_{MIN} = \frac{(P_{AH} - P_{VH}) - \rho G z \Delta H}{R_C} \tag{7}$$

In other words, blood flow is possible only if the perfusion pressure is higher than the hydrostatic pressure of the blood

column going from the heart to the head, meaning that it would be zero at approximately +4.5 Gz. The flow rate predicted by the model is somewhere between the "siphon" and the "waterfall", meaning that some pressure recovery is always present as the bloods descend towards the heart.

Elevated blood pressure has positive effect on cerebral blood flow since it reduces the narrowing of the jugular vein. If the pressure increase is sufficiently high, jugular veins cease to be collapsed and the normal blood flow is restored. Further increase in blood pressure has no effect since, at that point, the venous resistance is very low.

Autoregulation significantly improves cerebral perfusion at moderate $+Gz$ but is ineffective at higher $+Gz$. There are two reasons for this. First, at very high $+Gz$ the jugular resistance dominates and a reduction of the cranial vascular resistance has little effect on the blood flow. Second, the autoregulation mechanism itself becomes less effective for very small cerebral perfusion pressures (see the Appendix) which is the case for high $+Gz$.

CSF pressure

Rushmer *et al* [6] measured blood and CSF pressure in cats exposed to positive and negative Gz and concluded that P_{CSF} and venous pressure always stay roughly the same. Our model leads to the same conclusions using the assumption that the cranial blood volume is conserved, meaning that any increase of the arterial blood volume must be matched by an equivalent decrease of the venous blood volume. If P_{CSF} is to produce exactly the same volume change on the arterial and venous side, it should be much closer to venous than to arterial blood pressure, since the venous compliance is much higher than the arterial. Therefore P_{CSF} is only several millimeters of Hg higher than the cranial venous pressure.

5 CONCLUSIONS

The results show that a reduction of the cerebral blood flow during Gz stress may be caused by an increased vascular resistance on the venous side, outside of the skull. Though the extracranial veins are collapsed for $+Gz$, the gravitational effects play a role as the blood descends towards the heart. When the central blood pressures are elevated sufficiently, normal blood flow can be restored even at substantially high $+Gz$. The cerebral autoregulation is effective only at very moderate $+Gz$.

The cerebrospinal fluid pressure is a consequence of the cranial volume conservation and is directly influenced by the central venous pressure and the venous vascular resistance.

6 ACKNOWLEDGMENTS

This work has been generously supported by the Canadian Department of National Defence.
DCIEM Research Paper No. 98-P-xx.

7 REFERENCES

[1] Srdjan Cirovic, Colin Walsh, and William D. Fraser. A model of cerebral perfusion under high acceleration. In *Proceedings of the 1998 CSME Forum, Toronto*, 1998.

[2] P. Howard. The physiology of positive acceleration. In J. A. Gillies, editor, *A Textbook of Aviation Physiology*, pages 551 – 687. Pergamon Press, 1965.

[3] S. S. Kety, A. S. Henry, and C. F. Shmidt. The effect of increased intracranial pressure on cerebral circulatory function in man. *J. Clin. Invest*, 27:493 – 499, 1947.

[4] T. J. Pedley, B. S. Brooks, and R. S. Seymour. Blood pressure and flow rate in the giraffe jugular vein. *Phil. Trans. R. Soc. Lond.*, 352:855 – 866, 1996.

[5] W. H. Press, S. A. Teukolsky, W. T. Vetterling, and B. P. Flannery. *Numerical recipies in Fortran: the art of scientific computation.* Cambridge University Press, 1986.

[6] R. F. Rushmer, E. L. Beckman, and D. Lee. Protection of the cerebral circulation by the cerebrospinal fluid under the influence of radial acceleration. *Amer. J. Physiol.*, 151:459 – 468, 1947.

[7] Ascher H. Shapiro. Steady flow in collapsible tubes. *Journal of Biomechanical Engineering*, 99:126–147, 1977.

[8] T. Takemae, Y. Kosugi, J. Ikebe, Y. Kumangi, K. Matsuyama, and K. Saito. A simulation study of intracranial pressure increment using an electric circuit model of cerebral circulation. *IEEE Trans. Biom. Eng.*, 34:958 – 962, 1987.

[9] M. Ursino. A mathematical study of human intracranial hydrodynamics part 1 - the cerebrospinal fluid pulse pressure. *Ann. of Biomed. Eng.*, 16:379 – 401, 1988.

Appendix

Steady Inertial Flow in the Jugular Vein

We consider steady 1-D flow in a vertical elastic vessel. The vessel properties and the external pressure are spatially uniform. The 1-D steady state governing equations are:

$$Q = AU \tag{8}$$

$$U\frac{dU}{dx} + \frac{1}{\rho}\frac{dP}{dx} - G_z = -\frac{\mathcal{R}(A)Q}{\rho} \tag{9}$$

$$P_t = K_p\mathcal{P}(\alpha) \tag{10}$$

where

$$P_t = P - P_e \tag{11}$$

$$\alpha = \frac{A}{A_0} \tag{12}$$

The momentum equation (9) can be rewritten using equation (8) and the wave speed c as:

$$\frac{d\alpha}{dx} = \frac{\alpha[\rho G_z - \mathcal{R}(A)Q]}{\rho[c^2 - U^2]} \tag{13}$$

$$c^2 = \frac{A}{\rho}\frac{dP}{dA} \tag{14}$$

Next, we introduce functions for $\mathcal{P}$, c, and $\mathcal{R}$ following [4].

$$\mathcal{P}(\alpha) = \alpha^{20} - \alpha^{-3/2} \tag{15}$$

$$c^2 = \frac{\alpha K_p}{\rho}\frac{d\mathcal{P}}{d\alpha} = \frac{K_p}{\rho}(20\alpha^{20} + \frac{3}{2}\alpha^{-3/2}) \tag{16}$$

$$\mathcal{R} = \frac{8\pi\mu A_0^{1/2}}{A^{5/2}} = \frac{8\pi\mu}{A_0^2\alpha^{5/2}} \tag{17}$$

Substituting equations (15-17) into equation (15) and using $U^2 = Q^2/A^2 = Q^2/(A_0^2\alpha^2)$, we have

$$\frac{d\alpha}{dx} = \frac{\rho G_z\alpha - (8\pi\mu/A_0^2)Q\alpha^{-5/2}}{K_p(20\alpha^{20} + 3/2\alpha^{-3/2}) - (\rho Q^2/A_0^2)\alpha^{-2}} \tag{18}$$

This is a first order ordinary differential equation in terms of α. It can be solved if one boundary condition and the flow rate Q are known. Note that the area derivative is infinite for $U = c$. Consequently, a smooth transition to supercritical flow is only possible where the gravitational and dissipation effects cancel. Typically, the transition back to sub-critical flow occurs via an abrupt change in the area. This is analogous to the normal shock in gas dynamics.

Cerebral Autoregulation

The mathematical model of the cerebral autoregulation is taken from [9]. The model is based on the assumption that cranial resistance responds to the changes in cerebral perfusion pressure (cranial arterial minus cranial venous) and is described by the following equations:

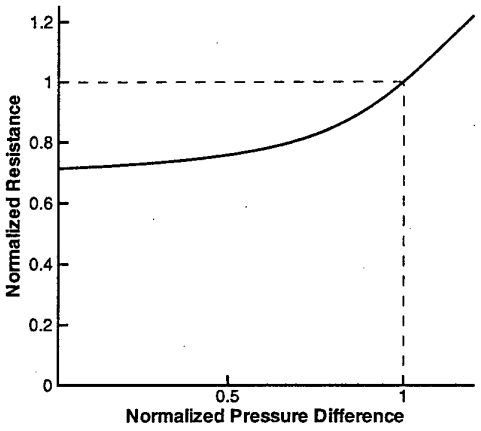

Figure 9: Normalized cranial resistance as a function of normalized cerebral perfusion pressure.

$$\frac{dy(t)}{dt} = -\frac{y(t)}{\tau} + \frac{1}{\tau}\left[\frac{P_{AC} - P_{VC}}{(P_{AC} - P_{VC})_n} - 1\right] \tag{19}$$

$$\frac{1}{Rc} = \frac{1}{Rc_n}\left[1 - \frac{1}{\pi}tan^{-1}(y(t)\pi)\right] \tag{20}$$

where τ is a time constant and subscript n denotes normal values (zero G_z).

The solution to equation (19) is

$$y(t) = \left[\frac{P_{AC} - P_{VC}}{(P_{AC} - P_{VC})_n} - 1\right] + K\exp(-\frac{t}{\tau}) \tag{21}$$

where K is a constant of integration. For the steady state

$$\lim_{t\to\infty} y(t) = \frac{P_{AC} - P_{VC}}{(P_{AC} - P_{VC})_n} - 1 \tag{22}$$

Substituting equation (22) into (20) and using $P_{AC} - P_{VC} = RcQ$ we have

$$\frac{1}{Rc} = \frac{1}{Rc_n}\{1 - \frac{1}{\pi}tan^{-1}[(\frac{QRc}{(P_{AC} - P_{VC})_n} - 1)\pi]\} \tag{23}$$

This is a nonlinear algebraic equation in terms of Rc which can be solved if Q is known. The relation between cerebral perfusion pressure and cranial resistance, normalized with respect to their respective normal values, is shown in figure 9.

DCIEM 98-P-88.

Linear and Nonlinear Models of the Physiological Responses to Negative-to-Positive Gz Transitions

A. Kapps
Engineering Services Inc.
5 King's College Rd.
Toronto, Ontario M5S 3G8
Canada

W.D. Fraser
Defence and Civil Institute of Environmental Medicine (DCIEM)
1133 Sheppard Avenue West
Toronto, Ontario M3M 3B9
Canada

1. SUMMARY

The identification and modeling of experimental data for negative-to-positive Gz (Push-Pull) transitions discussed in this paper is aimed at predicting typical and atypical physiological responses in order to develop Push-Pull countermeasures. A novel analysis of Push-Pull data in both the time and frequency domains was developed.

Eye-level blood pressure dynamics in response to Push-Pull transitions differ significantly from subject to subject. This individual sensitivity is much less profound in a sub-group of the tested subjects. Overall, the match between the predicted and measured eye-level blood pressure is much better with low Gz gradients than in the case of large Gz gradients. A model with a transfer function of low order (3 by 3) may be sufficient to match the behavior of eye-level blood pressure under both Push-Pull and positive Gz maneuvers. However, nonlinear models are required to fit blood pressure response data in a sub-group of subjects.

2. INTRODUCTION

The risk of G-induced loss of consciousness (GLOC) has become even more acute with the development of today's high performance aircraft that can withstand acceleration stress far in excess of a pilot's tolerance. Methods used to combat the fall in eye-level blood pressure include anti-G suit inflation, muscular straining manoeuvres, positive pressure breathing, or changes in the pilot's orientation with respect to the +Gz vector.

It is known that pilots' +Gz tolerance is reduced significantly when a +Gz exposure has been preceded by a -Gz exposure - the Push-Pull phenomenon [1]. This paper summarizes some early results of our research on the identification and analysis of dynamic models of the response of the cardiovascular systems of relaxed, unprotected subjects to Push-Pull transitions.

We applied a number of linear modeling techniques (e.g., recursive least squares, adaptive/recursive algorithms, and data segmentation based on AFMM (adaptive forgetting through multiple models)) to the experimental data [2]. These techniques enabled us to identify suitable model structures. Analysis of models for different subjects, as well as identification of discrepancies in responses of different subjects and the degree of correlation of their responses was undertaken. An attempt was also made to generalize individual models. A comparative analysis of a subject's physiological responses for positive-to-positive Gz transitions and negative-to-positive Gz transitions was performed. An attempt was also made to find out whether linear models are sufficient or nonlinear modeling is required.

3. MODELING OF PUSH-PULL EFFECTS

3.1 The Modeling and Prediction Algorithms

This section presents the results of the identification and analysis of a dynamic models representative of individual cardiovascular responses of relaxed, unprotected subjects exposed to Push-Pull manoeuvres, using data from the studies of Banks et al [1,3]. In the experiments reported in [1,3], Gz profiles were produced by moving a sliding bench back and forth along a track in a rotating horizontal plane. The blood pressure of the test subjects were measured using a Finapres device attached to a left-hand finger of the subject and secured over the right clavicle. Variable parameters of the Gz profiles were (i) time spent at -Gz and (ii) maximum +Gz exposure. Each experiment contained four types of runs:

- Zero Gz to +Gz (reference runs)
- Zero Gz to –Gz for t_1^- sec; then to +Gz and hold for t_1^+ sec; return to zero Gz.
- To -Gz for t_2^- sec; then to +Gz for t_2^+ sec; then to zero Gz.
- To -Gz for t_3^- sec; then to + Gz for t_3^+ sec; then to zero Gz.

Papers presented at the RTO HFM Specialists' Meeting on "Models for Aircrew Safety Assessment: Uses, Limitations and Requirements", held in Ohio, USA, 26-28 October 1998, and published in RTO MP-20.

In this preliminary study we examined data from the experiments performed on seven subjects. Input data used in the modeling investigation performed consisted of two files the measured Gz and the neck-level blood pressure. Neck-level blood pressure data were pre-processed in order to obtain the eye-level blood pressure.

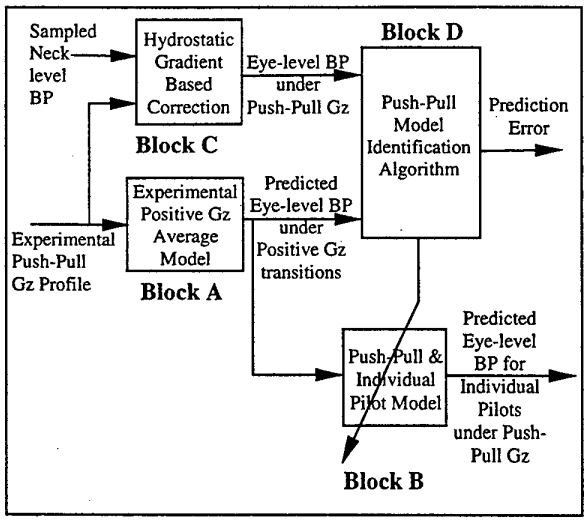

Figure 1: Push-Pull Modeling and Prediction Diagram

In these experiments, the subjects were fully restrained in a seated position on their backs, with their vertical axis (Gz axis) aligned with the direction of the seat movement along the track. Alternations in the subject's positive and negative Gz expsoure were achieved by repositioning the seat on the track and alternating the magnitude and direction of centripetal accelerations [1]. Positive Gz was obtained when the subject was positioned with feet facing outwards from the center of rotation, whereas the negative Gz corresponds to the subject positioned with his/her head facing outwards.

The modeling and prediction procedure developed in this paper for the case of Push-Pull responses is partially based on the transfer function (1) derived using the frequency domain response of the human body exposed to positive Gz transitions. The model (1) compares favourably to the model derived by Gillingham *et al.* [4]. The identification procedure developed in this report extends this Push-Push transfer function by adding a term that corresponds to the case of the Push-Pull Gz profiles. An important goal was to determine the possibility of using a unified model (expressed in terms of transfer functions) for both Push-Push and positive-to-positive Gz maneuvers. Another goal was to investigate and compare individual characteristics of subjects' responses and models under various Push-Pull maneuvers.

The scheme that has been implemented in order to model and predict a subject's eye-level blood pressure during Push-Pull manoeuvres is presented in Figure 1. The eye-level blood pressure is computed in **Block C** from the measured heart-level blood pressure corrected with the hydrostatic gradient from the heart to the eye. The Gz acceleration profile is an input into the simulation program that uses the empirical transfer function H(s) determined from positive-to-positive Gz transitions:

$$H(s) = \frac{BP(s)}{GZ(s)} = \frac{-3653.8s^6 - 1258.3s^5 - 9498.6s^4 - 1871.3s^3 - 4943.9s^2 - 508.6s - 20.8}{112.8s^7 + 121.6s^6 + 354.6s^5 + 316.8s^4 + 250.1s^3 + 159.8s^2 + 27.9s + 1} \quad (1)$$

The output of **Block A** is the predicted eye-level blood pressure. In general, this predicted blood pressure is not expected to fit the eye-level blood pressure in Push-Pull transitions since:

(i) the model in **Block A** has been computed from positive-to-positive Gz transitions while the Gz profiles used in this study are of the Push-Pull type;

(ii) the model in **Block A** does not take into account the individual physiological characteristics of each subject because it has been derived based on averaged data collected from a number of test subjects.

The purpose of the identification process in **Block D** is to calculate a corrective model to: (a) adapt the positive-to-positive Gz model to the Push-Pull blood pressure; and (b) account for the individual differences between subjects. The identification algorithm in **Block D** uses sampled (i.e., experimental) and predicted (based on the positive-to-positive Gz model) eye-level blood pressure values as its inputs. It produces two outputs:

(i) The Push-Pull correction model;

(ii) The standard deviation of the prediction errors.

Using the resulting Push-Pull correction model and the predicted eye-level blood pressure under Push-Push Gz (output of **Block A**), the predicted eye-level blood pressure for each individual subject under Push-Pull Gz is computed in **Block B** and compared with the experimental data. The predicted eye-level blood pressure for the individual subjects under the Push-Pull manoeuvres (output of **Block B**) is further used to evaluate eye-level blood pressure prediction accuracy for individual subjects under Push-Pull manoeuvres.

3.2 Push-Pull Modeling and Prediction Results

This section presents the results of modeling and prediction of a selected set of individual subject responses to different push-pull transitions. For each subject, data from one or two different push-pull experimental runs were analyzed. Two of the subjects were tested using the same Gz profile. Each figure below includes the following four plots:

1. the power spectra density of the neck-level blood pressure in dB of mmHg;
2. the eye-level blood pressure (solid line) predicted using the continuous transfer function defined by equation (1), together with the experimental eye-level blood pressure (dashed line);

3. the Gz profile;
4. the eye-level blood pressure (solid line) predicted using the new model identified for individual subjects that undergo Push-Pull transitions, together with the experimental eye-level blood pressure (dotted line).

Plots 2 and 4 of Figure 2 show the modeling results a subject during the Gz profile shown in plot 3. There is a poor match between the experimental and predicted blood pressure responses using the positive-to-positive Gz transfer function (1) during -Gz to +Gz transitions. However the match during +Gz to -Gz transitions is better.

The Push-Pull correction modeling did not significantly improved the match between the experimental and predicted blood pressure responses. The push-pull modeling algorithm (**Block D,** Figure 1) calculates coefficients of the transfer function polynomials, assuming initially that both the numerator and denominator are polynomials of degree 3. The resulting final optimal orders of the transfer function numerator and denominator polynomials, obtained by numerical trial and error, that yield the best fit are: 2 for the numerator and 2 for the denominator. The resulting transfer function is:

$$H(s) = 0.98 \frac{1+0.58s+0.07s^2}{1+0.34s+0.18s^2} \quad (2)$$

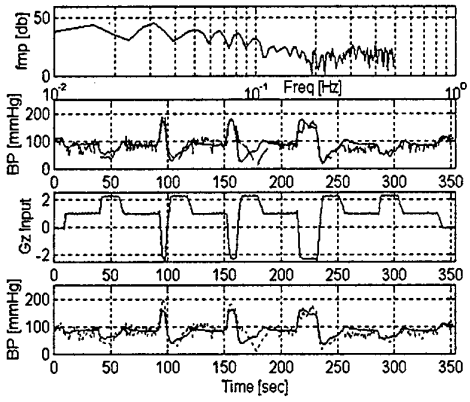

Figure 2: Modeling and Prediction Results for Session CA5

The gain of the transfer function (2) is close to 1 because the free term of the transfer function H(s) given by (1) has the correct steady state value. The frequency domain response presented in Plot 1 shows the presence of several relevant peaks at the following frequencies:

30 mHz, 50 mHz, 65 mHz, 80 mHz and 100 mHz.

The frequencies of the peaks are common (with very small variations) to all the test subjects during all push-pull exposures.

Figure 3 shows the prediction results for the same subject in a different Gz profile.

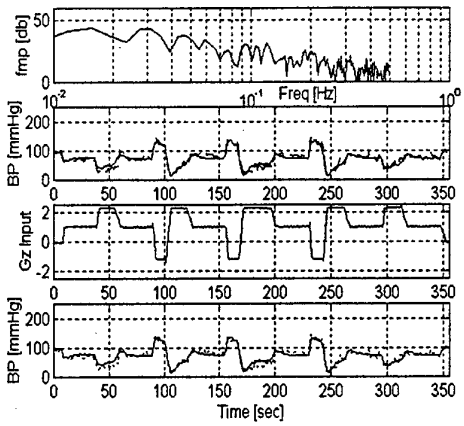

Figure 3: Modeling and Prediction Results for Session BC5

The modeling results show a good match between the experimental and predicted blood pressure responses during -Gz to +Gz transitions using the positive-to-positive Gz transfer function (1), as well as a very good fit during +Gz to -Gz transitions. The resulting optimal transfer function has 2 poles and 2 zeros, similar to the previous transfer function (2):

$$H(s) = 1.02 \frac{1+0.63s+0.17s^2}{1+0.55s+0.31s^2} \quad (3)$$

The degree of uncertainty in the identification of the transfer function polynomials is low with a standard deviation of 11.6 mmHg for the matching errors between the predicted eye-level blood pressure (based on the Push-Pull modeling) and the experimental eye-level blood pressure. This is only slightly lower than the variance of 12.6 mmHg in the matching errors between the experimental eye-level blood pressures and those predicted using the positive-to-positive Gz model (1) indicating that the positive-to-positive Gz model may also be used for the Push-Pull transitions of some subjects.

Plots 2 and 4 of Figure 3 show the modeling results another during the Gz profile shown in plot 3. There is a poor match between the experimental and predicted blood pressure responses during the -Gz to +Gz transitions using the positive-to-positive Gz transfer function (1), however,. the match during +Gz to -Gz portions is better. The Push-Pull correction did not significantly improve the match between the predicted and computed eye-level blood pressure

The transfer function for this case is given by:

$$H(s) = 0.96 \frac{1+0.54s+0.07s^2}{1+0.49s+0.26s^2} \quad (4)$$

Figure 4 shows the results of the simulation for same subject exposed to a different push-pull sequence.

The modeling and prediction results show a poor match between the experimental and predicted blood pressure responses during -Gz to +Gz transitions using the positive-to-positive Gz transfer function (1), whereas a better fit is obtained during +Gz to -Gz transitions. Compared with Plot 2, Plot 4 in Figure 4 shows that the Push-Pull correction modeling has improved the matching between the predicted and computed eye-level blood pressure. The transfer function for this case is given by:

$$H(s) = 0.9 \frac{1+0.51s+0.06s^2}{1+0.56s+0.26s^2} \quad (5)$$

The gain of the transfer function is smaller than (1), due to the poor matching between the eye-level blood pressure predicted based on equation (1) and the experimental eye-level blood pressure. The coefficients of the numerator and denominator polynomials in (5) are close to the values of the corresponding coefficients of (4).

The degree of uncertainty in the identification of the transfer function polynomials is of 13.6 mmHg for the matching errors between the predicted eye-level blood pressure (based on the Push-Pull modeling) and the experimental eye-level blood pressure. This is better than the variance of 18.1 mmHg in the matching errors between the experimental eye-level blood pressures and those predicted using the positive-to-positive Gz model (1) indicating that in this case the positive-to-positive Gz transition model (1) is not suitable for modeling the blood pressure responses to the Push-Pull transitions.

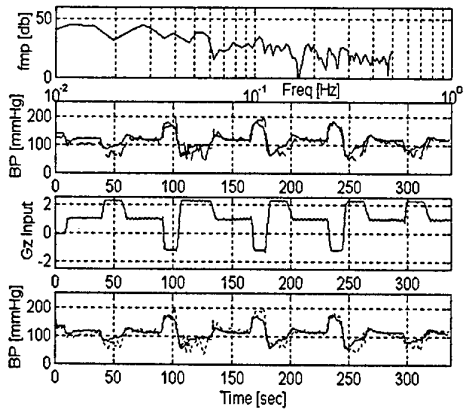

Figure 4: Modeling and Prediction Results for Session BB12

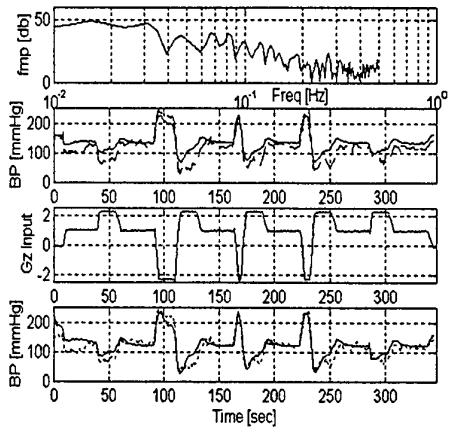

Figure 5: Modeling and Prediction Results for Session CC12

Plots 2 and 4 of Figure 5 show the modeling results for another subject during the Gz profile shown in plot 3. There is a poor match between the experimental and predicted blood pressure responses using the positive-to-positive Gz transfer function (1) during -Gz to +Gz transitions. The match during +Gz to -Gz transitions is better. The Push-Pull Correction has improved the match between the predicted and computed eye-level blood pressure. The transfer function for this case is similar to the previous subjects:

$$H(s) = 0.91 \frac{1+1.25s+0.22s^2}{1+2.1s+0.85s^2} \quad (6)$$

Based on the examples presented above, it is observed that in general:

1. either the prediction accuracy achieved with the transfer function (1) is good, or the Push-Pull correction improves the prediction accuracy significantly;
2. when the prediction accuracy of the transfer function (1) is poor, the DC (i.e., steady state) gain of the push-pull correction model is far from unity.

Specifically, the coefficients of the numerator and denominator polynomials in (6) differ significantly from the values of the corresponding coefficients in the other cases. The standard deviation of the matching errors between the eye-level blood pressure predicted based on the Push-Pull correction model and the eye-level blood pressure computed based on the measured neck-level blood pressure is 10.35 mmHg. This is better than the variance of 13.15 mmHg in the matching errors between the experimental eye-level blood pressures and those predicted using only the Push-Push model (1) and the eye-level blood pressure. In some cases the positive-to-positive Gz model (1) is not suitable for modeling the Push-Pull Gz transition and the Push-Pull Corrective Model has to be applied..

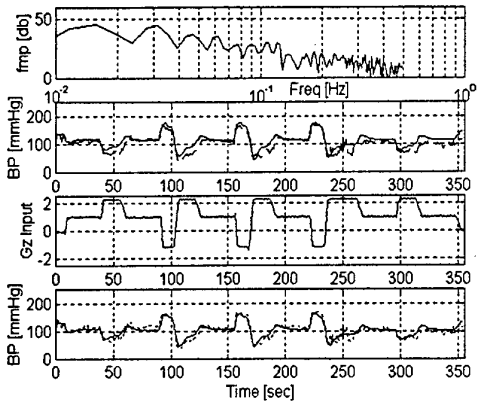

Figure 6: Modeling and Prediction Results for Session BE16

For other subjects, there was a poor match between the input the experimental and predicted eye-level using the trasnfer function (1) during *both* -Gz to +Gz and +Gz to -Gz transitions. In addition, the Push-Pull correction modeling did not improve the match. The physiological response of these subjects is nonlinear and a nonlinear modeling approach is required in these cases.

4. MODELING AND PREDICTION OF DIRECT PUSH-PULL MODEL

In order to further investigate the utilization of the positive-to-positive Gz averaged model given by Equation (1) for push-pull transitions, we have implemented a modeling and prediction scheme to compute a dynamic model of eye-level blood pressure as a function of the Push-Pull Gz signal based on direct experimental results. The purpose this section is to compare the following two models:

(i) **Model I:** The eye-level blood pressure model computed using the procedure described in section based on the combination of: (a) the positive-to-positive Gz averaged model computed from the frequency domain (1); and (b) the Push-Pull and individual subject corrective model as defined in Figure 1 discussed in Section 3;

(ii) **Model II:** The eye-level blood pressure model (called the *direct push-pull model* computed directly from: (a) the Push-Pull Gz profiles; and (b) the individual experimental eye-level blood pressures.

Figure 7 shows the prediction results for the experimental session CA17 with the Model II. The results in Figure 7 include the following plots:

1. the Gz profile;
2. the eye-level blood pressure (solid line) predicted using Model I, together with the experimentaleye-level blood pressure (dashed line);
3. the eye-level blood pressure (solid line) predicted using Model II, together with the eye-level blood pressure (dotted line) predicted using Model I;
4. the eye-level blood pressure (solid line) predicted using Model II and the experimental eye-level blood pressure (dotted line).

A signal pre-processing stage was needed in order to facilitate the computation of Model II. The pre-processing included a sign change and the *detrending* of the Gz and eye-level blood pressure signals.

The modeling and results show improved matching between the experimental eye-level blood pressure and the eye-level blood pressure predicted using Model II during both -Gz to +Gz and +Gz to -Gz transitions. The improvement is particularly noticeable in matching the blood pressure peak values. As compared with Plot 2, Plots 3 and 4 in Figure 7 show **the improved match of the blood pressure at both the maximum and minimum peaks.** However, it can be seen from Plot 4 that the Direct Push-Pull modeling not yield a perfect match between the dynamic time history of the predicted and the experimental eye-level blood pressure, since this subjects response is nonlinear. It can be also seen from Plot 3 that the dynamic time response of the eye-level blood pressure predicted using Model II is very similar to the eye-level blood pressure predicted using Model I and the standard deviation of the difference (3.15 mmHg) is caused mainly by the difference in the peak values of blood pressure.

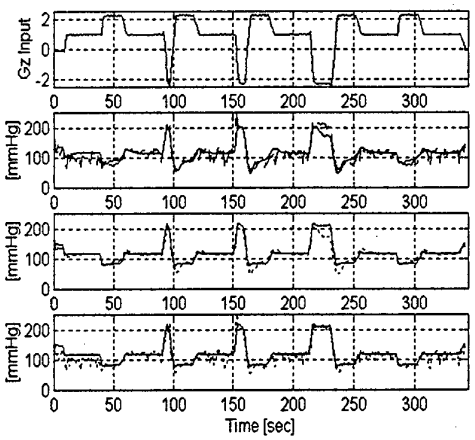

Figure 7: Modeling and Prediction Results for NCA17

The direct Push-Pull modeling algorithm calculates the coefficients of the transfer polynomials, assuming initially that both the numerator and denominator are polynomials of degree 4. The final optimal orders of the transfer numerator and denominator polynomials obtained by numerical trial and error

are 3 for the numerator and 3 for the denominator. The resulting TF is:

$$H(s) = -21.4 \frac{(1+0.56s+0.18s^2)\ (1+5.35s)}{(1+0.33s+0.21s^2)\ (1+3.32s)} \quad (7)$$

The transfer function defined by (7) consists of 3 terms:

(a) **First Term**: the gain of the steady state response, which is close to the theoretical value of -22 [4] and has the value identical to the steady state gain of the Rogers' model (eq. (6)-(10) in [5]);

(b) **Second Term**: a transfer function that is very similar to the function defined by (8) and represents the individual subject response;

(c) **Third Term**: a transfer function similar to the low-order transfer function of Rogers' model [5]:

$$H(s) = -21.4 \frac{(1+5.35s)}{(1+3.23s+5.17s^2)} \quad (8)$$

One apparent difference between Rogers' model and the direct push-pull model is that the direct Push-Pull model matches the *drift* in the blood pressure response during constant Gz segments (e.g., a subject at rest after a Gz transition). The term "drift" refers to the slow drop in the blood pressure during constant Gz segments following a sharp Gz transition (Figure 8)[4].

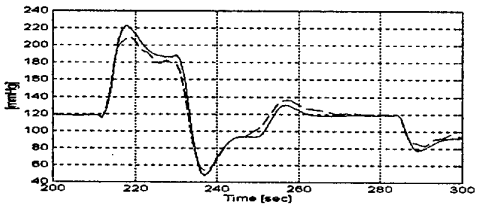

Figure 8: Detailed View of Eye-level BP Predicted by Rogers' and Push-Push Averaged Models *(Dashed line - Push-Push average model; Solid line- Rogers' Model)*

5. CONCLUSIONS

Blood pressure responses differ from subject to subject for relaxed Push-Pull and positive-to-positive Gz transitions. In the cases of subjects with extreme behavior, models of blood pressure responses seem to be more sensitive to the individual subject's responses than to the Gz transition type.

Overall, the match between the predicted eye-level blood pressure and the computed eye-level blood pressure is much better in the case of Gz profiles with low Gz gradients than in the case of Gz profiles with large Gz gradients. This is due to the nonlinear behavior and the lack of good matching for individual subjects with extreme behavior.

It appears from the modeling results that a model with a transfer function of low order (3 by 3) may be sufficient to match the behavior of eye-level blood pressure P under both Push-Pull and positive-to-positive Gz transitions. This model has been obtained by Direct Push-Pull Gz profile matching, and it is very close to the low-order Rogers' Model [5] with the exception that the Direct Push-Pull Model developed here captured the so-called drift behavior of the blood pressure. As a result, a low-order model may be used in the development of a model-based control scheme for the anti-G protection mask and suit valves.

All of the linear models investigated failed to match the eye-level blood pressure in cases of extreme behavior even when a model was computed using Direct Push-Pull modeling. And nonlinear modeling techniques must be used.

6. REFERENCES

[1] Banks, R.D., Grissett, J.D., Turnispeed, G.T., Saunders, P.L. and Rupert, A.H.,"The Push-Pull Effect", *Aviation, Space, and Environmental Medicine,* Vol. 65, No. 8, pp. 699-704, August, 1994.

[2] Ljung, L., System Identification: Theory for the User, Prentice Hall Inc., New Jersey, 1987.

[3] Banks, R.D., Grissett, J.D., Saunders, P.L. and Mateczun, A.J., "The Effect of Varying Time at -Gz on Subsequent +Gz Physiological Tolerance (Push-Pull Effect)", *Aviation, Space, and Environmental Medicine,* Vol. 66, No. 8, pp. 723-727, August, 1995.

[4] Gillingham, K.K., Freeman, J.J., McNee, R.C., "Transfer Functions for Eye-level Blood Pressure During +Gz Stress," *Aviation, Space, and Environmental Medicine,* Vol. 48, No. 11, pp. 1026-1034, 1977.

[5] Rogers, D.B., *A Model for the Energetic Cost of Acceleration Stress Protection in the Human,* Aerospace Medical Research Laboratory Report - AMRL-TR-79-58, July, 1979.

DCIEM 98-P-87.

Hierarchical modeling of the baroreceptor response to Gz acceleration and anti-Gz protective equipment

W. D. Fraser

Defence and Civil Institute of Environmental Medicine (DCIEM)
P O Box 2000
1133 Sheppard Avenue West
Toronto, Ontario M3M 3B9, Canada

1 Summary

The use of extended coverage anti-G suits and positive pressure breathing have enhanced the protection of aircrew exposed to high Gz and extreme altitudes. However, current systems do not provide optimal protection to the individual pilot during complex negative-to-positive Gz maneuvers nor do such systems adapt to changes in the physiological state of the pilot over the course of the mission, in part due to the hardware's inability to adapt to the complex response of the blood pressure regulating systems within the body. Current, medically relevant models of baroreceptor function are not suitable for the extreme changes in blood pressure and blood distribution in a body exposed to very high Gz levels of the tactical environment. Using a mix of first principle and data driven techniques, we are developing hierarchical models of baroreceptor function that include the interaction between the neuronal sub-components of the baroregulation centers of the central nervous system, the transient dynamics of pressure induced stretch in the baroreceptor organs, the effects of local pressure gradients within the aortic/carotid baroreceptor system, and the dynamic response of each of the subsystems during Gz exposures. All of these factors play a significant role in the individual's response to the Gz forces and the efficacy of the life support systems in preventing an adverse impact on cerebral blood flow and oxygenation of the brain.

2 Introduction

Environmental stresses such as acceleration, altitude, and thermal load can challenge the physiological capability of the crew of high performance tactical aircraft, such that sensory and cognitive function is degraded or even eliminated as in the extreme case of Gz induced loss of consciousness. Since World War II, experimental programs have been on-going to develop aircrew life support systems which provide an optimal degree of protection against the various stresses. However, development of computer controlled anti-G valves and breathing regulators, advances in garment technology, and the Gz stress and altitude extremes for which protection is required, makes the experimental test and validation of the systems more problematic.

Given the current environment of funding restrictions, increasing concerns regarding the short and long term hazards of acceleration and altitude exposure, and the increasing limitations imposed by ethics and human-use committees, the need for accurate models of the human response to these stresses and the efficacy of the life support systems, has become more critical. Both first principle and empirical models should be able to reduce experiment costs, minimize the exposure of test subjects to hazardous conditions, predict responses to stresses not available in experimental test facilities, and aid in predicting the short- and long-term risks associated with human experimentation as well as operational exposures.

The physiological response to high levels of negative or positive acceleration is, to a large extent, governed by the biomechanical responses of the various tissues. However, the autoregulatory mechanisms responsible for maintaining homeostasis, especially as regards blood pressure, play a critical role if the acceleration stresses last more than a few seconds. The modeling and simulation effort coordinated by DCIEM has focused on the development of rigourous 1-D finite element models of the stresses and strains in the heart during Gz exposure [6], 1-D lumped parameter models of the pressures and flows in the systemic [7] and cerebral circulations [2], along with extensive work on data driven empirical models of the physiological respones to Gz and life support equipment inflation protocols [3, 4, 5].

The body's ability to detect rapid changes in systemic blood pressure, and invoke various responses to change the capacitance and resistance of the blood vessels, as well as the rate and efficacy of the pumping heart, allows the body to adapt to a wide range of postures and exercise states. The abnormal acceleration, i.e., greater than $\pm$ 1 Gz, experienced by pilots in high performance aircraft, results in intense activation of the blood pressure control sys-

Papers presented at the RTO HFM Specialists' Meeting on "Models for Aircrew Safety Assessment: Uses, Limitations and Requirements", held in Ohio, USA, 26-28 October 1998, and published in RTO MP-20.

tem, which may have a benefical or a negative effect on the ability of the individual to tolerate the dynamic Gz environment.

This paper describes some preliminary work in developing models of the neural control of the resistance and capacitance of blood vessels.

3 Methods

Given the complexity of the baroreceptor system that regulates blood pressure in humans, there are numerous choices at what hierarchical level to model such a system. One approach is to use an empirical transfer function describing the relationship between the transmural pressure in the carotid artery and the systemic blood pressure. However, empirical models were developed to analyze the cardiovascular controls systems for humans in a 1 Gz environment. One motivation for modeling the baroreceptor system was to examine the effect of the hydrostatic pressure gradient that develops along the carotid baroreceptor in a high +Gz environment.

A modeling approach was chosen that allows a rigorous hierarchical approach to the baroregulation systems, enabling the incorporation of sub-models including the energy transformation in the mitochondria of the nerve cells, the action potential generation in the nerves of the carotid baroreceptor, the integrated signal processing and effector response of the central nervous system, involving tens of thousands of interconnected nerves, and the effector end-organs.

3.1 GENESIS

A considerable effort was undertaken to determine a modeling framework existed which would allow for this hierarchical modeling effort, without an overwhelming level of code development. Over the last decade the computational neuroscience community has been developing tools that address this problem, at least with respect to the nervous system. It was decided that the starting point for the development of a model of the baroregulation system would be one of the public domain packages extensively used by this community. Depending on the flexibility of the systems, these packages may allow the incorporation of the other modeling efforts under the umbrella of the computatational neuroscience software.

The GEneral NEural Simulation System (GENESIS) system was chosen for the development environment [1]. This freely available, public domain software has been under development at Caltech since 1985.

GENESIS was developed as a means of constructing biologically realistic neuronal simulations. The developers of GENESIS wanted a system that could address the problems of computational neuroscience at many levels of detail (i.e., parts of a neuron to many, many neurons) and most importantly, be open-ended and extensible (i.e., allow the inclusion of new software modules, including cardiovascular models). A key aspect of GENESIS that enables these desired features is the object-oriented approach. Simulations are constructed of modules which can perform well-defined functions and have a standardized method of communication. The level of detail, i.e., the hierarchical level which one is modeling, is determined by the detail that is incorporated in the modules. Modules can be combined in any fashion required and the level of detail can vary from module to module. The object-orientated design allows for the incorporation of new custom design models to extend GENESIS to incorporate software developed from the other modeling efforts at DCIEM.

GENESIS models are written in an interpreted object-oriented scripting language, similar to object PERL. Currently only an X-Windows/UNIX version of the software is available, though the underlying code is C/C++, so porting to the Windows95/NT environment is being considered. A parallellized version is available which allows for the use of numerous network based computers for the simulation. One major advantage of GENESIS is the flexible, easily programmed graphical user interface and plotting capabilities, which allow rapid investigation of the effects of changing model parameters.

3.2 A baroreceptor nerve

Baroreceptors are nerve endings embedded in blood vessesls, most abundant in the walls of the internal carotid artery and the carotid sinus. They are highly sensitive to the stretching of vessel walls. With changes in the transmural pressure across the arterial wall, the action potential generation rate or firing rate of the nerves changes. An increase in the action potential activity will inhibit the vasoconstrictor center in the medulla, reducing the tonic outflow of nerve impulses to the effector organs, including peripheral blood vessels and the heart. The increased vasodilation of the blood vessels and the

decreased heart rate and stroke volume will in turn reduce the systemic blood pressure and the pressure in the carotid sinus.

3.3 The nerves of the carotid baroreceptor

In order to model the effect of a pressure induced strain on the properties of the baroreceptor nerve, an equivalent electrical circuit model of the nerve membrane was developed. Neuronal membranes have properties of capacitance, resistance, and voltage sources. These passive properties define how electrical impulses are transmitted along the length of the nerve. In addition to these passive properties, neuronal membranes exhibit active properties, that are voltage or chemical agent dependent, and allow the nerves to transmit information over long distances via the initiation of action potentials.

Figure 1[1] shows the equivalent electrical circuit of one finite section of the membrane of a basic barorecptor nerve. V_m represents the membrane potential. As the conducting ionic solutions inside and outside of the cell are separated by the cell membrane, the compartment acts as a capacitor, which is charged or discharged by the current flowing into or out of the cell from adjacent segments of the nerve or across the cell membrane, or by leakage currents modulated by the strain induced in the membrane.

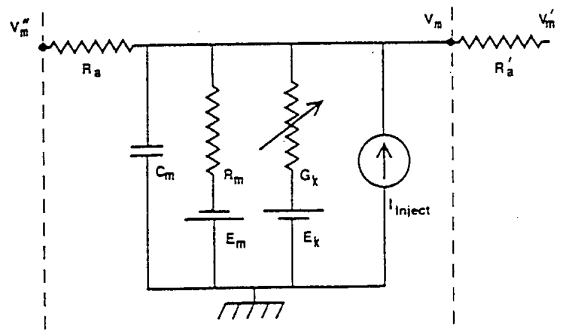

Figure 1. *Equivalent circuit model of a baroreceptor nerve*

The G_k term represents all of the various ionic conductances that give individual neurons and different neuron types their unique computational properties. Differences in the concentration of different ionic species on the inside and outside of the nerve membrane, result in a charge displacement, which in turn creates a voltage difference opposed to the flow. The fixed portion of the membrane conductance is represented by the term R_m, and is a function of the leakage current, which for most nerves is a constant.

The complexity of the model can be increased by splitting the general conductance term G_k into two components representing the flow of sodium and potassium ions. The conductances for these two predominant ions, G_K and G_{Na}, are complex functions of the membrane voltage and time, and are critical in the development of action potentials.

The deformation of the nerves embedded in the deforming arterial wall results in an increase in a strain dependent leakage current in the nerve membrane. The changes in the leakage current will in-turn change the action potential firing patterns of the nerve. The highly nonlinear response of the arterial wall will be reflected in the pattern of changes in the leakage current, and thus the firing rate.

The equivalent circuit model shown in Figure 1 can be modeled with the differential equation [1]:

$$C_m \frac{dV_m}{dt} = \frac{(E_m - V_m)}{R_m} + \sum_k [(E_k - V_m)G_k] + \frac{(V'_m - V_m)}{R'_a} + \frac{(V''_m - V_m)}{R_a} + I$$

The leakage current, I_{leak}, is in turn a complex function of the transmural pressure P across the wall of the carotid baroreceptor, i.e,

$$I_{leak} = f(P, dP/dt) \tag{1}$$

This simple model of the baroreceptor nerve forms the basic building block to investigate a number of different physiological responses, as I_{leak} can be related to changes in the Gz environment. There are several different types of nerves in the baroreceptor, distinguished by the different firing patterns with changes in transmural pressure, as well as the speed of the action potential propogation to the brain stem neurons. The blood pressure, or more precisely, the transmural pressure across the wall of the carotid artery at the level of the carotid baroreceptor is a complex function of time, posture, and Gz forces, i.e.,

$$P = f(t, Gz(t), \alpha(t)) \tag{2}$$

where α is the angle of the deviation of the body from the horizontal axis. In addition, P is function of external influences on the systemic circulation, such as high levels of positive pressure applied at the mouth and nose, and external counter-pressure applied to the legs and abdominal areas. Under the stress imposed by the transmural pressure gradient across the carotid arterial wall, the tissue in turn will deform in a complex frequency and time dependent manner. Models of both the deformation of the carotid tissue, and the deformation of the nerve cell membrane will have to be incorporated into the simulation.

We can extend the model by incorporating the interaction between the strain in the wall in the carotid artery and the strain in the membrane that evokes the leakage current and the effects of the viscoelastic properties of the carotid wall tissue and the neural membrane, including time-dependent relaxation and hysterisis. These may be used to explain some of the more complex firing pattern responses of individual carotid nerves.

3.4 Response to variable pressure

There are hundreds of different individual nerve endings in a human carotid baroreceptor. The threshold firing of theses nerves is pressure dependent, with various sub-populations of nerves acting in different ways to both absolute, relative, and time dependent pressure changes.

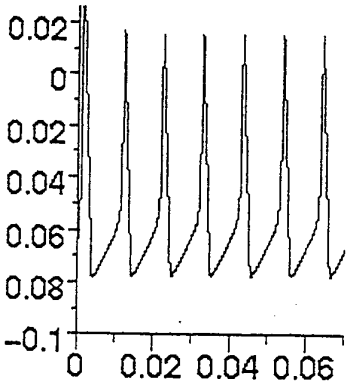

Figure 2. *Firing pattern of a carotid baroreceptor nerve at 1 Gz.*

A simple application of the equivalent circuit model can demonstrate the complexity of the Gz environment. The carotid baroreceptor extends along the carotid artery for approximately 1 cm. In a normal 1 Gz environment, even in a upright posture, the pressure gradient along the carotid baroreceptor will be less than 1 mmHg. However, at 10 Gz, as a result of the hydrostatic effects alone, and along with a change in the absolute transmural pressure, there is now a gradient of transmural pressure along carotid baroreceptor of approximately 10 mmHg. We used our model described above to examine the firing patterns of a nerve during 1 Gz and 10 Gz exposures.

Figure 2 shows the identical firing pattern of two nerves at opposite ends of the carotid baroreceptor in a 1 Gz environment. The input to the higher processing centres in the brain stem is identical.

Figure 3a shows shows the firing pattern from the nerve in the lower portion of the baroreceptor during exposure to 10 Gz. Figure 3b shows the firing pattern from a similar nerve in that portion of the carotid baroreceptor closer to the brain. The transmural pressure at this point in the carotid artery is such that the nerve has ceased to generate any action potentials, as the leakage current has dropped below a threshold.

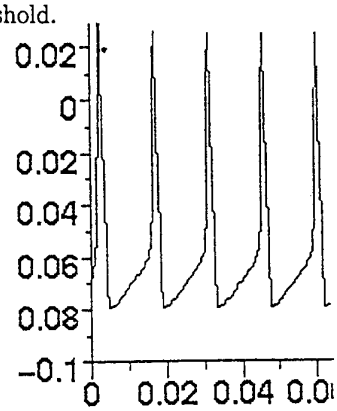

Figure 3a. *Firing pattern of a carotid baroreceptor nerve in the lower part of the carotid baroreceptor during high Gz exposure.*

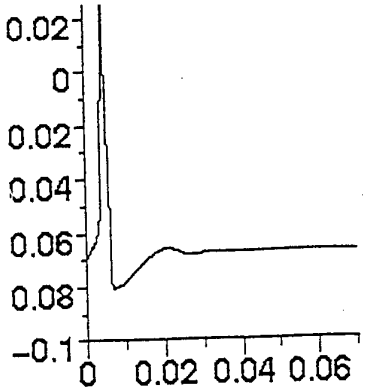

Figure 3b. *Firing pattern of a carotid baroreceptor nerve in the upper portion of the carotid baroreceptor during high Gz exposure.*

The integration of the total signal output of the carotid baroreceptor is done in the brainstem by a

number of different processing centers. A system, evolved to deal with the summed output behaviour of a wide variety of nerves responding in the 1 Gz environment, may be substantially disrupted by the effect seen in Figures 3a and 3b. Thus, the overall effector organ response calculated by the brain stem processing centers may in turn, be substantially different.

4 Discussion

In this preliminary model only a single nerve of the carotid baroreceptor sensory structure has been modeled. In the future we plan to develop a comprehensive model of the integrated response of the large population of nerves that are embedded in the carotid baroreceptor organ, the transmission of the stimulus information to the central nervous system, the integration of the sensory output of the carotid baroreceptor with other sensory input, including chemoreceptors, models of the effector nerves providing input to the peripheral blood vessels and the heart, and the response of these end organs.

An ongoing process is the integration of all of our modeling efforts into the development of a comprehensive simulation package, to provide a tool for the design and simulation of advanced aircrew life support systems.

References

[1] Bower JM, Beeman D. The Book of Genesis. TELOS 1997.

[2] Cirovic S, Walsh C, Fraser WD. A model of cerebral blood flow during sustained acceleration. In: Models for aircrew safety assessment: uses, limitations and requirements. NATO 1998, 1998; .

[3] Fraser WD, Kapps A, Askari V, Lu Z. A physiological modeling data analysis toolbox for the analysis of acceleration data. In: Models for aircrew safety assessment: uses, limitations and requirements. NATO 1998, 1998; .

[4] Fraser WD, Kapps A, Lu Z, Askari V. Modelling of the physiological respones to non-linear g-suit and positive pressure breathing schedules. In: Models for aircrew safety assessment: uses, limitations and requirements. NATO 1998, 1998;

[5] Kapps A, Fraser WD. Linear and nonlinear models of the physiological responses to negative-to-positive gz transitions. In: Models for aircrew safety assessment: uses, limitations and requirements. NATO 1998, 1998; .

[6] Tabarrok B, Behdinan K, Fraser WD. Effect of high +gz accelerations on the left ventricle. In: Models for aircrew safety assessment: uses, limitations and requirements. NATO 1998, 1998; .

[7] Walsh C, Cirovic S, Fraser WD. A model of cardiovascular performance during sustained acceleration. In: Models for aircrew safety assessment: uses, limitations and requirements. NATO 1998, 1998; .

Modeling of the Physiological Responses to Non-linear G-suit and Positive Pressure Breathing Schedules

W. D. Fraser
Z. Lu*
V. Askari*
A. Kapps*

Defence and Civil Institute of Environmental Medicine (DCIEM)
1133 Sheppard Avenue West, Toronto, Ontario M3M 3B9 Canada

* Engineering Services Inc. (ESI)
5 King's College Road, Toronto, Ontario M5S 3G8 Canada

1. SUMMARY

Heart level blood pressure responses to G-suit pressures (2~8 psi) with and without Positive Pressure Breathing (5~60 mm Hg) at +1Gz were investigated in this paper for six test subjects. Various models were developed and tested to simulate these responses. The results show that a single-zero, two-pole, output-error model is suitable for characterizing the blood pressure responses to G-suit and Positive Pressure Breathing (PPB) pressures. A single-input model is used for the case of G-suit pressure with and without synchronized PPB, whereas a double-input model is used for the case of G-suit pressure with asynchronic PPB. The suitability of the models developed to high +Gz environment is investigated based on the data from a prior centrifuge test of one subject. Special dynamic indices are used to quantify the characteristics of the blood pressure responses. Significant variations in the dynamic indices of individual subjects and the same subject observed at different time instances are seen. These variations indicate that a fixed standard G-suit pressure schedule might not necessarily be capable of providing adequate Anti-G protection for all subjects and even for the same subject at different time instances. The models developed in this paper can be used in an adaptive feedback control system for real-time identification and update of subjects' Anti-G protection requirements. Consequently, the G-suit pressures can be adjusted based on these models to provide most adequate Anti-G protections and compensate the variations in subject's physiological state.

LIST OF SYMBOLS

Gs	static gain
PO	percentage of overshoot
Tr	rise time
Tp	peak time
Ts	settling time
Fn	resonant frequency
Fc	cut off frequency
Fq	Nyquist frequency

2. INTRODUCTION

Due to large differences and irregularities in physiological responses to +Gz stress and G-suit pressure, the protection provided by a standard pressure schedule could be sub-optimal and even unsuitable for some pilots. An effective way to solve this problem is to adjust G-suit pressure schedules based on the physiological status of each individual subject. Modern computer and sensor technologies enable us to consider the development of a real-time controller aimed at enhancing the performance of existing standard Anti-G systems.

To design a real-time G-suit pressure controller based on biofeedback, a model of the system controlled is typically required. As shown in Figure 1, such a model would reflect the relationship between system inputs (G-suit and PPB pressures) and system outputs (physiological variables). For instance, eye-level blood pressure can be regarded as a controlled physiological variable, and G-suit and PPB pressures adjusted so that eye-level blood pressure is maintained around the required values at different levels of Gz. In such a case, knowledge regarding the eye-level blood pressure response to G-suit pressure is essential for designing a suitable Anti-G controller. Unfortunately, very little work has been done on modeling of blood pressure responses to G-suit and PPB pressures.

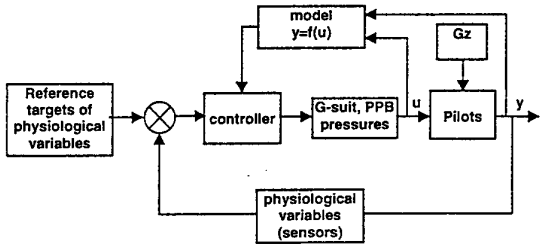

Figure 1. Schematic diagram of a biofeedback based G-suit pressure control system

There exist two general approaches to deriving a mathematical model of a dynamic system. Both methods are valid for the design of a real-time Anti-G controller. The major effort in the first approach is to identify fundamental physical laws that govern the dynamic behavior of a system in question. These laws are usually expressed through a set of differential equations. The models derived using this approach are easy to understand and provide an insight into the dynamic behavior of the systems. However, since the human body is a very complicated biological system, it is extremely difficult to

Papers presented at the RTO HFM Specialists' Meeting on "Models for Aircrew Safety Assessment: Uses, Limitations and Requirements", held in Ohio, USA, 26-28 October 1998, and published in RTO MP-20.

obtain such a model. The other approach is to use *system identification techniques* based on observed **input-output** data for the system in question. The major effort in this latter approach is to find a proper shape of parameterized equations that are capable of adequately mapping the system inputs into its outputs. In this work, the latter method is used to establish the system model.

3. MATERIALS

3.1 Subjects

Six subjects (two females and four males) with mean age of 35 ± 3.7 years, height of 171.9 ± 11.5 cm, and weight of 73.1 ± 16.0 kg participated in the study. All subjects were members of the DCIEM Acceleration Team (A-Team) and passed DCIEM medical examinations that included a full cardiovascular test required by the DCIEM Human Subjects Ethics Committee for the participation in G-suit and PPB studies. Three different sizes of STING[1] Anti-G suit (small, medium, and large) were used to ensure proper individual fit.

3.2 Experimental Setup

Figure 2 shows the experimental setup. Subjects were placed in a seated (15^0 seatback angle) relaxed position and wore the STING Anti-G suit. The subjects were exposed to three different pressure categories:

(i) G-suit pressure without PPB, the pressure varied from 2 to 8 psi with onset rates from 0.3 to 3 psi/sec;

(ii) G-suit pressure (2~8 psi) with synchronized[2] PPB (5~60 mm Hg); and

(iii) G-suit pressure (2~8 psi) with asynchronic[3] PPB, and different ratios between PPB and G-suit pressures (1:5 to 1:2).

Each category included five pressure profiles: step (square wave), ramp, pulse, sinusoidal, and random inputs. Four subjects completed three categories of pressure profiles, one subject completed categories 1 and 3, and one subject completed category 1.

Figure 2. Ground test experimental setup

[1] Sustained Tolerance INcreased G (STING).

[2] G-suit and PPB were controlled by a single valve, and PPB pressure was proportional to G-suit pressure.

[3] G-suit and PPB were controlled by two separate valves.

3.3 Physiological Sensors

The recorded parameters in this set of experiments were heart-level blood pressure, ECG, respiratory rate, G-suit and PPB pressures. Height, weight, and the distance between heart and eye levels were also recorded for each test subject. An arterial volume clamp plethysmograph (Finapres, Ohmeda Inc.) was used for continuous monitoring of blood pressures. The heartbeat rate and respiratory rate were recorded using a three-lead electrocardiogram and Respitrace devices, respectively. Finally, the G-suit and PPB pressures were monitored using two customized pressure transducers (Motorola pressure transducer MPX10 and MPX100).

4. METHODS

A dynamic system model can be expressed in three domains: continuous-time domain, frequency domain, and discrete-time domain. Since it is straightforward to implement discrete-time models on a computer system, a discrete-time model is used in this work.

A discrete-time model can have several different structures, such as ARX, ARMAX, Output Error (OE) and Box-Jenkins (BJ). These structures can be formulated in a general form as proposed in [1]:

$$A(q^{-1})y(k) = \frac{B(q^{-1})}{F(q^{-1})}u(k-n) + \frac{C(q^{-1})}{D(q^{-1})}e(k) \qquad (1)$$

where $y(k)$, $u(k)$, and $e(k)$ are the system output, input and disturbance respectively. k represents the time at k-th sampling moment. q^{-1} is the delay operator defined as follows: $q^{-1}y(k) = y(k-1)$. n is the time delay in the system output. In our case, the output is a subject's blood pressure, the controlled inputs are G-suit and PPB pressures, the disturbances are all (uncontrollable) factors that might influence the blood pressure, other than the control inputs.

Four different models (ARX, ARMAX, OE, and BJ) with various orders and delays were attempted, and their performance was tested with respect to various reference factors, such as robustness to the noise in data, mean square fit (an index quantifying the model errors), pole-zero cancellations, and residuals of the models. Finally, an Output-Error (OE) model with a single-zero, two-poles and one-delay was selected as the most suitable. The general shape of OE models is given as follows:

$$y(k) = \frac{b_1 + b_2 q^{-1}}{1 + a_1 q^{-1} + a_2 q^{-2}} u(k-1) + e(k) \qquad (2)$$

For each individual subject, the model parameters b_1, b_2, a_1 and a_2 were identified using different input (G-suit and PPB) combinations. Time-domain and frequency-domain characteristics were also examined. The sampling rate of the data in model identification process was 5 Hz.

5. RESULTS

5.1 Blood Pressure Responses to G-suit Pressure without PPB

In this set of experiments, G-suit pressure was applied without PPB. Figure 3 shows a typical systolic blood pressure (sbp) response of a subject to a step input of G-

suit pressure. The typical response behavior can be described as a two-phase dynamic process:

- *Phase 1*, a transient phase that includes an ascending course with 5~6 seconds rise time, followed by a descending course;
- *Phase 2*, a slowly changing convergence course to a steady pressure level.

It is understood that the inflation of G-suit causes a transitory displacement of blood volume (about 250 ml) from the peripheral vessels to the chest (a temporary increase in venous return) [2]. This displacement increases the effective filling pressure of the right ventricle, and induces an increase in blood pressure and cardiac output. While the equilibrium is gradually restored, the blood pressure is decreasing. On the other hand, as G-suit pressure increases the resistance to the inflow of blood, the blood pressure changes accordingly to maintain a certain level of cardiac output. These two mechanisms: (i) displacement of blood volume to the chest and (ii) an increase in blood vessel resistance may explain the two-phase behavior of blood pressure response to G-suit pressure.

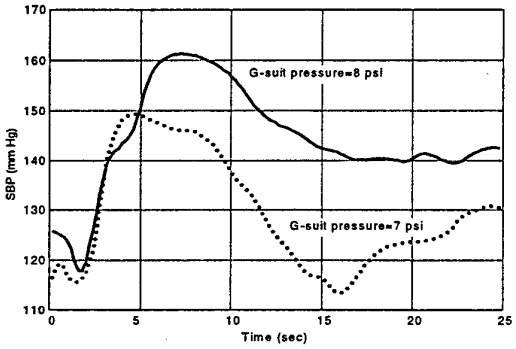

Figure 3. Typical responses of systolic blood pressure to step inputs of G-suit pressure

Table 1. Model parameters (no PPB)

subject	Number of inputs, G-suit pressure range	mean square fit (mm Hg)	model parameters: b_1, b_2, a_1, a_2
1	24, 2~8 psi	9.1	0.2057, -0.1905, -1.948, 0.9540
2	24, 2~8 psi	8.7	0.3218, -0.3115, -1.9394, 0.9431
3	24, 2~8 psi	7.2	0.2191, -0.2160, -1.918, 0.9225
4	17, 2~8 psi	6.6	0.3347 -0.3286 -1.9392 0.9448
5	21, 2~8 psi	7.5	0.2915 -0.2876 -1.9197 0.9228
6	9, 4~8 psi	8.1	0.5403 -0.5382 -1.8827 0.8855

The observed blood pressure responses from different subjects were quite different in terms of static gain, overshoot percentage and rise time. Based on the responses of systolic blood pressure to G-suit pressures ranging from 2 to 8 psi, a set of model parameters was obtained for each subject. Following the definitions in Equation (2), the model parameters are given in Table 1. The dynamic indices of the models are listed in Table 2 based on the definition of these indices in Figure 4. Figures 4 and 5 show typical step and frequency responses of the model.

Table 2. Dynamic indices of the model (no PPB)

subject	Gs	PO (%)	Tr sec	Tp sec	Ts sec	Fn Hz	Fc Hz	Fq Hz
1	2.5	60	2.5	6	26	0.06	0.11	2.5
2	2.9	61	2.3	5.8	24	0.05	0.1	2.5
3	0.8	180	0.8	4	13	0.06	0.2	2.5
4	1.3	150	1.1	4	17	0.06	0.3	2.5
5	1.2	132	1.0	4.5	20	0.05	0.15	2.5
6	1.3	180	0.8	4	22	0.06	0.18	2.5

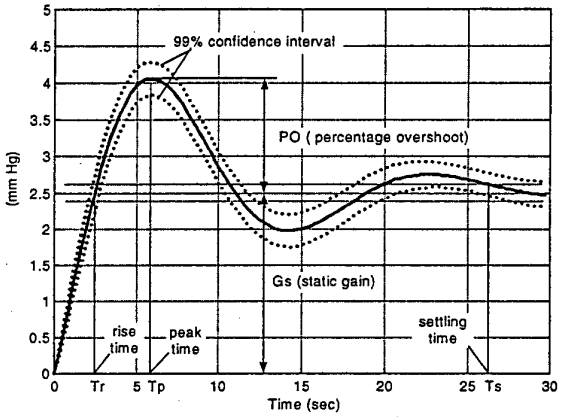

Figure 4. Step response of the systolic blood pressure model to G-suit pressure

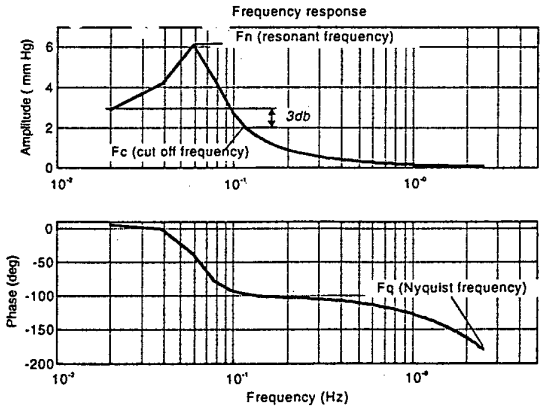

Figure 5. Frequency response of the model

It can be seen from Table 2 that the first two subjects have large static gain, relatively small overshoot and long rise time, whereas the other four have high overshoot, small static gain and short rise time. The frequency constants are quite similar for all the subjects. The subjects possess the

same resonant frequency of 0.06 Hz, which is also similar to the resonant frequency found in the responses of eye-level blood pressure to +Gz in [3].

5.2 Blood Pressure Response to G-suit Pressure with PPB

Two different types of electronic Anti-G valves were used in this set of experiments: (i) an NGL valve designed by Normalair Garrett Ltd., and ii) a SAMCAV valve designed by ESI. The NGL valve initiates PPB after G-suit pressure reaches 4 psi. The ratio of PPB to G-suit pressure is fixed. Therefore, one NGL valve can only produce a nearly synchronized PPB that is strongly correlated with G-suit pressure. To generate asynchronic PPB, two electronic SAMCAV valves were used to control G-suit and PPB pressures independently. In the following two subsections we discuss the responses to synchronized and asynchronic PPB schedules.

5.2.1 Model for synchronized PPB

In general, the model of Equation (2) for a two-input system can be written as follows:

$$y(k) = \frac{B_1(q^{-1})}{A_1(q^{-1})}u_1(k-1) + \frac{B_2(q^{-1})}{A_2(q^{-1})}u_2(k-1) + e(k) \qquad (3)$$

where u_1 is G-suit pressure, u_2 is PPB pressure. B_1, A_1, B_2, and A_2 are coefficient vectors and have the same structure as in Equation (2). Since synchronized PPB pressure can be expressed as a linear function of G-suit pressure, such as $u_2 = k * u_1$, Equation (3) can be re-written as follows:

$$y(k) = \left\{\frac{B_1(q^{-1})}{A_1(q^{-1})} + k\frac{B_2(q^{-1})}{A_2(q^{-1})}\right\}u_1(k-1) + e(k)$$

$$= \frac{B_e(q^{-1})}{A_e(q^{-1})}u_1(k-1) + e(k). \qquad (4)$$

Since the system (4) has only one independent input (G-suit pressure), a single-input model defined by $B_e(q^{-1})$ and $A_e(q^{-1})$ can be used to simulate the blood pressure responses. In such a case, the model maps the total protection input (generated by G-suit and PPB pressures) into one output (blood pressure). Figure 6 presents systolic blood pressure responses (for the same subject; similar to in Figure 3) to step inputs of G-suit pressure with PPB using NGL valve.

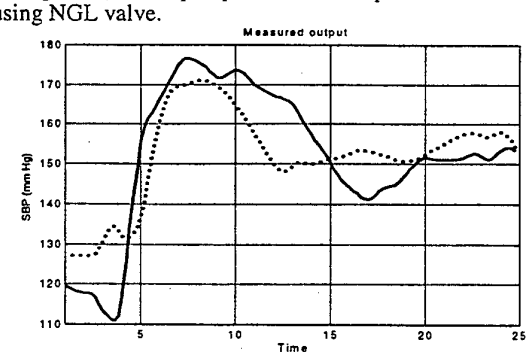

Figure 6. Two responses of systolic blood pressure at heart level to step inputs of G-suit pressure of 8 psi with PPB of 38 mmHg

Table 3. Model parameters (with synchronized PPB)

subject	number of inputs, G-suit pressures, PPB pressures	mean square fit (mm Hg)	model coefficients: b_1, b_2, a_1, a_2
1	18, 5~8 psi, 15~38 mm Hg	7.7	0.5159, -0.4807, -1.8916, 0.9028
3	9, 5~8 psi, 15~38 mm Hg	8.5	1.2524, -1.2152, -1.6847, 0.7086
4	6, 5~7 psi, 15~29 mm Hg	6.9	1.7082, -1.6714, -1.7004, 0.7092
5	17, 5~6 psi, 15~25 mm Hg	8.8	1.8016 -1.7557 -1.5463 0.5545

Table 4. Dynamic indices of the model (with synchronized PPB)

subject	Gs	PO (%)	Tr sec	Tp sec	Ts sec	Fn Hz	Fc Hz	Fq Hz
1	3.3	50	1.7	3.4	25	0.08	0.18	2.5
3	1.8	100	0.5	1.5	15	0.12	0.65	2.5
4	4.3	35	0.7	2.1	12	0.08	0.5	2.5
5	5	0	1.		10		0.2	2.5

The model parameters and dynamic indices for each subject are summarized in Tables 3 and 4. With PPB, the blood pressure responses for all the subjects have higher static gain and faster response speed than without PPB (refer to Table 2). These two features are clearly shown in Figure 7. Since the PPB pressure is directly applied to the chest to raise heart-level blood pressure, higher and faster responses are anticipated.

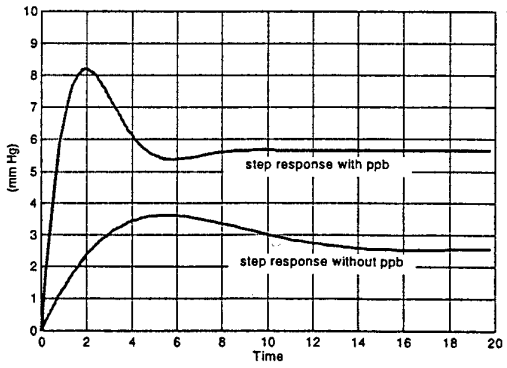

Figure 7. Step responses of the models with and without PPB

5.2.2 Model for asynchronic G-suit Pressure and PPB

A single-input model (4) cannot predict a subject's physiological response if the inputs are not correlated. In general, a separate model for each input is required to predict the total response to the independent inputs. To accomplish this task, the inputs should be generated in

such a way that they are not correlated with each other. For this purpose, two SAMCAV valves were used to control G-suit and PPB pressures independently. In this set of experiments, the profile of G-suit pressure consisted of a series of square waves with periods changing randomly from 2 to 5 seconds. The amplitude of the square waves varied from 1 to 4 psi. The profile of PPB was a step input with a plateau level of 25 mmHg.

A two-input model given by Equation (3) was used. Typical responses to each independent input are presented in Figures 8 and 9. The model parameters for each subject are presented in Table 5. Figure 8 shows that the response to the G-suit pressure raises slowly, and there exists no overshoot. As described in subsection 5.1, the displacement of blood volume to the chest by G-suit pressure might be the main factor contributing to the initial increase and overshoot in blood pressure. However, the displacement would be greatly reduced by the counteracting pressure in the lungs produced by PPB. A comparison of Figures 4 and 8 shows that the static gain of the model with PPB is much higher than that without PPB. This affirms the well-known fact that the protective effect of G-suit pressure is expected to be a function of PPB; it increases as PPB increases.

On the other hand, Figure 9 shows that PPB causes a rapid increase in the blood pressure only in the first few seconds following its application, and then its effect gradually vanishes. Overall, the net gain in the blood pressure will depend on a subject's physiological responses to both G-suit and PPB pressures. Because of the counteracting functions of G-suit and PPB, it can be anticipated that for a certain level of G-suit pressure, there exists an optimal level of PPB such that the gain in blood pressure is maximized.

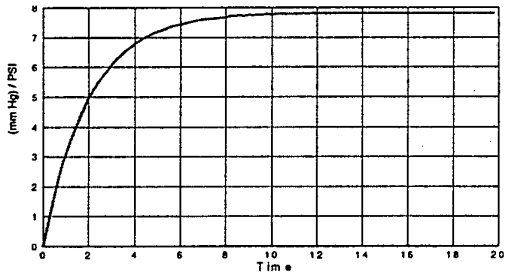

Figure 8. Step response of SBP model to G-suit pressure input with constant PPB of 25 mmHg

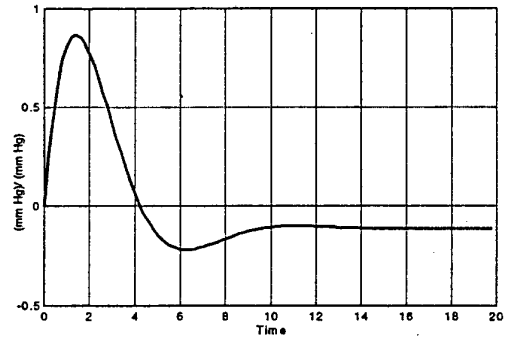

Figure 9. Step response of SBP model to PPB pressure input without G-suit pressure

Table 5. Model parameters (asynchronic PPB)

subject	Number of inputs, G-suit pressure, PPB pressure	mean square fit (mm Hg)	model parameters: $b_{11}, b_{21}, a_{11}, a_{21}$ for input 1 (G-suit) $b_{11}, b_{21}, a_{11}, a_{21}$ for input 2 (PPB)
1	1, 1~4 psi, 25 mm Hg	7.3	2.06, -0.61, 0.01, -0.82 0.26 -0.26, -1.81 0.83
4	1, 1~4 psi, 25 mm Hg	5.4	5.45, -4.49, -0.18, -0.67 0.34, -0.32, 1.66, 0.71
5	1, 1~4 psi, 25 mm Hg	7.1	3.09, -1.70, -0.26, 0.12 0.34, -0.31, -1.72, 0.77
6	1, 1~4 psi, 25 mm Hg	5.0	2.56, -1.41, -0.72, 0.32 0.35, -0.33, -1.71, 0.75

The responses to the G-suit pressure with a constant PPB were quite different from those to G-suit pressure without PPB (refer to Figure 4). As concluded from the previous work (e.g., [4]), the influence of G-suit and PPB pressures on the heart function are coupled and not additive. We can express blood pressure responses in a general form as a function of G-suit and PPB pressures:

$$bp = f(G_suit, PPB) \tag{4}$$

$$\Delta bp = \frac{\partial f}{\partial G_suit}\bigg|_{\substack{PPB=\\ const}} \times \Delta G_suit + \frac{\partial f}{\partial PPB}\bigg|_{\substack{G_suit=\\ const}} \times \Delta PPB \tag{5}$$

Considering the input profiles in the experiments, where PPB is constant and G-suit pressure varies, we can see that the model response shown in Figure 8 only represents a linearized relationship of the first term on the right-hand side of Equation (5) about the point $PPB = 25\ mmHg$. To establish the entire model (3), we have to conduct more experiments with different input profiles, such as varying G-suit pressure at different level of PPB and varying PPB at different level of G-suit pressure.

5.3 Comparison of Responses at +1Gz and High +Gz

The experiments described above were conducted at +1 Gz. It is important to investigate whether the similar models can be applied to the physiological responses exhibited in high Gz environment. Since one subject (subject 1) participated in a centrifuge experiment with the same G-suit (STING), we used the data from that experiment to estimate his model parameters. These parameters are shown in Table 6 to 9. The values of mean square fit (Tables 6 and 8) are quite small, which implies that the same model structure can be used to predict the blood pressure responses in high +Gz environment. By comparing the results in Tables 6-9 with the results in Table 1-4, we can see that the changes in the model parameters and dynamic indices are small. Hence, for this subject, the same model with minor revision in the parameters can be applied in a high +Gz environment.

Table 6. Model parameters (no PPB)

Subject	number of inputs, G-suit pressure, Gz	mean square fit (mm Hg)	model coefficients: b_1, b_2, a_1, a_2
1	5, 3.4~5 psi, 4.3~5 Gz	3.5	0.1312, -0.1139, -1.9554, 0.9632

Table 7. Dynamic indices of the model (no PPB)

subject	Gs	PO (%)	Tr	Tp	Ts	Fn	Fc	Fq
1	2.2	15%	2	3	15	0.13	0.24	2.5

Table 8. Model parameters (synchronized PPB)

subject	Number of inputs, G-suit pressure, PPB pressure, Gz,	mean square fit (mm Hg)	model coefficients: b_1, b_2, a_1, a_2
1	5, 5~7 psi, 17~30 mmHg, 5~6 Gz	4.9	-0.1038, 0.2877, -1.705, 0.7603

Table 9. Dynamic indices of the model (with synchronized PPB)

subject	Gs	PO (%)	Tr sec	Tp sec	Ts sec	Fn Hz	Fc Hz	Fq Hz
1	3.3	15	2.6	5.8	25	0.07	0.14	2.5

5.4 The Physiological Phenomena Observed in Blood Pressure Responses

5.4.1 Non-linearity in Blood Pressure Responses With Respect to the Level of G-suit Pressure

To find out whether there exists an inherent non-linearity in the blood pressure response with respect to the level of G-suit pressure, we categorized the experimental data into several groups according to the level of G-suit pressure. A set of model parameters was estimated for each group of data. By comparing these parameters, we can see that for some subjects, the models with relatively low G-suit pressure input have higher static gains (that is gains in Anti-G protection) than those with high-pressure inputs (Figure 10). This demonstrates that the static relationship between the blood pressure and G-suit pressure is non-linear, i.e., the amount of gain in blood pressure per each psi of G-suit pressure will gradually decrease as the G-suit pressure increases. At the same time, the blood pressure responses of some subjects have low sensitivity and, correspondingly, small gains in blood pressure to low G-suit pressures. Moreover, typical responses to low G-suit pressures undergo more fluctuations than those to high G-suit pressures.

5.4.2 Timing factor in Blood Pressure Response

The cardiovascular system is a time-varying system. To find out how subjects' responses vary with time, we classified the data with the same G-suit pressure inputs into several groups according to the time sequence at which these G-suit pressures were applied. For each group, a set of model parameters was obtained. By comparing these parameters, we could observe that in most cases the blood pressure responses to G-suit pressure profiles applied early in the experiment are lower and exhibit larger fluctuations than those applied later (see Figure 11).

If we also check the model zero-pole patterns in a z-plane (Figure 12), we can observe significant shifts in the zero-pole locations. This manifests a significant change in dynamic behavior of the system during the period from early to late G-suit inputs. If the same G-suit pressure profile is repeated at the beginning and the end of an experiment, the response to the later is usually smaller than that to the earlier (see Figure 13). These phenomena may be caused by factors such as warm up, fatigue and cardiovascular reflex functions.

5.4.3 Response Speed of Diastolic vs. Systolic Blood Pressure

It has been observed in our experiments that the response of diastolic blood pressure to the G-suit pressure is faster than systolic blood pressure (see Figure 14). Since the diastolic pressure is mainly affected by the peripheral resistance [5], which is directly increased by the inflation of G-suit, this may have contributed to the fast response of diastolic pressure.

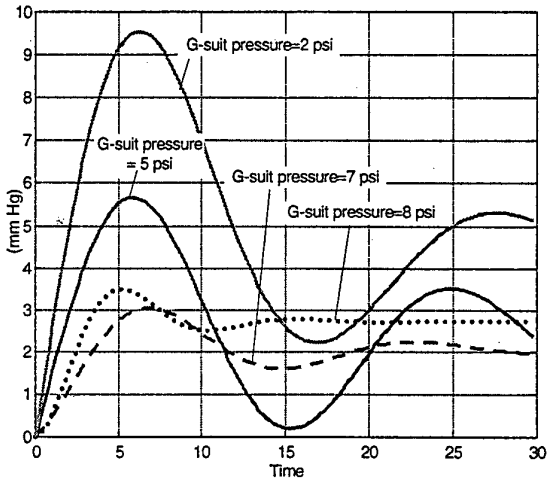

Figure 10. Step responses of the models obtained at different levels of control inputs

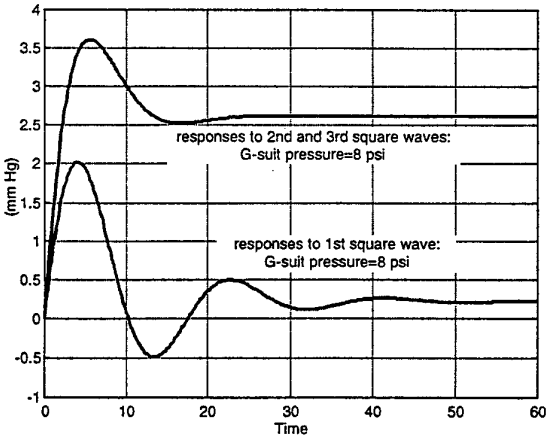

Figure 11. Responses to three square-wave profiles of G-suit pressure applied in sequence

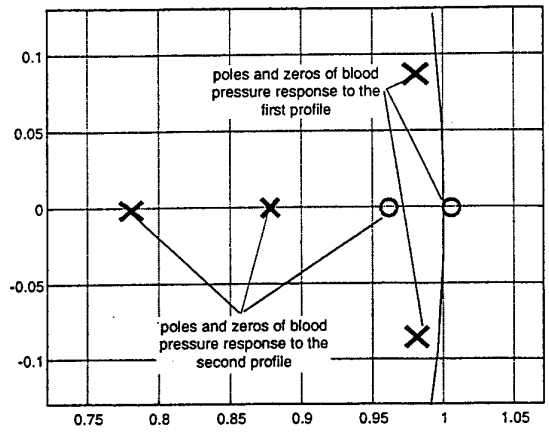

Figure 12. Poles and zeros of blood pressure responses

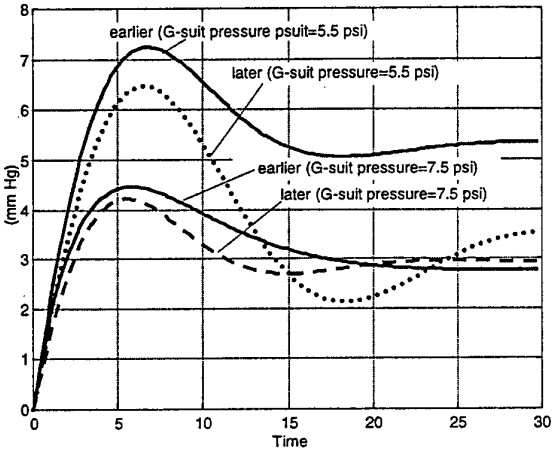

Figure 13. Response to the same G-suit pressure profiles applied at different stages of an experiment

6. DISCUSSION

The human cardiovascular system is inherently non-linear. However, certain linear models with the capability for moderately accurate prediction of physiological responses under Gz have been obtained in the past [3]. On the other hand, since there exist many factors that influence a biological system, it is unrealistic to assume that one model with fixed parameters would be either suitable for all subjects, or can be used for one subject at all time instances. Therefore, one major purpose of this work has been to identify a suitable model structure so that for each subject there would exist such a set of model parameters that the model output could match this subject's blood pressure responses under any circumstances. As long as a proper model structure is identified, its parameters can be estimated and updated in real-time within an adaptive control system framework.

In this work, four different types of model structures have been tested. In most cases, the ARX and ARMAX models have been found too 'smooth' to track physiological transition courses. The BJ model can sometimes track the responses well, yet in some cases it has produced an unstable model for the application in question. It also appears that of all the four models, BJ models are the least robust to the disturbances. Finally, the OE model has been selected as the most suitable. This model gives a reasonable tracking accuracy, and it is more stable than others. With regard to the selection of model orders, a single-zero, two-pole model has been found as sufficient in most cases. Two-zero, two-pole models may give a minor improvement in tracking transition courses, yet it may also induce oscillations in the model responses.

To further increase the model accuracy, some non-linear components may be introduced into the model. For example, to model the non-linearity between the steady level of blood pressure and G-suit pressure, a feasible way is to add a non-linear term $f(c, u)$ to Equation (2) as follows:

$$y(k)=f(c,u(k-1))\frac{b_1+b_2 q^{-1}}{1+a_1\ q^{-1}+a_2\ q^{-2}}u(k-1)+e(k), \qquad (6)$$

where c is the new set of parameters to be identified. The function $f(c,u)$ should be linear with respect to the parameter c so that the conventional identification methods, such as least-squares estimation can be applied.

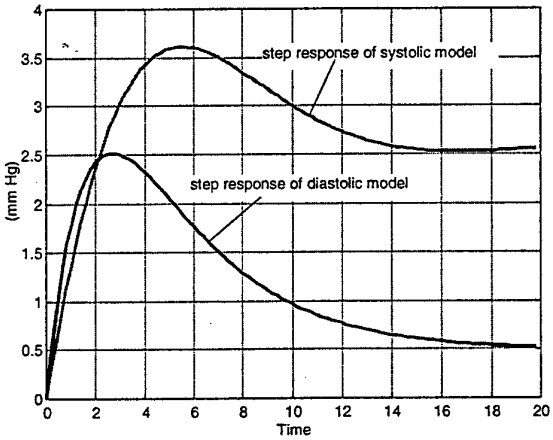

Figure 14. Step responses of the diastolic and systolic models

Since the effects of PPB and G-suit pressures on blood pressure are non-linear and not additive, it is difficult to get a true model for each of them separately. However, in practice it may often be the case that the schedule of PPB is synchronized with G-suit pressure and, therefore, only the ratio κ of PPB over G-suit pressure may be set at some optimal values κ_i. In such a case, we can express blood pressure responses as follows:

$$bp_i=f(G-suit,\kappa_i) \qquad (7)$$

$$\Delta bp_i=\left.\frac{\partial f}{\partial G_suit}\right|_{\kappa_i}\times\Delta G_suit \qquad (8)$$

A set of model parameters can be estimated for each particular value of κ_i. The sets of model parameters can be used to describe the overall model relationship. The model can be used in, for instance, a so-called 'gain scheduling controller' [6]. According to the operating conditions, such as subjects' physiological status and Gz intensity, a proper optimal κ_i and the corresponding model parameters could be chosen by the controller automatically.

Large discrepancies in the subjects' blood pressure responses have been encountered in our modeling work. Some subjects (1 and 2) have significant response to Anti-G protections ($Gs \geq 2.5$), whereas some others (subjects 3 to 6) have much less profound response ($Gs \leq 1.3$; refer to Table 1). For some subjects, the PPB pressure has a crucial influence on the blood pressure responses, such as for subjects 4 and 5. Without PPB, their static gains (and, correspondingly, G tolerance) are very low, much lower than those for subjects 1 and 2. With PPB, however, the gains increase significantly and become higher than those for subject 1 (refer to Table 4). Since G-suit pressure alone provides little protection for those subjects, PPB pressure should be initiated earlier than suggested by a standard pressure schedule. For subject 3, protection gains with and without PPB are very low. It can be expected that an optimal pressure schedule for this subject would be higher than the standard one.

It is also noted that significant changes in dynamic physiological behavior of the same subject could occur over a short time period. This atypical behavior can be compensated if a real-time Anti-G controller based on physiological sensory feedback is used. The controller would monitor changes in a subject's status online and regulate G-suit pressure and PPB to achieve the required responses. This approach has been successfully tested in our recent centrifuge experiments.

7. CONCLUSIONS

An OE model with a single-zero and two-poles has been found adequate to model the response of a subject's blood pressure to G-suit pressure with and without PPB at +1Gz. A single-input model is adequate for the case of G-suit pressure with synchronized PPB. The same model structure may also be used to simulate the responses to G-suit pressure at high Gz levels. This has been validated based on the data collected in centrifuge experiments performed on one of our test subjects. Significant variations in blood pressure responses have been found from subject to subject and for the same subject observed at different time instances.

8. REFERENCES

1. Ljung, L. "System Identification - Theory for the User", Prentice-Hall, Englewood Cliffs, N. J, 1987.
2. Gillies, J.A., "A Textbook of Aviation Physiology", Pergamon Press, 1965.
3. Gillingham, K., Freeman, J., and Mcnee, R.C., "Transfer functions for eye-level blood pressure during +Gz stress", Aviation, Space, and Environmental Medicine, November 1977, pp1026~1034.
4. Goodman, L.S., Yang, L.D., Kelso, B., and Liu, P., "Cardiovascular Effects of Varying G-suit Pressure and Coverage During +1 Gz Positive Pressure Breathing", Aviation, Space, and Environmental Medicine, Vol. 66, No. 9 September 1995, pp 829-836,
5. Rushmer, R.F., "Cardiovascular Dynamics", W. B. Saunders Company, 1976.
6. Astrom, K.J., Wittenmark, B., "Adaptive Control", Addison-Wesley Publishing Company Inc, 1995.

DCIEM 98-P-89.

A PHYSIOLOGICAL DATA ANALYSIS TOOLBOX FOR THE ANALYSIS OF ACCELERATION DATA

W. D. Fraser
V. Askari*
Z. Lu*
A. Kapps*

Defence and Civil Institute of Environmental Medicine (DCIEM)
1133 Sheppard Avenue West, Toronto, Ontario M3M 3B9 Canada

* Engineering Services Inc. (ESI)
5 King's College Road, Toronto, Ontario M5S 3G8 Canada

1. SUMMARY

As an alternative to using traditional first principle-based modeling of a protected subject's physiological responses to real-life acceleration trains (both positive and negative-to-positive Gz transitions), a nontraditional systematic approach is being designed to facilitate the evaluation and prediction of human cardiovascular responses to G-suit and Positive Pressure Breathing (PPB) pressure schedules. The purpose of this work is to develop novel improved Anti-G protection schedules optimized for individual pilots in general and push-pull protection in particular. The proposed nontraditional systematic models are based on input-output relationships supplemented by expert knowledge. Therefore, both the experimental design and physiological data processing architecture are critical in this project. Six subjects (two females and four males) participated in the initial experimental effort. Persistently excited non-linear G-suit and PPB pressure schedules, which are not direct linear functions of Gz levels, have been applied using two types of electronic valves: (i) a combined Breathing Regulator and Anti-G valve (BRAG valve)[1]; and (ii) two custom-designed electronic (SAMCAV)[2] valves. The recorded parameters were heart-level blood pressure, ECG, respiratory rate, G-suit and PPB pressures. Among other issues, this paper describes a Physiological Data Analysis Toolbox (Φ-DAT) that integrates statistical, fuzzy and linear trend investigations with higher-order spectrum analysis of the experimental data. Φ-DAT has been designed as a preprocessor of the nontraditional systematic modeling architecture and proven very efficient in establishing correlation and trend dependencies between the non-linear pressure schedules employed and responses obtained.

2. INTRODUCTION

Currently, the pressurization of anti-G-suits and positive pressure breathing (PPB) is controlled by mechanical valves that generate pressure schedules linearly dependent on momentary acceleration measurements. However, the physiological responses to acceleration trains and pressure schedules are non-linear due to time delays and complex reflex functions of the cardiovascular dynamics. Using modern microprocessor-controlled electronic valves and fast computer technologies, this project is aimed at the development of an Expert System for offline and online adaptive generation and control of Anti-G counter-measures optimized for individual pilots and groups of pilots. To develop such an Expert System, there is a need to model and predict the physiological responses of individual subjects to candidate non-linear schedules of G-suit pressure and PPB. The nontraditional systematic modeling and prediction architecture is being developed mainly based on input-output experimental relationships and, therefore, both the experimental design and physiological data processing architectures are critical. It is typically not obvious how to design acceleration experiments so that maximum amount of information on the cardiovascular dynamics is obtained using a limited number of expensive manned experiments. This paper addresses the design of such experiments, as well as a systematic approach to analyzing the experimental data.

3. METHODS

3.1 Subjects

Six subjects (two females and four males) with the mean age of 35 ± 3.7 years, height of 171.9 ± 11.5 cm, and weight of 73.1 ± 16.0 Kg participated in the study. All subjects were members of DCIEM Acceleration Team and passed DCIEM medical examinations that included a full cardiovascular test required by the Human Subjects Ethics Committee for participation in G-suit and PPB studies. Three different sizes of STING[3] suit (small, medium, and large) were used to ensure proper individual fit.

3.2 Experimental Setup and Protocol

Figure 1 shows the experimental setup for both BRAG and SAMCAV valves. For the BRAG valve, the PPB outlet pressure was a function of G-suit pressure. To achieve independent control of G-suit and PPB, two SAMCAV valves were used to control the G-suit and PPB pressure individually. In general, the experiment was designed for three different system configurations: (i) G-suit without PPB (SAMCAV valve) with pressures varying from 2 to 8 psi and onset rates of 0.4 to 3 psi/sec; (ii) G-suit with PPB (SAMCAV valves) with pressures varying from 2 to 8 psi for G-suit and 0 to 60 mmHg for PPB; and (iii) G-suit with PPB (BRAG valve) with pressures varying from 2 to 8.8 psi and the corresponding PPB varying from 0 to 51

[1] "Combined regulator and Anti-G valve" designed by Normalair-Garrett Ltd. (NGL).

[2] "Computer-controlled valve" designed by ESI in co-operation with DCIEM.

[3] Sustained Tolerance INcreased G (STING).

Papers presented at the RTO HFM Specialists' Meeting on "Models for Aircrew Safety Assessment: Uses, Limitations and Requirements", held in Ohio, USA, 26-28 October 1998, and published in RTO MP-20.

mmHg. Each subject completed 46 runs in total. Subjects were wearing STING G-suit and seated on a 15° seatback reclined chair (see Figure 2).

3.3 Physiological Measures

The parameters recorded in this set of experiments were heart-level blood pressure, ECG, respiratory rate, G-suit and PPB pressures. Each subject's height, weight, and the distance between heart-level and eye-level were also recorded. An arterial volume clamp plethysmograph (Finapres, Ohmeda Inc.) was used for continuous monitoring of heart-level blood pressure. The heart rate and respiratory rate were recorded using a single channel electrocardiogram and Respitrace system, respectively. Finally, the G-suit and PPB pressures were monitored by two customized pressure transducers (Motorola pressure transducers MPX10 and MPX100).

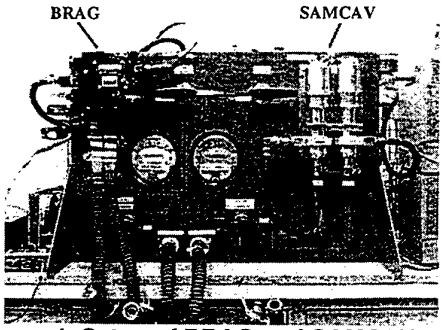

Figure 1. Setup of BRAG and SAMCAV valves

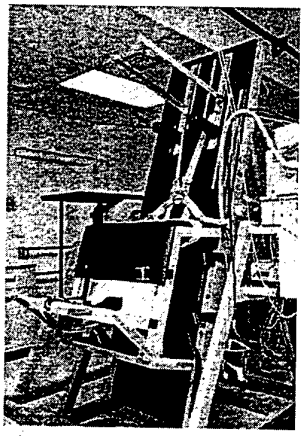

Figure 2. Layout of the experimental setup

4. EXPERIMENT DESIGN

A well-designed experiment is an efficient method of learning about the world [1]. In reality, when confronted with an identification problem, it is typically not obvious which signal to manipulate as the input and which to monitor as an output. The common-sense observation is that the output should be sensitive to changes in the input over the frequency range where the model is required to be accurate. Based on the previous work [2, 3] and the results of preparatory experiments, a protocol was designed for ground test experiments as the first run at modeling the physiological responses of individual subjects to non-linear G-suit and PPB schedules.

The design of the experimental protocol included several major steps, such as the selection of input and output signals, strategy of signal measurements, etc. In general, the choice of input signals has a very substantial influence on the data observed. The input signal determines the operating point of the system as well as the system components and modes that will be excited during the experiment. Moreover, it includes some practical aspects, such as how to condition the output signals before sampling and how to process them afterwards [4]. However, the first and most important step in the experimental design is to establish which inputs should be manipulated to excite the system and what sensors should be used to collect the output.

Figure 3 shows the G-suit pressure profiles (input signals) used in experiments[4]. Different ratios of G-suit to PPB pressures were applied in the ground-test experiments. For modeling purposes, some profiles of PPB pressures were intentionally not synchronized with the G-suit pressures to generate uncorrelated inputs. Each category of runs included five pressure profiles and their combinations: step (square wave), ramp, pulse, sinusoidal and random inputs. The periods, duration of plateaus, magnitudes, onset rates, frequencies, etc. used for the ramp and step inputs were chosen based on the previous research work [2, 3] and the results of preliminary tests conducted in the course of this project. In general, the linear dependency between the G-suit and PPB pressures would result in a set of correlated input signals, which is not a proper choice for the system identification. Finally, it should be mentioned that the safety issues and hardware limitations have been considered in the design of inputs.

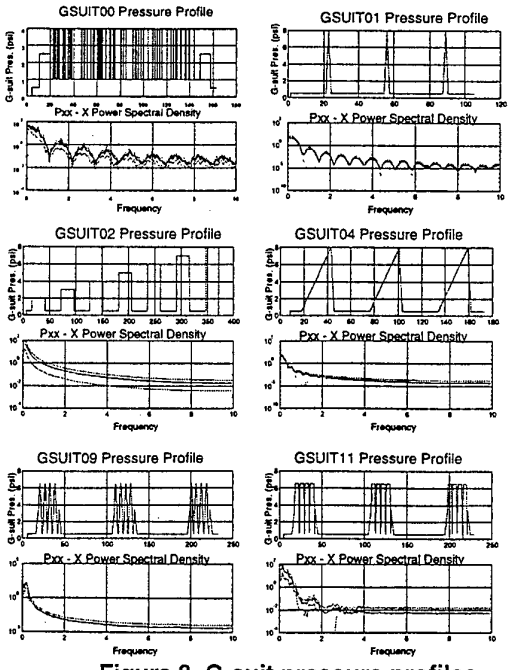

Figure 3. G-suit pressure profiles

[4] The PPB pressure profiles are the same as G-suit pressure profiles with different magnitudes and timings.

5. EXPERIMENTAL DATA ANALYSIS

One of the central features in the development of a physiological model based on input/output data is the preliminary analysis of experimental data. When the experimental data have been collected, it is not likely to be suitable for immediate use in the identification process. There might exist several possible deficiencies that should be addressed to properly prepare the data. Among those deficiencies; are the presence of high-frequency disturbances above the characteristic dynamic frequencies of the system, occasional bursts and outliers, drift and offset, and low-frequency disturbances of periodic nature.

To resolve the aforementioned problems, a systematic data processing approach has been custom designed to perform the preliminary data analysis[5]. Since the physiological responses of a subject are generated sequentially in time, they can be regarded as a time series. In general, digital or discrete signal data presented as a function of a suitable time index form a time series [5]. The time series can be either deterministic or random. If it is random, the statistical properties may or may not change with time, corresponding to nonstationary or stationary time series, respectively. Time series analysis is required whenever certain time-dependent information is to be extracted from the measured data. Time series data can be classified into different groups (e.g., linear or non-linear). The custom designed data analysis toolbox (Φ-DAT) has been used to analysis the collected data. The toolbox is written in MATLAB®[6]. and has the following features (see also Figure 4):

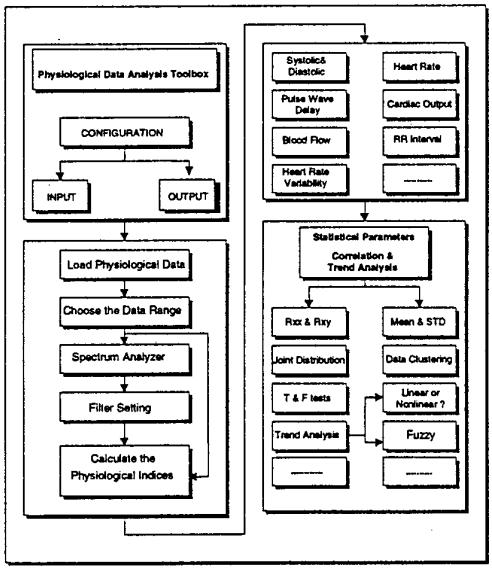

Figure 4. Data analysis toolbox structure

[5] A toolbox was written in MATLAB® to assist the user in preliminary data analysis (Physiological Data Analysis Toolbox, "*Φ-DAT*").

[6] The MathWorks Inc. 24 Prime Park Way, Natick, Mass. 01760-1500.

Loading the physiological data

The data file can be loaded by choosing the experimental data filename. All outputs for the selected data set will be loaded automatically.

Selecting the data range

To start the analysis, a set of plots will be automatically generated for the loaded data. At this stage, it is possible to choose any portion of the data for further analysis. If this step is skipped, the program will use the whole range of data for further analysis.

Calculation of heart rate and blood pressure indices

Based on the collected data (Finapres, ECG, etc.), all major physiological indices can be calculated. For example, heartbeat rate, pulse rate variability matrices, pulse wave delay (PWD), pulse wave pressure, systolic, diastolic, and mean blood pressure can be calculated based on arterial blood pressure, ECG, ear opacity, etc.

Filtering and decimating the signals

Power spectrum plots for each signal will be generated in order to show the energy and frequency contents of each signal at different frequencies. These plots will be used for selecting optimal filtering parameters. Based on the power spectra plots, a filter for smoothing the collected signals can be chosen at this stage. A Butterworth filter is currently used for filtering the data, but it is possible to select other filter types, such as Chebyshev, Elliptic, Bessel, etc. The reason for choosing the Butterworth filter is that the filter is characterized by a magnitude response that is maximally flat in the passband region and is monotonic overall [6]. Decimating the data is the next step. The decimation process filters the input data with a lowpass filter and then resamples the resulting smoothed signal at a lower rate [6]. The decimation decreases the computational time required for further data processing.

Joint distribution, trend analysis, and hystresis plots

To study the behavior of input/output signals, it is necessary to investigate the qualitative behavior of the signals. Scatter diagrams (joint distribution plots) of input/output and output/output signals reveal qualitative information about the structure of input/output dependency (e.g., linearity or non-linearity). The qualitative information contained in these plots can be used for modeling purposes. The trend analysis is used to define a quantitative approach to analyzing the scatter plots. Two types of trend analysis are considered in the toolbox: (i) fuzzy trend (fuzzy index) [7, 8]; and (ii) linear trend (linear index) [9].

A *Hysteresis plot* is conceptually similar to scatter diagrams. Hysteresis plots check the consistency of a subject's physiological response to certain pressure profiles (G-suit and PPB). In general, the narrower the plot, the more repeatable a subject's physiological response.

Statistical parameters of the calculated signals

The statistical parameters of each signal convey useful information about the system (e.g. mean, variance, etc.). Using these parameters, it is possible to answer several questions such as whether the recorded data are reliable and meaningful and the type of input/output dependency (linear or non-linear). To answer these questions, the standard deviation "σ" and mean value "μ" of

"*conditional*" and "*unconditional*" outputs were compared to check their effect on the inputs. Observations of mean values can provide information on the significance and type of a model dependency on its input variables. The *t*-statistic has also been used for testing the null hypothesis [10, 11].

Auto-correlation and cross-correlation

The primary purpose of linear correlation analysis is to measure the strength of a linear relationship between two variables. This tool can also be used in designing experiments. The quantitative information contained in the correlation plots can be used at the modeling stage. Initially, it is not generally clear what type of model may be appropriate for a batch of data. The shape of the auto-correlation plot can be used for preliminary analysis of this issue. In general, the shape of the auto-correlation function reveals the properties and order of the process [5]. Moreover, it can be used to evaluate whether the input variables (G-suit and PPB pressures) have been varied independently.

Higher order spectral analysis

Auto-correlation and power spectrum analysis cannot reveal all the information contained in a stochastic non-Gaussian or deterministic signal. Higher-order spectra analysis looks into the higher-order momenta or cumulants of a signal. The Higher-Order Spectral Analysis (HOSA) Toolbox [12] is implemented in Φ-DAT for this purpose.

In addition to generating the pertinent analyses described above, Φ-DAT generates an output (report) file that contains the relevant parameters and calculated indices for the data being analyzed. The output file is used for proper clustering the experimental results in a database and further non-traditional modeling (system identification), prediction, and generation of optimal Anti-G protections by the Expert System mentioned in Section 2.

6. DESIGN OF EXPERIMENTS

6.1 Design of Inputs

The performance of the input pressure profiles designed for this study was evaluated using the correlation analysis. The results (Figures 5-8) indicate a high degree of correlation between inputs (G-suit and PPB pressures) and outputs (systolic and diastolic blood pressures). Figures 5 and 6 show the correlation analysis results for G-suit, and G-suit with PPB in the experiments with subject No.1 (dubbed "S1"), respectively. The correlation analysis results for the BRAG valve are shown in Figure 7. It should be mentioned for the case of the BRAG valve that G-suit and PPB pressures are linearly dependent. This dependency between G-suit and PPB pressures is not desirable in the comprehensive model identification process.

Figure 8 shows the correlation results for a group of five subjects. It can be noticed again that the inputs and outputs are highly correlated. Moreover, it has been found in our work [13] that the random pressure profile resulted in a very comprehensive model for the case of G-suit and PPB applied together. To develop a comprehensive model for the case of G-suit and PPB applied independently, there is a need of more experiments with different levels of PPB combined with randomly changing G-suit pressure (that is, uncorrelated G-suit and PPB pressures) [13]. In conclusion, from the point of view of the experimental design, the correlation analysis can be used for evaluating the input signals designed, such as G-suit and PPB pressure profiles.

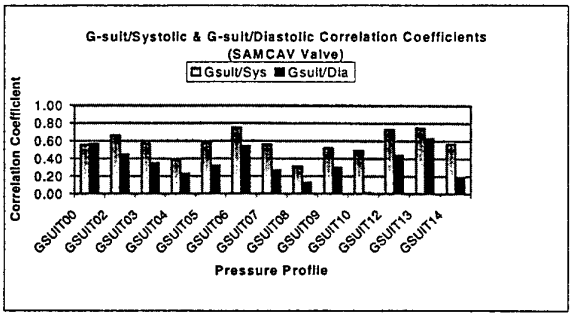

Figure 5. Correlation coefficients for S1: Gsuit with SAMCAV valve

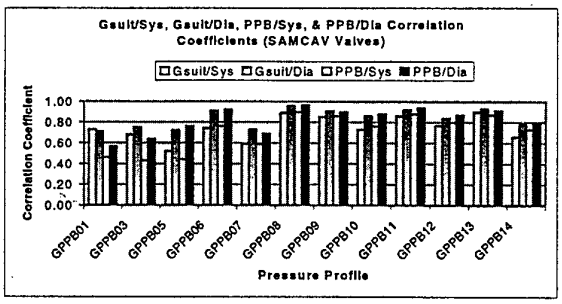

Figure 6. Correlation coefficients for S1: Gsuit and PPB with SAMCAV valves

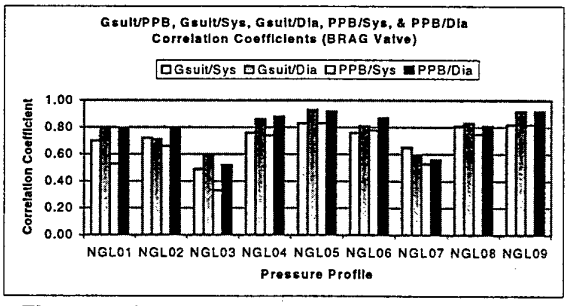

Figure 7. Correlation coefficients for S1: Gsuit and PPB with BRAG valve

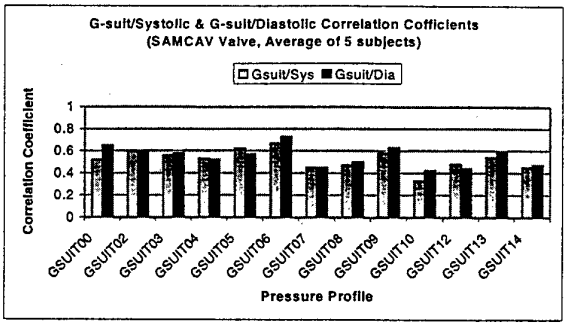

Figure 8. Correlation coefficients for five subjects - Gsuit and SAMCAV valves

6.2 Results of Experimental Data Analysis

The first step in any modeling and system identification process is to perform a close and careful observation of data sampled from the system. Such an observation is to answer the following two questions: i) whether the recorded data is meaningful; and ii) what is the degree of dependency between input/input and output/input.

6.3 Statistical Analysis of the Signals Collected

To answer the questions posed in the previous subsection, certain statistical parameters, such as *standard deviation* σ and *mean value* μ, must be calculated for conditional (i.e., output due to a certain level of input) and unconditional (i.e., output due to all different levels of input) output populations. In general, the input can be categorized into different ranges of values. For example, for the case of multi-level step input, the input can be categorized into the several ranges shown in Figures 9-11. To explain the variability in the system output due to its input, the standard deviation for the conditional population (fixed pressure level) should be smaller than for the unconditional one ($\sigma_{uncond} > \sigma_{cond}$). This proposition can be also used in multi-input cases. Tables 1-3 show a comparison between unconditional and conditional standard deviations for the systolic, diastolic, and heartbeat rate indices.

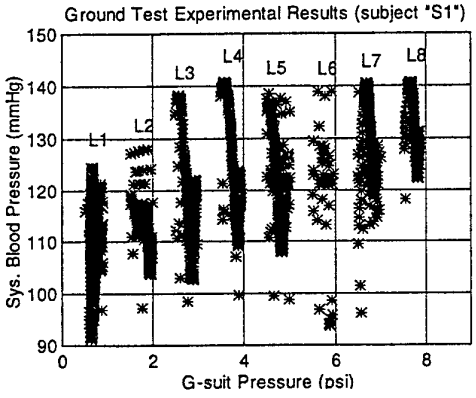

Figure 9. Systolic blood pressure as a function of G-suit pressure

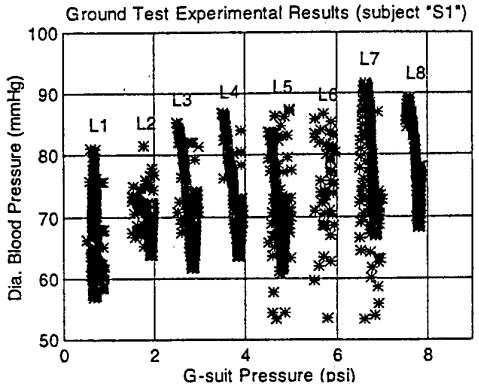

Figure 10. Diastolic blood pressure as a function of G-suit pressure

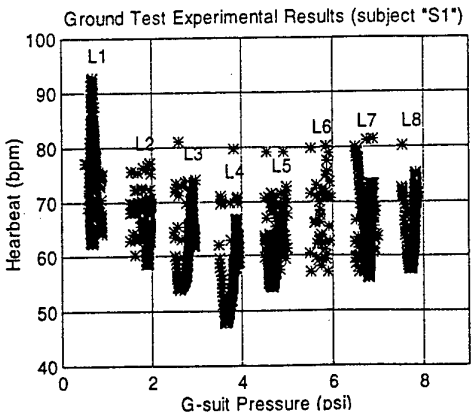

Figure 11. Heartbeat rate as a function of G-suit pressure

Table 1. Conditional and unconditional standard deviations of systolic blood pressure

Pres. Profile		Conditional, Systolic Blood Pressure (mmHg)							
Unconditional		*L1*	*L2*	*L3*	*L4*	*L5*	*L6*	*L7*	*L8*
Profile	σ	$\sigma 1$	$\sigma 2$	$\sigma 3$	$\sigma 4$	$\sigma 5$	$\sigma 6$	$\sigma 7$	$\sigma 8$
S1gsuit00	8.2	5.9	6.2						
S1gsuit01	7.9	7.8	4.7						
S1gsuit02	9.9	6.2	3.7	6.7	9.5	8.3	10	7.5	5.4
S1gsuit03	11	7.8	10	6.0	6.4	10			
S1gsuit04	8.1	5.3	9.3						
S1gsuit06	14	6.9	10						
S1gsuit13	14	8.1	3.7	4	3				
S1gppb03	15	11	11	9.7	5.3	10			
S1gppb05	18	14	13	13	12	12			
S1gppb07	13	8.0	12						
S1gppb14	12	9.1	10						

Table 2. Conditional and unconditional standard deviations of diastolic blood pressure

Pres. Profile		Conditional, Diastolic Blood Pressure (mmHg)							
Unconditional		*L1*	*L2*	*L3*	*L4*	*L5*	*L6*	*L7*	*L8*
Profile	σ	$\sigma 1$	$\sigma 2$	$\sigma 3$	$\sigma 4$	$\sigma 5$	$\sigma 6$	$\sigma 7$	$\sigma 8$
S1gsuit00	5.9	4.8	4.5						
S1gsuit01	5.5	5.0	3.0						
S1gsuit02	6.3	4.6	3.4	3.8	6.6	6.8	8.0	7.6	6.0
S1gsuit03	6.8	5.7	6.8	7.1	6.9	9.6			
S1gsuit04	6.4	5.5	6.2						
S1gsuit06	8.6	5.5	8.1						
S1gsuit13	9.1	8.6	2.1	2.4	2.5				
S1gppb03	9.2	5.6	5.3	4.6	2.7	4.8			
S1gppb05	13.	7.0	7.5	7.9	9.8	11			
S1gppb07	7.1	5.4	5.2						
S1gppb14	9.3	5.5	6.8						

Table 3. Conditional and unconditional standard deviations of heartbeat rate

Pres. Profile		Conditional, Heartbeat Rate (bpm)							
Unconditional		*L1*	*L2*	*L3*	*L4*	*L5*	*L6*	*L7*	*L8*
Profile	σ	$\sigma 1$	$\sigma 2$	$\sigma 3$	$\sigma 4$	$\sigma 5$	$\sigma 6$	$\sigma 7$	$\sigma 8$
S1gsuit00	3.5	2.4	2.7						
S1gsuit01	7.2	7.2	4.3						
S1gsuit02	7.0	4.9	4.2	3.7	7.1	5.1	6.1	6.3	5.7
S1gsuit03	8.2	6.1	6.5	6.4	5.6	8.2			
S1gsuit04	8.1	4.2	6.6						
S1gsuit06	11.	5.7	8.7						
S1gsuit13	7.0	2.6	2.0	3.0	1.6				
S1gppb03	14.	7.8	15.	12.	7.1	16.			
S1gppb05	16.	12.	15.	16.	16.	12.			
S1gppb07	13.	4.1	12.						
S1gppb14	7.7	7.9	7.6						

It is shown in Tables 1-3 that the criteria of having the smaller standard deviation for the conditional population than for the unconditional one is satisfied in most of the cases considered. This comparison also reveals the quality of the experiment conducted. Moreover, observation of the mean values can reveal important information on the effect and relationship of input to the output.

A t-statistics test [10, 11] with 95% confidence level has been performed on the conditional population to find out whether the input is capable of explaining the output variation. Table 4 shows the result of the t-test for subject "S1" with a multi-step G-suit pressure input. The quantifier '1' in Table 4 indicates that the variation in output is due to the input, which corresponds to the rejection of null hypothesis [10], and 0 states that the input cannot explain the output variation, which means the acceptance of null hypothesis. This is preliminary step can be used for eliminating the unacceptable data. It also shows the performance (effectiveness) of the designed inputs.

Figures 12-14 show the conditional means trends for systolic and diastolic blood pressures, and heartbeat rate for subject "S1." It can be seen from the figures that there exists a linear trend for systolic and diastolic blood pressure. This is not valid for the case of heartbeat rate. In general, the trend analysis technique reveals information about the input/output relationship. This relationship can be linear or non-linear. However, a non-linear relationship can be approximated by a higher-order polynomial. It should be mentioned that we are interested in the dynamic relationship between input and outputs over a time period.

Table 4. T-test results

S1Gsuit02	*L1*	*L2*	*L3*	*L4*	*L5*	*L6*	*L7*	*L8*
H0 (Sys)	1	1	0	1	1	1	1	1
H0 (Dia)	1	1	1	1	1	1	1	1
H0 (Hb)	1	1	1	1	1	1	1	1

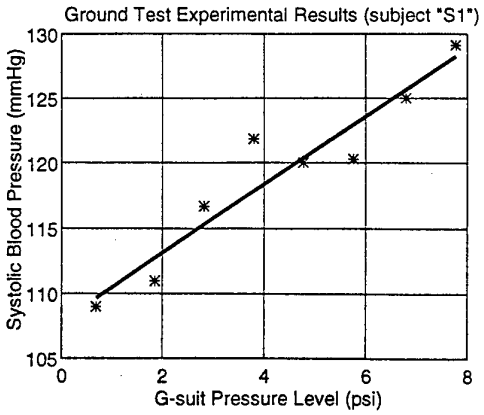

Figure 12. Conditional means for experiment S1Gsuit02 (Systolic blood pressure)

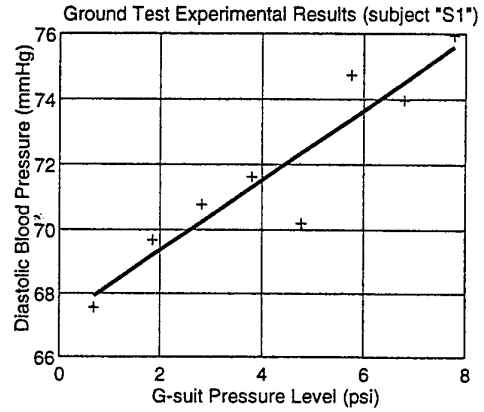

Figure 13. Conditional means for experiment S1Gsuit02 (Diastolic blood pressure)

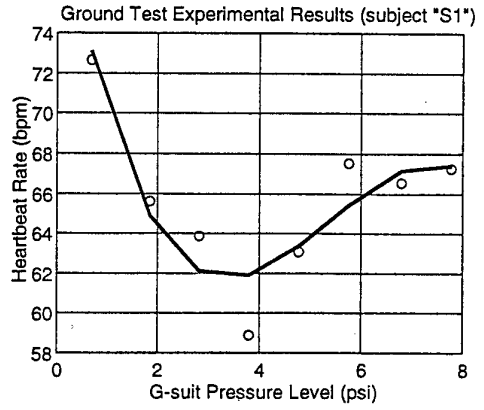

Figure 14. Conditional means for experiment S1Gsuit02 (Heartbeat rate)

6.4 Joint distribution, trend analysis, and hysteresis plots

To study the dynamics of input/output signals, it is necessary to investigate the qualitative behavior of the signals. Scatter diagrams (joint distribution plots) of input/output and output/output signals reveal qualitative

information about the structure of input/output dependency (e.g., linearity or non-linearity). A plot of the input or output signal versus an (input or output) signal delayed by time τ will show the degree of dependency of each present value of the signal on: (i) the previous values of its own states, such as the relationship of **output** to (**output-τ delays**); and (ii) the other signals, such as the relationship of **output** to (**input-τ delays**). The qualitative information contained in these plots can be used in system modeling. Also, the trend analysis can be used to define a quantitative approach for analyzing the scatter plots. Figures 15-17 show the joint distribution for the case of input (delayed) versus output (delayed) and output (delayed) versus output (current).

Two different types of trend analysis (fuzzy trend and linear trend) have been considered in the investigation of the nature of relationship between delayed input and output. The trend analysis can be used to determine [9]:

⇒ whether there exists a trend of increase in means as the level of the independent variable increases. The existence of this trend would correspond to the linear input/output relationship; or

⇒ whether the function which relates the means and the level of the independent variable is significantly curved. This would correspond to a non-linear input/output relationship.

The F-test statistics is used to investigate this type of dependency (e.g., linear or non-linear). It has been proved in [9] that the ratio of fitting curve mean square to its group mean square (F-ratio) has a so-called F-distribution. This means that if the F-ratio is high, the corresponding type of relationship exists between an input and output. For example, Table 5 shows the F-ratio results for the subject "S1" (the case of random G-suit profiles).

Table 5. F-ratios

Type of relation	Linear	Quadratic	Cubic
Systolic	72.10	0.13	1.20
Diastolic	83.50	4.70	0.62
Heart rate	50.10	7.70	2.50

It is clear from the F-ratio results (Table 5) that only the linear component of systolic and diastolic blood pressures, and linear and quadratic components of heartbeat rate are significant. Using this unique feature of F-ratio, it is possible to group the collected data into different groups. Also, the idea behind the fuzzy trend analysis is to define a number (fuzzy index) for comparing the qualitative results of the trend and scatter plot analysis.

Finally, a hysteresis plot has been defined for qualitative analysis of input/output data. Figures 18 and 19 show examples of such plots. The X-axis of the plot is either G-suit or PPB pressure. A physiological signal (e.g., systolic blood pressure) normalized by the G-suit or PPB pressure is plotted as the Y-axis. In general, the narrower the plot, the more repeatable the physiological response.

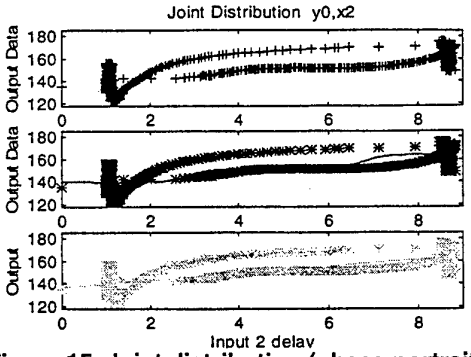

Figure 15. Joint distribution (phase portrait) for output versus (input-2 delays)

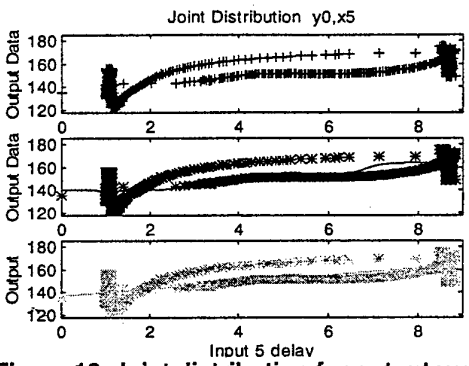

Figure 16. Joint distribution for output versus (input- 5 delays)

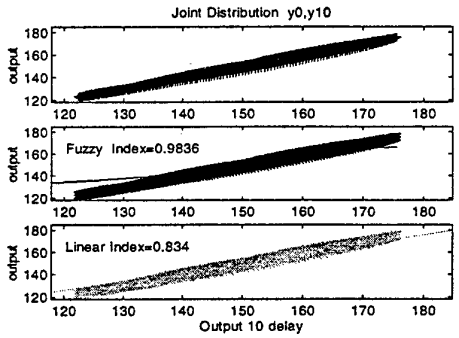

Figure 17. Joint distribution for output versus (output-10 delays)

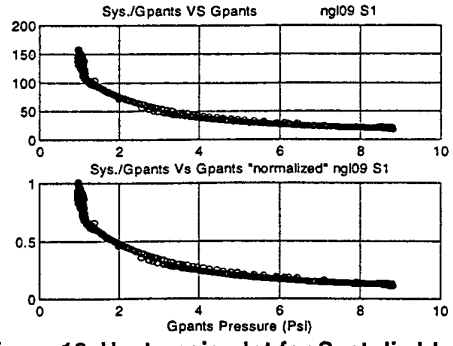

Figure 18. Hysteresis plot for Systolic blood pressure normalized by G-suit pressure

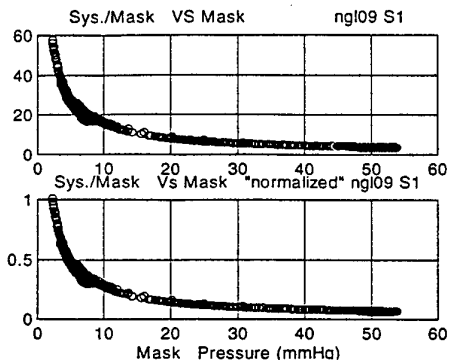

Figure 19. Hysteresis plot for Systolic blood pressure normalized by PPB pressure

6.5 Auto-correlation and Cross-correlation

The primary purpose of linear correlation analysis is to measure the strength of a linear relationship between two variables. This tool can also be used in the design of an experiment. In general, the trend analysis reveals the existence of a linear or non-linear relationship between the input/output signals. In the physiological systems, the maximum value in correlation analysis indicates the maximum dependency between input/output data in the case of linear relationship. Also, the sign and position of the maximum show the direction of relationship and lag or lead of the system, respectively. Therefore, the correlation analysis is a tool for obtaining more information about the characteristics of the system. Finally, it should be mentioned that the correlation analysis is very sensitive to the interval (sampling rate) of the data set. To eliminate this dependency, the bootstrap technique is typically used [10]. Figures 20-22 show the auto-correlation and cross-correlation for the case of a BRAG valve (NGL09) experiment. It has been mentioned earlier that the G-suit and PPB pressures are linearly dependent for the BRAG valve results.

6.6 Higher Order Spectral Analysis

Auto-correlation and power spectrum analysis cannot reveal all the information contained in a stochastic or deterministic signal. Higher-order spectral analysis looks into the higher-order momenta or cumulants of a signal to find out more information about the process. This feature has not yet been fully implemented for the analysis of the ground-test experimental data.

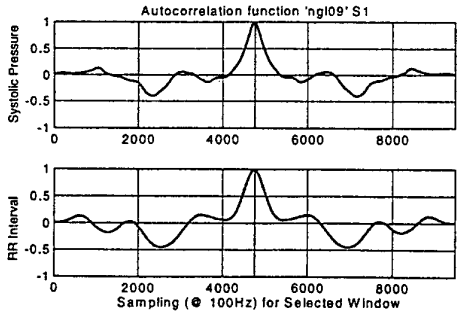

Figure 20. Auto-correlation (Sys. & RR interval)

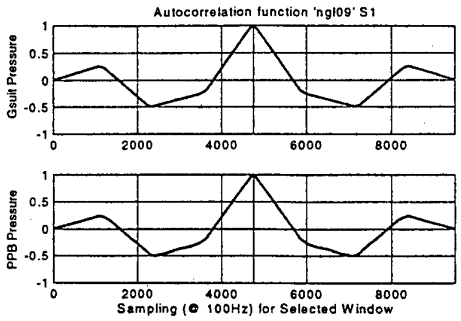

Figure 21. Auto-correlation (G-suit & PPB)

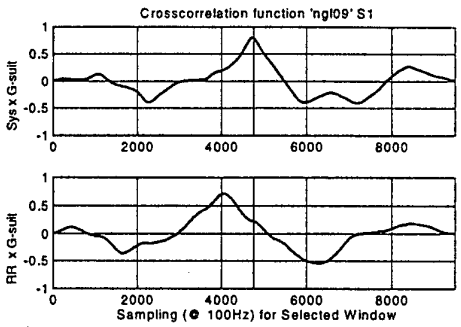

Figure 22. Cross-correlation (G-suit versus Sys. and G-suit versus RR interval)

7. CONCLUSIONS

A generic toolbox has been developed for analyzing the results collected in physiological experiments aimed at the development of advanced non-linear Anti-G countermeasures. The toolbox called **Physiological Data Analysis Toolbox (Φ-DAT)** has been applied to the analysis of physiological data collected in Gz experiments. This tool can be also used at the experiment design stage. If Φ-DAT is used for the preliminary analysis of physiological data, it yields important information that can be further used at the modeling stage [5]. Finally, it should be mentioned that Φ-DAT toolbox can be used to analysis different types of physiological experimental data.

8. REFERENCES

1. Atkinson, A.C., Donev, A.N., "Optimum Experimental Design", Oxford Science Publications, 1992.
2. Jaron, D. Moore, T.W., etc., "Increased Acceleration Tolerance Using a Pulsating Anti-G Suit", Proc. IEEE, National Aerospace and Electronics Conference, 1987.
3. Moore, T., et al., "An Experimental Microcomputer Controlled System for Synchronized Pulsating Anti-Gravity Suit", Technical note, Biomedical Engineering and Science Institute, and Dept. of Electrical and Computer Eng., Drexel University, Philadelphia, PA 19104, July 1986.

4. Kantz, H., Schreiber, T., "Non-linear Time Series Analysis", Cambridge university press, 1997.
5. Box, G.E.P, Jenkins, G.M., Reinsel, G.C., "Time Series Analysis: Forecasting and Control", Prentice-Hall Inc., 1994.
6. Krauss, P. T., Shure, L., Little, N. J., "Signal Processing Toolbox", The Mathworks Inc., 1994.
7. Emami, M. R., "Observational Study of the DCIEM Data", Robotics and Automation Laboratory, University of Toronto, Internal Report, Sept. 1997.
8. Lin, Y., Cunningham, G. A., "A fuzzy Approach to Input Variable Identification", Proc. of IEEE Conference on Fuzzy Systems, Orlando, pp. 2031-2036, 1994.
9. Myers, L. J., Well, A. D., "Research Design and Statistical Analysis", Harper Collins Publisher, 1981.
10. Bradley, J., "Matlab Statistics Toolbox", The Mathworks Inc., 1997.
11. Hicks, C., "Fundamental Concepts in the Design of Experiments", Holt, Rinehart and Winston Inc., 1964.
12. Swami, A., Mendel, J.M., Nikias, C.L., "Higher-Order Spectral Analysis Toolbox", The Mathworks Inc., 1995.
13. Fraser, W. D., Lu, Z., Askari, V., Kapps, A., "Modeling of the Physiological Responses to Non-linear G-suit and Positive Pressure Breathing Schedules", To be presented in North Atlantic Treaty Organization, Ohio, 26-28 October 1998.

DCIEM 98-P-90.

Model Derived Timing Requirements For Gz Protection Methods

Dana B. Rogers Ph.D.
University of Dayton
5482 Stonegate Ct
Dayton, Ohio 45469, US

Studies of GLOC during Gz maneuvers highlight the need for further understanding of both orthostatic and transient behavior of blood pressure driven quantities in response to a variety of Gz profiles. Important in the analysis are duration, rates of change, direction and magnitude of transition and system memory (time at previous G level). The wide variety and number of profiles that need to be explored is intractable for human experimentation, indicating the need for functional models that provide a method for analyzing transient Gz equivalence under multiple profile conditions.

The Stoll (5) curve provides the first graphic indication that there is a transient behavior of the cardiovascular system that complements the steady state or long term behavior.

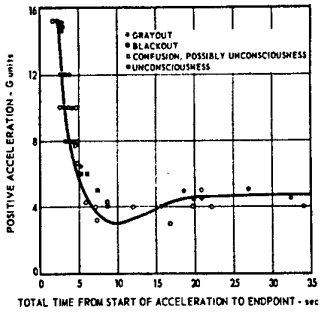

Figure 4–11. Time to unconsciousness as a function of varying rates of positive acceleration (G_z) onset, G amplitudes, and exposure times. (After Stoll, 1956)

Figure1 (After Stoll)

A FIR model was proposed in 1975 by Rogers (3). This model based on the Stoll curve shape represents only an approximation of what the transient behavior might be. Gillingham's experiments in 1977 (2) provided the first direct evidence that quantified the transient values. Gillingham's data provided an impetus for a number of Gz to Blood pressure transfer functions that replicate with some fidelity the cardiovascular parameters related to blood pressure. The transfer function forms which exhibit the greatest flexibility are those which develop a linear separation of the orthostatic values from the transient function of the system response to Gz. In these forms the orthostatic gain is dependent upon anatomical parameters and Pascal's Law of fluids. The dynamic or Effective G component responds only to derivative values of the input function and has a steady state gain of 1.

The model used for this study uses a normalized set of Gillingham's data that is analyzed in a log amplitude and log frequency plot. The model is designed by the method of asymptotes for use in aircraft simulators. (1978)

$$G(s) = K \frac{(1+a_1)}{(1+b_1 s+b_2 s^2)}$$

$a_1=5.31 \quad b_1=3.23 \quad b_2=5.17 \quad K=1$

The mathematical description is represented in the frequency domain for design and then transformed to the time domain for analysis. The model experiments are designed so that the forcing functions are a parametric set of G profiles representing onset rates from base G level to a fixed end point. The functions are represented as "Applied Gz.". The surface map of this forcing function is shown in Figure 2.

Theoretical Experiments

The first model experiment uses ramps from 0.2G/sec. to 5G/sec. in a profile set which begins at 1G and terminates at 3.8 G The companion mapping of the transient response is shown in Figure 3.

The resulting 3D surface map is the Effective G Surface where the response level in the early part of the profile rises to as much as two G above the applied level. There appears to be very little difference in the peaks of the higher onset rates from 2G/sec. to 5G/sec.

The Effective G Surface is now rotated slightly around a vertical axis to change the perspective view to an edge view. The figure is then rotated 180 degrees around a horizontal axis to obtain Figure 4. This representation now corresponds with a G tolerance view. The parametric set of G ramps is clearly seen as the framework of the transient dimming area envelop.

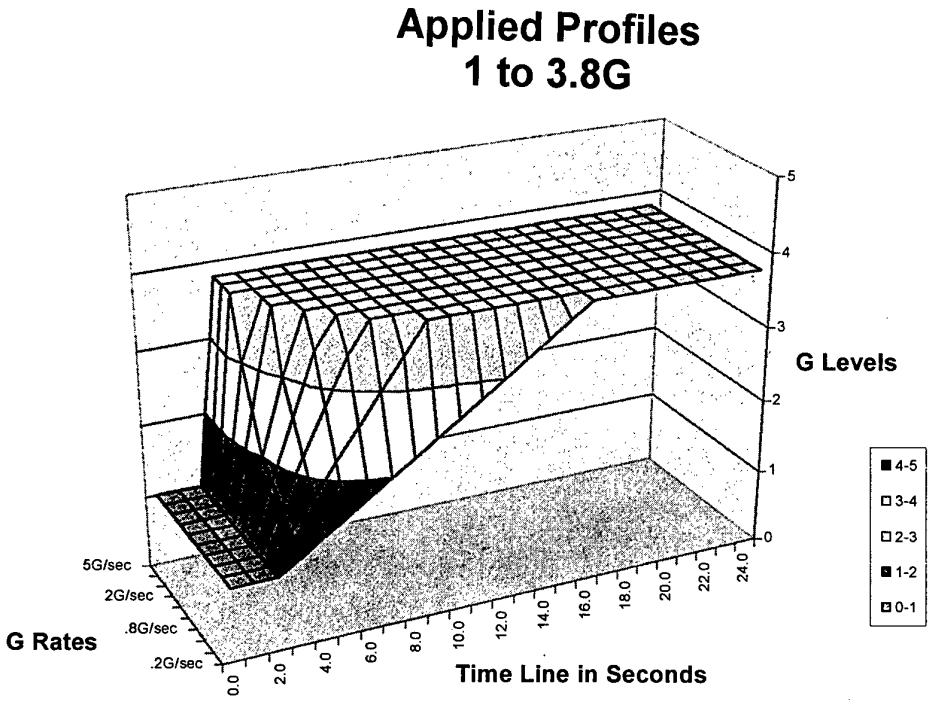

Figure 2. Applied Gz Profiles for 1 to 3.8 Gz.

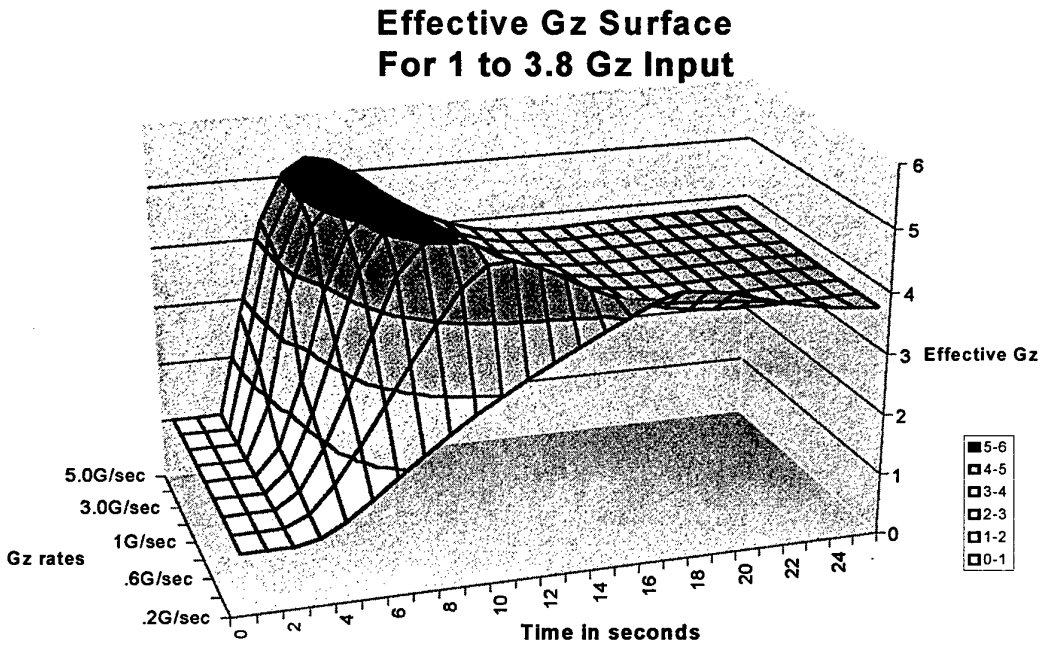

Figure 3. effective G surface for 1 to 3.8 Gz

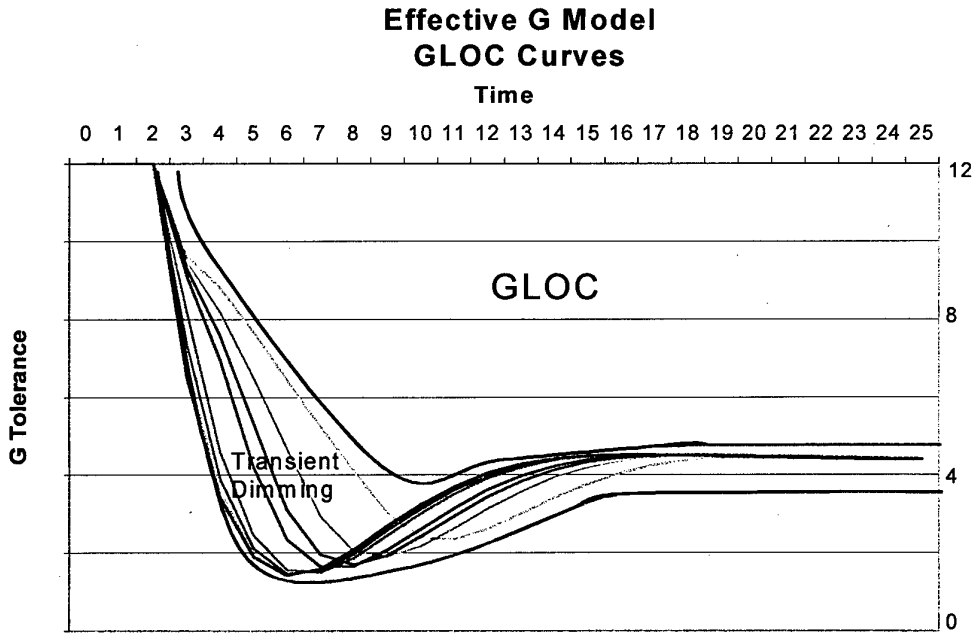

Figure 4. G Tolerance Curves from the Effective G Model

The first model experiment uses profiles which represent "push-pull" or -/+ Gz. This experiment uses a transition from –2 to +3 Gz with onset rates from 0.2G/sec to 5G/sec. Figure 5 is the Applied Gz Surface. The Effective G surface resulting from the push-pull forcing function is seen in Figure 6. It is interesting to note that the Effective Peak G at the higher onset rates reaches well above the 5G level in the presence of a 3G applied profile. Also note the small differences between the Effective G peaks for onset rates above 2G/sec.

The second model experiment compares the Applied and Effective G using a 1G/sec ramp from –2 to +3Gz. There are three elements used in the comparison. The Tolerance Deficit is defined as the difference between the Effective G level and the subject's relaxed G tolerance. The Time Deficit is measured from the crossover time of the Effective G value and the relaxed tolerance level to the point where countermeasures become effective. There can be more than one Time Deficit in any evaluation representing a variety of protection methods. The Protection Deficit represents the difference between the actual protection provided by a countermeasure and the effective G value at any time. The graphical representation of the evaluation is found in Figure 7.

A view of G tolerance as related to the Effective G rather than the Applied G suggests a modified view of activation criteria for the suit-valve system and straining maneuvers.

The third experiment explores differences between Effective G values generated by a centrifuge starting from a nominal baseline of 1.6 Gz and an aircraft starting from a 1.0G baseline. A 1G/sec ramp to a final level of 4G is used in the evaluation. Note that the time signature of the two profiles varies by as much as 0.3 G for this simple example as shown in Figure 8.

A modeling approach to analysis of G protection methods, profiles, and the concept of Effective G has brought several questions to bear. What is the maximum onset rate needed to stimulate the cardiovascular system? Is the model constrained by a lack of data at high onset rates or is the high frequency rolloff accurate? What is an acceptable difference when using moderate baseline levels to start centrifuge profiles in view of the G memory shown by the model? Should a modified approach to centrifuge control be used to shape the applied G profile? Would this insure a higher fidelity in the Effective G response?

1. Burns, J.W. G Protection Basis/Acceleration Physiology. AGARD LS-202. May 1995

2 Gillingham, K. K. Transfer Functions for Eye Level Blood Pressure During +G Stress. Aviation Space and Environmental Medicine. 1977

3. Rogers, D. B. A Linear Model for Acceleration. AsMA Meeting May 1975.

4. Rogers, D. B AMRL-TR-79-58

5. Stoll A. Aviation Space and Environmental Medicine 1965.

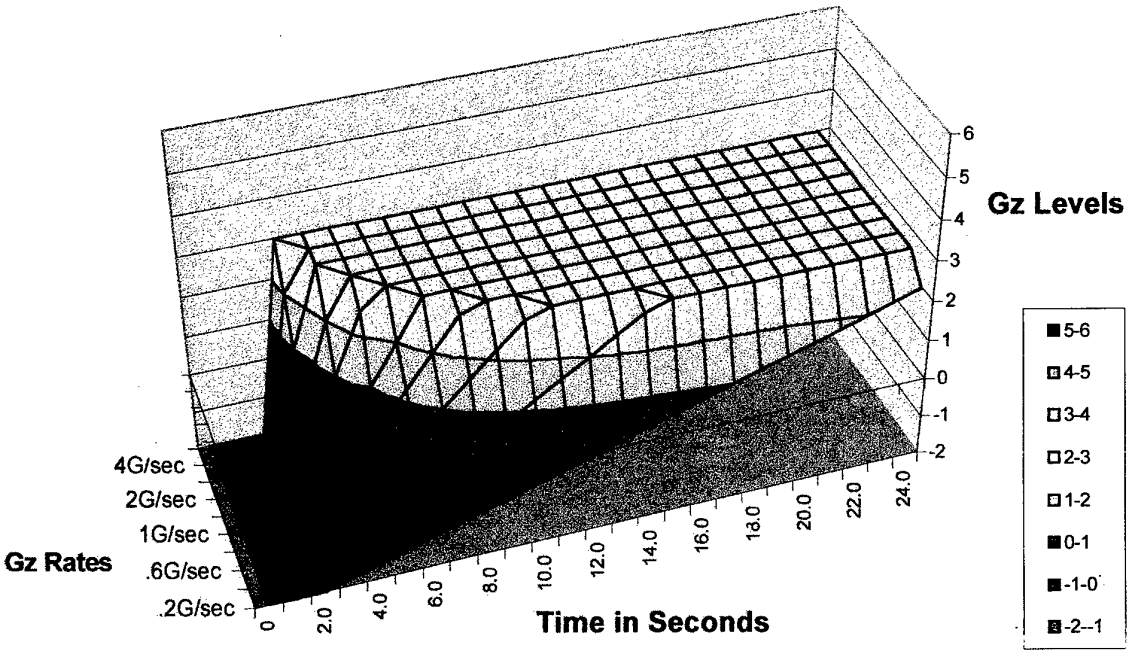

Figure 5. Applied Ramps from -2 to 3 Gz.

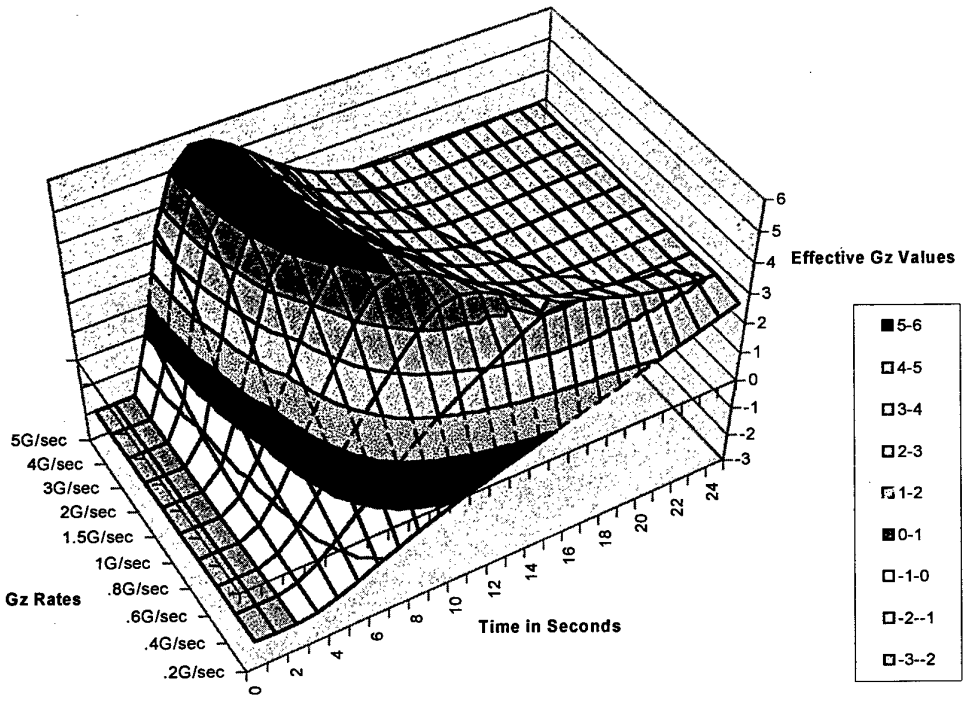

Figure 6. Effective G Surface for applied Gz from –2 to 3Gz.

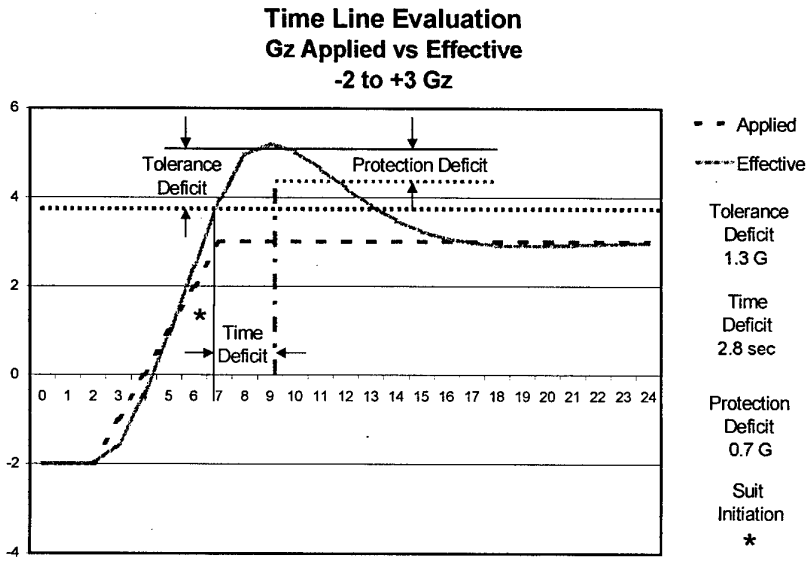

Figure 7. 1G/sec profile showing the time and Protection Deficits as related to Effective Gz.

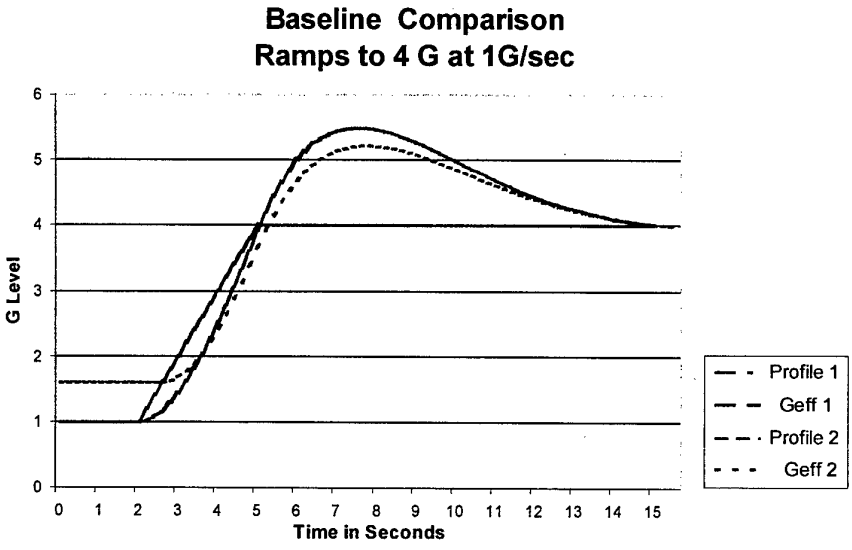

Figure 8. Effective G comparison between 1Gz baseline and 1.6 Gz baseline with a 1G/sec ramp to 4G

Mathematical Models for Predicting Human Tolerance to Sustained Acceleration

Russell R. Burton
Senior Scientist
Human Effectiveness Directorate
Air Force Research Laboratory
2509 Kennedy Circle
Brooks AFB, TX 78235-5118, USA

1. SUMMARY

Mathematical models that predict G-level and G-duration tolerances are reviewed. These models are subdivided into relaxed and straining tolerances. The latter tolerance predicts G levels of subjects that are performing an anti-G straining maneuver. These models are equations based on hydrostatic pressure mathematics: $G = (P_a \bullet d)/h$; where: $G = +G_z$ level tolerance; P_a = mean arterial blood pressure in mm Hg (100) at heart level; d = specific density of Hg (i.e.13.6); and, h = eye-heart vertical distance in mm (350 mm). The G-duration tolerance model is based on tolerance data obtained from subjects exposed to the same continuous level of G to fatigue. These G tolerance models were validated using published data. These G-level and duration models predict, with high accuracy, tolerances for relaxed or straining subjects using various anti-G protective systems/methods.

2. INTRODUCTION

Human tolerance to sustained G has two dimensions: (1) G-level tolerance and (2) G-duration tolerance. The former is most commonly measured and frequently referred to as simply G tolerance. The latter is a tolerance measurement that has only been considered separate from G-level tolerance during the last decade (3). None the less, these two tolerances are distinctly different with different physiologic bases and different tolerance dimensions. Therefore models that have been developed for each type of G tolerance are reviewed and reported herein.

Several G-level tolerance mathematical models have been developed for various reasons and by different laboratories. Cohen (11) published a G-level tolerance model that considered the use of the anti-G straining maneuver (AGSM), reclined seat-back seat designs, and the anti-G suit. He developed his model summing the protective systems (named the "linear additive model") based on relaxed G tolerances using data obtained from centrifuge studies. He noted that the reclined seat derived its protection from a reduction in the eye-heart vertical distance. The maximum G tolerance protection that he predicted using a combination of G protective systems was slightly more than 6 G.

Harding and Bomar (13) did not develop a model *per se*, but used published data and an early version of my model (4) to explain the G protection derived from positive pressure breathing during G (PBG) and the anti-G suit. They did note that an arterial pressure (P_a) of 22 mm Hg does equate to 1 G of tolerance and that an increase in intrathoracic pressure does directly increase P_a. These assumptions are critical in the development of my mathematical G tolerance models.

Buick et al (1) using data obtained from centrifuge subjects similar to the methods of Cohen (11) developed a mechanical model that incorporated PBG and the AGSM. His model correctly predicted that the combination of PBG and AGSM is additive in increasing P_a although he was unable to validate it with his experimentation. The additive nature of PBG and AGSM was a major step forward in developing a more predictable G-level tolerance model for higher G levels, as this relationship had not been predicted previously (4).

My first G-level tolerance model was published nearly a decade ago and was based entirely on the hydrostatic pressure equation (4). Human G-level tolerance to increased sustained acceleration (G) is a function of hydrostatic pressures that develop within the intravascular system with an increase in G. These hydrostatic pressures develop immediately as described by the hydrostatic pressure equation:

$$P_H = h \bullet d \bullet g \quad \ldots\ldots (1)$$

Where: P_H = hydrostatic pressure (mm Hg);
h = height of the column (mm);
d = specific density of a fluid relative to Hg (1/13.6); and,
g = ambient accelerative force (G is the inertial force).

Relaxed G-level tolerances can be predicted therefore using eq (1) by solving for "g" for subjects seated upright and exposed to rapid onset G (ROR; G onset ≥ 1 G/s):

Papers presented at the RTO HFM Specialists' Meeting on "Models for Aircrew Safety Assessment: Uses, Limitations and Requirements", held in Ohio, USA, 26-28 October 1998, and published in RTO MP-20.

$G_{LR}=(P_a \bullet d)/h$.....(2)

Where: G_{LR} = relaxed ROR +G_z level tolerance;
P_a = mean arterial blood pressure in mm Hg (100) at heart level;
d = specific density of Hg (i.e.13.6); and,
h = eye-heart vertical distance in mm (350 mm).

This equation serves as the basis for models for predicting changes in G-level tolerances with: (1) various designs of anti-G suits; (2) reclined seatback angles; (3) types of anti-G straining maneuver (AGSM); (4) levels of Positive pressure Breathing during G (PBG); (5) rapid and gradual onset of G; (6) muscle contractions (handgrip); and, (7) leg elevation (4, 5, 6, 7, 8). Indeed this model is useful to scientists and engineers for aircraft cockpit design, advanced development of personal equipment, validation of G-tolerance determination methods and in teaching the physiologic basis of G tolerance. Also these tolerance models were used to validate a G-duration profile used to test subjects for G-level tolerances (8).

The principal reason that this model is effective in predicting G tolerances is that hydrostatic pressures dominate the cardiovascular physiology leaving the body without effective countermeasures. The results are major intravascular pressure changes that are predictable with the hydrostatic pressure equation. Consequently an examination of eq (2) shows clearly that G-level tolerances can only be altered directly by changing the eye-heart vertical distance (h of eq 2) or the arterial pressure within the body (P_a of eq 2).

Also G-duration tolerances (models to be discussed later in this article) are tightly coupled with these G-level tolerances, thus depending significantly upon "h" and P_a as well. Indeed a method, system, or technique that is theorized for increasing G tolerances, must affect "h" or "P_a" of eq 2 if it is to be effective in increasing G tolerance. With this concept in mind the following mathematical models that I have recently developed for G-level and G-duration tolerances are now presented.

3. G-LEVEL TOLERANCE MODELS

Since my last mathematical G-level tolerance model was develop in 1986, more experimental data have become available that validated many aspects of this early model. Also I found this information could be used to develop a more detailed and accurate G-level tolerance model (4). Therefore a G-level mathematical model was developed based on these new data yet using the same concept of hydrostatic pressure (5, 7).

Two types of G-level tolerance models have been developed. The first one described involves a predictive model for relaxed G-level tolerances. The other model predicts G-level tolerances for subjects/pilots that are using the AGSM and/or PBG called the straining G-level tolerance model. Detailed descriptions of these models are to be published elsewhere (5, 7).

3.1 Relaxed G-level tolerance models

Using eq 2 as a basis for predicting relaxed G-level tolerance without G protection, the following two equations, based on the onset rate of G, using conventional anti-G methods were developed:

Rapid Onset G-level Tolerance:

$G_{LR} = (P_a + P_g + kP_p) \bullet d/(h - (k \bullet 6\text{ mm} \bullet \text{psi}))$..... (3)

Where: G_{LR} = relaxed ROR G-level tolerance;
P_p = pressure of PBG ((G – 4) • 12) to a maximum of 60 mm Hg;
P_g = 3 mm Hg per psi anti-G suit pressure;
k = h/350;
psi = anti-G suit pressure that directly depends on h; and,
Other symbols same as eq (2).

Gradual Onset (GOR) G-Level Tolerance (eq 4):

$G_{LG} = (P_a + kP_b + k_1P_g + P_m + kP_p) \bullet d/(h - (k \bullet 6\text{ mm} \bullet \text{psi}))$

Where: G_{LG} = relaxed GOR G-level tolerance (G onset of 0.1 G/s);
k_1 = factor of 2 for lower body anti-G suit coverage > 50%;
P_m = 15 mm Hg, after 20-30 s of handgrip;
P_b = 25 mm Hg from baroreceptor after 8-10 s of onset of G; and,
Other symbols same as eqs (2) and (3).

These equations predict changes in G-level tolerances with the use of all current and advanced operational anti-G systems by relating them to P_a or changes in "h" in eq 2. Indeed the bases of their capabilities must be explained by eq 2. Even increasing venous return (VR) with a greater coverage anti-G suit, must affect P_a in order for it to increase G-level tolerance; i.e. k_1 of eq 4.

In eq 3, P_g and (k • 6 mm • psi) explain the function of the anti-G suit; i.e. it directly increases P_a and reduces "h" by elevating the diaphragm as a function of the pressure applied. The pressure used in PBG protection, P_p has been standardized (i.e. ((G – 4) • 12) to a maximum of 60 mm Hg). Since reclining the seat-back angle affects P_b, the applied level of PBG, and the effect of the anti-G suit on "h", a constant "k" is included that is dependent upon "h". Incidentally the seat-back angle that this eq will accommodate is restricted to $\leq 55°$ (details are available, 7).

The baroreceptor response (P_b) and the increase in P_a with handgrip directly increase heart-level P_a. However these

responses require several s of sustained increased G before they become effective. Hence they are included only in GOR tolerance determinations. The effects of P_b and P_m on P_a have been measured.

An increase in anti-G suit coverage will increase VR, in turn increase P_a, but only during GOR. Advanced anti-G suits (e.g. Advanced Technology Anti-G Suit (ATAGS)) increase their lower body coverage from 30% to 85%. Rapid G onset tolerances are not influenced by changes in VR.

3.2 Straining G-level tolerance model

Pilots are required to maneuver high performance aircraft at G levels far in excess of protected relaxed G-level tolerances (eqs 3 and 4). Operational fighter aircraft routinely obtain 9 G within 1 s. Therefore, rapidly increasing G-level tolerances to high-G operational levels can only be accomplished using the AGSM (M-1 or L-1 types of straining maneuvers) and PBG either alone or in combination. The application of the AGSM results in another G-level tolerance model called "Straining-G Level Tolerance". As discussed previously, the key in increasing G-level tolerances is increasing P_a. That increase is accomplished at high G levels with the AGSM that directly increases intrathoracic pressure (P_i) and indirectly heart-level P_a.

$$G_{LS} = (P_a + 0.75P_i + kP_p) \bullet d/(h - (k \bullet 6 \text{ mm} \bullet \text{psi})) \quad \ldots\ldots(5)$$

Where: G_{LS} = Straining G level tolerance with an "h" of ≥ 250 mm;
P_i = intrathoracic pressure from AGSM (max of 125 mm Hg); and,
Other symbols = same as eqs 2 and 3.

P_i directly affects P_a at heart level and therefore plays a crucial role in protecting pilots at high levels of G. The quantitative relationship of P_i to heart-level P_a for the AGSM has been determined to be 0.75; i.e. 1 mm Hg increase in P_i results in an increase of approximately 0.75 mm Hg of P_a (5). P_i relationships to P_a using PBG has been determined to be approximately 1 (12).

This model predicts rapid-onset high-sustained G-level tolerances for subject seated in an upright posture or reclined with an "h" of ≥ 250 mm (55° back-angle equivalent) and using conventional anti-G methods. A model for predicting straining G-level tolerances for seat-back angles > 55° (h = 250 mm) has been developed and published elsewhere (7).

To summarize, all conventional anti-G systems/methods have been incorporated into these G-level tolerance models. Calculations of G-level tolerances using these models have been accomplished and compared with G-level tolerances measured on centrifuge subjects. To validate these models, calculated and measured values were compared mathematically (5) with the following results; i.e. (X% ± SD) with n = studies used in the validation: (1) ROR relaxed w/o anti-G suit (n = 22): 99.2 ± 8.06; (2) ROR w/ anti-G suit (n = 9): 98.9 ± 8.95; (3) ROR w/ handgrip (n = 1): 100; (4) ROR w/ anti-G suit and handgrip (n = 1): 100; (5) ROR w/ anti-G suits and PBG (n = 6): 103.8 ± 2.99; (6) GOR w/o anti-G suit (n = 18): 97.7 ± 10.40; (7) GOR w/ anti-G suit (n = 8): 91.8 ± 6.73; (8) GOR w/ handgrip (n = 1): 104; and, (9) GOR w/ anti-G suit and handgrip (n = 1): 90.

Straining G-level tolerance predictions for ≤ 55° were reasonably accurate with limited data available for validation (2). Using the AGSM at different seat back angles the following values were compared (calculated/measured): 12° = 9.1/9.0 and 9.5/10.7; 30° = 10.1/10.9; 55° = 12.7/11.7. Using PBG: 12° = 12.4/12.0; 30° = 12.9/12.0+; 55° = 15.6/12.0+ (i.e. centrifuge exposures were limited to 12 G).

A schema of the increases in G-level tolerance with various G-protective methods/systems as determined using the above G-level tolerance models is shown in figure 1.

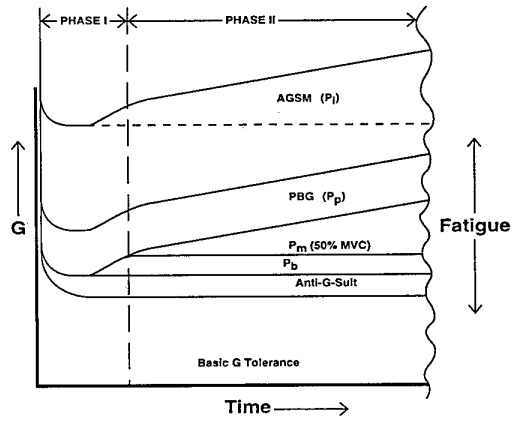

Figure 1: Schema of G protection relationships with time at G (6).

4. G-DURATION TOLERANCE MODELS

G-duration tolerances, quite unlike G-level tolerances, are measured as the duration time that subjects can tolerate increased G exposures continuously until they become fatigued. These G exposures can be at a single level or various levels of G. The latter is a G profile that is called a simulated aerial combat maneuver (SACM). Duration tolerances for sustained single levels of G (0.5 to 1G increments) from 3G up to and including 9G have been measured. G-duration tolerances are a function of G-level tolerances since subjects must achieve levels of G of the exposure to fatigue. G-duration models have been developed from data obtained from subjects exposed to constant G levels until the development of fatigue (Figure 2; ref 3).

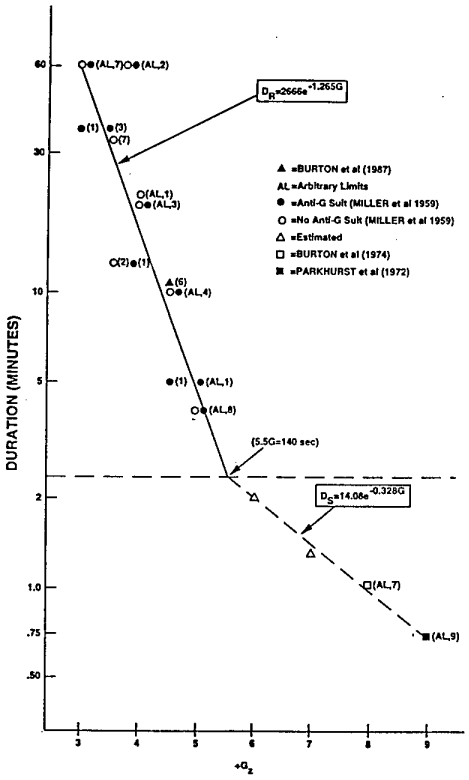

Figure 2: Durations (min) that subjects tolerated continuous exposures to a constant level of G until fatigued (3, 9).

4.1 Relaxed G-duration Tolerance Model

This model is based on data determined on centrifuge subjects exposed to sustained G levels of 3G to and including 5G (Figure 2). The G-duration tolerance equation for 3-5G follows:

$$D_R = 2666e^{-1.265G} \quad \ldots\ldots (6)$$

Where: D_R = Duration (min) tolerance for relaxed subjects until the onset of fatigue that includes the baroreceptor reflex (P_b) of 25 mm Hg; and,
G = G_D for G levels of exposure ≤ 5 G but ≥ 3 G.

G of eq 6 is determined as G_D using $G_L = P_a \bullet d/h$ (eq 2). $G_D = G_L$ for subjects seated upright with "h" = 350mm. In the upright seat at 5 G the P_a required at heart level is 129 mm Hg (that includes the baroreceptor reflex), with the duration tolerance of 4.9 min. If a subject is seated at reclined seat-back angles to ≤ 55° at ≥ 3 G to ≤ 5 G G_D must be calculated as follows. The example of a subject at 5 G seated at 45° reclined seat back; e.g. "h" at 45° = 280 mm calculates the P_a required at 5 G at 45° using: $P_a = G \bullet h/d$ or $5 \bullet 280/13.6 = 103$ mm Hg. Using 103 mm Hg for P_a of eq 2 with an "h" = 350 mm G_D is calculated to be 4.0 G. Using 4 G in eq 6 the D_R = 17 min duration for someone at 5 G seated at 45°. The G-duration tolerance of a subject seated in a 55° seat back ("h" = 250 mm) using eq 2 is predicted with a G_D of 3.6 to be 28 min.

4.2 Staining G-Duration Tolerance Model

G-duration tolerances for G-levels predicted using eq 5, a straining G-duration tolerance model has been developed. This model is based on data obtained from subjects wearing the operational anti-G suit and performing the AGSM as required.

$$D_s = 16.2\, e^{-0.328\,G} \quad \ldots\ldots (7)$$

Where: Ds = Straining G-duration tolerance until subject fatigue (min) that includes P_b, P_m, P_i as required and the operational anti-G suit (eq 4).

Eq 7 differs from the regression equation shown in figure 2 for G tolerances > 5G. The slope is the same but the intercept is higher. The reasoning behind this difference is that these subjects were not completely fatigued. This model was validated using isometric contraction duration data that included the dynamics of performing the AGSM during long duration exposures to G (for details see ref 6).

This model accurately predicts duration tolerances for exposures to a constant level of G for subjects seated upright, using the operational anti-G suit and performing an AGSM as required. This model also predicts approximate duration tolerances for subjects exposed to various types of SACMs. SACM predictions were usually less duration than determined experimentally. This relationship would be expected since the lower G level exposures of the SACM provide time for subjects to rest. This relationship with various types of SACM is summarized as follows:

1. 3.5-5.5 G (10 s at each level).....129%
2. 4.0-7.0 G (10 s at each level)..... 132%
3. 4.5-7.0 G (15 s at each level)..... 124%
4. 5.0-9.0 G (10 s at each level)..... 79%

The one exception on SACM prediction was the 5.0-9.0 G profile that was shorter than predicted. This difference would also be expected since the lowest level of G is 5 G that does not allow for adequate rest and too increasing the G level frequently by 4 G (5G to 9G) is in itself extra fatiguing.

G-duration tolerances can also be predicted for subjects using reclining seat backs and PBG with eq 7. G_L = G level attained by the subject with protective systems is calculated as for reclining seat backs shown for eq 6 (see eq 8). However with the use of PBG, G level is increased but with less fatigue than

found with the AGSM. Therefore PBG pressures used are not included or substituted for portions of the AGSM in calculating G_D as shown in eq 9.

$$G_L = (P_a + 0.75P_i + P_p) \bullet d/(h - (k \bullet 6\ mm \bullet psi)\ldots\ldots\ldots\ldots(8)$$

$$G_D = (P_a + 0.75P_i + P_p - P_p) \bullet d/(h - (k \bullet 6\ mm \bullet psi)\ldots\ldots(9)$$

Where: Symbols same as eqs (4) and (5).

The maximum G level (G_L) that can be obtained with a subject seated upright using a maximum P_i of 125 mm Hg and 60 mm Hg of P_p with an anti-G suit pressure of 10 psi and a "h" of 350 mm calculates to be 11.9 G using eq 8. However the G duration – level (G_D) that represents the effort used by the subject at 11.9 G is calculated using eq 9 without P_p thus P_a + 0.75(125) = 194 • 13.6/290 = 9.1 G. Therefore 9.1 G is used in eq 7 resulting in a G duration tolerance of 50s. Theoretically therefore a subject using PBG should tolerate 11.9 G for 50 s.

Unfortunately these studies have never been accomplished and may never be done but this example demonstrates the power of this model. Similar calculations can be made for reclined seat-back angles and combinations of reclined seat-back angles and PBG at very high levels of G.

5. DISCUSSION

My earlier model that was published in 1986 predicted G-level tolerances quite accurately. A comparison of calculated high-sustained G-level tolerances of this model, with those measured in various laboratories using the human-use centrifuge, shows a combined correlation coefficient ("r") of 0.96 at 7 seatback angles using data from 6 different published studies (4). The models developed and reported herein are more detailed and now include G-duration tolerance predictions. Consequently, these have considerably greater power and value.

Some of my reasons for developing physiologic based mathematical models are to collect and organize available pertinent information and provide a method to use that information, usually to predict G-level tolerances with subjects using new anti-G systems. These G tolerance models describe physiologic and physical interactions with simple calculations, thus forming a mathematical understanding of the basis of G tolerance. Mathematical models are also useful in teaching as they clearly illustrate the interactions of important physiologic parameters involved in humans accommodating to a changing environment. Indeed, these models, as with my earlier model, can be used also as a simple teaching tool as it provides a basic understanding of human tolerance to G. These models have been used in this manner in reference books (used as textbooks) in environmental physiology/medical courses (9, 10).

Useful models are best known for their ability to use experimental data to predict outcomes that can not be tested because of various confounding factors or testing is too complicated, time consuming, or expensive. Considering high-G research, all of the above factors apply with one major confounding factor being level of safety risk to the subject. A major value in predicting G tolerances is to quickly evaluate the application of new designs of operational methods/systems to increase G tolerances. Simply making design changes on paper, inserting them into the model and calculating the design benefits to G tolerance as an isolated system or in combination with other anti-G systems makes this model a very powerful tool. Also and very important is that these tests can be conducted at any G level since safety is not an issue.

Also the G-tolerance benefits of the application of operational systems, used in other environments, to the increased G environment can be predicted. For instance, PBG is based on breathing positive pressure used as an operational high-altitude protection system for pilots. The capability of PBG to increase G-level tolerance above operational levels with pilots performing the AGSM and wearing anti-G suits, was tested with both G-level and G-duration tolerance models. G-level tolerances with PBG were predicted at 12° seat back angle to be 11.9 G and measured by Burns (2) to be 12.0 G. Reclining subjects to 55° predicted a G tolerance of 15.5 G however since the Burns study was limited to 12.0 G they were unable to measure the maximum G-level tolerance (2). Also we were able to predict G-duration tolerances using PBG and straining with subjects seated upright at 11.9 G to be 50s. The study that is required to validate this value will probably never be attempted because of the safety risks involved. None the less scientists and engineers interested in this G-duration tolerance will have a reasonable estimate using this G-duration model.

In some situations models can give additional information that is not available with experimentation that has been completed and published. One example is the use of these models in validating a GOR G tolerance testing profile used recently in a G-tolerance study testing advanced G anti-G suits (14). The profile used was a gradual onset of G until the subject reached visual criteria commonly used in G-level tolerance testing. This same profile has been used to select candidate pilots for G-level tolerance as well as to test anti-G systems for increases in G-level tolerance. Using these models, it was demonstrated that this G tolerance measurement was not a G-level tolerance but was a measure of G-duration tolerance. Consequently changes in anti-G systems that were reported to have raised G-level tolerance using this profile had instead increased G-duration tolerance. Clearly such a misunderstanding of the identity of the tolerance measurement can become a safety issue (8).

6. REFERENCES

1. Buick F, Hartley J, Pecaric M. Maximum intra-thoracic pressure with PBG and AGSM. In: AGARD-CP-516, High Altitude and High Acceleration Protection for Military Aircrew. 1991; Oct 7.1-7.9.

2. Burns JW. Upper limits of +Gz protection. Avia. Space Environ. Med., 69:222, 1998.

3. Burton RR. Human physiologic limitations to G in high-performance aircraft. Chapt. 10. In: Physiological Functions in Special Environments. Eds. Paganelli CV, Farhi LE, Springer-Verlag, NY, 1988; 123-37.

4. Burton RR. A conceptual model for predicting pilot group G tolerance for tactical fighter aircraft. Aviat. Space Environ. Med. 1986; 57:733-44.

5. Burton RR. Mathematical models for predicting G-level tolerances. Presented at the 69th Ann. Sci. Mtg. Aerosp. Med. Assoc., Seattle WA, 1998.

6. Burton RR. Mathematical models for predicting G-duration tolerances. Aviat. Space Environ. Med. (submitted) 1998.

7. Burton RR. Mathematical models for predicting straining G-level tolerances in reclined subjects. J. Grav. Physiol. (in press) 1998.

8. Burton RR. Straining GOR tolerance determinations are a measure of G-duration not G-level tolerance. Presented at the SAFE Ann. Sym., Phoenix AR, 1998.

9. Burton RR, Smith AH. Adaptation to acceleration environments. Chapt. 40 In: Environmental Physiology. Vol II. Eds. MJ Fregly and CM Blatteis. Oxford Univ. Press. 1996; 943-70.

10. Burton RR., Whinnery JE. Biodynamics:Sustained acceleration. Chapt. 9. In: Fundamentals of Aerospace Medicine. Ed. RL DeHart. Williams and Wilkins, Pub. 1996; 201-60.

11. Cohen MM. Combining techniques to enhance protection against high sustained accelerative forces. Aviat. Space Environ. Med. 1983; 54:338-342.

12. Ernsting J. Some effects of raised intrapulmonary pressure in man. AGARDograph 106. WJ Mackay Co. Pub. 1966.

13. Harding RM, Bomar JB. Positive pressure breathing for acceleration protection and its role in prevention of inflight G-induced loss of consciousness. Aviat. Space Environ. Med. 1990; 61:845-9.

14. Paul MA. Extended-coverage-bladder G-suits can provide improved G-tolerance and high G_z foot pain. Aviat. Space Environ. Med. 1996; 67:253-5.

MODEL VALIDATION

Ints Kaleps
Air Force Research Laboratory
AFRL/HEPA
2800 Q Street - Bldg 824 - RM 206
Wright-Patterson AFB, OH 45433-7947, USA

SUMMARY

For models to be acceptable tools for the purposes of predicting system response, better understanding of phenomena, or use in design, they must have undergone some degree of validation. This paper seeks to provide an appreciation of the necessity for model validation, presents suggestions for model development to facilitate later validation, addresses degree of desired validation for various applications, and discusses the validation process. It particularly discourages the use of unnecessary degrees of freedom for model responses that can not be measured.

NEED FOR MODEL VALIDATION

We often hear that beauty is in the eye of the beholder. That one quite often sees what they want to see. It seems that model validation is viewed the same way. As modelers we often talk about model validation. We claim that our model is validated by comparing curves generated by models to empirical data, and making claims of successful validation. Sometimes the correspondence is so close that one wonders if the data have been adjusted. On other occasions the curves are so dissimilar that one wonders whether the wrong curves may have been presented. Generally claims are made about correspondence of peak amplitudes, the timing of peaks, rise times, decays, and sometimes the root-mean-square difference between the two response curves. Even though the model often has a number of degrees of freedom, usually only a few are compared for purposes of demonstrating validation. Some models are shown to match a set of empirical data quite well, but it is not clear whether these are predictive models and will provide an equally good fit for a modified system or are models that are strictly descriptive and only reflect the input data. Ultimately, if a model is to be accepted, it must have some validation pedigree. Let us examine what a model is, the process of model development, and the process of model validation.

In the simplest sense, a model is a representation of the real world. We generally think of a system on which we can make observations, we then identify fundamental response mechanisms which can be mathematically expressed, couple these to properly reflect the system interactions, exercise the model, and compare its predicted results to observations on the real system. While there are various types of models, we will only consider here models that are predictive in nature and are based on fundamental response mechanism for which material or other properties can specifically be measured. This precludes models that are merely data representations or systems identification models that can produce proper input-output characteristics, but cannot provide predications for specific changes to the system.

WHY MODELS?

First let us consider why we develop and use models as these reasons may dictate what level of validation is appropriate for various applications:

Better Insight into Physical Phenomena: Models and their sub-mechanisms can provide a better insight into the real physical process that they represent. They can effectively show response tendencies resulting from parameter or input changes and serve as a tool for concept explorations.

Reconstruction Tool for Physical Events: This approach allows for the reconstruction of a physical event where only partial data are available. The model serves as an interpolation and a partial extrapolation tool to reassemble an event that has not been fully observed.

Design Tool: Models can provide specific design criteria for development and modification of systems. Quantitative information is used to make design decisions.

System Simulation: For this application the model must adhere very closely to the system response, must have comparability between all system and model variables, and can be used to determine proper system response.

For these application areas the validation requirements become progressively more stringent. To get better insight into physical phenomena, it may be sufficient that the model is a proper idealization of the real system. Highly precise parameter properties are not necessary and a criterion of being physically reasonable may be sufficient. A typical application may be the investigation of the effects of differently shaped ejection seat acceleration pulses on crewmember acceleration.

The reconstruction of a physical event requires that the model have some general validation, but it must only have agreement at specific variable trajectory points. However, there is still physical reasonableness requirement throughout the full trajectory. An example this application could be an aircraft crash from which it is known what the ground impact deceleration was as well as points and forces of crewmember contact with the aircraft interior.

Papers presented at the RTO HFM Specialists' Meeting on "Models for Aircrew Safety Assessment: Uses, Limitations and Requirements", held in Ohio, USA, 26-28 October 1998, and published in RTO MP-20.

For use of models as a design tool, validation requirements become more stringent. The model in this case is used to provide quantitative information that will be used for specific design. An example could be the cockpit dimensions to provide clearance for an ejecting crewmember.

Use of models for simulations require the highest fidelity. These types of model applications are used to check the system design for deficiencies, and must have full fidelity and all variables require validation. A typical application is that of a controller for an ejection seat. Here every combination of input parameters is explored to ensure that the right output occurs.

MODEL DESIGN CONSIDERATIONS

There are a number of considerations that are integral to model development and its eventual validation:

Complexity: The number of degrees of freedom, their coupling, and their observability. A variable that cannot be observed, obviously, cannot be validated.

Completeness of Representation: Are all the degrees of freedom represented? Generally a trade-off is made between the completeness of the representation and the added complexity which requires additional data for validation.

Accuracy of Observation: Any human, mechanical, or analog system will have some observation error. It is possible to model digital or logical decision-making systems in which perfectly accurate observations can be made.

Range of Validity: Models are compositions of sub-mechanisms which have their domains of applicability. These may be property constraints such as linearity or algorithm constraints such as ones that limit large rotations.

MODEL BUILDING PROCESSES

After the system to be modeled has been properly identified, there are there three model-building processes that must be performed:

The Idealizations Properly Characterize the Model Responses: For a dynamic model, this would require that proper geometry, masses, flow, and connective properties are defined. Also that proper characterizations for the sub-mechanisms are selected, e.g. constitutive equations, equation of state.

The Analytic Formulation: The equations describing the model must be generated and written in a form amenable to solution.

The Solution of the Equations: The equations are solved either in closed form or, more likely, numerically on a computer.

VERIFICATION AND VALIDATION

After the modeler has completed his creation, apprehensively, but with great expectations, he submits it to the test. Inevitably, there will be compilation, code and other errors. But, hopefully, in time there will be results. These results will be subjected to two tests: *verification* and *validation.* Another process that has more recently been defined is a *confidence assessment*, but in effect it is no more than an elaborate verification and validation process.

The *verification* process may be viewed as the domain of the mathematician and ensures that the equations are being properly solved. The *validation* process is the domain of the researcher who ensures that the real system has been properly idealized, that the proper algorithms have been selected for the various sub-mechanisms, and the database of parameters is appropriate. The *confidence assessment* can be viewed as the domain of the bureaucracy, which seeks to provide a high level sanctioning process for a model. It has in part been the outgrowth of a concern by the General Accounting Office (GAO) that there is no standard of validity for models bought by the Department of Defense. A confidence assessment guidebook has been developed that provides a highly elaborate process that stresses teaming and involvement of experts, but fundamentally still deals with conceptual model validation, model implementation verification, and testing on the real system.

In the *verification* process coding errors and incorrect solutions for algorithms are the most common problems. Computer diagnostics will generally identify coding errors. Checking of algorithms is best done by comparing results to closed-form solutions. Checks can be performed either on individual algorithm subroutines or limited model runs may be performed in which only a portion of the model is exercised.

The *validation* process requires comparison of the predicted and real system variables. Judgement of validity is based on differences between the model predictions and the real system responses.

In developing a model and in anticipation of the requirement for ultimate model validation, certain approaches will make the validation process easier and will also lead to better model acceptance.

Use only enough degrees of freedom to capture the essential responses of the system. More variables will make the validation process more difficult, distract from the variables of real interest, and may couple with the primary variables to produce unclear responses.

Clearly define each component and its properties that is being modeled. The mass, constitutive properties, geometry, links to other components, etc. should be clearly related to the equivalent components in the real system. Effective properties may occasionally be used, but these may somewhat undermine the models validity since they cannot be directly measured on the real system.

Do not have variables in the model that cannot at least conceptually be measured. Ideally, have only variables that can be directly measured. Hidden variables cannot be validated and, unless there is a compelling hypothesis for some underlying mechanism, their use will cast doubt on the model's validity.

For the validation process, identify response characteristics that are most relevant in comparing model to system responses. These may not always be the primary system response variables. In dynamic systems, time histories of acceleration, velocity, displacement, and forces provide the best basis for comparison. However, point-by point comparisons can be highly misleading due to real system non-linearities. These cause slight phase shifts that can produce large least-square-mean values while the overall time histories may be quite similar. Contact force magnitudes can also be misleading since precise stiffnesses of contacting surfaces are difficult to quantify. Real system acceleration data that are derived from velocity or displacement data have magnified noise that may make comparisons to model data difficult. Comparisons that may be more appropriate for judging how well the model matches the real system include time history peak values, the time between peaks, impulses calculated from accelerations or contact forces, energy absorption, and frequency content.

REFERENCES

1. Carson, E.R., Cobelli, C., and Finkelstein, L. *The Mathematical Modeling of Metabolic and Endocrine Systems.* New York: John Wiley & Sons, 1983.
2. Knepell, P.L. and Arangno, D.C. *Simulation Validation: A Confidence Assessment Methodology.* Los Alamitos: IEEE Computer Society Press, 1993.
3. McLeod, J. *Computer Modeling and Simulation: Principles and Good Practice.* La Jolla: A Society for Computer Simulation, 1982.

A biomechanical approach to evaluating the health effects of repeated mechanical shocks

Morrison, J.B.*, Robinson, D.G., Nicol, J.J., Roddan, G., Martin, S.H., Springer, M.J-N., Cameron, B.J., and Albano, J.P**

BC Research Inc., 3650 Wesbrook Mall, Vancouver, B.C. CANADA, V6S 2L2
*School of Kinesiology, Simon Fraser University, Burnaby, B.C. CANADA, V5A 1S6
**U.S. Army Aeromedical Research Laboratory, Fort Rucker, AL, USA, 36362-0577

1. SUMMARY

Operators of industrial and military vehicles are routinely exposed to repeated mechanical shocks. Numerous studies have associated these exposures with an increased incidence of low back pain and degenerative disorders of the spine. This paper describes a method of evaluating the effect of repeated mechanical shocks on the health of vehicle operators. The method provides a health hazard assessment (HHA) in which the risk of injury to the operator is related to the acceleration measured at the vehicle seat. The HHA process consists of four stages. Dynamic response models are used to predict accelerations of the lumbar spine in the x, y and z axes from accelerations at the seat. Compressive forces at the L4/L5 vertebral joint are estimated from peak lumbar accelerations using relationships derived from biomechanical analysis. The effect of repeated compressive loading is calculated using a dose model based on the fatigue failure properties of tissue and the compressive strength of the vertebral joint. The risk of injury to the operator is then determined from the accumulated compressive dose, the fatigue life of the system, the variance of vertebral joint strength data, and the cumulative probability of failure. The HHA model can be used to predict the risk of injury from a single exposure or from the cumulative effects of a life time. The HHA was tested using a range of repeated shock profiles. Results indicate that the risk of injury predicted by the HHA compares favorably with human tolerance data obtained from acute exposures and with injury incidence data obtained from chronic exposure of vehicle operators.

2. INTRODUCTION

Operators of industrial and military vehicles are routinely exposed to high levels of whole body vibration (WBV > 1.0 $m.s^{-2}$ rms) and repeated mechanical shocks (MS > 10 $m.s^{-2}$ peak). Numerous studies have been published in which vibration levels of 1.0 to 2.5 $m.s^{-2}$ have been reported (1). Although there is less information available regarding levels of shocks in vehicles, studies have indicated that repeated mechanical shocks of greater than 10 $m.s^{-2}$ are not uncommon (1). Epidemiological studies have shown high levels of low back pain and degenerative disorders of the spine in vehicle operators. A major limitation of some studies is the absence of control groups to provide comparative incidence rates in non-exposed workers. The manner in which data is gathered, and the criteria used for evaluating low back pain also vary. Information on ride conditions and duration of exposure are limited and methods of reporting are inconsistent. Although most studies report rms vibration levels, others provide rmq vibration or vibration dose value (VDV). There is generally no information as to whether the exposures contain repetitive shocks. Nevertheless there is good evidence of increased low back pain in vehicle operators, although it is difficult to establish a dose response relationship. There is also evidence of an increase in the spinal degenerative process with high levels of vibration (1.5 $m.s^{-2}$). Although not reported, it is likely that these exposures also contain repetitive shocks.

The International Organization for Standardization has published a method of measuring and reporting human exposure to whole body vibration (2). This standard also included an indication of the rms vibration levels at which daily exposure is likely to cause health effects. The standard is restricted to measurement and analysis of whole body vibration and is not considered applicable to exposures containing repeated mechanical shocks. A revision of the ISO 2631 was published in 1997 (3) which provides guidelines for evaluating repetitive shocks. This involves the use of a running rms value, or alternatively calculation of a vibration dose value (VDV) based on the fourth power of acceleration. The standard does not provide a means of relating these measures to health effects. Both methods have been criticised for the lack of a physiological or biomechanical basis. It has been suggested that a VDV of 15 is approximately equivalent to the existing rms exposure limit for health effects.

An alternative method for evaluating mechanical shocks was proposed by Payne (4). This method

Papers presented at the RTO HFM Specialists' Meeting on "Models for Aircrew Safety Assessment: Uses, Limitations and Requirements", held in Ohio, USA, 26-28 October 1998, and published in RTO MP-20.

referred to as the dynamic response index (DRI) utilises a simple second order system consisting of a mass, spring and damper to simulate upper body motion in response to a single shock. Although originally designed for single impact events such as aircraft ejection, the DRI model has been extended to the evaluation of repetitive shocks. Payne (4) adopted a theory of material fatigue failure (5) to predict the effects of repeated mechanical shocks. The successive values of DRI were summed in a dose function and related to fatigue failure of vertebrae. Although there is data to support the application of the DRI to single, large amplitude shocks, the use of this method to predict chronic health effects of repeated mechanical shocks has not been validated.

The present study was instigated due to concerns about the health effects of repeated mechanical shocks on the operators of military vehicles. New tactical ground vehicles are lighter and capable of higher speeds than their predecessors. These vehicles operate at high speeds over rough terrain, which results in high levels of whole body vibration and repetitive mechanical shocks that are transmitted to the occupants through the vehicle seats. The objectives of this study were to ascertain the type of shock exposure occurring in military vehicles travelling over rough terrain, to investigate the nature of human response to mechanical shocks, and to develop a model which will predict the probability of injury due to repeated shock exposure.

3. METHODS

A literature review was conducted in which existing data of human exposure to shock in vehicles and the possible health effects were examined (1). A number of records of whole body vibration and shock were obtained from a selection of military vehicles operating on test tracks and across open country. These records represented a range of conditions including vehicle type, speed, loading, and position within the vehicle. A classification of shocks by peak amplitude, fundamental frequency, and decay rate was employed to analyse the shocks recorded during the operation of the tactical ground vehicles (6). The shock and vibration characteristics of these vehicles were simulated in a series of synthesised signatures. Each shock consisted of a single damped sinudoid characterised by its amplitude and waveform frequency.

Experimental data on the human response to shocks was collected using a multi axis ride simulator (MARS) at the US Army Aeromedical Research Laboratory, Ft. Rucker, AL. (7). The MARS consists of a shake table which can be driven in three orthogonal axes by hydraulic actuators governed by a multi channel servo controller (Shenck Pegasus 5900). The MARS has a frequency response of 2 to 40 Hz and an amplitude range of $\pm$ 40 $m.s^{-2}$.

The study was reviewed by an ethics review board. Volunteer subjects selected from military personnel completed informed consent forms prior to exposure to a series of shock signatures of the amplitude and period (or shock frequency) identified in military vehicles. Volunteers were carefully selected and clinically screened to exclude previous injury or existing conditions that may have predisposed them to injury. Subjects were positioned on a rigid seat bolted to the MARS table. The seat consisted of a metal frame and surface. A thin beanbag type cushion was taped to the surface of the seat in order to distribute the pressure between the seat and the subject. Ten subjects were exposed to a series of simulated vehicle rides of approximately 330 seconds duration. Each exposure contained between 16 and 34 shocks superimposed on a background of random vibration. In each simulation, shocks of 0.5 to 4 g were delivered in the x, y, or z axes.

Acceleration inputs to the subject were measured at the seat using a flexible seat pad containing accelerometers mounted in the x, y, and z axes. Human response was measured by miniature accelerometers (Entran EGAX $\pm$ 25 g) attached to the skin surface over the spinous process at the T1, T2, T3, and L2, L3, and L4 vertebrae. Muscle activity (surface emg) was recorded from the extensor muscles at the level of T9 and L3. A rectal probe containing a miniature pressure transducer was used to measure the internal pressure fluctuations in response to individual shocks. Data were collected to a VAX 3000 computer at a sampling rate of 500 s^{-1}. Spinal posture and displacement data were collected at 200 s^{-1} using an Optotrak system coupled to a 486 personal computer. Infrared emiting diodes (IREDs) were attached over the spinous process at C7, T4, T6, T8, T9, T10, T12, L1, and L5.

Subjective response data were collected from subjects in response to each shock. Subjects were asked to rate shock severity on a scale of 1 to 7 where 1.0 represented barely perceptible and 7.0 represented the limit of tolerance. Due to the wide range of shock inputs at the seat and the ability of the subjects to discriminate between the sensations of each shock, subjective responses were reported in increments of 0.1, providing an effective 70 point scale.

Sustained operations in tactical ground vehicles may require soldiers to be exposed to a motion environment for prolonged periods of time. In a second series of experiments, ten subjects were exposed to a simulated vehicle ride containing shocks of $\pm$ 2 g peak magnitude in the x, y, and z axes and + 4 g in the z axis. During each five minute period subjects were

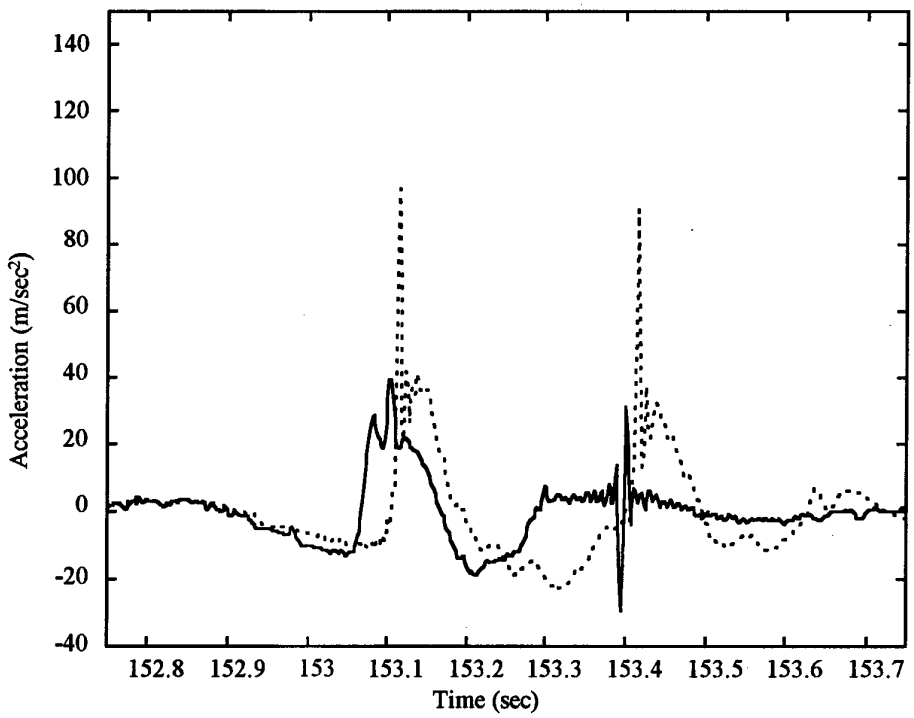

Figure 1. Acceleration at the seat and lumbar spine for a +4 g, 4 Hz z axis shock. Dotted line: Lumbar L4 z; solid line: Seat Sz.

exposed to 128, 2 g shocks and 2, 4 g shocks. Each subject was exposed to the simulated vehicle ride for a maximum of eight hours which included two 15 minute rest periods and one 30 minute rest period. During the experiment the subjects rated the severity of the shock, their level of comfort, and tiredness. Subjects were also asked to report their predicted tolerance time for the exposure condition. Measures of acceleration, internal pressure and posture were collected as described in the previous experiment.

4. RESULTS

Study of acceleration data measured at the seat of military vehicles during cross country operations indicated that shocks varied in magnitude from 0.5 to 6 g in the z axis with the majority being less than 4 g. Shocks measured in the x and y axes were generally smaller in magnitude with maximum values of approximately 4 g. It was also noted that z axis shocks occurred in both positive (upward) and negative (downward) directions.

Analysis of experimental data obtained from the simulated vehicle rides indicated that shock transmission to the lumbar spine was attenuated in the x and y axes with the highest transmission occurring at the lowest shock frequency measured (2 or 4 Hz). As the frequency of the shock waveform increased, transmission decreased from about 0.5 at 4 Hz to 0.2 at 20 Hz. The shock transmission was approximately linearly related to amplitude in both the x and y axes.

The pattern of spinal response to z axis shocks was more complex than in the x and y axes. Transmission ratios, which were greatest at the lower shock frequencies (4 to 6 Hz), were non-linear with input shock amplitude. Transmission ratios decreased from in excess of 1 at 4 Hz to approximately 0.5 at 20 Hz. Higher transmission ratios were measured in response to the larger magnitude shocks. This non linearity was particularly prevalent for the lower frequency shock waveforms. A typical acceleration response to a 4 g z axis shock is shown in Figure 1.

From subjective measures obtained following extended exposure to the simulated vehicle ride it was clearly demonstrated that exposure to these shock and vibration conditions resulted in residual soreness and pain. Given the lack of objective evidence of injury and the relatively low levels of muscle activity indicated by emg data it was likely that this soreness was related to inflamation or damage to spinal structures.

5. HEALTH HAZARD ASSESSMENT

Any health hazard assessment method capable of predicting the risk of injury from repeated mechanical shocks must be based on data from a wide range of studies encompassing human response, injury

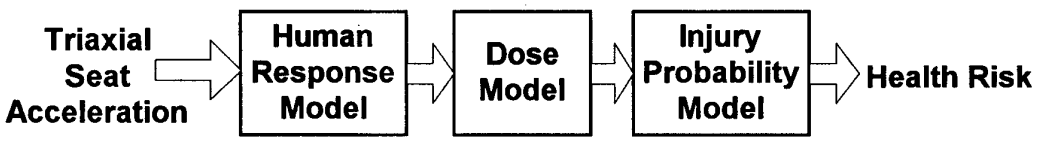

Figure 2. Structure of Health Hazard Assessment method

incidence, material properties, and theoretical models. Therefore, the approach adopted in this study was to construct a HHA method which is based on components selected from existing models, human response data, tissue characteristics and injury data. The structure of the HHA method is shown in Figure 2.

5.1 Dynamic Response Models

As the lumbar acceleration response in the x and y axes was approximately linear, the response was modelled as a second order linear system of the form proposed by Payne (4). The parameters of the model were then adjusted to give the best fit to the experimental data using indexes of rms and rmd error. Results indicated that the best prediction was obtained with a natural frequency f_n = 2.125 Hz and critical damping ratio ς = 0.22 for both the x and y axes.

As the response to z axis shocks was non-linear, a different strategy was adopted to model the response. A recurrent neural network (RNN) was developed and trained to represent the system dynamics using the acceleration data obtained from the experiments (8). The RNN predicted acceleration output at the lumbar spine based on the previous acceleration inputs at the seat and previous predicted outputs. The final RNN consisted of 12 input elements, seven hidden layer processing elements, and one output processing element.

5.2 Biomechanical Model

A biomechanical model of the upper torso was developed to estimate the compressive and shear forces acting at the L4/L5 lumbar joint in response to shock input at the seat. Input to the biomechanical model consisted of spinal posture, acceleration data, and internal pressure. Posture was obtained from the location of the IREDs at C7, T4, T8, T10, L1 and L5. The coordinates of these points were used to determine the vector directions of the long axis of the spine at three levels within the torso. The centre of mass of each segment and the corresponding linear and angular accelerations (flexion-extension and lateral rotation) were calculated from the coordinate data. It was assumed that there was no rotation about the long axis of the torso.

The upper torso was represented as a six compartment lumped parameter model. It was assumed that the high frequency components of acceleration (> 20 Hz) observed in the acceleration data were transmitted through the stiffer tissues of the vertebral column. The mass of the torso was therefore subdivided into two compartments representing the spinal mass and soft tissue mass. Acceleration of the soft tissue mass was low pass filtered at 20 Hz (based on the frequency spectrum of the internal pressure data). In order to accommodate the flexion of the spinal column (which was observed in the IRED data in response to shocks) the torso was further subdivided into three spinal levels. These compartments were treated as linked segments having individual linear and angular accelerations.

Moments Mx and My acting at the L4/L5 joint were calculated from the accelerations, segment masses and coordinate data measured from the experimental subjects. The resultant joint moments were equilibrated by forces in the extensor, abdominal and lateral oblique muscles, and the internal pressure which was assumed to act on the diaphragm. The resultant joint compression force at L4/L5 was calculated by summing the forces due to acceleration, internal pressure and muscle tension.

The peak compressive forces were calculated in response to shock wave forms in the range 0.5 to 4 g magnitude and 2 to 20 Hz frequency in the x, y and z axes. The peak compressive force at the L4/L5 lumbar joint was compared with the corresponding peak lumbar acceleration (in the direction of the shock inpupt at the seat) predicted by the dynamic response model for the x, y or z axis respectively. A series of regression equations was developed to transform the output of each dynamic response model (i.e., predicted peak lumbar acceleration in the direction of the shock) to the resultant peak lumbar compressive force. The peak lumbar compressive forces in response to repeated mechanical shocks in the x, y and z axes could then be summed to provide a joint compression dose function.

5.3 Repetitive Shock Dose Model

Mechanical fatigue due to repetitive loading has been proposed as a mechanism for chronic degenerative changes to spinal structures (9, 10). A fatigue dose model was therefore developed using a theory of material fatigue (5). This approach has been suggested by several authors in connection with

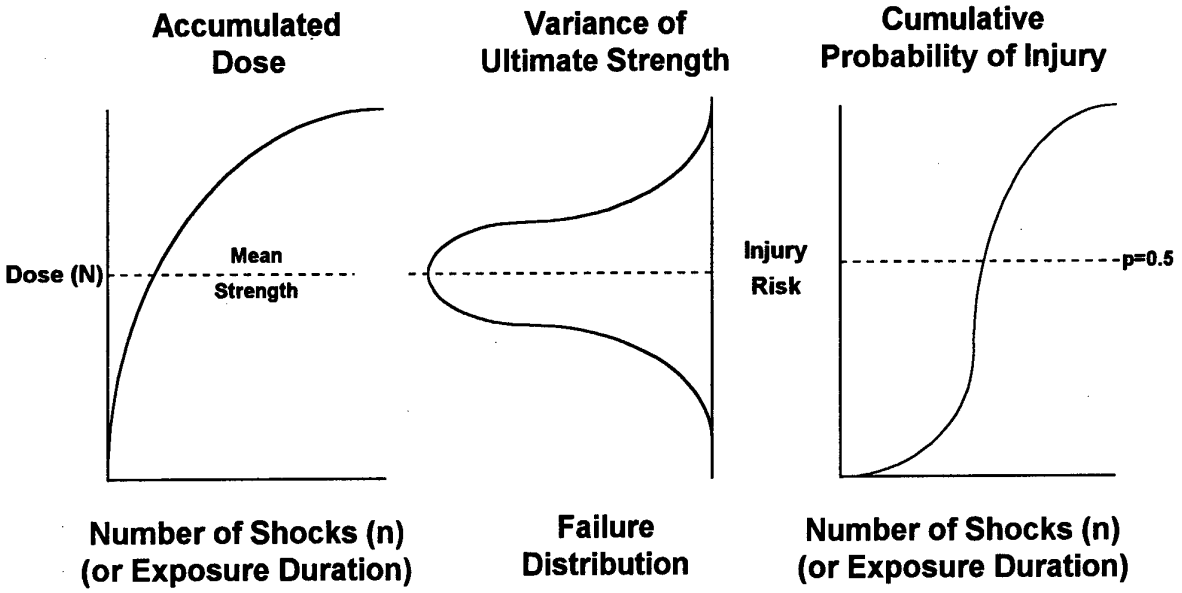

Figure 3. Conceptual illustration of the relationship between the computed dose value (N) and failure distribution, which combine to estimate the risk of injury (cumulative probability function).

repetitive loading of the spine due to mechanical shock (4, 9,11).

Miner (5) proposed that the degree of fatigue (D) of a material subject to repeated stress can be expressed by the ratio (n_i / N_i), where n_i = the number of cycles completed at stress S_i and N_i = the number of cycles required to cause failure. In addition, the number of cycles to failure can be expressed as

$$N_i = (S_u/S_i)^x$$

where S_u = static failure stress,
and S_i = applied repetitive stress level.

This relationship can be generalised to any number of stress levels and cycles, where the degree of fatigue = Σ (n_i / N_i). The effective stress "dose" can be expressed as

$$S_e = \{ \Sigma [n_i (S_i)^x] \}^{1/x}$$

where S_e, represents an equivalent single static stress which will produce the same degree of fatigue. In this configuration the repetitive stress dose function produces failure when $S_e = S_u$. This relationship has a similar form to the existing DRI acceleration dose function for assessing shocks (12).

The parameters of the model were determined from the published experimental data of fatigue failure in bone, and the material properties of the lumbar joints. The peak compressive force estimated in response to each shock is summed to obtain a resultant compression "dose" at the L4/L5 joint

$$F_e = \{ \Sigma [n_i (F_i)^6] \}^{1/6}$$

where F_i = prediction of peak compressive force (N) for each shock
and F_e = the equivalent static load (N).
The value x = 6 was selected as a conservative estimate of the rate of fatigue in bone (13, 14, 15, 16).

5.4 Injury Risk Model

The cumulative dose function provides a value of equivalent static load F_e for a series of repetitive shocks at the seat. The ultimate strength of the L4/L5 joint was estimated from the experimental data of Hutton et al. (17), and Porter et al. (18). These authors tested complete spinal units selected from male cadavers with an average age of 27 years (range 19 to 46). Data were obtained from 34 samples of lumbar joints and adjusted for spinal level. The mean ultimate strength of F_u = 10,093 N ($\pm$ 1926 sd) was calculated for the L4/L5 joint.

Rather than associate injury with single dose value, the distribution of compressive strength was used to represent the likelihood of injury within a population. This was achieved by relating the computed dose value F_e to a cumulative probability function based on the population variance of the cadaver data. Thus a dose value of $F_e = F_u$ represents a 50% probability of injury. This concept is illustrated in Figure 3.

Table 1. Results of Health Hazard Assessment using seat acceleration data from simulated vehicle rides.

Ride Description	Acceleration (rms) - $m.s^{-2}$	Exposure Duration	Probability of Injury	Compression Dose (N)
Vibration (2-40 Hz)	0.63	10 years	0	0
0.3 g shocks (32/5 min) + 0.6 g shocks (32/5 min) 2 to 20 Hz	0.63	10 years	0.013	5811
0.5 g shocks (32/5 min) + 1 g shocks (32/5 min) 2 to 20 Hz	1.1	10 years	0.11	7716
2 g shocks (32/5 min) 6 Hz	1.6	1 year	0.95	13237
2 g shocks (64/5 min) + 4 g shocks (2/5 min) 6 Hz	2.65	6 hours	0.19	8447

5.5 Integration of Model Components

Information from the dynamic response models, biomechanical model, dose model and injury risk model were combined to produce a method of health hazard assessment (HHA). Given input seat acceleration time series in the x, y and z axes, the HHA method computes the probability of injury for a specified exposure duration. The biomechanical data are used to correlate the predicted peak lumbar acceleration response to each shock with the peak compressive force at the L4/L5 joint. This information is then used to construct a compression dose using a theory of material fatigue. The corresponding probability of injury is estimated from the joint ultimate strength and population variance.

6. MODEL VALIDATION

Validation of the health hazard assessment method and its component models is limited by the lack of available information regarding the human response to repeated mechanical shocks. Few experiments have measured both the input shock acceleration at the seat and the response in terms of spinal acceleration or injury. No publications were located that measure internal spinal forces in response to repeated spinal shocks. Therefore, validation was based on the data measured during the experimental phases of this study, existing standards for whole body vibration, and a few relevant epidemiological studies.

The HHA method was tested using a selection of repeated mechanical shock signatures and exposure durations varying from 6 hours to 10 years. Input data for this process were obtained from the simulated vehicle rides developed for the experimental phase of the study. The seat acceleration profiles, rms acceleration levels, duration of exposure, probability of injury predicted by the assessment method, and compression "dose" are reported in Table 1.

The lower end point for safe exposure was evaluated using the ISO 2631 limits for steady state vibration (2). Chronic exposure (of 6 hours/day) to vibration of approximately 0.63 $m.s^{-2}$ rms resulted in a dose value of zero with no likelihood of injury. The acceleration peaks contained in this signal did not exceed the minimum acceleration threshold of 3 $m.s^{-2}$ utilized in the model for determining the presence of shocks. However, a signal containing 0.3 g and 0.6 g shocks with a rms level of 0.63 $m.s^{-2}$ registered a probability of injury of 0.01 after ten years' exposure. A similar signal containing 0.5 g and 1 g shocks at rates of 32 per 5 min. interval yielded a probability of injury of 0.11 after ten years.

The relatively low probability of injury for a lifetime exposure to 0.63 $m.s^{-2}$ rms vibration is confirmed by epidemiological studies (1). These studies also show that vehicles producing rms vibrations of 1.5 to 2.5 $m.s^{-2}$ cause significant degenerative changes to spinal structures.

An upper end point for extreme exposure was established using the most severe condition tested in the experimental phase when subjects were exposed to repeated shocks of 2 g and 4 g for a period of up to seven hours. The HHA method predicted that this

condition could cause some injury within one day. This prediction is supported by subjective reports of muscle soreness and pain. Exposure was terminated voluntarily after only three hours in one case, and only two subjects completed the seven hour experiment.

7. CONCLUSIONS

There are a number of limitations to the HHA method which will affect the accuracy of the hazard assessment. The probability of injury is based on a small amount of data describing vertebral fracture in the spinal units of cadavers. There is evidence in the literature that micro fractures may occur at stress levels well below failure (10). The model needs to be more rigorously tested against chronic injury data due to long term exposures to WBV and repeated shocks. The model does not account for either the ability of biological material to repair, or the decline of vertebral strength with age. It represents male vehicle operators within an age range of approximately 20 to 40 years. However, the model structure forms the basis of a general HHA method, within which sub-components and parameters can be adjusted as experimental and epidemiological data becomes available.

8. DISCLAIMER

This work was supported by the U.S. Army Medical Research and Development Command under Contract No. DAMD17-91-C-1115. The views, opinions and/or findings contained in this report are those of the authors and should not be construed as an official Department of the Army position, policy or decision unless so designated by other documentation. In the conduct of research where humans are the subjects, the investigators adhered to the policies regarding protection of human subjects as prescribed by 45 CFR 46 (Protection of Human Subjects).

9. REFERENCES

1. Village, J., Morrison, J., Robinson, D., Roddan, G., Rylands, J., Cameron, B., Brammer, A., and Smith, M. 1995. Development of a standard for the health hazard assessment of mechanical shock and repeated impact in army vehicles Phase 1. U.S. Army Aeromedical Research Laboratory, Fort Rucker, AL. Report CR-95-1

2. International Organization for Standardization 1974. ISO 2631: Guide to the evaluation of human exposure to whole-body vibration.

3. International Organization for Standardization 1997. ISO 2631-1 Mechanical Vibration and shock - Evaluation of human exposure to whole-body vibration - Part 1: General requirements.

4. Payne, P. 1976. On quantitizing ride comfort and allowable acceleration, AIAA 76-873. American Institue of Aeronatuics and Astronauts/Society of the Naval Architects and Marine Engineers Conference on Advanced Marine Vehicles, Arlington, Virginia.

5. Miner, M.A. 1945. Cumulative Damage in Fatigue. Journal of Applied Mechanics. 12: 159-164

6. Roddan, G., Brammer, T., Village, J., Morrison, J., Remedios, B., Brown, D. 1995. Development of a Standard for the Health Hazard Assessment of Mechanical Shock and Repeated Impact in Army Vehicles: Phase 2. U.S. Army Aeromedical Research Laboratory, Fort Rucker, AL. Report No. CR-95-2.

7. Cameron, B., Morrison, J., Robinson, D., Vukusic, A., Martin, S., Roddan, G, and Albano, J.P. 1996. Development of a Standard for the Health Hazard Assessment of Mechanical Shock and Repeated Impact in Army Vehicles: Phase 4. U.S. Army Aeromedical Research Laboratory, Fort Rucker AL. Report CR-96-1.

8. Morrison, J., Robinson, D., Roddan, G., Nicol, J., Springer, M. J-N., Martin, S., Cameron, B. 1997. Development of a standard for the health hazard assessment of mechanical shock and repeated impact in army vehicles: Phase 5. U.S. Army Aeromedical Research Laboratory, Fort Rucker AL. Report CR-96-1.

9. Sandover, J. 1983. Dynamic loading as a possible source of low-back disorders. Spine. 8: 652-658.

10. Brinckmann, P. 1985. Pathology of the vertebral column. Ergonomics. 28: 77-80.

11. Allen, G.R. 1977. Human tolerance of repeated shocks. In Proceedings of the European Space Agency Life Sciences Research in Space, 343-349. Germany

12. Air Standardization Coordinating Committee. 1982. Human tolerance to repeated shock. Air Standardization Coordinating Committee ADV PUB 61/25 : 1-6.

13. Lafferty, J.L. 1978. Analytical Model of the Fatigue Characteristics of Bone. Aviation Space and Environmental Medicine. 49: 170-174.

14. Carter, D.R., Caler, W.C., Spengler, D.M., and Frankel, V.H. 1981. Uniaxial Fatigue of Human Cortical Bone. The Influence of Tissue Physical Characteristics. Journal of Biomechanics. 14: 461-470

15. Hansson, T., Keller, T.S., and Spengler, D.M. 1987. Mechanical behavior of the human lumbar spine. II. Fatigue strength during dynamic compressive loading. Journal of Orthopedic Research. 5: 479-487.

16. Brinckmann, P., Biggeman, M. and Hilweg, D. 1988. Fatigue fracture of juman lumbar vertebrae. Clinical Biomechanics. 4 (Supplement 2): S1-S23.

17. Hutton, W.C., and Adams, M.A. 1982. Can the lumbar spine be crushed in heavy lifting? Spine. 7(6): 586-590.

18. Porter, R.W., Adams, M.A., and Hutton, W.C. 1989. Physical activity and the strength of the lumbar spine. Spine. 14(2): 201-203.

THE DEVELOPMENT OF A LUMPED-PARAMETER MODEL FOR SIMULATING THE VIBRATION RESPONSE OF THE HUMAN BODY

S. D. Smith
Air Force Research Laboratory
Noise and Vibration Branch
AFRL/HESN, 2610 7th Street
Wright-Patterson AFB, OH 45433-7901, USA

SUMMARY

Seating systems provide a mechanism for minimizing the transmission of vehicle vibration to the occupant. Human vibration data has indicated that differences exist in the distribution of the mass, stiffness, and damping characteristics between the smaller female and larger male which may be important when designing seating systems. Mathematical models may provide a useful tool for the development and evaluation of seating systems for vibration mitigation. However, in order to be effective, these models must adequately simulate and predict the range of vibration response characteristics observed in the human body. A five degree-of-freedom (DOF) model was developed based on the dynamic response characteristics of major anatomical regions or structures in the human body. The model was recently modified to represent the legs as a two DOF system based on vibration response data collected in this laboratory. This paper summarizes the development, modification, and effectiveness of the five DOF model in simulating the differences between representative female and male vibration responses. The model is also evaluated on its ability to predict the effects of seat cushions on human body vibration response.

1. INTRODUCTION

Prolonged exposure to whole-body vibration is known to occur in the operation of military air, ground, and water vehicles. These exposures can have adverse effects on the comfort, performance, and even the health of the crewmembers. Back pain is the most common symptom reported by military helicopter pilots and vibration has been considered one of several factors contributing to these symptoms. Low back pain and general discomfort were reported in a survey of Black Hawk helicopter pilots who attributed the discomfort to the seat configuration (1). The pilots indicated that the seatpan cushions were too thin and concentrated loading on the ischial tuberosities.

The seating system provides one possible mechanism for minimizing the adverse effects of vibration. However, the majority of current seat cushion designs have been shown to increase the transmission of vibration at low frequencies (in the vicinity of the major body resonance of 4 - 8 Hz) and attenuate vibration at higher frequencies (2, 3, 4, 5). For some vehicles, the addition of a suspension system can improve the vibration attenuation at low frequencies but their use in military aircraft is limited due to the requirements for crashworthiness.

Mathematical models may be a useful tool for optimizing seating system design for vibration mitigation. Lumped-parameter models of the human body have been used for simulating and predicting human vibration response. In particular, most of these models were developed for simulating the driving-point impedance or apparent mass response of the human body at the major resonance located between 4 and 8 Hz. These models have ranged from a simple single degree-of-freedom (DOF) system to more complex multi-DOF systems which include the representation of several body regions or structures (6, 7). However, none of these models have undergone rigorous comparison to measured data to determine if they effectively predict the dynamic response of the represented anatomical regions. This has partly been due to the lack of data. This laboratory has conducted a series of studies to characterize the vibration response of

Papers presented at the RTO HFM Specialists' Meeting on "Models for Aircrew Safety Assessment: Uses, Limitations and Requirements", held in Ohio, USA, 26-28 October 1998, and published in RTO MP-20.

major anatomical regions in the human and to determine the contribution of these regions to whole-body vibration response (8). These data, has well as some limited data collected by others, were used to develop a five DOF human body model based on the known dynamic characteristics of the contributing anatomical regions, and which was capable of simulating and predicting the coupling effects between regions or structures. The model was shown to be quite effective in simulating the effects of acceleration level on the driving-point mechanical impedance response and was used to quantify changes in the mass, stiffness, and damping characteristics of the lumped anatomical regions as a function of acceleration (9). Recently, the model was expanded to include the addition of a seat cushion and a simple low frequency suspension system and was evaluated for its effectiveness in simulating both the impedance and transmissibility responses from data collected in this laboratory (10). The model was shown to be relatively effective in predicting the increases in the peak driving-point impedance and peak chest transmissibility at low frequencies (4 - 8 Hz) with the use of cushions, but overestimated the magnitude of the peak chest response. The model was also effective in simulating the two prevalent transmissibility peaks observed in the spine transmissibility data; the first peak (5 - 6 Hz) associated with dynamic coupling with the chest or upper torso. However, the magnitude of the major peak in the spine occurring at higher frequencies (15 - 20 Hz) was underestimated by the model. The model did show the relative damping effect of seat cushions at these higher frequencies. The model included a single DOF representation for the legs. The simulations for the leg transmissibility coincided with the peaks observed in the transmissibility data collected at the knee (between 5 and 9 Hz) (8). Data collected at the thigh have shown two transmissibility peaks for the males; the first coinciding with the response of the lower leg (5-9 Hz), and the second located between 10 and 15 Hz. The model did predict a peak in the higher frequency range (10-15 Hz) for the single DOF system representing the response of the lower torso.

For a model to be effective, it must be capable of simulating the broad range of vibration responses observed among humans. Mechanical impedance data have shown differences between the response characteristics of smaller females (weighing less than 60 kg) and larger males (weighing greater than 70 kg) (11). The primary impedance peak located between 4 and 8 Hz was expected to be higher in the larger male. However, with an acceleration level of 0.59 m/s^2 rms, the smaller females showed a second peak between about 7 and 10 Hz whose magnitude was similar to or greater than the primary peak. This peak was associated with the response of the legs and has been observed in some larger males at lower acceleration levels (0.347 m/s^2 rms) (9). These findings and the resonance behavior observed in the thigh transmissibility data led to the modification of the five DOF model in which the upper and lower legs were represented as a coupled two DOF system. The objective of this paper is to evaluate the effectiveness of the modified five DOF human vibration model in simulating the differences observed in the vibration responses of the smaller female and larger male. A summary is provided on the human vibration data collection scheme and model modification process. In addition, the modified model is evaluated on its ability to predict the effects of seat cushions on human body vibration response.

2. METHODOLOGY

2.1 Human Vibration Data

Details on the human vibration data collection scheme used in this laboratory are provided in (11). In summary, an Unholtz-Dickie electrodynamic vibration platform was used to provide the vertical motion. A rigid seat was mounted on top of the platform. The seat included a seatpan and seatback oriented at 90 degrees and weighed approximately 12 kg. A lapbelt and double shoulder harness were used to loosely restrain the subjects. The transmitted force of the combined seat and subject was measured from three load cells located between the seat and moving platform. Two accelerometers were

located beneath the seat for measuring the input acceleration and phase, respectively. Miniature accelerometers were attached, via double-sided tape, at various anatomical regions including the chest (at the manubrium), spine (in the vicinity of the seventh cervical vertebra over the spinous process), the head using a bitebar, and the leg (at mid-thigh). In an earlier study, accelerations were also measured at the top of the knee (distal end of the tibia) (8).

The input profiles typically included sinusoidal vibration at discrete frequencies, as well as sum-of-sines profiles generated with different crest factors (ratio of peak acceleration to rms acceleration). The frequency range for all exposures was 3 to 21 Hz in one-Hz increments. All frequency components were generated at the same acceleration level. The overall rms acceleration for the profiles ranged from 0.49 - 2.35 m/s^2 rms. The input profiles were computer-generated and an iterative process was used to minimize the error between the actual and desired input.

The calculated responses included driving-point mechanical impedance and transmissibility. Driving-point impedance was defined as the complex ratio between the transmitted force at the seat and the input velocity at the seat (calculated from the input acceleration). The magnitude and phase were plotted as functions of frequency. Peaks in the response profiles indicated a resonance in the body, although the anatomical region(s) contributing to the response could not be determined from this calculation. The transmissibility for each of the anatomical regions was defined as the magnitude ratio between the acceleration measured at the region or structure (chest, spine, leg) and the input acceleration at the seat. Again, the responses were plotted as a function of frequency. A peak in the transmissibility frequency response was also an indication of resonance but the motion could be due to coupling with another resonant structure.

Subjects were tested in the rigid seat (no cushion) and with the use of seat cushions. The legs were unsupported (no footrest). Two seat cushions were used for the modeling effort. The first cushion (Cushion 1) was obtained from a Black Hawk helicopter. The cushion was fabricated with three layers of foam. The bottom layer was made of high density plastic foam and varied in thickness from about 1 cm at the back to 6 cm at the front providing a contoured seating surface. Air vents ran from the front to back on the inside surface. The top layer was made of polyurethane foam about 2.5 cm in thickness. The middle layer was approximately 1.5 cm in thickness and made of polyurethane foam of greater density than the top layer. The cushion was covered in 2.5 cm thick black lambswool and weighed approximately 920.0 gm. The second cushion (Cushion 2) was fabricated entirely of rate-sensitive foam and was approximately 3 cm thick. The cushion was encased in a cotton material with the top and side surfaces covered with a 2.5 cm thick treated wool fabric. The cushion was flat and weighed 1678.5 gm. The cushions were additionally tested using two rigid masses weighing 38.5 kg and 68.0 kg.

2.2 Five Degree-of-Freedom (DOF) Lumped-Parameter Model

Figure 1 illustrates the modified five DOF model which represents the leg as a two DOF coupled system.

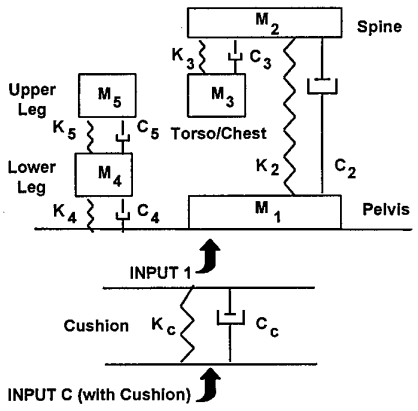

Figure 1 Five Degree-of-Freedom Model

The equations of motion for the mass systems represented in the model are:

$$M_1\ddot{x}_1 + K_2(x_1 - x_2) + C_2(\dot{x}_1 - \dot{x}_2) + K_4(x_1 - x_4) + C_4(\dot{x}_1 - \dot{x}_4) = F_{T1} \quad (1)$$

$$M_2\ddot{x}_2 + K_2(x_2 - x_1) + C_2(\dot{x}_2 - \dot{x}_1) + K_3(x_2 - x_3)) + C_3(\dot{x}_2 - \dot{x}_3) = 0 \quad (2)$$

$$M_3\ddot{x}_3 + K_3(x_3 - x_2) + C_3(\dot{x}_3 - \dot{x}_2) = 0 \quad (3)$$

$$M_4\ddot{x}_4 + K_4(x_4 - x_1) + C_4(\dot{x}_4 - \dot{x}_1) + K_5(x_4 - x_5) + C_5(\dot{x}_4 - \dot{x}_5) = 0 \quad (4)$$

$$M_5\ddot{x}_5 + K_5(x_5 - x_4) + C_5(\dot{x}_5 - \dot{x}_4) = 0. \quad (5)$$

By definition,

$$F_{T1} = F_{T1}e^{i\omega t} \quad (6)$$

$$x_i = \frac{v_i e^{i\omega t}}{i\omega} \quad (7)$$

$$\dot{x}_i = v_i e^{i\omega t} \quad (8)$$

$$\ddot{x}_i = i\omega\, v_i e^{i\omega t} \quad (9)$$

where $F_{T1}e^{i\omega t}$ is the transmitted force at the seat (Input 1) and $v_i e^{i\omega t}$ is the velocity of mass M_i. Eqs. 6 - 9 were substituted into Eqs. 1 - 5. From the resultant relationships, the complex driving-point impedance was determined by solving for $Z_T = F_{T1}/v_1$. The impedance magnitude was expressed as the absolute value of the complex impedance. The phase angle between the force and velocity was expressed as the arc tangent of the ratio between the imaginary and real components of the complex impedance. The transmissibilities were expressed as the absolute values of the ratios between the velocities of the mass elements representing the anatomical regions (v_i) and the input velocity at Input 1 (v_1) given the relationships provided by Eqs. 1 - 9.

Figure 1 shows that the cushions were represented as spring and damper elements combined in parallel and attached to the base of the model. The single DOF representation for the cushions was based on the results of the rigid mass tests. The addition of a cushion redefined the driving-point impedance calculated at the seat and the transmissibilities calculated between the motions of the anatomical regions or structures and the input motion at the seat. The transmitted force is defined at Input C in Figure 1 at the base of the cushion as:

$$K_c(x_c - x_1) + C_c(\dot{x}_c - \dot{x}_1) = F_{Tc}. \quad (10)$$

The driving-point impedance was redefined at Input C as F_{Tc}/v_c where v_c is the velocity at Input C. The transmissibilities were also redefined as the absolute values of v_i/v_c given the relationships provided by Eqs. 1 - 10.

2.3 Model Coefficients

The initial distribution of mass among the modified model elements was based on previous modeling efforts and on human body mass data (12). Initial stiffness coefficients were estimated from the frequency location of the peak responses observed in the data. The model coefficients were adjusted to produce the best simulation of the major resonance peaks observed in the impedance and transmissibility data. The sinusoidal response data from a small 56 kg female and a 75 kg male collected at 0.59 m/s^2 rms were used to estimate the coefficients and to evaluate model effectiveness.

The cushion stiffness and damping coefficients were calculated by assuming a one DOF system for the cushion responses using rigid masses. It was found that the impedance increased with increasing mass with no dramatic change in the transmissibility. Therefore, the cushion stiffness and damping coefficients were estimated from the rigid mass data based on the total weight of each subject.

3. RESULTS

3.1 Human Mechanical Impedance and Transmissibility Response Data

Table 1 summarizes the frequency ranges where peak responses (resonances) have been observed in the impedance and transmissibility calculations from various data collected in this laboratory as well as data found in the literature. Figure 2 illustrates the driving-point impedance response data for the 56 kg female and 75 kg male. The figure includes the responses using the rigid seat (no cushion) and the two seat cushions (Cushions 1 and 2). For the rigid seat, both subjects showed

Table 1 Frequency Ranges of Peak Responses

DRIVING-POINT IMPEDANCE	
PRIMARY PEAK	4 - 8 Hz
SECOND PEAK	7 - 10 Hz
THIRD PEAK	10 - 15 Hz
FOURTH PEAK	16 - 19 Hz
TRANSMISSIBILITY	
CHEST (Upper Torso)	4 - 7 Hz
SPINE (C_7)	4 - 7 Hz; 12 - 20 Hz
UPPER LEG (Thigh)	4 - 10 Hz; 10 - 15 Hz
LOWER LEG	5 - 9 Hz

the expected impedance peak between 4 and 8 Hz. A second higher peak was observed around 10 Hz for the female. The male showed a peak associated with the third peak region (Table1) around 15 Hz. The peaks observed in the female (10 Hz) and male (15 Hz) have been associated with the dynamic response of the legs as described below. Both the female and male showed some increase in the magnitude of the primary peak with the use of the cushions; Cushion 1 showing the highest response. There was a tendency for the second peak observed in the female to slightly decrease with the use of cushions; Cushion 1 showing the most dampened response. The male showed a more dramatic dampening of the response at higher frequencies with the use of cushions; Cushion 1 producing the most dampened response. The dampened response was also observed in the peak located around 15 Hz.

Figure 3 illustrates the transmissibility frequency response data for the chest, spine, and leg using the rigid seat and the two seat cushions. For the rigid seat, both subjects showed a peak in the chest transmissibility around 5 - 6 Hz and showed an increase in the peak chest response using Cushion 1. The female subject also showed the increase with Cushion 2. For the rigid seat, the female and male showed the two transmissibility peaks previously observed in the spine and occurring at about 5 - 6 Hz and 17- 19 Hz in these subjects. The first peak was associated with coupling between the chest and spine. The figure shows that the magnitude and frequency location of the second peak tended to be higher for the male subject. Both subjects showed an increase in the first spine peak with the use of cushions; Cushion 1 showing the highest response. At the second spine peak, the female and male showed a notable dampening of the response using Cushion 1. Although a small transmissibility peak was observed around 5 Hz for the female thigh, the major peak was observed between 9 and 10 Hz and coincided with the prominent impedance peak occurring in this frequency range. A second relatively prominent peak was observed around 15 Hz in the female. The female subject also showed that the thigh response increased with increasing frequency above about 17 Hz, with the generation of an additional peak at 20 Hz. Since data were only collected to 21 Hz, it was not clear if this peak represented an additional resonance in the leg. There was no clear effect of cushions on the prominent peak occurring around 9 - 10 Hz in the female, although the cushions did significantly dampen the peak occurring around 15 Hz. Cushion 2 also significantly dampened the thigh response at higher frequencies. The small peak observed around 5 Hz did increase with the use of Cushion 1. For the rigid seat, the male showed a small peak around 7 Hz. The second, and the highest peak occurred between 12 and 15 Hz. The higher peak coincided with the impedance peak observed around 15 Hz. The first peak was increased with the use of cushions; the highest response occurring with Cushion 1, similar to the

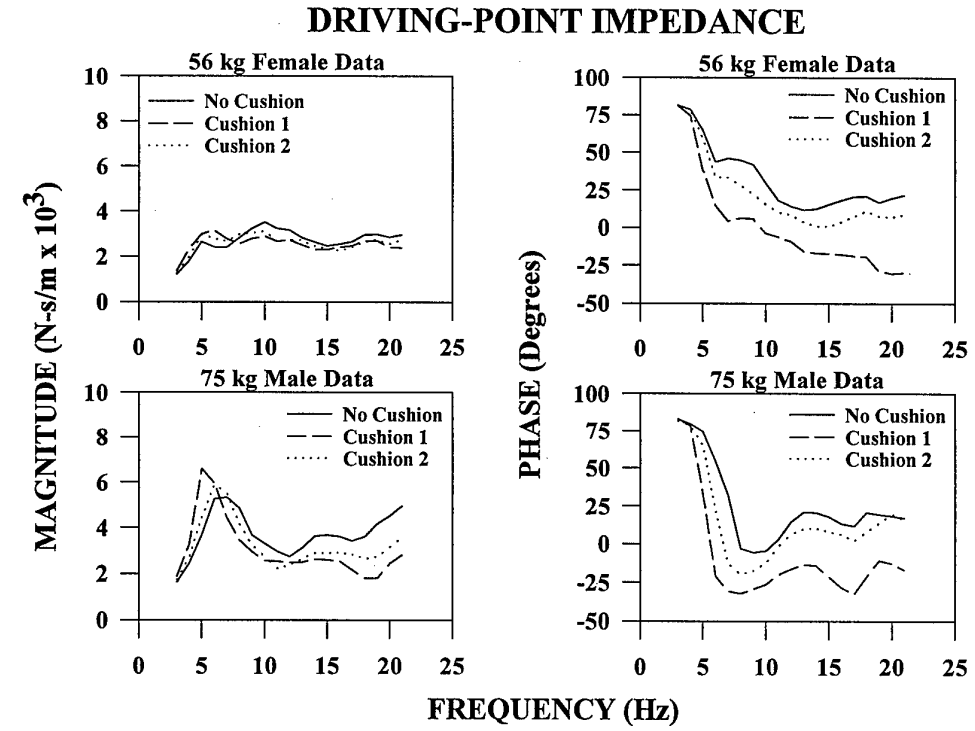

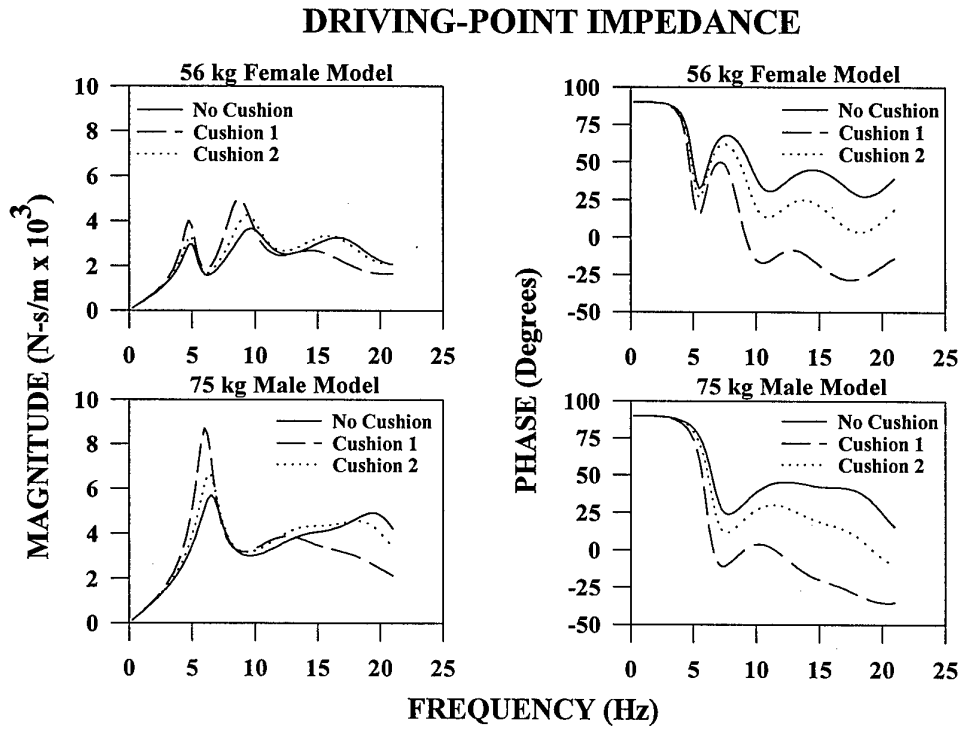

Figure 2 Driving-Point Impedance Human Data and Model Simulations

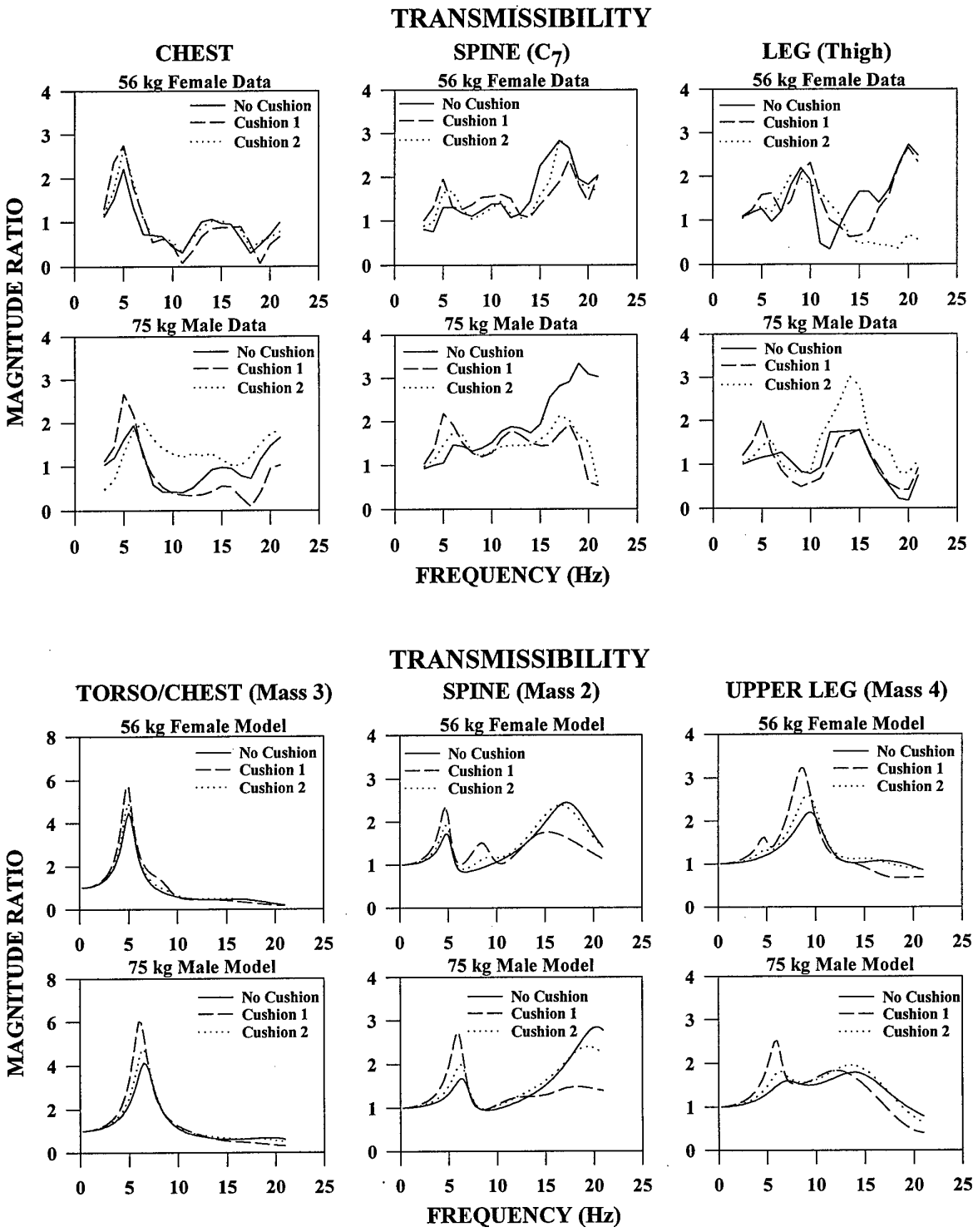

Figure 3 Transmissibility Human Data and Model Simulations

results observed in the female. The frequency location of this peak was also reduced from 7 Hz (no cushion) to 5 Hz (Cushion 1). While Cushion 1 had no effect on the male thigh response between 12 and 15 Hz, there was a significant increase in the peak thigh response with Cushion 2. This finding was in contrast to the results observed for the 86 kg male (used in the previous modeling effort) who showed a dampened response with the use of cushions. Larger males weighing over 100 kg have shown a tendency for an increase in the peak thigh response occurring between 10 and 15 Hz with the use of cushions, although there was no clear effect on the magnitude of the peak responses at the lower frequencies. However, the frequency location of the peak occurring at lower frequencies was reduced with the use of cushions (13).

There were additional peaks observed in the data which were not represented in the current model formulation. They included the transmissibility peaks observed around 15 Hz in the chest response of both subjects (magnitude below 1.0), and the peaks observed in the spine occurring around 10 Hz and 20 Hz in the female and around 12 Hz in the male. Finally, the small peak in the female thigh at 5 Hz was not represented in the model.

3.2 Five DOF Model Simulations

Figure 2 includes the model simulations for the driving-point impedance. For the rigid seat, the model was quite effective in simulating the impedance responses of the two subjects, particularly the higher peak occurring around 10 Hz in the female. For both subjects, the model predicted the relative increase in the primary impedance peak with the use of cushions, particularly for Cushion 1. However, while the measured impedance showed a slight decrease in the second peak observed around 10 Hz in the female with the use of cushions, the model predicted an increase in the response. The model did predict the dampened responses observed in in the male at higher frequencies with the use of cushions (particularly Cushion 1).

Figure 3 includes the model simulations for the torso (Mass 3), spine (Mass 2), and upper leg (Mass 4) transmissibility responses. For the rigid seat, the modified model improved the simulation of the peak chest transmissibility (Mass 3) although the prediction was still higher than observed in the data. The lower peak observed in the data may be due to the external measurement site used to estimate the acceleration of a lumped region which included the chest, shoulders, and viscera. For the rigid seat, the modified model provided a significant improvement in the simulation of the second spine transmissibility peak (Mass 2), and showed the relative differences observed between the female and male responses. While the model simulated the major peak observed in the thigh of the female (9-10 Hz) (Mass 4), it did not effectively simulate the peak observed around 15 Hz, nor did it predict the mass-like increase in the leg response at higher frequencies. (The peak observed at 20 Hz was not represented in the modified model.) For the rigid seat, the model did simulate the two peaks observed in the male thigh (Mass 4), the peak around 7 Hz being associated with coupling to the lower leg. Although not shown, the magnitude of the peak for the lower leg (Mass 5) was overestimated compared to previously collected data (8). However, there are no data available to confirm the location and magnitude of the lower leg peak for the small female.

The increase in the peak chest transmissibility in the female and male with the use of cushions was effectively predicted by the model. The model also predicted the relative increase in the peak spine transmissibility at low frequencies (around 5 - 6 Hz) and the dampened response at higher frequencies (15-20 Hz) for both the female and male. With the use of cushions, a peak was observed in the female spine transmissibility between 8 and 9 Hz; Cushion 1 showing the more prevalent peak. It was speculated that the peak represented coupling between the spine and legs via the seat cushion. The data also showed this peak for the rigid seat. This raised questions about the source of this peak since the legs were considered uncoupled to the spine. The model also predicted the generation of a peak in the

female thigh response at 5 Hz with the use of cushions; Cushion 1 producing the highest peak. This coincided with the increase in the small peak observed around 5 Hz which was not represented in the model. Again, these observations suggested that there was coupling between the legs and the torso/spine via the seat cushion. The model predicted that the cushions would have no significant effect on the response of the upper leg in the male. However, the data showed a dramatic increase in the peak response with Cushion 2 as described previously. The modeled peak observed in the male thigh at 7 Hz was also increased and the frequency location shifted downward with the use of cushions, similar to the trends observed in the data.

3.3 Female vs Male Leg Responses

Table 2 lists the model coefficients selected for the modified model and used for simulating the responses of the 56 kg female and 75 kg male.

Table 2 Model Coefficients

MODEL COEFFICIENTS	FEMALE (56 kg)	MALE (75 kg)
M_1 (kg)	20.7	28.1
M_2 (kg)	6.8	11.8
K_2 (N/m))	66997.0	162671.1
C_2 (N-s/m)	35.0	17.5
M_3 (kg)	13.2	17.2
K_3 (N/m)	16857.7	37230.6
C_3 (N-s/m)	175.1	332.7
M_4 (kg)	10.9	10.9
K_4 (N/m)	91531.6	87808.6
C_4 (N-s/m)	385.3	175.1
M_5 (kg)	4.5	7.3
K_5 (N/m)	26630.2	16102.6
C_5 (N-s/m)	175.1	262.7
K_{c1} (N/m)	239768.2	321623.7
C_{c1} (N-s/m)	851.1	1143.5
K_{c2} (N/m)	890937.9	663464.7
C_{c2} (N-s/m)	3775.55	2812.4
Total Weight (kg)	56.1	75.3

Table 3 lists the undamped natural frequencies (f_n) associated with the modeled anatomical regions. The modified five DOF model coefficients showed a dramatic difference in the distribution of the leg masses and produced a difference in the coupling behavior between the upper and lower legs for the smaller female and larger male. Interestingly, the modeled mass for the upper leg was identical for the female and male suggesting a greater contribution of the thigh to the observed whole-body response in the smaller female. The significance of this contribution was observed in the impedance response where the highest response in the female (using the rigid seat) coincided with the peak response in the thigh (9 - 10 Hz). The undamped natural frequencies shown in Table 3 for the upper and lower legs indicated that the lower leg had a significant influence on the response of the upper leg in the female; the primary peak in the upper leg (thigh) coincided closely with the undamped natural frequency calculated for the lower leg. As mentioned, data on the lower leg response were not available for the smaller female. These data would help clarify whether the small peak observed at 5 Hz should be represented in the model. Based on the assumptions made in this study, it is speculated that the peak response in the lower leg of the smaller female occurs at the higher end of the frequency range shown in Table 1 (8 - 9 Hz). Data collected on males weighing over 100 kg do show a more pronounced peak in the thigh around 7 Hz as compared to the data presented in this paper (13), suggesting a greater influence of the lower leg on the response of the upper leg as compared to the results for the 75 kg male.

Table 3 Undamped Natural Frequencies

REGION	FEMALE (f_n)	MALE (f_n)
Spine (Mass 2)	17.9	21.0
Torso (Mass 3)	5.0	6.6
Upper Leg (Mass 4)	18.1	15.9
Lower Leg (Mass 5)	9.8	6.8

It must be emphasized that the data reported by this laboratory were for the unsupported legs (no footrest). This seating configuration may have a significant influence on the leg response and the coupling behavior between the upper and lower legs. Subsequent studies will address this issue.

4.0 CONCLUSIONS

1. The modified five DOF model was effective in simulating the driving-point impedance responses of the smaller female and larger male (rigid seat).

2. The modified model improved the simulation of the chest and spine transmissibility responses (rigid seat).

3. The model effectively simulated the coupled response of the lower and upper leg in the male, but did not effectively simulate the higher frequency response observed in the female (rigid seat).

4. The model was relatively effective in predicting the increases in the driving-point impedance, and the increases in the chest and spine transmissibilities occurring at low frequencies (4 - 8 Hz) in both the female and male with the use of cushions. The model did predict the relatively dampened response occurring in the impedance and spine at higher frequencies with the use of cushions.

5. The model was not effective in predicting the effects of cushions on the peak thigh transmissibility occurring around 9 - 10 Hz in the female and between 12 - 15 Hz in the male. However, the model was relatively effective in predicting the effects of cushions on the thigh response at low frequencies (5 - 7 Hz).

6. The model predictions suggest that there is some coupling of responses between the legs, torso, and spine via the seat cushions.

7. The results of this study strongly suggest the need for further modification of the leg representation in the model. The data also indicates that there may be additional anatomical regions and/or coupling between regions which should be considered in future modifications of the model.

5.0 REFERENCES

1. VanIngen-Dunn, C. and Richards, M. K., "Feasibility of Reducing the Incidence of Low Back Pain in Helicopter Pilots Using Improved Crewseat Cushions", Armstrong Laboratory, WPAFB, OH, SR-1991-0009, 1991.

2. Fairley, T. E. and Griffin, M. J., "A Test Method for the Prediction of Seat Transmissibility", Society of Automotive Engineers, International Congress and Exposition, February 1986, SAE Paper 860046.

3. Pope, M. H., Broman, H. and Hansson, T., "The Dynamic Response of a Subject Seated on Various Cushions", Ergonomics, 23,10, 1989, pp 1155-1166.

4. Mansfield, N. J., "Prediction of the Transmissibility of a Vehicle Seat in the Vertical Direction", UK Informal Group Meeting on Human Response to Vibration, Army Personnel Research Establishment, Ministry of Defence, Farnborough, England, September, 1993.

5. Smith, S. D., "The Effects of Military Aircraft Seat Cushions on Human Vibration Response", UK Informal Group Meeting on Human Response to Vibration, Institute of Naval Medicine, Alverstoke, Gosport, Hants, England, September, 1994a.

6. Payne, P. R., "A Four-Degree-of-Freedom Lumped Parameter Model of the Seated Human Body", Aerospace Medical Research Laboratory, WPAFB, OH, AMRL-TR-70-35, January 1971.

7. Mertens, H., "Nonlinear Behavior of Sitting Humans Under Increasing Gravity", Aviation, Space and Environmental Medicine, January, 1978.

8. Smith, S. D., "Comparison of the Driving-Point Impedance and Transmissibility Techniques in Describing Human Response to Whole-Body Vibration", UK Informal Group Meeting on Human Response to Vibration, Army Personnel Research Establishment, Farnborough, England, September, 1993.

9. Smith, S. D., "Nonlinear Resonance Behavior in the Human Exposed to Whole-Body Vibration", Shock and Vibration, 1,5,1994b, pp 439-450.

10. Smith, S. D., Cushions and Suspensions: Predicting Their Effects on the Biodynamic Responses of Humans Exposed to Vertical Vibration", Heavy Vehicle Systems, International Journal of Vehicle Design, 4, 2-4, 1997, pp 296-316.

11. Smith, S. D., "Comparison of the Effects of Whole-Body Vibration Exposure Between Females and Males", US Army Medical Research and Materiel Command, ADA309219, May, 1996.

12. Cheng, H., Obergefell, L., and Rizer, A., "Generator of Body Data (GEBOD) Manual", Armstrong Laboratory, WPAFB, OH, AL/CF-TR-1994-0051

13. Smith, S. D., "The Effects of Prototype Helicopter Seat Cushion Concepts on Human Body Vibration Response", Journal of Low Frequency Noise, Vibration and Active Control, 17, 1, 1998, pp 43-53.

Modelling Motion Sickness

J.E. Bos & W. Bles
TNO Human Factors Research Institute
P.O. Box 23
3769 ZG Soesterberg
the Netherlands
tel: +31 346 356371 fax: +31 346 353977 e-mail: bos@tm.tno.nl

1. SUMMARY

To analyze and or anticipate air crew performance pre-, per- and post-flight, we present a model that predicts spatial orientation and motion sickness. We first demonstrate a close linkage between spatial orientation and motion sickness, resulting in the postulation that sickness only arises when sensed and expected estimates of gravity change differently. Including observer theoretical considerations, this concept lead to predictions of seasickness corresponding with experimental data. The model offers the possibility to predict all types of motion sickness, including simulator sickness.

2. INTRODUCTION

To give a quantitative prediction of the percentage of motion sick people, literature reveals only a few descriptions (e.g. McCauley et al., 1976; Griffin, 1990; ISO 1997). These models are all based on extensive, and largely overlapping data gained with simulator experiments and obtained at sea. These models, however, relate sickness incidences exclusively to vertical motions, that is they predict seasickness.

If these models were to be extended to include not only linear vertical motions, but also other linear and all angular motions (three dimensional space has six degrees of freedom), the exploration of sickness related to motion is a well nigh impossible task. Inter- and intra-individual variability in sickness sensitivity is large, and motions may be complex (multiple frequency components, phase angles, interactions, etc.). Hence, thousands of subjects would be needed to obtain sufficient statistical significance of the parameters of the (arbitrarily chosen) functions that fit these data best. Moreover, such models are accordingly mere descriptive and lack a vestibular basis, whereas the vestibulum plays an essential role: people without a functioning vestibular system do not get sick from motions.

Experiences with sickness induced by combined roll and pitch motions in a simulator (Wertheim et al., 1997), by on- and off-vertical axis rotations, and by hypergravity in a human centrifuge (Bles et al., 1997), merged with insights in control systems theory (Oman, 1982), brought us to a vestibular based motion sickness model. The crux of this model is threefold: *1)* using multisensory information, the central nervous system resolves a vector representing the magnitude and direction of the sensed gravity, *2)* in addition, it creates an anticipated vertical based on previous experiences, and *3)* sickness results from a conflict between these two verticals.

Because our estimate of gravity, or subjective vertical, is directly linked to spatial (dis)orientation, this concept predicts that motion sickness (and hence also air sickness) results from spatial orientation irregularities. Elaborating this concept for passively endured vertical motions typical at sea, results in a model that predicts sea sickness characteristics as observed. So, not only because sea and air sickness have the same incapacitating effect, but also because sea sickness is far better charted than air sickness, naval and aerospace knowledge should further be integrated to be of better aid to all defence divisions where humans work in a moving environment.

3. THEORY

3.1 Subjective vertical mismatch

Generally motion sickness (MS) is considered to occur when there is a conflict between signals related to accelerations originating from visual (vis), somatosensory (som), vestibular (vest), and/or auditive (aud) cues, and/or experience (exp, see Fig. 1). This theory is described by Reason & Brand (1975).

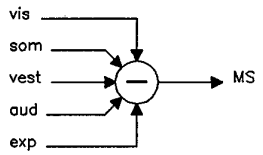

Fig. 1 Classical conflict theory on motion sickness.

We hypothesize, however, that this theory is only partially true. The basis of our model is the observation that people get far more severe sick when gravity (true or expected) changes with respect to their body, than when gravity remains unaltered. If, for example, otherwise immobile subjects are rotated in the dark about an axis that is perfectly aligned with gravity, hardly anybody gets sick. If then only the orientation of the rotation axis is changed off-vertical, most people do get sick (see Fig. 2).

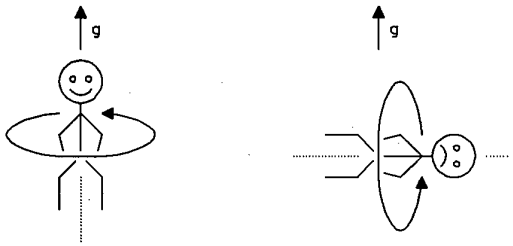

Fig. 2 Rotation about an earth vertical axis is by far less sickness provoking than about an off-vertical axis.

From this and other examples (Bles et al., 1998) we

assume that *motion sickness only correlates with a difference between the vertical as determined by integrated multisensory information and a vertical as expected based on previous experience* (see Fig. 3).

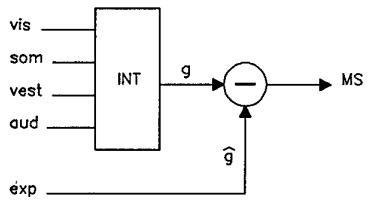

Fig. 3 Motion sickness only correlates with a vertical mismatch.

Though vision, proprioception, hearing, and even cognition are involved in spatial orientation and motion sickness, we currently restrict to vestibular inputs. This is not only an attractive attitude because the vestibular system plays a key role in motion sickness, but also because the transfer functions of the otoliths to detect linear accelerations, and semicircular canals to detect angular accelerations are well known. In addition, reasonable estimates of central nervous system processing of otolith and canal afferents are available. It will be described how these signal processings can be modelled.

3.2 A systems concept

The primary path: Within each inner ear otoliths respond to linear accelerations (including gravity), and semicircular canals respond to angular motions. Within the frequency range in which motion sickness occurs, the otoliths are known to be almost perfect acceleration sensors, that is, their afferents are linearly related to linear acceleration. The canals, however, function as first order high pass velocity sensors with a time constant of some 5 s. This means that the canals do not respond to a constant angular velocity. Fig. 4 gives a solution to the way the central nervous system resolves a vertical from these two afferents (Bles et al., 1998). Basically, this process consists of a low pass filter (LP) to deliver gravity, which is assumed to be constant (Mayne, 1974). Because gravity is only constant in an earth fixed frame, canal information is used to rotate the head fixed frame into an earth fixed frame (R) and back again after the low pass filtering (R^{-1}). In this model the estimate of gravity is called a subjective vertical (SV), and its high-pass counterpart the subjective translations (ST). In fact a model like this is the essence of any spatial orientation model.

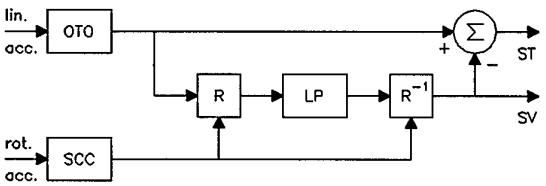

Fig. 4 Resolving a vertical from linear and angular accelerations.

A simple controller: To control body posture, a sense of gravity is of value. Classically, such a control loop is obtained by a simple servo system, as sketched in Fig. 5.

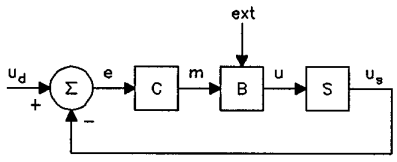

Fig. 5 Servo system to control body posture.

Here, an error between some desired (u_d) and a sensed (u_s) posture is input to a controller (C) that generates motor commands (m). These motor commands, together with externally enforced motions (ext), yield true posture (u), which is sensed by our senses (S). The functioning of this model, however, depends strongly on the accuracy of the sensors. Especially the canals are not accurate enough in many flying conditions.

Observer theory: One way of desensitising the model for sensor anomalies and to model experience, is to add copies (labelled with hats, all together called an internal model) of the body dynamics and sensor transfer functions as sketched. Then the primary feedback ($\hat{u}$) is our expected body posture, as predicted by motor commands (efference copy) and primary sensory output. A weighting coefficient K may account for noise and other uncertainties.

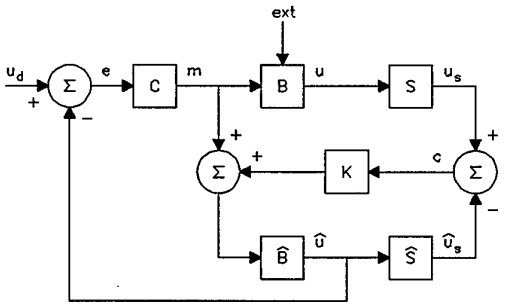

Fig. 6 Extended body posture control system.

This model was presented by Oman (1982), and inherently generates a conflict (c). In our opinion, the conflict to generate motion sickness should now be only one between the components of u_s and $\hat{u}_s$ that represent gravity. If we take the magnitude of their vector difference to be the basic sickness conflict, it is obvious that this conflict needs some further processing. First it should be rectified, and secondly it should be maximized, people can not get sicker than sick (i.e. vomiting). A function that fulfils these needs is a Hill-function: $h = P/(1+c^2/b^2)$, with b some fixed point, and P the maximum percentage of people getting sick anyhow. Lastly this conflict should be integrated over time to include the cumulation of sickness over the endured time of motion. These last stages are depicted in Fig. 7.

3. EXAMPLE

If we omit all but the vestibular cues, and restrict to vertical motions only, we are left with a characteristic condition at sea. The model should then be capable of

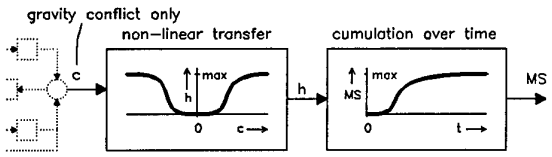

Fig. 7 (nonlinear) Conflict transformations.

predicting sea sickness as observed by McCauley et al. (1976) for example. They exposed over 500 subjects to pure sinusoidal vertical motions in a motion simulator, one at a time, and varied frequency and amplitude. They scored the number of subjects that vomited within two hours of motion exposure. Data points and ad hoc mathematical fits are shown in Fig. 8.

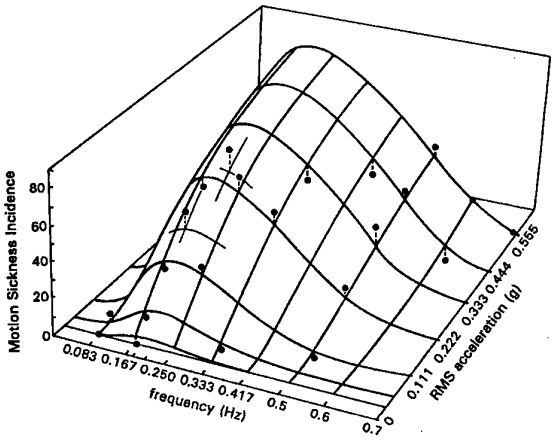

Fig. 8 Observed (points) and fitted motion sickness incidences versus frequency and RMS acceleration according McCauley et al. (1976).

To implement a model for numerical analysis mimicking these conditions, angular motions are of no concern. Accordingly, we only had to fix the time constant of the low pass filter. This time constant was determined by us in experiments measuring the subjective vertical by means of a joy stick in a human centrifuge (de Graaf et al., 1997), and rounded off to 5 s. The maximum percentage of people getting sick anyhow was set to 85%. The remaining parameters, K, b, and the cumulation time constant (μ), were varied to get an optimum performance of the model (K = 5 s^{-1}, b = 0.7 m/s^2, μ = 12*60 s). These figures gave the result as shown in Fig. 9.

The model predicts a peak in sickness incidence about 0.16 Hz. The location of this peak is independent of the post conflict transformations!

4. DISCUSSION: USES, LIMITATIONS AND REQUIREMENTS

Air crew performance certainly depends on both spatial disorientation phenomena and on air sickness. Here, we demonstrated the close linkage between these two. The current model may therefore be an indispensable tool in analyzing pre-, per- and post-flight crew performance considered in whatever framework.

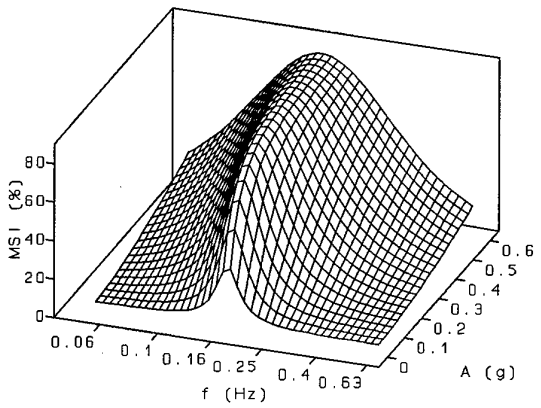

Fig. 9 Model predictions of motion sickness incidence.

In further refining the general conflict theory on motion sickness, sea sickness characteristics could be successfully predicted. This success results from the notice that gravity is the key conflict component, and additional low pass filters to isolate the gravity components, introduce a time lag. When body posture is only externally controlled and not by self generated motor commands (passenger behaviour), the internal model lag is not compensated for by an appropriate efference copy of the motor commands, and a conflict may cumulate to give motion sickness.

Most importantly, the model predicts a peak in sickness severity versus frequency, a phenomenon that was not understood previously. The location of this peak was independent of the post conflict processing, and mainly depends on the time constant of the otolith low pass filter. This has been demonstrated elsewhere (Bos & Bles, 1998). The time constant was gained from different kinds of experiments, and not varied to obtain the presented data. In addition, the feed back factor K could be used for fine tuning.

The considerations that led to the model were all based on the behaviour of an average population. The model itself, on the other hand, was build as if it represented the functioning of an individual. For some parameters (like the low-pass filter time constant) an individual guess may give a prediction on his or her individual behaviour with respect to motion sickness. On the other hand, inter-, but also intra-individual differences in more complex situations may be that large that such individual predictions need much more refinement of the model than presently incorporated.

The model in its present concept is apt to predict other types of motion sickness. We are currently working on a three-dimensional model with all six degrees of freedom incorporated. Calibration by Coriolis effects seems appropriate, be it that cross-coupled Coriolis stimulation may result in sudden sickness, as opposed to the slowly cumulating sea sickness. But it is our belief hat the same principles that led to the successful prediction of sickness in response to vertical motions only, will also lead to successful predictions of sickness to all kinds of complex motion.

Vision can also be included in the model. It is known that visual frame information (horizontal and vertical structures) is of paramount importance to our final estimate of gravity. It therefore seems sound to add this information somewhere downstream the model. In addition, vision may include optical flow information (angular velocity for example), which we assume is introduced in our spatial orientation system at the output level of the canals, that is, it should be added to canal angular velocity at the stage of R and R^{-1} in Fig. 4. Then the model will not only give predictions in more realistic situations, but it may also be of use to predict simulator sickness, for example.

But even then the model is not yet complete. Long term adaptation, for example, seems to be of relevance, be it more for naval, than for air crew. Of special importance to air crew seems the modelling of the controller (C), because only then the model is applicable not only to passengers, but also to the pilot himself.

5. ACKNOWLEDGEMENT

This work was funded by the Royal Netherlands Navy and Air Force.

6. REFERENCES

To be numbered consecutively throughout the paper

Bles W, de Graaf B, Bos JE, Groen E. (1998) The motion sickness provoking conflict. *Report TNO Human Factors Research Institute, Soesterberg, Netherlands.* TM-98-A033.

Bos JE, Bles W. (1997) A vestibular based motion sickness incidence model. *Report TNO Human Factors Research Institute, Soesterberg, Netherlands.* TM-97-A032.

Graaf B de, Bos JE, Tielemans W, Rameckers F, Rupert AH, Guedry FE. (1996) Otolith contribution to ocular torsion and spatial orientation during acceleration. *Technical Memorandum Naval Aerospace Medical Research Laboratory*, Pensacola, Fl. 96-3.

Griffin MJ. (1990) *Handbook of Human Vibration*, Academic Press, London.

International Organization for Standardization (1997) *Mechanical vibration and shock - Evaluation of human exposure to whole-body motion - Part 1: General Requirements.* Geneva, ISO 2631-1:1997(E).

Mayne R. (1974) A systems concept of the vestibular organs. In: *Handbook of sensory physiology IV-2: Vestibular system.* Kornhuber HH (ed). Spinger Verlag, Berlin. :493-580.

McCauley ME, Royal JW, Wylie CD, O'Hanlon JF, Mackie RR. (1976) Motion sickness indidence: exploratory studies of habituation, pitch and roll, and the refinement of a mathematical model. *Human Factors Research Inc. Technical Report* 1733-2.

Oman CM. (1982) A heuristic mathematical model for the dynamics of sensory conflict and motion sickness. *Acta Otolaryngol. Suppl.* 392.

Reason JT, Brand JJ. (1975) *Motion Sickness.* Acad. Press, London.

Wertheim AH, Wientjes CJE, Bles W, Bos JE. (1995) Motion sickness studies in the TNO-TM Ship motion simulator (SMS). *Report TNO Human Factors Research Institute, Soesterberg, Netherlands* TNO-TM 1995 A-57.

ALTITUDE DECOMPRESSION SICKNESS (DCS) RISK ASSESSMENT COMPUTER (ADRAC)

L.J. Petropoulos
N. Kannan*
A.A. Pilmanis**
AFRL/HEPR
2504 Gillingham Dr., Ste 25
Brooks AFB, TX, 78235-5104
US (Wyle Labs, San Antonio)
*University of Texas at San Antonio, TX 78249
**AFRL/HEPR, Brooks AFB, TX 78235, US

1. INTRODUCTION

Decompression sickness (DCS) is caused by exposure to significant reductions in environmental pressure. These situations are encountered during diving, high altitude exposures or artificially induced pressure changes in hyperbaric or hypobaric chambers. For large and rapid pressure reductions, supersaturation occurs as a result of the inability of tissue gas exchange processes to expel excess nitrogen. These gases, which come out of solution when tissues are sufficiently supersaturated, collect as bubbles in the tissue. The size and location of these bubbles are thought to have a significant effect on the resulting DCS symptoms. The risks can be minimized or prevented with sufficient denitrogenation by prebreathing pure oxygen before such exposures.

The risk of DCS increases with extended exposure times, very high altitudes, and greater physical activity during the exposure. The assessment of DCS risk for both civilian and military personnel under specified flight protocols is a critical problem that the USAF deals with on a regular basis. To provide answers to these questions, and also to obtain a clearer understanding of the effects of denitrogenation, the High Altitude Protection Function of the Air Force Research Laboratory is developing an appropriate model to predict DCS risk using physical and physiological principles.

2. PRIOR MODELING ATTEMPTS

Most altitude DCS modeling has focused on mathematical models describing bubble growth. Van Liew et al. [1] developed a probabilistic model of altitude DCS. The mechanistic principles used in the model were based on the premise that the risk of DCS is related to the number of bubbles and the volume of gas that can be liberated from a unit of tissue. The authors developed equations that incorporated these premises, and used these equations in the risk function. They tested several models to determine the one that best fit the data. The covariates (risk factors) used in the model were duration of 100% oxygen at ground level (prebreathing), atmospheric pressure after ascent, and exposure duration. Gerth and Vann [2] developed an extensive model for bubble dynamics to provide an assessment of DCS. The bubble dynamic equations were similar to those used by Van Liew et al. In the report, the percentage of individuals with DCS was used as the response variable and maximum likelihood methods were used to estimate the model parameters. In an appendix, the authors discussed the need for including onset times of DCS to improve the predictions from the model.

Kumar et al. [3], [4], [5], [6] in a series of papers, recognized that survival analysis techniques are the most appropriate to model DCS risk. They developed logistic and loglinear models to predict DCS as a function of Tissue Ratio, which is a measure of tissue nitrogen decompression stress. Another covariant used was CMB (circulating microbubbles) status. The models used the logarithm of time to DCS and maximum likelihood techniques to estimate the model's parameters. The articles allude to the fact that censoring occurs for individuals who did not exhibit any symptoms of DCS. Conkin et al [7] in a recent paper discussed in some detail the use of survival times and censoring using the loglogistic model. They also discussed different forms of the risk functions using certain mechanistic assumptions similar to those of Van Liew and others

The survey of current literature in the area of altitude DCS shows the limitations of the models that are currently in use. The description of the bubble growth dynamics using approximate (quasi-steady state) models for example, is one of them. Such an approach, due to the

Papers presented at the RTO HFM Specialists' Meeting on "Models for Aircrew Safety Assessment: Uses, Limitations and Requirements", held in Ohio, USA, 26-28 October 1998, and published in RTO MP-20.

equilibrium assumption inherent in it, cannot account for the influence of any initial conditions. Approximate models were selected in order to obtain a non-complicated numerical solution leading most of the times as showed in [8] to erroneous results. Moreover, most of them examine the effect of one or two factors on the DCS risk. In reality, the risk of DCS is affected by a number of competing factors like the preoxygenation time, exposure time, exercise status, symptom and VGE (Venus Gas Emboli) onset times, and altitude. In order to develop a model that adequately describes the phenomenon of DCS, all these factors should be included in a survival model. This would determine the relative importance of the different factors, and possibly provide a method of controlling the risk of DCS. There is clearly a need for a comprehensive model that includes all these factors and the proper utilization of the bubble data information.

3. METHODS

We have conducted experiments on human subjects in a hypobaric chamber for the past several years, creating a unique database of over 2000 altitude exposures with a variety of flight profiles. The subjects were exposed to different altitudes, varying preoxygenation times, and different prebreathing mixtures. The subjects were monitored continuously and were required to report any unusual pain or other symptoms. If the symptoms were indicative of DCS, the experiment was terminated with the subject being brought down to ground level. Several measurements were recorded during the experiment including onset time of DCS, physical activity and time spent in the chamber. During each exposure, venous gas emboli were recorded by precordial 2-D echocardiography. All of the data that were collected are now included in the AFRL Hypobaric Research Database.

Pressure levels in the database ranged from 141 mmHg (40,000 ft) to 380 mmHg (18,000 ft). The preoxygenation times ranged from 0 to 240 minutes, and the exposure time ranged from 120 minutes to 480 minutes. The subjects performed different types of exercise. They were classified as rest, mild exercise, and heavy according to the amount of oxygen consumption. When we analyzed the data we found that subjects who performed mild exercise in flights of moderate/long duration (240 minutes or longer) were more likely to have high bubble grades. For individuals at rest with low prebreathing times, high grades were also observed. If prebreathing times were moderate or high, the individuals almost always had very low bubble grades. The time at which the maximum grade is attained could be interpreted as a 'survival time' and modeled accordingly. We therefore used two separate models: one that did not include bubble data (prebreathe times larger than 30 minutes) and one that included them (0-30 minutes of preoxygenation time).

The models used to fit the data were based on the loglogistic distribution, with survival function given by:

$$S(t) = \frac{1}{1+(\lambda * t)^{\gamma}} \quad (1)$$

The cumulative distribution function (Cdf) is defined as F(t) = 1-S(t), i.e. the probability of developing symptoms by time t. The risk function for the loglogistic curve is given by:

$$r(t) = \frac{\lambda\gamma(\lambda * t)^{(\gamma-1)}}{1+(\lambda * t)^{\gamma}} \quad (2)$$

The parameter $\gamma = 1/\sigma$, where σ is a scale parameter. If $\sigma < 1$, the risk function of the loglogistic curve increases to a peak, and then decreases towards zero. This is the shape, which accurately describes the risk of DCS over time. The parameter λ depends on the vector of risk factors $\vec{x}$ through the following equation:

$$\lambda = \exp(-\beta'\vec{x}) \quad (3)$$

where beta is a vector of unknown parameters which will be estimated from the data. Using the functions defined above, we can write the likelihood function:

$$L(\beta,\gamma) = \prod_{i=1}^{M} f(t_i) \prod_{j=1}^{N-M} S(t_j) \quad (4)$$

where M is the number of uncensored observations and N is the total number of observations in the data set. Here f (t)=F'(t) is the probability density function. We used the statistical software package SAS to maximize the likelihood and obtain estimates of the unknown parameters. The results are provided in Tables 1-2. The tables provide the estimates of the parameters, the standard error of the estimates,

and a chi-square value used to assess the relative importance of the different risk factors.

The weights for the various groups are displayed in the two tables below (PRES = pressure, BRTALT = ratio of prebreathing time/time at maximum altitude, EX = exercise code, MAXT = onset time of maximum venus gas emboli). The first table does not include bubble data, meanwhile the second one does. It is clear that in Table 2 the MAXT covariant dampens the effect of all the other covariates. The EX covariate, in table 2, was found to be nonsignificant in this model. However, exercise is still a part of the predictions because it has an effect on MAXT.

Variable	DF	Estimate	Std. Err.	Chi-sq.	p-value
INT	1	-8.00	2.45	10.63	0.0011
PRES	1	2.53	0.44	32.57	0.0001
BRTALT	1	1.29	0.39	11.26	0.0008
EX	1	-0.53	0.14	13.68	0.0002
SCALE	1	0.60	0.03		

Table 1. Parameter estimates for the weighted model

Variable	DF	Estimate	Std. Err.	Chi-sq.	p-value
INT	1	-3.66	1.80	4.12	0.0424
PRES	1	1.34	0.31	17.37	0.0001
BRTALT	1	0.96	0.30	10.21	0.0014
MAXT	1	0.01	0.00	183.58	0.0001
SCALE	1	0.37	0.02		

Table 2. Parameter estimates for the weighted model including bubble data

The risk vector has five inputs. Four of them must be entered manually by the user and the fifth one is being calculated automatically by calling a subroutine. The four risk parameters are the altitude, the exposure time at that altitude, the exercise level, and the preoxygenation time. Once those parameters are known the program calls subroutine "bubgrow". Its function is to calculate the onset time of the maximum bubble radius (MAXT) in order to provide the main program with the fifth and final risk factor. This is a very complicated process and is described in detailed in the next section. If the preoxygenation time is more than 30 minutes it skips subroutine "bubgrow" and continues to calculate the probability from the cumulative distribution function.

4. BUBBLE GROWTH MODEL

Subroutine "bubgrow" is a program that solves numerically a system of equations describing bubble growth due to a hypobaric decompression. It returns a single value, and that is the onset time of the maximum bubble radius. The equations used are described in detail in [8] but we will also present them here in brief. The model consists of an advection-diffusion equation coupled with two ordinary differential equations named: the conservation of mass and momentum equations. The system is in spherical coordinates and it describes the growth of a single bubble surrounded by a limited amount of tissue. Since blood leaving the capillaries removes nitrogen gas from the system, a sink term in the diffusion equation (Equation 5) was added to account for this tissue nitrogen loss (due to capillary-tissue gas exchanges that take place in a uniformly perfused region of the body).

Initially, the gas concentration is assumed to be uniformly distributed throughout the tissue with magnitude equal to C_o depending on the duration of prebreathe prior to ascent to altitude. At altitude, the bubble expansion (due to Boyle's law) reduces the bubble pressure and induces a concentration gradient in the tissue (since the bubble pressure is related to the concentration, in the tissue layer adjacent to the bubble, through Henry's law). In turn, this initiates the bubble growth process that is governed by the following equations (dots denote differentiation with respect to time):

Bubble growth model equations

$$\frac{\partial C}{\partial t} + u_r \frac{\partial C}{\partial r} = \frac{D}{r^2}\frac{\partial}{\partial r}\left(r^2 \frac{\partial C}{\partial r}\right) - kC \quad ; R(t) < r < \delta(t) \qquad (5)$$

$$\frac{d}{dt}\left(\frac{P_g R^3 M}{R_g T}\right) = 3\rho D R^2 \left(\frac{\partial C}{\partial r}\right)_{r=R} \qquad (6)$$

$$\rho\left(\frac{1}{2}(\xi^{4/3} - 1)R\dot{R}^2 - (\xi^{1/3} - 1)(R^2\ddot{R} + 2R\dot{R}^2)\right) = (P_g - P_{f_a})R - 2\sigma + 4\eta(\xi - 1)\dot{R} \qquad (7)$$

where r=R(t) is the location of the bubble surface, r=δ(t) is the radius of the outer shell that encloses the bubble, $\xi=R^3 / (V+R^3)$ (ξ is nondimensional), P_{fa} is the equilibrated (at ambient level) pressure of dissolved N_2 outside the tissue shell, $V=\delta^3 - R^3$ is $3/4\pi$ times the tissue volume surrounding the bubble, D is the diffusion constant, u_r is the velocity of the radial flow field induced by the bubble surface motion, k is the perfusion rate constant, R_g is the gas-law constant, T is the temperature, M is the molecular weight of the gas, ρ is the density associated with the concentration measured in moles of dissolved gas per unit volume of tissue, P_g is the partial pressure of the diffusing gas inside the bubble, σ is the surface tension, η is the viscosity of the tissue surrounding the bubble and C is the gas concentration (which is a function of time and space). The initial condition for the concentration is:

$$C(r,0) = C_o \quad (8)$$

Since there are other bubbles growing in close proximity, the amount of dissolved gas in the tissue available for each bubble is finite. The concentration gradient at the outer boundary of the tissue shell is assumed zero at all times (no flux through the outer boundary of the shell). Nevertheless, the amount of gas in the tissue and the bubble is not constant, due to the sink term in the diffusion equation, which accounts for the perfusion effect on bubble growth. Hence the boundary conditions for Equation 5 are as follows:

$$C(R,t) = K_h P_g \quad (9)$$

$$\frac{\partial C(\delta,t)}{\partial r} = 0 \quad (10)$$

where K_h is the Henry's law constant.

5. RESULTS

Here we test the model over a wide spectrum of altitude profiles and the results are compared with the equivalent research exposures taken from the database (see Table 3).

The first profile describes a 35,000-ft flight with 75 minutes of preoxygenation time and 180 minutes exposure time. The exercise level conducted by the subjects is considered heavy and all of them breathe 100% oxygen throughout the entire flight profile. The ascent rate is 5000 ft/min. The predicted DCS risk from ADRAC was 91.7 %. For the exact same profile but with mild exercise, ADRAC predicted a 58.8% risk. The observed risks, taken directly from the database, were 96.6% and 56.6% respectively. As one can see the predicted and observed values are very close and well within a reasonable error range.

Next we will test the model's capability of predicting risk for two different preoxygenation

schedules. Both exposures are at 30,000-ft, breathing 100% oxygen. The ascent rate is again 5000 ft/min and the preoxygenation times are 90 and 240 minutes respectively. The predicted risks computed by ADRAC were 60.7% for the 90 minutes of preoxygenation time, and 43.8% for the 240-minute one. During both of the exposures the subjects were performing mild exercises. Once again, the observed risks, from the database, were 56.0% and 45.3%.

Altitude is one of the most important risk parameters. The next two flight scenarios examine how altitude affects the risk of DCS and how ADRAC performs when altitudes are altered. The first profile represents an exposure to 25,000-ft with zero preoxygenation time, 5000 ft/min ascent rate, mild exercise breathing 100% oxygen throughout the entire exposure. The second profile is an exposure to 21,200-ft under the same conditions described above. The exposure times were 4 and 6 hours respectively. The calculated risks for those two flights were 80.8% and 16.9%. The equivalent observed values were 81.3% and 17.5%.

In Table 3 we summarize the results and a straight comparison with the observed values can conclude that all of the tested profiles were within +/- 5% error.

Altitude Profiles	% of DCS Risk taken from the Armstrong Laboratory Hypobaric DCS Research Database	% of DCS Risk calculated from ADRAC
35,000 ft altitude, 75 minutes of preoxygenation time, 180 minutes of exposure time, heavy exercise	96.6%	91.7%
35,000 ft altitude, 75 minutes of preoxygenation time, 180 minutes of exposure time, rest	56.6%	58.8%
30,000 ft altitude, 90 minutes of preoxygenation time, 240 minutes of exposure time, mild exercise	56.0%	60.7%
30,000 ft altitude, 240 minutes of preoxygenation time, 240 minutes of exposure time, mild exercise	45.3%	43.8%
25,000 ft altitude, 0 minutes of preoxygenation time, 240 minutes of exposure time, mild exercise	81.3%	80.8%
21,200 ft altitude, 0 minutes of preoxygenation time, 360 minutes of exposure time, mild exercise	17.5%	16.9%

Table 3

REFERENCES

1. Van Liew, H. D., Conkin, J. and Burkard, M. E., "Probabilistic model of altitude decompression sickness based on mechanistic premises", J. Appl. Physiol., vol. 76, pp. 2726-2734, 1994.

2. Gerth, W. A. and Vann, R. D., "Statistical bubble dynamics algorithms for assessment of altitude decompression sickness incidence", AL/CF-TR-1995-0037, 1995.

3. Kumar, K., Waligora, J. and Calkins, D., "Threshold altitude resulting in decompression sickness", Aviat. Space Environ. Med., vol. 61, pp. 685-689, 1990.

4. Kumar, K., Calkins, D., Waligora, J., Gilbert III, J. and Powell, M., "Time to detection of circulating microbubbles as a risk factor for symptoms of altitude decompression sickness", Aviat. Space Environ. Med., vol. 63, pp. 961-964, 1992.

5. Kumar, K., Waligora, J., Gilbert III, J. and Powell, M., "Epidemiology of decompression sickness under simulated space extravehicular activities", Aviat.

Space Environ. Med., vol. 64, pp. 1032-1039, 1993.

6. Kumar, K. and Powell, M., "Survivorship models for estimating the risk of decompression sickness", Aviat. Space Environ. Med., vol. 65, pp. 661-665, 1994.

7. Conkin, J., Kumar, K., Powell, M., Foster, P. and Waligora, J., "A probabilistic model of hypobaric decompression sickness based on 66 chamber tests", Aviat. Space Environ. Med., vol. 67, pp. 001-008, 1996.

8. Petropoulos, L.J., Petropoulos, P.G. and Pilmanis, A.A., "Mathematical analysis of bubble growth models applied to altitude decompression sickness", J. Math. Biosci. (In review).

New Methodology for the Assessment of Battlefield Insults and Injuries On the Performance of Army, Navy, and Air Force Military Tasks

Mr. David N. Neades
Dr. J. Terrence Klopcic
Dr. Edward G. Davis

U. S. Army Research Laboratory
Survivability/Lethality Analysis Directorate
ATTN: AMSRL-SL-BE
Aberdeen Proving Ground, MD 21005, U.S.A.

SUMMARY

To address known limitations, shortfalls, and lack of a comprehensive standardized casualty assessment methodology, across the military services as well as within services, a new methodology has been developed for triservice use that allows the assessment of soldier performance following weapon-induced injury. This new methodology, embodied in the Operational Requirement-based Casualty Assessment (ORCA) modeling system, permits casualty assessments to be performed in a consistent manner across virtually all types of military platforms, jobs, and weapon-induced threats. The ORCA computer code enables the analyst to calculate anatomical damage and the effect on individual performance as a result of exposure to one or more insult types including kinetic energy (fragments), chemical, and blast overpressure. The ORCA modeling system incorporates previously developed as well as newly developed injury criteria models, algorithms, and scoring systems to characterize human bioresponse to trauma from various types of battlefield insults and derives estimates of soldier performance degradation. Future ORCA developments will enable the presence of body armor or other protective barriers to be taken into account. It is envisioned that use of the ORCA Modeling System will provide the tri-service survivability/ lethality / vulnerability community with a useful and standardized crew casualty analysis process and analytical assessment tool.

1. INTRODUCTION

In 1965, Kokinakis and Sperrazza published curves of probability of incapacitation given a hit, or P(I/H), correlated to fragment mass and striking velocity raised to the 3/2 power ($MV^{3/2}$).[1] In the years since, these curves have been used to compute P(I/H) as a common measure of weapon effectiveness throughout a wide segment of the military operational research community. Although these data apply strictly to situations involving fragment impacts against infantry soldiers, they are often mis-applied to personnel in non-infantry roles as well, usually due to the lack of platform specific criteria. In other segments of the analysis community, the vulnerability of on-board crew personnel and their contribution to the vulnerability of the weapon system are not explicitly computed.

Papers presented at the RTO HFM Specialists' Meeting on "Models for Aircrew Safety Assessment: Uses, Limitations and Requirements", held in Ohio, USA, 26-28 October 1998, and published in RTO MP-20.

In general, comparable methodology to deal with the effects of other damage mechanisms, such as blast overpressure, thermal, *etc.*, on land, air, or sea platforms has been inadequate or lacking altogether. The lack of a standard, comprehensive methodology has prevented, among other things, direct comparisons of operational casualty estimates due to soldier exposure to the same or different weapon-induced threats, across service as well as within a service.

2. BACKGROUND

The present work has its origins in a series of casualty workshops,[2] sponsored by the U.S. Office of the Secretary of Defense (OSD), which identified many of the limitations and shortfalls cited previously, and the need for a comprehensive casualty assessment methodology. That need led eventually to the formation of the Crew Casualty Working Group (CCWG) which, in 1992, became part of the Joint Technical Coordinating Group for Munitions Effectiveness (JTCG/ME). Shortly thereafter, the essential common interest of the JTCG/AS (Aircraft Survivability) in the same crew casualty assessment issues was recognized. The CCWG at that point became a joint JTCG/ME and JTCG/AS working group.

2.1 The Crew Casualty Working Group

An executive committee consisting of five representatives, one each from the Army, Navy, Air Force, OSD, JTCG/ME and JTCG/AS, heads the CCWG tri-service organization. The executive committee is supported by technical inputs from throughout the personnel vulnerability and human factors community through representatives from the services, other government agencies, academia, and industrial groups/contractors.

The primary goals of the CCWG are as follows:

1. To develop and publicize a comprehensive, Department of Defense-accredited personnel vulnerability assessment methodology.

2. To establish a consistent set of working definitions.

3. To support key projects that are triservice applicable and needed to fill identified voids.

4. To ensure hat outputs of crew casualty projects are compatible with their uses/ users.

5. To aid dissemination of results, in particular, through JTCG channels.

6. When appropriate, to transition to a subgroup under one of the permanent JTCG Working Groups.

The remainder of this paper describes the status of work driven by the first goal.

3. ORCA MODELING APPROACH

The foundation of the Operational Requirement-based Casualty Assessment (ORCA) Modeling System and the underlying CCWG methodology is a new taxonomy that characterizes the analytical casualty assessment process. The taxonomy has proven to be most useful, not only for ensuring completeness and coordination of the technical tasks but also for developing an overall management plan for the work of the CCWG. As shown in Figure 1, the taxonomy divides logically into three parts: the determination

of the injury resulting from an insult, the resulting impairment of certain human elemental capabilities, and the effect of such impairment on the performance of military jobs.

The ultimate objective of the process, then, is to determine if an individual would be an *Operational Casualty* as a result of his/her exposure to the insult. An Operational Casualty is defined here as "An impaired individual whose available elemental capabilities are less than those required for successful performance of a specified military job."

It should be noted at this point, that the original scope of the CCWG project was limited to evaluating the residual performance of an individual after a potentially damaging environment had actually impinged upon him/her. Thus, the degradation of a threat by protective armor, or other external factors that may influence the characteristics of the threat prior to its reaching the individual, had to be taken into account before beginning the CCWG process. This constraint has now been removed in order to be more responsive to the needs of the analysis community. It should also be noted that no attempt has been made to account for any effect that variables, such as motivation and fear, might have on performance. We are attempting to simulate only the physical effects of injury in order to assess what an individual *could* do, not what he/she *would* do.

The basic steps involved in the analytical crew casualty assessment process are as follows:

1. Assemble the parameters that quantify a battlefield Insult.

2. Evaluate the anatomical/ physiological Injury produced by that Insult.

3. Relate that Injury to the attendant Impairment, expressed as a degradation of Elemental Capabilities.

4. Independently, establish the Requirements for satisfactory performance of a military job, also in terms of Elemental Capabilities.

5. Compare the *available* (degraded) Elemental Capabilities to the *required* Elemental Capabilities to determine if the incurred injury constitutes an Operational Casualty for an individual in the specified military job.

4. THE ORCA COMPUTER MODELING SYSTEM

The computer code written to carry out these steps is referred to as the ORCA Modeling System, or the ORCA Model. The assessment of an operational casualty using the ORCA Model begins by specifying the potentially damaging mechanism or *Insult.* The weapon-induced insults addressed in the ORCA model at this stage of development follow:

- Blast Overpressure
- Penetration
- Thermal
- Directed Energy (lasers)
- Toxic Substance Inhalation/ Contact
- Blunt Trauma

- Acceleration

It is an important attribute of the ORCA Modeling System that it incorporates previously developed or newly developed models, algorithms and scoring systems to characterize the weapon-induced insult to injury phenomenon. Each of these models, algorithms, or scoring systems were identified, reviewed, and adopted by consensus of subject matter experts from the military tri-service survivability/ lethality vulnerability (SLV) community, academia, and industry. The major models that characterize the insult-to-injury phenomenon within ORCA are presented in Figure 2 and identification of these models follows.

Penetrating injuries are modeled using the Army Research Laboratory ComputerMan Model methodology to conduct wound ballistics assessments.[3,4] Non-auditory blast overpressure injuries are modeled using the INJURY Model jointly developed by the U.S. Army Walter Reed Army Institute of Research (WRAIR) and JAYCOR, Inc. (San Diego, CA).[5] Blast overpressure induced auditory injuries are characterized using a combination of the WRAIR/JAYCOR INJURY Model and an Army model developed by Price and colleagues.[6,7] Injuries associated with rapid acceleration are modeled using the U.S. Air Force's Articulated Total Body (ATB) Model[8] to define the physical forces on the human body and the U.S. Army's BLAST Model developed by Alem at the Aeromedical Research Laboratory to characterize the acceleration injuries to the human body.[9] Laser eye damage is modeled using an ocular injury model developed by Miller and Carver.[10] Thermal and burn injuries are characterized using the BURNSIM Model developed by U.S. Army and U.S. Air Force researchers Knox and colleagues.[11] Chemical insults and resulting injury are modeled using the U.S. Army Chemical Computer Man - Chemical Agent Response Simulation (CARS) Model developed by Davis and Mioduszewski.[12]

4.1 Insult Specification

An Insult is quantified by a set of parameters, {P} which characterizes the damage mechanism in useful terms. As an example, for a blast overpressure event, that set might consist of a pressure-time curve and a body orientation with respect to the blast wave. In many cases, ORCA users will have the option of selecting from predefined insult characterizations (e.g., a wave form, along with a peak pressure and "A-duration" in the case of blast overpressure) or providing their own data. When appropriate, the body can be articulated or placed into different postures relative to the Insult. For example, a soldier being subjected to fragment impacts can be positioned in a standing, seated, crouching, or prone position.

4.2 Injury Characterization

ORCA contains state-of-the-art algorithms and supporting data to calculate the anatomical damage to a human body as a result of an Insult. In the ORCA code, all injuries are recorded in a standard form via a vector (A vector) whose elements refer to the state of over 470 body parts that have been defined to constitute the human body. Each element has an associated scale through which the severity of the damage is recorded. Again, with the blast overpressure example, the lungs and ears, being the main organs at risk, are the relevant elements of the A vector. A numerical value ranging from 1 to 5 is used to indicate the severity of damage to the lung as a result of the blast Insult. In addition to producing direct physical damage, an insult can initiate certain deleterious processes, such as bleeding or

reduced respiratory functions that further reduce elemental capabilities. These factors are recorded as B-Processes and are used in connection with the A vector damage to compute impairment as a function of time after injury.

The determination of medical casualties is not within the CCWG charter. However, since ORCA's inception, it was considered important that a commonality of human injury description was sought to describe injury for the operational casualty as well as the medical casualty assessment process. In fact, a significant effort was made during the development of ORCA to make injury descriptions consistent and potentially applicable to modeling needs of the medical research and analysis community, as well to the operational casualty SLV community. To this end, significant care has been taken to define and record injuries in such a way as to potentially serve future medical analysis needs. In particular, for penetrating fragment injuries ORCA determines and keeps track of each injury's Abbreviated Injury Score – 1985 Revision (AIS-85),[13] a standard measure of individual anatomical injury severity that is commonly used throughout the civilian medical community for this purpose. The AIS system is also the basis for anatomical severity summary measures used to describe an individual's overall severity of injury, such as the Injury Severity Score (ISS),[14,15] Anatomic Profile (AP),[16] modified-Anatomic Profile (mAP),[17] and Revised Injury Severity Score (RISS).[18] Future ORCA developmental efforts will evaluate updating the anatomical injury description to the Abbreviated Injury Score – 1990 Revision (AIS-90).[19]

4.3 Elemental Capability Impairment

Significant work has been devoted to correlating the various types and levels of injury to the impairment of an individual's capabilities. These capabilities are formally recorded via the Elemental Capability Vector, or "ECV" for short. The elements of the ECV are representative of the capabilities that humans use to accomplish tasks. The 24 ORCA Elemental Capabilities are presented in Figure 3.

Each of these elements is quantified by a set of parameters that permits us to consider various levels of capability. The 24 elemental capability elements can be grouped into the following general categories:

Visual - Vision is critical for almost every imaginable task, including battlefield surveillance, driving a tank, or loading weapons.

Auditory - Hearing is measured in decibels for two threshold frequencies. Crew-members likely to require hearing capability include communication personnel, combat vehicle crewmembers, infantry soldiers, and pilots.

Mental - Cognitive, visual, auditory, and psychomotor mental processing refers to the brain responses needed to interpret or understand the stimuli received by the senses. The ability to reason and make decisions is critical for many tasks in the field.

Vocal - Vocal capability is measured by the amount of vocal power needed and speech intelligibility. The ability to communicate can be important on the battlefield as well as in communication activities.

Physical - Physical tasks are broken down by body segment. Strength and movement capabilities of the legs, arms, hands, torso, and neck are measured in the ECV. Minor

physical tasks, such as pushing a button or turning a knob can be modeled as well as major tasks, such as walking, climbing, pushing or pulling, or swimming.

Endurance - Other capabilities, such as endurance, balance, and a sense of touch, are modeled in the ECV. Endurance will play an important role in determining casualties because many injuries can affect the blood or oxygen supply to the body.

In ORCA, the Elemental Capability vector serves two important functions. First, as described previously, the ECV is used to quantify the capabilities that a particular, possibly wounded, individual possesses. In this application, the ECV is referred to by the symbol $\underline{X}$. The same vector form is used to quantify the capabilities required to perform specific military tasks or jobs. In this application, the ECV is referred to by the symbol $\underline{Z}$. Therefore, it is a straightforward matter to determine whether a wounded individual is capable of performing a particular task or job. ORCA compares his capabilities ($\underline{X}$) with the task requirements ($\underline{Z}$).

4.4 Time Dependence

In the ORCA formulism, an injury is characterized at the time it occurs. However, it is recognized that the effects of an injury may change over time. To capture this effect, ORCA calculates a number of $\underline{X}$ vectors, one for each of six post-injury times: Immediate, 30 seconds, 5 minutes, 1 hour, 24 hours, and 3 days. Each $\underline{X}$ vector is, in turn, compared to the job requirements to determine job performance, or casualty status over time.

4.5 Task Requirements

As previously stated, an operational casualty is defined with respect to a particular job or task (a "job" is a group of tasks). Thus, in addition to defining the insult, the job and associated tasks required of an individual must be input using Military Occupational Specialty (MOS), Navy Enlisted Code (NEC), or Air Force Specialty Code (AFSC) job description information. These military jobs have been defined by a list of basic physical, cognitive and sensory tasks. Each basic task description such as running, carrying, or speaking is described using the elemental capability vector. For instance, a pilot's job contains several tasks such as operating controls, reaching above, visual mental processing, communication, and hearing. Each task is described by the ECV, and the pilot's job will consist of the summation of all needed tasks. ORCA contains a library of tasks and jobs that have been quantified in terms of their elemental capability requirements. In addition, ORCA contains a very friendly user interface to help an ORCA user to describe his own tasks and jobs through common terms and images. Military occupations or jobs currently incorporated or under development in ORCA are presented in Figure 4. The number of tasks and unique task elements associated with each military job are presented in Figure 5.

It is recognized that job performance is usually not a "Go-No Go" proposition; rather, most jobs can be performed at various levels of effectiveness. ORCA models this by allowing different levels of requirements to describe different levels of performance. Standard practice with ORCA is to specify requirements for full performance and the requirements for marginal performance. Again, the user interface helps the user to specify different levels of effectiveness or to select them from the ORCA internal library.

4.6 Individual Characterization

ORCA allows the user to characterize the individual being studied. Although a 50th percentile individual is the default condition, the user can specify the initial capabilities of the individual or randomly select initial capabilities via Monte Carlo draws from distributions of capabilities. This feature also allows the user to account for other relevant and circumstantial attributes that may mitigate the insult-to-injury effects. For example, the presence of protective items like chemical protective clothing or other items that may restrict movement or vision or otherwise cause the individual's initial starting conditions or circumstances to be less than a fully capable or considered not in a fully optimal state.

5. CURRENT STATUS OF THE ORCA COMPUTER CODE

Currently, the ORCA code exists in an alpha-test version that contains the complete structure of the methodology; the Blast, Chemical, Thermal, Directed Energy, and Kinetic Energy fragment portion of the Penetrating Insult Modules and required data; the military occupational database; and the graphical user interface. The entire ORCA project, as originally envisioned in 1992 as a five-year program, is essentially complete. In addition to completing the Acceleration Insult module, a number of other refinements are scheduled for 1999 along with two verification and validation (V&V) efforts. Future planned model refinements include the addition of enhancements ("wrappers") to permit body armor coverage of specified body regions and computation of soldier survival probability to augment the current performance-based outputs. Configuration management issues are also being addressed to ensure that the code remains in sync with current developments elsewhere in the SLV community and relevant to the needs of the military analyst.

REFERENCES

[1] Kokinakis, W. and Sperrazza J., "Criteria for Incapacitating Soldiers with Fragments and Flechettes", Ballistic Research Laboratory Report No. 1269, U.S. Army Ballistic Research Laboratory, Aberdeen Proving Ground, MD, January 1965.

[2] Director, Live Fire Testing, Office of the Director, Defense Research and Engineering, "Proceedings of the Live Fire Test Crew Casualty Assessment Workshop Held 18-19 October 1988 at the Naval Submarine Base, Groton, Connecticut", October 1988.

[3] Clare, V.R., Ashman, W., Broome, P., Jameson, J., Lewis, J., Merkler, J., Mickiewicz, A., Sacco, W., Sturdivan, L., Lamb, D., Sylvanus, F., "The ARRADCOM Computer Man: An Automated Approach to Wound Ballistics." ARCSL-TR-80021, U.S. Army Chemical Systems Laboratory, Aberdeen Proving Ground, MD, November 1980.

[4] Saucier, R., Kash, H.M., III, "ComputerMan Model Description," U.S. Army Research Laboratory Technical Report No. ARL-TR-500. U.S. Army Research Laboratory, Aberdeen Proving Ground, MD, August 1994.

[5] JAYCOR, Inc. (San Diego, CA), "INJURY User's Manual (Version 4.00 Beta)", May 1995.

[6] Price, G.R., Kalb, J.T., "A New Approach to a Damage Risk Criterion for Weapons Impulses." *Scand. Audiol. Suppl.*, 34, 1991, pp 21-37.

[7] Price, G.R., et al., "Insights Into Hazards From Intense Impulses From a Mathematical Model of the Ear." *J. Accoust. Soc. Amer.*, 90,1, 1991, pp 219-227.

[8] Obergefell, L.A., Gardner, T.R., Kaleps, I., Fleck, J.T., "Articulated Total Body Model Enhancements, Vol II – User's Guide", U.S. Air Force Research Laboratory Report No. AAMRL-TR-88-043, U.S. Air Force Research Laboratory, WPAFB, OH, 1988.

[9] Alem, N.M., "Mine Blast, Acceleration, Injury Assessment: Methods, Criteria, and Software." U.S. Army Aeromedical Research Laboratory Technical Report No. USAARL-97-28, U.S. Army Aeromedical Research Laboratory, Ft. Rucker, AL, July 1997.

[10] Miller, R.E., Carver, B., "A Submodel for Combat Casualty Assessment of Ocular Injury from Lasers – Final Report." VERIDIAN, Inc., Brooks AFB, TX, June 1998.

[11] Knox, F.S., III, Bonetti, D., Perry, C., "User's Manual for BURNSIM: A Burn Hazard Assessment Model." U.S. Army Aeromedical Research Laboratory, Ft. Rucker, AL, and the U.S. Air Force Laboratory, WPAFB, OH, USAARL Report No. 93-13, Army Aeromedical Research Laboratory, 1993.

[12] Davis, E.G., Mioduszewski, R.J., "Chemical Computer Man: Chemical Agent Response Simulation (CARS)", U.S. Army Chemical Research, Development, and Engineering Center Technical Report No. CRDEC-TR-88067. U.S. Army Chemical Research, Development, and Engineering Center, Aberdeen Proving Ground, MD, March 1988.

[13] American Association for Automotive Medicine. "The Abbreviated Injury Scale 1985 Revision (AIS-85)", Committee on Injury Scaling, Des Plaines, IL, 1985.

[14] Baker, S.P., O'Neill, B., Haddon, W., Long W.B, "The Injury Severity Score: A Method for Describing Patients with Multiple Injuries and Evaluating Emergency Care", *Journal of Trauma,* 14,3, 1974, pp187-196.

[15] Baker, S.P., O'Neill, B, "The Injury Severity Score: An Update", *Journal of Trauma, 16, 11,* 1976, pp 882-885.

[16] Copes, W.S., Champion, H.R., Sacco, W.J., Lawnick, M.M., *et al.*, "Progress in Characterizing Anatomic Trauma", *Journal of Trauma, 30, 1,* 1990, pp 1200-1207.

[17] Sacco, W.J., MacKenzie, E.J., Champion, H.R., Davis, E.G., *et al.*, "Injury Severity Score (ISS), New Injury Severity Score (NISS), ICD-9-based Injury Severity Score (ICISS), Anatomic Profile (AP), and Modified-Anatomic Profile (mAP): A Scientific Study", (Manuscript in preparation).

[18] Davis, E.G., "Characterization of Trauma: Evaluation and Refinement of Indices of Severity and Survival Probability Models", Ph.D. Dissertation, The Johns Hopkins University School of Hygiene and Public Health / Johns Hopkins Medical Institutions, Baltimore, MD, June 1998.

[19] American Association for Automotive Medicine, "The Abbreviated Injury Scale 1990 Revision (AIS-90)", Committee on Injury Scaling, Des Plaines, IL, 1990.

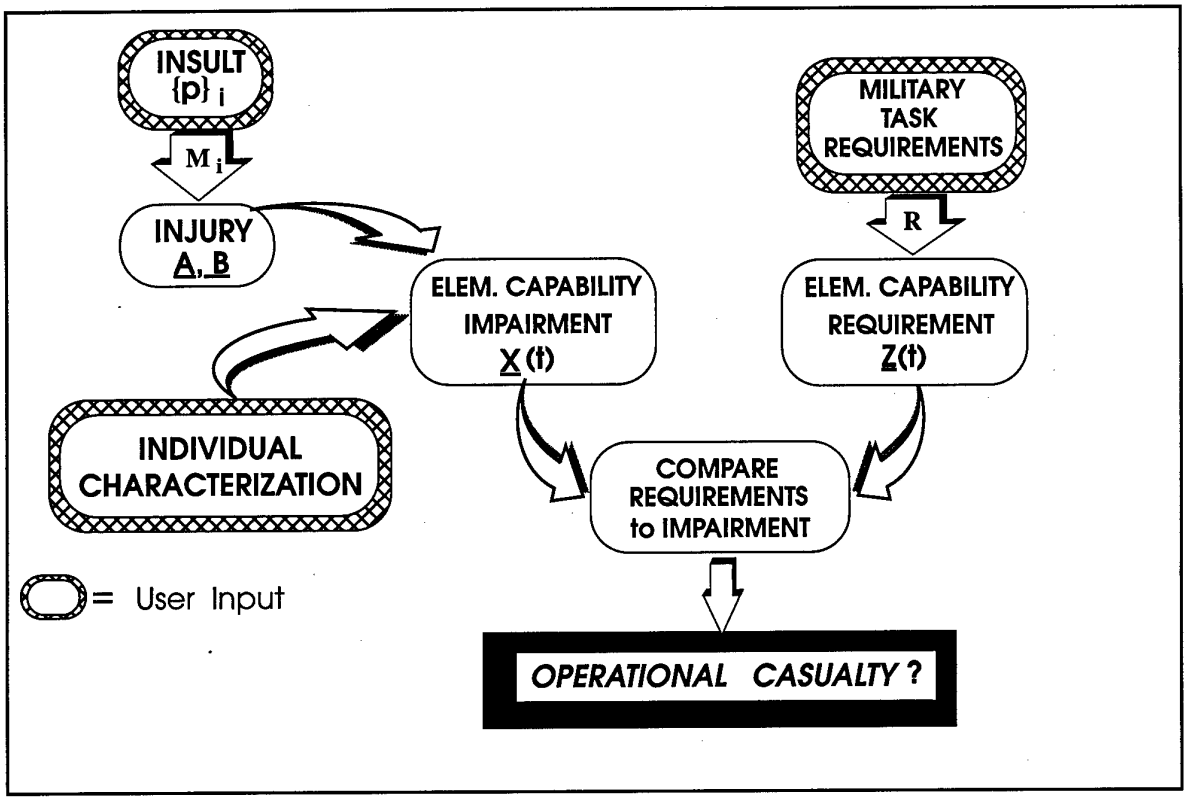

Figure 1. Taxonomy for the Crew Casualty Assessment Process

INSULT	SUBMODEL (S)
Penetrating	ComputerMan (USA)
Blast Overpressure	INJURY (USA) / Price Ear Model (USA)
Directed Energy (Laser)	ILPEM(USAF)
Chemical	Chemical Man (USA) / OSHA
Thermal	BURNSIM (USAF)
Acceleration	Articulated Total Body (USAF) / BLAST (USA)

Figure 2. ORCA Insult to Injury Submodels (M_i)

ECV No.	Capability	ECV No.	Capability
1.	Visual Acuity & Color Discrimination	14.	Speech Articulation
2.	Night Vision	15.	Vocal Power
3.	Visual Field of View		
4.	Visual Binocularism & Motility	16.	Right Leg Strength
		17.	Left Leg Strength
5.	Hearing Threshold - Low Frequency	18.	Left Arm/Hand Strength
6.	Hearing Threshold - High Freauency	19.	Right Arm/Hand Strength
7.	Binauralism	20.	Left Arm/Hand Dexterity
		21.	Right Arm/Hand Dexterity
8.	Somatic Senses	22.	Torso Support
9.	Balance	23.	Head/Neck Movement
10.	Cognitive Mental Processing	24.	Endurance
11.	Visual Mental Processing		
12.	Auditory Mental Processing		
13.	Psychomotor Mental Processing		

Figure 3. Elemental Capability Vector, $\overline{X}$

JOB	SERVICE	OCCUPATION CODE
Infantry Rifleman	Army	11B
AH64 Apache Pilot	Army	152F
Firefinder Radar Operator	Army	13R
Ammunition Specialist	Army	55B
Combat Engineer	Army	12B
Artilleryman (M-109 Gunner)	Army	13B
M1A1 Abrams Crewman (Gunner)	Army	19K
Installation Security Specialist	Army	95B
Medical Care Provider-Combat Medic	Army	91B
Combat Pilot (F/A-18)	Navy	8528
EOD Technician	Navy	5332
Damage/Casualty Control/Recovery/Reconfig	Navy	Various
Damage Control Specialist	Navy	DC3
C-130 Hercules Pilot	Air Force	1045
Radioman (Airborne Commo Systems)	Air Force	1A3X1
Combat Operations Control Specialist	Air Force	1A1X1
Motor Transport Operator	Army	88M
LAV Crewman (Driver)	Marine	0313

Figure 4. ORCA Occupations

JOB	TASKS	TASK ELEMENTS
Infantry Rifleman	64	266
AH64 Apache Pilot	86	377
Firefinder Radar Operator	67	234
Ammunition Specialist	23	187
Combat Engineer	42	315
Artilleryman (M-109 Gunner)	34	173
M1A1 Abrams Crewman (Gunner)	99	706
Installation Security Specialist	75	313
Medical Care Provider-Combat Medic	77	368
Combat Pilot (F/A-18)	136	555
EOD Technician	15	255
Damage/Casualty Control/Recovery/Reconfig	40	599
Damage Control Specialist	40	356
C-130 Hercules Pilot	109	214
Radioman (Airborne Commo Systems)	15	255
Combat Operations Control Specialist	9	224
Motor Transport Operator	8	56
LAV Crewman (Driver)	38	227
Common Tasks - Army	10	70
Common Tasks - Navy	13	100
Totals	1,000	5,810

Figure 5. ORCA Task Database

DOSIMETRY MODELS USED TO DETERMINE THE BIOEFFECTS OF DIRECTED ENERGY EXPOSURE

WILLIAM D. HURT and PATRICK A. MASON[1]
Air Force Research Laboratory
Human Effectiveness Directorate
Radiofrequency Bioeffects Branch
8308 Hawks Road
Brooks AFB, TX 78235-5324, USA

1. SUMMARY

Determining the bioeffects of directed energy exposure is essential for establishing safety standards to protect military personnel and the general public. However, internal temperature measurements are invasive in nature, and therefore difficult or impossible to obtain. Furthermore, it would be unethical to expose human subjects to those field parameters producing substantial thermal increases. An alternative method to obtain the necessary information is the development of accurate anatomical models incorporating permittivity values for the major tissue types. Using the VisableMan dataset available from the National Library of Medicine, we have converted each of the 1870 photographic images into a color-coded image representing permittivity values. Each color corresponds to an entry in a look-up-table containing the permittivity properties of that tissue. The resulting dataset is imported into a mathematical model to predict electrical fields and specific absorption rate (SAR) values. Various mathematical models are available including the finite-difference time-domain code. Processing such a large dataset is best accomplished using parallel computer system. Combining anatomical and mathematical models provide the technology required to begin understanding the distribution of localized SAR values in the human resulting from directed energy exposure.

2. INTRODUCTION

The radio frequency (RF) region of the electromagnetic (EM) spectrum extends over a wide range of frequencies, from about 3 kHz to 300 GHz. Over the last several years, the use of devices that emit RF radiation has increased dramatically. RF devices include radio and television transmitters, military and civilian radar systems, a variety of communications systems, microwave ovens, industrial RF heat sealers, and various medical devices.

The proliferation of RF devices has been accompanied by increased concern about ensuring the safety of their use. Throughout the world many organizations, both government and nongovernment, have established RF safety standards or guidelines for exposure. Theoretical and experimental methods are used to extrapolate or relate effects observed in animals to similar effects expected to be found in people. Safety standards can be revised if knowledge is obtained about previously unknown adverse RF effects on the human body.

An essential element of the research examining the biological effects of RF exposure is dosimetry: the determination of energy absorbed by an object exposed to the EM fields composing the RF spectrum. Since the energy absorbed is directly related to the internal EM fields (that is, the EM fields inside the object, not the EM fields incident upon the object), dosimetry is also interpreted to mean the determination of internal EM fields. The internal and incident EM fields can be quite different, depending on the size and shape of the object, its electrical properties, its orientation with respect to the incident EM fields, and the frequency of the incident fields. Because any biological effects will be related directly to the internal fields, any cause-and-effect relationship must be formulated in terms of these fields, and not the incident fields. However, direct measurement of the incident fields is easier and more practical than measuring the internal fields, especially in people, so we use dosimetry to relate the internal fields to the incident fields. As used here, the term "internal fields" is to be broadly interpreted as the fields that interact directly with the biological system. In general, the presence of the body causes the internal fields to be different from the incident fields.

The rigorous analysis of a realistically shaped inhomogeneous model for humans or experimental animals is an enormous theoretical task. Because of the difficulty of solving Maxwell's equations, which form the basis of this analysis, a variety of special models and techniques have been used, each valid only in a limited range of frequency or other parameters. Early analyses were based on plane-layered, cylindrical, and spherical models. Although these models are relatively crude representations of the size and shape of the human body, experimental results show that calculations of the average specific absorption rate (SAR), one of the most important dosimetric values, agree reasonably well with measured values. Calculations of the local distribution of the SAR, even though being much more difficult, are now becoming possible. SAR is discussed later in this paper.

3. INTERACTION OF EM FIELDS WITH MATERIALS

Electric (E) and magnetic (H) fields interact with materials in two ways. First, the E- and H-fields exert forces on the charged particles in the material, thus altering the charge patterns that originally existed. Second, the altered charge patterns in the materials produce additional E- and H-fields (in addition to the fields that were originally applied). Materials are usually classified as being either magnetic or nonmagnetic. Magnetic materials have magnetic dipoles that are strongly affected by applied magnetic fields, nonmagnetic materials do not. Biological material is almost exclusively nonmagnetic.

In nonmagnetic materials, it is mainly the applied E-field that effects the charges in the material. This occurs in three primary ways:

1. Polarization of bound charges.
2. Orientation of permanent dipoles.
3. Drift of conduction charges (both electronic and ionic).

Materials primarily affected by the first two ways are called dielectrics; materials primarily affected by the third way are called conductors.

[1] Veridian, Brooks AFB, TX

Papers presented at the RTO HFM Specialists' Meeting on "Models for Aircrew Safety Assessment: Uses, Limitations and Requirements", held in Ohio, USA, 26-28 October 1998, and published in RTO MP-20.

The polarization of bound charges is illustrated in Figure 1(a). Bound charges are so tightly controlled by restoring forces in a material that they can move only very slightly. Without an applied E-field, positive and negative bound charges in an atom or molecule are essentially superimposed upon each other and effectively cancel out. When an E-field is applied, the forces on the positive and negative charges are in opposite directions and the charges separate, resulting in an induced electric dipole. A dipole consists of a combination of a positive and a negative charge separated by a small distance. In this case the dipole is said to be induced because it is a result of the applied E-field; when the field is removed, the dipole disappears. When the charges are separated by the applied E-field, the charges no longer cancel. In effect the charge distribution is altered, called polarization charge, which creates new fields that did not exist previously.

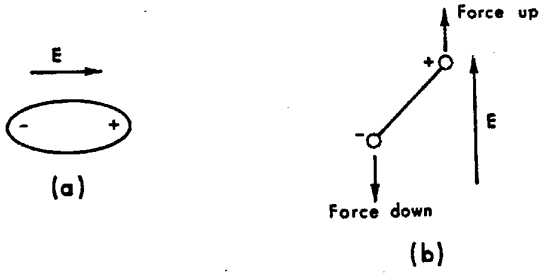

Figure 1. (a) Polarization of bond charges. (b) Orientation of permanent dipoles.

The orientation of permanent dipoles is illustrated in Figure 1(b). The arrangement of charges in some molecules produces permanent dipoles that exist regardless of whether an E-field is applied to the material. With no E-field applied, permanent dipoles are randomly oriented because of thermal excitation. With an E-field applied, the resulting forces on the permanent dipoles tend to align the dipole with the applied E-field. This orientation effect is only slight because the thermal excitation is relatively strong, but on the average there is a net alignment of dipoles over the randomness that existed without an applied E-field. Like induced dipoles, this net alignment of permanent dipoles produces new fields.

The drift of conduction charges in an applied E-field occurs because these charges are free enough to move significant distances in response to forces of the applied field. Both electrons and ions can be conduction charges. Movement of the conduction charges is called drift because thermal excitation causes random motion of the conduction charges, and the force due to the applied fields superimposes only a slight movement in the direction of the force on this random movement. The drift of conduction charges amounts to a current, and this current produces new fields that did not exist before the E-field was applied.

The two effects--creation of polarization charges by an applied field and creation of new fields by these new charge distributions--for both induced dipoles and orientation of permanent dipoles are taken into account by a quantity called permittivity. Permittivity is a measure of how easily the polarization in a material occurs. If an applied E-field results in many induced dipoles per unit volume or a high net alignment of permanent dipoles per unit volume, the permittivity is high. The drift of conduction charges is accounted for by a quantity called conductivity. Conductivity is a measure of how much drift occurs for a given applied E-field. A large drift means a high conductivity. For sinusoidal steady-state applied fields, complex permittivity is defined to account for both dipole charges and conduction-charge drift. Complex permittivity is usually designated as:

$$\varepsilon^* = \varepsilon_o(\varepsilon' - j\varepsilon'') \quad \text{F/m},$$

where ε_o ($8.85 \cdot 10^{-12}$ farad/meter) is the permittivity of free space, $\varepsilon' - j\varepsilon''$ is the complex relative permittivity, ε' is the real part of the complex relative permittivity (ε' is also called the dielectric value), j is the imaginary unit, and ε'' is the imaginary part of the complex relative permittivity. ε'' is related to the effective conductivity by:

$$\varepsilon'' = \sigma/\omega\varepsilon_o,$$

where σ is the effective conductivity in siemens/meter, and

$$\omega = 2\pi f \quad \text{radians/s}$$

is the radian frequency of the applied fields. The ε' of a material is primarily a measure of the relative amount of polarization that occurs for a given applied E-field, and the ε'' is a measure of both the friction associated with changing polarization and the drift of conduction charges.

4. ELECTRICAL PROPERTIES OF BIOLOGICAL TISSUE

The permeability of biological tissue is essentially equal to that of free space; in other words, biological tissue is essentially nonmagnetic. The permittivity of biological tissue is a strong function of frequency. Figure 2 shows the average ε' and σ for the human body as a function of frequency. Calculations have shown that the average ε' and σ for the whole human body are equal to approximately two-thirds that of muscle tissue.

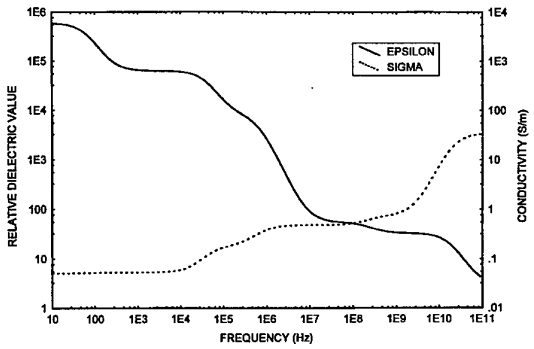

Figure 2. Average permittivity of the human body as a function of frequency.

The dielectric value generally decreases with frequency. This results from the inability of the charges in the tissue to respond to the higher frequency applied fields, thus resulting in lower dielectric values.

In tissue, the ε'' represents mostly ionic conductivity and absorption due to relaxational processes, including friction associated with the alignment of electric dipoles and with vibrational and rotational motion

in molecules.

Energy transferred from applied E-fields to materials is in the form of kinetic energy of the charged particles in the material. The rate of change of the energy transferred to the material is called SAR, the standard quantity for RF dosimetry.

A typical manifestation of average (with respect to time) SAR is heat. The average SAR results from the friction associated with movement of induced dipoles, permanent dipoles, and drifting conduction charges. If there were no friction in the material, the average SAR would be zero.

A material that absorbs a significant rate of energy for a given applied field is said to be a lossy material because of the loss of energy from the applied fields. A measure of the lossiness of a material is ε". The larger the ε", the more lossy the material. In some tables, a quantity called the loss tangent is listed instead of ε". The loss tangent, often designated as tanδ, is defined as:

$$\tan\delta = \varepsilon''/\varepsilon'.$$

The loss tangent usually varies with frequency. For example, the loss tangent of distilled water is about 0.04 at 1 MHz and 0.265 at 25 GHz. Sometimes the loss factor is called the dissipation factor. Generally speaking, the wetter a material is, the more lossy it is; the drier it is, the less lossy it is. For example, in a microwave oven a wet piece of paper will get hot as long as it is wet. When the paper dries out, the oven's EM fields will no longer heat it. Much biological tissue is considered to be wet material. Gabriel [1] has measured the permittivity for over 30 tissue types over a frequency range as large as from 10 Hz to 20 GHz.

5. SPECIFIC ABSORPTION RATE

For steady-state sinusoidal fields, the time-averaged rate of energy absorbed per unit volume at a point inside an absorber is given by:

$$P = \sigma|E|^2 = \omega\varepsilon_o\varepsilon''|E|^2 \quad W/m^3,$$

where |E| is the root-mean-square (rms) magnitude of the E-field vector at that point inside the material. To find the total rate of energy absorbed by an object, the value of P must be calculated at each point inside the body and summed (integrated) over the entire volume of the body.

In dosimetry, the transfer of energy from electric and magnetic fields to dipoles and charged particles in an absorber is described in terms of the specific absorption rate. "Specific" refers to the normalization to mass; "absorption", the absorption of energy; and "rate," the time rate of change of the energy absorbed. SAR is defined, at a point in the absorber, as the time rate of change of energy transferred to an infinitesimal volume at that point, divided by the mass of the infinitesimal volume.

$$SAR = P/\rho_m = \sigma|E|^2/\rho_m = \omega\varepsilon_o\varepsilon''|E|^2/\rho_m \quad W/kg,$$

where ρ_m is the mass density (kg/m^3) of the object at that point. If the E-field and the conductivity are known at a point inside the object, the SAR at that point can easily be found; conversely, if the SAR and conductivity at a point in the object are known, the E-field at that point can be calculated. This is called the local SAR or SAR distribution to distinguish it from the whole-body average SAR. The whole-body average SAR is defined as the time rate of change of the total energy transferred to the absorber, divided by the total mass of the body. In practice, the term "whole-body average SAR" is often shortened to just "average SAR."

6. CALCULATION METHODS

In principle, the internal fields in any object irradiated by EM fields can be calculated by solving Maxwell's equations. In the past, this has been very difficult and could be done only for a few very special cases (idealized models, such as planar slabs, spheres, infinitely long cylinders, spheroids, or ellipsoids). Because of the mathematical complexities involved in calculating SAR, a combination of techniques was used to obtain SAR for various models as functions of frequency. Each of these techniques provided information over a limited range of parameters. Combining the information thus obtained gave a reasonably good description of SAR as a function of frequency over a wide range of frequencies for a number of useful models.

The theoretical techniques used to calculate the SAR in models of humans and animals can be divided into three basic approaches, based on the degree of complexity of the model's shape. One-dimensional models are the simplest and are particularly useful at higher frequencies where body curvature can be neglected. Such models, however, cannot predict body resonance, which occurs in models of finite sizes. Two-dimensional models are basically single- or multi-layered infinite cylindrical geometries suitable to simulate limbs, thighs, or arms. Three-dimensional models include both idealized shapes (such as spheres, spheroids, and ellipsoids) and block models. Although the latter models are the most complicated and can be solved only numerically, they give the best estimates of the average SAR, the resonance frequency, and the SAR distribution.

Although planar models do not represent humans well, analyses of these models have provided important qualitative understanding of energy-absorption characteristics. When a planewave is incident on a planar dielectric object, the wave transmitted into the dielectric attenuates as it travels and transfers energy to the dielectric. For very lossy dielectrics, the wave attenuates rapidly. This characteristic is described by skin depth: the depth at which the E- and H-fields have decayed to e^{-1} (0.368) of their value at the surface of the dielectric. Skin depth is also the depth at which the Poynting vector has decayed to e^{-2} (0.135) of its value at the surface. At higher frequencies, the skin depth is very small; thus most of the energy from the fields is absorbed near the surface. As an example, for humans and animals at 2450 MHz the skin depth is about 2 cm; at 10 GHz, it is about 0.4 cm.

Other models--spheres, cylinders, spheroids, ellipsoids, and block models (cubical mathematical cells arranged in a shape like a human or animal body)--have been used to represent the human or animal body for calculating and measuring energy absorbed during plane wave irradiation [2-5]. Especially important for nonplanar objects are the effects of the polarization of the incident fields. The orientations of incident E- and H-fields with respect to the irradiated object have a very strong effect on the strength of fields inside the object. This orientation is defined in terms of the polarization of the incident fields. The incident-field vector--E, H, or k--that is parallel to the long axis of the body defines polarization for objects of revolution (circular symmetry about the long axis). The polarization is called E-polarization if the E-field is parallel to the long axis, H if the H-field is parallel to the long axis, and K if the direction of propagation (k vector) is parallel to the long axis. This definition is illustrated in terms of prolate spheroids in Figure 3.

With the availability of improved computer technology, numerical techniques such as the admittance method [6], the impedance method [7], and the finite-difference time-domain (FD-TD) method [8, 9] have been developed for the solution of EM field interactions with objects having irregular geometries and inhomogeneous dielectric composition.

The admittance and impedance methods are applicable to objects that are small compared to the wavelength of the exposure fields since they are based on dividing the medium into electrical current nodes or meshes. The FD-TD numerical approach is unique because it involves discrete, time-domain computations of differential equations applicable for all size objects within the limits of the speed and memory of the computer used for making the calculation. Imperfect boundary condition information does not degrade the accuracy of these techniques significantly. These and other advantages have made these numerical analysis techniques popular for solving related, non-biological, EM field problems. Recent adaptations of the FD-TD method to complex biological problems have utilized models divided into many thousands of rectangular cells. One problem associated with the implementation of the FD-TD method is the need for a very powerful computer to solve problems involving many thousands of cells. However, currently available workstations now have sufficient power to run many of the models and are approaching that required to run even the largest models such as the full-sized human.

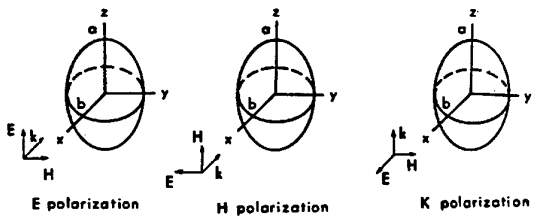

Figure 3. Polarization of the incident field with respect to an irradiated object.

7. MODEL DEVELOPMENT

The computer modeling efforts in our laboratory began in 1994. At that time, accurate anatomical models of the Sprague-Dawley rat, pigmy goat, and rhesus monkey were required in a digital format. After reviewing the literature, we concluded that these models were not available. Detailed description of how the magnetic resonance imaging (MRI) scans of the Sprague-Dawley rat (370 gm), pigmy goat (20 kg), and rhesus monkey (7.1 kg) were acquired appears in an earlier publication [10]. MRI scans, which did not adequately code tissue types, were converted into a format that would allow tissue types to be manually encoded with a color. Each of the selected tissue types was assigned dielectric and conductivity values obtained from Gabriel [11, 12]. These permittivity values are also available on the World Wide Web (WWW) at: www.brooks.af.mil/AFRL/HED/hedr/reports/Title/Title.html. Each tissue was assigned a specific Red-Green-Blue (RGB) color value. RGB 24-bit color rather than 8-bit color was used since some software programs modify colors in the 8-bit images. All pixels on each image were then "painted" manually with the RGB colors representing the appropriate tissue types. MRI atlases [13, 14] and atlases of the rat [15, 16], goat [17], and monkey [18], and skeletons of the rat and monkey were used to identify the location of each tissue type.

Due to the size constraints of the General Electric Signa MRI scanner, the goat's front and back legs were stretched outwards. In order to intubate the monkey during scanning, its neck was tilted backwards. We have developed algorithms that aid in moving and rotating body parts and have successfully rotated the monkey's head from its original tilted back position to that consistent with those of our RF-exposed monkeys. However, these rotations still require extensive manual interaction to ensure correct tissue alignment.

In 1996, we initiated efforts to produce a man dosimetry model. At that time, the following man models were being developed or used. The model described by Sullivan *et al.* [19] was comprised of 1.3 cm cubical cells. The model was developed using cross-sectional diagrams of the human body at spacings 1 inch apart [20]. Furse and Gandhi [21] used a 6 mm resolution man model developed from MRI scans to calculate electrical fields and induced currents. The human was actually scanned at a 3 mm resolution. Due to the immense size of the dataset and the limited computer processing power available to run such a dataset, voxels were combined by taking the dominant tissue in each group to produce the 6 mm cubical cells. Dawson et al. [22] developed a 3.6 mm cubed model of a man to compute electrical fields. This model was developed using a combination of head and torso MRI images obtained from Yale Medical School [23] and MRI and CT images of the arms and legs from the Visible Human project (National Library of Medicine, www.nlm.nih.gov/research/visible/visible_human.html). A 7.2 mm cubed man was produced by applying a 3 x 3 x 3 median filtering algorithm to the above dataset. The National Radiological Protection Board (Chilton, UK) developed a man dosimetry model using MRI scans. The axial scans were approximately 10 mm apart and the data volume was rescaled and interpolated to produce 2-mm cubical voxels [24]. The desire to have a 1 mm cubed voxel model of the entire man led us to use the photographic images of the Visible Human and computer-segmented images (CieMed, a collaboration between National University of Singapore and John Hopkins University) of this dataset to develop a man dosimetry model. Images from the Visible Man project are now used as a standard anatomy reference. This dataset consists of 1878 axial images, each voxel being 1 mm cubed. This resolution permits the inclusion of fine detail, such as small blood vessels and nerves, in the dosimetry model. Structural detail and voxel size are both important factors to consider when selecting a dosimetry model. MRI and anatomical atlases of the human [13, 14, 25, 26], numerous WWW sites pertaining to the Visible Human project, and human cadavers were used to aid in identifying the location of each tissue type. The tissues were color coded in the same manner as described above. The Visible Man was missing a tooth and one testicle, so these were added during the color-coding process. As described above for the monkey's head, the feet of the man are currently being rotated upwards and inwards. This will change each foot from a drop foot position to that required to properly ground the man for plane-wave exposure simulations.

Images were checked for unknown pixel values and for pixel values located in incorrect locations (i.e., heart pixel value located in the leg) using WaveAdvantage™ (Visual Numerics, Inc., Houston, TX) software. To predict electrical fields and SAR values, each TIF image file was converted to an 8-bit binary file and imported into a mathematical model.

8. SAR VERSUS FREQUENCY

SAR is an important quantity in dosimetry both because it gives a measure of the energy absorption that can be manifest as heat, and because it gives a measure of the internal fields which could affect the biological system in ways other than through ordinary heating. The internal fields, and hence the SAR, are a strong function of the incident fields, the frequency, and the properties of the absorber. Since any biological effects would be caused by internal fields, not incident fields, the ability to determine internal fields or SARs in people and experimental animals for a given radiation exposure situation is very important. Without such a determination in both animal models used for experimentation and for humans, we could not meaningfully extrapolate observed biological effects in irradiated animals to similar effects that might occur in irradiated people.

The general dependence of average SAR on frequency is illustrated by Figure 4 for the model of an average-sized man for the three standard polarizations. For E-polarization, the maximum SAR value occurs at about 80 MHz. Therefore, this portion of the curve is refereed to as the resonance condition. From this graph it can be inferred that the resonance frequency is related to the length of the body, and indeed it is. In general, resonance occurs for long, thin, metallic objects at the frequency for which the length of the object is approximately one-half of the free-space wavelength. For biological bodies, resonance occurs at the frequency for which the length of the body is about equal to four-tenths of a wavelength. For frequencies below resonance, the SAR varies approximately as f^2; just beyond the resonance frequency, SAR varies as f^{-1}.

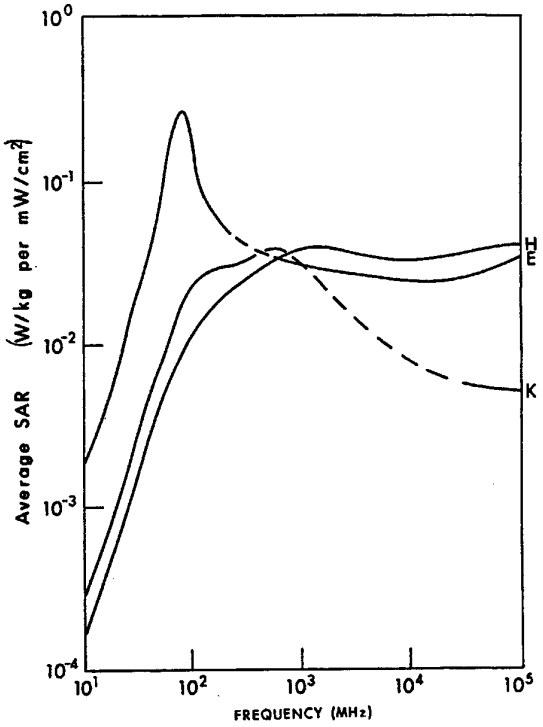

Figure 4. Whole-body average SAR versus frequency for an average man.

Figure 4 also indicates that below the resonance frequency, the SAR is generally higher for E-polarization, intermediate for K, and lowest for H-polarization. Again, this is generally true. These characteristics can be explained by two qualitative principles:

1. The SAR is higher when the incident E-field is more parallel to the body than perpendicular to it.
2. The SAR is higher when the cross section of the body perpendicular to the incident H-field is larger than when it is smaller.

The average SAR is higher for E-polarization because the incident E-field is more parallel to the body than perpendicular to it, and the cross section of the body perpendicular to the incident H-field is relatively larger (see Figure 3). For H-polarization, however, the incident E-field is more perpendicular to the body than parallel to it, and the cross section of the body perpendicular to the incident H-field is relatively smaller. Both conditions contribute to a lower average SAR. The average SAR for K-polarization is intermediate between the other two because the incident E-field is more perpendicular to the body, contributing to a lower SAR. However, the cross section perpendicular to the incident H-field is larger, contributing to a larger SAR.

When a man is standing on a perfectly conducting ground plane, with E-polarization the ground plane has the effect of making the man appear to be electrically about twice as tall. This lowers the resonance frequency to approximately half of that for free space. For a man on such a ground plane, the graph of SAR versus frequency for E-polarization would therefore be similar to the one in Figure 4, but shifted to the left by approximately 40 MHz. Another important qualitative characteristic is that when the incident E-field is mostly parallel to the body, the average SAR goes up if the body is made longer and thinner. The data shown in Figure 4 are used to help set the RF safety standard for permissible exposure levels.

9. MEASUREMENT METHODS

Generally, accepted methods of measurement of SAR include the measurement of the rate of temperature rise within the exposed object or the measurement of the internal E-field strength. The temperature rise may be characterized by a whole-body-averaged (calorimetric) measurement, a point measurement (via a thermometer implanted in the body being exposed), or thermographic camera analysis of bisected phantom models that have been exposed to large RF fields. The internal E-field strength may be measured with an implantable E-field probe.

Average SAR may be measured using calorimetric methods. In the past, such methods have been used predominantly with small animals or animal models [27-30], recently, however, calorimetric twin-well methods have been successfully used to measure SAR in a full-size human model [31]. The heart of the measurement system is the calorimeter device itself. Gradient-layer devices are also commonly used. Gradient-layer calorimeters have a convenient voltage output signal that is proportional to the rate of heat energy flowing out of the device. However, the Dewar-flask method of calorimetry is a relatively simple, straight-forward way of determining the whole-body average SAR of small-bodied animals [32]. The calorimetric technique of determining a whole-body average temperature requires that the cadaver be immersed in a Dewar-flask containing a medium, such as water, at a known temperature; then the temperature of the cadaver, following irradiation, can be determined by noting the final temperature of the cadaver/medium mixture.

Certain temperature probes can be used successfully to make SAR measurements. The minimum requirements are that the temperature sensor and associated leads should be nonperturbing to the EM fields, and the SAR should be large enough to produce a measurable temperature rise during a period of less than about 20 seconds. The first requirement is usually satisfied by using highly resistive material or fiber optics, instead of metal components, for the temperature-sensing element leads [33]. The second requirements entails the measurement of SARs no lower than a few mW/g. This lower limit exists because the resolution of most temperature probes is typically 0.01 to 0.1°C, and the longest practical duration of irradiation that allows reasonably accurate SAR measurement is typically 5 to 30 seconds. Irradiation of

an inert, lossy dielectric object for longer durations causes local "hot spots" to lose their thermal energy to the surrounding area via conduction, diffusion, and convection. In living biological systems, active thermo-regulation also degrades accuracy. It is acceptable to use an ordinary metal-wire temperature probe for RF dosimetry when the probe is not in place during irradiation, but is in place immediately before and after. The use of metallic probes during irradiation is not acceptable. Even when the probe's metallic leads appear to be oriented orthogonal to the incident E-field, the depolarization of fields within finite sized dielectric objects induces errors. The objective is to measure the time rate of irradiation-induced temperature rise ($\Delta T/\Delta t$) at a specific location in tissue or phantom material. The SAR, which is proportional to ($\Delta T/\Delta t$), can then be determined.

A method for rapid evaluation of the distribution of SAR throughout an entire planar surface of a biological object or a model that is composed of heterogeneous dielectric materials is described by Cetas [34], D'Andrea [27], and Johnson [35]. The method involves the use of a thermographic camera for recording the rate of rise of temperature in a plane that bisects an entire model (phantom) or a cadaver of a biological subject under study. The temperature distribution before, and immediately after brief, high-power irradiation, is observed on the precut surface on each half of the bisected model. This is done to prevent cooling by evaporation or flow of the wet synthetic tissue out of its shell (usually composed of synthetic fat or rigid plastic foam). This procedure is also used to measure heating patterns on the surface of subjects exposed to RF fields [36].

Miniature isotropic, implantable E-field probes with high impedance feed lines, which have been commercially available for a number of years [37], have been used to measure SAR distributions in phantom models and in living, anesthetized animals [38, 39]. These probes have much higher sensitivity than thermal probes and are especially suitable for measuring E-fields within simulated or actual biological tissues of moderate to high water content, i.e., brain and muscle. While it is possible to measure SARs of the order of 1 mW/g using sensitive and precise thermal measurements ($\Delta T/\Delta t \approx 0.1°C/30$ s), it is well within the domain of E-field probes to measure SARs as low as 10 μW/g [40]. Recent improvements in decoupling the diodes from the high resistance line have led to the realization of true rms sensors [41]. To reduce the magnitude of the effort of taking data throughout a volume of tissue, data can be taken while the probe is scanned through the volume. Since the E-field probe has a response time of the order of a few milliseconds, continuous line scans of the internal E-field may be dynamically recorded by means of a robot that generates position data as the probe is moved along a path. Extensive data in an object can, thus, be plotted in a relatively short period of time, and the possibility of missing a local peak is reduced.

10. CONCLUSIONS

RF dosimetry is the process of determining the SAR that results from exposure to EM fields. Approximations of whole-body average SAR are calculated by using homogeneous cylindrical and prolate spheroidal models. The reliability of these values has been confirmed with measurements made in the laboratory. Taken together with biological data, experts have been able to establish RF safety standards. Iterative numerical techniques such as FD-TD are being used to solve Maxwell's equations for anatomically accurate block models. These results not only give the average SAR, but the SAR distribution, so that better mechanisms for explaining RF bioeffects can be generated. This improved understanding of dosimetry and RF bioeffects can then be used to evaluate current RF safety standards and, if appropriate, update existing RF safety standards.

11. NOTES

Views presented are those of the authors and do not reflect the official policy or position of the Department of the Air Force, Department of the Navy, Department of Defense, or U.S. Government. Trade names of materials and/or products of commercial or nongovernment organizations are cited as needed for precision. These citations do not constitute official endorsement or approval of the use of such commercial materials and/or products.

12. ACKNOWLEDGMENTS

Research was funded by U.S. Air Force Contracts F33615-90-C-0604 and F41624-96-C-9009, HQ Human Systems Center, Air Force Materiel Command, Brooks AFB, TX, 78235-5000, and Air Force Office of Scientific Research awards (1995, 1996) to Mr. William Hurt.

13. REFERENES

1. Gabriel, C. (June 1996) *Compilation of the Dielectric Properties of Body Tissues at RF and Microwave Frequencies, AL/OE-TR-1996-0037,* Armstrong Laboratory, Brooks Air Force Base, TX 78235.
2. Durney, C.H., Massoudi, H. and Iskander, M.F. (October 1986) *Radiofrequency Radiation Dosimetry Handbook (Fourth Edition), USAFSAM-TR-85-73,* USAF School of Aerospace Medicine, Brooks Air Force Base, TX 78235.
3. IEEE Recommended Practice for the Measurement of Potentially Hazardous Electromagnetic Fields--RF and Microwave, IEEE Std C95.3-1991, Institute of Electrical and Electronics Engineers, Inc., New York, NY (August 21, 1992).
4. Hurt, W.D. (December 4-8, 1988) Specific absorption rate measurement techniques, in: Proceeding of the Twenty-second Midyear Topical Meeting on Instrumentation:139-151, Health Physics Society, San Antonio, Texas.
5. Hurt, W.D. (1997) Dosimetry of radiofrequency (RF) fields, in: *Non-Ionizing Radiation: An Overview of the Physics and Biology,* Health Physics Society 1997 Summer School, K. Hardy, M. Meltz, and R. Glickman, ed., Medical Physics Publishing, Madison, Wisconsin.
6. Armitage, D.W., LeVeen, H.H., and Pethig, R. (1983) Radiofrequency-induced hyperthermia: computer simulation of specific absorption rate distributions using realistic anatomical models, *Phys. Med. Biol.* **28 (1),** 31-42.
7. Orcutt N. and Gandhi, O.P. (1988) A 3-D impedance method to calculate power deposition in biological bodies subjected to time varying magnetic fields, *IEEE Trans. Biomed. Eng.* **BME-35 (8),** 577-583.
8. Kunz K.S. and Luebbers R.J. (1993) *The Finite Difference Time Domain Method for Electromagnetics*, CRC Press, Inc., Boca Raton, Florida.
9. Taflove, A. (1995) *Computational Electrodynamics: The Finite-Difference Time-Domain Method,* Artech House, Inc., Norwood, Massachusetts.
10. Mason, P.A., Walters, T.J., Fanton, J.W., Erwin, D.N., Gao, J.H., Roby, J.W., Kane, J.L., Lott, K.A., Lott, L.E. and Blystone, R.V. (1995) Database created from magnetic resonance images of a Sprague-Dawley rat, rhesus monkey, and pigmy goat, *FASEB J.* **9,** 434-440.
11. Gabriel, C., Gabriel, S., and Courthout, E. (1996) The dielectric properties of biological tissues: 1. Literature survey, *Phys. Med. Biol.* **41**, 2231-2250.
12. Gabriel, S., Lau, R.W., and Gabriel, C. (1996) The dielectric properties of biological tissues: 2. Measurement in the frequency range 10 Hz to 20 GHz, *Phys. Med. Biol.* **41**, 2251-2269.

13. Barrett, C.P., Anderson, L.D., Holder, L.E., and Poliakoff, S.J. (1994) *Primer of Sectional Anatomy with MRI and CT Correlation*, Williams & Wilkins, Baltimore, MD.
14. Mai, J.K., Assheuer, J., and Paxinos, G. (1997) *Atlas of the Human Brain*. Academic Press, London, England.
15. Olds, R.J. and Olds, J.R. (1979) *A Colour Atlas of the Rat - Dissection Guide*. Wolfe Medical Publications, Ltd., Ipswich, England.
16. Popesko, P., Rajtova, V., and Horak, J. (1992) *A Color Atlas of Anatomy of Small Laboratory Animals. Vol. II: Rat, Mouse, and Hamster*. Wolfe Publishing Ltd., London, England.
17. Hopkins, Sr., C.E., Hamm, Jr., T.E., and Leppart, G.L. (1972) *Atlas of Goat Anatomy. Part II. Serial Cross Sections. Edgewood Arsenal Report, 1972-EA-TR-4626*, Edgewood Arsenal, MD.
18. Dalrymple, G.V. (1965) *An Atlas of Cross-Sectional Anatomy of the Macaca Mulatta for use in Radiobiolgical Experiments. USAF School of Aerospace Medicine Reports, USAF-TR-65-32*, Brooks Air Force Base, TX.
19. Sullivan, D., Gandhi, O., and Taflove, A. (1988) Use of the finite difference time-domain method in calculating EM absorption in man models, *IEEE Trans. Biomed Eng.* **BME-35**, 179-185.
20. Eycleshymer, A.C. and Schoemaker, D.M. (1911) *A Cross-Section Anatomy*, Appleton, New York.
21. Furse, C.M. and Gandhi, O.P. (1998) Calculation of electric fields and currents induced in a millimeter-resolution human model at 60 Hz using the FDTD method, *Bioelectromagnetics* 19, 293-299.
22. Dawson, T.W., Cupata, K., and Stuchly, M.A. (1997) Influence of human model resolution on computed currents induced in organs by 60-Hz magnetic fields, *Bioelectromagnetics* **18**, 478-490, 1997.
23. Zubal, I.G., Harrell, C.R., Smith, E.O., Rattner, Z., Gindi, G.R., and Hoffer, P.H. (1994) Computerized three dimensional segmented human anatomy. *Med. Phys. Biol.* **21**, 299-302.
24. Dimbylow, P.J. (1995) The development of realistic voxel phantoms for electromagnetic field dosimetry, in P.J. Dimbylow (ed.), *Voxel Phantom Development, Proceedings of an International Workshop held at the National Radiological Protection Board*, Chilton, UK, 1-7.
25. Netter, F.H. (1989) *Atlas of Human Anatomy*, CIBA-GEIGY Corp., Summit, New Jersey.
26. Spitzer, V.M. and Whitlock, D.G. (1998) *Atlas of the Visible Human Male*, Jones and Bartlett Publishers, Sudbury, MA.
27. D'Andrea, J.A., Emmerson, R.Y., Bailey, C.M., Olsen, R.G., and Gandhi, O.P. (1985) Microwave radiation absorption in the rat: frequency-dependent SAR distribution in body and tail, *Bioelectromagnetics* **6**, 199-206.
28. Olsen, R.G. (June 1-5, 1986) Localized specific absorption rate (SAR) in a full-sized man model near a shipboard monopole antenna: effects on near-field, reradiating structures and of whole-body resonance, *Eighth Annual Meeting—Abstracts of the Bioelectromagnetics Society*, 34.
29. Allen, S.J. and Hurt, W.D. (1979) Calorimetric measurement of microwave energy absorption in mice after simultaneous exposure of 18 animals, *Radio Sci.* **14 (6S)**, 1-4.
30. Blackman, C.F. and Black, J.A. (1977) Measurement of microwave radiation absorbed in biological systems, 2, analysis of Dewar-flask calorimetry, *Radio Sci.* **12**, 9-14.
31. Olsen, R.G. and Griner, T.A. (1989) Outdoor measurements of SAR in a full-size human model exposed to 29.2 MHz near-field irradiation, *Bioelectromagnetics* **10**, 162-171.
32. Padilla, J.M. and Bixby, R.R. (1986) *Using Dewar-flask Calorimetry and Rectal Temperatures to Determine the Specific Absorption Rates of Small Rodents, USAFSAM-TP-86-3*, School of Aerospace Medicine, Brooks Air Force Base, TX 78235.
33. Hochuli, C. (1981) *Procedures for Evaluating Nonperturbing Temperature Probes in Microwave Fields, FDA 81-8143*, Food and Drug Administration, Rockville, MD 20857.
34. Cetas, T. and Conner, W.G. (1978) Practical thermometry with a thermographic camera—calibration, transmission, and emittance measurements, *Rev-Sci Instn.* **49 (2)**, 245-254.
35. Johnson, C.C. and Guy, A.W. (1972) Nonionizing electromagnetic wave effects in biological material and systems. *Proc. IEEE* **60**, 692-718.
36. Walters, T.J., Blick, D.W., Johnson, L.R., Adair, E.R., and Foster, K.R. (submitted) Heating and pain sensation produced in human skin by millimeter waves. *Health Phys.*
37. Cheung, A. (Dec. 1976) Experimental calibration of a miniature electric field probe within simulated muscular tissues, *Selected Papers of the USNC/URSI Annual Meeting, Boulder, CO, October 20-23, 1975, vol. II, DHEW Publication (FDA) 77-8011*, 324-327.
38. Bassen, H.I., Herchenroeder, P., Cheung, A., and Neuder, S.M. (1977) Evaluation of implantable electric field probes within finite simulated tissues, *Radio Sci.* **12 (6S)**, 15-23.
39. Stuchly, S. (1987) *Specific Absorption Rate Distribution in a Heterogeneous Model of the Human Body at Radiofrequencies, Report PB87-201356*, Ottawa University, Ontario.
40. Balzano, Q., Garay, O., and Manning, Jr., T.J. (1995) Electromagnetic energy exposure of simulated users of portable cellular telephones, *IEEE Trans. Veh. Tech.* **VT-44 (3)**, 390-403.
41. Pokovic, K., Schmid, T., and Koves, N. (June 23-25 1996) ***E***-field probes with improved isotropy in brain simulating liquids, in: *ELMAR Proceedings*, Zadar, Croatia.

A Submodel for Combat Casualty Assessment of Ocular Injury from Lasers

R. E. Miller, II
B. Carver
Veridian
9601 McAllister Freeway
Suite 1165
San Antonio, TX 78216-4605, USA

1. SUMMARY

In an effort to standardize casualty assessments for DoD, the Joint Service Technical Coordination Group/Munitions Effectiveness and Aircraft Survivability Crew Casualty Working Group (CCWG) developed the Operational Requirements based Casualty Assessment (ORCA) model. The ORCA system consists of a functioning software code that will predict the effects of insult-to-injury-to-operational casualty from various types of trauma at specific times post-insult.

As an integral part of ORCA, this submodel was designed to predict the probability for ocular injury from insult on the battlefield by directed energy, i.e., lasers, and assess casualty status. A unique, integrated, and multifaceted approach was devised to compute the effects of laser insult on the elemental capabilities of vision, or visual taxons. The methodology is based on using equations and algorithms to calculate a functional index of ocular damage, utilizing this index to quantify the effects of combat injuries on the visual taxons, and applying the resultant values to a notional scale to determine the potential for combat casualty in terms of mission completion. This submodel also provides a capability to differentiate operational casualties from medical casualties in a format that is compatible with the ORCA system.

2. INTRODUCTION

The Joint Service Technical Coordination Group/Munitions Effectiveness and Aircraft Survivability Crew Casualty Working Group (CCWG) is working to standardize casualty assessments for DoD. Accordingly, the CCWG developed a combined threats casualties model called the Operational Requirements-based Casualty Assessment (ORCA) software system. The ORCA model consists of a functioning code that can predict the effects of insult-to-injury-to-operational casualty from various types of trauma at specific times post-insult, e.g., immediate (0 sec), 30 sec, 5 min, 1 hour, 24 hours, and 72 hours.

This submodel is the ocular component for the ORCA model and was designed to predict the potential for eye injuries from insult by directed energy, or lasers. The components of the submodel include: (1) Laser Insult Parameters- type, wavelength, radiant energy density, and insult duration; (2) Ocular Injury Assessment- corneal damage/photokeratitis, flashblindness, and retinal damage; (3) ORCA Body Components- right eye, left eye, right retina, and left retina; (4) Elemental Capability Vectors (visual taxons)- Visual Acuity, Night Vision, Field of View, and Binocular Vision.

Several equations and algorithms were refined to calculate the effects on the visual taxons of injury from various types of laser radiation. A novel approach was employed which is based on computing a functional index to quantify the extent of ocular injury. This is translated into a format compatible with ORCA by using a notional logarithmic scale that relates visual taxon injury to combat casualty status in terms of mission completion as follows:

Scale	Injury	Casualty Status
3	None	Normal (default value)
2	Mild	Can complete mission
1	Moderate	Operational casualty
0	Severe	Medical casualty

For this scale, an operational casualty is defined as one without life threatening injury but where the mission can not be completed, as differentiated from a medical casualty, which is one that requires definitive medical assistance for survival. Thus, a unique and multifaceted submodel was developed to predict, assess, and quantify the effects of laser insult on the four visual taxons and determine individual casualty status.

Papers presented at the RTO HFM Specialists' Meeting on "Models for Aircrew Safety Assessment: Uses, Limitations and Requirements", held in Ohio, USA, 26-28 October 1998, and published in RTO MP-20.

3. BACKGROUND

A laser is a device that emits an intense and narrow beam of light at a specific wavelength. Lasers are classified according to whether they emit radiation in the visible, ultraviolet (UV), or infrared (IR) spectral ranges, and as continuous wave (CW) or in a short burst or bursts (pulsed). The number of pulses that a pulsed laser emits within a given duration is called the pulse repetition frequency (PRF). Some pulsed lasers can emit all of their energy compressed into time periods as brief as nanoseconds or less.

Because lasers have very little beam divergence, most of their radiant power can be directed over very small areas even at great distances. The radiant power output of a laser at a given instant is defined, as for any light source, in watts. A measure of the radiant power at a position in space is called irradiance, which is specified in units of Joules (1 J = 1 watt/sec). While a measure of the radiant energy, at a position in space, is called radiant exposure, which is specified in units of Joules per sq. cm. The radiant exposure of a laser is equal to its irradiance multiplied by the duration of time (seconds) that the irradiance is present at the position in question, e.g., the cornea.

The rapid growth of laser science and technology has resulted in the increased use of lasers by the military. Modern warriors are not only at risk from exposure to enemy lasers but also from accidental exposures from friendly forces. Many lasers have sufficient energy to produce eye injuries at distances of a kilometer or more. The potential for ocular injury is intensified by the fact that laser radiation is gathered through a 2-7 mm pupil, depending upon the ambient luminance, and sharply focused by the optical system of the eye (cornea and crystalline lens). This can increase the retinal irradiance by a factor of 100,000 over that which is incident at the cornea. Therefore, even a moderately powerful laser can produce significant ocular injury because of the efficient focusing system of the eye.

In general, the cornea and lens absorb all UV radiation, the retina absorbs visible and near IR energy, and far IR radiation is absorbed by the water molecules in the cornea. Eye damage is proportional to the amount of laser energy the tissue absorbs which is dependent upon the wavelength, exposure duration, pulse width, PRF, and irradiance. A laser is more likely to strike both eyes, unless one eye is inadvertently protected by closure or being shielded by the nose, because the diameter of the laser beam at most operationally encountered distances is wider than the head.

To be compatible with the ORCA system, the submodel originates when laser radiation strikes the surface of the cornea. Accordingly, it includes the effects of intraocular light scatter but excludes all extraocular effects. Omitted in the submodel are the following: visual target information; use of life support equipment including night vision goggles (NVGs), chemical defense gear, or laser eye protection devices; optical scatter effects from the atmosphere or aircraft/vehicle windscreen; wearing of optical aides including binoculars, visors, spectacles, contact lenses, etc.

The methodology was simplified by employing standard constants where appropriate. Time durations for laser insult were defined as $\leq$ 10 sec for UV and IR lasers, but 0.25 sec or less for visible lasers (see 4.1.6). Also, an ocular pupil diameter constant of 7 mm was used to simulate nighttime on the battlefield and worse-case scenarios. In addition, only laser strikes that occur from directly in front of the subject, i.e., on the visual axis, were considered. Including off-axis laser insults, which affect the peripheral retina, would have induced a high degree of complexity in assessing ocular physiological effects that are essentially secondary elements of visual function. However, it is recommended that future versions of this submodel be expanded to cover a larger range of parameters including off-axis laser insults.

4. SUBMODEL METHODOLOGY

The Operational Requirements-based Casualty Assessment computer program is a DoD accreditable model that provides a comprehensive personnel vulnerability assessment of the human body based on selected insults. The taxonomy for this submodel, which is the element of ORCA that covers ocular insult from directed energy, contains the following components: Laser Insult Parameters; Injury Assessments; ORCA Body Components; and Elemental Capability Vectors. Of primary importance are the four Elemental Capability Vectors for vision, or visual taxons, which were previously defined in Reference 1 as (1) Visual Acuity, (2) Night Vision, (3) Field of View, and (4) Binocular Vision. Each component will be described in more detail in the following sections.

4.1 LASER INSULT PARAMETERS

4.1.1 Type of Laser
The type of laser is either CW or pulsed. A pulsed laser emits bursts of energy in a repeating cycle. If a pulsed laser is selected, then values for both the pulse repetition frequency (PRF) and the pulse width must also be entered (see 4.1.3 and 4.1.4).

4.1.2 Wavelength
The ocular tissue affected and the severity of the eye injury is dependent upon the spectral range of the laser radiation. In this submodel any value from 0.200 μm to 1.400 μm can be selected for the laser wavelength. However, the lasers are automatically grouped into three spectral ranges: ultraviolet (UV)- 0.200 to 0.399 μm; visible- 0.400 to 0.700 μm; near infrared (IR)- 0.701 to 1.400 μm. The use of far IR lasers was excluded due to their potential limitations in many military environments. This is because radiation above 1.400 μm is absorbed by water molecules and does not readily penetrate through smoke, haze, or clouds (Ref 2).

4.1.3 Pulse Repetition Frequency (PRF)
Only required if the laser type is pulsed, it is a value from 1 to 10^6 in cycles per second (Hertz).

4.1.4 Pulse Width
Only required if the laser type is pulsed, the value is selected from a range of 10^{-9} to 10 seconds. The pulse width is always less than 1/PRF.

4.1.5 Laser Radiant Exposure
Radiant exposure is defined as the radiant energy of the laser at the surface of the cornea. Entered as a finite value in Joules/cm^2 from within a range of arbitrary choices. Note that this submodel requires specifying the laser radiant energy at the cornea and not the actual power output of the laser. In order to be compatible with the ORCA system architecture, all external optical effects were excluded, e.g., attenuation of the laser intensity which occurs as the beam passes through the atmosphere or through any intermediate material such as aircraft canopies, visors, eyeglasses, or contact lenses. Accordingly, the user should be cautioned not to confuse this parameter with the rated power output of the laser.

4.1.6 Insult Duration
The insult duration is the total time that the laser radiation strikes the cornea and is a value that ranges from 10^{-9} to 10 seconds. If the wavelength of the laser is in the visible spectral range, the duration is always less than or equal to a constant of 0.25 seconds. This is the standard constant that corresponds to the ocular blink reflex and/or physiological aversion response to intensely bright light. For UV or near IR lasers, the maximum duration at the cornea is equal to 10 seconds which is a time constant that represents worse-case exposures from invisible lasers (Ref 3).

4.1.7 Eyes Affected
ORCA Body Components (OBCs) include left eye, right eye, left retina, and right retina. The OBCs for left and right eyes are used to model all-or-none (on or off) types of responses to ocular injuries. However, the OBCs for left and right retinas are used to model retinal injuries using a gradual scale of damage. This approach provides greater accuracy and precision in quantifying multiple effects of eye injuries.

4.2 OCULAR INJURY ASSESSMENT
Three possible ocular injuries are assessed in this submodel: (1) corneal damage/photokeratitis; (2) flashblindness; (3) retinal damage. Other potential laser induced effects such as glare or injury to the ocular crystalline lens were appropriately excluded from consideration. This is because glare is not an injury, although it can be a significant problem for mission performance; and, laser radiation can damage the crystalline lens, e.g., induce cataracts, but the effects are long term and delayed far beyond the 72 hour time frame in the ORCA model.

Specific guidelines for when to use each of the three injury assessments is as follows:

- For a UV laser, use only the assessment for corneal damage/photokeratitis;
- For a visible laser, both the flashblindness and retinal damage assessments may apply dependent upon the total radiant exposure;
- For a near IR laser, use only the assessment for retinal damage.

4.2.1 Corneal Damage/Photokeratitis
Ultraviolet lasers may cause significant corneal injury because the cornea readily absorbs UV radiation. Absorption by the cornea is total for UV radiation below 0.295 μm and partial for UV radiation from 0.295 μm to 0.399 μm. All UV radiation not absorbed by the cornea is absorbed

by the crystalline lens which prevents any UV from reaching the retina. Corneal damage can also occur from exposure to far IR lasers because the water molecules in the corneal stroma have strong absorption bands in the far IR. Far IR lasers, however, were not included in this submodel as discussed in section 4.1.2.

The injury to the cornea induced by excessive UV exposure is called photokeratitis. Photokeratitis is often referred to as snow blindness because it commonly occurs in skiers who do not wear appropriate eye protection from UV radiation reflected by snow. Fresh snow reflects 88% of UV radiation as compared to 1% reflected from grass or soil and 20% reflected from water. Mild corneal injuries caused by laser induced photokeratitis include edema with resultant clouding and haze that often degrades vision. Moderate burns of the cornea may cause it to become white and opaque. Severe burns can even cause a rupture of the cornea and an iritis with consequent pupillary miosis.

The signs and symptoms of injury from a UV laser are not immediate but only occur after a finite time period. The length of time from initial insult to the manifestation of significant swelling of the cornea, and the total time that vision is degraded, are both dependent upon the total amount of energy absorbed by the cornea. Values for the time until manifestation of corneal injury and the duration of the injury effect were based on clinical and aeromedical experience (Ref 2). The values for UV laser radiation capable of inducing photokeratitis were extrapolated from Maximum Permissible Exposure (MPE)[1] values found in the American National Standards Institute (ANSI) tables (Ref 4), and ED50[2] values found in the Integrated Laser Personnel Effects Model (ILPEM) at Brooks AFB TX (Ref 5). In this submodel, ten times the MPE is used as a first order approximation of the ED50 value.

Corneal damage from UV lasers was arbitrarily divided into two broad categories that correlate logarithmically with the MPE as follows:

Category 1- if the UV laser radiant exposure is $\geq$ 10 x MPE (32 J/cm^2) but < 100 x MPE (320 J/cm^2), then time until onset of photokeritis is 4 hours and the duration of the effect is 24 hours;
Category 2- if the UV laser radiant exposure is $\geq$ 320 J/cm^2, then time until onset of corneal clouding and haze is 2 hours and the duration of the effect is $\geq$ 72 hours.

An illustration of the scenario for corneal damage, including injury onset and duration times for the 2 categories, is provided in Figure 1.

4.2.2 Flashblindness

Flashblindness describes the temporary blindness induced by the photochemical bleaching of the rod and cone photoreceptors in the retina by extremely bright light. It is a phenomena of ocular light and dark adaptation; and, it is scientifically defined as an increase in visual threshold for detecting luminance differences after retinal exposure to a high luminance light source.

When triggered by laser insult, flashblindness initially renders the eyes completely blind for a brief period of time, usually a few seconds or less. An afterimage subsequently forms which creates a transient blind spot (scotoma) on the retina. This is a relative scotoma which means that it is a blind spot where the visual sensitivity, although considerably depressed, is not totally absent. The size of the scotoma created by the afterimage is equivalent to the corresponding visual field defect, as measured in degrees of arc, and is a function of the total energy (brightness and duration) of the laser insult. The time delay for the scotoma to disappear and vision to return to normal is also dependent on the total energy of the insult.

The criteria in this submodel for laser insult to induce flashblindness is as follows:

- the wavelength of the laser must be in the visible spectral range (0.400 to 0.700 μm);
- the laser radiant energy at the cornea must be greater than 50% of the ED50 value (5 times the MPE value) for producing a visible lesion on the retina.

If these conditions are met, flashblindness will be induced and the OBC eyes are set to off for the immediate time frame (0 seconds post insult). Subsequently, the OBC eyes are set to on and the afterimage phase of flashblindness, with the presence of a relative scotoma, then applies to the

[1] MPE is the amount of laser radiation to which a person may be safely exposed without hazard.
[2] ED50 is the amount of laser energy that has a 50% probability of producing a visible lesion.

OBC retinas. Normally, flashblindness is bilateral unless one eye is inadvertently protected.
The effects of flashblindness and the diameter of the scotoma can be calculated by using the data provided in Tables 1and 2. First, determine the ED50 estimate from Table 1 for the specified laser insult, assume that it is a CW laser[3], and divide by 2. Second, divide this value into the effective laser radiant energy at the cornea to obtain the flashblindness index. Third, compare the index to the values in Table 2 to determine the size of the scotoma in degrees. This value for the scotoma size applies to the OBC retinas and remains constant until recovery. Finally, to calculate the length of the recovery time (RT) from flashblindness (FB), use the formula:

$$\mathbf{RT = (0.012) \times (FB\ Index)^2}$$

At the end of the recovery time, the temporary damage due to flashblindness ceases and the OBC retinas are reset to normal. However, the retinal damage assessment may now apply if the insult and injury was severe enough to produce a retinal lesion. A visible retinal lesion creates an absolute scotoma, which is a permanent blind spot devoid of light perception. The format for calculating retinal damage will be presented in the next section.

The effects of flashblindness prevail for a finite time period after which retina damage effects, if any, apply. A schematic representation of the scenario for flashblindness, including subsequent retinal damage, is shown in Figure 2. Also, a sample calculation of flashblindness, with recovery time and follow-on retinal damage, can be found in Example 1 of the Annex.

4.2.3 Retinal Damage

Retinal damage is defined as a laser insult of sufficient intensity to cause a visible lesion to develop on the retina. Damage to the retina is characterized by the size of the retinal lesion, and the corresponding absolute scotoma, which creates a permanent blind spot because retinal tissue does not regenerate.

Estimating the size of the lesion in degrees of visual angle is a complex process that has been greatly simplified in this submodel. Essentially, the wavelength and duration of the laser radiant energy are correlated to ten times the ANSI Maximum Permissible Exposure value, as found in Table 1, which is used interchangeably as an estimate of the ED50 value. The actual laser radiant energy at the cornea is divided by the ED50 estimate to calculate the retinal damage index value which is used to determine the retinal lesion/scotoma size from Table 2. The data in Table 2 was extrapolated from the ILPEM model at the Air Force Research Laboratory, Brooks AFB TX (Ref 5). It incorporates the McLin Modification for enhancing the accuracy of the diameter of the scotoma size and resultant visual acuity values.

For retina damage to occur in this submodel, the following conditions apply:

- the laser wavelength must be in the visible or near IR spectral range (0.400-1.400 μm);
- the laser radiant energy at the cornea must be greater than the ED50 estimate in Table 1.

To calculate retinal damage from a CW laser, find the ED50 estimate in Table 1 for the appropriate laser wavelength and time duration. Then, compute the retinal damage index value by dividing the actual laser radiant energy striking the cornea by the estimated ED50 and round off to the nearest whole integer. Next, locate in Table 2 this ED50 index and read the retinal damage scotoma size. If the ED50 index for retina damage is greater than 50, the OBC eye(s) should be set to off and considered to be so severely injured as to not be functional.

To determine the ED50 estimate for a pulsed laser, select the smaller of: (1) the ED50 estimate based on a single pulse with a correction factor of $n^{-1/4}$ where n is the number of pulses; or (2) the ED50 estimate as if it were a CW laser. The specific procedure is to calculate the ED50 for a single pulse, multiply it by the correction factor of $n^{-1/4}$, and multiply this value by the total number of pulses to get the ED50 estimate for method 1. Then, compare this value to the one obtained by method 2, which presumes a CW laser, and select the smaller of the two estimates. Next, determine the retinal damage index value by dividing the actual laser radiant energy by this estimated ED50 and round off to the nearest whole integer. Finally, locate the index in Table 2 and read the value for retinal damage. Sample calculations of retinal

[3] For the assessment of flashblindness, pulsed lasers will be treated the same as CW lasers.

damage from both CW and pulsed lasers are provided in examples 2-4 of the Annex.

4.3 ORCA BODY COMPONENTS (OBCs)

In the ORCA model there are 470 numbered OBCs for the whole body of which four are ocular: left eye; right eye; left retina; and right retina. For this submodel, the left and right OBC eyes have defined vulnerability categories of all-or-none, i.e., either on or off. The left and right OBC retinas, however, have vulnerability categories which quantify the scotoma and/or retina lesion size in terms of a graded scale from 0 (no damage) to 8.00 degrees. By definition, the OBC eye(s) must be set to on before any damage effects can be computed in the corresponding OBC retina(s). If the OBC eye(s) are set to off, then the OBC retina(s) must also be off.

4.4 ELEMENTAL CAPABILITY VECTORS

There are 24 Elemental Capability Vectors (taxons) listed for the human body in the ORCA model. Four of these taxons are ocular and, accordingly, are called visual taxons. The visual taxons are defined as Visual Acuity (includes Color Vision), Night Vision, Field of View, and Binocular Vision (includes Ocular Motility). Detailed descriptions of the visual taxons and their injury metrics can be found in Reference 1. The methodology used to quantify laser injury effects for each of the following visual taxons, except field of view, is to apply the notional scale listed in Section 2 to the calculated values from Tables 1and 2.

4.4.1 Visual Acuity (includes Color Vision)

If both OBC eyes, left and right, are set to off, then visual acuity should be set to 0 on the injury scale in Table 3. If either or both OBC eyes are set to on, then the impact on visual acuity is determined by the damage to the OBC retina or retinas. The injury effects for scotoma size and resultant visual acuity are calculated using Tables 1 and 2 and then inserted into Table 3 to predict the relative scale of casualty. The criteria used to derive the scale values in Table 3 were based on typical clinical standards for visual acuity (Ref 6). Visual acuity of 20/40 is universally regarded as the minimum requirement for driving; and, a best corrected visual acuity of 20/200 (or less than 20/100) is considered to be legal blindness.

It should be noted that color vision was included as part of the taxon for visual acuity because the effects of a central scotoma are relatively similar for both color vision and visual acuity. In the future, however, color vision may need to be considered as a separate visual taxon because of its increased importance in multicolor displays and the night vision systems used in new military weapons.

4.4.2 Night Vision

If both OBC eyes are set to off, then night vision should be set to 0 on the injury scale in Table 4. If both OBC eyes are set to on, the impact on night vision is determined by the retinal damage values calculated from Tables 1 and 2 and plugged into Table 4. The level of injury found in Table 4, however, may require modification. If only one OBC eye is injured but the other is set to on, the scale value from Table 4 is modified by multiplying it by a factor of 1.41. If one OBC eye is set to off but the other is injured, the scale value in Table 4 is modified by dividing it by a factor of 1.41. This correction factor is necessary because the eyes function essentially as 2 sensors for purposes of visual detection. Accordingly, two eyes together are better detectors at night than one eye alone by the factor of the square root of 2 which is equal to 1.41. Thus, the constant of 1.41 is used to modify the scale value for night vision as appropriate. The criteria used to derive the scale values in Table 4 are essentially based upon aeromedical considerations for mesopic, scotopic, and night visual function found in Reference 7.

4.4.3 Field of View (FOV)

If both OBC eyes are set to off, then FOV as determined from the injury scale in Table 5 is equal to 0. If only one OBC eye is set to off, the FOV per Table 5 equals 1. However, if both OBC eyes are set to on, then FOV is based upon the extent of peripheral retinal damage as specified in Table 5. It should be noted that the parameters for FOV loss are <u>not</u> based upon induced scotoma size but on total FOV size in degrees. The values in table 5 are unrelated to scotoma size and were derived from standard tables for visual efficiency and industrial health (Ref 6).

4.4.4 Binocular Vision (includes Ocular Motility)

Binocular vision is dependent upon the interaction of both eyes and, in this submodel, stereopsis is considered to be the primary component. When either or both OBC eyes are set to off, then binocular vision equals 0 as listed in the injury scale in Table 6. If both OBC eyes are set to on, then binocular vision is determined by the extent of

the scotoma effect on stereopsis in the more damaged retina according to the scale in Table 6. The criteria used to derive the scale values in Table 6 were based on military medical standards and basic aeromedical requirements for stereopsis and binocular vision (Ref 7). It should be noted that the visual taxon for binocular vision is inherently more affected by mechanical trauma to the eye muscles and orbital area than to insult from directed energy.

5. ACKNOWLEDGEMENTS

The authors would like to express their sincere gratitude to the Executive Committee of the CCWG. This submodel represents completion of Phase II of contractual work conducted in support of the CCWG and their efforts to model the casualty effects of various types of trauma for the DoD. Phase I was previously documented in Reference 1. Deep appreciation is also extended to the personnel of the Optical Radiation Division, Armstrong Laboratory, Brooks AFB TX (now part of the Air Force Research Laboratory) for providing access to data in the Integrated Laser Personnel Effects Model (Ref 5).

6. REFERENCES

1. Miller, R.E. II, Barsalou, N., and Cartledge, R.M. "Review of the Elemental Capability of Vision: Primary Visual Taxons", AL/OE-TR-1996-0103, Aug 1996.

2. Green, R.P. Jr., Cartledge, R.M.,Cheney, F.E., and Menendez, A.R. "Medical Management of Combat Laser Eye Injuries", USAFSAM-TR-88-21, Oct 1988.

3. Military Handbook for Laser Range Safety, MIL-HDBK-828-15, Apr 1993.

4. American National Standard for the Safe Use of Lasers, ANSI Z136.1, American National Standards Institute Inc., New York, NY, 1993.

5. Integrated Laser Personnel Effects Model (ILPEM), Optical Radiation Division, Armstrong Laboratory, Brooks AFB Texas, 1997.

6. Physicians Desk Reference for Ophthalmology, 24th Edition, Medical Economics Co., Montvale, New Jersey, 1996.

7. Miller, R.E. II and Tredici, T.J., "Night Vision Manual for the Flight Surgeon", Armstrong Laboratory Special Report, AL-SR-1992-0002, Brooks AFB TX, Aug 1992.

Figures

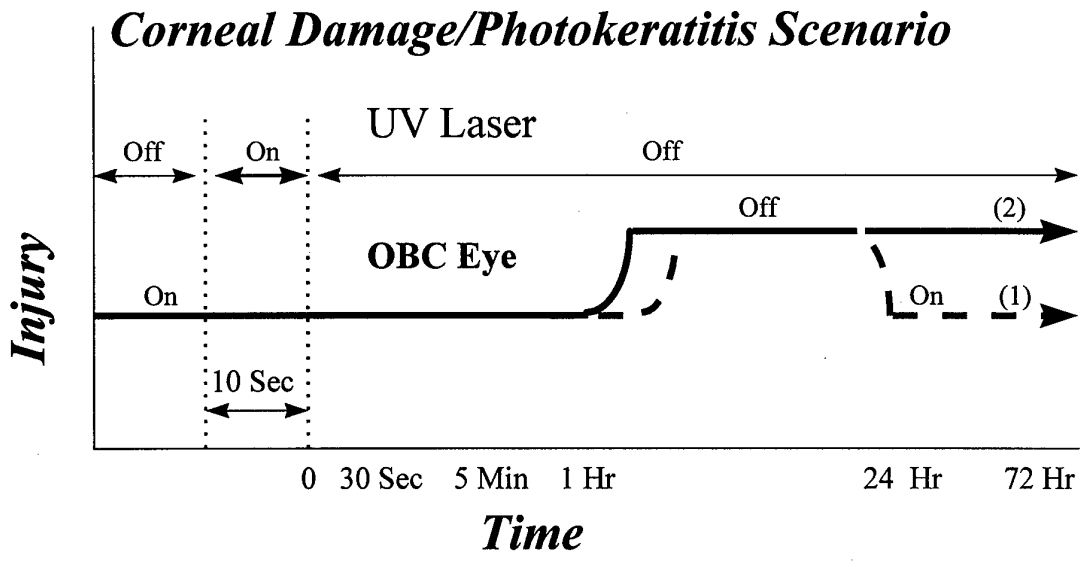

Figure 1. Corneal damage/photokeratitis scenario for category 1 and 2 injuries (notional time scale).

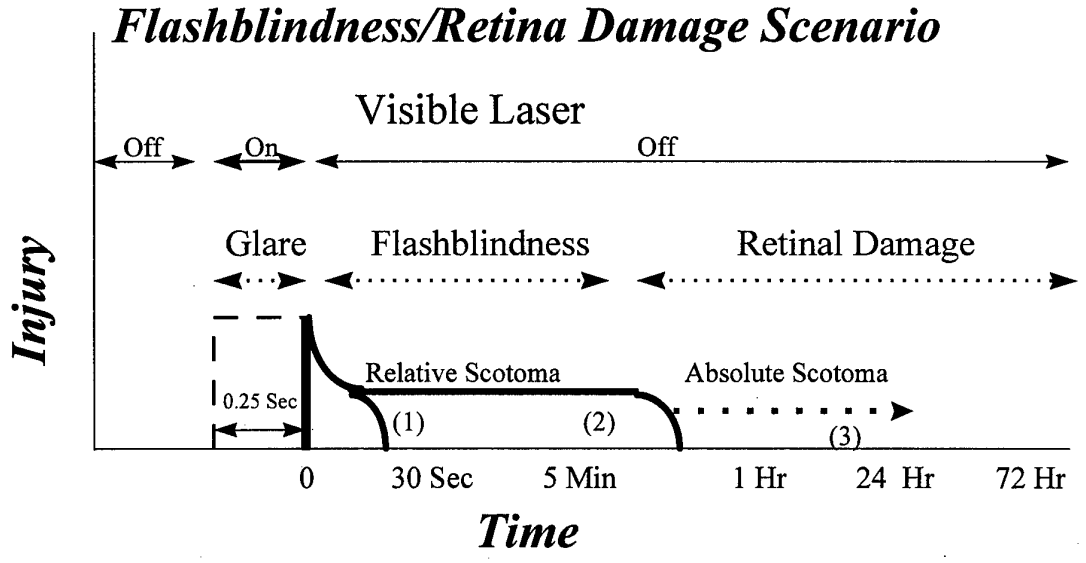

Figure 2. Scenario for flashblindness (FB) and subsequent retina damage for the following conditions: (1) mild FB; (2) moderate FB with relative scotoma; (3) severe FB with retinal damage and absolute scotoma (notional time scale).

Tables

Table 1: ED50 Estimate for flashblindness and retinal damage based on laser wavelength and duration of exposure at the surface of the cornea.

Wavelength (um)	Duration (seconds)	ED50 Estimate (Joules/sq.cm)
0.400 to 0.700	10^{-9} to 18 $x10^{-6}$	5 Ca $x10^{-6}$
0.400 to 0.700	18 $x10^{-6}$ to 10	1.8 Ca $t^{3/4}$ $x10^{-2}$
0.701 to 1.400	10^{-9} to 18 $x10^{-6}$	5 Ca $x10^{-6}$
0.701 to 1.400	1 $x10^{-6}$ to 10	1.8 Ca $t^{3/4}$ $x10^{-2}$

Note: $C_a = 1.0$ when the wavelength is 0.400 to 0.700μm; $C_a = 10^{\{2(\text{wavelength}-0.700)\}}$ when the wavelength is 0.701 to 1.400 μm; and t = duration time in seconds.

Table 2: ED50 Index for flashblindness and/or retinal damage with resultant scotoma size in degrees and visual acuity in denominator of 20/20.

ED50 Index	Scotoma size	20/Acuity	ED50 Index	Scotoma size	20/Acuity
1	0.20	22.50	26	5.40	87.50
2	0.60	27.50	27	5.54	89.25
3	1.04	33.00	28	5.68	91.00
4	1.50	38.75	29	5.82	92.75
5	1.84	43.00	30	5.94	94.25
6	2.12	46.50	31	6.06	95.75
7	2.38	49.75	32	6.20	97.50
8	2.56	52.00	33	6.30	98.75
9	2.80	55.00	34	6.40	100.00
10	2.94	56.75	35	6.50	101.25
11	3.14	59.25	36	6.60	102.50
12	3.32	61.50	37	6.70	103.75
13	3.46	63.25	38	6.80	105.00
14	3.64	65.50	39	6.90	106.25
15	3.80	67.50	40	7.00	107.50
16	4.00	70.00	41	7.10	108.75
17	4.14	71.75	42	7.20	110.00
18	4.28	73.50	43	7.30	111.25
19	4.42	75.25	44	7.40	112.50
20	4.56	77.00	45	7.50	113.75
21	4.70	78.75	46	7.60	115.00
22	4.84	80.50	47	7.70	116.25
23	4.98	82.25	48	7.80	117.50
24	5.12	84.00	49	7.90	118.75
25	5.26	85.75	50	8.00	120.00

Note: The McLin Modification was incorporated into this table to provide a correction factor for the inherent difference between visible retinal lesion size, visual field scotoma size, and resultant visual acuity.

Tables (Continued)

Table 3: Scale for resultant visual acuity from flashblindness or retina damage.

Injury Metric for Visual Acuity	Scale	Retina Damage/Scotoma Size (Degrees)
20/20 or better in each eye	3	0 in both eyes
20/20-20/40 in better eye; ≤ 20/25 in worse eye	2	≥ 0 to ≤ 1.5 in better eye; ≥ 0.2 in worse eye
20/50-20/100 in better eye; ≤ 20/50 in worse eye	1	> 1.5 to ≤ 6.4 in better eye; ≥ 1.5 in worse eye
worse than 20/100 in each eye	0	> 6.4 in better eye

Table 4: Scale for resultant night vision from flashblindness or retina damage.

Injury Metric for Night Vision	Scale	Retina Damage/Scotoma Size (Degrees)
Normal mesopic/scotopic sensitivity	3	≤ 1
Mild loss	2	>1 to < 3
Moderate loss	1	≥ 3 to ≤ 8
Severe loss	0	> 8

Table 5: Scale for resultant field of view from ocular injury.

Injury Metric for Field of View	Scale	FOV (Degrees)
Full binocular FOV	3	≥180
Mild reduction	2	<180 to ≥140
Moderate reduction	1	<140 to >20
Severe reduction	0	≤20

Table 6: Scale for resultant binocular vision from flashblindness or retina damage.

Injury Metric for Binocular Vision	Scale	Retina Damage/Scotoma Size (Degrees)
Normal BV and stereopsis	3	0
Mild reduction	2	<2.0
Moderate reduction	1	≥2.0 to ≤8.0
Severe reduction	0	>8.0

Annex

Sample Calculations

Example 1. Calculate the flashblindness effect from a 0.488 μm CW Argon laser with a 7.50×10^{-5} Joules/cm^2 insult for 10^{-7} seconds to both eyes as follows:

1. Determine the radiant energy at the cornea: 7.5×10^{-5} Joules/cm^2.
2. Find the ED50 estimate from **Table 1** = 5.0×10^{-6} Joules/cm^2.
3. Compute the flashblindness index by dividing the energy at the cornea, by ½ the ED50 estimate = $7.5 \times 10^{-5} / 1/2 \times (5.0 \times 10^{-6}) = 30$.
4. Because the index is > 1.0, same as the input being more than 50% of the ED50 estimate, flashblindness occurs. Accordingly, the OBC eyes are set to off for the immediate time post insult (0 sec), but subsequently they are reset to on at 30 sec post-insult time.
5. Plug the index into**Table 2** to determine that the flashblindness scotoma size equals 5.94 degrees and use this value for both OBC retinas.
6. Calculate recovery time (4.2.2) from the flashblindness: RT= $0.012 \times 30^2 = 10.8$ minutes.
7. The effects of flashblindness disappear after 10.8 minutes, however, the retina damage assessment may now apply. To determine if there is any follow on retina damage, compute the retina damage assessment. In this example, the retina damage index is found to be 15 which equates to a retinal lesion/scotoma of 3.8 degrees for each eye.

Example 2. The retinal damage from a 0.6328 μm CW Helium-Neon laser with a 1.210×10^{-3} Joules/cm^2 insult for 8×10^{-4} seconds to both eyes is calculated as follows:

1. Determine the radiant energy at the cornea = 1.210×10^{-3} Joules/cm^2.
2. Find the ED50 estimate from **Table 1** = $1.8 \times 10^{-2}(.0008)^{3/4} = 8.6 \times 10^{-5}$ Joules/cm^2.
3. Divide the radiant energy by the ED50 estimate to find the index = $1.21 \times 10^{-3} / 8.6 \times 10^{-5} = 14$.
4. Plug the index value into **Table 2** and read that the scotoma size is 3.64 degrees in each eye.

Example 3. The retinal damage from a 0.6943 μm, 100 Hz pulsed Ruby laser with a pulse width of 10^{-3} seconds and a 4.2×10^{-2} Joules/cm^2 insult for 0.25 seconds to both eyes is calculated as follows:

1. Determine the ED50 for a single pulse: $1.8(10^{-3})^{3/4} \times 10^{-2} = 1.01 \times 10^{-4}$ Joules/cm^2.
2. Multiply the single pulse ED50 by the correction factor of ($n^{-1/4}$) and the number of pulses (PRF x t): $1.01 \times 10^{-4} \times (100 \times 0.25)^{-1/4} \times (100 \times 0.25) = 1.1375 \times 10^{-3}$ Joules/cm^2.
3. Find the ED50 estimate in **Table 1** assuming that it was a comparable CW laser: $1.8 \times (0.25)^{-3/4} \times 10^{-2} = 6.4 \times 10^{-3}$ Joules/cm^2.
4. Select the smaller value of the two, which is 1.1375×10^{-3}, and compute the index by dividing this value into the input radiant energy: $4.2 \times 10^{-2} / 1.1375 \times 10^{-3} = 37$.
5. Plug the index into **Table 2** and read that the scotoma = 6.70 degrees in each eye.

Example 4. The retinal damage from a 1.200 μm CW near IR tunable laser with a 1.50×10^{-3} Joules/cm^2 insult for 18×10^{-7} seconds to the right eye only is calculated as follows:

1. Determine the radiant energy at the cornea = 1.50×10^{-3} Joules/cm^2.
2. Find the ED50 estimate from **Table 1** = $5 (10)^{\{2(1.200-0.700)\}} \times 10^{-6} = 5.0 \times 10^{-5}$ Joules/cm^2.
3. To find the retina damage index, divide the radiant energy at the cornea by the ED50 estimate: $1.50 \times 10^{-3} / 5.0 \times 10^{-5} = 30$.
4. Plug the index into **Table 2** and read that the scotoma = 5.94 degrees in the right eye.

Burn Prediction Using BURNSIM and Clothing Models

F.S. Knox, Ph.D., D.B. Reynolds*, Ph.D., A. Conklin**, B.S., C.E. Perry, M.S.
Human Effectiveness Directorate, Air Force Research Laboratory
2800 Q Street, Wright-Patterson AFB, OH 45433-7901, USA
*Department of Biomedical and Human Factors Engineering
Wright State University, Dayton, OH 45435, USA
**Veridian
5200 Springfield, Ste 200
Dayton, OH 45431, USA

ABSTRACT

The development of BURNSIM, an interactive burn prediction model, has been previously presented at SAFE. Recently, a user who was incorporating BURNSIM into a larger Crew Casualty Model (ORCA) came to us for documentation of BURNSIM's validation. This prompted us to pull together several previously unpublished studies of BURNSIM's ability to accurately predict both human and porcine (pig) burns. The paper discussed the degree to which BURNSIM's predictions agree with data published by: Stoll (human), University of Rochester Atomic Energy Project (pig), Fort Knox (human), Moritz and Henriques (pig), and Knox *etal* (pig). This paper adds to that discussion by introducing efforts to model the protective effects of clothing. Three approaches have been taken: first, making experimental observations of how much heat is transferred through fabric to a sensor or pig skin: second, treating clothing as a simple filter and finally, describing clothing analytically as a multi-layered system through which heat must flow. Each method has its uses and problems. For example, the analytical model is the most general but requires that the user specify many things about the clothing system e.g. size of spaces, thermal properties of the fabric etc. These are not often known and may be difficult to obtain. BURNSIM was able to predict with reasonable accuracy when the initial conditions and thermal inputs are adequately defined.

1. INTRODUCTION

Burns are one of the most traumatic, possibly life threating, injuries anyone can experience, and require more medical care than any other trauma. Post-burn psychological trauma follows the physical burn and may last much longer, and is daily reinforced by the disfigurement which often accompanies severe burns. Burn trauma teams now recognize this and employ psychological specialists who start therapy right along with the medical/physical therapy. The physical and psychological trauma resulting from burns requires extensive care and thus great expense.

For all concerned, the best course is to prevent fires through good design practice. For example, the US Army was able to cut the incidence of burn injuries in survivable crashes to nearly zero by equipping its helicopters with crashworthy fuel systems and having its aviators wear protective flight suits. Part of the justification for this retrofit program was based on the cost of treating burned aviators and training their replacements. The retrofit program turned out to be both the humanitarian and cost effective thing to do.

Part of calculating the cost/benefit of proposed fire safety measures is to be able to assess burn hazard with some accuracy. For example, one protective device worn by today's military pilots is their fire retardant flight ensemble. Historically these uniforms were tested in several ways. First, basic simple flammability tests showed which fabrics

Papers presented at the RTO HFM Specialists' Meeting on "Models for Aircrew Safety Assessment: Uses, Limitations and Requirements", held in Ohio, USA, 26-28 October 1998, and published in RTO MP-20.

might be good candidates. The next step was to assess burn protective capability of various fabrics and fabric constructions. This protective capability was assessed by passing ensembles through fuel fires in an outdoor fire pit or by testing fabrics using pigs as aviator surrogates or by using heat flux sensors to measure heat transmitted through the ensemble and then using math models to predict the burn damage.

Beginning in the 1960's, the US Army Aeromedical Research Laboratory (USAARL) at Fort Rucker, Alabama, became involved in quantifying the burn hazard associated with post-crash fires and the protective capability of flight clothing. USAARL staff (including the author) conducted a number of field studies using burning helicopters to establish the severity and time course of post-crash fires (Knapp and Knox, 1982). They also 1) built and used two fire simulators to study the effect of simulated post-crash fires on pigs as human analogs (Knox et al, AGARD, 1978), 2) placed fabrics between the fire and the pigs to study their protective capability (Knox et al, ASMA, 1979), 3) assembled a large porcine (pig) burn database using this bioassay method (Knox, Final Report, 1979), and 4) developed the model, BRNSIM (now BURNSIM), to decrease the workload associated with using the bioassay method to assess fabric protective capabilities (Knox, 1979). It has been shown that the heat transmitted through fabric as measured by heat flux sensors can be used by BURNSIM to accurately predict burn severity, time to pain, and time to burn.

In assessing burn hazards, its is important to be able to predict the burn injury expected by crewmen dressed as they fight. The purpose of this paper is to review the burn prediction model, BURNSIM, and its validation against a number of data bases. The model was originally developed to replace the use of pigs in testing protective fabrics, but subsequently has been applied to other cases such as side-by-side ejection seats, live fire testing and aerothermal heating. The remainder of the paper will present efforts to model the transfer of heat through clothing. This heat flux is then input to BURNSIM. A preliminary validation of a simple fabric model that has been developed is described by heat flux measurements through NOMEX III. Finally, a sensitivity analysis of BURNSIM is presented so that inaccuracies of the fabric model can be assessed.

2. BACKGROUND

Aircraft fires vary widely depending on the fuel source, the aircraft type, and environmental factors. Light aircraft, such as utility helicopters, tend to heat up rapidly to as much as 2400°F (1315°C) in less than 20 seconds, while large cargo or passenger planes can resist burn-through for up to several minutes. Large fuel fires tend to have a high radiant component, while hot gas or hot surfaces can be convective or conductive. The spectrum of the thermal radiation will determine whether the energy is absorbed mostly at the surface or in depth. Once the energy is absorbed the heat is conducted within the skin or convectively removed by the blood. The net energy increase or decrease changes the temperature and when the temperature is above 44°C damage will result. Other thermal threats include: jet exhaust from thrust vector controlled engines, rocket exhaust from ejection seats in side-by-side configuration, live fire, terrorist bombs and lasers.

Knapp and Knox (1982) discussed the nature of aircraft fires and the testing of flight suit ensembles in some detail. Those who refer to that paper will find that the extensive bibliography was not published. The reader will find an expanded version of that bibliography in the BURNSIM User's Manual (Knox 1993) available from the authors.

BURNSIM is a computer model which allows the user the convert heat flux incident to bare skin to a predicted burn depth. The requirement for such a model first arose when there was a need to

quantify the thermal protective properties of new flight suits. Techniques employed in the 1960's and very early 1970's did not predict the full range of burns from no burn to full thickness and failed to take into account both initial conditions of the skin and its adaptive behavior when heated.

The starting point for building BURNSIM (short for Burn Simulation) was the work of Alice Stoll who based her model on Moritz and Henriques' damage integral (Moritz and Henriques, 1947). She had collected data from human volunteers on the time/heat flux relationships resulting in threshold transepidermal necrosis. This burn is represented by minor blister formation. To explain her results, she added a consideration of damage occurring during cooling as well as during the heating phase (Figure 1). Stoll chose the constants (Stoll and Greene, 1969) in her model to fit her human data on threshold burns; more severe burns were not at first considered. Later, Stoll (Weaver and Stoll, 1969) proposed an extension of her first model to include more severe burns without experimental basis.

The first model to come out of the USAARL program was that of Art Takata of IITRI (Takata, 1974) who worked for USAARL as a contractor. He started with Stoll's approach and added water boiling as a way of handling blister formation. He then adjusted the constants, activation energy (P) and frequency factor (ΔE) (see equation (7)), to predict USAARL's more severe porcine burns.

The current BURNSIM model expands on these earlier efforts (Henriques, 1947; Weaver and Stoll, 1969; Mehta and Wong, 1973; Morse et al, 1973; and Takata, 1974). It is an interactive model originally written in both FORTRAN and ZBASIC running on PDP 11/40, 11/03, 11/24, VAX 11/780, Macintosh and IBM compatible PC's. The latest version is written in C++ and Visual Basic to run on a PC in an MS Windows environment.

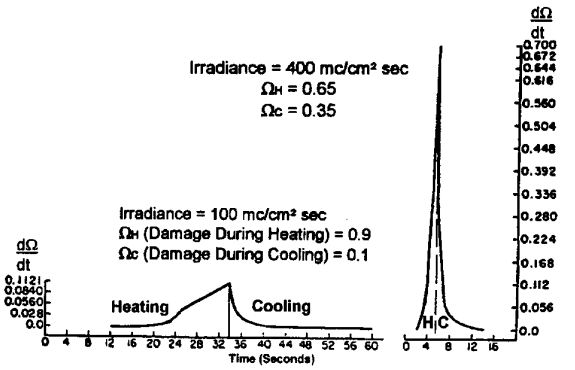

Figure 1. Damage Coefficient for Both Heating and Cooling at Two Different Irradiances

While much work has been reported on analysis and modeling of skin burns, much less has been done related to the response of protective clothing or fabrics to external heating. Morse et al (1973) seems to be one of the first groups to model the thermal response of protective clothing to heating produced by a JP-4 fuel fire. Their model accounts for two fabric layers separated by an air gap followed by another air gap before the skin. The latter is also modeled with a burn model similar to BURNSIM. Each fabric layer is further subdivided into two nodes, resulting in front and back side temperature predictions. According to Morse et al, they were the first to attempt to predict pyrolysis, ignition and combustion of fabrics from fundamental principles. Other aspects also considered were water evaporation in the fabric, air gap thermal conductance as a parallel conductance due to radiation between layers, and air conductivity. Shrinkage effects on local fabric density and air gap width were also considered. Shrinkage effects also played a role in estimating the optical properties of the fabrics, as they measured radiation absorption as a function of shrinkage. In addition, in later model versions, incoming radiation could be partitioned among the nodes of the fabric layers, not just at the surface of the outermost layer.

3. BURNSIM MODEL DESCRIPTION

BURNSIM considers the skin to be represented as 12 chunks or nodes (0,200,400...2200 um). Seven additional nodes can be inserted between the first and second nodes when exposures are mild and burn damage is likely to be shallow (Figure 2). BURNSIM solves the Fourier heat conduction equation to find temperature as a function of time at each node. Then total damage at each node is found by computing the damage integral at each depth. The transition between normal and damaged skin is defined as that depth where the damage integral is equal to one.

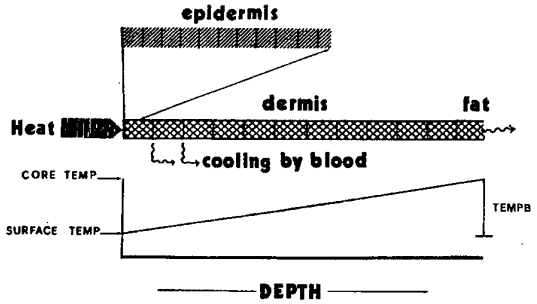

Figure 2. Skin Response to External Heating

3.1 Analytical Model

When Weaver and Stoll (1969) proposed extending Stoll's earlier model (Stoll and Greene, 1959) to heat fluxes higher than those used in obtaining her experimental data, they also found that the effective conductivity changed during the exposure and subsequent cool-down period. Takata (1974), using preliminary data from USAARL's Thermal Project, formulated a model which not only predicted threshold burns but deep burns and tissue water boiling as well. Starting with the work of Henriques (1947), Stoll and Greene (1959), Weaver and Stoll (1969), Mehta and Wong (1973) and Takata (1974), an analytical model was formulated as follows:

Human skin is essentially opaque to thermal radiation from exposures such as post-crash or in-flight fires, and can be considered to transfer energy internally by conduction only. Since exposure durations are no longer than the minimum response times reported for increased thermoregulatory system activity (1954) , thermal energy transfer in skin can be described by the Fourier heat conduction equation as follows:

$$r * Cp * \frac{\partial T}{\partial t} = \frac{\partial}{\partial x}\left(K * \frac{\partial T}{\partial x} \right) + q \qquad (1)$$

where,

r = density, gm/cm^3
Cp = heat capacity, cal/gm-^{o}C
K = thermal conductivity, cal/cm-sec-^{o}C
T = temperature, ^{o}C
x = distance, cm
q = energy source, for the first nodal volume, cal/cm^3-sec

Since skin is considered to be opaque to radiant energy from a post-crash fire and since the source term is due only to radiant energy[1], equation (1) applies only to the surface of the skin. For all conditions in which x > 0, equation (1) reduces to the following:

$$r * Cp * \frac{\partial T}{\partial t} = \frac{\partial}{\partial x}\left(K * \frac{\partial T}{\partial x} \right) \qquad (2)$$

Solution of equations (1) and (2) requires two boundary conditions for x, preferably at x = 0 and x = L, and initial conditions at t = 0 for all positions 0 < x < L. If one assumes that there is no backward flux of thermal energy at x = 0 (all conduction is into the skin), then the energy flux at x = 0 is zero and, consequently, dT/dx = 0. Similarly, if the problem assumes that an adiabatic back wall condition prevails at x = L, the fatty tissue, then the net flux out of the system at x = L is 0, dT/dx=0. These two boundary conditions

[1] Simplifying assumption based on the predominance of the radiate mode of heating. May be less valid with fabrics. In actuality a correction is made to q to account forconvective heating, surface absorptivity, and attenuation of radiant heating by hair.

indicate that the system is closed and that all thermal energy added to the system, $0 \leq x \leq L$, is distributed within the system and cannot escape. Initial conditions specified a uniform temperature for all locations, $0 \leq x \leq L$, at time $t = 0$.

Consequently, the system may be defined by the following mathematical model:

$$r*Cp*\frac{\partial T}{\partial t} = \frac{\partial}{\partial x}\left(K*\frac{\partial T}{\partial x}\right) + q \quad @\ x = 0 \qquad (3a)$$

$$r*Cp*\frac{\partial T}{\partial t} = \frac{\partial}{\partial x}\left(K*\frac{\partial T}{\partial x}\right) \quad @\ 0 \leq x \leq L \qquad (3b)$$

T_L = CORE TEMPERATURE = TEMPI0 + TEMPB

$$T = T_0,\ 0 \leq x \leq L,\ t = 0 \quad \text{Initial Conditions} \qquad (4)$$

$$\frac{\partial T}{\partial x} = 0,\ x = 0,\ 0 \leq t \leq x \quad \text{Boundary conditions 1} \qquad (5)$$

$$\frac{\partial T}{\partial x} = 0,\ x = L,\ 0 \leq t \leq x \quad \text{Boundary conditions 2} \qquad (6)$$

3.2 Solution of Mathematical Model

(Reneau and O'Young, 1976, 1977, 1978)

An analytical solution to equation set (3) was not considered feasible due to the variable nature of q, Cp and K, so explicit differencing methods of numerical analysis were employed to solve the equations. Reneau and O'Young (1976, 1977, 1978) employed the Crank-Nicholson six point implicit differencing (Crank and Nicholson, 1947) to the second-order partial derivatives and corresponding explicit methods to the first order partials. This method is noted for the characteristics of stability and convergence when using correct increment sizes. The first model was implemented in FORTRAN IV using solution techniques of Thomas as described by Bruce et al (1953). This initial model was revised to make it more realistic by allowing: energy flux across the surface, x = 0, during heating; convective heat loss at the skin surface during cooling; heat transfer into deep tissues including conduction into fat; convective cooling via the blood; tissue water boiling; a temperature gradient from surface to fat; and a gradient of thermal properties based on measured tissue water. The model, BURNSIM, is run interactively with the input and output variables, listed in Table 1, changeable per run.

From the relationship for first order kinetics, assumed to apply in damaging tissue protein, we have:

$$\text{Damage Rate} = \frac{d\Omega}{dt} = Pe^{-\Delta E/RT} \qquad (7)$$

$$\text{Total Damage} = \int_0^{\text{ETIME}} d\Omega/dt + \int_{\text{ETIME}}^{\text{ITIME}} d\Omega/dt \qquad (8)$$

If $P = N \times 10^y$ and $\Delta E/R = DE$, then:

$$\ln\frac{d\Omega}{dt} = \ln N + y\ln 10 - E(T) = P_1 - DE*T_1 \qquad (9)$$

where:

$$E(T) = \frac{\Delta E}{R} * \frac{1}{T}\ ,\ P_1 = PL + PLN\ ,\ T_1 = \frac{1}{T + 273}$$

Thus, for damage calculations, the following constants are entered:

PL_1 (44°C - 50°C) = 1.46
PL_2 (50°C - 100°C) = 2.24
PLN_1 (44°C - 50°C) = 147.37
PLN_2 (50°C-100°C) =239.47
DE_1 (44°C-50°C) = 50,000
DE_2 (50°C-100°C) = 80,000

The program outputs $d\Omega/dt$, for each node at each time step, total damage for each node and a threshold depth where $\Omega = 1$. This depth is found using inverse interpolation on two or three w's nearest 1 using either y or log(y). Time to pain is also determined when the temperature at 175 um exceeds 44°C. Since the first presentations (Knox, Wachtel, and Knapp, 1978a, 1978c) BURNSIM has undergone further development.

Table1. Interactive Model Parameters

INPUTS:
TEMPI0 = Initial Surface Temp. (°C); 32.5 °C for man
DENS = Density of skin, 1.0 gm/cm^3
Q1 = Incident Heat Flux either constant or as a File of Fluxes, cal/cm^2-sec
BL = Skin thickness, 2200 um
AK = Calculation interval, nominally .01 sec. For short exposures, the calculation interval must be at least a hundred times less than the exposure duration.
JINC = Number of Nodes, nominally 12
TEMPB = Differences between TEMPI0 and backwall temp. (fat/core), °C. Note: TEMPI0 + TEMPB = Core Temp.
ABSORB = Absorptivity usually .613 assuming 10% convective and 90% radiative heating ; .94 for blackened skin
BOIL = Temperature when water boiling occurs, 100.15 °C
ETIME = Exposure Time, seconds
ITIME = Maximum calculation time usually 80-100 seconds *NXTRA* = Number of extra nodes between the surface and node #2 at 200um, initially set at seven, used for superficial burns Note: The seventh node must be at 175um for an accurate time to pain prediction.
BLOOD = Factor to adjust amount of convective cooling by blood usually set at .001
DE1 & DE2 = ΔE/R from Arrehenius relationship for tissue temperatures from 44°C to 50°C, or over 50°C, respectively
DAMAGE RATE CONSTANTS = PL1, PLN1, PL2, PLN2, DE1, DE2 (for Nodes 2-12) APL1, APLN1, APL2, Constants APLN2, ADE1, ADE2 (for Nodes 1 and Extra Nodes)

OUTPUTS:
Flux (I) - tabulated heat flux as a function of time
DAMAGE, Ω - at each Depth (Node)
Maximum Temperature
Threshold Depth - in um (microns)
Time to Pain
Final Time - total calculation time
File of calculated temperatures - for later plotting by a standard graphics packages.
File summarizing simulation
File of temperature - as printed each second on the terminal

4. USES OF BURNSIM

4.1 Side-by-side Ejection Seats

As Figure 3 shows, the T-46 had side-by-side ejection seat. During testing, it was noticed that the flight suit of the second manikin to eject was damaged by the rocket of the first seat. BURNSIM was used to assess the effect of the rocket exhaust. Heat flux measurements were used as input to BURNSIM. The results showed a chance of burn damage could be averted if the ignition of the first rocket were delayed a small amount.

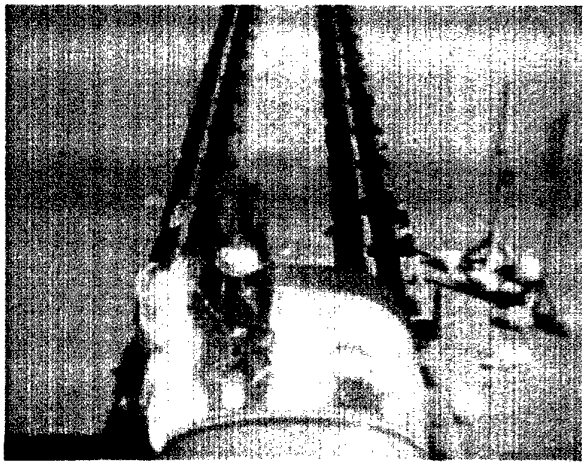

Figure 3. Manikin Ejection from a T-46 Forebody During Sled Test at Holloman AFB

4.2 High Mach Escape

Computational fluid dynamics was used to simulate the aerothermal heating expected to occur as a pilot ejects at supersonic speeds. BURNSIM was used by McDonnell Douglas to find the speeds and altitudes where burn injury was a problem. During an ejection of the Russian K-36D seat at 50k+ feet and Mach 2.5, some heating of the flight ensemble was noted. BURNSIM showed that there was no danger of burns at these conditions.

4.3 Fabric Insulating Capability

Seven fabrics were subjected to a 2.2 cal/cm^2*sec radiant (quartz lamp) source for about six seconds. The plots in Figure 4 show the difference between the fabrics. Two were obviously good insulators. In a similar study, four fabrics and several pigs were subjected to a JP-4 fuel fire. Heat transfer was measured by calorimeter and by actual burns on the pigs. Figure 5 shows that the burn depths predicted by BURNSIM match the observed burns in the pigs using the four different fabrics.

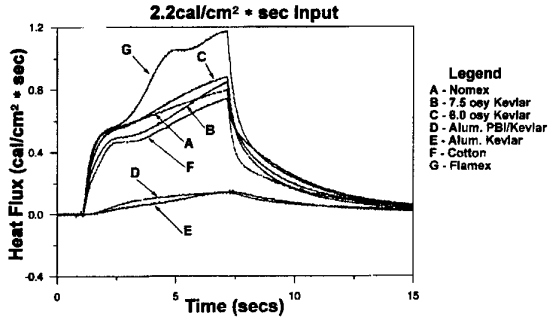

Figure 4. Transmitted Flux for Various Fabric Samples Exposed to a 2.2 cal/cm^2 *sec Flux Input

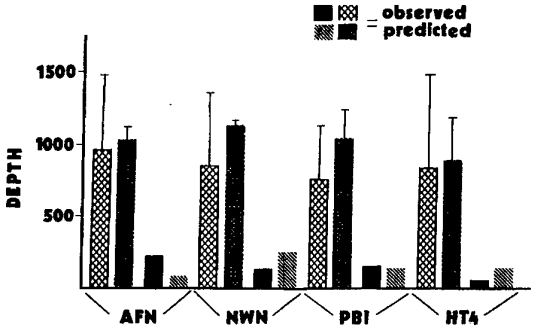

Figure 5. Predicted Burn Depths Under Four Different Fabrics at Two Different Heat Flux Inputs

4.4 Burn Hazard During Live Fire

An F-15 fuselage was instrumented with heat flux sensors (Figure 6a) and then shot with various types of ammunition. The fluctuating heat flux recorded at the right hand of the manikin (Figure 6b) was sufficient to cause a deep dermal (1413 um) burn at the right hand. This case illustrates that BURNSIM handles any shape time varying flux as an input. Thus, it is ideal for analyzing data from aircraft fire tests where the flux fluctuates. It also points out that the next addition to the model needs to account for the clothing worn by the crew exposed to the fire. Both an analytical and a filter approach have been explored. A simple first-order filter can be used quite successfully to simulate the insulating properties of a single layer. Filters can also be cascaded for more complex ensembles.

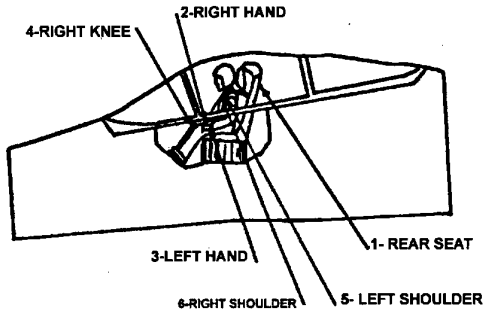

Figure 6a. Live Fire Heat Flux Sensor Placement

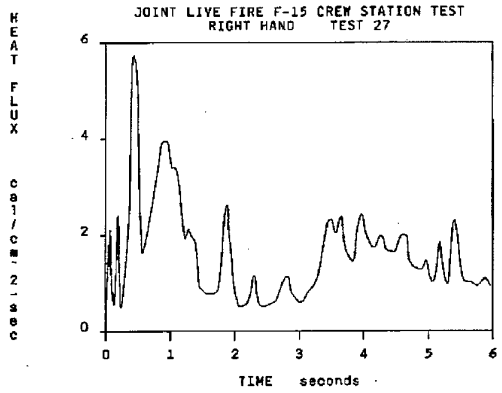

Figure 6b. Heat Flux Measured at Right Hand of Manikin During Live Fire Test

5. FABRIC MODELING

5.1 Overview

As previously stated, Morse et al (1973) seem to be one of the first groups to model the thermal response of protective clothing to heating produced by a fuel fire. Some of the main conclusions from the Morse et al study pertinent to our recent studies are:

(1). Optical properties of transmittivity ($\Im$) and absorbtivity (α) of fabric are of paramount importance in thermal protection. Low α keeps energy out of the clothing system and low $\Im$ prevents a direct heating of the skin.

(2). Thermal conductivity of the fabric is of much lesser importance, especially when an air gap(s) of reasonable width is maintained. For example, we calculate that an air gap of 0.4mm has about the same thermal resistance as a single layer of 7.5 oz/yd Nomex. We should note here, however, that the thermal conductivity values for air reported by Morse et al (1973) seem low by a factor of about 11 (Byrd (1990) also noted this error). Thus it is possible that some conclusions drawn by Morse et al regarding the relative importance of radiation vs. air conduction heat transfer may be suspect.

(3). Thermal capacitance of the fabric is important in relation to the absorbed heat and thus the heat load to the skin after the incident flux is removed. For example, after leaving a fire vicinity, cooling the clothing surface should be done immediately for any beneficial effect because waiting as short a time as 3 to 5 s would release most of the stored heat to the skin.

In 1990, Byrd formulated a relatively comprehensive model of heat transfer through single and multiple fabric layers and included the effects of the skin surface properties. In his model, each fabric layer is divided into 3 regions and fabric layers were separated by an air layer. He included heat transfer by convection and radiation to the outermost layer, conduction through a layer and radiation and conduction in the air space between layers. A one-dimensional energy balance could then be used to write equations for each of the fabric regions and air spaces. Radiation followed the Stefan-Boltzmann 4^{th} power law and was confined to fabric surface nodes except for a portion which is directly transmitted without interaction. Thermal properties were allowed to have temperature dependence in the general model (the model was run only with constant properties however) and the resulting equation set was nonlinear due to radiation and variable properties. The skin node was simplified to have constant thermal properties and constant backside temperature rather than adiabatic backside.

As mentioned above, the model as run had constant thermal properties. One of the interesting results obtained for a single fabric layer is that the middle node fabric temperature is lower than the inner node temperature for about 10 s. This is due to the reflected radiation from the skin warming the inner fabric surface faster than the thicker interior region can warm by conduction from the surface. For two fabric layers, Byrd reported that the protective effect increased more than fivefold, i.e., the heat flux to the skin with two layers was less than one-fifth that for a single layer.

This study uses a simplified version of Byrd's model to analyze and predict heat flux through fabrics. This is a lumped capacitance model in which a fabric layer is simulated by single or multiple regions which have thermal resistance(s) and capacitance(s) related to thermophysical properties of the fabric and air. The resistance is the familiar "R" value used in comparing commercial insulation but in a modified cgs unit system which uses calories as the energy unit. The R=L/k, where L is fabric thickness and k is fabric thermal conductivity. R can be thought of as the temperature difference required to produce a

unit value of heat flux in the medium. For example, compare the R values of 1 cm of the following materials at room temperature: air has an R of 16100, styrofoam has an R of 12700 and solid Nomex III polymer has an R of 3220 °C/(cal/cm^{2}s) (Dupont Product Specification Sheet). The thermal capacitance C relates to the ability of the material to store heat and represents the change in energy storage per unit surface area per unit change in temperature. Thermal capacitance C=ρcL, where ρ is the density and c is the heat capacity. In our model, we have attributed C to the fabric fibers and not the air trapped by the fibers because air has a much smaller density and heat capacity. Compare C for 1 cm of air and Nomex polymer at room temperature: C=0.00028 for air and for Nomex, C=0.40 cal/(cm^2°C), thus Nomex fiber has 1400 times the heat storage capacity of air. On the other hand, both the fiber and the air contribute to R, as shown later. A schematic for the analysis is shown in Figure 7. A portion of the incident heat flux is directly transmitted through the fabric, and we assume that this does not interact with the fabric. Another part of the incident flux is absorbed by the fabric, assumed to be at the surface only. The fabric itself may be arbitrarily divided up into one or more sub-layers, each having a uniform temperature. An air gap may be included between the back side of the fabric layer and the heat flux sensors, although in most experiments, no gap was intentionally included. An energy balance at the front side surface and energy balances for each sublayer may be written. In addition, a back side sensor relationship may be written, which includes sensor dynamics. We have found the latter to be well described by a first order system, characterized by a time constant τ_c. In more recent experiments, the time constant includes the recorder dynamics as well.

The surface energy balance can be written:

$$\alpha G'' + q''_{conv} = q''_{rad} + q''_{cond} \qquad (10)$$

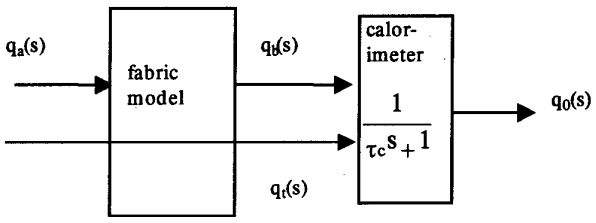

Fig 7. Block Diagram of Fabric and Calorimeter Models with Inputs and Outputs in Laplace (s) Domain

where α is the surface absorptivity, G" is the surface irradiation, q"$_{conv}$ is the heat convected to the surface, q"$_{rad}$ is the net radiation emitted by the surface and q"$_{cond}$ is heat flux conducted into the fabric. Note that α depends upon the surface and the spectrum of the incident source, characterized by its absolute temperature. The quartz tube bank approximates a blackbody radiator with peak temperature increasing with percentage of rated voltage. On the other hand, q"$_{rad}$ depends upon the fabric surface emissivity ε, which may be a function of fabric surface temperature, and view factor F to cooler surrounding surfaces. In our analysis, we have neglected q"$_{rad}$ because we have assumed F is small because the heater bank is placed close to the fabric. With this assumption, the only unknown in (10) is α because we measure G" and the total incident heat flux (G" + q"$_{conv}$).

The simplest model has a single fabric layer over the sensor without an air gap. We use the lumped capacitance method and perform an energy balance on the layer, i.e.

$$E''_{in} - E''_{out} + E''_{gen} = E''_{sto} \qquad (11)$$

where E"$_{in}$, E"$_{out}$ are energy fluxes into and out of the layer, E"$_{gen}$ is internal heat generated within the layer per unit surface area (assumed zero) and E"$_{sto}$ is the thermal energy stored within the layer per unit surface area. E"$_{in}$ is thus given

by (10), E''_{out} is the heat loss to the back side flux sensor, modeled by (T-Ts)/R and E''_{sto} is given by m"c dT/dt. In these expressions, T is the fabric temperature, Ts is the sensor temperature (assumed constant over the short exposures in these experiments), R is the effective thermal resistance to heat transfer between the fabric and sensor and m"c (product of fabric mass per area and fiber heat capacity) is the fabric thermal capacitance C. Thus, (11) becomes the following:

$$\alpha G''+q''_{conv}-(T-T_S)/R = CdT/dt \qquad (12)$$

Finally, if the system dynamics are first order, the following equation holds:

$$(T-T_s)/R + q_t = q_0 + \Im_c\, dq_0/dt \qquad (13)$$

where q_t is the directly transmitted heat, q_0 is the system output and $\Im_c$ is the heat flux sensor/system time constant.

Equations (12) and (13) can be solved analytically using Laplace transforms, for example. For a step input in incident heat flux, the solution for the system output and fabric temperature are given by

$$q_0(t) = q_a\left(1-\left(\frac{\Im_f}{\Im_f-\Im_c}\right)e^{-t/\Im_f}+\left(\frac{\Im_c}{\Im_f-\Im_c}\right)e^{-t/\Im_c}\right) + q_t\left(1-e^{-t/\Im_c}\right) \qquad (14a)$$

$$T(t) = T_c + q_a R(1-e^{-t/\Im_f}) \qquad (14b)$$

where $q_a = \alpha G'' + q''_{conv}$ and $\Im_f = RC$, which we call the fabric time constant.

5.2 Parameter Estimation

The thermal resistance R between the fabric and sensor is the total resistance connecting the fabric node temperature to the sensor temperature. For close contact between fabric and sensor, we assume this is the conduction resistance of the fabric only, i.e. we are neglecting contact resistance between fabric and sensor and any internal sensor resistance. Conduction resistance $R = L/k_f$, where L is the fabric thickness and k_f is the fabric thermal conductivity.We used an equation given by Morse et al (1973) to compute k_f, given below:

$$k_f = x(Vk+(1-V)k_a)+(1-x)\left(\frac{kk_a}{(1-V)k+Vk_a}\right) \qquad (15)$$

where x is the fraction of parallel pathways for conduction, (1-x) is the fraction of series pathways, V is the volume fraction of fiber, (1-V) is the volume fraction of air, k is fiber thermal conductivity and k_a is air thermal conductivity. For the Nomex III tested in this study, we computed V=0.28 from the known fabric weight and the measured thickness. As in the Morse et al (1973) report, we chose x=0.3. Now k and k_a increase with temperature (Morse et al, 1973) and it's difficult to choose an average without having measured fabric temperature. So we compute a value of k_f=9.5 x 10^{-5} cal/(cm·s·°C) at T=20 °C from Eq.15. At T=260 °C, k_f=14.2 x 10^{-5} cal/(cm·s· °C), almost a 50 % increase. Thus nominally $R = L/k_f = 0.066\text{cm}/9.5\text{x}10^{-5}$ cal/(cm·s·°C) = 695 (cm^2·s·°C)/cal. Note that k_f would likely be larger and at higher temperatures, R would be smaller.

Thermal capacitance C = m"c = (2.54x10^{-2} g/cm^2) (0.29 cal/gm °C) = 7.37 x 10^{-3} cal/cm^2 °C at 20°C. As noted by Morse et al (1973), this essentially is all due to the fiber mass, i.e. thermal capacity of air is negligible. Thus, the fabric time constant for NOMEX, $\Im_f = RC = 5.1$ s. Because we have likely used too high a value of R as indicated above, $\Im_f = 5.1$ s may be high. In any case, adjusting the $\Im_f$ downward is not unreasonable.

Because in the series of experiments described here we directly measured the transmitted radiation, the only other unknown parameter is the fabric absorptivity α. Using values from other studies with NOMEX may be hazardous because the particular fabric and incident spectrum may be different, both of which affect α. For example, for the virgin state NOMEX tested by Morse et al (1973) (which is probably a quite different version and color of NOMEX than we tested), $\alpha = 0.57$ for a blackbody radiant heating source at a peak temperature of 980°C and 0.32 for one at 2480°C. These peak temperatures and corresponding heat fluxes are controlled by voltage supplied to the lamp. In this study, for a measured incident heat flux of 2.2cal/(cm^2·s), a peak lamp temperature of 2280°C (2553K) was estimated from the manufacturer's literature (Research Inc., Minneapolis, lamp 2000T3/CL/HT). However, this is not enough information to allow us to use Morse et al (1973) data for the α value. Surface characteristics of the fabric must also be similar.

6. FABRIC STUDIES AND MODEL PREDICTIONS

6.1 Experimental Method

The thermal protective performance testing was conducted using 7.5 osy (oz/yd^2) Nomex III sample fabric and a quartz lamp heater panel (Research Inc, model 4553-10-12) set to a nominal heat flux output of 2.2 cal/cm^2s. We controlled the exposure of the fabric to the heater with a computer-timed shutter in order to precisely limit the time of exposure to six seconds. A single radiometer/total heat flux sensor (Medtherm, Huntsville AL, model #64-500T-500R-20989) was mounted flush with the front surface of the insulating board, and a second sensor was mounted in direct contact with the back side of the fabric. This is shown in Figure 8. This allowed for the separation of transmitted radiative flux from the total heat flux. The output of the heat flux sensors was then measured via stripchart recorder whose output was in turn digitized using Un-Scan-It (Silk Software). We made the decision to use stripchart recorders for the initial analysis due to the inherent electromagnetic noise produced by quart lamp heaters.

The quartz heater panel shown in Figure 8 measures 12 inches by 12 inches and was placed 9.75 inches from the surface of the fabric. The panel has twelve 10 inch tubular quartz lamps (Research Inc., Model 2000T3) with a rated voltage of 240 V. The lamps are positioned horizontally to prevent sagging of the heating elements. All fabric test samples had an exposed diameter of 2 inches.

6.2 Results and Discussion

For an incident total heat flux of 2.2 cal/cm^2/s with an exposure time of 6 seconds, the output heat flux (behind the fabric) can be seen in Figure 9 labeled as Test Data. It is interesting to note that the measured data seems to rise very quickly for almost half a second at which point it begins to rise more slowly. This seems to suggest a greater than first order respond for the system. It is also interesting to note that the data appears to reach an asymptote after about 3.5 seconds.

For the case of 2.2 cal/cm^2/s with an exposure time of 12 seconds, shown in Figure 10 as Test Data, the data for the first 6 seconds of exposure looks very similar to the results of the 6 second test. Again the data rises very quickly in the first half seconds with a slower rise time afterwards. This data also seems to reach an asymptote around 3.5 seconds but then begins to again increase almost linearly after 6.5 seconds. It appears as if some type of physical change must be taking place in the fabric after about 6.5 seconds of exposure.

6.3 Modeling and Analysis

Using the testing method described above, the following values for 7.5 osy Nomex III were measured. The heat flux absorbed by the fabric, q_a, was found to be .0194 cal/cm^2s. The time constant of the fabric, τ_f, as described in equation

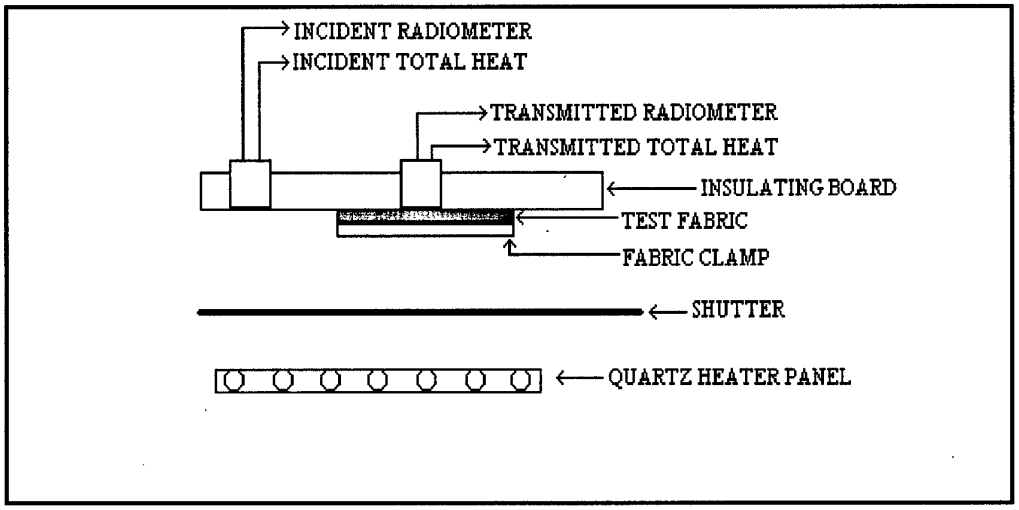

Figure 8. Schematic Showing Top View of Test Facility for Fabric Thermal Analysis

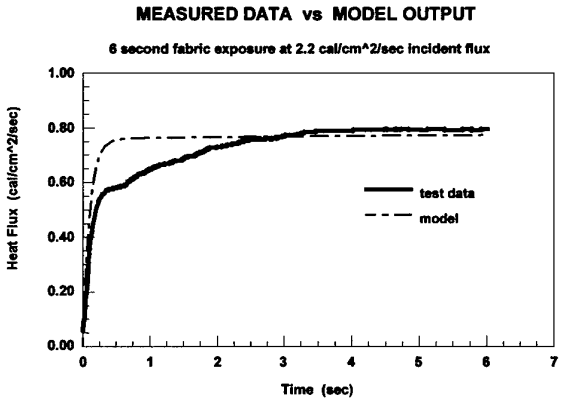

Figure 9. Measured Heat Flux Behind Fabric Versus Model Output For 6 Second Exposure

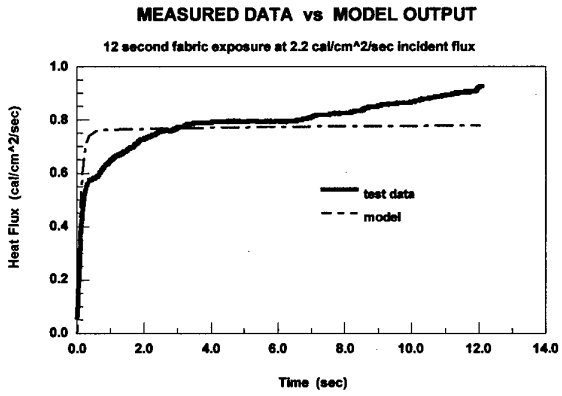

Figure 10. Measured Heat Flux Behind Fabric Versus Model Output For 12 Second Exposure

14, was calculated to be 5.1 seconds. The time constant of the system, τ_s, was measured at 0.1seconds. The transmitted radiative heat flux, q_t, was determined to be 0.76 cal/cm^{2}s. A graphical fit of the model can be seen in figure 9. And represents a mere 4.8% pointwise average absolute error. Using Burnsim, the measured test data results in a burn depth of 315.9 microns while the model data results in a burn depth of 332.1 microns. This difference is insignificant regardless of which measurement system of table 1 you use. We can conclude therefore that the model closely corresponds to the actual test data both in terms of numerical error and in terms of actual burn damage done to the skin.

Figure 10 shows that the model can use the values determined in the 6 second test to predict the burn depth of a 12 second test. This represents a 100% increase in prediction capability from the 6 second test. Using the test data for a 12 second exposure, Burnsim predicts a burn depth of 1213 microns. Similarly, the model data results in a burn depth of 1164 microns. Again, this difference is neither numerically or clinically significant.

7. BURNSIM SENSITIVITY

In order to determine how precise the clothing model must be, a study was made of the sensitivity of Burnsim, and thus the skin, to various heat flux input ranges as well as exposure times. This was done by using Burnsim to predict the depth of damage in the skin for several heat flux vs. exposure time scenarios.

The representative scenarios were chosen to reflect cases which can often be found in actual JP-4 fuel fires resulting from aircraft crashes. A fully developed JP-4 fuel fire produces a heat flux between 3.5 and 4 cal/cm^2/s. After extensive testing of actual aircraft fires and open field fuel fires with instrumented human surrogates, the worst credible environment is defined as a six-second radiant exposure of skin to a radiant wall of heat at 2100 ° F (Knox et al 1978).

Figure 11 shows the burn depth predictions of BURNSIM for plus and minus ten percent of several key heat fluxes, namely 1, 3, and 5 cal/cm^2/s with exposure times ranging from 0 to 10 seconds. In all cases, the initial skin temperature was assumed to be 32.5 ° C.

The average decrease in burn depth for a ten percent reduction in heat flux from 1 cal/cm^{2}s is 134.5 microns, while the average increase in burn depth for a ten percent increase in heat flux is 99.2 microns. For the 3 cal/cm^{2}s exposure, the average decrease in burn depth for a 10% reduction was 88.3 microns, while average increase in burn depth for a 10% increase was 70 microns. Similarly, for the 5 cal/cm^{2}s exposure, the average decrease for a 10% reduction was 35.5 microns and the average increase for a 10% increase in heat flux was 32.4 microns.

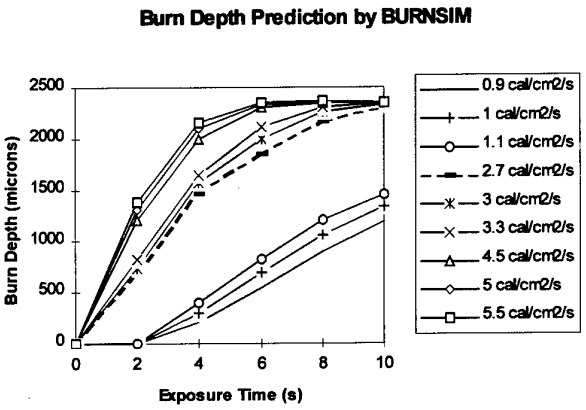

Figure 11. Prediction of Burn Depth by BURNSIM as a Function of Exposure Time and Flux Level

From the above analysis we can see that ten percent error in a model is not significant when the heat flux exposure produced by that model is in the range of 3-5 cal/cm^{2}s. The error does become significant, however, when the exposure is near 1 cal/cm^{2}s since a increase or decrease of around 100 microns can mean the difference between first and second degree burns as shown in Table 2.

Table 2. Identification of Degree of Burn or Thermal Injury

Standard	Reed (1994)	Knox (1978)	Knox Depth (1978)
1st degree	Below Threshold	1- Cell damage without acidophilism 2- Partial epidermal acidophilism 3- Complete epidermal acidophilism	1-20 μ 20-50 μ 50-100 μ
2nd degree	Partial Thickness	4- Partial dermal-epidermal separation 5- Complete dermal-epidermal separation 6- Superficial dermal 7- Mid dermal 8- Deep dermal	100-150 μ 150-250 μ 250-500 μ 500-1000 μ 1000-1500 μ
3rd degree	Full Thickness	9- Complete dermal to adipose border 10- Adipose	1500-2000 μ >2000μ

It is also important to note however, that after around four seconds, 10% error loses its significance for the 3 and 5 cal/cm^{2}s cases since the skin has already suffered a third degree burn and the error merely increases or decreases the depth of the burn. This same point can be made for the 1 cal/cm^{2}s case after approximately 10 seconds. We can therefore conclude that for heat fluxes above 3 cal/cm^{2}s, 10% error is not significant, and that for exposures of 1 cal/cm^{2}s, 10% error is not significant if the exposure is greater than 10 seconds.

8. OTHER MODELS IN USE

Since the publication of BURNSIM, various other authors have used finite element models to study the effect of burns. Diller and Hayes (1983), and Torvi (1992), for example, have written finite element models and studied their performance in predicting burn injury resulting from hot surface contact (Diller and Hayes) and flash fires (Torvi). Behnke, Geshury, and Barker (1992) and Dale et al (1992) have employed models with instrumented mannequins to assess the protective capability of fabrics. More recently, Lawton and Laird (1993), employed such a model to investigate skin burns behind defeated armor. They showed that, for high temperature thermal sources, in-depth absorption of heat flux improves the accuracy of burn predictions. The general success of BURNSIM and all the other models supports their use in assessing the burn hazard associated with aircraft fires. Experimentally, it is only necessary to measure heat flux as a function of time during the fire and then use BURNSIM or similar model to process the data. Predictions of time-to-pain, maximum temperature and burn depth are possible. If an instrumented mannequin is used, then burn area can be assessed as well. To our knowledge BURNSIM is the only such model set up to be interactive to facilitate conducting what-if studies as well as data reduction.

9. CONCLUSIONS

BURNSIM is available for those wishing to conduct analyses of data collected during experiments with protective clothing, aircraft fires, high-speed ejection seats and other cases when what-if studies are called for. It can quite easily be fine tuned to fit particular experimental situations such as where the thermal source has shorter wavelength or where longer exposures

result in blood flow and thermal property changes.

10. REFERENCES

Behnke, W.P., Geshury, A.J., Barker, R.L. 1992. Thermo-Man® and Thermo-Leg: large scale test methods for evaluating thermal protective performance. Philadelphia, PA: Performance of Protective Clothing: 4th Volume, ASTM STP 1133, James P. McBriarty and Norman W. Henry, Eds., American Society for Testing and Materials.

Byrd, L.W. 1990 Heat Transfer Through Multiple Layers of Fabric. Final Report, Air Force Office of Scientific Research: USAF Summer Faculty Research Program through Univeral Energy Systems Inc., Contract F49620-88-C-0053.

Crank, J., and Nicholson, P. 1947. Proceedings Cambridge Philological Society. 43:50

Dale, J.D., Crown, E.M., Ackerman, E.L., and Rigakis, K.B. 1992. Instrumented mannequin evaluation of thermal protective clothing. Philadelphia, PA: Performance of Protective Clothing: 4th Volume, ASTM STP 1133, James P. McBriarty and Norman W. Henry, Eds., American Society for Testing and Materials.

Davis, Thomas P. 1959. A theoretical and experimental investigation of the temperature response of pig skin exposed to thermal radiation. Rochester NY, The University of Rochester Atomic Energy Project. AEC Research and Development Report UR-553.

Diller, K.R. and Hayes, L.J. 1983. A finite element model of burn injury in blood-perfused skin. Journal of Biomechanical Engineering. 105(8):300-307.

Henriques, F. C. 1947. Studies of thermal injury. V. The predictability and the significance of thermally induced rate processes leading to irreversible epidermal injury. Archives of Pathology. 43:489-502.

Incropera, F.P. and DeWitt, D.P. 1996. Chapter 5, *Fundamentals of Heat and Mass Transfer*, 4th Ed., Wiley & Sons, New York.

Knapp, S. C., and Knox, Francis S., III. 1982. Human response to fire and personnel protection measures. AGARD/NATO PEP lecture series no. 123 on "Aircraft Fire Safety," 7-16 June, at Oslo, Norway, London, England and Washington DC.

Knox, F.S., Wachtel, T.L., Travethan, W.P., McCahan, G. R. Jr., and Brown, R.J. 1978. A Porcine Bioassay Method for Analysis of Thermally Protective Fabrics: A Histological and Burn Depth Grading System. USAARL report No. 78-11, U.S. Army Aeromedical Research Laboratory, Fort Rucker AL.

Knox, F. S., III, Wachtel, T. L., and Knapp, S. C. 1978a. How to measure the burn-preventive capability of nonflammable textiles: A comparison of the USAARL porcine bioassay technique with mathematical models. Burns. 5(1):19-29. Also reprinted as USAARL Report No. 79-5. 1979. (Uses model and sensor output to predict burns.)

Knox, F. S., III, Wachtel, T. L., and Knapp, S. C. 1978b. Biomedical constraints on thermal protective flight clothing design: A bioengineering analysis. In Operational Helicopter Aviation Medicine: AGARD/NATO Panel Specialists' Meeting, May 1-5; Fort Rucker AL. London: Technical Editing and Reproduction Ltd. Pp. 63-1--63-11. AGARD-CP-255.

Knox, F. S., III, Wachtel, T. L., and Knapp, S. C. 1978c. Mathematical models of skin burns induced by simulated postcrash fires as aids in thermal protective clothing design and selection. In Proceedings of the Army Science Conference, June 20-22; West Point NY, 267-281. Vol II (AD-A056437). Also published as USAARL Report No. 78-15.

Knox, F. S., III, Knapp, S. C., McCahan, G. R., Jr., and Wachtel, T. L. 1979. Bioassay of thermal protection afforded by candidate flight suit fabrics. Journal of Aviation, Space, and Environmental Medicine. 50(10):1023-1030.

Knox, F. S., III. 1979. Predictability of burn depth: Data analysis and mathematical modeling based on USAARL's experimental porcine burn data. Shreveport LA: Louisiana State University School of Medicine, Department of Physiology and Biophysics. Contract DAMD17-77-7004.

Knox, F. S, III, Wachtel, T. L., and Knapp, S. C. 1980. Burn prediction model for thermally protective clothing evaluation. Paper presented at the annual meeting of the Aerospace Medical Association, 12-15 May.

Knox, F. S., III, Wachtel, T. L., McCahan, G. R., Jr., and Knapp, S. C. 1986. Thermal properties calculated from measured water content as a function of depth in porcine skin. Burns. 12(8):556-562.

Knox, F. S., III, Bonetti, D., and Perry, C. 1993. User's manual for BURNSIM: A burn hazard assessment model. USAARL, Fort Rucker AL and AL/CFBE, Wright-Patterson AFB OH. USAARL Report No. 93-13.

Lawton, B., and Laird, M. 1993. Assessment of skin burns behind defeated armor. In Proceedings of the 14th International Symposium on Ballistics, September 26-29, Quebec, Canada, 785-794.

Mehta, A., and Wong, F. 1973. Measurement of flammability and burn potential of fabrics. (Summary report December 1971-January 1973.) Cambridge MA: Fuels Research Laboratory, Massachusetts Institute of Technology Project DSR 73884.

Moritz, A. R. 1947. Studies of thermal injury. III. The pathology and pathogenesis of cutaneous burns, an experimental study. American Journal of Pathology. 23:915-941.

Morse, H. L., Thompson, J. G., Clark, K. J., Green, K. A., and Moyer, C. B. 1973. Analysis of the thermal responses of protective fabrics. Wright-Patterson Air Force Base OH: Air Force Materials Laboratory, Air Force Systems Command. Technical Report AFML-TR-73-17.

Reed, M.P., Schneider, L.W., and Burney, R.E. 1994. Laboratory Investigations and Mathematical Modeling of Airbag-Induced Skin Burns. Proceedings of the 38th Stapp Car Crash Conference, Society of Automotive Engineers, Warrendale PA.

Reneau, D. D., and O'Young, Nelson. 1976, 1977, 1978. Consultation report to F. S. Knox. Shreveport, LA: Louisiana State University Medical Center, Department of Physiology and Biophysics. US Army Contract Nos. DABT01-75-C-0257 and DAMD17-77-C-7004.

Reynolds, D.B. 1997. Modeling Heat Flux Through Fabrics Exposed to a Radiant Source and Analysis of Hot Air Burns. Final Report No. 32, Air Force Office of Scientific Research: USAF Summer Faculity Research Program through RDL, Inc.

Rushmer, R. F., Buettner, K. J. K., Short, J. M., and Odland, G. F. 1966. The skin. Science. 154(3747):343-348.

Stoll, A., and Greene, L. C. 1959. Relationship between pain and tissue damage due to thermal radiation. Journal of Applied Physiology. 14:373.

Stoll, A. M., and Chianta, M. A. 1971. Heat transfer through fabrics as related to thermal injury. Transactions-New York Academy of Science. Vol 33(7):649-670. November.

Takata, A. 1974. Development of criterion for skin burns. Aerospace Medicine. 45(6):634-637.

Torvi, David A. 1982. A finite element model of heat transfer in skin subjected to a flash fire.

(Master of Science Thesis). Edmonton, Alberta: University of Alberta, Department of Mechanical Engineering.

Weaver, J. A., and Stoll, A. M. 1969. Mathematical model of skin exposed to thermal radiation. Aerospace Medicine. 40:24-30.

THERMAL OUTPUT OF PYROTECHNIC COMPOSITIONS AND EVALUATION OF SKIN BURNS

Dr B Lawton
Royal Military College of Science
Cranfield University
Shrivenham, Swindon, Wilts SN6 8LA, UK.

Dr R. Merrifield
Health and Safety Executive
Chemicals and Hazardous Installations Division
St Anne's House, Stanley Precinct
Bootle, Merseyside, L20 3RA, UK.

Dr R K Wharton
Health and Safety Laboratory
Health and Safety Executive
Harpur Hill, Buxton
Derbyshire, SK17 9JN, UK.

1. SUMMARY

This paper presents a method of computing the heat dose for first, second, and third-degree burns from convection or radiation sources. Henriques' theory of skin burns is used with a simple numerical model of one-dimensional, transient heat conduction through skin. Allowance is made, where necessary, for heat absorption due to penetration of the skin by short wavelength radiation. The theory is used to compute the quantity-distance-burns relation for fires burning various pyrotechnic compositions of commercial and military interest.

2. INTRODUCTION

The incidence of burns casualties in war has been about 3% historically but in recent conflicts the incidence has risen to 10-12%. In the Falkland Islands conflict, 18% of British casualties suffered burns, while in the October 1973 war in the Middle East, Nili and Kadem (1984) report that 10.5% of all injured troops were burnt. The very high incidence of burns in armoured fighting vehicles led the Israeli defence forces to institute burn prevention measures such as protective clothing and improved vehicle design. In the Lebanon War of 1982, the incidence had declined to 8% of all injured troops, and the severity of burn was less.

There are numerous occasions when it is necessary to assess the risk of skin burns in humans. For example, when a shaped charge jet penetrates and defeats armour plate on a military vehicle the interior of the vehicle is subjected to blast pressures, toxic fumes and a thermal pulse which may cause serious burns to exposed skin. Similarly, accidental fires of stores such as pyrotechnic compositions or gun propellants may cause radiation burns to people who, necessarily, have to work in close proximity. Numerous other risk situations could be cited. Clearly, it is a matter of some importance to determine the effects of thermal exposure on personnel and equipment and on their prospects for escape and survival. Since only limited testing can use human volunteers, extensive tests have been done on anaesthetised or dead pigs. In its response to burns, porcine flesh is remarkably similar to human flesh. Such methods are now considered both undesirable and frequently unnecessary. The data generated in such experiments can be modelled with good accuracy using an appropriate theory of skin burns and a suitable model of skin heat transfer. In risk assessment trials, the heat dose absorbed by a suitable skin simulant may be measured and used as the input data to a computer code. This code uses the theory of skin burns presented in this paper to predict the onset of pain, or burn severity (first, second or third-degree burns).

The theory of burns was first put forward by Henriques (1947), and Henriques and Moritz (1947), and relates the lifetime of a skin cell to its temperature using the Arrhenius equation. Henriques' equation was later modified by Weaver and Stoll (1969) and by Takata (1974). However, such modifications are unnecessary. It will be shown that Henriques' original equation may be used to predict all types of skin burns, including those from high temperature sources, if a proper allowance is made for the penetration and absorption of thermal radiation, and if a reasonable computer model is used to predict the fluctuation of cell temperature with time. The computer model used in this paper is based on the numerical solution of the one-dimensional heat diffusion equation with constant thermal properties and internal heat generation by

Papers presented at the RTO HFM Specialists' Meeting on "Models for Aircrew Safety Assessment: Uses, Limitations and Requirements", held in Ohio, USA, 26-28 October 1998, and published in RTO MP-20.

penetrating, high temperature, radiation.

Observation of skin burns has usually been made under idealised conditions in which radiation or convection is constant. In real fires, the radiation or convective conditions usually fluctuate during the exposure period. Published burns data, therefore, may not be applicable and the influence of such variations needed to be investigated. Details of the size, duration, and radiation emitted by fires of several pyrotechnic compositions are described and the distance for pain, second-degree and third-degree burns are determined. Methods of protection against skin burns are not discussed.

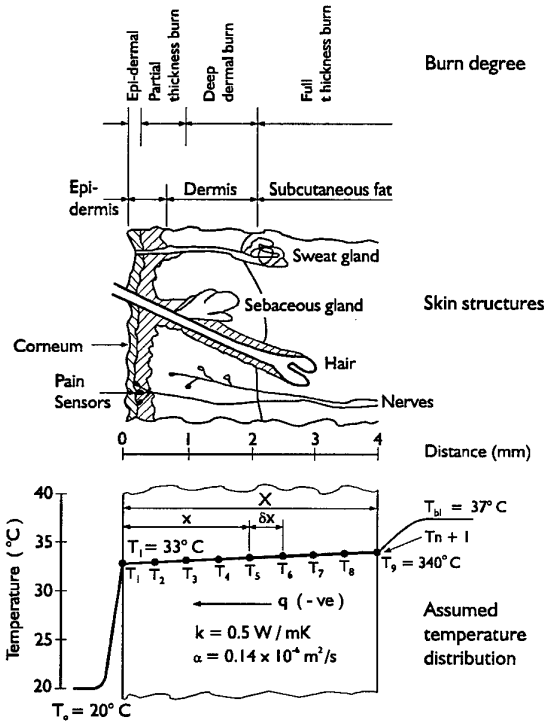

Fig.1 Assumed temperature distribution, skin structure and burns depths.

3. THEORY OF SKIN BURNS

Fig.1 shows a cross-section through human skin and illustrates its main structures. Healthy skin consists of two layers: the epidermis and dermis. The epidermis is about 100 to 150 μm thick and has an outer layer of dead cells and a thin layer of epithelial cells containing the pigment melanin. Dead cells flake constantly from the outer surface and are replaced by new cells at the base of the epidermis. The dermis makes up most of the skin thickness and varies from about 0.5 mm on the eyelids to about 5 mm in the centre of the back; an average thickness is 2 mm. The dermis is usually perfused with blood and it contains structures such as hair follicles, the sweat and sebaceous glands and nerve endings.

The sensation of pain is thought to originate at the nerve endings; certainly, it is true that if a skin burn exceeds a certain depth then pain is no longer experienced. The pinprick test is commonly used to help assess the burn depth and severity. Hair follicles play an important part in the re-growth of skin after severe burns because they are lined with epithelial cells which act as growth points. If the skin burn depth is greater than the follicle depth then re-growth is slow or even impossible. If a scar is to be avoided, a skin graft is necessary.

Cell structures die naturally, due to their internal processes, and they are continually replaced. When skin is heated, these processes occur at an enhanced rate that is related to the cell temperature in the same way as other chemical reactions are related to temperature, namely through the Arrhenius equation. Blood temperature is 37 °C (310 K) and skin surface temperature is usually in the range 28 to 35 °C. If skin temperature rises above 50 °C then pain is triggered and, if heating continues, the blood vessels in the dermis dilate to allow blood to flow closer to the surface. This causes a reddening and the resulting burn is referred to as a superficial or first-degree burn. Cell death does not occur and the process is reversible. Further application of heat, however, will cause cell death. When all the cells in the epidermis die the burn is referred to as a partial thickness or second-degree burn and blisters usually form. If the cells are destroyed to the depth of the follicles, the burn is referred to as a deep dermal, or third-degree burn, and skin grafts are necessary. These data are summarised in Table 1.

Table 1. Classification of Burns.

Burn Degree	Burn Description	Burn Depth
1st Degree	Superficial	Reversible
2nd Degree	Partial Thickness	0.1-0.5 mm
3rd Degree	Deep Dermal	0.5-2 mm

Henriques (1947) determined the constants in the Arrenhius equation for skin burns, namely:

$$\frac{d\omega}{dt} = exp(226.78 - 75000 / T) \qquad 1$$

where T is the cell temperature and ω is the degree of cell damage which is defined such that $\omega = 1$ corresponds to cell destruction. If the cell temperature is constant as might occur when skin is in contact with a solid surface or with flowing hot water, then Equ.1 may be integrated to give the time to cell death.

$$t_d = exp(75000 / T - 226.78) \qquad 2$$

According to this relation cell life is about 44 days at normal temperature (310 K) but falls to about 33 s if temperature rises by 20 °C to 330 K. If the cell is 100 μm from the surface then we have a second-degree burn (blistering) whereas if the cell is 2 mm from the surface we have a third-degree burn. Henriques found that first-degree burns (reddening) occurred when $\omega = 0.53$ and thus Equ.2 should be multiplied by 0.53 for first-degree burns. Pain usually occurs when the skin surface temperature reaches about 50 °C.

In general the cell temperature is not constant but fluctuates during the exposure time so Equ.1 cannot be solved analytically. However, it can be solved numerically if measured temperatures are available or if skin temperatures can be predicted using a suitable numerical model.

4. COMPUTER MODEL

One dimensional, transient heat conduction through skin may be modelled by the energy equation and Fourier's law of conduction and written in the form of a diffusion equation

$$\frac{\partial T}{\partial t} = \alpha \frac{\partial^2 T}{\partial x^2} + \frac{R}{\rho c_v} \qquad 3$$

Heat absorption rate per unit volume (R), when it exists, is usually due to the penetration of skin by incident radiation. The skin is modelled either as an opaque or as a semi-transparent wall of finite thickness and constant thermal properties, Fig.1. Wall thickness and the initial temperature distribution must be specified. The heat dose required to produce a given burn depends somewhat on the initial temperature of the skin.

The diffusion equation, Equ.3, may be solved by a suitable numerical method, Smith (1978), Crank and Nicolson (1947), using appropriate boundary and initial conditions. For example, it may be approximated as a set of finite difference equations. The position of imaginary nodes, distance δx apart, is shown in Fig.1. The surface node is T_1 and there are n nodes so the inner node temperature is T_{n+1}. If a simple, explicit, finite difference scheme is used then Equ.3 may be written as

$$F_i = (1 - 2p) T_i + p(T_{i+1} + T_{i-1}) + u R_i$$

$$i = 2,3,4 - --, n \qquad 4$$

$$p = \frac{\alpha \ \delta t}{\delta x^2} < 0.5 \qquad u = \frac{\delta t}{\rho \ c_v}$$

The restriction on the parameter p is necessary to avoid numerical instability in the solution. Since this equation cannot be used for surface nodes 1 and n+1 the temperature at these boundaries must be determined from the boundary conditions. If the heat input at the skin surface is q_0 and the inside wall is assumed to be cooled by convection to the blood stream, then the simplest expressions for the boundary temperatures are

$$F_1 = (1 - 2p) T_1 + 2p(T_2 + v \, q_0) + u \, R_1$$

$$u = \delta t / \rho c_v \qquad v = \delta x / k \qquad 5$$

$$F_{n+1} = [1 - (2 + w)p] T_{n+1} + p(2T_n + wT_b) + uR_{n+1}$$

$$w = 2 \, \delta x \, h_b / k$$

The surface heat input, q_0 may be time dependent and may arise from convection or from radiation. Other expressions for the boundary temperatures are used when Equ.5 is inadequate. For example, the surface temperature gradient may be represented as a fourth or fifth order equation, which gives greater accuracy at high rates of heat transfer. If the heat transfer coefficient is very large, the surface temperature

may be calculated from:

$$T_1 = \frac{v T_f + T_2 + 2T_3 - T_4}{2 + v}$$

$$v = 2\ \delta x\ h_f / k \qquad 6$$

$$q_0 = h_f\ (T_f - T_1)$$

Alternatively, Equ. (4) and (5) may be re-written in Crank-Nicolson form. This has the considerable advantage of being more accurate and stable for all values of the parameter p and the slight disadvantage of being an implicit rather than an explicit scheme.

The thermal properties of skin have been measured by numerous workers, Buettner (1952), Henriques (1947), Lipkin and Hardy (1954), Perkins et al (1952), Stoll and Greene (1959). The thermal properties are similar to those of water and have been summarised in Roth (1968). Weaver and Stoll (1969) found that skin conductivity increased dramatically at temperatures close to 33 °C. Takata (1974) and Kilminster (1974) have accepted these measurements, for example, but such non-linear behaviour is unlikely and has not been confirmed. The thermal properties used in this work are based on measurements made by Lawton and Laird (1989) and are summarised in Table 2; they are in general agreement with previously quoted sources. These properties vary somewhat from person to person and from place to place over the body.

Thermal conductivity varies with distance from the surface and with the state of vaso-dilation. As noted above, skin thickness varies from 0.5 mm at the eyelids to about 5 mm in the centre of the back; 2 mm is the average thickness. Thermal conductance, U, is a commonly used quantity in relation to body metabolism. It is defined as the heat lost from the body per unit area, divided by the difference between the body temperature (310 K) and the skin surface temperature. It is thus a measure of skin thickness, conductivity and the heat transfer coefficient of the blood supply to the skin, that is

$$\frac{T_b - T_1}{q_0} = \frac{1}{U} = \frac{X}{k} + \frac{1}{h_b} \qquad 7$$

The conductance varies over the body, being about 10 W/m^2K on the head and thighs and about 30 W/m^2K on the hands. An average value is about 17 W/m^2K. It also changes from about 17 to about 50 W/m^2K when the blood vessels dilate. The normal value, 17 W/m^2K, implies that the heat transfer coefficient between the skin and the blood is about 18 W/m^2K and the term X/k in Equ.7 may be ignored. When dilated the effective heat transfer coefficient increases to about 62 W/m^2K. It seems preferable to assume a finite skin thickness with a heat transfer coefficient derived from the known conductance rather than assume that the skin is semi-infinite.

Table 2. Thermal Properties of Skin

Thermal Conductivity, k	0.51	W/mK
Volumetric Specific Heat, ρc_v	3.67	MJ/m^3K
Thermal Diffusivity, α	1.39×10^{-7}	m^2/s
Thermal Inertia $k\rho c_v$	1.87×10^6	N^2/m^2K^2s
Skin Thickness, X	2	mm
Conductance,U	17	W/m^2K
Normal Heat Loss, Q	125	W
Surface Area, A	1.8	m^2
Surface Temperature, T_1	33 310	°C K

Table 3. Optical Properties of Skin

Source Temperature	< 2000 K	> 4000 K
Reflectivity	0.05	0.42
Emissivity	0.95	0.58
Penetration Depth	< 0.2 mm	2 mm

The optical properties of skin are required if the heat source is radiation. These properties depend on the wavelength of the incident radiation and, therefore,

on the temperature of the emitting source. Buettner (1952) has measured the reflectivity of skin, Fig.2a, and finds that it is constant for radiation source temperatures less than 2000 K and is substantially constant if it exceeds 4000 K. Buettner's data for white skin is summarised in Table 3.

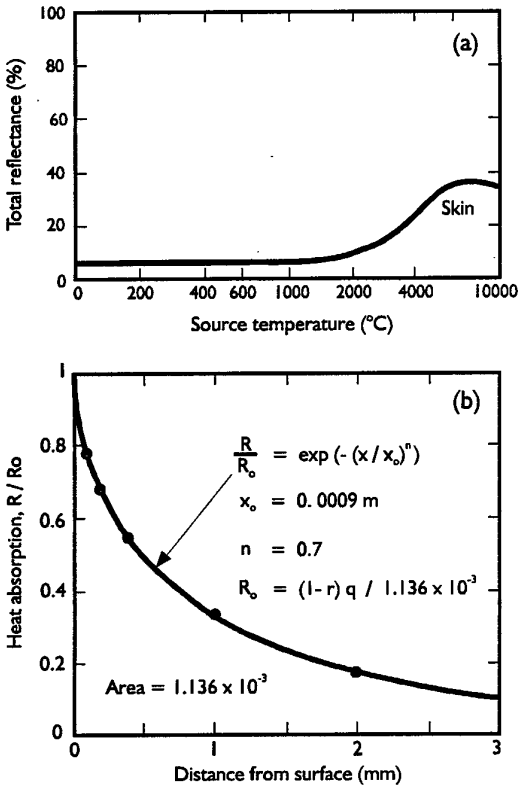

Fig.2 a. Total reflectance of white skin and b. Absorption of penetrating radiation. Buettner (1952)

The penetration depth gives some indication of the depth to which radiation will penetrate the skin before it is absorbed. For low temperature radiation, it is sufficiently accurate to assume that the incident radiation is absorbed at the surface. However, for high temperature radiation, above 2000 K, is better to use the experimental data of Buettner (1952), who found that white skin reflected 42% of incident radiation and absorbed 58% and that:

45.0% passed 0.1 mm depth,
39.6% passed 0.2 mm depth,
32.0% passed 0.4 mm depth,
19.0% passed 1.0 mm depth, and
10.2% passed 2.0 mm depth.

These data may be adapted to give the heat absorption rate per unit volume as

$$R = \frac{(1-r)\,q_0}{1.136x10^{-3}} \exp\left(-\left(\frac{x}{0.0009}\right)^{0.7}\right) \quad 8$$

Buettner's data on heat absorption and reflectivity Equ.8, are plotted in Fig.2b.

5. TYPICAL SKIN BURNS

Equ. (4), (5), (6), (7) and (8) form the basis a computer program. The program was checked for accuracy against standard analytical solutions for opaque thick slabs, Carslaw and Jaeger (1990) and for semi-transparent slabs, Lane (1990). These checks included

i. constant heat flux at one surface and constant temperature at the other surface,
ii. constant heat flux at one surface and zero heat flux at the other,
iii. constant radiation into a semi-infinite slab with a constant absorption coefficient.

In each case the error between the computed and analytical value was less than 0.3% and was usually less than 0.1%. The program was then used to compute skin burns for various conditions of heat input, and the length of time required to produce a first, second or third-degree skin burn determined. The program was tested against a wide range of experimental data for skin burns, and was found to predict the burn time with good accuracy. Before comparing the computed and experimental data, it is useful to examine the computed results in some detail.

For example, Fig.3a shows the skin temperature, heat dose, and burn damage during and after a 1.96 s exposure to hot water. In Fig.3a, the calculation is made for a depth of 1 mm. The temperature at this depth rises by about 20 °C after 4.5 s and then declines whereas the heat dose rises to about 150 kJ/m^2 at 1.96 s and then remains constant. The burn damage function 1 mm from the surface does not begin to rise until 2.5 s, that is, until about 0.5 s after exposure has ended. This is because it takes a finite time for heat to diffuse from the surface. The burn function rises to 1.0 after 24 s. The burn damage caused after exposure to the hot source may be called afterburning. The afterburning period can be quite

long, several minutes in some cases, and justifies the advice given to first aid workers, namely, that burn severity may be reduced by immersion in cold water immediately after exposure. In Fig.3a the afterburning period is about 22 s. It is a matter of trial and error to adjust the heat input to produce zero slope at ω=1.

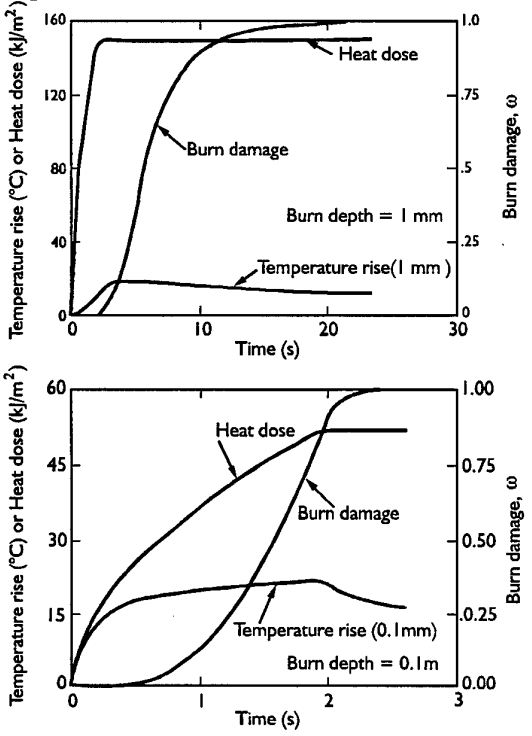

Fig. 3 Computed thermal reaction of skin exposed to hot flowing water. Exposure time is 1.96 s. Top. 3rd degree (1 mm) burn. Bottom. 2nd degree (0.1 mm) burn.

A slightly smaller heat dose causes a very large increase in burn time whereas a slightly larger heat dose gives a non-zero slope when the burn function is 1.0. Thus the heat dose required to produce a burn is well defined.

Fig.3b shows a similar set of results calculated for a burn depth of 0.1 mm. In this case, the exposure time remains the same, 1.96 s, but the water temperature is decreased to produce a second-degree burn. The temperature at 0.1 mm rises quickly by about 20 °C and then declines. At times greater than the exposure time, 1.96 s, the heat dose remains constant at about 52 kJ/m^2, the skin temperature falls, and the burn function continues to rise, reaching 1.0 at 2.95 s. In this case, the afterburning period is quite short, about 1 s. Again, a small decrease in heat dose makes it impossible for the burn function to reach 1.0 whereas a slight increase in heat dose gives a non-zero slope when the burn function is 1.0. When calculating the heat dose to produce skin burns it is important to include the afterburning period. Very misleading results may be obtained if the calculation is stopped when the exposure to heat ends. This is particularly important for short exposure times, intense heat transfer rates, and for deep dermal burns.

6. COMPARISON OF COMPUTED AND OBSERVED HEAT DOSE

Fig.4 shows the observed and computed burn times for skin in contact with flowing water at various temperatures. The experimental data are those of Henriques (1947) and the computed curves assume the surface heat transfer coefficient is 1 kW/m^{2}K, skin thickness is 2 mm and conductance is 17 W/m^{2}K. The skin temperature rises to a constant value for t > 100 s and so Equ.2 fits the observed results. For t < 100 s the skin temperature is unsteady but may be computed numerically; the resulting burn times are then in good agreement with Henriques observations.

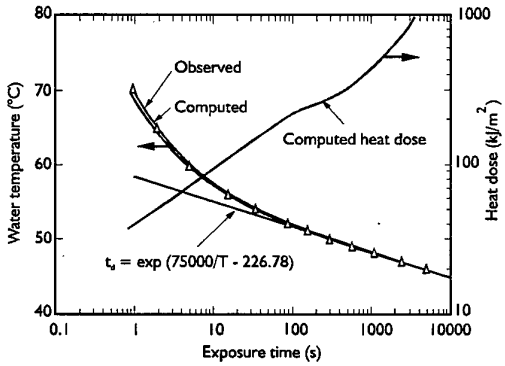

Fig.4 Comparison of computed and observed time for 2nd degree burns by contact with hot flowing water.

It is more usual to plot the heat dose required to produce a given burn against the burn time and so Fig.4 shows the computed heat dose for these conditions. An advantage of this plot is that the heat dose required to produce a burn is almost independent of fluctuations in the heat flux during the exposure time. It is found that the computed results for constant surface temperature, constant surface heat flux, convection, or non-penetrating radiation, all lie close to the same curve and give similar predictions for second-degree burns. This is illustrated in Fig.5

where the line for low temperature, non-penetrating radiation burns is almost identical to that calculated for convection burns in Fig.4. Moreover, the computed curve is in good agreement with measurements made by Stoll and Greene (1959) for second-degree burns using non-penetrating radiation.

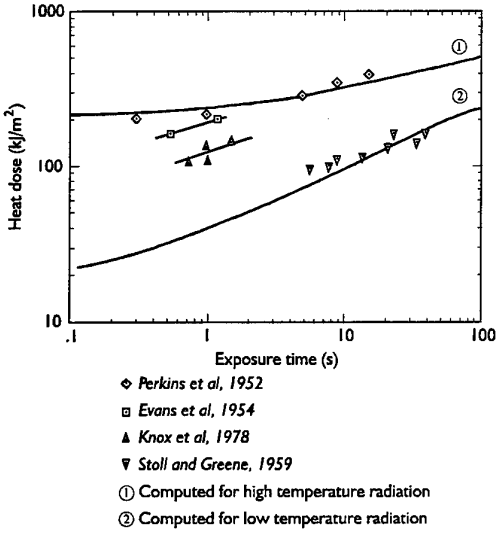

Perkins et al, 1952
Evans et al, 1954
Knox et al, 1978
Stoll and Greene, 1959

Fig.5 Comparison of computed and observed heat dose for 2nd degree burns (0.1 mm burn depth)

However, flash burns caused by penetrating radiation from a high temperature source, have been measured by Evans et al (1955), Knox et al (1978) and by Perkins et al (1952). Their results show that much greater heat doses are required to produce second-degree burns. The reason for this is that 42% of such incident radiation is reflected and the remaining 58% must penetrate the skin for 2 mm or so before it is absorbed. The incident energy is spread through a larger mass of material and this produces a smaller temperature rise. Such radiation is much less damaging than radiation from a low temperature source from which only 5% is reflected and penetration is only about 0.2 mm. As can be seen in Fig.5, the computer models this behaviour with good accuracy without having to change the constants in Henriques equation. The computed curve for high temperature radiation is for the extreme case where 42% of incident radiation is reflected and the remainder is absorbed at various depths as specified by Equ.8; all other data remain unchanged. The required heat dose is between 150% and 900% greater for penetrating radiation than for non-penetrating radiation. The computed results show very good agreement with the measurements of Perkins et al (1952). The heat doses measured by Evans et al (1954) and by Knox et al (1978) are smaller because these workers used cooler, less penetrating, radiation sources.

Fig.6 compares experimental and computed heat doses required to produce deep dermal (third-degree) burns from penetrating radiation. The computed curves are for second-degree and third-degree burns and the experimental results are those of Perkins et al (1952). For short duration burns there are marked differences between the heat doses required for different burn depths, but for long exposures the required heat doses are almost the same. During long exposures, the heat input is low and there is adequate time for conduction. The skin temperature is nearly uniform and the heat required for a burn on the surface is nearly the same as that required for a skin burn at 2 mm depth.

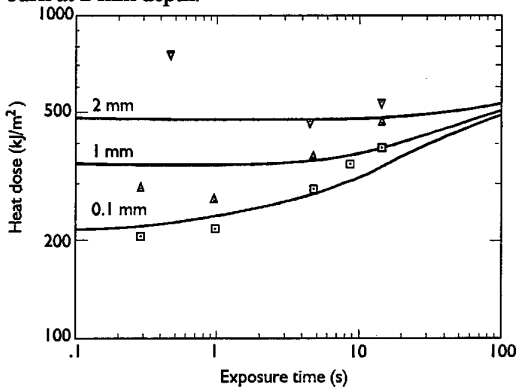

Fig.6 Computed and observed 3rd degree burns from a high temperature radiation source.

Perkins et al have attempted to assess burn depth by classifying their results as superficial dermal, mid dermal or deep dermal; but they do not specify burn depth numerically. It appears that mid dermal burns are about 1.5 mm deep whereas deep dermal burns are in excess of 2 mm deep.

7. APPLICATIONS OF BURNS THEORY

7.1 Pyrotechnic Fires

In the above analysis, a constant heat flux is assumed and this corresponds to the usual test conditions. However, real fires are characterised by a fluctuating heat flux and this causes burns at greater or lesser heat dose, depending on the how the heat flux varies with time. The U.K. Health and Safety Executive

has recently completed a study to determine the size and duration of fireballs produced by a number of pyrotechnic compositions. These were selected to provide representative examples of the range of potential fire hazards posed by materials manufactured and handled in the U.K. The chemical composition is specified by Wharton and Merrifield (1997). The experimental programme, Wharton et al (1995), examined quantities of material in the range 1-25 kg and included the measurement of the surface emissive power (radiation heat flux) of the fireballs. The pyrotechnic compositions and quantities tested are listed in Table 4.

Table 4. Pyrotechnic compositions tested

Pyrotechnic	Test Quantity (kg)
Gunpowder	1, 5, 10, 22.7, and 25
Flare Composition 1	1, 5, and 25
Flare Composition 2	0.8, 1, 5, and 19
Star Composition 1	1, 5, and 25
Star Composition 2	1, 5, and 25
Priming Composition 1	1, and 5
Priming Composition 2	1, 5, and 25
Delay Composition	1, 5, and 25

Test samples were spread to an even thickness in a circle on flat wooden boards supported by a metal frame. Ignition was by a remotely ignited electric fuse-head taped to a length of fast cord and buried in the sample. Visual records were made by video and high-speed film cameras and the images scaled by comparison with marker poles having 1 m bands. It was possible to measure the flame dimensions with an accuracy of 0.1m. The flame was assumed to correspond to either a sphere or a cylinder. In the latter case, the diameter of a sphere of equivalent volume is determined. The surface emissive power was measured using three fast response radiometers that had been calibrated against a black body source. The radiometers were positioned equally around the flame and were focussed on the point where the centre of the fully formed fireball was likely to occur.

Table 5. Fireball radius

Pyrotechnic	Fireball Radius m		
	1 kg	5 kg	25 kg
Gunpowder	1.6	2.4	4.5
Flare Composition 1	0.6	0.6	1.2
Flare Composition 2	1.0	2.4 (19 kg)	
Star Composition 1	1.7	3.5	-
Star Composition 2	0.8	1.4	2.1
Priming Composition 1	0.4	0.5	-
Priming Composition 2	1.2	2.2	2.9
Delay Composition	-	0.5	0.8

7.2. Burns Injuries

The maximum fireball diameter of the pyrotechnics tested is specified in Table 5 below and Fig.7a shows a typical heat flux measurement made during combustion of 1 kg of gunpowder. The heat flux is measured at the surface of the fireball at three positions 120 ° apart but for simplicity, only one result is shown. The time integral of the heat flux is the heat dose, which is also plotted in Fig.7a. The maximum value of the fireball radius is 1.6 m. To determine the radius at which a second-degree burn

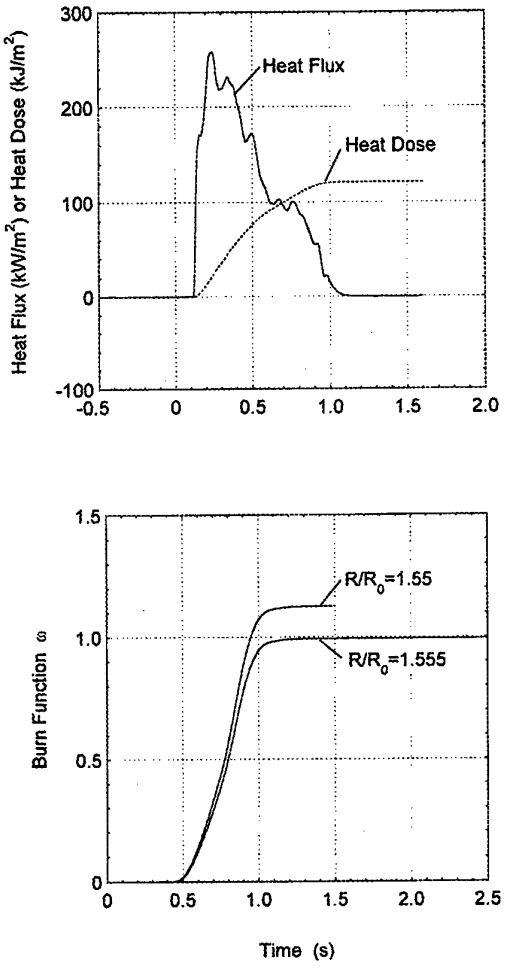

Fig.7 Top. Surface emissive power (heat flux) and heat dose measured during burning of 1 kg of gunpowder.
Bottom. Henriques' burn damage function at two slightly different radii from the fire.

occurs the measured heat flux (q_0) is used as input for the computer program which solves Equ.1, 4, 5, 6, 7, and 8. This heat flux is scaled using an inverse square law to estimate the heat flux at any radius R from the centre of the fireball. The burn damage ω at 0.1 mm from the skin surface is calculated at this radius. If $\omega < 1$ then the radius R is decreased and the calculation repeated. If $\omega > 1$ then the radius R is increased and the calculation repeated. If $\omega = 1$ after a sufficiently long time, then this is the radius at which a second-degree burn occurs. The procedure is illustrated in Fig.7b. For a third-degree burn, the same procedure is used but the burn function is calculated at a depth in excess of 0.5mm.

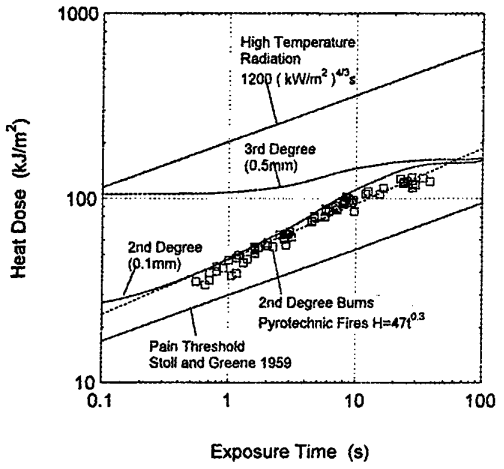

Fig.8 Second degree burns in the pyrotechnic fires compared with idealised (constant heat flux) fires. The pain threshold, 3rd degree burn, and 2nd degree (high-temperature radiation) burns are also illustrated.

The calculation procedure was repeated for all the pyrotechnic compositions and the results, for a second-degree burn, are plotted in Fig.8. Exposure times vary from 0.5 s to about 50 s and the trials data lies quite close to the theoretical second-degree burns line. The latter is computed for a constant radiation flux so the difference is caused by the variation in the measured radiation flux. The figure also shows, for information, the pain threshold determined by Stoll and Greene (1959), and the heat dose for third-degree burns (0.5 mm deep). If the exposure time is short then a third-degree burn requires three times more heat than a second-degree burn. However, if the exposure time is long the curves converge and the heat dose for second and third degree burns is almost the same. This is because during slow heating the temperature difference across the skin is small and thus cells deep in the skin layer are subjected to almost the same temperature as cells at the surface. Fig.8 also illustrates the high temperature (nuclear) radiation burns criterion, 1200 $(kW/m^2)^{4/3}$ s, that is often used in assessing thermal radiation burns, see Hymes et al (1996). It is, strictly, only applicable to radiation from nuclear explosions, or other very hot explosions.

8. QUANTITY-DISTANCE-BURN CURVES

In addition to giving the heat dose for second-degree burns, the computer progam also gives the radius at which this burn is sustained. Fig.9 illustrates the relation between second-degree burn radius and charge mass for two pyrotechnics, gunpowder and Flare Composition 2. The scatter in the experimental results is caused partly by slight crosswinds that cause some radiometers to record high and others to record low. The experimental results may be represented by a simple power law having an index between 0.33 and 0.5.

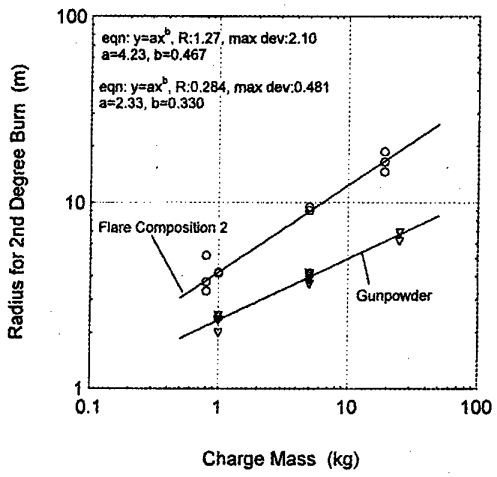

Fig.9 Relation between radius for 2nd degree burns and charge mass for gunpowder and flare composition 2.

The quantity-distance-burn relations for all pyrotechnic compositions have been determined for two conditions, namely, an "infinite" exposure and a five-second exposure. In "infinite exposure", the subject is exposed to the pyrotechnic fire for the whole period and does not move. In the "five-second exposure" the subject receives heat for the first five seconds only. After this, the subject is assumed to move away very quickly or seek shelter. Of course, an infinite exposure and a five-second exposure are the

Table 6. Quantity-Distance-Burn Relations for Various Pyrotechnics.
R=radius (m) and m = charge mass (kg) * indicates 5 s exposure.

Pyrotechnic	Third –degree	Second –degree	Pain
Gunpowder	$R=1.57m^{0.323}$	$R=2.33m^{0.33}$	$R=2.94m^{0.328}$
Flare Composition 1	$R=1.81m^{0.308}$ $*R=1.25m^{0.150}$	$R=2.12m^{0.29.2}$ $* R=1.71m^{0.153}$	$R=2.85m^{0.296}$ $*R=2.15m^{0.150}$
Flare Composition 2	$R=2.91m^{0.512}$	$R=4.22m^{0.467}$	$R=5.53m^{0.471}$
Star Composition 1	$R=2.45m^{0.588}$	$R=3.90m^{0.522}$	$R=4.82m^{0.531}$
Star Composition 2	$R=1.85m^{0.489}$	$R=2.49m^{0.469}$	$R=3.23m^{0.474}$
Priming Composition 1	$R=1.26m^{0.345}$ $*R=1.22m^{0.215}$	$R=1.49m^{0.360}$ $*R=1.56m^{0.265}$	$R=1.95m^{0.370}$ $*R=1.95m^{0.265}$
Priming Composition 2	$R=2.12m^{0.317}$	$R=3.06m^{0.303}$	$R=3.56m^{0.331}$
Delay Composition	$R=0.873m^{0.457}$ $*R=0.510m^{0.362}$	$R=0.973m^{0.465}$ $* R=0.686m^{0.364}$	$R=1.33m^{0.462}$ $*R=0.864m^{0.367}$

same if the exposure time is less than five seconds. In a real fire a subject may suffer infinite exposure if he is injured or trapped or is otherwise unable to move, but the five second exposure may be more realistic in the majority of cases. The quantity-distance-burn relations for all the pyrotechnic compositions and for both five-second and infinite exposures are specified in Table 6.

10. CONCLUSIONS

Henriques' theory of skin burns may be used to predict second and third-degree burns regardless of the heat source. The theory predicts conductive, convective, and low-temperature radiation burns. The heat dose for such burns depends mainly on the exposure time and is almost, but not quite, independent of transient variations in the incident heat flux. Radiation from a high-temperature source is much less damaging than radiation from a low-temperature source. This is because high-temperature radiation is reflected from the skin to a greater degree and because it penetrates the skin to a depth of about 3 mm before it is absorbed. The computer program models this behaviour and it is not necessary to modify Henriques' original theory.

Application of the theory to pyrotechnic fires has enabled the quantity-distance-burn relations to be determined for the tested pyrotechnics and provides a means of defining the level of exposure to which personnel may be subjected.

11. NOTATION

c_v	specific heat
h_b	blood-skin heat transfer coefficient
h_f	fluid-skin heat transfer coefficient
H_C	heat dose by convection
H_R	heat dose by radiation
F_i	temperature at node i at time t+δt
k	thermal conductivity
q	heat flux
q_0	surface heat flux
r	reflectance
R	heat absorption rate per unit volume or
R	distance from origin of fire
R_0	maximum fireball diameter
t	time

t_d	time to cell death
T	temperature
T_b	blood temperature
T_i	temperature at node i at time t
T_f	fluid temperature
U	skin conductance
x	distance from skin surface
X	skin thickness
α	thermal diffusivity, $k/\rho c_v$
δt	time increment
δx	distance between nodes
ΔT_i	initial temperature difference (probe-skin)
ΔT_p	change in probe temperature
ρ	density
ω	Henriques' thermal damage function

12. REFERENCES

Buettner, K.,1952, "Effects of Extreme Heat and Cold on Human Skin", *Journal of Applied Physiology*, Vol.5, pp 207-220.

Carslaw, H.S., and Jaeger, J.C.,1990, "Conduction of Heat in Solids", Oxford Science Publications, Clarendon Press, Oxford.

Crank, J and Nicolson, P.,1947, "A Practical Method for Numerical Evaluation of Solutions of Partial Differential Equations of the Heat Conduction Type", *Proc Camb Phil Soc*, Vol.43, pp 50-67.

Evans, E.I.,et al,1955, "Flash Burn Studies on Human Volunteers", *Recent Advances in Surgery, Surgery*, pp 239-297.

Henriques, F.C, 1947, "Studies of Thermal Injury: The Predictability and the Significance of Thermally Induced Rate Processes Leading to Irreversible Epidermal Injury", *Archives of Pathology*, Vol.43, No.5, pp 489-502

Henriques, F.C, and Moritz, A.R., 1947, "Studies of Thermal Injury: The Conduction of Heat Through the Skin and the temperature Attained Therein. A Theoretical and experimental Investigation", *American Journal of Pathology*, 23, pp 531-549.

Hymes, I, Boydell, W, Prescott, B.L., "Thermal Radiation: Physiological and Pathological Effects", I. Chem. E, Major Hazards Monograph, ISBN 0 85295 328 3.

Kilminster, D.T., 1974, "A Model to Predict Human Skin Burns". Ballistics Research Laboratory, Report AD/A-003, 918, Aberdeen Proving Ground, Maryland.

Knox, F.S, Watchel, T.L., and Knap, S.C., 1978, "Mathematical Models of Skin Burns Induced by Simulated Postcrash Fires as Aides in Protective Clothing Design and Selection", USAARL Rep 78-15, Fort Rucker, Al, US Army Medical Research Lab.

Lane, D.W., 1991,"The Optical Properties and Laser Irradiation of Some Common Glasses", *J. Phys.D:Appl.Phys*, Vol.23, pp 1727-1734.

Lawton, B., and Laird, M., 1989, "Assessment of Skin Burn Severity Behind Defeated Armour", Report SMMCE/TN/TP/0307/15, RMCS. Shrivenham, Wilts, UK.

Lawton, B., and Laird, M., 1993, "Assessment of Skin Burns Behind Defeated Armour", American Defence Preparedness Association, *14th International Symposium on Ballistics*, Quebec City, Canada, pp 785-794.

Lipkin, M., and Hardy, J.D., 1954, "Measurement of Some Thermal Properties of Human Tissues", *Journal of Appl Physiology*, Vol.7, No.2, pp 212-217.

Nili, E., and Kedem, R., 1984, "Burn Injury and Prevention in the Lebanon War, 1982", *Israeli Journal of Medical Science*, Vol20, p311.

Perkins, J.B., Pearse, H.E., and Kingsley, H.D., 1952, "Studies on Flash Burns: The Relation of Time and Intensity of Applied Thermal Energy to the Severity of Burns", Atomic Energy Report UR 217, Univ of Rochester, NY.

Roth, B.M., 1968, "Compendium of Human Responses of the Aerospace Environment", NASA-CR 1205, National Aeronautics and Space Administration, Washington, DC.

Smith, G.D., 1978, "Numerical Solution of Partial Differential Equations", Clarendon Press, Oxford.

Stoll, A.M., and Greene, L.C., 1959, "Relationship Between Pain and Tissue Damage Due to Thermal Radiation", *Journal of Applied Physiology*, Vol.14, No.3, pp 373-382.

Takata, A,, 1974, "Development of Criterion for Skin Burns", *Aerospace Medicine*, Vol.45, pp 634-637.

Weaver, J.A., and Stoll, A.M., 1969, "Mathematical Model of Skin Exposed to Thermal Radiation", *Aerospace Medicine*, 40, pp24-30.

Wharton, R.K., Harding, J.A., Barratt, A.J., and Merrifield, R., 1995, "Measurement of the Size, Duration and Thermal Output of Fireballs Produced by a Range of Pyrotechnics", Proc. 21st IPS, Moscow, Russia, 916.

Wharton, R.K. and Merrifield, R., 1997, "Thermal Hazards from Accidental Ignition of Pyrotechnic Compositions", *Journal of Pyrotechnics*, Number 6, pp1-8.

BIOMECHANICAL MODELING OF INJURY FROM BLAST OVERPRESSURE

James H. Stuhmiller, Paul J. Masiello, Kevin H. Ho
Jaycor
9775 Towne Centre Drive, P. O. Box 85154
San Diego, California 92186-5154, USA

Maria A. Mayorga, Nancy Lawless, Greg Argyros
Walter Reed Army Institute of Research
Building 511, Trailers-Forest Glen Annex
Silver Spring, Maryland 20910, USA

SUMMARY

The loading of the body by blast overpressure, often generated by explosives or weapon noise, can rapidly collapse the air-containing organs of the body and cause local injury. These effects can range from isolated pathologies, with no observable physiological consequences, to rupture of critical organs and death. Following World War II, animal models were used to study lethality, while in the past two decades the US Army Medical Research and Materiel Command has used animal models to study injury. The lethality data was correlated with pressure-duration characteristics of the free field blast, but these correlations become ambiguous in reverberant environments. Correlations have been proposed based on the motion of the thorax, but without a biomechanical basis, they do not provide insight into injury location or scaling with species and gender. A model of the thoracic injury process has been developed that provides both a biomechanical understanding and a good correlation of experimental observation. This paper reviews the mathematical model, the data supporting the choice of material properties, and the correlation of calculated internal stress with observed injury.

INTRODUCTION

The occupational standard for allowed exposures to short-duration, high-intensity noise, called impulse noise, is governed by Military Standard 1474 (1991). This standard is designed to protect against auditory injury by providing limits expressed in terms of peak pressure and B-duration, which is approximately the time between the first and last occurrence of pressures that exceed 10% of the peak. Each limitation is in the form of a line in the coordinates of peak pressure and B-duration. Personnel without hearing protection are limited to a peak no greater than 140 dB (the "W-line"). For personnel with single hearing protection, either earplugs or earmuffs, exposure is limited to 1000 repetitions per day for conditions at or below the "X-line," which allows increasing peak pressure at decreasing duration. When double hearing protection is worn, exposure is limited to 1000 repetitions at or below the "Y-line," which is 5 dB higher than the X-line. These levels may be increased if there are fewer exposures per day, according to a logarithmic trading rule.

The standard contains an absolute upper limit on exposures, no matter what the hearing protection and no matter how few repetitions, called the "Z-line," which is 6.5 dB above the Y-line. This limit is to protect against "nonauditory" injury, that is, injury to other organs that will not be protected by ear muffs and plugs. The nature and location of these injuries is not specified.

In the late 1970s, new howitzers were introduced in training, fitted with anti-recoil muzzle brakes, that deflect a significant part of the propulsion gasses back toward the crew area. The large peak pressures measured in the crew area exceeded the Z-line. Over the following years, other systems, such as shoulder-fired anti-tank weapons, also exceeded the nonauditory limits. As weapons were fired from enclosures, the reverberations led to long durations, which also caused the Z-line to be exceeded.

Although there were anecdotal complaints from soldiers training with the weapons, it was generally felt that the Z-line was too conservative. Beginning with the howitzers, human volunteer studies were conducted to confirm that the levels were safe. This case-by-case approval of training conditions was very expensive and time-consuming and further delayed the deployment and training of new weapon systems.

Despite the probable overstatement of risk at the Z-line, blast overpressure is known to cause serious injury and death. Following World War II, a long-term research effort was conducted at the Kirtland Air Force Base in New Mexico to establish the parameters causing lethality. A wide range of animal species was studied (from mice to oxen) under free-field explosive and shock tube generated blast waves. The results were summarized in the so-called Bowen curves, which correlated 50% lethality with peak pressure and A-duration, the time the pressure remains positive (White, et al., 1971). All large animal results could be made to agree with a single curve by scaling the duration by a power of the body mass. All small animal results collapsed to a different, single curve. The Bowen results do not provide estimates of injury levels or thresholds and so cannot be used as a replace-

Papers presented at the RTO HFM Specialists' Meeting on "Models for Aircrew Safety Assessment: Uses, Limitations and Requirements", held in Ohio, USA, 26-28 October 1998, and published in RTO MP-20.

ment for the Z-line. It was speculated that the Bowen curves could be arbitrarily reduced in peak pressure to provide a nonauditory criterion, but there was no credible data supporting those limits. Furthermore, the long durations seen in enclosures led to unrealistic estimates of lethality when the Bowen curve was used.

Starting in the early 1980s, the US Army Medical Research and Materiel Command (MRMC) took over the Kirtland Blast Overpressure Test Site and began a series of studies aimed at determining nonauditory injury modes and threshold levels. A single species, sheep, was selected because of its anatomical similarity with the human thorax. Over the next 15 years, over 1100 animal exposures were conducted in the free field and in enclosures.

About the same time, the MRMC began a parallel program to develop a biomechanical understanding of blast overpressure injury that could be used to correlate the animal data, extrapolate to man, and provide a basis for making health hazard assessments for exposures exceeding the Z-line. The work initially investigated abdominal and upper respiratory injuries, but eventually concentration on injuries to the lung. By the late 1980s, the mechanism of lung contusion was understood and a biomechanical-based method of estimating lung injury was developed. Medical personnel at the Walter Reed Army Institute of Research (WRAIR) have used this methodology since that time to prospectively validate the model predictions and to make health hazard assessments for new systems without requiring human exposure testing. A review of that work can be found in Stuhmiller, et al. (1996).

The final phase of the MRMC effort is to transition these findings into a revision of the Military Standard. Several activities are being pursued, all aimed at obtaining peer review and consensus. This paper deals with one of those aspects: the estimation of chest wall motion under blast loading. To put the importance of chest wall motion in perspective, we review previous findings.

PREVIOUS RESULTS

All organs injured by blast overpressure are air-containing or are stressed by neighboring air-containing organs. Gross compression of the lung, however, is not a source of injury since these volumetric changes are within the normal physiological range. Attempts to correlate injury to overall compression have proven to be negative (Josephson, et al., 1988).

On the other hand, the importance of local compression within the lung, especially compression waves, has been suspected for a long time. Clemedson and Jönsson (1962) observed compression waves in the lungs of rabbits injured by blast. However, it was the work conducted at the University of California, San Diego, under MRMC sponsorship, that quantitatively linked this waves to tissue damage and the formation of edema (Yen, 1988). The exact mechanism of tissue damage is unknown, although speculated upon (Fung, et al., 1988). Nonetheless, the correlation of observed injury patterns with wave concentration points is compelling (Stuhmiller, et al., 1989).

The origin of these compression waves is also well known: the piston-like motion of the chest wall into the lung parenchyma. Because the lung tissue is composed of trapped air regions, the lung has compressibility of gas, but the inertia of tissue. This combination leads to a compression propagation speed of 30-50 m/s that has been well documented (Rice, 1983, Fung, 1985). The chest wall can obtain velocities of 10-30 m/s during blast loading, resulting in internal pressure waves with peak values of 60 kPa or more, which are further amplified by internal reflections. These pressures dwarf those generated by gross compression of the lung or the minuscule sound wave pressures transmitted through the thoracic wall.

Estimation of the magnitude of these waves turns out to be rather easy. Experiments with lung surrogate materials (Yu, et al., 1990) found that the wave pressure (without internal reflections) was proportional to the chest wall velocity. Numerical studies (VanderVorst, et al., 1990)

NOMENCLATURE

p_w	kPa	Pressure in lung compression wave
ρ	kgm/m^3	Mass density of lung
v	m/s	Velocity of chest wall
M/A	kgm/m^2	Areal mass density of thorax
p_{load}	kPa	Pressure loading on chest due to blast
W	---	Normalized energy in lung compression wave
T	sec	Time
P_{atm}	kPa	Atmospheric pressure
V_{lung}	m^3	Volume of lung
P	---	Probability of lung injury
b_0,b_1	---	Coefficients in log-logistic regression
N	---	Number of exposure repetitions
M_1	kgm	Mass of skin layer over "sternum"
C_{12}	N-S/m	Damping coefficient for skin layer
A_F	m^2	Area of moveable section of chest wall
A_B	m^2	Frontal area of body

showed that the experimental results could be understood from the composite (gas-tissue) nature of the lung. Finally, an analytic form of the result can be derived from an analogy with gas dynamics (Landau and Lifshitz, 1959), which includes the nonlinear effects as the chest wall approaches the wave speed (shock formation). For all threshold conditions, the linear form in adequate

$$p_w(t) = \rho\, c\, v(t) \quad (1)$$

Here ρ is the mass density and c is the speed of sound in the lung parenchyma and v(t) is the inward velocity of the chest wall.

The chest wall moves under the influence of the external blast wave loading, P_{load} (t), the reaction force of the compressed lung tissue, p_w (t), and the mechanical forces that develop within the thoracic wall (ribs, musculature, etc.). Limited data on chest wall motion (Dodd, 1987) under blast loading indicated that the thoracic forces were negligible during high intensity, short duration blast loading. Consequently, the Pleural Surface Model (PSM) of chest wall dynamics was proposed

$$(M/A)\, dv/dt = P_{load}(t) - p_w(t) \quad (2)$$

where (M/A) is the areal mass density of the thorax.

Local injury patters are associated with the details of the wave motion, but for the purposes of estimating threshold injury, the total energy in the wave, normalized to the thermodynamic energy in the lung gasses, was selected as a correlate

$$W = [\int dt\, p_w(t)\, v(t)]/[P_{atm}\, V_{lung}] \quad (3)$$

where P_{atm} is the atmospheric pressure and V_{lung} is the volume of the lung. This normalized work, W, proved to be an excellent correlate of injury, pathology, and lethality and to provide a natural scaling across animal species, reproducing the Bowen curves. A complete discussion is found in Stuhmiller, et al. (1996).

MODEL EXTENSION

The Pleural Surface Model (PSM) of chest wall motion, combined with normalized work, has satisfactorily correlated lung contusion injury data over a wide range of blast conditions, both retrospectively and prospectively. Nonetheless, there are reasons to validate the thoracic response model directly against chest wall motion data.

First, on general principles, every aspect of a model should be confirmed. Although no *blast-driven* chest wall motion data are available, there are data on *blunt impact* to man available in the car crash literature. To make this comparison, the PSM must be extended to impact loading.

Second, the PSM does not account for whole body motion, which can be significant in some blast environments. The model tacitly assumes that the lung tissue is at rest. In actuality, the lung moves with the whole body and it is the relative velocity of the chest to lung tissue that provides the compression and generates the waves.

Finally, there is a growing interest in estimating the injury from nonpenetrating projectile impact. The PSM deals only with distributed forces (pressure) and distributed inertia (M/A) and so cannot be directly used to estimate the chest wall motions associated with local impact. In fact, the extent of the thoracic wall that is in motion is not defined in this model.

One alternative is to use finite element analysis (FEA) instead of the simplified model. In principle, all loading conditions can be described and normalized work can be computed from the resulting, three-dimensional chest wall motion. In practice, FEA introduces too much complexity for an operational safety criterion.

Another alternative is to use the thoracic motion model, developed by the automotive industry (Lobdell, 1972) that has been calibrated for large mass impacts against human cadavers. This model has the converse problem, it defines the thorax by a mass, without specifying the area. Therefore, we do not know how to apply a blast pressure force. In addition, the Lobdell model is not biomechanically based, that is, its many parameters (masses, springs, dampers) have been selected to fit thorax response data. They are not related to anatomical features and they have not been determined by independent material property tests. Nonetheless, it is the best (only) simple response model accounting for chest wall forces.

This paper describes the use of FEA of thoracic response to both local and distributed loading to extend the Lobdell model to blast loading.

THORACIC FINITE ELEMENT MODEL

A finite element model (FEM) was constructed in LS-DYNA-3D software from the Visible Man data set. Representative slices from the shoulder to the abdomen were taken from the photographic image set. The images were categorized into tissue classes: chest wall, right and left lung lobes, heart, and abdominal contents. Three dimensional block elements were chosen to conform to the geometry seen in each slice and to minimize the distortion between slices. The diaphragm was not resolved as a separate material. Details are found in Masiello (1997).

The material properties varied with each tissue type. The heart and abdominal contents were treated as low shear modulus, incompressible liquids. The lung was modeled as a hydrodynamic-elastic material, the elastic component representing the lung tissue and the hydrodynamic part providing the gas compressibility. The properties were selected to reproduce the proper compression wave speed.

The thorax wall was modeled as a single, elastic material with properties approximating the composite properties of bone, muscle, and cartilage. No attempt was made to resolve internal structure, such as the ribs and spinal processes, but the correct anatomical variation of wall thickness was preserved. The material properties were based on Sundaram and Feng (1977). The Young's modulus of the composite material was adjusted, within the range of component properties, to gain agreement with frontal impact tests. Values are shown in the following table.

Component	Density gm/cm^3	Young's Modulus dynes/cm^2	Shear Modulus dynes/cm^2	Poisson's Ratio	Sound Speed cm/sec
Thorax Wall:					
Outer band	1.0	6.0×10^6	---	0.30	---
Inner band[1]	1.5	5.0×10^7		0.10	
Lungs	0.1	---	7.33×10^3	---	3000
Heart	1.06	---	7.96×10^4	---	---
Abdomen	0.95	6.89×10^5	---	0.30	---

FEM RESPONSE RESULTS

The human cadaver impact tests of Kroell (1971) were simulated as a contact-impact problem. These test data were used by Lobdell to calibrate his model. The 6-inch diameter impactor was simulated as a separate, rigid object and allowed to hit the model in the frontal and oblique directions, corresponding to the reported test conditions.

The force-displacement curves are reasonably reproduced by the model (Figures 1 and 2). The thorax wall properties were adjusted to give agreement with the frontal impacts. The oblique impact was at an angle of 60°. The force increases rapidly within an initial displacement of a fraction of an inch and then is approximately constant until the maximum displacement is reached. The expansion of the thorax proceeds along an entirely different trajectory.

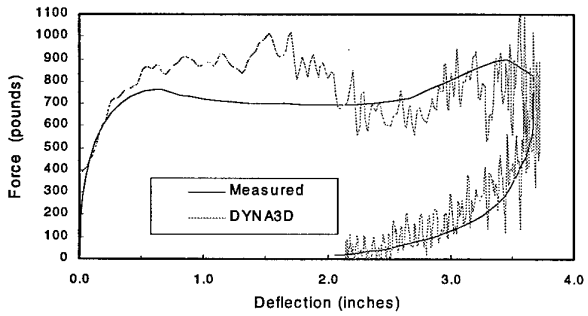

Figure 1. Finite element model simulation of frontal impact tests of Kroell, et al. (1971).

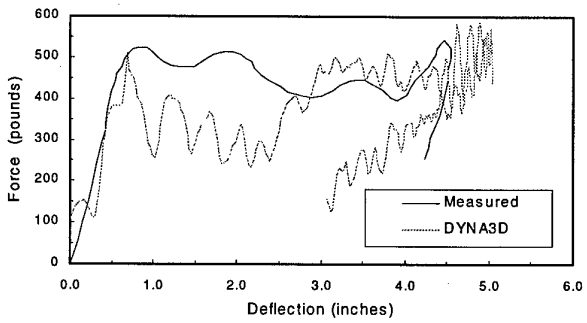

Figure 2. Finite element model simulation of oblique impact tests of Kroell, et al. (1971).

In addition to demonstrating the validity of the model to these blunt impacts, the results underscore the nature of the thoracic response. At large chest wall velocities, the forces are nearly independent of displacement (not spring-like) and in fact are dominated by velocity-dependent forces. Only when the displacements are large (several inches) and the velocities reduced, do the elastic components dominate. At these displacements, rib fracture is likely. This extreme motion will not be reached under blast loading.

FEM INJURY DISTRIBUTION COMPARISON

Internal compression waves are generated by all parts of the thorax under motion and these waves combine internally and are amplified at locations of internal reflection. Consistent with the observation that these internal pressure waves are the mediators of lung contusion, we expect to see a correlation between regions of high pressure and observed injury. The injury pattern seen in a free field blast exposure, in which only one side of the body experiences the principal blast loading, is primarily on the exposed side and concentrated at the tips of the diaphragmatic lobes. This same pattern is observed in the pressure contours produced by the simulation (Figure 3). When the blast exposure occurs in an enclosure, both sides of the thorax are loaded by the blast wave and lung contusion is more distributed among the lobes. Again, this pattern is reflected in the calculated pressure distribution (Figure 4).

EXTENDED LOBDELL MODEL

The FEM model is used to extend the Lobdell model so that it will be applicable to both small and large area impacts and to the distributed loading of blast. First, the conceptual framework is extended to allow the "body" mass to have a frontal area. This area is necessary so the blast wave can deliver momentum to the whole body. See Figure 5. Next, a mass is added corresponding to the skin layer over the sternum. In the original Lobdell model the

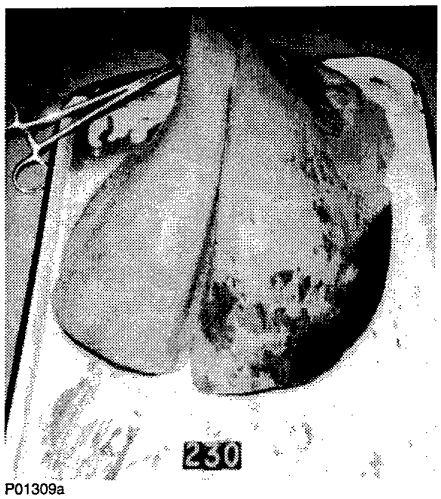

P01309a

(a) Pathology photograph

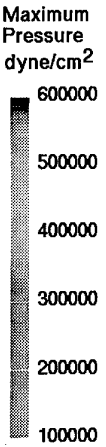

DYNA3D CALCULATION WITH SEVERE INJURY LOADING

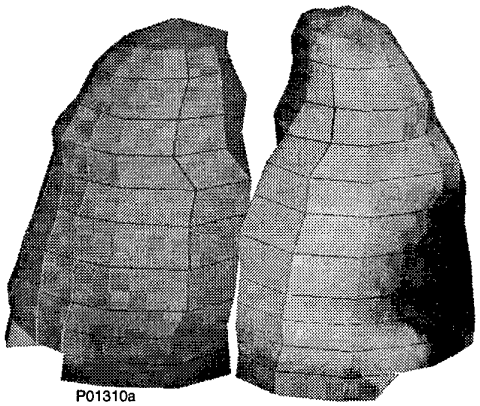

P01310a

(b) FEM simulation

Figure 3. Comparison of maximum internal pressure distribution in lung with observation of pleural surface contusion. Loading is from a right side incident blast wave.

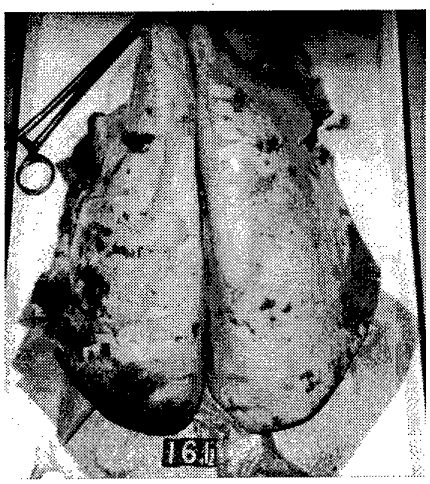

P01317

(a) Pathology photograph

DYNA3D SIMULATION OF COMPLEX WAVE LOADING

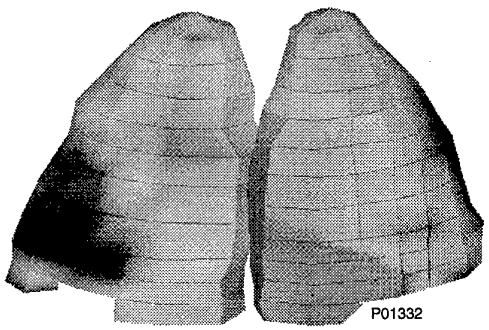

P01332

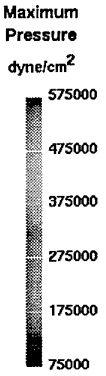

DORSAL VIEW

(b) FEM simulation

Figure 4. Comparison of maximum internal pressure distribution in lung with observation of pleural surface contusion. Loading is from a whole body blast wave in an enclosure.

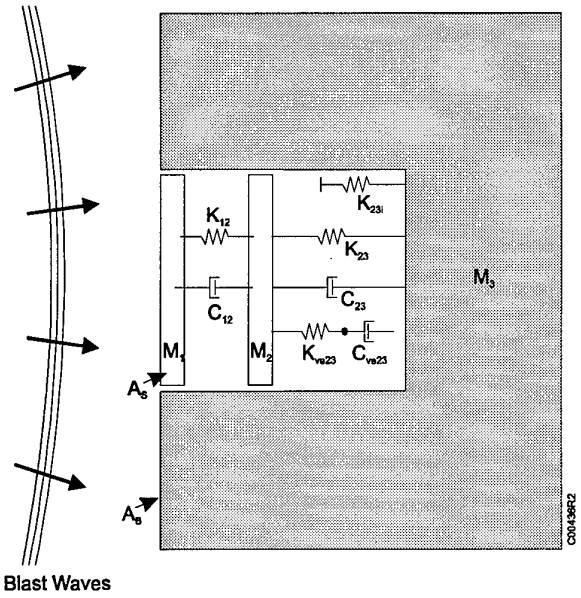

Figure 5. Schematic diagram of modified Lobdell model of thoracic response. Modified model includes a skin mass (M_1), a skin damping coefficient (C_{12}), and areas associated in the moveable part of the chest (A_S) and the rest of frontal body area (A_B). Other parameters are the same as proposed by Lobdell (1972).

skin was represented by the spring, K_{12}, so that impacting masses would gradually transfer their momentum. The skin mass is chosen to be $1/100^{th}$ of the sternum mass, so there is no effect on previous impactor results. A damper, C_{12}, is added based on Hill skin data quoted in Fung (1981).

The effective area of motion under loading, the "sternum" area, is selected so that the total energy in the lung compression wave is equal to that computed by the FEM. For small area impacts, the effective area is found to be 95 cm^2, while for blast loading over the entire front, the effective area is found to be 175 cm^2. Finally, the total frontal area presented to the blast is estimated to be 885 cm^2.

CORRELATION OF LUNG INJURY

As in the case of the Pleural Surface Model, we use the MRMC Blast Pathology Database to determine a correlation with observed lung contusion. This database contains over 1100 animal exposures (sheep) to blasts in the free field, in enclosures, and from simulated weapon firing. The data includes pressure traces, necropsy photographs, and pathological observations. All organ systems and many organ subsystems were recorded. Over the 15 years that the data was collected, the injury grading system took on greater and greater detail. The injury scoring that could be applied across the entire database is based on the percent of lung area contused (none, trace = a few petechia, slight < 5%, moderate < 20%, severe > 40%). There are 776 animal exposures in the database with complete enough pressure and pathology to correlate model predictions.

The loading prescription follows that described in Stuhmiller, et al. (1966). Where the Blast Test Device (a thorax-sized cylinder with flush mounted load gages in each quadrant) data is available, the loads were used as measured. Where only free field gages were available, the frontal load is assumed to be equal to a reflected wave and the other quadrants equal to the incident wave. The normalized work is the sum of the work computed from each orientation.

Log-logistic regression is used to determine the correlation, with normalized work, W, and number of exposures, N, as independent variables and occurrence of any lung contusion as the dependent variable. The coefficients were estimated with maximum likelihood and the computations made with Statistica©. The probability of lung injury, P, follows the correlation

$$\ln(P/1\text{-}P) = b_0 + b_1 \ln (W * N^{0.125}) \qquad (4)$$

with $p < 0.0001$. The comparison of the regression and the animal data is shown in Figure 6. For visualization purposes, the data has been placed in groups of 25, ordered by $W * N^{0.125}$. All but one of these groups falls within the 95% confidence bands of the correlation.

From this correlation a new exposure standard can be determined. Currently a criterion based on 95/95 values (95% confidence of 95% protection) is under review by WRAIR and MRMC.

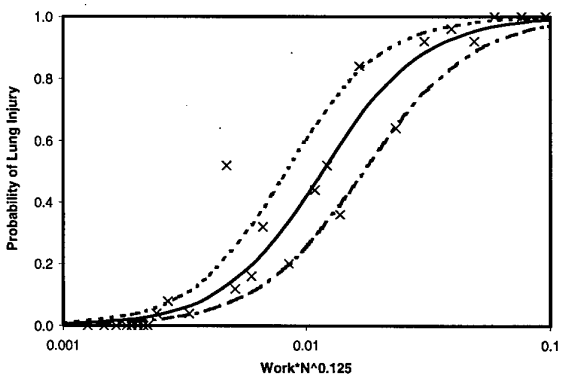

Figure 6. Comparison of log-logistic regression (——) and 95% confidence trends (---) with animal injury rates as computed for groups of 25 (X).

CONCLUSIONS

A model for the chest wall response to blast loading has been developed, based on a previously used model for crash tests. The effective area of the thoracic motion has been calibrated by finite element analysis. The resulting model reproduces previous large impactor tests and small projectile and blast loading.

The correlate of lung injury, total energy in the lung compression wave, is based on previous direct observations of lung injury. A correlation between this normalized work, the number of exposures and lung injury was found with log-logistic regression using 776 tests from the MRMC Blast Pathology Database. A safe exposure level determined by 95% confidence of 95% protection is under consideration as a new standard.

ACKNOWLEDGEMENTS

The authors acknowledge the support of the US Army Medical Research and Materiel Command under Contract DAMD-17-96-C-6007.

REFERENCES

Clemedsen, C.J. and Jönsson, A. (1962). Distribution of Extra- and Intra-thoracic Pressure Variations in Rabbits Exposed to Air Shock Waves. *Acta. Physiol. Scand.*, 54: 18-29.

Dodd, K.T. (1987). Analysis of Field Test Results of the Biophysical Response of Sheep to Blast Loading. In Proceedings of the Tenth International Symposium of Military Applications of Blast Simulation, Bad Reichenhall, West Germany.

Fung, K.C., Yen, M.R. and Zeng, Y.J. (1985). Lung Dynamics and Mechanical Properties Determination. Volume 3 of Characterization and Modeling of Thoraco-Abdominal Response to Blast Waves. Final Report for Contract DAMD17-82-C-2062, Jaycor, San Diego, California.

Fung, Y.C. (1981). Biomechanics, Mechanical Properties of Living Tissues. Springer-Verlog, New York.

Fung, Y.C., Yen, R.T., Tao, Z.L. and Liu, S.Q. (1988). A Hypothesis on the Mechanism of Trauma on Lung Tissue Subjected to Impact Load. *J. Biomech. Eng.*, 110: 50-56.

Josephson, L.H. and Tomlinson, P. (1988). Predicted Thoracic-abdominal Response to Complex Blast Waves. *J. Trauma*, 28: S116-S124.

Kroell, C.K., Schneider, D.C., and Nahum, A.M. (1971). Impact Tolerance and Response of the Human Thorax. In Proceedings of the 15th STAPP Car Crash Conference, Coronado, California.

Landau, L.D. and Lifshitz, E.M. (1959). Fluid Mechanics. Pergamon Press, London.

Lobdell, T.F. (1972). Impact Response of the Human Thorax. In Proceedings of the Symposium: Human Impact Response Measurement and Simulation. Plenum Press, New York.

Masiello, P.J. (1997). A Finite Element Model for Analysis of Thoracic Injury. Technical Report under Contract DAMD17-96-C-6007, Jaycor, San Diego, California.

Military Standard: Noise Limits for Military Materiel. (1991). Mil-Std 1474(C).

Rice, D.A. (1983). Sound Speed in Pulmonary Parenchyma. *J. Appl. Physiol.: Respir. Envir. Exercise Physiol.*, 54: 304-308.

Stuhmiller, J.H., Chuong, C.J., Phillips, Y.Y., and Dodd, K.T. (1988). Computer Modeling of Thoracic Response to Blast. *J. Trauma,* 28: S132-S239.

Stuhmiller, J.H., Ho, K.H-H., Vander Vorst, M.J., Dodd, K.T., Fitzpatrick, T. and Mayorga, M. (1996). A Model of Blast Overpressure Injury to the Lung,", *J. Biomech.*, 29: 227-234.

Sundaram, S.H. and Feng, C.C. (1977). Finite-Element Analysis of the Human Thorax. *J. Biomech.*, 10: 505-516.

Vander Vorst, M.J. and Stuhmiller, J.H. (1990). Calculation of the Internal Mechanical Response of Sheep to Blast Loading. Technical Report under Contract DAMD17-85-C-5238, Jaycor, San Diego, California.

White, C.S., Jones, R.K., Damon, E.G., Fletcher, E.R., and Richmond, D.R. (1971). The Biodynamics of Airblast. Technical Report DNA 2738T, Lovelace Foundation for Medical Education and Research, Albuquerque, New Mexico.

Yen, R.T., Fung, Y.C., and Liu, S.Q. (1988). Trauma of Lung Due to Impact Load. *J. Biomech.*, 21: 745-753.

Yu, J.H.Y., Ho, H.H. and Stuhmiller, J.H. (1990). A Surrogate Model of Thoracic Response to Blast Loading. Technical Report under Contract DAMD17-85-C-5238, Jaycor, San Diego, California.

REPORT DOCUMENTATION PAGE

1. Recipient's Reference	2. Originator's References	3. Further Reference	4. Security Classification of Document
	RTO-MP-20 AC/323(HFM)TP/7	ISBN 92-837-1017-7	UNCLASSIFIED/ UNLIMITED

5. Originator Research and Technology Organization
North Atlantic Treaty Organization
BP 25, 7 rue Ancelle, F-92201 Neuilly-sur-Seine Cedex, France

6. Title

Models for Aircrew Safety Assessment: Uses, Limitations and Requirements

7. Presented at/sponsored by

the Human Factors and Medicine Panel (HFM) Specialists' Meeting held at Wright-Patterson Air Force Base, Ohio, USA, 26-28 October 1998.

8. Author(s)/Editor(s)	9. Date
Multiple	August 1999
10. Author's/Editor's Address	**11. Pages**
Multiple	360

12. Distribution Statement There are no restrictions on the distribution of this document. Information about the availability of this and other RTO unclassified publications is given on the back cover.

13. Keywords/Descriptors

Aviation safety
Flight crews
Computerized simulation
Models
Impact analysis
Escape systems
Acceleration stresses (physiology)
Acceleration tolerance
Motion sickness
Decompression sickness
Altitude
Mechanical shock
Overpressure
Blast effects
Biodynamics
Vibration
Human factors engineering
Man machine systems
Finite element analysis
Protective equipment
Safety engineering
Stress (physiology)
Push-pull effect
Protective clothing
Anti-g suits
Battlefields
Traumatic disorders
Data bases
Dummies
Ejection seats
Anthropometry
Biomechanics
Casualties
Evaluation
Windblast
Directed energy
Live fire

14. Abstract

These proceedings include the Technical Evaluation Report, a tribute to Dr. Henning E. von Gierke, Director Emeritus, Wright-Patterson Air Force Base (WPAFB), OH, three Keynote Addresses and 32 invited papers of a Specialists' Meeting sponsored by the NATO/RTO Human Factors and Medicine Panel. It was held at WPAFB from 26-28 October 1998.

Significant advances have been made in modelling human physical and physiological responses to extreme environments. Technological advances in computer speed and power have made modelling a feasible research and design tool. Computer simulations are being used extensively for predicting human physical and physiological responses, for reducing testing requirements, for rapidly designing improved protective systems, and for performing human safety-systems analyses. A variety of models were reviewed at this Specialists' Meeting including lumped-parameter, rigid-body, finite-element, statistical, physiologic, and empirical models. Topics covered included modelling human-body responses to environmental stressors, and the systems with which the body interacts to: impact, emergency escape, sustained acceleration, vibration, mechanical shock, motion sickness, high altitude, blast, extreme thermal conditions, directed energy and live firing.

These proceedings will be of interest to military and civilian scientists and engineers interested in exploiting data bases, tolerance criteria, and new models and methods in the research of physiological systems and in simulating the design, test set up and evaluation of safety systems.

NORTH ATLANTIC TREATY ORGANIZATION

RESEARCH AND TECHNOLOGY ORGANIZATION
BP 25 • 7 RUE ANCELLE
F-92201 NEUILLY-SUR-SEINE CEDEX • FRANCE
Télécopie 0(1)55.61.22.99 • E-mail mailbox@rta.nato.int

DIFFUSION DES PUBLICATIONS
RTO NON CLASSIFIEES

L'Organisation pour la recherche et la technologie de l'OTAN (RTO), détient un stock limité de certaines de ses publications récentes, ainsi que de celles de l'ancien AGARD (Groupe consultatif pour la recherche et les réalisations aérospatiales de l'OTAN). Celles-ci pourront éventuellement être obtenues sous forme de copie papier. Pour de plus amples renseignements concernant l'achat de ces ouvrages, adressez-vous par lettre ou par télécopie à l'adresse indiquée ci-dessus. Veuillez ne pas téléphoner.

Des exemplaires supplémentaires peuvent parfois être obtenus auprès des centres nationaux de distribution indiqués ci-dessous. Si vous souhaitez recevoir toutes les publications de la RTO, ou simplement celles qui concernent certains Panels, vous pouvez demander d'être inclus sur la liste d'envoi de l'un de ces centres.

Les publications de la RTO et de l'AGARD sont en vente auprès des agences de vente indiquées ci-dessous, sous forme de photocopie ou de microfiche. Certains originaux peuvent également être obtenus auprès de CASI.

CENTRES DE DIFFUSION NATIONAUX

ALLEMAGNE
Fachinformationszentrum Karlsruhe
D-76344 Eggenstein-Leopoldshafen 2

BELGIQUE
Coordinateur RTO - VSL/RTO
Etat-Major de la Force Aérienne
Quartier Reine Elisabeth
Rue d'Evère, B-1140 Bruxelles

CANADA
Directeur - Recherche et développement - Communications et gestion de l'information - DRDCGI 3
Ministère de la Défense nationale
Ottawa, Ontario K1A 0K2

DANEMARK
Danish Defence Research Establishment
Ryvangs Allé 1, P.O. Box 2715
DK-2100 Copenhagen Ø

ESPAGNE
INTA (RTO/AGARD Publications)
Carretera de Torrejón a Ajalvir, Pk.4
28850 Torrejón de Ardoz - Madrid

ETATS-UNIS
NASA Center for AeroSpace Information (CASI)
Parkway Center
7121 Standard Drive
Hanover, MD 21076-1320

FRANCE
O.N.E.R.A. (ISP)
29, Avenue de la Division Leclerc
BP 72, 92322 Châtillon Cedex

GRECE
Hellenic Air Force
Air War College
Scientific and Technical Library
Dekelia Air Force Base
Dekelia, Athens TGA 1010

HONGRIE
Department for Scientific Analysis
Institute of Military Technology
Ministry of Defence
H-1525 Budapest P O Box 26

ISLANDE
Director of Aviation
c/o Flugrad
Reykjavik

ITALIE
Centro documentazione tecnico-scientifica della Difesa
Via Marsala 104
00185 Roma

LUXEMBOURG
Voir Belgique

NORVEGE
Norwegian Defence Research Establishment
Attn: Biblioteket
P.O. Box 25
NO-2007 Kjeller

PAYS-BAS
NDRCC
DGM/DWOO
P.O. Box 20701
2500 ES Den Haag

POLOGNE
Chief of International Cooperation Division
Research & Development Department
218 Niepodleglosci Av.
00-911 Warsaw

PORTUGAL
Estado Maior da Força Aérea
SDFA - Centro de Documentação
Alfragide
P-2720 Amadora

REPUBLIQUE TCHEQUE
VTÚL a PVO Praha /
Air Force Research Institute Prague
Národní informační středisko obranného výzkumu (NISČR)
Mladoboleslavská ul., 197 06 Praha 9

ROYAUME-UNI
Defence Research Information Centre
Kentigern House
65 Brown Street
Glasgow G2 8EX

TURQUIE
Millî Savunma Başkanliği (MSB)
ARGE Dairesi Başkanliği (MSB)
06650 Bakanliklar - Ankara

AGENCES DE VENTE

NASA Center for AeroSpace Information (CASI)
Parkway Center
7121 Standard Drive
Hanover, MD 21076-1320
Etats-Unis

The British Library Document Supply Centre
Boston Spa, Wetherby
West Yorkshire LS23 7BQ
Royaume-Uni

Canada Institute for Scientific and Technical Information (CISTI)
National Research Council
Document Delivery
Montreal Road, Building M-55
Ottawa K1A 0S2
Canada

Les demandes de documents RTO ou AGARD doivent comporter la dénomination "RTO" ou "AGARD" selon le cas, suivie du numéro de série (par exemple AGARD-AG-315). Des informations analogues, telles que le titre et la date de publication sont souhaitables. Des références bibliographiques complètes ainsi que des résumés des publications RTO et AGARD figurent dans les journaux suivants:

Scientific and Technical Aerospace Reports (STAR)
STAR peut être consulté en ligne au localisateur de ressources uniformes (URL) suivant:
http://www.sti.nasa.gov/Pubs/star/Star.html
STAR est édité par CASI dans le cadre du programme NASA d'information scientifique et technique (STI)
STI Program Office, MS 157A
NASA Langley Research Center
Hampton, Virginia 23681-0001
Etats-Unis

Government Reports Announcements & Index (GRA&I)
publié par le National Technical Information Service
Springfield
Virginia 2216
Etats-Unis
(accessible également en mode interactif dans la base de données bibliographiques en ligne du NTIS, et sur CD-ROM)

Imprimé par le Groupe Communication Canada Inc.
(membre de la Corporation St-Joseph)
45, boul. Sacré-Cœur, Hull (Québec), Canada K1A 0S7

NORTH ATLANTIC TREATY ORGANIZATION

RESEARCH AND TECHNOLOGY ORGANIZATION
BP 25 • 7 RUE ANCELLE
F-92201 NEUILLY-SUR-SEINE CEDEX • FRANCE
Telefax 0(1)55.61.22.99 • E-mail mailbox@rta.nato.int

DISTRIBUTION OF UNCLASSIFIED RTO PUBLICATIONS

NATO's Research and Technology Organization (RTO) holds limited quantities of some of its recent publications and those of the former AGARD (Advisory Group for Aerospace Research & Development of NATO), and these may be available for purchase in hard copy form. For more information, write or send a telefax to the address given above. **Please do not telephone.**

Further copies are sometimes available from the National Distribution Centres listed below. If you wish to receive all RTO publications, or just those relating to one or more specific RTO Panels, they may be willing to include you (or your organisation) in their distribution.

RTO and AGARD publications may be purchased from the Sales Agencies listed below, in photocopy or microfiche form. Original copies of some publications may be available from CASI.

NATIONAL DISTRIBUTION CENTRES

BELGIUM
Coordinateur RTO - VSL/RTO
Etat-Major de la Force Aérienne
Quartier Reine Elisabeth
Rue d'Evère, B-1140 Bruxelles

CANADA
Director Research & Development
Communications & Information
Management - DRDCIM 3
Dept of National Defence
Ottawa, Ontario K1A 0K2

CZECH REPUBLIC
VTÚL a PVO Praha /
Air Force Research Institute Prague
Národní informační středisko
obranného výzkumu (NISČR)
Mladoboleslavská ul., 197 06 Praha 9

DENMARK
Danish Defence Research
Establishment
Ryvangs Allé 1, P.O. Box 2715
DK-2100 Copenhagen Ø

FRANCE
O.N.E.R.A. (ISP)
29 Avenue de la Division Leclerc
BP 72, 92322 Châtillon Cedex

GERMANY
Fachinformationszentrum Karlsruhe
D-76344 Eggenstein-Leopoldshafen 2

GREECE
Hellenic Air Force
Air War College
Scientific and Technical Library
Dekelia Air Force Base
Dekelia, Athens TGA 1010

HUNGARY
Department for Scientific Analysis
Institute of Military Technology
Ministry of Defence
H-1525 Budapest P O Box 26

ICELAND
Director of Aviation
c/o Flugrad
Reykjavik

ITALY
Centro documentazione
tecnico-scientifica della Difesa
Via Marsala 104
00185 Roma

LUXEMBOURG
See Belgium

NETHERLANDS
NDRCC
DGM/DWOO
P.O. Box 20701
2500 ES Den Haag

NORWAY
Norwegian Defence Research
Establishment
Attn: Biblioteket
P.O. Box 25
NO-2007 Kjeller

POLAND
Chief of International Cooperation
Division
Research & Development
Department
218 Niepodleglosci Av.
00-911 Warsaw

PORTUGAL
Estado Maior da Força Aérea
SDFA - Centro de Documentação
Alfragide
P-2720 Amadora

SPAIN
INTA (RTO/AGARD Publications)
Carretera de Torrejón a Ajalvir, Pk.4
28850 Torrejón de Ardoz - Madrid

TURKEY
Millî Savunma Başkanliği (MSB)
ARGE Dairesi Başkanliği (MSB)
06650 Bakanliklar - Ankara

UNITED KINGDOM
Defence Research Information
Centre
Kentigern House
65 Brown Street
Glasgow G2 8EX

UNITED STATES
NASA Center for AeroSpace
Information (CASI)
Parkway Center
7121 Standard Drive
Hanover, MD 21076-1320

SALES AGENCIES

NASA Center for AeroSpace Information (CASI)
Parkway Center
7121 Standard Drive
Hanover, MD 21076-1320
United States

The British Library Document Supply Centre
Boston Spa, Wetherby
West Yorkshire LS23 7BQ
United Kingdom

Canada Institute for Scientific and Technical Information (CISTI)
National Research Council
Document Delivery
Montreal Road, Building M-55
Ottawa K1A 0S2
Canada

Requests for RTO or AGARD documents should include the word 'RTO' or 'AGARD', as appropriate, followed by the serial number (for example AGARD-AG-315). Collateral information such as title and publication date is desirable. Full bibliographical references and abstracts of RTO and AGARD publications are given in the following journals:

Scientific and Technical Aerospace Reports (STAR)
STAR is available on-line at the following uniform resource locator:
http://www.sti.nasa.gov/Pubs/star/Star.html
STAR is published by CASI for the NASA Scientific and Technical Information (STI) Program
STI Program Office, MS 157A
NASA Langley Research Center
Hampton, Virginia 23681-0001
United States

Government Reports Announcements & Index (GRA&I)
published by the National Technical Information Service
Springfield
Virginia 22161
United States
(also available online in the NTIS Bibliographic Database or on CD-ROM)

Printed by Canada Communication Group Inc.
(A St. Joseph Corporation Company)
45 Sacré-Cœur Blvd., Hull (Québec), Canada K1A 0S7

ISBN 92-837-1017-7